NEAR-FAULT FORWARD-DIRECTIVITY ASPECTS OF STRONG GROUND MOTIONS IN THE 2010-11 CANTERBURY EARTHQUAKES

A THESIS
SUBMITTED TO THE UNIVERSITY OF CANTERBURY
IN PARTIAL FULFILMENT OF THE REQUIREMENTS
FOR THE DEGREE OF
MASTER OF ENGINEERING

Department of Civil and Natural Resources Engineering
College of Engineering
University of Canterbury
Christchurch, New Zealand

Varun Anil Joshi
November 2013

Abstract

The purpose of this thesis is to conduct a detailed examination of the forward-directivity characteristics of near-fault ground motions produced in the 2010-11 Canterbury earthquakes, including evaluating the efficacy of several existing empirical models which form the basis of frameworks for considering directivity in seismic hazard assessment.

A wavelet-based pulse classification algorithm developed by Baker (2007) is firstly used to identify and characterise ground motions which demonstrate evidence of forward-directivity effects from significant events in the Canterbury earthquake sequence. The algorithm fails to classify a large number of ground motions which clearly exhibit an early-arriving directivity pulse due to: (i) incorrect pulse extraction resulting from the presence of pulse-like features caused by other physical phenomena; and (ii) inadequacy of the pulse indicator score used to carry out binary pulse-like/non-pulse-like classification. An alternative 'manual' approach is proposed to ensure 'correct' pulse extraction and the classification process is also guided by examination of the horizontal velocity trajectory plots and source-to-site geometry. Based on the above analysis, 59 pulse-like ground motions are identified from the Canterbury earthquakes , which in the author's opinion, are caused by forward-directivity effects. The pulses are also characterised in terms of their period and amplitude. A revised version of the B07 algorithm developed by Shahi (2013) is also subsequently utilised but without observing any notable improvement in the pulse classification results.

A series of three chapters are dedicated to assess the predictive capabilities of empirical models to predict the: (i) probability of pulse occurrence; (ii) response spectrum amplification caused by the directivity pulse; (iii) period and amplitude (peak ground velocity, PGV) of the directivity pulse using observations from four significant events in the Canterbury earthquakes. Based on the results of logistic regression analysis, it is found that the pulse probability model of Shahi (2013) provides the most improved predictions in comparison to its predecessors. Pulse probability contour maps are developed to scrutinise observations of pulses/non-pulses with predicted probabilities.

A direct comparison of the observed and predicted directivity amplification of acceleration response spectra reveals the inadequacy of broadband directivity models, which form the basis of the near-fault factor in the New Zealand loadings standard, NZS1170.5:2004. In contrast, a recently developed narrowband model by Shahi & Baker (2011) provides significantly improved predictions by amplifying the response spectra within a small range of periods. The significant positive bias demonstrated by the residuals associated with all models at longer vibration periods (in the M_w7.1 Darfield and M_w6.2 Christchurch earthquakes) is likely due to the influence of basin-induced surface waves and non-linear soil response.

Empirical models for the pulse period notably under-predict observations from the Darfield and Christchurch earthquakes, inferred as being a result of both the effect of nonlinear site response and influence of the Canterbury basin. In contrast, observed pulse periods from the smaller magnitude June (M_w6.0) and December (M_w5.9) 2011 earthquakes are in good agreement with predictions. Models for the pulse amplitude generally provide accurate estimates of the observations at source-to-site distances between 1 km and 10 km. At longer distances, observed PGVs are significantly under-predicted due to their slower apparent attenuation. Mixed-effects regression is employed to develop revised models for both parameters using the latest NGA-West2 pulse-like ground motion database. A pulse period relationship which accounts for the effect of faulting mechanism using rake angle as a continuous predictor variable is developed. The use of a larger database in model development, however does not result in improved predictions of pulse period for the Darfield and Christchurch earthquakes. In contrast, the revised model for PGV provides a more appropriate attenuation of the pulse amplitude with distance, and does not exhibit the bias associated with previous models.

Finally, the effects of near-fault directivity are explicitly included in NZ-specific probabilistic seismic hazard analysis (PSHA) using the narrowband directivity model of Shahi & Baker (2011). Seismic hazard analyses are conducted with and without considering directivity for typical sites in Christchurch and Otira. The inadequacy of the near-fault factor in the NZS1170.5: 2004 is apparent based on a comparison with the directivity amplification obtained from PSHA.

Acknowledgements

I would firstly like to thank my supervisor, Dr. Brendon Bradley for providing me with continuous support and excellent guidance from the beginning of my journey as a postgraduate student till the very end. I feel privileged to have worked with you and more importantly, you have had an extremely positive impact in my personal and professional development over the last two years.

I would also like to thank Dr. Mark Davidson for encouraging me to undertake postgraduate study during the final year of my Bachelor's degree. I can safely say that I do not regret the decision and have thoroughly enjoyed my six years at the University of Canterbury.

This thesis would not have been possible without the significant financial support from the University of Canterbury, New Zealand Earthquake Commission and Natural Hazards Research Platform. I am extremely grateful to all three institutions for their contribution in allowing this research to be realised.

I would like to thank the Civil and Mathematics departments at the University of Canterbury for providing me with several teaching assistant roles over the past four years. The experience I have gained from tutoring has been invaluable and has been particularly useful in improving my communication skills. I am also extremely appreciative of the administrative support provided by Ms. Louise Barton, Ms. Elizabeth Ackermann and Mr. Alan Jolliffe. The seismic hazard analyses in this research would have not been possible without the computational resources provided by the Mathematics department and I wish to thank Mr. Steve Gourdie for making these resources available at short notice.

I wish to also thank Dr. Shrey Shahi of Virginia Tech and Dr. Paul Somerville of URS Corporation for their insightful comments and prompt response on several issues related to this research.

I have shared some fond memories with my friends and colleagues at the University of Canterbury and in particular, a special thanks goes to Adi Ramakanth, Sam McHattie,

James O'Neill, Andrew Baird, Tobias Smith, Dennis Pau, Maxim Millen, Zeinab Chegini, Gareth Morris, Lake Carter, Chris Watson, Matthew MacDonald, Harry Johnston, Daniel Moroder and Francesco Sarti. I will surely miss our daily coffee trips to Cafe 101 and light-hearted interactions. I wish to thank my office mates for creating a great working environment including Kishore Gopalakrishnan, Fazly Patath, Calvin Lim and more recently, Andy Pan, Deepak Chouhan, Gautham Praburam and Reza Esfandiari. More importantly, I have thoroughly enjoyed your company during my time on the third floor. I would also like to thank my past and present flatmates for making the past five years of flatting a truly enjoyable experience.

I am particularly grateful to my aunt, Dr. Vijaya Dharan and uncle, Ravi Auradkar for having a significant role in my formative years and for their constant encouragement in pursuing my goals.

Finally, I would like to thank my parents, Sandhya and Anil Joshi for their unwavering support and love. They have provided me with all possible opportunities over the past 24 years and I would like to dedicate this thesis to them.

Varun Anil Joshi

21 November 2013

Table of Contents

List of Figures

List of Tables

1 Introduction

1.1 Motivation

Forward-directivity effects produce pulse-like ground motions which can potentially place larger demands on structures located in the near-fault region than so-called 'ordinary' or 'far-fault' ground motions. The tremendous damage potential of this ground motion phenomenon has been observed in major worldwide earthquakes such as the 1971 San Fernando, 1994 Northridge and 1995 Kobe earthquakes. Until recently, the study of directivity effects in New Zealand has been restricted by a lack of near-fault ground motions resulting from moderate-to-large magnitude earthquakes. The 2010-11 Canterbury earthquake sequence produced severe ground motions which were well-recorded by a dense array of high quality instrumentation in Christchurch and the surrounding Canterbury Plains. Recent studies (e.g. Bradley & Cubrinovski, 2011; Bradley, 2012) have identified clear evidence of significant forward-directivity effects in near-source ground motions from the 4 September 2010 M_w7.1 Darfield and 22 February 2011 M_w6.2 Christchurch earthquakes.

A rigorous examination of the ground motions from the Canterbury earthquakes is required in order to appropriately identify forward-directivity effects and their implications for seismic design and assessment. Such an examination forms the initial focus of the present study. In addition to the events mentioned above, ground motions from smaller (yet significant) magnitude earthquakes which occurred on 13 June 2011 (M_w5.3 and 6.0) and 23 December 2011 (M_w5.8 and 5.9) are also considered. Empirical ground motion modelling of forward-directivity effects requires: (i) pulse probability models; (ii) models to predict the period and amplitude of the directivity pulse; and (iii) models which account for the response spectrum amplification caused by the directivity pulse. Observations from the Canterbury earthquakes can be used to scrutinise the predictive capabilities of these models, which are typically calibrated using data from overseas earthquakes and therefore, may not entirely reflect source, path and site effects which are important in NZ. The results of this empirical analysis will allow the explicit inclusion of near-fault directivity in NZ-specific seismic

hazard analysis. In doing so, appropriate comparisons can be made with current seismic design guidelines in the NZ seismic design standard, NZS1170.5:2004 (Standards New Zealand, 2004), to account for directivity effects.

1.2 Objectives

The key research objectives of this thesis are as follows:

1. Document the observations of forward-directivity in strong ground motions recorded during the 2010-11 Canterbury earthquakes and quantify their salient characteristics.
2. Examine the adequacy of several existing empirical models which predict the probability of directivity pulse occurrence and the resulting amplification of pseudo-acceleration response spectra using observations from the Canterbury earthquakes.
3. Examine the adequacy of several empirical models, including those developed as part of this study, which predict the directivity pulse period and amplitude, using observations from the Canterbury earthquakes.
4. Explicitly implement and quantify the effect of near-fault directivity in New Zealand-specific probabilistic seismic hazard analysis.

1.3 Organisation

The thesis is organised into chapters as follows:

Chapter 2 presents the findings of a detailed literature review on several relevant aspects related to near-fault ground motions with a strong focus on the directivity phenomenon.

Chapter 3 illustrates the identification of observed forward-directivity effects in the 2010-11 Canterbury earthquakes using two wavelet-based pulse classification algorithms. More specifically, the considered events include: (i) 4 September 2010 M_w 7.1 Darfield earthquake; (ii) 22 February 2011 M_w 6.2 Christchurch earthquake; (iii) 13 June 2011 M_w 5.3 and M_w 6.0 earthquakes; and (iv) 23 December 2011 M_w 5.8 and M_w 5.9 earthquakes. Discussion of potential issues associated with these stand-alone automated approaches is carried out using specific examples from the Darfield and Christchurch earthquakes. In an

effort to overcome these issues, alternative approaches are proposed and used to 'correctly' identify forward-directivity characteristics of recorded ground motions in the above events. Furthermore, due to the complexity of the multiple fault rupture process in several events, the pulse orientations of the observed forward-directivity ground motions are also examined.

Chapter 4 initially provides a review of the empirical models developed in previous research to quantify the probability of pulse occurrence for the near-fault region. Subsequently, observations from four events in the Canterbury earthquake sequence are used to assess these models in term of their bias (accuracy) and precision (variability). This assessment procedure allows the most suitable model to be selected for use in Chapters 5 and 7. Furthermore, pulse probability contour maps are developed for the four events and compared to observations of pulse-like and non-pulse-like ground motions.

Chapter 5 presents the results associated with the assessment of several models which aim to capture the amplification of pseudo-acceleration response spectra due to forward-directivity. Discussions on the adequacy of these models is provided and the reasons for the observed bias, if any, are presented using observations from the Canterbury earthquakes.

Chapter 6 consists an assessment of several existing empirical prediction equations for the amplitude and period of the directivity pulse using observations from the Canterbury earthquakes. In an effort to determine whether improved predictions of these two metrics can be obtained using a recent dataset of pulse-like ground motions (known as the NGA-West2 database), empirical models are developed for the two parameters and their predictions are compared to the observations. Statistical analyses are carried out to identify trends in the bias and variability exhibited by the models.

Chapter 7 firstly discusses the incorporation of a recently developed narrowband directivity model by Shahi & Baker (2011) in the Bradley (2010) ground motion prediction equation. This is followed by example applications of the adopted approach to account for near-fault directivity effects in NZ-specific PSHA. The resulting directivity amplification is compared with the near-fault factor prescribed in the NZS1170.5:2004 (Standards New Zealand, 2004).

Chapter 8 outlines the main conclusions drawn from the present study.

1.4 References

Bradley, B. A. (2012). Strong ground motion characteristics observed in the 4 September 2010 Darfield, New Zealand earthquake. *Soil Dynamics and Earthquake Engineering*, **42**, 32–46. doi:10.1016/j.soildyn.2012.06.004

Bradley, B. A., & Cubrinovski, M. (2011). Near-source Strong Ground Motions Observed in the 22 February 2011 Christchurch Earthquake. *Seismological Research Letters*, **82**(6):853–865. doi:10.1785/gssrl.82.6.853

Bradley, Brendon A. (2010). *NZ-Specific Pseudo-Spectral Acceleration Ground Motion Prediction Equations Based on Foreign Models* (Research Report No. 2010-03) (p. 316). Department of Civil and Natural Resources, University of Canterbury.

Shahi, S. K., & Baker, J. W. (2011). An empirically calibrated framework for including the effects of near-fault directivity in probabilistic seismic hazard analysis. *Bulletin of the Seismological Society of America*, **101**(2):742–755. doi:10.1785/0120100090

Standards New Zealand. (2004). *NZS1170.5:2004, Structural Design Actions, Part 5: Earthquake actions- New Zealand*. Wellington, New Zealand.

2 Literature Review

2.1 Overview

In the past, a significant amount of research has been conducted in the seismological and earthquake engineering research communities on various aspects of near-fault ground motions. The purpose of this literature review is to provide a concise overview of the relevant topics associated with near-fault ground motions considered in this study and is not exhaustive by any means. In order to familiarise the reader with the near-fault forward-directivity phenomenon, a summary of the characteristics and importance of strong ground motions in the near-fault region is initially provided. This is followed by a concise description of the salient aspects of the well-recorded near-fault ground motions during the 2010-11 Canterbury earthquakes. Focus then shifts to the available approaches for the identification of pulse-like ground motions; empirical models which can be used to account for the effects of directivity on response spectra; and models which predict the peak velocity and period of the directivity pulse. Finally, available approaches for the inclusion of the near-fault directivity phenomenon in probabilistic seismic hazard analyses and its consideration in seismic design guidelines are discussed.

2.2 Characteristics and importance of near-fault ground motions observed in previous earthquakes

The so-called “near-fault region” is typically assumed to be bound by a distance of approximately 20km from the causative fault (Bray & Rodriguez-Marek, 2004). Within this region, observed strong ground motions often exhibit the effects of forward-directivity and fling step. Forward-directivity occurs due to the alignment of the rupture front, direction of slip, and the source-to-site direction (Bradley, 2012a). The occurrence of the forward-directivity phenomenon is highlighted by the presence of a large long-period pulse in the velocity time series, which occurs at the beginning of the record and represents the cumulative effect of almost all of the seismic radiation from the fault (Somerville et al., 1997). This pulse is typically observed in the fault-normal component of the velocity time series due to the constructive interference of shear waves (S-waves) propagating towards a site. On the other hand, fling step refers to the permanent ground displacement at a particular site resulting from permanent tectonic movement (Bray & Rodriguez-Marek, 2004). It is commonly observed as a discrete step in the displacement time-series that occurs parallel to the strike of the fault in strike-slip events, and in the dip direction for dip-slip events. The focus of the present study is on the observed forward-directivity effects in the Canterbury earthquakes, and therefore the remainder of the literature review will focus on this particular characteristic of near-fault ground motions.

In seismological literature, the term 'directivity' is used exclusively for rupture propagation effects. However, in engineering literature, this term refers to the azimuthally-varying amplitude, frequency content and duration of strong ground motions recorded in the near-fault region. As noted by Somerville et al. (1997), the necessary conditions for generating forward rupture directivity effects are readily met in strike-slip faulting, where the rupture propagates horizontally, either unilaterally or bilaterally along strike, and the fault slip direction is oriented horizontally in the direction along the fault strike. Hence, forward-directivity conditions are typically largest near the end of the fault when the rupture front is moving towards the site in strike-slip events (Rodriguez-Marek, 2000). Similarly, the alignment of the rupture and slip direction up-dip on the fault plane produces rupture directivity effects at sites located around the surface exposure of the fault (Somerville, 2003). It is pertinent to note that forward-directivity effects are not observed at all near-fault sites.

Firstly, if the rupture propagates locally away from the site, backward directivity effects are observed in the form of low amplitude and long duration ground motion. Secondly, if the rupture occurs towards a site located at the end of a fault and the slip is also concentrated near the end of the fault, forward-directivity effects may not exist although the conditions for observing this phenomenon are met (Rodriguez-Marek, 2000).

The directivity phenomenon has long been known and studied by a number of theoretical geophysicists, prior to the confirmation of its existence by means of recorded strong ground motion records (Rowshandel, 2010). For example, Ben-Menahem (1961, 1962) carried out two studies on the effects of surface (Rayleigh and Love) and body (P and S) waves, respectively. One of the main findings associated with these studies was that the amount of energy radiated in the direction of the rupture can be significantly larger than the amount radiated in the opposite direction, thereby implicitly alluding to the directivity phenomenon.

As mentioned previously, the effects of forward-directivity in near-fault ground motions are evident from the presence of well-defined velocity pulses. The first identification of a recorded fault-normal velocity pulse was the Station 2 accelerogram recorded during the 1966 Parkfield (California) earthquake (Housner & Trifunac, 1967). However, it was not until the 1971 San Fernando (California) earthquake, during which the well-known Pacoima Dam record exhibited a large amplitude velocity pulse in the fault-normal component, that earthquake engineers began to consider the implications of such velocity pulses on structural response. Figure 2.1 shows the fault-normal (strike-normal) component of the Pacoima Dam velocity time-series, as well as the fault-parallel (strike-parallel) component to provide a comparison of the distinct waveforms and peak ground velocities observed in the two directions.

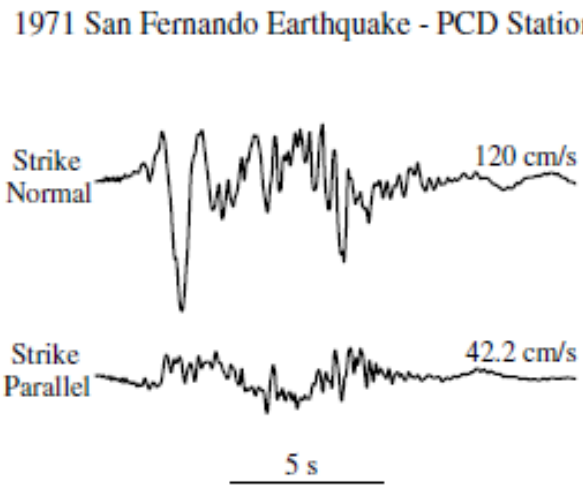

Figure 2.1: Fault-normal and fault-parallel components of the velocity time-series observed at Pacoima Dam during the 1971 San Fernando earthquake (after Mavroeidis & Papageorgiou, 2003).

Following an extensive study of heavy structural damage sustained by the Olive View hospital during the San Fernando earthquake, Bertero et al. (1978) attributed the sustained damage to "only a few large displacement excursions" caused by the low-frequency velocity pulse as opposed to repeated small amplitude cycles caused by the high frequency (low period) component of the ground motion. Figure 2.2 provides visual evidence of the destructive potential associated with forward rupture directivity effects using the Olive View Hospital[1] case as an example.

[1] In addition to the severe ductility demand imposed by the strong velocity pulse on the first floor columns, the sustained damage was also attributed to inadequate ductility capacity due to insufficient transverse reinforcement.

Figure 2.2: Observed damage at Olive View Hospital following the 1971 San Fernando earthquake (after Bertero & Godden, 1997).

Anderson and Bertero (1987) subsequently investigated the effects of forward-directivity ground motions from the San Fernando earthquake on flexible steel frame structures, and concluded that nonlinear structural response is particularly sensitive to the pulse duration relative to the fundamental period of the structure. Due to the presence of the velocity pulse, they also suggested that the acceleration response spectrum must be amplified in the long-period region ($1s \leq T \leq 3s$) for the design of structures located in near-fault regions. For shorter period structures, these authors recommended that the ductility requirement must be increased in the design codes due to the increase in the ratio of the pulse duration to the period of the structure.

Unfortunately, the implications of the above findings were not widely realised by the earthquake and structural engineering research communities until the 1994 Northridge (USA) and 1995 Kobe (Japan) earthquakes, which occurred in populated urban areas and caused tremendous losses due to structural damage. As a consequence, several researchers decided to concentrate their efforts on investigating the effects of near-fault ground motions on the performance of conventionally designed structures by means of response history analyses (e.g. Hall et al., 1995; Chopra & Chintanapakdee, 2001; Alavi & Krawinkler, 2004; and more recently, Sehhati et al. 2011). The results from these studies indicate that the induced lateral displacement and shear forces under forward-directivity ground motions are much higher

than those under 'ordinary' ground motions which do not exhibit such effects. More importantly, these findings hold true principally because the peak ground velocities (PGV) associated with the forward-directivity set of ground motions were significantly larger than those observed in the 'ordinary' ground motion set, for similar values of peak ground acceleration (PGA) values. Hence, results from the above studies clearly highlight the importance of PGV as an effective intensity measure of near-fault ground motions and its contribution to the significant non-linear behaviour exhibited by structures subjected to these ground motions.

2.3 The 2010-2011 Canterbury earthquakes

The M_w7.1 Darfield (4 September 2010) and M_w6.2 Christchurch (22 February 2011) earthquakes occurred on previously unmapped faults and resulted in strong ground motions in Christchurch and the surrounding Canterbury Plains. These ground motions caused partial or total collapse of several commercial, residential and industrial structures in Christchurch as well as significant damage to lifelines due to severe liquefaction of surficial soils (Bradley, 2012b). In general, there has been a paucity of strong ground motion recordings at small source-to-site distances worldwide, primarily due to the infrequent nature of moderate-to-large earthquakes and the lack of instrumentation in place to record the resulting strong ground motions. However, for New Zealand (NZ) in particular, the strong ground motions resulting from the two main events in the Canterbury region and subsequent significant earthquakes (collectively referred to as the 'Canterbury earthquakes' hereafter) have been well recorded. More importantly, the dense array of strong motion instrumentation in Christchurch and the Canterbury Plains has provided a large number of strong ground motion recordings in the near-fault region. This is illustrated in Figures 2.3 and 2.4, which show the observed fault-normal horizontal acceleration time-series at numerous sites in the Christchurch region during the Darfield and Christchurch earthquakes, respectively. Although the main focus of the present study is on directivity effects, it is important to gain a holistic understanding of the physical reasons for the observed ground motions. Therefore, the following sub-sections provide an overview of the salient features of the near-fault ground motions recorded during both events, based on a thorough review of important studies by several researchers including Bradley (2012c) and Bradley & Cubrinovski (2011), among others.

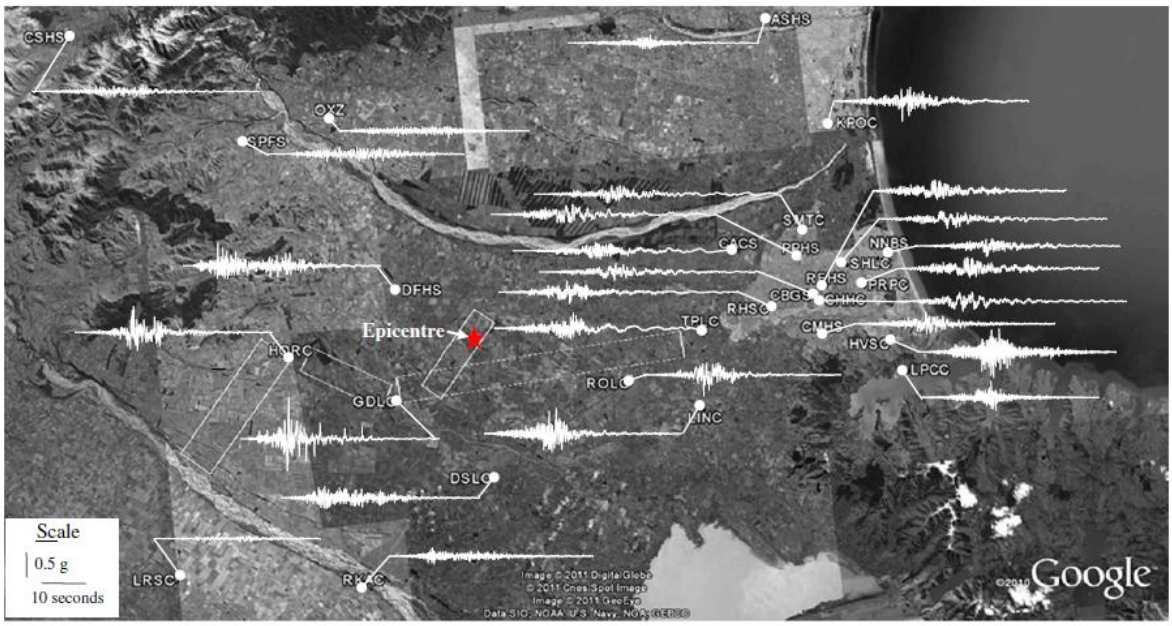

Figure 2.3: Observed fault-normal horizontal acceleration time-series at various locations in the Christchurch region during the M_w7.1 Darfield earthquake (after Bradley, 2012a).

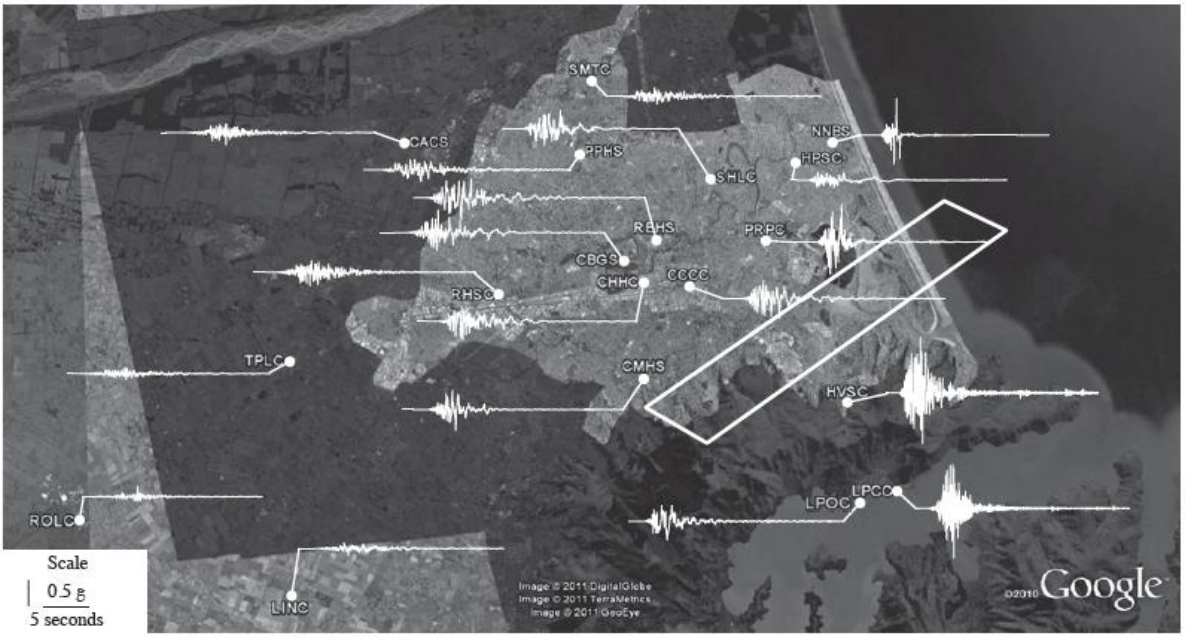

Figure 2.4: Observed fault-normal horizontal acceleration time-series at various locations in the Christchurch region during the M_w6.2 Christchurch earthquake (after Bradley & Cubrinovski, 2011).

2.3.1 Rupture complexity

The complexity of the rupture process during the M_w7.1 Darfield earthquake has been highlighted by the differences in estimates of the focal mechanism of the earthquake. While the first motion and regional moment tensor focal mechanisms were in good agreement, and showed reverse faulting (Gledhill et al., 2011), teleseismic moment tensor solutions indicated

a strike-slip source mechanism. The latter being consistent with the surface rupture trace of the predominantly right-lateral strike-slip Greendale fault. Based on a comparison of the teleseismic and regional moment tensor solutions, Beavan et al. (2010) suggested that the rupture was initiated by means of a reverse-faulting mechanism, with a majority of energy being released by means of strike-slip faulting.

The understanding of the complex rupture process associated with the Darfield earthquake was also influenced by the uncertainty in finite-fault modelling. An initial finite-fault model (FFM) proposed by Beavan et al. (2010) included six fault planes which provided a good representation of the observed displacement field. Based on the inferred slip distribution, it was found that the largest asperity (with an inferred slip of up to 5 m) occurred on the central section of the approximately 29.5 km east-west striking Greendale fault segment. The FFM subsequently developed by Holden et al. (2011) included four fault planes as shown in Figure 2.3, and was based on a simplified version of the Beavan et al. (2010) model. It can be observed that the central and eastern segments of the Greendale fault discussed in Beavan et al. (2010) are represented by a single fault plane with a 30 km along-strike dimension. The western segment of the Greendale fault, Charring Cross (north of the Greendale fault) and Hororata blind thrust faults (west of the Greendale fault) are represented by segments with along-strike dimensions of 10 km, 10 km, and 15 km, respectively. This model also indicates that the rupture process began on the Charring Cross blind fault followed by bilateral rupture of the Greendale fault, and ended with the rupture of the Hororata thrust fault. A more recent FFM developed by Beavan et al. (2012) shown in Figure 2.6 includes seven fault planes to more accurately account for the total moment release during the earthquake. The model also differs from its predecessors because the modelled fault plane follows the surface rupture trace (not shown in Figure 2.6) of the central Greendale fault segment to obtain a better fit to the GPS (global positioning system) displacement data.

An appreciation of the source complexity during the Darfield earthquake can also be gained by examining the recorded strong ground motions. For example, the ground motion recorded at Darfield High School (DFHS) in Figure 2.5 clearly illustrates the arrival of separate energy sources. In this case, the first energy is interpreted by Bradley (2012c) as arriving from the initiating Charring Cross fault, followed by energy from rupture along the other fault segments.

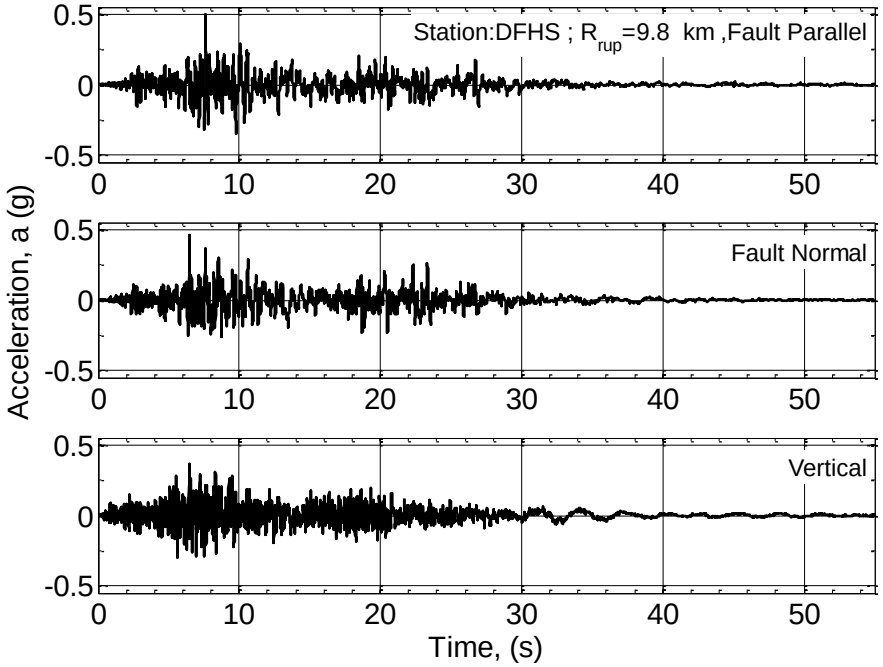

Figure 2.5: Evidence of rupture complexity in the strong ground motion recorded at Darfield High School (DFHS) during the M_w7.1 Darfield earthquake (after Bradley, 2012c).

In addition to the rupture complexity for the Darfield earthquake discussed in the above paragraphs, source complexity was also observed in the M_w 6.2 Christchurch earthquake. According to an initial geodetic FFM developed by Beavan et al. (2011), the M_w6.2 Christchurch earthquake occurred along a previously unrecognised steeply dipping blind fault, as shown in Figure 2.4. The along-strike and down-dip dimensions of this fault plane are 15 km and 8 km, respectively. A mix of reverse-faulting and right lateral strike-slip faulting was inferred from the slip distribution. However, in the same study, Beavan et al. (2011) also found that the large amount of geodetic ground displacement data is significantly better fit by two fault planes. The first plane corresponds to the FFM described above with a region of oblique slip and the second plane is a vertical fault with right-lateral strike-slip located southwest of the first plane. More recently, Beavan et al. (2012) presented an updated geodetic FFM which included three fault planes as shown in Figure 2.6. This model indicates that the Christchurch earthquake was mixed right-lateral and reverse, with a left-stepping offset interrupting an ENE (East North-East)-striking rupture (Beavan et al., 2012). Hence, it is clear that the Christchurch event was also characterised by a complex rupture process with different faulting mechanisms.

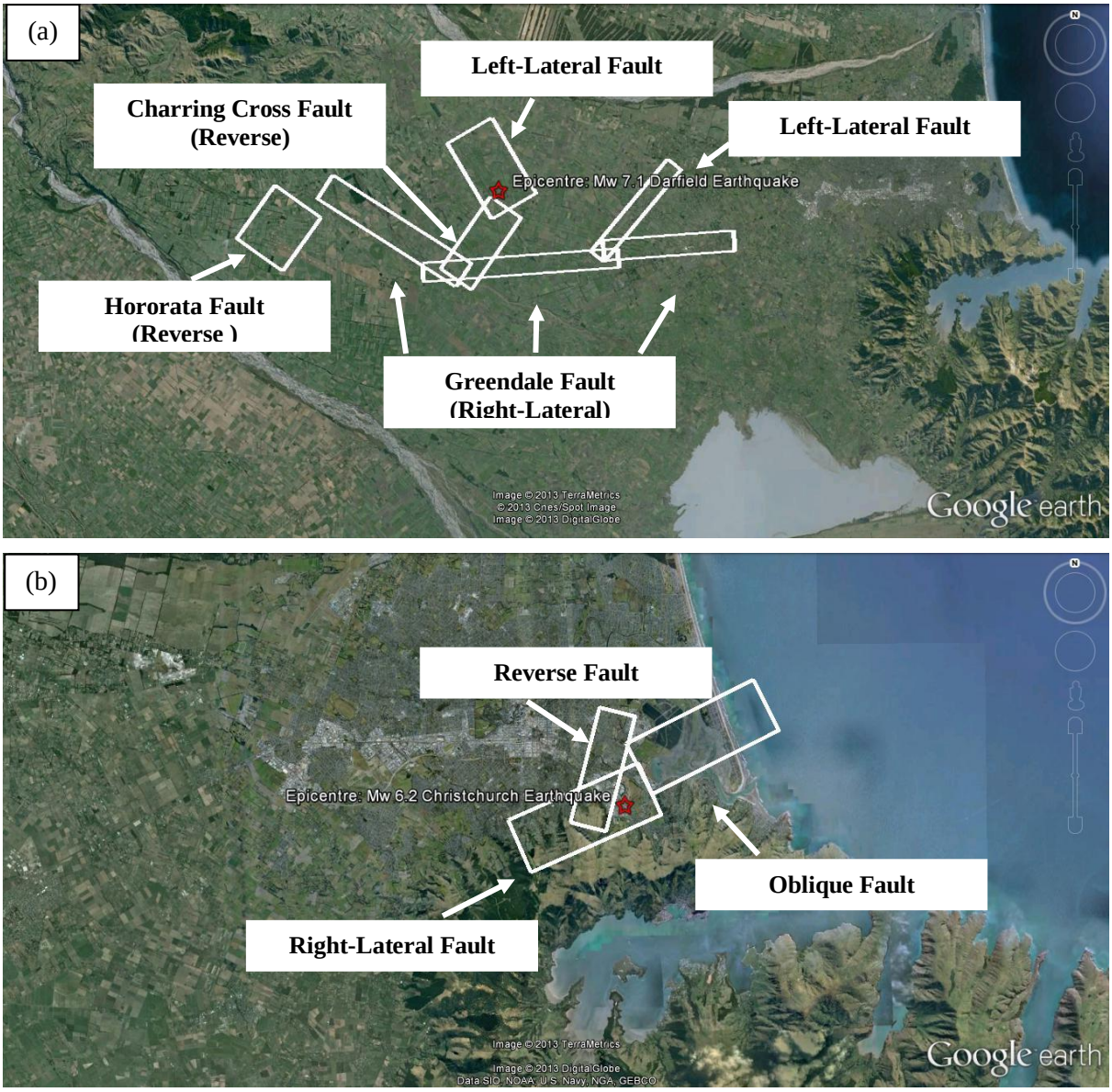

Figure 2.6: Finite fault models developed by Beavan et al. (2012) for: (a) M_w7.1 Darfield earthquake; and (b) M_w6.2 Christchurch earthquake. Note that the red star denotes the location of the epicentre for each event (adapted from Beavan et al. (2012)).

2.3.2 Forward-directivity effects

Bradley (2012c) and Bradley & Cubrinovski (2011) identified the presence of forward-directivity effects in the near-fault ground motions resulting from the Canterbury earthquakes. The phenomenon was significant in the Darfield earthquake, which can be explained by the size of the event (M_w 7.1), strike-slip faulting mechanism and rupture propagation of the central and eastern section of the Greendale fault toward Christchurch (Bradley, 2012c; Holden et al., 2011). In contrast, according to Bradley & Cubrinovski (2011), forward-directivity effects from the Christchurch earthquake were only prevalent

over a smaller area in the eastern suburbs of Christchurch due to the misalignment between the direction of slip and inferred direction of rupture propagation on the causative reverse thrust fault. Figure 2.7 illustrates the observed velocity time-series at Rolleston (ROLC) and Pages Road (PRPC) during the Darfield and Christchurch earthquakes, respectively. Evidence of forward-directivity is clearly demonstrated by the pulses (shown in blue) arriving at the beginning of the fault-normal velocity time-series. At both sites, the observed peak ground velocities (PGV) in the fault-normal direction (approximately 108 cm/s and 95 cm/s, respectively) are large in relation to the fault-parallel direction (approximately 67cm/s and 38cm/s, respectively).

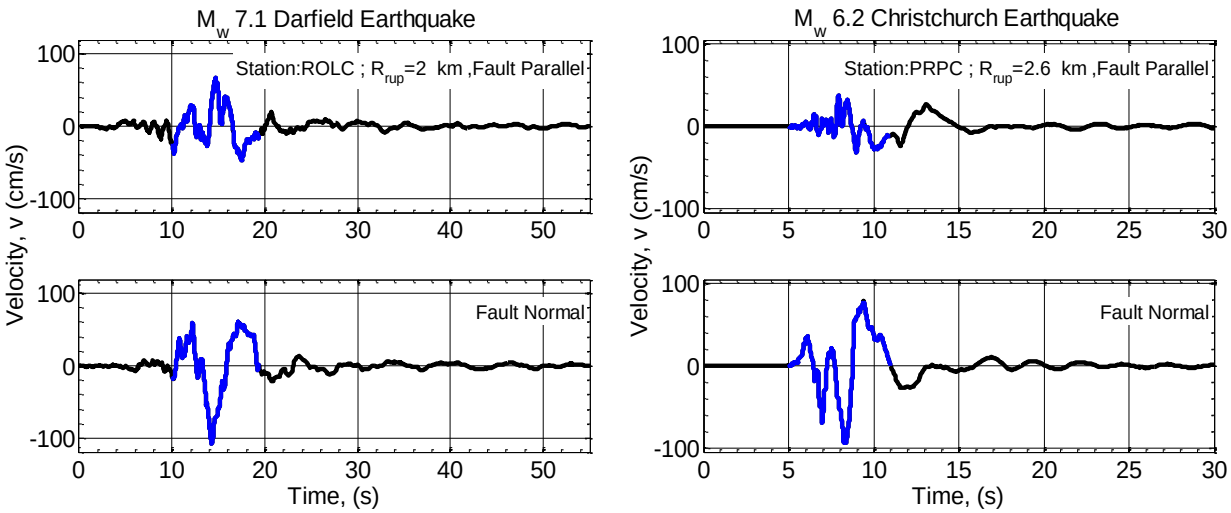

Figure 2.7: Evidence of strong forward-directivity effects in the fault-normal velocity time-series recorded at Rolleston (ROLC) during the M_w7.1 Darfield earthquake (left); and Pages Road (PRPC) during the M_w6.2 Christchurch earthquake (right) (adapted from Bradley, 2012c and Bradley & Cubrinovski, 2011).

2.3.3 Basin-generated surface waves

In addition to strong long period ground motion resulting from forward-directivity effects in the Darfield and Christchurch earthquakes, significant long period ground motion was also observed at several sites during both events due to basin-induced surface wave effects (Bradley, 2012c; Bradley & Cubrinovski, 2011). It is important to note that Christchurch is situated on a sedimentary fan deposit with the volcanic rock of Banks peninsula to the south-east (Brown & Weeber, 1992). This gives rise to the 'waveguide effect', where the large post-critical incidence angles of seismic waves entering the basin-basement rock interface (at shallow incidence angles) causes total internal reflection (Choi, 2005). Hence, the seismic waves are effectively trapped within the surficial soil layers,

thereby resulting in large long period ground motion amplitudes and shaking duration (Bradley & Cubrinovski, 2011). Figure 2.8 illustrates the three-component velocity time-series recorded at Templeton (TPLC) during the Darfield earthquake. It can be observed that the fault-normal component is characterised by an initial forward-directivity pulse followed by several cycles of large amplitude and long period ground motion due to basin-induced surface wave effects (Bradley, 2012c). These effects are also visible in the fault-parallel and vertical components, although to a lesser extent.

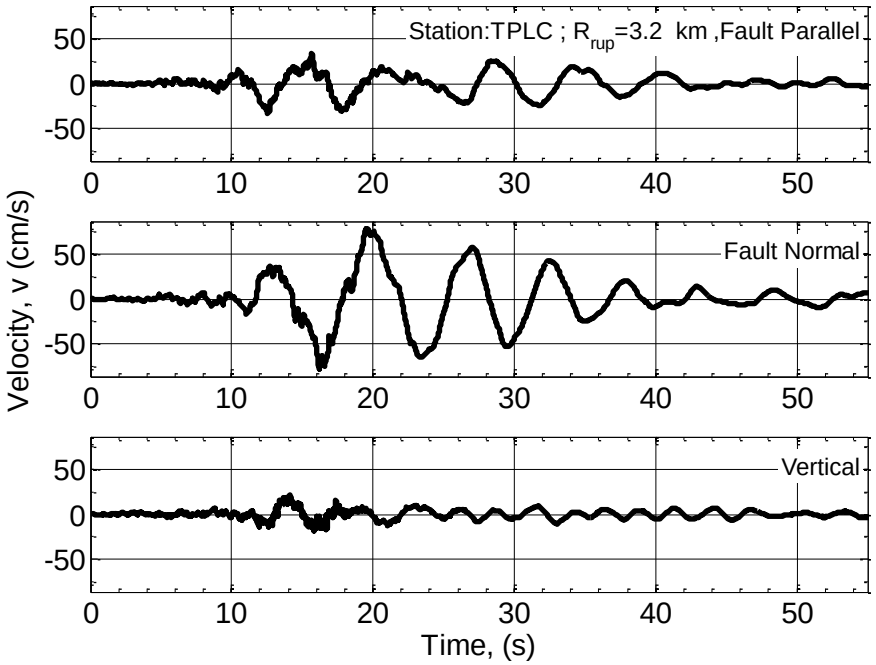

Figure 2.8: Illustration of significant basin-generated surface waves at Templeton (TPLC) during the M_w7.1 Darfield earthquake (after Bradley, 2012c).

2.3.4 Site response effects

Recent studies by Bradley (2012c) and Bradley & Cubrinovski (2011) have highlighted the inferred contribution of nonlinear soil behaviour to the amplification of long period ground motion in the Canterbury earthquakes. In order to provide a clear illustration of nonlinear soil behaviour, Bradley & Cubrinovski (2011) compared the two ground motions recorded at Lyttleton Port (located southeast of the Christchurch central business district as illustrated in Figure 2.4) during the M_w6.2 Christchurch earthquake. One of the ground motions was recorded at a strong motion station (LPCC) located on 'engineering' bedrock, whereas the other ground motion was recorded at a strong motion station (LPOC) located on

a thin layer of colluvium (Bradley & Cubrinovski, 2011). Figure 2.9 illustrates the pseudo-acceleration response spectra of the geometric mean horizontal ground motion component at the two sites. It is evident that the nonlinear response of the surficial soil layer at LPOC results in significant amplification of long period ground motion amplitudes and reduction in the short period ground motion amplitudes. The nonlinear response is characterised by large shear deformation of the near-surface soil layers in the horizontal plane, which consequently leads to a reduction in the shear stiffness and increased hysteretic damping (Bradley & Cubrinovski, 2011). This explains the significant differences between the ground motions observed at the two stations.

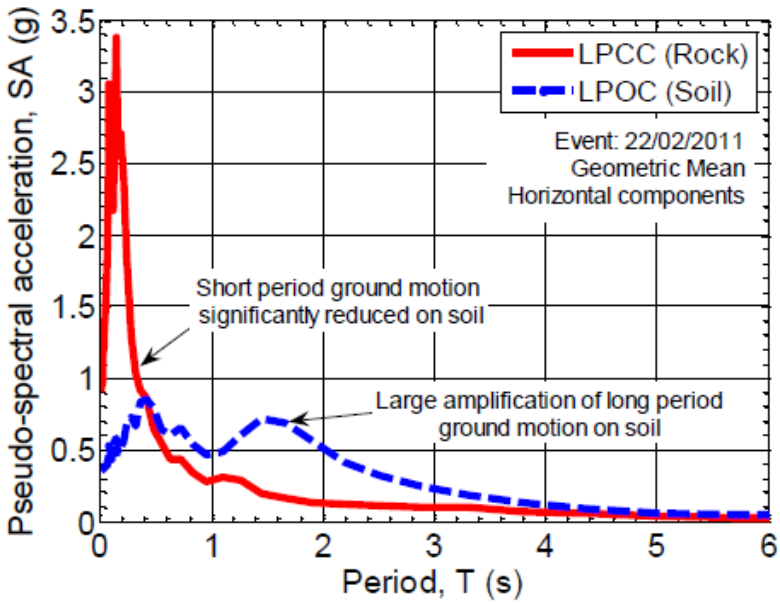

Figure 2.9: Comparison of the geometric mean horizontal component pseudo-acceleration response spectra at Lyttleton Port during the M_w6.2 Christchurch earthquake illustrating the significance of surficial soil response (after Bradley & Cubrinvoski, 2011).

2.3.5 Strong vertical ground motion

In addition to strong ground motion in the two horizontal components at numerous sites in the Canterbury earthquakes, large vertical ground motion amplitudes were also observed, particularly in the M_w6.2 Christchurch earthquake. For example, peak vertical accelerations of 1.88 g and 2.21 g were observed at Pages Road (PRPC) and Heathcote Valley (HVSC), respectively (refer to Figure 2.4 for strong motion station locations). These significant vertical accelerations can be physically explained by: (i) the relatively steep dip angle of the fault plane (using the single-fault FFM of Beavan et al. (2011)) of 69^o, which

results in a large component of slip in the vertical direction, and (ii) the conversion of inclined SV waves to P waves at the sedimentary basin interface for soil sites, which are amplified and refracted toward vertical incidence due to the basin P-wave gradient (Bradley & Cubrinovski, 2011). Figure 2.10a illustrates the observed geometric mean horizontal and vertical pseudo-acceleration response spectra at Pages Road (PRPC), Christchurch Hospital (CHHC) and Riccarton High School (RHSC). The corresponding vertical-to-horizontal (V-to-H) ratios are also shown in Figure 2.10b as a function of vibration period. It can be observed that the largest V-to-H ratios occur at high frequencies with values significantly greater than 1.0. However, the ratios reduce rapidly with increasing source-to-site distance (2.5 km, 3.8 km and 6.5 km for PRPC, CHHC and RHSC, respectively), and also for periods greater than T = 0.1 s (Bradley & Cubrinovski, 2011).

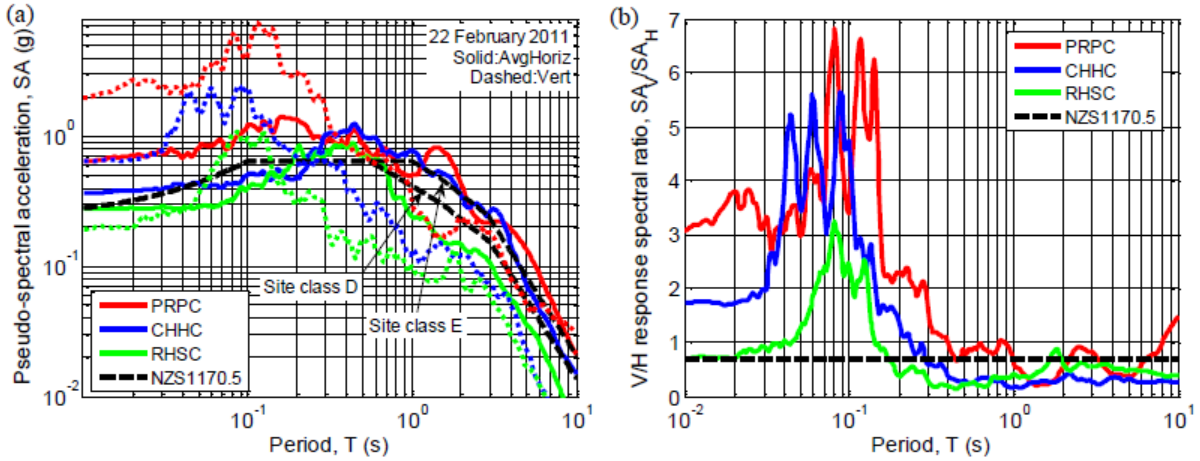

Figure 2.10: (a) Geometric mean horizontal and vertical response spectra observed at several near-fault locations during the M_w6.2 Christchurch earthquake; and (b) the corresponding vertical-to-horizontal spectral ratios. (after Bradley & Cubrinvoski, 2011).

2.3.6 Comparison of ground motions observed in the Darfield and Christchurch earthquakes

In order to obtain further insight into the ground motions observed in the Darfield and Christchurch earthquakes, Bradley & Cubrinovski (2011) compared the geometric mean horizontal and vertical response spectra at several strong motion stations from both events, as shown in Figure 2.11. It is immediately obvious that the spectral amplitudes corresponding to a majority of vibration periods of engineering interest in the Christchurch earthquake are significantly larger than those observed in the Darfield earthquake. However, at longer periods (T > 2 s), the spectral amplitudes observed at Christchurch Cathedral College (CCCC), Riccarton High School (RHSC) and Canterbury Aero Club (CACS) in the latter event are larger due to the aforementioned phenomena such as forward-directivity effects and the longer duration of shaking (Bradley & Cubrinovski, 2011). Despite the different source locations of the two events (i.e. the Christchurch and Darfield earthquakes occurred approximately 10 km southeast and 30 km west of the Christchurch central business district, respectively), it can be observed that the response spectral shapes at a given site from both events in Figure 2.11 are remarkably similar. For example, the response spectral shapes of the horizontal and vertical components observed at CACS and RHSC during both events are very similar for vibration periods less than T = 2 s. At periods greater than 2 s, there is a deviation of the spectral shapes due to the significance of the source effects discussed previously. From the observations above, the importance of local site effects on the recorded ground motion at the surface are further elucidated at high to moderate frequencies. More importantly, the comparisons in Figure 2.11 are useful in highlighting the advantages of carrying out site-specific response analysis in comparison to using simplified code-based site classification schemes to characterise the surficial soil conditions (Bradley, 2012b).

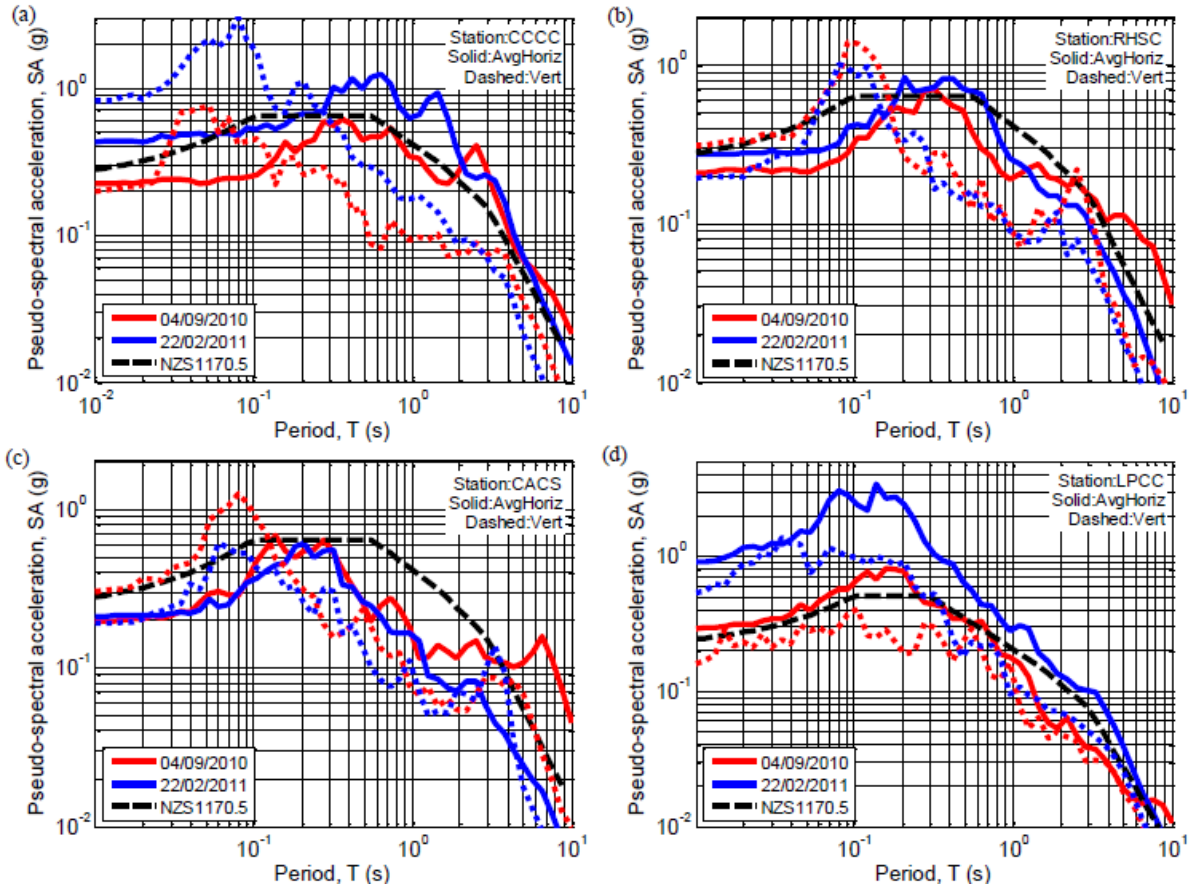

Figure 2.11: Comparison of geometric mean horizontal and vertical pseudo-acceleration response spectra observed at various strong motions stations in the M_w6.2 Christchurch and M_w7.1 Darfield earthquakes (after Bradley & Cubrinovski, 2011).

2.4 Identification of pulse-like ground motions

The compilation of databases containing pulse-like ground motions in the past (e.g. Mavroeidis & Papageorgiou, 2003; Bray & Rodriguez-Marek, 2004) has largely relied on user judgment and qualitative evidence. For example, the presence of a large amplitude velocity pulse occurring at the beginning of the fault-normal velocity time-series has traditionally been a strong indicator of a forward-directivity ground motion. The identification process has also been aided by the preferred direction taken by the horizontal velocity trajectory plot and/or examination of the source-to-site geometry. However, it is important to note that forward-directivity effects are not solely responsible for producing pulse-like ground motions in the near-fault region. For example, if a site is located near an asperity (an area on a fault that ruptures with a high velocity and stress drop) in the fault rupture, the observed ground motion could potentially display a characteristic pulse-like

feature. Furthermore, it is possible for seismic waves passing through the edge of a sedimentary basin (e.g. Canterbury basin) to become essentially trapped in the surficial soil layers, which leads to the "waveguide effect" (Bradley, 2012a), as discussed previously in the context of the Canterbury earthquakes. Consequently, the seismic waves are forced to propagate in a confined medium and produce large amplitude pulse-like ground motion. The present study requires the identification of forward-directivity ground motions observed in the Canterbury earthquakes, for which a suitable method is required. Several approaches for identifying pulse-like ground motions in an automated manner have been proposed in the recent past. Hence, it is appropriate to carry out a review of these methods in order to find a suitable option for this study.

2.4.1 Baker (2007) pulse classification algorithm

In order to avoid subjectivity and reproducibility issues associated with qualitative classification of pulse-like ground motions, Baker (2007) developed a quantitative and automated pulse classification algorithm. This algorithm uses a form of signal processing known as wavelet analysis, which is computationally inexpensive and provides reproducible results. According to Baker (2007), a basic understanding of wavelet analysis can be obtained using the Fourier analysis analogy. For example, Fourier analysis represents a signal using a linear combination of sine waves, with each wave having its own frequency and being represented by a signal of infinite length. On the other hand, wavelet analysis represents a signal using a summation of basis functions known as wavelets that are localised in time and represent a narrow range of frequencies (Baker, 2007). The basis function at time t is defined as follows:

$$\Phi_{s,l}(t) = \frac{1}{\sqrt{s}}\Phi\left(\frac{t-l}{s}\right) \tag{2.1}$$

where $\Phi(\cdot)$ is the mother wavelet function[2], s is the scale parameter that 'dilates' the wavelet, and l is the location parameter that translates the wavelet in time. As mentioned

[2] There are several types of wavelet prototypes that can be used to decompose a signal. A prototype function is known as a mother wavelet. For example, the Daubechies wavelet of order 4 is used as the mother wavelet in

above, any signal $f(t)$ can be represented as a linear combination of the basis functions, and the coefficients for this linear combination can be determined using a convolution integral (similar to the Fourier transform) as shown in Equation (2.2):

$$C_{s,l} = \int_{-\infty}^{\infty} f(t) \frac{1}{\sqrt{s}} \Phi_{s,l}(t) dt = \int_{-\infty}^{\infty} f(t) \frac{1}{\sqrt{s}} \Phi\left(\frac{t-l}{s}\right) dt \tag{2.2}$$

where $C_{s,l}$ is the coefficient associated with a wavelet having a scale, s and location, l.

The wavelet decomposition procedure used by the Baker (2007) pulse classification algorithm to extract the main pulse-like feature from a ground motion is summarised below:

1. The ground motion under consideration (i.e. the fault-normal velocity time-series recorded at Rinaldi during the 1994 Northridge earthquake in Figure 2.12a) is evaluated by computing the continuous wavelet transform (i.e. Equation 2.2) of the velocity time-series, and the coefficient with the largest absolute value is identified (Baker, 2007). The scale and location associated with the largest wavelet coefficient is associated with a concentration of energy in a small time and frequency range, which is a characteristic typically associated with a velocity pulse.
2. The period and location of the pulse in the velocity time-series are identified using the wavelet associated with the coefficient from Step 1, as illustrated in Figure 2.12a.
3. The continuous wavelet transform is computed for the residual ground motion (calculated by subtracting the wavelet with the largest coefficient from the original ground motion) in order to find the second largest wavelet coefficient in the vicinity of the original wavelet (within $\pm$ one-half of the width, s of the original wavelet), as shown in Figure 2.12b.
4. Steps 2 and 3 are repeated until a total of ten coefficients are extracted in the vicinity of the original wavelet to obtain a detailed representation of the pulse. Figure 2.12c and Figure 2.12d illustrate the extracted pulse using ten coefficients and the residual ground motion after the pulse has been removed, respectively.

this pulse classification algorithm because it effectively represents the shape of velocity pulses. Further details regarding wavelets in regard to ground motion applications can be found in Baker (2007) and references therein.

Hence, the largest pulse-like feature from a particular component of the velocity time-series under consideration can be identified and extracted using the wavelet decomposition procedure described above. In addition, the algorithm is also capable of characterising the period and amplitude of the extracted pulse. The period of the pulse is defined as the period at which its maximum Fourier amplitude is reached and the peak ground velocity (PGV) is used to define the pulse amplitude.

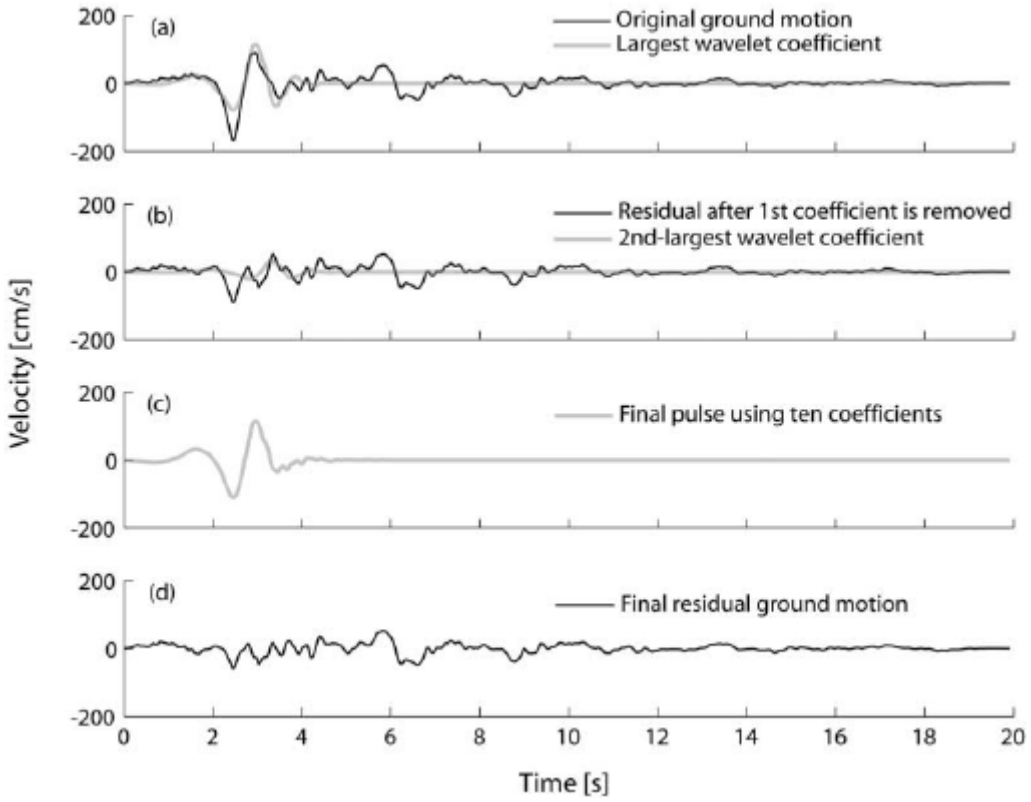

Figure 2.12: Illustration of the wavelet decomposition procedure used in extracting the pulse-like feature from the fault-normal velocty time-series recorded at Rinaldi during the 1994 Northridge earthquake (after Baker, 2007).

It is important to note that the wavelet analysis algorithm extracts a pulse from the original velocity time-series regardless of whether or not a significant pulse (due to forward-directivity for example) exists. In order to quantify the significance of the extracted pulse, Baker (2007) qualitatively classified potential pulse-like and non-pulse-like ground motions based on the results of the wavelet analysis carried out on fault-normal ground motions in the Next Generation Attenuation (NGA) ground motion database (Chiou et al., 2008) (with source-to-site distance, R_{rup} < 30 km and magnitude, M_w > 5.5). For example, the ground motion illustrated in Figure 2.12 was classified as being potentially pulse-like due to its early-arriving and large amplitude velocity pulse (Baker, 2007). These manual classifications were

subsequently used to calibrate a logistic regression equation for calculating a 'pulse-indicator' score, which predicts the likelihood of a given ground motion being pulse-like. Based on the results of linear discriminant analysis, Baker identified two predictor variables that provided good predictions: (i) the 'PGV ratio' and (ii) the 'energy ratio'. The PGV and energy (represented by the cumulative squared velocity as described subsequently) ratios represent the ratios of PGV and energy associated with the residual and original ground motions, respectively. The cumulative squared velocity is defined as shown in Equation (2.3):

$$CSV(t) = \int_0^t V^2(u)\, du \tag{2.3}$$

where $CSV(t)$ represents the cumulative squared velocity at time t and $V(u)$ is the ground motion velocity at time u. Equation (2.4) shows the predictive relationship developed by Baker (2007) for the pulse indicator (PI) score. It was concluded that a ground motion is pulse-like if the PI score predicted by the equation is greater than 0.85 and non-pulse-like for scores below 0.15.

$$PI\ Score = \frac{1}{1 + e^{-23.3 + 14.6(PGV\ Ratio) + 20.5(Energy\ Ratio)}} \tag{2.4}$$

It is worth re-iterating the fact that a ground motion exhibiting forward-directivity effects is typically characterised by a large amplitude velocity which arrives at the beginning of the record and is potentially damaging to well-engineered structures. Hence, in order to determine whether a ground motion is potentially pulse-like due to forward-directivity effects, Baker (2007) proposed the following two additional criteria:

1. The PGV of the ground motion record must be greater than 30 cm/s.
2. The pulse reaches 10% of its total CSV ($t_{10\%,pulse}$) before the original ground motion reaches 20% of its CSV ($t_{20\%,original}$).

The first criterion ensures that the ground motion under consideration is of engineering significance, whereas the second criterion allows the algorithm to check whether the pulse arrives early. Baker (2007) employed the wavelet analysis algorithm in conjunction with the three classification criteria described above to produce a database of 91 pulse-like ground

motions from a total of 3,551 three-component ground motions in the NGA database. Although this method provides defensible pulse classifications, Baker (2007) does advise that in some cases, it may be incapable of classifying the ground motion using the binary criteria of pulse-like and non-pulse-like. In such cases, qualitative judgement (e.g. examination of source-to-site geometry) on the part of the user is warranted during the classification process. The importance of this statement will become apparent in Chapter 3 where evidence of forward-directivity effects in the Canterbury earthquakes is identified and documented.

2.4.2 Shahi (2013) pulse classification algorithm

One of the main limitations associated with the pulse classification algorithm developed by Baker (2007) is its inability to classify pulse-like ground motions using multi-component ground motion time-series. Upon recognising this limitation, Shahi (2013) developed a pulse classification algorithm which is capable of analysing multi-component velocity time-series and classifying pulses in arbitrary orientations. Similar to its predecessor, this recently developed algorithm also makes use of wavelet analysis in identifying pulses from ground motions. For the purposes of brevity, the discussion herein is restricted to aspects of the Shahi (2013) pulse classification algorithm that are novel in relation to the Baker (2007) algorithm (hereafter referred to as the B07 and S13 algorithms in this chapter).

In order to account for both horizontal components of ground motions, the S13 algorithm calculates the continuous wavelet transform (CWT) of two orthogonal components of the velocity time-series and combines them linearly to provide coefficients for any arbitrary orientation. Hence, for each given scale (s) and location (l), these coefficients are used to compute the maximum wavelet coefficients over all non-redundant orientations (i.e. between 0 and 180 degrees). In contrast, the B07 algorithm is typically used to compute the CWT for the fault-normal component of the velocity time-series, which only yields the maximum wavelet coefficient in one orientation. This issue can be resolved by performing the wavelet analysis on one component of the ground motion rotated through all non-redundant orientations as suggested by Shahi & Baker (2011) in a related study (discussed subsequently in Section 2.5.2). However, according to their approach, the ground motion is considered pulse-like if the classification criteria are met in any orientation and non-pulse-like only if the classification criteria are not met in all orientations. The stricter classification criteria imposed for non-pulse-like ground motions significantly increases the chance of

false-positive classifications i.e. non-pulse-like ground motions classified as pulse-like. In order to alleviate the possibility of such false-positive classifications, the algorithm proposed by Shahi (2013) uses improved classification criteria (discussed subsequently) while compromising between the use of one orientation and all possible orientations.

Shahi (2013) also recognised the fact that the original B07 classification algorithm and the modified approach followed in the Shahi & Baker (2011) study are capable of producing false negative classifications i.e. pulse-like ground motions classified as non-pulse-like. This finding was based on the observation that in certain cases, wavelets other than the largest wavelet in the velocity time-series can be more dominant (i.e. in terms of amplitude). In order to avoid this issue, the S13 algorithm uses five potential pulses in the classification process. This is followed by the calculation of the orientation in which each potential pulse was found (refer to Shahi (2013) for further details). In this manner, the original ground motion in each of the five cases corresponds to the velocity time-series rotated to the calculated orientation. Steps 2 and 3 outlined in the wavelet decomposition procedure for the B07 algorithm are carried out ten times subsequently to obtain a refined shape for the extracted pulse. It is possible for more than one potential pulse to be classified as pulse-like using the criteria described above. In such cases, the pulse with the largest wavelet coefficient is classified as the dominant pulse (Shahi, 2013).

Although the classification criteria adopted by Shahi (2013) for identifying pulse-like ground motions follows the approach taken by Baker (2007), the selected threshold pulse indicator scores and PGV values in the former algorithm have a firm basis. For example, the pulse indicator (PI) score equation for the S13 algorithm was developed using superior statistical tools such as principal component analysis and support vector machines (Shahi, 2013). Equation (2.5) defines the PI score:

$$PI = -1 \cdot (13.819 + 9.384 \cdot PC^2 + 0.0004 \cdot PGV^2 \\ -17.189 \cdot PC - 0.625 \cdot PGV + 0.585 \cdot PC \cdot PGV) \quad (2.5)$$

where PC (principal component) is a linear combination of the PGV ratio and Energy ratio (i.e. $PC = 0.63 \cdot (PGV\ ratio) + 0.777 \cdot (Energy\ ratio)$) obtained using principal component analysis to reduce the number of variables required in the classification process.

A ground motion evaluated using the S13 algorithm is considered pulse-like if the PI score is positive. Nonetheless, upon comparing the classification bounds used by both algorithms in terms of PI score, Shahi (2013) concluded that they agree well with each other. Hence, the major difference in classification criteria arises from the PGV threshold adopted in both algorithms. While Baker (2007) chose an arbitrary value of 30 cm/s, the threshold for the S13 algorithm is obtained directly from the data, thereby highlighting the improved nature of the classification criteria developed by Shahi (2013). Upon using the algorithm to evaluate all 8,661 ground motions in the more recent NGA-West2 database (Ancheta et al., 2013), Shahi (2013) identified 244 pulse-like ground motions and found that 145 ground motions were most likely caused by forward-directivity effects based on manual filtering.

2.5 Response spectra-based modelling of forward-directivity effects

In the near-fault region, the effects of forward-directivity can be considered by two types of response spectra-based models referred to as 'broadband' and 'narrowband' directivity models. Both models involve the modification of the elastic pseudo-acceleration response spectrum obtained using conventional ground motion prediction equations (GMPE). The term 'broadband' is used to classify models which capture the effects of directivity (forward and backward) by either monotonically increasing or decreasing the spectral ordinates over a broad range of periods. Conversely, the term 'narrowband' is used to classify models which amplify the response spectra within a small range of periods surrounding the directivity pulse period (T_p).

2.5.1 Broadband directivity models

Somerville et al. (1997) produced the first broadband directivity model (hereafter referred to as the S97 broadband directivity model). They identified that the spatial variations in ground motion amplitude and duration due to rupture directivity effects in the near-fault region become significant at a vibration period of 0.6 s. In addition to the modification of the average horizontal response spectra predicted by the Abrahamson & Silva (1997) GMPE (which represents the average of the fault-normal and fault-parallel SA values at each vibration period), the model also included modifications to the ratio of fault-normal to fault-

parallel response spectra, and the duration of the ground motion. These modifications were based on the empirical analysis of near-fault data obtained from major earthquakes including the San Fernando (1971), Imperial Valley (1979), Loma Prieta (1989), Northridge (1994) and Kobe (1995) earthquakes. However, the model is not entirely empirical as it takes into account the basic physics of the directivity phenomenon. The model assumes that variations in ground-motion amplitude due to fault rupture directivity depends on two geometrical parameters: (i) the angle between the direction of rupture and direction of travelling waves from the source to the site (θ for strike-slip faults and φ for dip-slip faults),'and (ii) the fraction of fault rupture surface (X for strike-slip faults and Y for dip-slip faults) that lies between the hypocentre and the site (Somerville et al., 1997). An illustration of the important geometric parameters used in the calibration of the model is shown in Figure 2.13a and 2.13b for strike-slip and dip-slip faults, respectively. From a physical viewpoint, it is obvious that the smaller the angle, the larger the directivity effects that are experienced at a given site. Similarly, if a larger fraction of the fault lies between the site and hypocentre, the effects of directivity are larger. A further modification to the directivity model was made by Abrahamson (2000) (hereafter referred to as the AB00 model) in order to incorporate a directivity saturation effect and to taper it at small magnitudes and large distances for strike-slip events.

There are two main limitations associated with the S97 broadband directivity amplification model as identified by Rowshandel (2006) below:

- The model implicitly assumes that rupture along a fault surface is unidirectional by separating faults into purely strike-slip and dip-slip.
- For dip-slip faults, the near-source region affected by directivity affects is arbitrarily delineated in the model by two lines from the surface projection of the fault surface as shown in Figure 2.14, which form 22.5^{o} angles with the fault edges. This could potentially impact the distribution of seismic hazard in regions surrounding dip-slip faults.

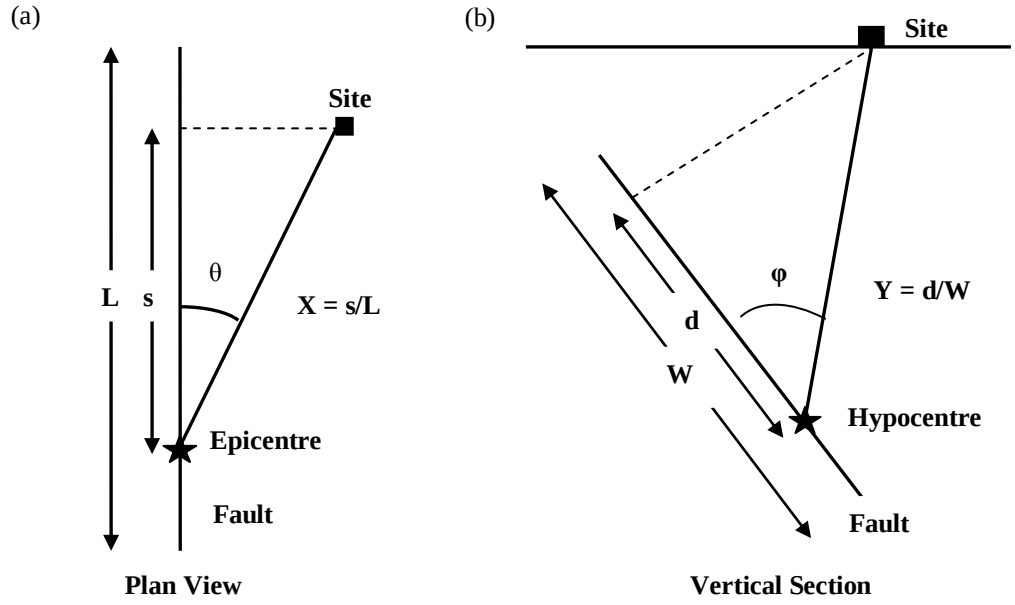

Figure 2.13: Geometric parameters used in the calibration of the Somerville et al. (1997) broadband directivity model for (a) a strike-slip fault; and (b) a dip-slip fault (adapted from Somerville et al., 1997).

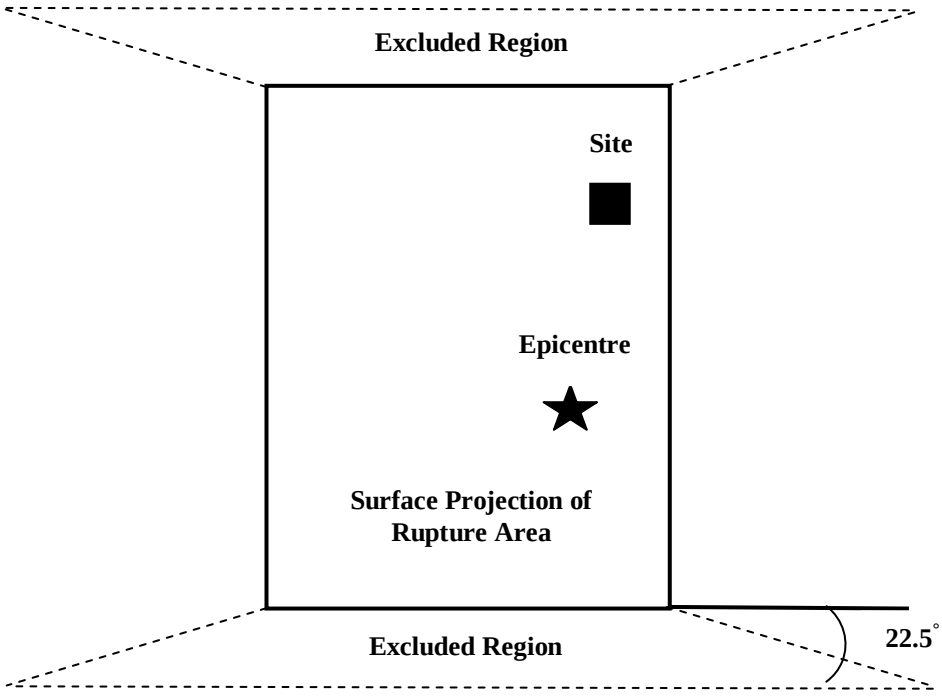

Figure 2.14: Region off the end of dip-slip faults excluded from the Somerville et al. (1997) broadband directivity model (adapted from Somerville et al., 1997).

In an effort to overcome the limitations identified above, Rowshandel (2006) developed a generalised version of the S97 directivity model, which assumes that the effect of rupture directivity is proportional to the fraction of the fault surface area that ruptures towards the site. A directivity parameter, ξ_j which is proportional to the "effective" fraction of the fault area that ruptures towards a site and source-to-site azimuth (θ), was used in the model development. Rowshandel (2006) adopted the same broadband functional form as Somerville et al. (1997) for the directivity amplification of spectral ordinates predicted by four different ground motion prediction equations between vibration periods of 0.1 s < T < 3 s. The geometric directivity parameter, ξ_j for a given fault plane can be calculated as shown in Equation (2.6):

$$\xi_j = \frac{\sum_{i=1}^{N} \zeta_i . \Delta A_i . \overrightarrow{r_1} . \overrightarrow{r_2}}{\sum_{i=1}^{N} \Delta A} \tag{2.6}$$

where ΔA_i is an increment of the fault area which ruptures in the direction represented by the unit vector $\overrightarrow{r_1}$; $\overrightarrow{r_2}$ represents the unit vector which defines the direction from the rupturing area increment $\Delta A_i$to the site j; and ζ_i is a parameter which accounts for the heterogeneity of the rupture and can be assumed to be 1 when the focus is solely on modelling the directivity phenomenon (Rowshandel, 2006). Hence, by accounting for the multi-directional nature of the rupture process along a fault, this model is able to capture the along-strike directivity effects in dip-slip events and up-dip effects in strike-slip events. More recently, as part of the NGA project (Power et al., 2008), Rowshandel (2010) applied this model to the latest NGA GMPEs developed by Boore and Atkinson (2008), Campbell and Bozorgnia (2008), Chiou and Youngs (2008), and Abrahamson and Silva (2008). This study further highlighted that the influence of rupture directivity on the resulting ground motion intensity is dependent upon the fault geometry, orientation of the fault surface in relation to the site, and the location of the hypocentre. Furthermore, it was shown that upon correcting the four GMPEs for directivity, reductions ranging from a few percent for short-period ground motion to approximately 20% for moderate-to-long period ground motion could be achieved in the intra-event standard deviation associated with the predictions.

Similar to Rowshandel (2010), Spudich et al. (2004) and Spudich & Chiou (2008) recognised the importance of incorporating near-fault directivity effects in ground motion modelling by developing a physics based model using isochrone theory, which provides directivity correction factors for earlier versions of the four NGA GMPEs listed above. According to Rowshandel (2010), isochrone theory is particularly useful in studying ground motions in the near-fault region because the low-frequency contribution of the radiated seismic energy from the ruptured fault, including surface waves, are ignored. As a result, only the high frequency seismic waves are considered, thereby making the method particularly advantageous for the near-fault region. However, it should be noted that the development of the isochrone directivity model was carried out using synthetic ground motions due to the lack of azimuthally well-distributed observed strong ground motion recordings for a given earthquake event in the NGA database. Based on the earlier investigative efforts of Spudich et al. (2004), an isochrone directivity parameter (IDP) was used to develop the broadband model of Spudich & Chiou (2008) and is defined in Equations (2.7)-(2.9) as follows:

$$IDP = CSR_{ri} \tag{2.7}$$

$$C = \frac{\left(\min\left(\widetilde{c'}, 2.45\right) - 0.8\right)}{2.45 - 0.8} \tag{2.8}$$

$$S = \ln\left[\min\left(75, \max(s, h)\right)\right] \tag{2.9}$$

The parameters in the equations displayed above are calculated for a site (x_s) with a given source-to-site geometry as illustrated in Figure 2.15. It can be observed that the s and h parameters in Equation (2.9) represent the along-strike distance from the hypocentre (x_h) to the point (x_c) on the fault closest to the site; and the down-dip distance from the top of the rupture to the hypocentre, respectively. C is the normalised version of the isochrone velocity ($\widetilde{c'}$), which captures the rupture directivity amplification around a fault (Spudich and Chiou, 2008). The isochrone velocity is defined as the ratio of the rupture velocity (v_r) and shear wave velocity (β). In fact, the authors liken the parameter S and C to X and $\cos(\theta)$ in the S97 model, respectively. Finally, R_{ri} is a scalar radiation pattern amplitude and is explained in further detail by Spudich & Chiou (2008). Based on a comparison with the directivity amplification (or deamplification) of response spectra predicted by the S97 and AB00 models, it was found that the isochrone directivity model predicts approximately half the

amplification (or deamplification) at every period in relation to the former model, and similar predictions in comparison to the latter model.

In addition to overcoming the aforementioned limitations associated with the S97 directivity model, the Rowshandel (2010) and Spudich & Chiou (2008) models are also applicable for fault ruptures involving multiple fault segments. This is particularly useful in the present study where recently developed finite fault models by Beavan et al. (2012) for the M_w7.1 Darfield and M_w6.2 Christchurch earthquakes indicate that rupture occurred along multiple fault planes. Furthermore, the performance of these models has not been assessed by comparing their predictions to empirical observations. Hence, the large set of near-fault ground motions recorded during the Canterbury earthquakes provide a good opportunity to carry out this exercise.

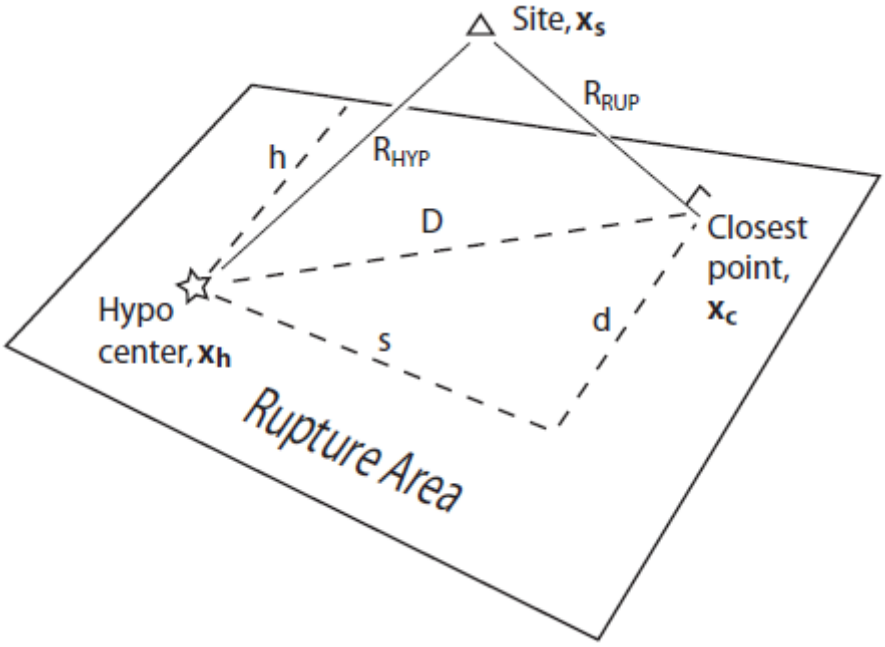

Figure 2.15: Illustration of a fault plane and source-to-site geometry (after Spudich & Chiou, 2008).

2.5.2 Narrowband directivity models

Upon close examination of near-fault ground motion recordings from the 1999 Chi-Chi (Taiwan) and Kocaeli (Turkey) earthquakes, Somerville (2003) confirmed that the near-fault rupture directivity pulse is a narrowband pulse whose period increases with magnitude. The period of this pulse was related to source parameters such as the rise time (duration of slip at a point on the fault) and the fault dimensions, which generally increase with magnitude. In fact, Somerville (2003) indicated that near-fault ground motions cannot be adequately described by uniform scaling of a fixed response spectral shape. This is because the shape of the intermediate and long period part of the response changes as the level of spectrum and earthquake magnitude increase. For example, it was found that the elastic spectra of near-fault forward-directivity recordings of earthquakes with M_w6.7-7.0 are much stronger than those of larger magnitude (M_w7.2-7.6) in the intermediate period range of 0.5-2.5 s, but are weaker at longer periods (Somerville, 2003). This observed magnitude scaling is contrary to the previously described ground motion spectral scaling model developed by Somerville et al. (1997), which assumes that spectral amplitudes increase monotonically at all periods.

Based on the evidence above, Somerville (2003) developed a preliminary narrowband directivity model which included the magnitude dependence of the directivity pulse period. In essence, the model scales the response spectrum obtained using a conventional ground motion prediction equation (GMPE) by a cosine-shaped function centred at a period of approximately 75% of the directivity pulse for a certain magnitude (M_w). Because the response spectrum produced by the GMPE is assumed to be representative of the fault parallel component of ground motion, the scaled response spectrum represents the fault-normal component (Somerville, 2003). Figure 2.16 provides a comparison between the response spectra predicted by the narrowband model of Somerville (2003), broadband model of Somerville et al. (1997) and the GMPE developed by Abrahamson & Silva (1997), which does not explicitly account for directivity effects. The comparisons have been shown for rock and soil sites. While the broadband model predicts a monotonic increase in spectral acceleration amplitudes with magnitude at all vibration periods (T), the narrowband model predicts larger amplitudes at moderate periods (i.e. 0.5 s < T < 2 s) for M_w less than 7.5 and smaller amplitudes at all periods for M_w greater than 7.5 (Somerville, 2003).

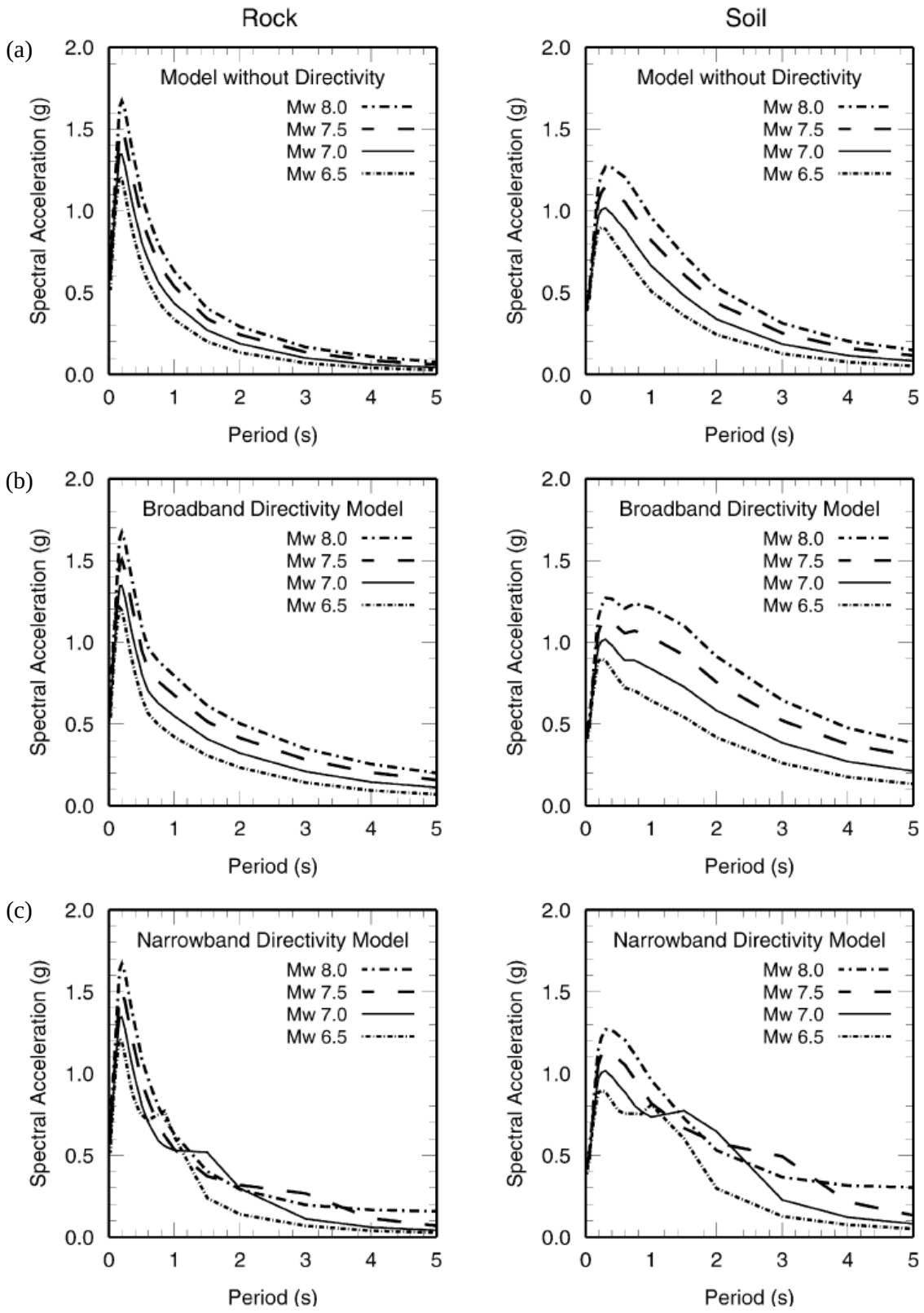

Figure 2.16: Comparison of pseudo-acceleration response spectra predicted using: (a) Abrahamson & Silva (1997) GMPE without any directivity modification; (b) Somerville et al. (1997) broadband directivity model; and (c) Somerville (2003) narrowband directivity model for rock and soil sites located 5km from a strike-slip fault (after Somerville, 2003).

More recently, Shahi & Baker (2011) developed the first comprehensive narrowband model for predicting the effect of forward-directivity on elastic response spectra. The model was empirically calibrated using the observed recordings of pulse-like ground motions from the Next Generation Attenuation (NGA) strong ground motion library. In doing so, they developed empirical equations for the amplification of pseudo-spectral acceleration predicted by conventional GMPEs for a range of periods centred about the period of the pulse. Consequently, ground motion scaling could be carried out to meet the observed magnitude scaling of the directivity pulse by Somerville (2003). This is in stark contrast to the previously discussed broadband directivity models where the following two features were evident, as highlighted by Spudich et al. (2012): (i) the peak directivity amplification of spectral ordinates always occurs at the longest vibration period for all earthquake magnitudes and (ii) the models predict very small or no directivity amplification for earthquakes with M_w less than 6.0.

2.5.3 Assessment of response spectra-based directivity models

The strong ground motion data in the near-fault region from the Canterbury earthquakes has created an excellent platform for the examination of the adequacy of the previously discussed response spectra-based models in a NZ context. A similar type of exercise has been carried out in the United States by Howard et al. (2005) in order to assess the capabilities of the Somerville et al. (1997) model using ground motion recordings representing California's active tectonic environment. The results illustrated that the model, as modified by Abrahamson (2000) was able to provide satisfactory predictions for strike-slip events. Conversely, the model provided significant under-prediction of spectral ordinates for reverse faulting events. Nonetheless, the latter comparison was based predominantly on observations from ground motions recorded during the 1994 Northridge earthquake, where amplification of longer period spectral ordinates was influenced by basin effects and buried rupture effects, in addition to directivity effects (Howard et al., 2005). Another important point to make in passing is the fact that the Somerville et al. (1997) model has not been well validated on soft soil sites. A majority of the near-fault strong ground motion stations in the Canterbury region are located on soft soil sites (Site Class D and E according to NZS1170.5 (2004)), thereby providing an incentive to carry out the aforementioned validation process.

This is also applicable to the more recent narrowband model developed by Shahi & Baker (2011).

2.5.4 Directivity models for the Next Generation Attenuation West 2 (NGA-West2) Project

As part of the NGA-West2 Project, improved preliminary versions of the directivity models discussed in the previous sections have been developed by their respective researchers using the larger NGA-West2 (NGAW2) strong ground motion database (Ancheta et al., 2013). This database contains 8,661 three-component accelerograms (compared to 3,551 three-component accelerograms in the NGA-West database) and includes the ground motions recorded in the M_w7.1 Darfield and M_w6.2 Christchurch earthquakes. In addition to using an updated dataset for model development, an aim of this project is to produce directivity models that can be included as additional terms in the development of new NGA-West2 GMPEs, with the coefficients associated with model being ascertained in the same regression as the other GMPE coefficients (Spudich et al., 2012), although this aim has not been achieved at present. Conversely, the older versions of these models were developed in order to provide directivity correction factors that can be applied to conventional GMPE predictions. At the time of writing, published final versions of these newer directivity models were not available and are therefore not considered in the present study. Nonetheless, based on the preliminary results presented by Spudich et al. (2012), it is anticipated that the NGA-West2 directivity models will not provide significantly improved predictions in comparison to their predecessors. The only exception to the above statement is the more recent narrowband model of Shahi & Baker (2011) which has been considered in the project without modification, and will also be considered in the present study.

2.6 Characterisation of forward-directivity ground motions in the time-domain

As mentioned earlier, forward-directivity in near-fault ground motion recordings is characterised by the arrival of most of the seismic energy in a single large pulse of motion at the beginning of the fault-normal velocity time-series. Conventional seismic design practice in NZ i.e. NZS1170.5:2004 (Standards New Zealand, 2004) and overseas (e.g. Uniform

Building Code in the United States) has favoured the use of a pseudo-acceleration response spectra because it indirectly reflects strong ground motion characteristics such as amplitude, frequency content and to a lesser extent, duration (Kramer, 1996, p. 74). In particular, the effects of forward-directivity are incorporated by means of a spectral amplification factor (discussed subsequently in Section 2.7), which is typically a function of the source-to-site distance and vibration period of interest. However, several researchers (Alavi & Krawinkler, 2000; Bray & Rodriguez-Marek, 2004; Mavroeidis & Papageorgiou, 2003; Somerville, 2003; Somerville, 1998) have demonstrated that a so-called 'time-domain' representation is able to better characterise the effects of near-fault ground motions, primarily because elastic response spectra are highly simplified representations of nonlinear inelastic structural response. The desirability of these time-domain models over response spectra-based models can be attributed to the fact that the use of response spectra for the seismic design and assessment of inelastically responding structures typically assumes that the ground motion is well represented as a stationary stochastic process, having a relatively uniform distribution of energy throughout the duration of the ground motion (Rodriguez-Marek, 2000).

The common theme underlying the aforementioned studies is the approximation of the velocity time-series by means of equivalent pulse shapes. For example, Alavi & Krawlinker (2000) developed three basic pulse shapes representing the impulsive characteristics of near-fault ground motions in order to assess their suitability for seismic performance assessments. In each case, the acceleration pulse was first defined, followed by mathematical integration to obtain the velocity and displacement pulse shapes. The pulse period (T_p), in this case, was identified from the location of a global peak in the pseudo-velocity response spectrum (Alavi & Krawinkler, 2000). Similarly, Somerville (2003) developed simple triangular pulse shapes whose period increased with magnitude as defined by the empirical equations obtained from a limited set of near-fault ground motions. These equations were developed using the period of the largest cycle of the fault-normal velocity waveform for both rock and soil sites.

Although the simplified velocity waveforms developed in the models described above are useful in capturing the salient features of structural response, their reliability can be severely compromised if they do not capture the time-domain and response spectrum characteristics of actual near-fault ground motions. In fact, researchers made no attempt to validate their respective models by comparing the predicted and observed time-series and

response spectra. This motivated Mavroeidis & Papageorgiou (2003) to develop a simple analytical model which is capable of providing synthetic ground motions that account for the impulsive character of near-fault recordings in a qualitative and quantitative manner. A modulated harmonic function (also known as a wavelet) was proposed to define the velocity pulse in this case. The calibration of this model was carried out using a large number of recorded pulse-like ground motions from well-known earthquake events and the period of the pulse was determined upon fitting the modulating function to the observed velocity waveform. Unlike the models described previously, the model devised by Mavroeidis & Papageorgiou (2003) successfully simulated the entire set of time-series (displacement, velocity and in most cases, acceleration) as well as the corresponding response spectra used in its development. Another important note to make in passing is the fact that PGV is widely used in defining the amplitude of the equivalent velocity pulses represented by the models above. These time-domain models will not be considered in the present study and are mentioned here for completeness. This can be attributed to the fact that the focus of immediate studies is on simulating the near-fault ground motions recorded during the Canterbury earthquakes using physics-based broadband simulation methodologies (Bradley personal communication, 2012). Such site-specific simulations are expected to offer new insights into the complex interaction of source-, path- and site-effects that resulted in the severe near-source ground motions recorded during these earthquakes. It is also expected that the as-recorded and simulated ground motions will be used to conduct seismic response analyses (both structural and geotechnical) in an effort to validate the broadband ground motion simulation procedure.

As identified previously in Section 2.1, previous research (e.g. Alavi & Krawinkler, 2000) has shown that the non-linear response of structures in the near-fault region is particularly sensitive to the amplitude and period of the directivity pulse. Based on this evidence, several studies have focused on developing predictive relationships for these important parameters (e.g. Bray et al., 2009; Bray & Rodriguez-Marek, 2004; Shahi & Baker, 2011; Somerville, 1998). However, these relationships were developed using a deprecated NGA ground motion database. As mentioned earlier, the more recent NGA-West 2 database is significantly larger than its predecessors, thereby providing an opportunity to investigate whether improved predictions of the directivity pulse period and amplitude can be obtained

based on augmented datasets. The observations from the Canterbury earthquakes will act as a springboard to carry out this validation process.

2.7 Forward-directivity effects in probabilistic seismic hazard analysis and seismic design

2.7.1 Frameworks developed in previous research

The quantification of seismic hazard in a site-specific study is traditionally carried out using probabilistic seismic hazard analysis (PSHA). However, conventional ground motion models used in PSHA (e.g. Kramer, 1996; McGuire, 2004) do not account for the effects of forward-directivity ground motions (Shahi & Baker, 2011). This could potentially lead to an under-prediction of the seismic hazard at sites located in the near-fault region. The need to include the effects of rupture directivity in probabilistic seismic hazard analyses was first highlighted by Abrahamson (2000), who subsequently used a modified version of the Somerville et al. (1997) model in conjunction with the Abrahamson & Silva (1997) GMPE to develop a framework for its inclusion. In doing so, a 30% increase in the SA value at T = 3 s was found upon comparing the results obtained from traditional and modified PSHAs for the San Francisco-Oakland Bay Bridge. The growing recognition that a ground motion with a distinct velocity pulse has a tendency to cause heightened elastic response only in a narrow period range (close to the pulse period, T_p) led Tothong et al. (2007) to develop an approach to incorporate these narrowband characteristics in PSHA. However, the use of this methodology was restricted by the unavailability of narrowband response spectra-based models. Shahi & Baker (2011), upon developing their narrowband model were able to extend the PSHA framework proposed by Tothong et al. (2007).

Figure 2.17 illustrates the uniform hazard spectra for an exceedance probability of 2% in 50 years obtained using three approaches: (i) conventional PSHA without considering the effect of pulse-like ground motions; (ii) PSHA including the effect of forward-directivity ground motions using the broadband Abrahamson (2000) approach; and (iii) PSHA including the effect of forward-directivity ground motions using the narrowband Shahi & Baker (2011) approach. It should be noted that these hazard calculations were performed by Shahi & Baker (2011) for a site located 6.7 km from the fault responsible for the 1979 M_w6.5 Imperial Valley earthquake. They propose that the results obtained using the narrowband approach are

superior because it is consistent with seismological theory. The details of this framework are omitted here for the purposes of brevity and will be discussed in further detail in Chapter 7.

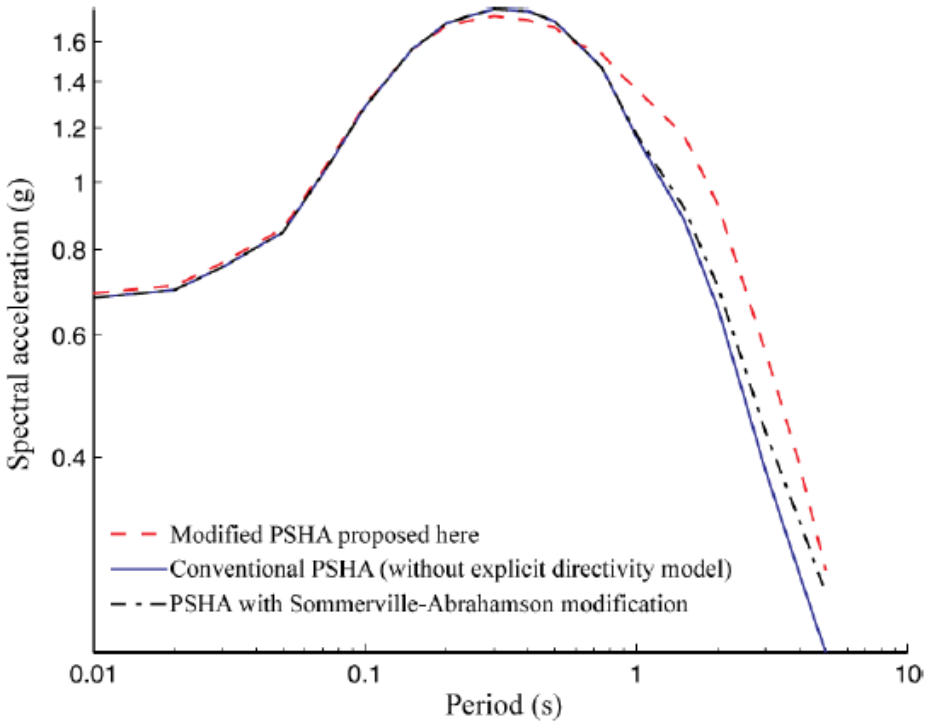

Figure 2.17: Illustration of the 2% in 50 year uniform hazard spectra obtained using three approaches (i) conventional PSHA; (ii) PSHA including directivity effects using the Abrahamson (2000) broadband approach; and (c) PSHA including directivity using the Shahi & Baker (2011) narrowband approach (after Shahi & Baker, 2011).

2.7.2 Consideration of forward-directivity effects in seismic design guidelines

The seismic design of structures is carried out using the NZS1170.5:2004 (Standards New Zealand, 2004) design standard in NZ. For conventional design, the 475-year return period acceleration response spectrum (which corresponds to a probability of 10% in 50 years) is typically used and the effects of forward-directivity in the near-fault region are accounted for by the near-fault factor, $N(T, D)$. This factor amplifies the spectrum based on the annual probability of exceedance, source-to-site distance and fundamental period of the structure (Standards New Zealand, 2004). It is important to note that the near-fault factor is based on the Somerville et al. (1997) horizontal geometric mean component forward-directivity amplification. Since the strong ground motion intensity at a particular site can be modified by the local site conditions (e.g. rock, soft soil), the design code considers 5 distinct

site class conditions (A: Hard Rock, B: Rock, C: Shallow Soil, D: Deep or Soft Soil, E:Soft Soil) and hence prescribes 5 different design acceleration response spectra based upon these site classifications. In addition, the near-fault factor prescribed in NZS1170.5 (2004) also bears significant resemblance to the near-fault factors N_V and N_A from the 1997 Uniform Building Code (UBC) used in North America to amplify the intermediate (velocity-controlled) and short period (acceleration-controlled) parts of the design acceleration response spectrum, respectively (Rodriguez-Marek, 2000).

The inadequacy of the near-fault factor was clearly exhibited in a recent study by Bradley (2012a). A comparison of the observed fault-normal and fault-parallel acceleration response spectra from the Darfield earthquake at 2 sites in the Christchurch central business district (classified as site class D) with the design response spectrum from NZS1170.5 (Standards New Zealand, 2004) (which includes the maximum permissible increase in the spectral amplitudes due to near-fault directivity effects) was carried out. From the comparison illustrated in Figure 2.18, it is evident that the observed fault-normal spectral acceleration (SA) values, which show a peak at approximately T = 2.5 s primarily due to forward-directivity effects (Bradley, 2012a), exceed the amplified design spectra. The broadband effect of the near-fault factor is also clearly illustrated in this figure. This comparison has highlighted the need for an improved representation of near-fault directivity effects in the seismic design standard. The present study aims to do so by incorporating the recently developed PSHA framework by Shahi & Baker (2011), which include the effects of directivity, in NZ-specific probabilistic seismic hazard analyses.

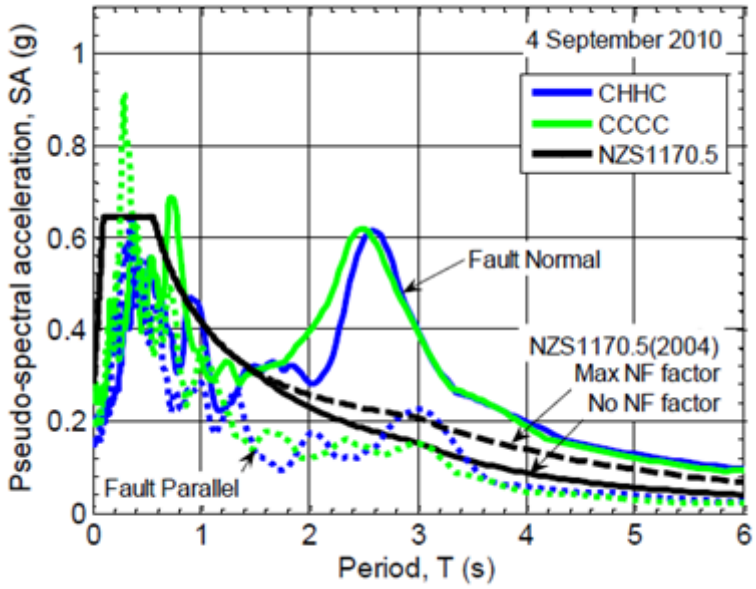

Figure 2.18: Comparison of the observed pseudo-acceleration response spectra at two CBD sites during the Darfield earthquake with the 475-year return period elastic site hazard spectrum for site class D (after Bradley, 2012a).

Conventional ground motion prediction equations (GMPE) such as those developed by Bradley (2010) and McVerry et al. (2006) for the NZ tectonic environment do not explicitly consider the effects of forward-directivity (Bradley, 2012b). This was one of the primary reasons for their under-prediction of observed *SA* values at various near-fault locations from the Darfield earthquake at longer periods. As a result, Bradley (2012b) recommended that the effects of forward-directivity should be explicitly considered in seismic hazard analyses in NZ, including those that form the basis of hazard spectra in future seismic design standards. This also provides an impetus for examining the effect of including directivity in NZ-specific PSHA in the present study.

The recent major earthquakes in the Canterbury region were a direct result of rupture along previously unknown faults. While it can be argued that these type of faults are accounted for by the background seismicity model in the most recent national seismic hazard model of NZ (Stirling et al., 2012), there are several limitations associated with this argument. For example, one of the limitations as highlighted by Bradley (2012a) is that such earthquakes are treated as point sources with a minimum depth of 10 km (whereas the centroid depths i.e. 'the centre of radiated energy' of the Darfield and Christchurch earthquakes were as low as 4 km). The use of point-sources in the seismicity model is inconsistent with the use of finite-fault based parameters (which form the basis of GMPE

development) in ground motion modelling, which results in un-conservatively lower surface ground motions, especially in the near-fault region of significant background earthquakes (Bradley, 2012b). In this study, the point sources representing background seismicity in NZ will be considered as finite-fault sources in an effort to determine the increase in seismic hazard for regions (e.g. Christchurch) where the background seismicity has a major contribution to the overall seismic hazard.

2.8 References

Abrahamson, N. A. (2000). Effects of rupture directivity on probabilistic seismic hazard analysis. In *Proceedings of the 6th International Conference on Seismic Zonation*. Palm Springs, California.

Abrahamson, N. A., & Silva, W. J. (1997). Empirical response spectral attenuation relations for shallow crustal earthquakes. *Seismological Research Letters*, **68**(1):94–127.

Abrahamson, N., & Silva, W. (2008). Summary of the Abrahamson & Silva NGA Ground-Motion Relations. *Earthquake Spectra*, *24*(1), 67–97. doi:10.1193/1.2924360

Alavi, B., & Krawinkler, H. (2000). Consideration of near-fault ground motion effects in seismic design. In *Proceedings of the 12th World Conference on Earthquake Engineering*. Auckland, New Zealand. Retrieved from http://www.iitk.ac.in/nicee/wcee/article/2665.pdf

Alavi, B., & Krawinkler, H. (2004). Behavior of moment-resisting frame structures subjected to near-fault ground motions. *Earthquake engineering & structural dynamics*, **33**(6): 687–706.

Ancheta, T. D., Darragh, R. B., Stewart, J. P., Seyhan, E., Silva, W. J., Chiou, B. S., … Boore, D. M. (2013). *PEER NGA-West2 Database*. Retrieved from http://peer.berkeley.edu/publications/peer_reports/reports_2013/webPEER-2013-03-Ancheta.pdf

Anderson, J. C., & Bertero, V. V. (1987). Uncertainties in establishing design earthquakes. *Journal of Structural Engineering*, *113*(8), 1709–1724.

Baker, J. W. (2007). Quantitative classification of near-fault ground motions using wavelet analysis. *Bulletin of the Seismological Society of America*, **97**(5):1486–1501. doi:10.1785/0120060255

Beavan, J., Fielding, E., Motagh, M., Samsonov, S., & Donnelly, N. (2011). Fault location and slip distribution of the 22 February 2011 Mw 6.2 Christchurch, New Zealand, Earthquake from geodetic data. *Seismological Research Letters*, **82**(6):789–799. doi:10.1785/gssrl.82.6.789

Beavan, J., Wallace, L., Samsonov, S., Ellis, S., Motagh, M., & Palmer, N. (2010). The Darfield (Canterbury) earthquake: geodetic observations and preliminary source model. *Bulletin of the New Zealand Society for Earthquake Engineering*, **43**(4):228.

Beavan, J., Motagh, M., Fielding, E. J., Donnelly, N., & Collett, D. (2012). Fault slip models of the 2010–2011 Canterbury, New Zealand, earthquakes from geodetic data and

observations of postseismic ground deformation. *New Zealand Journal of Geology and Geophysics*, **55**(3):207–221. doi:10.1080/00288306.2012.697472

Ben-Menahem, A. (1961). Radiation of seismic surface-waves from finite moving sources. *Bulletin of the Seismological Society of America*, **51**:401–435.

Ben-Menahem, A. (1962). Radiation of seismic body-waves from finite moving sources. *Bulletin of the Seismological Society of America*, **67**:345–350.

Bertero, V. V., & Godden, W. G. (1997). Uniform and Continuous Distribution of Mass, Stiffness, Strength and Ductility. Retrieved January 7, 2013, from http://www.cartage.org.lb/en/themes/arts/architec/architecturalstructure/StructuralElements/ProperSelections/UniformContinuous/UniformContinuous.htm

Bertero, V. V., Mahin, S. A., & Herrera, R. A. (1978). Aseismic design implications of near-fault San Fernando earthquake records. *Earthquake Engineering & Structural Dynamics*, *6*, 31–42.

Boore, D. M., & Atkinson, G. M. (2008). Ground-Motion Prediction Equations for the Average Horizontal Component of PGA, PGV, and 5%-Damped PSA at Spectral Periods between 0.01 s and 10.0 s. *Earthquake Spectra*, *24*(1), 99–138. doi:10.1193/1.2830434

Bradley, B. A. (2012a). *Ground Motion and Seismicity Aspects of the 4 September 2010 and 22 February 2011 Christchurch Earthquakes* (Technical report prepared for the Canterbury Royal Commission) (p. 62). Department of Civil and Natural Resources Engineering, University of Canterbury.

Bradley, B. A. (2012b). Ground motions observed in the Darfield and Christchurch earthquakes and the importance of local site response effects. *New Zealand Journal of Geology and Geophysics*, *55*(3), 279–286. doi:10.1080/00288306.2012.674049

Bradley, B. A. (2012c). Strong ground motion characteristics observed in the 4 September 2010 Darfield, New Zealand earthquake. *Soil Dynamics and Earthquake Engineering*, **42**:32–46. doi:10.1016/j.soildyn.2012.06.004

Bradley, B. A. (2010). *NZ-Specific Pseudo-Spectral Acceleration Ground Motion Prediction Equations Based on Foreign Models* (Research Report No. 2010-03) (p. 316). Department of Civil and Natural Resources, University of Canterbury.

Bradley, B. A., & Cubrinovski, M. (2011). Near-Source Strong Ground Motions Observed in the 22 February 2011 Christchurch Earthquake. *Bulletin of the New Zealand Society for Earthquake Engineering*, **44**(4):181–194.

Bray, J. D., & Rodriguez-Marek, A. (2004). Characterization of forward-directivity ground motions in the near-fault region. *Soil Dynamics and Earthquake Engineering*, **24**(11): 815–828. doi:10.1016/j.soildyn.2004.05.001

Bray, J. D., Rodriguez-Marek, A., & Gillie, J. L. (2009). Design ground motions near active faults. *Bulletin of the New Zealand Society for Earthquake Engineering*, **42**(1):1.

Brown, L. J., & Weeber, J. H. (1992). *Geology of the Christchurch urban area* (p. 110). Geological and Nuclear Sciences.

Campbell, K. W., & Bozorgnia, Y. (2008). NGA Ground Motion Model for the Geometric Mean Horizontal Component of PGA, PGV, PGD and 5% Damped Linear Elastic Response Spectra for Periods Ranging from 0.01 to 10 *s*. *Earthquake Spectra*, *24*(1), 139–171. doi:10.1193/1.2857546

Chiou, B., Darragh, R., Gregor, N., & Silva, W. (2008). NGA Project Strong-Motion Database. *Earthquake Spectra*, **24**(1):23–44. doi:10.1193/1.2894831

Chiou, B.-J., & Youngs, R. R. (2008). An NGA Model for the Average Horizontal Component of Peak Ground Motion and Response Spectra. *Earthquake Spectra*, *24*(1), 173–215. doi:10.1193/1.2894832

Choi, Y. (2005). Empirical Model for Basin Effects Accounts for Basin Depth and Source Location. *Bulletin of the Seismological Society of America*, **95**(4):1412–1427. doi:10.1785/0120040208

Chopra, A. K., & Chintanapakdee, C. (2001). Comparing response of SDF systems to near-fault and far-fault earthquake motions in the context of spectral regions. *Earthquake engineering & structural dynamics*, **30**(12):1769–1789.

Gledhill, K., Ristau, J., Reyners, M., Fry, B., & Holden, C. (2011). The Darfield (Canterbury, New Zealand) Mw 7.1 Earthquake of September 2010: A Preliminary Seismological Report. *Seismological Research Letters*, **82**(3):378–386. doi:10.1785/gssrl.82.3.378

Hall, J. F., Heaton, T. H., Halling, M. W., & Wald, D. J. (1995). Near-Source Ground Motion and its Effects on Flexible Buildings. *Earthquake Spectra*, **11**(4):569–605.

Holden, C., Beavan, J., Fry, B., Reyners, M., Ristau, J., Van Dissen, R., … Quigley, M. (2011). Preliminary source model of the Mw 7.1 Darfield earthquake from geological, geodetic and seismic data. In *Proceedings of the Ninth Pacific Conference on Earthquake Engineering: Building an Earthquake-Resilient Society* (pp. 14–16). Retrieved from http://www.nzsee.org.nz/db/2011/164.pdf

Housner, G. W., & Trifunac, M. D. (1967). Analysis of Accelograms: Parkfield Earthquake. *Bulletin of the Seismological Society of America*, **57**(6):1193–1220.

Howard, J. K., Tracy, C. A., & Burns, R. G. (2005). Comparing Observed and Predicted Directivity in Near-Source Ground Motion. *Earthquake Spectra*, **21**(4):1063–1092. doi:10.1193/1.2044827

Kramer, S. L. (1996). *Geotechnical Earthquake Engineering*. Upper Sadle River, New Jersey: Prentice Hall.

Mavroeidis, G. P., & Papageorgiou, A. S. (2003). A mathematical representation of near-fault ground motions. *Bulletin of the Seismological Society of America*, **93**(3): 1099–1131.

McGuire, R. K. (2004). *Seismic Hazard and Risk Analysis*. Berkeley, California: Earthquake Engineering Research Institute.

McVerry, G. H., Zhao, J. X., Abrahamson, N. A., & Somerville, P. G. . (2006). New Zealand acceleration response spectrum attenuation relations for crustal and subduction zone earthquakes. *Bulletin of the New Zealand Society for Earthquake Engineering*, **39**(4):1–58.

Power, M., Chiou, B., Abrahamson, N., Bozorgnia, Y., Shantz, T., & Roblee, C. (2008). An Overview of the NGA Project. *Earthquake Spectra*, **24**(1):3–21. doi:10.1193/1.2894833

Rodriguez-Marek, A. (2000). *Near-Fault Seismic Site Response*. University of California, Berkeley.

Rowshandel, B. (2006). Incorporating source rupture characteristics into ground-motion hazard analysis models. *Seismological Research Letters*, **77**(6):708–722.

Rowshandel, B. (2010). Directivity Correction for the Next Generation Attenuation (NGA) Relations. *Earthquake Spectra*, **26**(2):525–559. doi:10.1193/1.3381043

Sehhati, R., Rodriguez-Marek, A., ElGawady, M., & Cofer, W. F. (2011). Effects of near-fault ground motions and equivalent pulses on multi-story structures. *Engineering Structures*, **33**(3):767–779. doi:10.1016/j.engstruct.2010.11.032

Shahi, S. K. (2013, January). *A probabilistic framework to include the effects of near-fault directivity in seismic hazard assessment*. Stanford University, Stanford.

Shahi, S. K., & Baker, J. W. (2011). An empirically calibrated framework for including the effects of near-fault directivity in probabilistic seismic hazard analysis. *Bulletin of the Seismological Society of America*, **101**(2):742–755. doi:10.1785/0120100090

Somerville, P. (1998). Development of An Improved Representation of Near-Fault Ground Motions. In *SMIP98 Seminar on Utilization of Strong-Motion Data* (pp. 1–20). Woodward-Clyde, Pasadena, California.

Somerville, P. G. (2003). Magnitude scaling of the near fault rupture directivity pulse. *Physics of the Earth and Planetary Interiors*, **137**(1-4):201–212. doi:10.1016/S0031-9201(03)00015-3

Somerville, P. G., Smith, N. F., Graves, R. W., & Abrahamson, N. A. (1997). Modification of empirical strong ground motion attenuation relations to include the amplitude and duration effects of rupture directivity. *Seismological Research Letters*, **68**(1):199–222.

Spudich, P., & Chiou, B. S. J. (2008). Directivity in NGA Earthquake Ground Motions: Analysis Using Isochrone Theory. *Earthquake Spectra*, **24**(1):279–298. doi:10.1193/1.2928225

Spudich, P., Chiou, B. S. J., Graves, R. W., Collins, N., & Somerville, P. G. (2004). *A Formulation of Directivity for Earthquake Sources Using Isohrone Theory* (Open-File Report No. 2004-1268). U.S. Geological Survey.

Spudich, P., Watson-Lamprey, J., Somerville, P., Bayless, J., Shahi, S., Baker, J. W., … Chiou, B. (2012). Directivity models produced for the Next Generation Attenuation West 2 (NGA-West 2) project. In *Proceedings of the 15th World Conference on Earthquake Engineering*. Lisbon, Portugal. Retrieved from http://www.stanford.edu/~bakerjw/Publications/Spudich_et_al_(2012)_NGAW2_directivity,_WCEE.pdf

Standards New Zealand. (2004). *NZS1170.5:2004, Structural Design Actions, Part 5: Earthquake actions- New Zealand*. Wellington, New Zealand.

Stirling, M., McVerry, G., Gerstenberger, M., Litchfield, N., Van Dissen, R., Berryman, K., … Jacobs, K. (2012). National Seismic Hazard Model for New Zealand: 2010 Update. *Bulletin of the Seismological Society of America*, *102*(4), 1514–1542. doi:10.1785/0120110170

Tothong, P., Cornell, C. A., & Baker, J. W. (2007). Explicit directivity-pulse inclusion in probabilistic seismic hazard analysis. *Earthquake Spectra*, **23**(4):867–891. doi:10.1193/1.2790487

3 Observed Forward-Directivity Effects in the Canterbury Earthquakes

3.1 Overview

In this chapter, the near-fault ground motions resulting from the 2010-11 Canterbury earthquakes are examined to identify and document evidence of forward-directivity effects. The following events are considered in the present study:

- M_w7.1 Darfield Earthquake (4 September 2010)
- M_w6.2 Christchurch Earthquake (22 February 2011)
- M_w5.3 and M_w6.0 Earthquakes (13 June 2011)
- M_w5.8 and M_w5.9 Earthquakes (23 December 2011)

A wavelet-based pulse classification algorithm developed by Baker (2007) is used to classify pulse-like ground motions. Several important issues in using this stand-alone automated approach are identified and illustrated by means of examples from the Darfield and Christchurch earthquakes. In order to overcome these issues, alternative approaches are proposed and used to correctly identify (in the author's interpretation) forward-directivity characteristics of recorded ground motions. Furthermore, the extracted pulses from the algorithm are characterised in terms of their amplitude and period. In an effort to determine whether improved pulse classifications can be obtained, a more recent wavelet-based pulse classification algorithm developed by Shahi (2013) is also applied to the near-fault ground motions from the two main events (i.e. 4 September 2010 and 22 February 2011). Specific examples are used to make comparisons between the results obtained using both methods. Based on these comparisons, the most appropriate method of pulse classification is identified. Finally, an evaluation of the pulse periods obtained using wavelet analysis and the pseudo-velocity response spectrum is carried out to choose the most suitable method for use in the

assessment of empirical models (in Chapters 5 and 6). Due to the complexity of the causative ruptures in the Canterbury earthquakes, the pulse orientations of the identified forward-directivity ground motions are also examined.

3.2 Near-fault ground motions of the Canterbury earthquakes

As mentioned in Chapter 2, the strong ground motions resulting from the 2010-11 Canterbury earthquakes were well-recorded by the dense array of strong motion instrumentation in Christchurch and the surrounding Canterbury Plains. In order to highlight the importance of these ground motions, Figure 3.1 illustrates the magnitude-distance distribution of recorded ground motions from active shallow crustal earthquakes in New Zealand until 2009. The distribution of ground motions from the 4 September 2010 M_w7.1 Darfield, 22 February 2011 M_w6.2 Christchurch, 13 June 2011 (M_w5.3 and M_w6.0) and 23 December 2011 (M_w5.8 and M_w5.9) earthquakes are also illustrated. It is evident from the figure that prior to the Canterbury earthquakes, the NZ database did not contain ground motion recordings at near-source locations (R_{rup} < 30 km) from moderate-to-large magnitude earthquakes. In addition to the events shown, the database has been further augmented by records from other significant events in the Canterbury earthquake sequence.

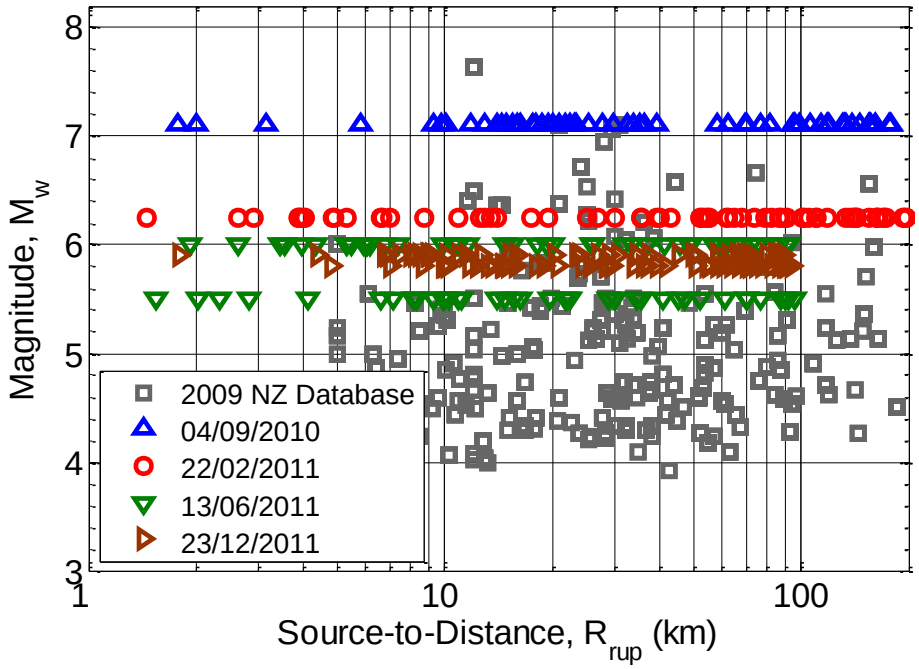

Figure 3.1: Magnitude-distance distribution of ground motions resulting from active shallow crustal earthquakes in the 2009 NZ strong motion database, and in the Canterbury earthquakes (modified from Bradley and Cubrinovski, 2011)

The raw near-fault ground motions (Volume 1 records obtained from GeoNet: www.geonet.org.nz) from the Darfield and Christchurch earthquakes were processed by Bradley (2012) and Bradley & Cubrinovski (2011), respectively, on a record-by-record basis using the approach prescribed by Chiou et al. (2008). This involved applying a low-pass causal Butterworth filter of 50 Hz and a high-pass filter with record-specific corner frequencies (Bradley, 2012). It should be noted that the strong ground motions recorded during the subsequent significant events were also processed using the same approach (Bradley, personal communication, 2013). As a result, reliable estimates of peak ground acceleration (PGA) and spectral ordinates for vibration periods between 0.01 s and 10 s could be obtained.

3.2.1 4 September 2010 M_w7.1 Darfield earthquake

The Canterbury earthquake sequence began with the M_w 7.1 Darfield earthquake, which occurred on 4 September 2010 in the Canterbury Plains. The locations of strong motion stations (SMS) in the near-fault region are illustrated in Figure 3.2 along with the causative fault planes from the finite fault model (FFM) of Holden et al. (2011) previously discussed in Chapter 2. It is worth re-iterating that this model consists of four fault planes: (i) the Charring Cross thrust fault (10 km along-strike); (ii) the Hororata thrust fault (15 km along-strike); (iii) the 10 km western segment of the strike-slip Greendale fault; and (iv) the 30 km central and eastern segment of the strike-slip Greendale fault. The epicentre of this earthquake, also illustrated in Figure 3.2, is located approximately 35 km west of the Christchurch CBD. According to the kinematic source model developed by Holden et al. (2011), the rupture commenced on the Charring Cross fault, followed by bilateral rupture of the eastern and western Greendale fault segments, and ended with the rupture of the Hororata fault. Nonetheless, this earthquake can be treated as a strike-slip event primarily because a majority of the seismic energy was released from the rupture of the 30 km Greendale fault segment (Holden et al., 2011; Beavan et al., 2010). Hence, the strike of this fault segment (85°) has been used herein to obtain the fault-parallel and fault-normal components of horizontal ground motion. However, in order to calculate the source-to-site distance (R_{rup}), all fault planes from the FFM of Holden et al. (2011) were included.

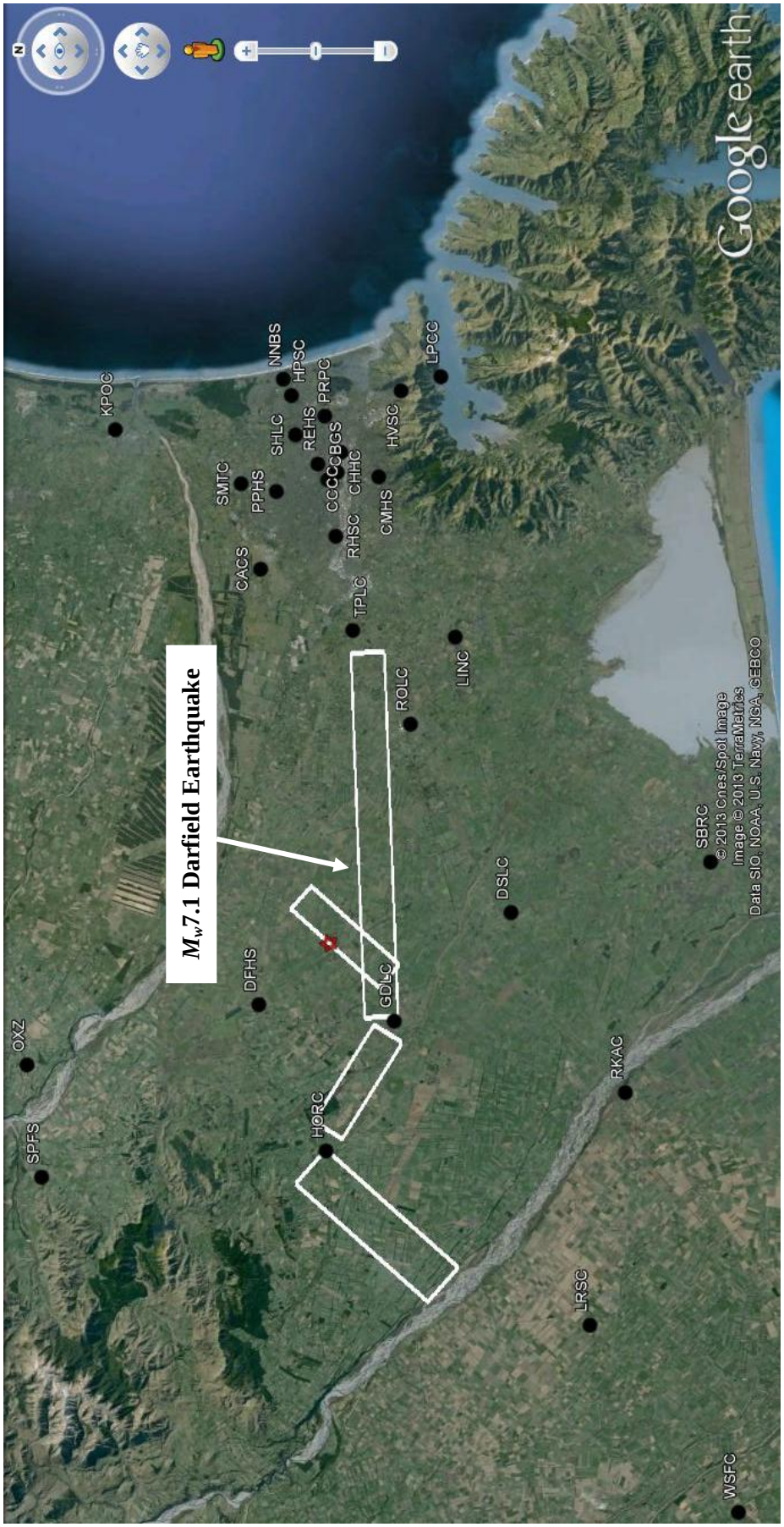

Figure 3.2: Strong motion stations located within 30 km of the causative fault in the 4 September 2010 M_w7.1 Darfield earthquake. Note that the red star denotes the epicentre of the event.

Table 3.1 provides a summary of the ground motions recorded within a source-to-site distance (R_{rup}) of 30km of the Darfield earthquake, including the site class (as defined by the New Zealand seismic design standard, NZS1170.5:2004 (Standards New Zealand, 2004)), peak ground acceleration (PGA), peak ground velocity (PGV), 5-75% significant duration (Ds_{5-75}) and 5-95% significant duration ($Ds_{,5-95}$) (representing the time interval between 5% & 75% and 5% & 95% of the total Arias Intensity, respectively (Kempton & Stewart, 2006)); and peak vertical ground acceleration ($PGA_{vert.}$). It should be noted that the PGA, PGV and significant duration parameters have been calculated for the geometric mean horizontal component, which in this case has been calculated as the geometric mean of the fault-normal and fault-parallel components. It is evident from Table 3.1 that a majority of the strong motion stations are located on deep or soft soil sites in the Canterbury Plains (i.e. Site Class D). The remaining stations include the LPCC station (Site Class B, or rock) in Lyttelton; Heathcote Valley (HVSC) at the base of the Port Hills (Site Class C, or shallow soil); three stations (HPSC, NNBS and PRPC) in the eastern suburbs of Christchurch (Site Class E, or very soft soil); and Kaiapoi (Site Class E). Due to the proximity of the strong motion stations to the causative faults in this earthquake (29, 21 and 7 stations within R_{rup}= 30 km, 20 km and 10 km, respectively), significant ground motion amplitudes were observed in the recorded ground motions. For example, the ground motion recorded at Greendale (GDLC), which is located 0.9 km from the Greendale fault, exhibited geometric mean horizontal peak ground acceleration, peak ground velocity and vertical peak ground acceleration of $PGA = 0.75$ g, $PGV = 109.9$ cm/s and $PGA_{vert} = 1.30$ g, respectively.

Table 3.1: Summary of observed ground motions at near-fault strong motion stations in the 4 September 2010 M_w7.1 Darfield earthquake.

Station Name	Station Code	Site Class	R_{jb}[1] (km)	R_{rup}[2] (km)	PGA (g)	PGV (cm/s)	$D_{s\ 5\text{-}75}$ (s)	$D_{s\ 5\text{-}95}$ (s)	$PGA_{vert.}$ (g)
Canterbury Aero Club	CACS	D	9.8	11.9	0.19	40.4	13.3	33.4	0.30
Christchurch Botanic Gardens	CBGS	D	13.9	14.4	0.16	35.3	10.8	24.9	0.12
Christchurch Cathedral College	CCCC	D	16.0	16.3	0.21	43.3	10.3	23.3	0.19
Christchurch Hospital	CHHC	D	14.5	14.8	0.17	38.3	10.6	23.9	0.15
Cashmere High School	CMHS	D	14.0	14.0	0.24	28.5	8.6	17.3	0.29
Darfield High School	DFHS	D	7.3	9.8	0.48	32.3	13.8	20.9	0.36
Dunsandel School	DSLC	D	9.2	9.3	0.26	54.3	11.5	19.0	0.32
Greendale	GDLC	D	0.3	0.9	0.75	109.9	5.2	12.9	1.30
Hororata School	HORC	D	0.1	1.8	0.49	87.4	6.8	8.5	0.79
Hulverston Drive Pumping Station	HPSC	E	21.1	21.7	0.15	39.4	11.3	22.9	0.14
Heathcote Valley School	HVSC	C	20.8	20.8	0.61	27.3	8.2	15.3	0.31
Kaiapoi North School	KPOC	E	25.9	27.7	0.32	33.7	9.4	19.0	0.09
Lincoln School	LINC	D	5.7	5.8	0.46	89.1	8.0	11.7	0.90
Lyttelton Port	LPCC	B	22.4	22.4	0.29	18.7	7.5	12.1	0.15
Lauriston	LRSC	D	11.3	12.9	0.09	15.8	13.7	24.4	0.10

Station Name	Station Code	Site Class	R_{jb}[1] (km)	R_{rup}[2] (km)	PGA (g)	PGV (cm/s)	$D_{s\ 5\text{-}75}$ (s)	$D_{s\ 5\text{-}95}$ (s)	$PGA_{vert.}$ (g)
North New Brighton School	NNBS	E	22.5	23.2	0.21	36.8	10.4	25.8	0.14
Papanui High School	PPHS	D	14.2	15.4	0.20	49.9	12.2	34.4	0.28
Oxford	OXZ	U*	23.1	23.2	0.14	11.9	17.8	22.9	0.11
Pages Road Pumping Station	PRPC	E	19.0	19.4	0.21	41.9	11.4	22.2	0.32
Christchurch Resthaven	REHS	D	15.3	15.9	0.25	38.8	11.6	26.7	0.22
Riccarton High School	RHSC	D	9.4	10.0	0.20	37.1	9.4	23.8	0.31
Rakaia School	RKAC	D	18.0	18.1	0.17	16.2	12.8	20.6	0.12
Rolleston School	ROLC	D	1.8	2.0	0.39	84.7	6.3	10.5	0.70
Southbridge School	SBRC	D	25.2	25.2	0.17	27.1	13.8	20.3	0.10
Shirley Library	SHLC	D	17.9	18.7	0.19	43.0	11.2	26.6	0.14
Styx Mill Transfer Station	SMTC	D	16.1	17.6	0.17	35.3	12.3	35.8	0.23
Springfield Fire Station	SPFS	D	20.1	20.1	0.18	21.1	15.6	22.3	0.11
Templeton School	TPLC	D	1.8	3.2	0.28	51.3	12.5	24.2	0.94
Westerfield	WSFC	D	29.4	29.7	0.07	10.0	15.2	27.8	0.07

[1] Joyner-Boore distance measured from the surface projection of fault plane to site.

[2] Closest distance from fault plane to site.

[*] Unknown site class

3.2.2 22 February 2011 M_w6.2 Christchurch earthquake

The 22 February 2011 M_w 6.2 earthquake, which occurred directly beneath Christchurch city (with an epicentre located approximately 6 km from the Christchurch central business district (CBD) (Bannister & Gledhill, 2012)) was significantly more devastating than the 4 September 2010 earthquake, both in terms of damage to structures and lifelines as well as number of casualties. As previously discussed in Chapter 2, this event was also characterised by a complex rupture process involving up to three fault planes according to the most recent FFM developed by Beavan et al. (2012). For the purposes of strong ground motion analysis, the one-fault model of Beavan et al. (2011) has been adopted herein. The inferred slip distribution of this model indicates that the Christchurch event was a mix of reverse and right-lateral strike-slip faulting. In addition to the fault plane obtained by Beavan et al. (2011) (with strike and dip angles of 59º and 69º respectively), Figure 3.3 also illustrates the locations of strong motion stations located in the near-fault region.

Table 3.2 provides a summary of the ground motions recorded within a source-to-site distance (R_{rup}) of 30 km in the same manner as Table 3.1 for the Darfield earthquake. The significance of this earthquake is evident with geometric mean horizontal peak ground accelerations and vertical peak ground accelerations as large as 1.30 g and 2.21 g (observed at Heathcote Valley (HVSC)). In order to further elucidate the importance of the ground motions recorded during the Canterbury earthquakes, the largest recorded horizontal PGA in New Zealand prior to the Darfield earthquake was 0.39 g, according to Bradley & Cubrinovski (2011).

Figure 3.3: Strong motion stations located within 30 km of the causative fault in the 22 February 2011 M_w6.2 Christchurch earthquake. Note that the red star denotes the epicentre of the event.

Table 3.2: Summary of observed ground motions at near-fault strong motion stations in the 22 February 2011 M_w6.2 Christchurch earthquake.

Station Name	Station Code	Site Class	R_{jb}[1] (km)	R_{rup}[2] (km)	PGA (g)	PGV (cm/s)	Ds 5-75 (s)	Ds 5-95 (s)	$PGA_{vert.}$ (g)
Canterbury Aero Club	CACS	D	12.9	12.9	0.20	20.2	3.9	12.0	0.19
Christchurch Botanic Gardens	CBGS	D	4.7	4.8	0.56	52.2	4.3	10.2	0.35
Christchurch Cathedral College	CCCC	D	2.7	2.9	0.44	56.7	4.0	9.8	0.79
Christchurch Hospital	CHHC	D	3.8	3.9	0.43	57.0	4.8	10.5	0.62
Cashmere High School	CMHS	D	1.1	1.5	0.37	46.8	3.1	4.8	0.85
Moorehouse Avenue	D06C	D	3.8	3.9	0.26	46.3	5.3	12.0	0.29
Hulverston Drive Pumping Station	HPSC	E	3.9	4.1	0.20	37.4	3.9	10.2	1.03
Heathcote Valley School	HVSC	C	1.3	3.9	1.30	73.2	3.2	5.8	2.21
Kaiapoi North School	KPOC	E	17.5	17.5	0.21	17.3	4.3	11.7	0.06
Lincoln School	LINC	D	13.4	13.5	0.12	13.9	5.7	12.5	0.09
Lyttelton Port	LPCC	B	4.6	7.0	0.90	47.3	1.9	4.1	0.51
Lyttelton Port Naval Point	LPOC	C	4.2	6.6	0.33	57.8	3.4	8.1	0.39
North New Brighton School	NNBS	E	3.9	4.0	0.67	38.8	1.8	2.4	0.80
McQueen's Valley	MQZ	B	12.2	14.0	0.13	7.0	3.0	8.7	0.07
Papanui High School	PPHS	D	8.7	8.8	0.21	37.3	5.9	12.9	0.21

Station Name	Station Code	Site Class	R_{jb}[1] (km)	R_{rup}[2] (km)	PGA (g)	PGV (cm/s)	Ds_{5-75} (s)	Ds_{5-95} (s)	$PGA_{vert.}$ (g)
Pages Road Pumping Station	PRPC	E	2.4	2.6	0.63	59.9	2.5	4.2	1.88
Christchurch Resthaven	REHS	D	4.8	4.9	0.55	76.1	3.8	8.6	0.51
Riccarton High School	RHSC	D	6.6	6.6	0.28	28.8	4.9	9.6	0.19
Rolleston School	ROLC	D	19.5	19.5	0.18	8.4	3.9	10.2	0.08
Shirley Library	SHLC	D	5.2	5.3	0.35	60.7	4.4	6.8	0.49
Selwyn Lake Road	SLRC	D	26.8	26.9	0.09	8.2	5.9	13.1	0.05
Styx Mill Transfer Station	SMTC	D	10.9	10.9	0.17	28.1	5.8	14.0	0.17
Swannanoa School	SWNC	D	25.1	25.2	0.21	12.5	2.7	7.4	0.07
Templeton School	TPLC	D	12.5	12.6	0.11	11.0	6.1	15.3	0.16

[1] Joyner-Boore distance measured from the surface projection of fault plane to site.

[2] Closest distance from fault plane to site.

3.2.3 Other significant events

Following the two main events discussed previously, the Canterbury region experienced several other significant earthquake events. In fact, since the Darfield earthquake, the Canterbury earthquake sequence has produced 2 events greater than M_w6.0, 11 events between 5.0 < M_w < 6.0, and 134 events between 4.0 < M_w < 5.0 (Cubrinovski et al., 2012). The ground motions resulting from four significant events following the 22 February, 2011 M_w6.2 Christchurch earthquake were also well-recorded by the strong motion instrumentation in Christchurch city and its suburbs. These include the two events which occurred on 13 June, 2011 approximately 80 minutes apart with magnitudes of M_w5.3 and M_w 6.0, respectively; as well as the M_w 5.8 and M_w 5.9 events which occurred on 23 December, 2011. In addition to the two main events, the present study also aims to investigate whether the ground motions resulting from these other events demonstrated evidence of significant forward-directivity effects.

3.2.3.1 13 June 2011 earthquakes

The two significant events which occurred on 13 June 2011 originated within close proximity to the suburbs located east of the Christchurch CBD along the Avon River (Avonside, Avondale, Bexley, Burwood and Dallington). These areas are founded on loose fluvial deposits with clean and fines-containing sands (Cubrinovski et al., 2012) and were subjected to significant levels of shaking (e.g. horizontal peak ground accelerations reached 2 g in Sumner and 0.4 g in the Christchurch CBD (Bannister & Gledhill, 2012)), thereby resulting in widespread liquefaction. It is pertinent to note that the eastern suburbs were also severely affected by liquefaction immediately following the Darfield and Christchurch earthquakes. In addition, the two June events caused further damage to weakened structures and infrastructure throughout the city in general.

Although a FFM has not been explicitly developed for the M_w 5.3 event (which occurred first), the regional moment tensor solution indicates a strike-slip faulting mechanism (GeoNet, 2011). Using this solution and the empirical M_w-A (moment magnitude-faulting area) scaling relationship developed by Berryman et al. (as cited in Stirling et al., 2007), the geometry of the finite fault plane was calculated. This allowed for a first-order computation of source-to-site distances in addition to a visual appreciation of the location and size of the faulting area. The finite-fault model developed by Beavan et al. (2012) for the subsequent M_w6.0 event indicates both onshore and offshore faulting. Figure 3.4 illustrates the surface projection of the finite fault planes for both events. It can be observed that the simplified finite fault (with strike and dip angles of 69° and 78°, respectively) developed for the first event (shown in white) is located in a similar position to the causative fault planes in the second event (shown in black). The modelled fault planes for the latter event include a left-lateral strike-slip fault (with strike and dip angles of 153º and 56º, respectively) and an oblique (reverse/right-lateral) fault (with strike and dip angles of 69º and 78º, respectively). Also shown in the figure are the strong motion stations located in the near-fault region and a summary of the ground motions resulting from the two events is provided in Appendix A.

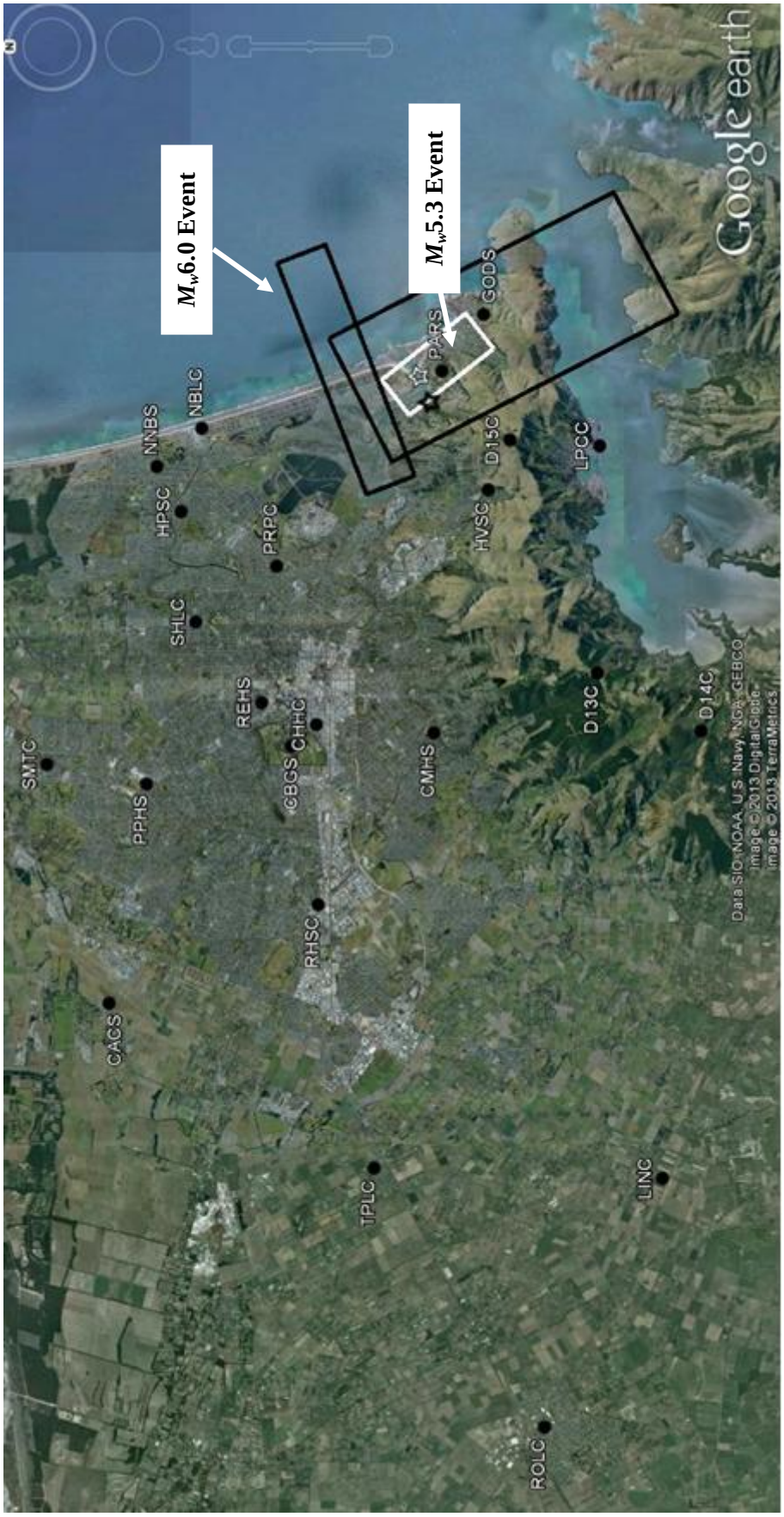

Figure 3.4: Strong motion stations located within 30 km of the causative faults in the 13 June 2011 events. Note that the stars denote the epicentre of each event. The M_w6.0 event is considered to be comprised of two fault planes

3.2.3.2 23 December 2011 earthquakes

On 23 December 2011, a series of 11 moderate magnitude earthquakes struck off the coast of New Brighton (20 km east of Christchurch (Ristau et al., 2013)) over a period of five hours. As previously mentioned, the two largest events had moment magnitudes of 5.8 and 5.9 respectively, and occurred approximately 90 minutes apart. Although these events did not cause notable structural damage relative to previous events, the suburbs located east of the Christchurch CBD experienced a recurrence of liquefaction due to their proximity to the earthquake source and susceptible nature of the soft sedimentary soils. In the CBD, horizontal peak ground accelerations ranged between 0.2-0.4 g, which are comparable to those observed during the M_w6.0 June and M_w7.1 Darfield earthquakes, but significantly lower than the values observed during the M_w6.2 Christchurch earthquake (Ristau et al., 2013). Vertical ground accelerations up to 0.96 g were observed at New Brighton Library (NBLC) in the M_w5.8 event. The regional moment tensor solution (GeoNet, 2011) of the first event indicates a reverse-faulting mechanism. This solution was combined with the M_w-A (magnitude-faulting area) scaling relationship of Berryman et al. (as cited in Stirling et al., 2007) to obtain the finite fault plane (with strike and dip angles of 45º and 63º, respectively) illustrated in Figure 3.5. Based on the available onshore displacement data, Beavan et al. (2012) developed a FFM for the second event, which is also illustrated in Figure 3.5. The inferred slip distribution (Beavan et al. 2012, Figure 3O) indicates largely reverse faulting, especially on the eastern extent of the fault plane (with strike and dip angles of 60° and 69°, respectively), where the largest slip occurred. Similar to the aforementioned 13 June 2011 events, a summary of the near-fault ground motions resulting from these December events is provided in Appendix A.

For the purposes of further reference, the three-component acceleration time-series and velocity time-series; horizontal velocity trajectory plots; pseudo-acceleration and pseudo-velocity response spectra corresponding to the fault-parallel, fault-normal and geometric mean horizontal components; and Husid plots, showing the build-up of Arias intensity of the fault-parallel and fault-normal components of ground motion with time; are provided in Appendices B and C for the two main events (i.e. M_w7.1 Darfield and M_w6.2 Christchurch earthquakes) in the Canterbury earthquake sequence, respectively.

Figure 3.5: Strong motion stations located within 30 km of the causative faults in the 23 December 2011 events. Note that the stars denote the epicentre of each event.

3.3 Identification and characteristics of forward-directivity ground motions

Previous documentation of observed forward-directivity in near-fault ground motions recorded during the Canterbury earthquakes (Bradley, 2012; Bradley & Cubrinovski, 2011) has largely been based on qualitative visual evidence, i.e. the presence of a pulse-like feature in the fault-normal velocity time-series as well as the preferred direction taken by the horizontal velocity trajectory (polar plot). Moreover, these investigative efforts have excluded other significant events (e.g. June 13, 2011 and December 23, 2011), which took place during the Canterbury earthquake sequence. Hence, it is important to rigorously evaluate these ground motions using quantitative approaches which supposedly minimise subjectivity issues associated with qualitative approaches. The following sections summarise the results obtained using the wavelet-based pulse classification algorithms of Baker (2007) and Shahi (2013) in identifying ground motions exhibiting pulse-like characteristics due to forward-directivity effects. These methods are subsequently assessed by comparing their relative performance in accurately characterising pulse-like ground motions.

3.3.1 Baker (2007) pulse classification algorithm

In order to assist in the quantification of forward-directivity effects, Baker (2007) (referred to herein as the B07 algorithm) developed an automated pulse classification algorithm which identifies pulse-like ground motions. Because the details of this method are covered extensively in Chapter 2, they are not repeated in this section and only the application of this method is discussed. However, it is worth repeating that the algorithm utilises wavelet analysis to extract the main pulse-like feature from a given component of the velocity time-series. Subsequently, a pulse indicator (PI) score, indicating the likelihood that a ground motion record is pulse-like, is calculated based on the PGV and energy (represented by the cumulative squared velocity) associated with the residual record (i.e. the original ground motion with the extracted pulse removed) and the original record (Baker, 2007). A high PI score (≥ 0.85) generally indicates a pulse-like record whereas a score of 0.15 or less indicates a non-pulse like record. The period of the extracted pulse is defined as the period at which the maximum Fourier amplitude is reached. In order to determine whether the ground motion is pulse-like due to significant forward-directivity effects, Baker (2007) proposed the

following two additional criteria: (i) the PGV of the ground motion record must be greater than 30 cm/s; and (ii) the pulse must arrive early in the velocity time-series, as indicated by the criterion developed using the cumulative squared velocity of the extracted pulse and original record (refer to Section 2.4.1 in Chapter 2).

3.3.1.1 4 September 2010 M_w7.1 Darfield earthquake

The results obtained using the B07 algorithm in identifying pulse-like ground motions from the Darfield earthquake are summarised in Table 3.3, including the peak ground velocity (PGV) of the original ground motion, pulse period (T_p), and pulse indicator score. It can be observed that only 5 out of 29 ground motions are classified as pulse-like by the automated classification method. Figure 3.6 shows the wavelet analysis procedure applied to the ground motions recorded at CBGS, DSLC, LINC, ROLC and TPLC. There is clear evidence of an early arriving directivity pulse in each case as highlighted in the original fault-normal velocity time-series. However, in the case of CBGS and TPLC, the ground motions are characterised as being pulse-like for arguably physically inappropriate reasons. In the two cases respectively, the algorithm extracts the half-cycle following the directivity pulse which is related to wave scattering (Bradley, 2012); and the second cycle of ground motion associated with basin-generated surface waves effects, which has a larger amplitude in comparison to the initial directivity pulse. In contrast, the ground motions observed at DSLC, LINC and ROLC are dominated by the directivity pulse and are hence classified as pulse-like by the B07 algorithm for a physically appropriate reason.

Table 3.3: Summary of the results obtained using the automated Baker (2007) pulse classification algorithm in identifying pulse-like ground motions from the M_w7.1 Darfield earthquake.

Station	PGV (cm/s)	Pulse Period, T_p (s)	Pulse Indicator Score	Late Arrival	Pulse-Like Motion
CACS	48.1	8.3	0.74	No	No
CBGS	62.0	9.9	0.93	No	Yes
CCCC	74.2	3.5	0.83	No	No
CHHC	70.6	3.7	0.12	No	No
CMHS	42.2	3.0	0.05	No	No
DFHS	29.4	5.0	0.00	No	No
DSLC	54.3	8.1	1.00	No	Yes
GDLC	119.0	6.3	0.36	Yes	No
HORC	83.1	9.2	0.06	Yes	No
HPSC	50.4	9.3	0.01	Yes	No
HVSC	28.9	10.0	0.02	Yes	No
KPOC	37.2	8.8	0.07	Yes	No
LINC	109.1	7.2	1.00	No	Yes
LPCC	20.6	10.2	0.62	No	No
LRSC	20.0	6.1	0.01	Yes	No
NNBS	48.3	6.9	0.72	No	No
OXZ	2.7	1.4	0.00	Yes	No
PPHS	72.9	8.9	0.59	No	No
PRPC	64.6	3.9	0.66	No	No
REHS	68.2	7.5	0.65	No	No
RHSC	56.3	9.8	0.91	Yes	No
RKAC	13.0	5.4	0.00	Yes	No
ROLC	107.9	7.2	1.00	No	Yes
SBRC	24.2	6.9	1.00	No	No
SHLC	58.2	7.2	0.75	No	No
SMTC	43.7	9.0	0.32	No	No
SPFS	20.7	1.1	0.02	Yes	No
TPLC	78.0	8.6	1.00	No	Yes
WSFC	8.8	11.1	0.12	No	No

(a)

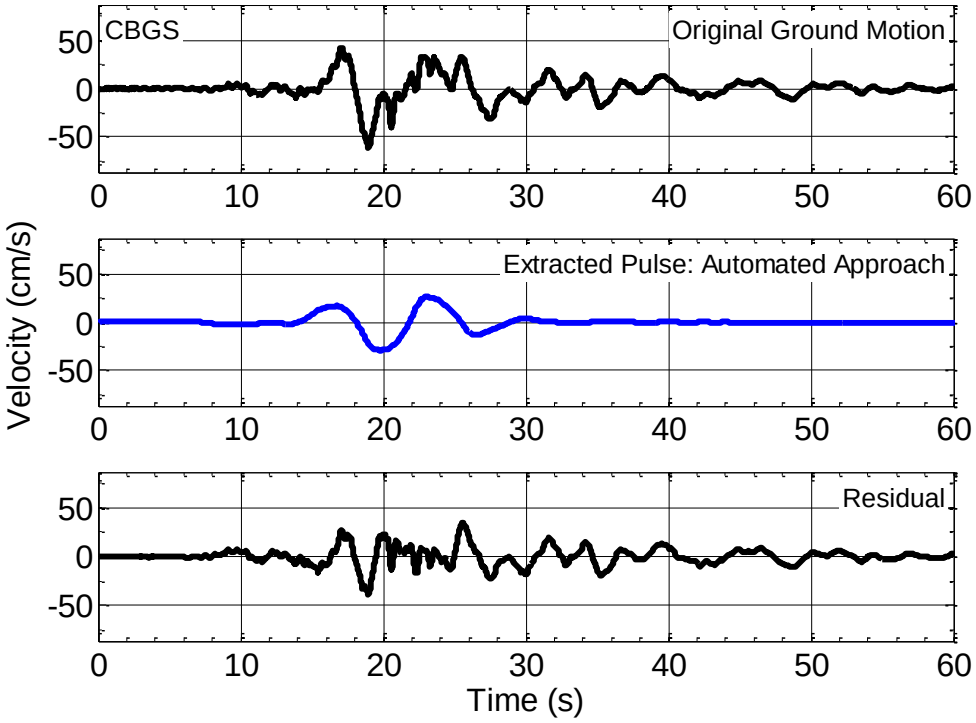
CBGS
Original Ground Motion
Extracted Pulse: Automated Approach
Residual
Velocity (cm/s)
Time (s)

(b)

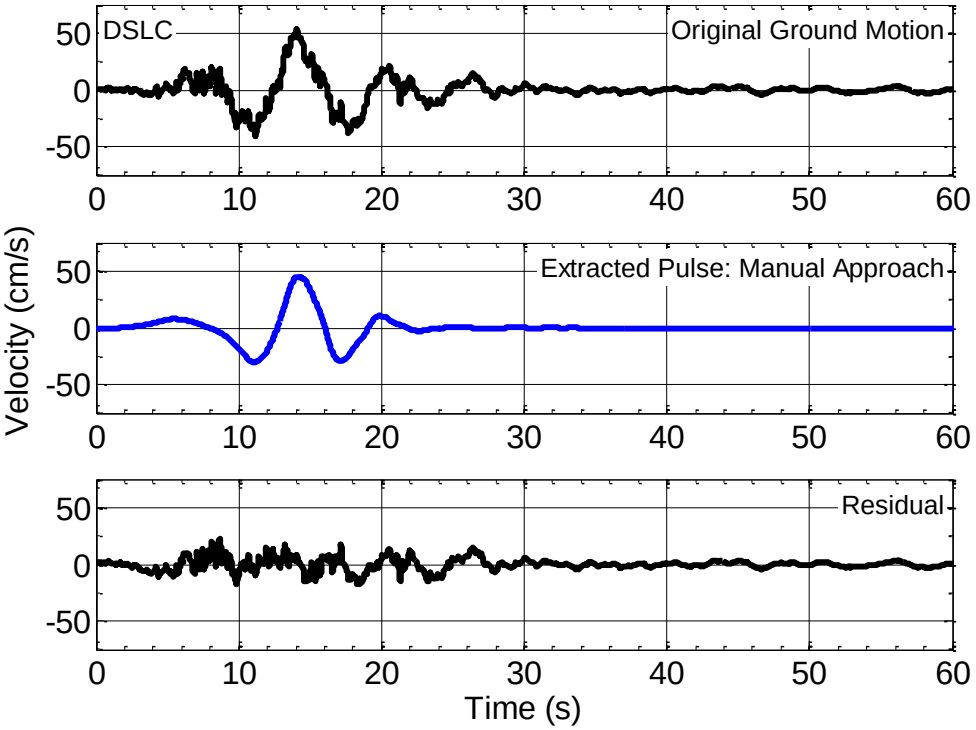
DSLC
Original Ground Motion
Extracted Pulse: Manual Approach
Residual
Velocity (cm/s)
Time (s)

(c)

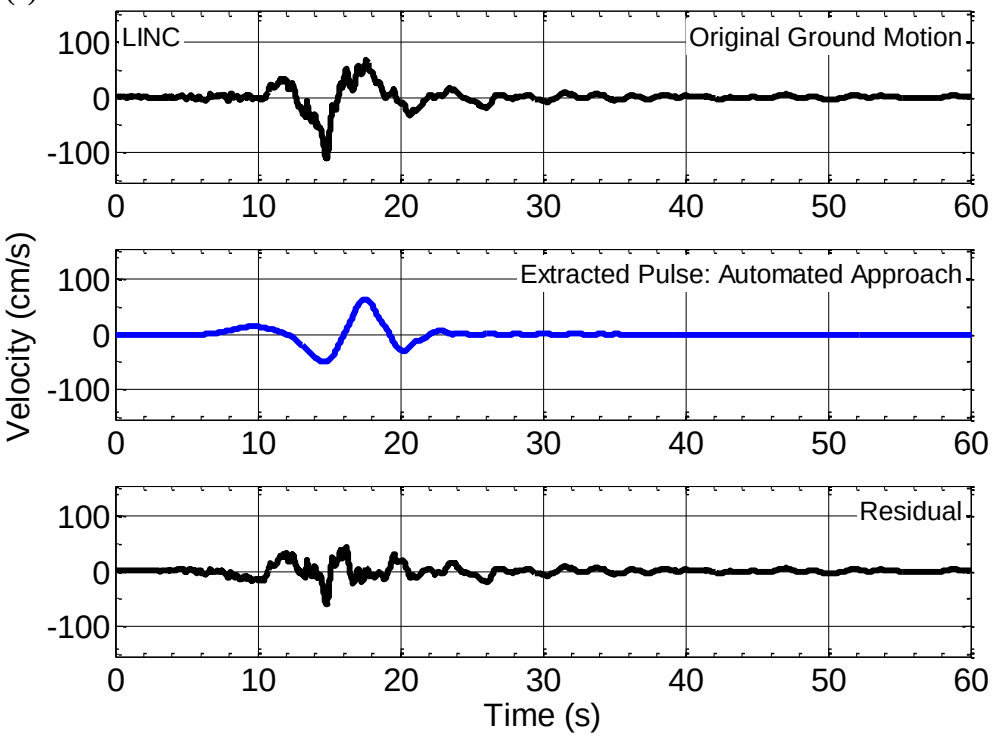
LINC
Original Ground Motion
Extracted Pulse: Automated Approach
Residual
Velocity (cm/s)
Time (s)
100
0
-100
0
10
20
30
40
50
60

(d)

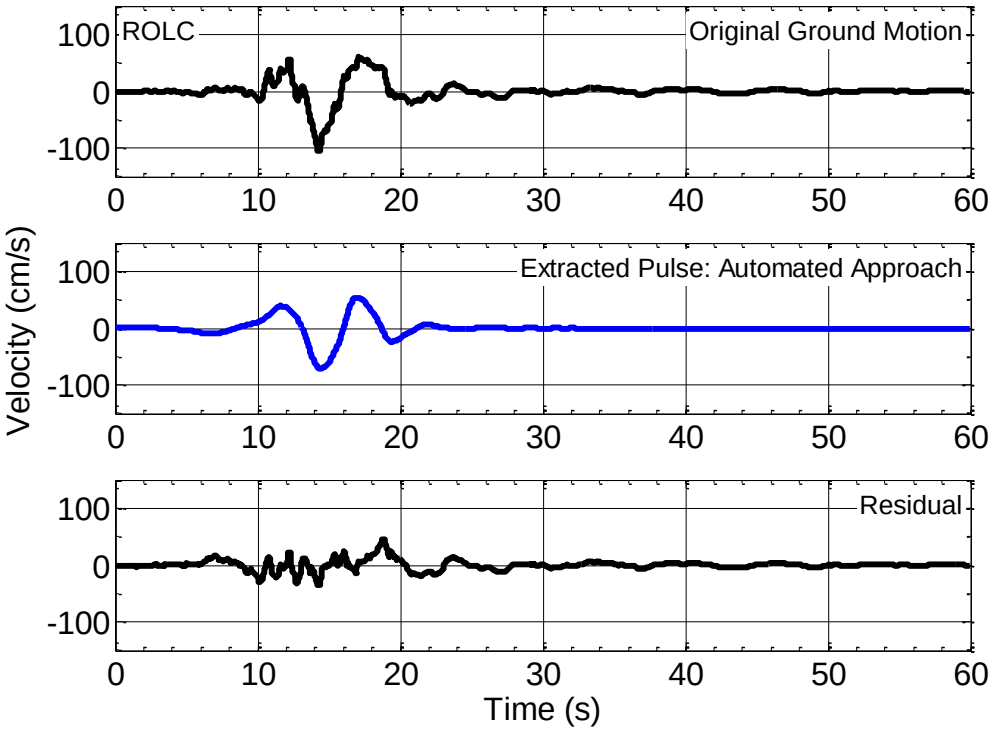
ROLC
Original Ground Motion
Extracted Pulse: Automated Approach
Residual
Velocity (cm/s)
Time (s)
100
0
-100
0
10
20
30
40
50
60

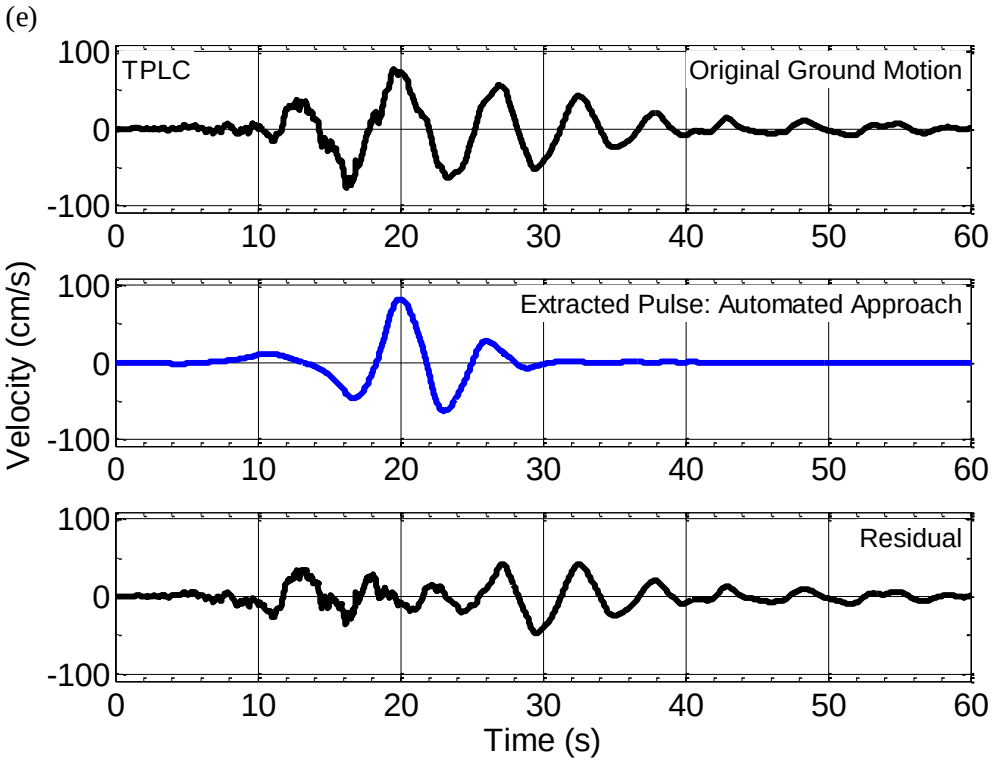

Figure 3.6: Ground motions observed at: (a) CBGS; (b) DSLC; (c) LINC; (d) ROLC; and (e) TPLC in the 4 September 2010 M_w7.1 Darfield earthquake, and identified as pulse-like using the automated Baker (2007) pulse classification algorithm.

In order to scrutinise the results obtained using the B07 algorithm in Table 3.3, the velocity time-series and polar plots of the two orthogonal components of all near-fault ground motions (fault-parallel and fault-normal) were subsequently examined on a case-by-case basis. The polar plots have also been included in Appendix B for further reference. This examination provided clear evidence of an early-arriving pulse in numerous ground motions with strong polarity in the fault-normal direction. Furthermore, the source-to-site geometry in each case also supported the above evidence.

In an effort to ensure correct pulse extraction from the original ground motion, a so-called 'manual' approach was adopted by slightly modifying the standard B07 algorithm. The ground motion recorded at TPLC is used to illustrate the use of the modified B07 algorithm in Figure 3.7. As shown previously in Figure 3.6, the automated algorithm incorrectly extracted the second predominant cycle associated with basin-induced surface wave effects. In order to overcome this limitation, a manual cut-off is applied at 18 s, as highlighted by the solid blue line in the original velocity time-series. In this manner, the algorithm is forced to extract the principal directivity pulse, which is subsequently analysed to determine whether

the ground motion is pulse-like. Thus, this example illustrates that additional criteria maybe required in the Baker (2007) algorithm in order to ensure that significant basin-induced surface waves are not incorrectly extracted.

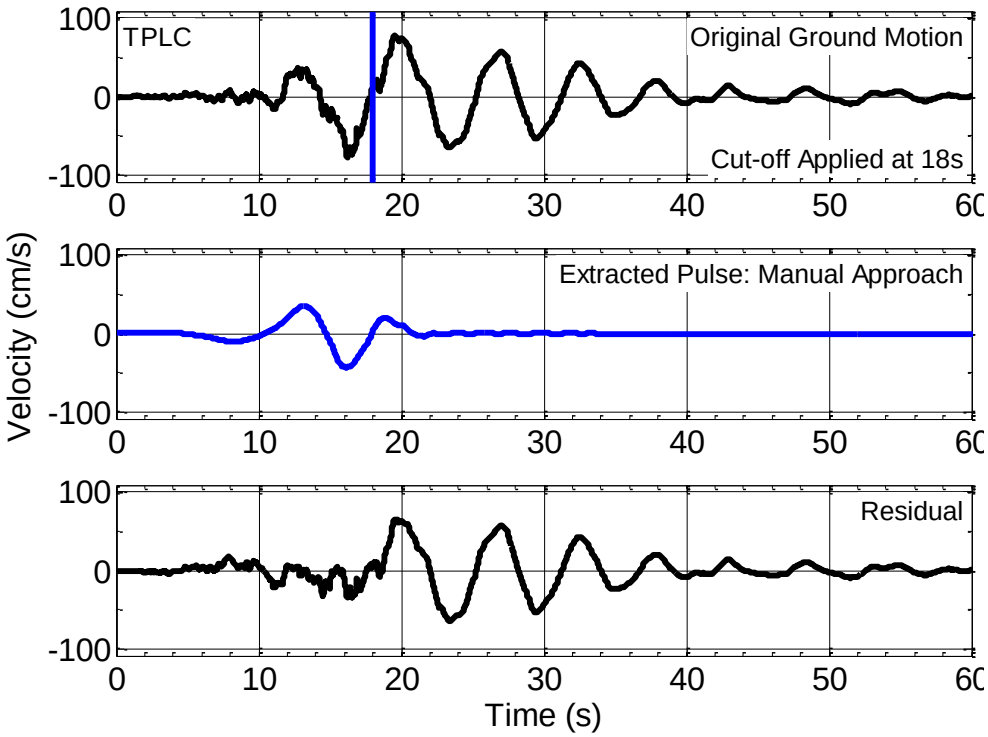

Figure 3.7: Illustration of the 'manual' approach applied to the ground motion recorded at TPLC in the 4 September 2010 M_w7.1 Darfield earthquake using the Baker (2007) pulse classification algorithm.

The pulse indicator (PI) score in the B07 algorithm as mentioned in Chapter 2 is repeated below in Equation (3.1):

$$PI = \frac{1}{1 + e^{-23.3 + 14.6(PGV\ Ratio) + 20.5(Energy\ Ratio)}} \tag{3.1}$$

From the logistic regression equation above, it is clear that the PI score is strongly dependent on the ratio of the PGV and energy (represented by the cumulative squared velocity) of the residual and original velocity time-series. It is also evident from the ground motion recorded at TPLC in Figure 3.6 that the automated algorithm cannot decipher between the directivity pulse and large amplitude ground motions associated with basin-induced surface waves. Although correct pulse extraction and characterisation (i.e. pulse period and amplitude) can be ensured using the manual approach in such cases (refer to Figure 3.7), the calculated PI score is usually extremely low. For example, the PI score using the automated and manual

approaches for the TPLC case is 1.00 and 0.01, respectively. This can be attributed to the relatively higher PGV and energy ratios in the latter case (0.85 and 0.76 respectively) compared to the former case (0.61 and 0.36 respectively) due to the presence of several cycles of large amplitude ground motion in the residual record. Hence, it is clear that the PI score alone is an ineffective classification measure for ground motions where the initial directivity pulse is followed by cycles of long period significant ground motion caused by other physical phenomena. It should also be noted that this aspect of the ground motions observed in the Canterbury earthquakes is not a common characteristic in other ground motions which have been documented as having significant forward-directivity, and hence it is not unexpected that the B07 approach does not work well without modification in such cases.

In addition to the ground motion recorded at TPLC, the 'manual' approach was applied to 11 other ground motions from the Darfield event for which the automated approach was deemed to give undesirable results, as illustrated in Figure 3.8. Although these ground motions have significant directivity pulses (i.e. peak ground velocities > 30 cm/s) which arrive early in the record, the PI scores of all but two (CBGS and NNBS) are below the threshold of 0.85 for reasons discussed above. As a result, these ground motions are still considered non-pulse-like by the algorithm and further highlight the limitations of the PI score as a sole classification metric. Nonetheless, based on the aforementioned visual examination of the velocity time-series, polar plots and source-to-site geometry, the remaining 9 ground motions were classified as pulse-like. Hence, these examples serve to illustrate the importance of user judgement in identifying ground motions exhibiting forward-directivity effects.

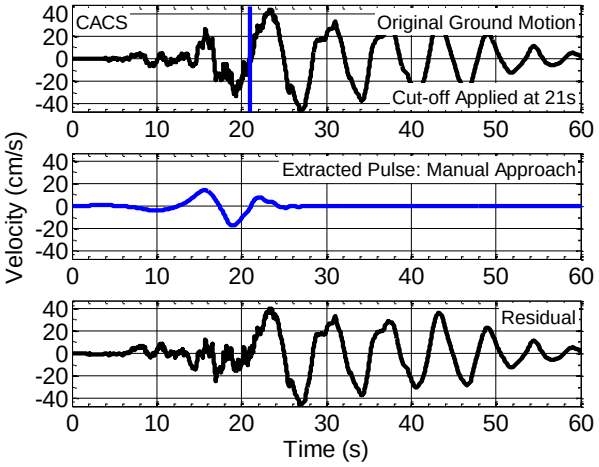
CACS
Original Ground Motion
Cut-off Applied at 21s
Extracted Pulse: Manual Approach
Residual
Velocity (cm/s)
Time (s)

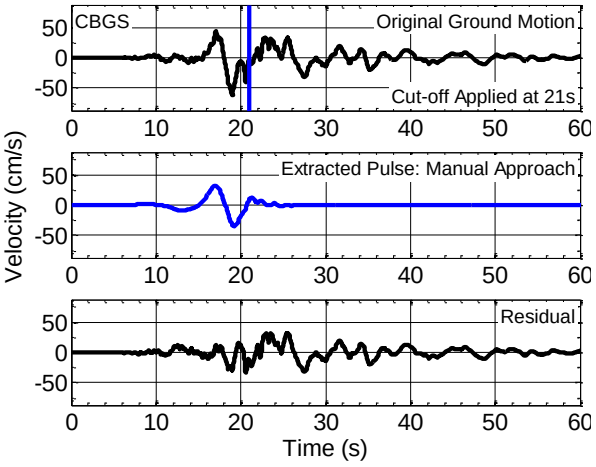
CBGS
Original Ground Motion
Cut-off Applied at 21s
Extracted Pulse: Manual Approach
Residual
Velocity (cm/s)
Time (s)

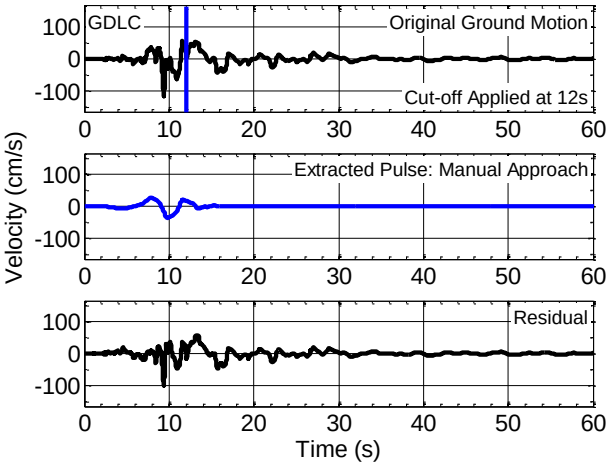
GDLC
Original Ground Motion
Cut-off Applied at 12s
Extracted Pulse: Manual Approach
Residual
Velocity (cm/s)
Time (s)

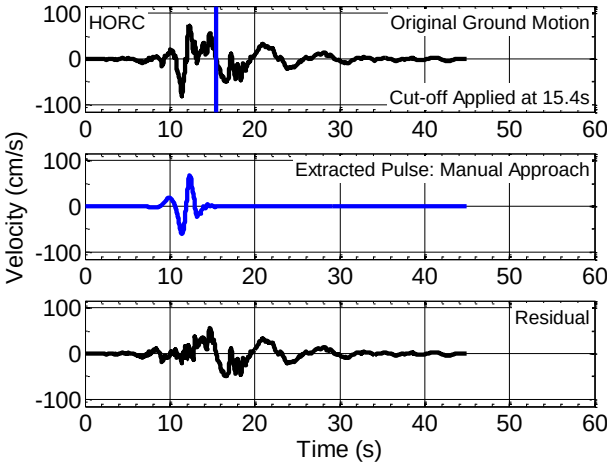
HORC
Original Ground Motion
Cut-off Applied at 15.4s
Extracted Pulse: Manual Approach
Residual
Velocity (cm/s)
Time (s)

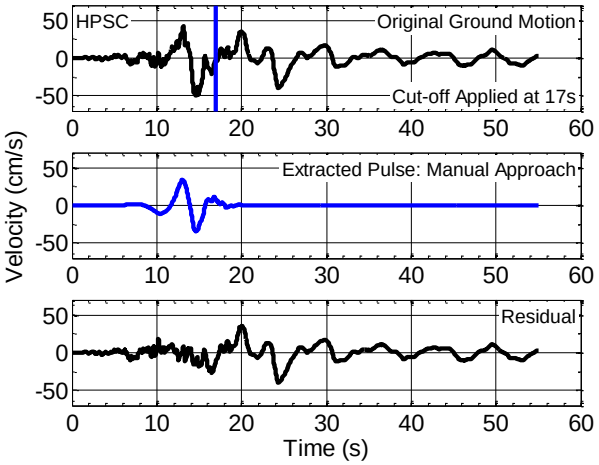
HPSC
Original Ground Motion
Cut-off Applied at 17s
Extracted Pulse: Manual Approach
Residual
Velocity (cm/s)
Time (s)

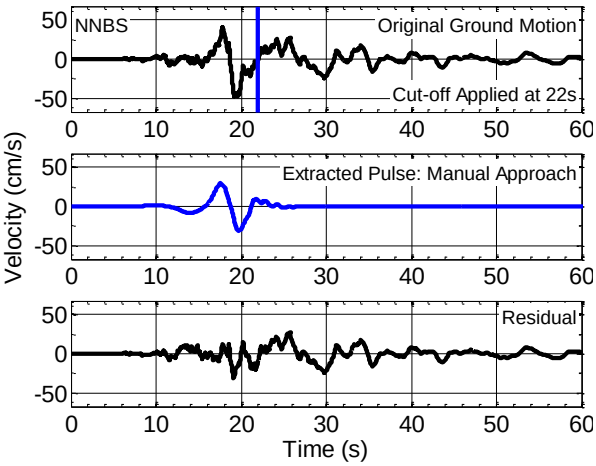
NNBS
Original Ground Motion
Cut-off Applied at 22s
Extracted Pulse: Manual Approach
Residual
Velocity (cm/s)
Time (s)

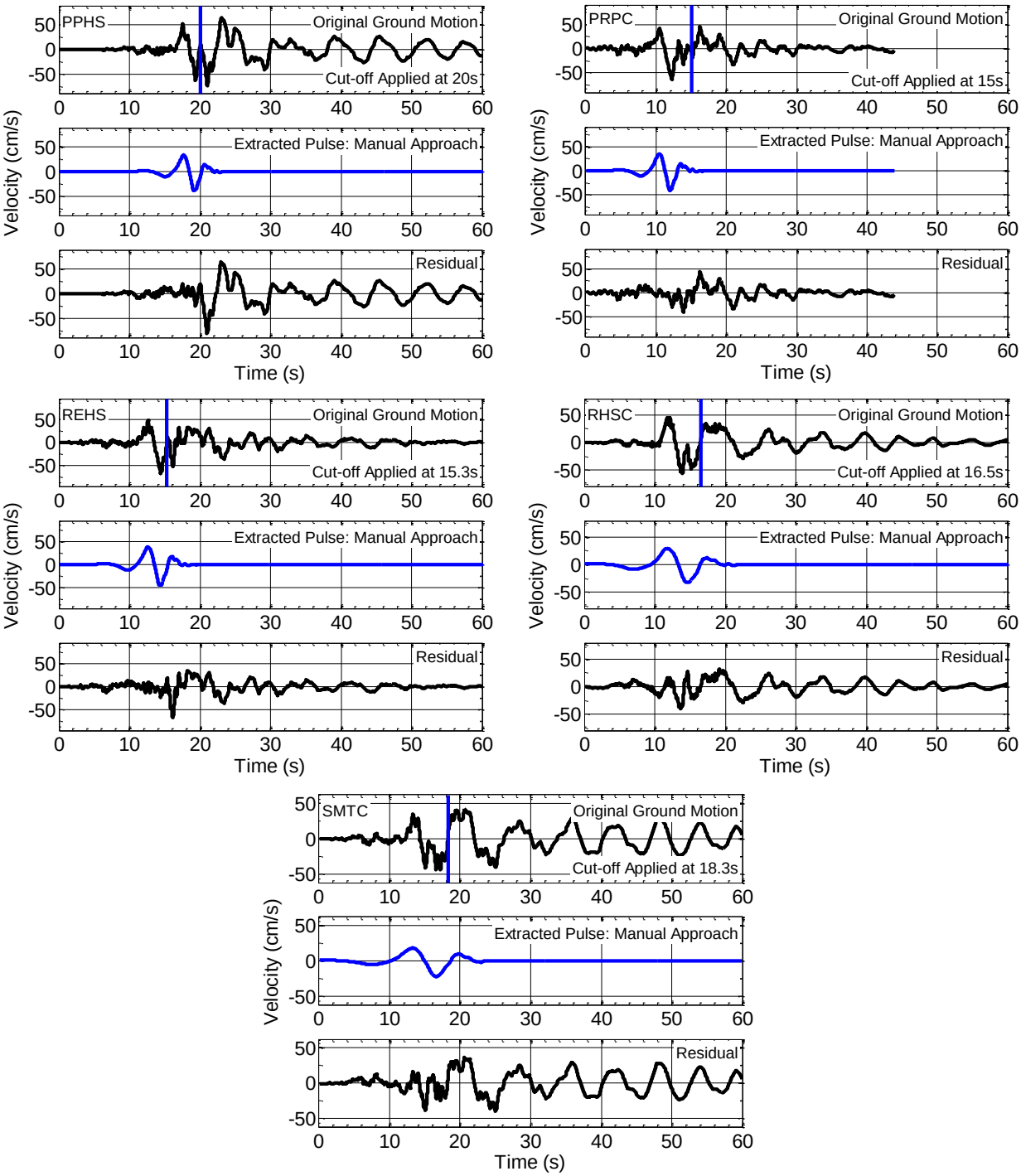

Figure 3.8: Illustration of the 'manual' approach applied to ground motions from the 4 September 2010 M_w7.1 Darfield earthquake using the Baker (2007) pulse classification algorithm, with a manual 'cut-off' to ensure appropriate pulse extraction.

Another identified limitation of the B07 algorithm is illustrated in Figure 3.9, which shows the fault-normal velocity time-series at four near-fault stations with significant forward-directivity effects, but were identified as non-pulse-like by the algorithm (because PI < 0.85) despite correct extraction of the directivity pulse. These are clearly cases of false-negative classification (i.e. pulse-like ground motions identified as non-pulse-like) and hence rely on qualitative judgement. In particular, the ground motions recorded at CHHC and CMHS are misclassified due to their low PI scores, whereas the CCCC and SHLC ground motions marginally fall short of the pulse classification threshold, with scores of 0.83 and 0.75, respectively.

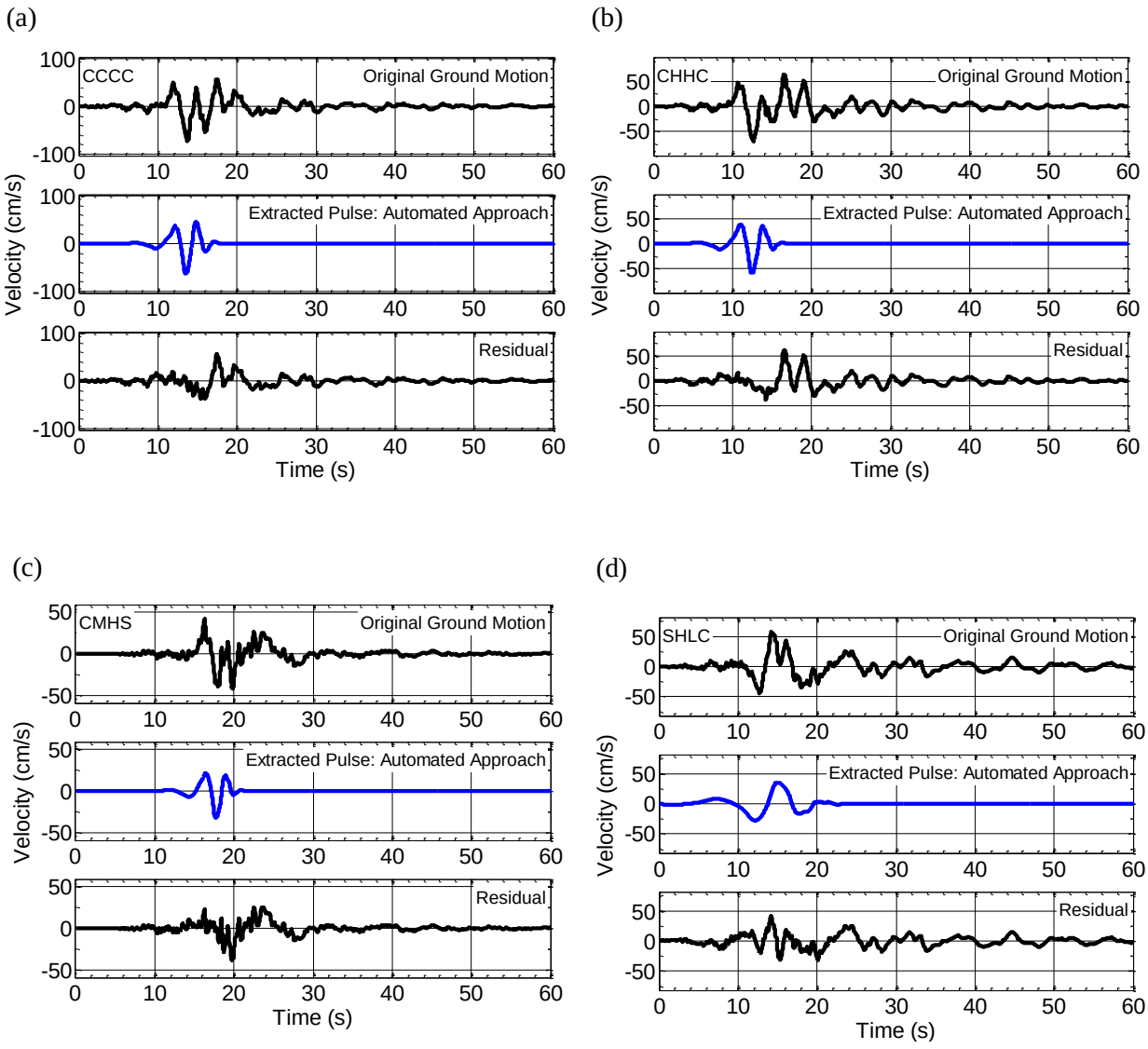

Figure 3.9: Examples of false-negative classifications from the 4 September 2010 M_w7.1 Darfield earthquake obtained using the Baker (2007) pulse classification algorithm.

Figure 3.10 illustrates the application of the wavelet analysis procedure to three ground motions (SBRC, HVSC and LPCC) which are classified as non-pulse-like by the B07 algorithm because their corresponding PGVs are lower than the threshold value of 30 cm/s. In classifying pulse-like ground motions, Baker (2007) assumed that velocity pulses with PGVs less than 30 cm/s do not possess any engineering significance. In order to understand the spatial distribution of forward directivity velocity pulses, it is however instructive to neglect this threshold. The aforementioned ground motions, which all feature an early-arriving directivity pulse, were manually classified as pulse-like as a result.

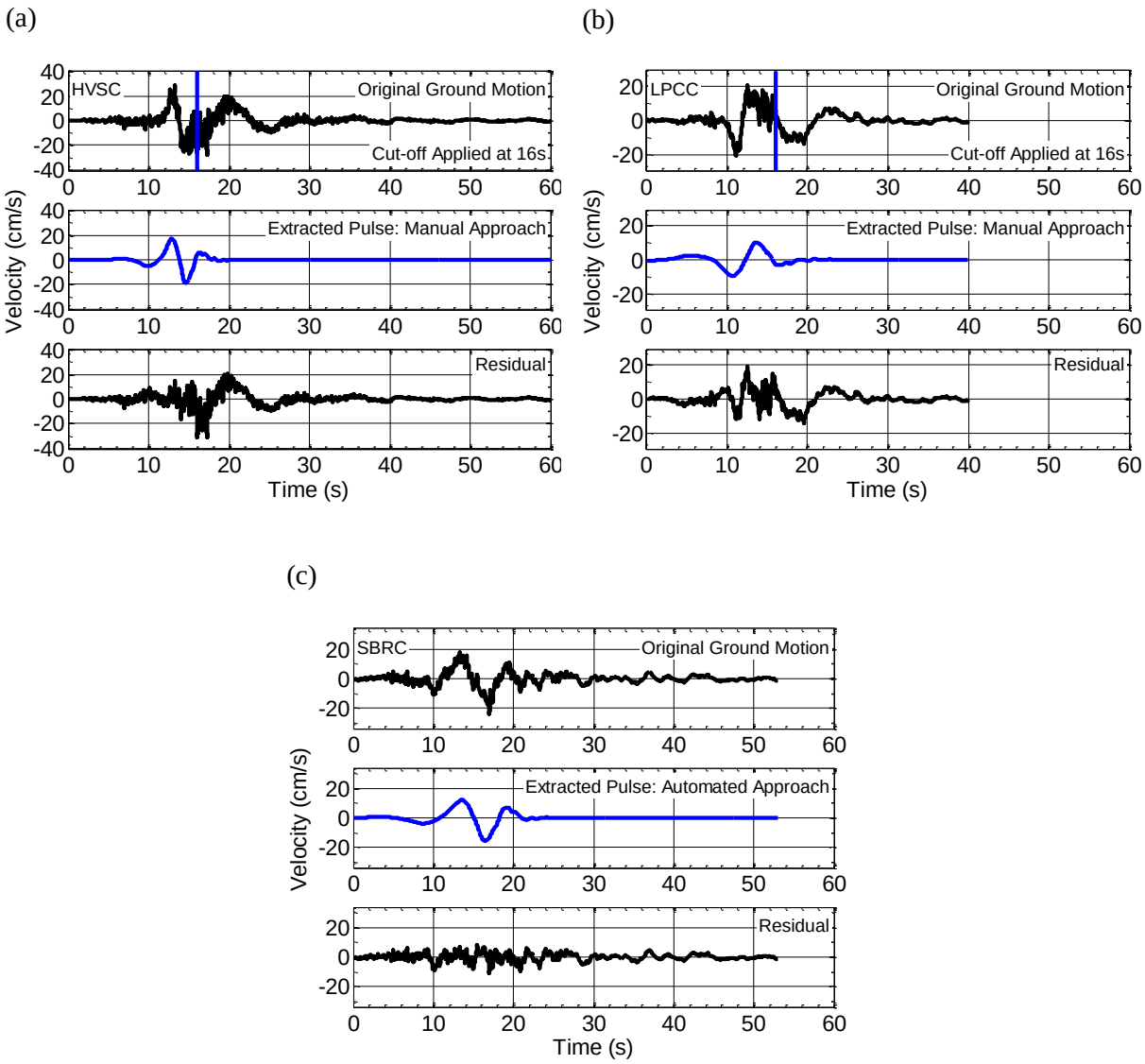

Figure 3.10: Illustration of the wavelet analysis procedure applied to pulse-like ground motions observed at (a) HVSC; (b) LPCC; and (c) SBRC in the 4 September 2010 M_w7.1 Darfield earthquake. Note that these ground motions were classified as non-pulse-like by the B07 algorithm because their PGVs are lower than the threshold of 30 cm/s.

Upon analysing the orthogonal components of the velocity time-series (i.e. fault-parallel and fault-normal) of all near-fault ground motions recorded in the Darfield earthquake, a clear difference between the characteristics of forward-directivity was observed at locations to the east of the causative faults in relation to locations near the central and western segments of the Greendale fault. In order to illustrate this difference, Figure 3.11 compares the orthogonal components of ground motion recorded at LINC and ROLC with those recorded at HORC and GDLC (refer to Figure 3.2 for the location of these recording stations). The PGVs associated with the directivity pulse in the fault-normal component at LINC and ROLC exceed 100 cm/s compared with approximately 60 cm/s in the fault-parallel component. This is consistent with the large amount of slip along the central and eastern portion of the Greendale fault, which ruptured towards the east in a predominantly strike-slip mechanism (Holden et al., 2011; Beavan et al., 2010).

In contrast to the observations at LINC and ROLC, the PGVs observed at HORC and GDLC in the two orthogonal components are comparable to each other. According to Bradley (2012), the different strike of the western segment of the Greendale fault, which ruptured towards HORC results in evidence of directivity in the fault-parallel component (corresponding to the strike of the central segment). Furthermore, due to the rupture directivity of the Hororata blind thrust fault (which ruptured after the Greendale fault), a velocity pulse is observed in the fault-parallel component (approximately between t = 14 s and t = 19 s) with an amplitude of approximately 90 cm/s. The location of the GDLC station near the mid-point of the Greendale fault results in another complex situation as illustrated in Figure 3.11. From the finite-fault model developed by Holden et al. (2011), it is inferred that the observed ground motion at this location is significantly influenced by the significant up-dip rupture of the Charring Cross fault, in addition to the subsequent rupture of the Greendale fault. This explains the previously mentioned large amplitude velocity pulses in both orthogonal components. It is also important to note that the amplitude of these pulses was further augmented by liquefaction effects, as inferred by Bradley (2012) from the 'spikes' in the acceleration time-series, which are indicative of cyclic mobility. This phenomenon occurs when the underlying soil layers experience large shear strain amplitudes during strong earthquake shaking, thereby resulting in a significant increase of the soil shear stiffness and subsequent propagation of high frequency ground motion (Bradley, 2012), as shown in Figure 3.12. Evidence of cyclic mobility can be clearly observed in both horizontal

components of the acceleration time-series recorded at GDLC from t = 11 s onwards. Hence, it is clear that the velocity pulses observed at this location occurred due to a combination of source and site effects.

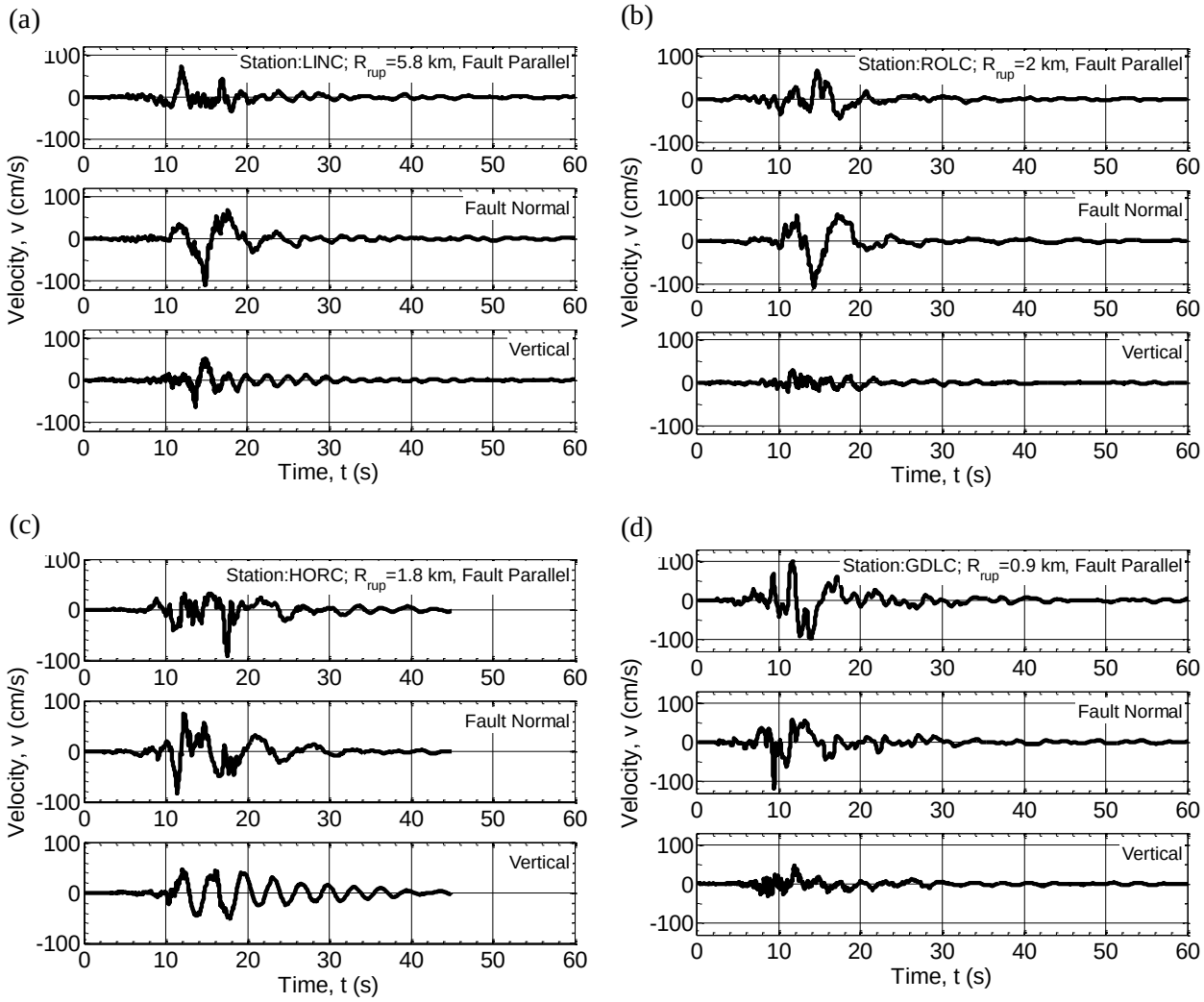

Figure 3.11: Comparison of the characteristics of forward-directivity observed at: (a) LINC; (b) ROLC; (c) HORC; and (d) GDLC in the 4 September 2010 M_w7.1 Darfield earthquake.

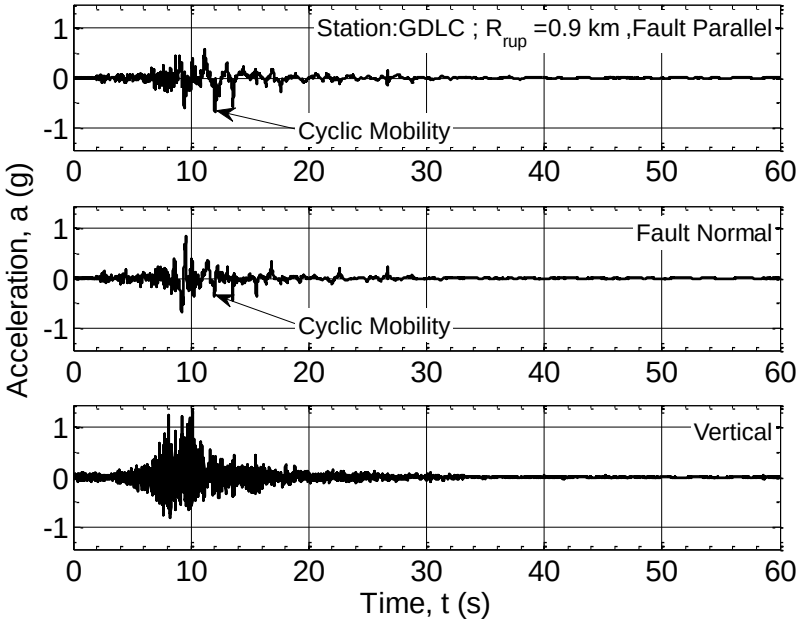

Figure 3.12: Evidence of liquefaction observed in the form of cyclic mobility at GDLC in both orthogonal horizontal acceleration time-series recorded in the 4 September 2010 M_w7.1 Darfield earthquake.

Table 3.4 lists the ground motions which showed strong evidence of forward-directivity effects in the M_w7.1 Darfield earthquake. The results obtained from applying the B07 algorithm are also summarised. It can be observed that 22 near-fault ground motions from the original database of 29 ground motions are classified as pulse-like based on either automated or manual classification procedures. The location of the strong motion stations which recorded these ground motions were previously illustrated in Figure 3.2.

Table 3.4: Forward-directivity ground motions identified using the Baker (2007) wavelet analysis algorithm in the 4 September 2010 M_w7.1 Darfield earthquake.

Station	Cut-Off Point[1] (s)	PGV (cm/s)	Pulse Period, T_p (s)	Pulse Indicator Score	Late Arrival	Pulse-Like Motion
CACS	21	33.4	8.3	0.00	No	Yes[3]
CBGS	21	62.0	5.7	0.93	No	Yes[2]
CCCC	-	74.2	3.5	0.83	No	Yes[3]
CHHC	-	70.6	3.7	0.12	No	Yes[3]
CMHS	-	42.2	3.0	0.05	No	Yes[3]
DSLC	-	54.3	8.1	1.00	No	Yes[2]
GDLC	12	118.9	5.1	0.01	No	Yes[3]
HORC	15.4	83.1	2.2	0.52	No	Yes[3]
HPSC	17	50.2	3.8	0.00	No	Yes[3]
HVSC	16	28.9	4.3	0.00	No	Yes[3]
LINC	-	109.1	7.2	1.00	No	Yes[2]
LPCC	16	20.6	7.6	0.07	No	Yes[3]
NNBS	22	48.3	5.4	0.88	No	Yes[2]
PPHS	20	63.2	3.8	0.00	No	Yes[3]
PRPC	15	64.6	3.8	0.67	No	Yes[3]
REHS	15.3	68.2	4.2	0.00	No	Yes[3]
RHSC	26.5	56.3	7.1	0.52	No	Yes[3]
ROLC	-	107.9	7.2	1.00	No	Yes[2]
SBRC	-	24.2	6.9	1.00	No	Yes[3]
SHLC	-	58.2	7.2	0.75	No	Yes[3]
SMTC	18.3	43.7	8.4	0.00	No	Yes[3]
TPLC	18	77.4	7.2	0.01	No	Yes[3]

[1] The symbol '-' indicates that the manual approach is not warranted as the automated approach extracts the initial directivity pulse correctly.

[2] As determined using the classification criteria proposed by Baker (2007).

[3] Classified as pulse-like based on visual examination of the velocity time-series, polar plot and source-to-site distance.

3.3.1.2 22 February 2011 M_w6.2 Christchurch earthquake

Forward-directivity effects are typically manifested in the form of a low frequency and large amplitude pulse in the velocity time-series corresponding to the fault-normal orientation. Similar to the Darfield earthquake, the automated B07 algorithm was initially applied to the ground motions (i.e. fault-normal velocity time-series) recorded within 30 km of the causative reverse thrust fault in the M_w 6.2 Christchurch earthquake. Table 3.5 summarises the results provided by the pulse classification algorithm for this event. It can be observed that only 3 out 24 ground motions are classified as pulse-like by the automated classification method.

Table 3.5: Summary of the results obtained using the automated Baker (2007) pulse classification algorithm in identifying pulse-like ground motions from the M_w6.2 Christchurch earthquake.

Station	PGV (cm/s)	Pulse Period, T_p (s)	Pulse Indicator Score	Late Arrival	Pulse-Like Motion
CACS	23.3	3.1	0.39	No	No
CBGS	40.6	3.5	0.02	Yes	No
CCCC	47.5	2.5	0.03	Yes	No
CHHC	45.3	3.3	0.01	Yes	No
CMHS	44.2	1.2	0.04	Yes	No
D06C	42.5	1.6	0.02	No	No
HPSC	35.3	7.0	0.98	Yes	No
HVSC	58.7	1.3	0.00	No	No
KPOC	15.3	6.8	0.00	Yes	No
LINC	14.9	5.0	0.02	Yes	No
LPCC	44.7	3.6	0.70	Yes	No
LPOC	77.1	1.9	0.99	No	Yes
NNBS	39.0	1.4	0.99	No	Yes
MQZ	6.0	5.6	0.11	No	No
PPHS	36.4	3.3	0.03	No	No
PRPC	95.0	4.5	1.00	No	Yes
REHS	59.1	3.0	0.00	Yes	No
RHSC	23.9	4.5	0.32	No	No
ROLC	8.3	5.0	0.05	Yes	No
SHLC	60.9	4.0	0.95	Yes	No
SLRC	8.5	6.4	0.00	Yes	No
SMTC	28.5	3.6	0.23	No	No
SWNC	10.3	3.6	0.01	Yes	No
TPLC	10.6	5.3	0.04	Yes	No

Figure 3.13 shows the wavelet analysis procedure applied to the ground motions recorded at Lyttelton Port (LPOC), North New Brighton School (NNBS) and Pages Road (PRPC). Although there is clear evidence of forward-directivity at LPOC and PRPC, the pulse-like feature observed at NNBS is a manifestation of the 'spikes' in the acceleration time-series which is inferred to have occurred due to liquefaction of the soil deposit beneath the ground surface and consequent cyclic mobility (refer to Figure 3.14). However, due to the objective nature of the automated algorithm, the ground motion is incorrectly classified as pulse-like.

(a)

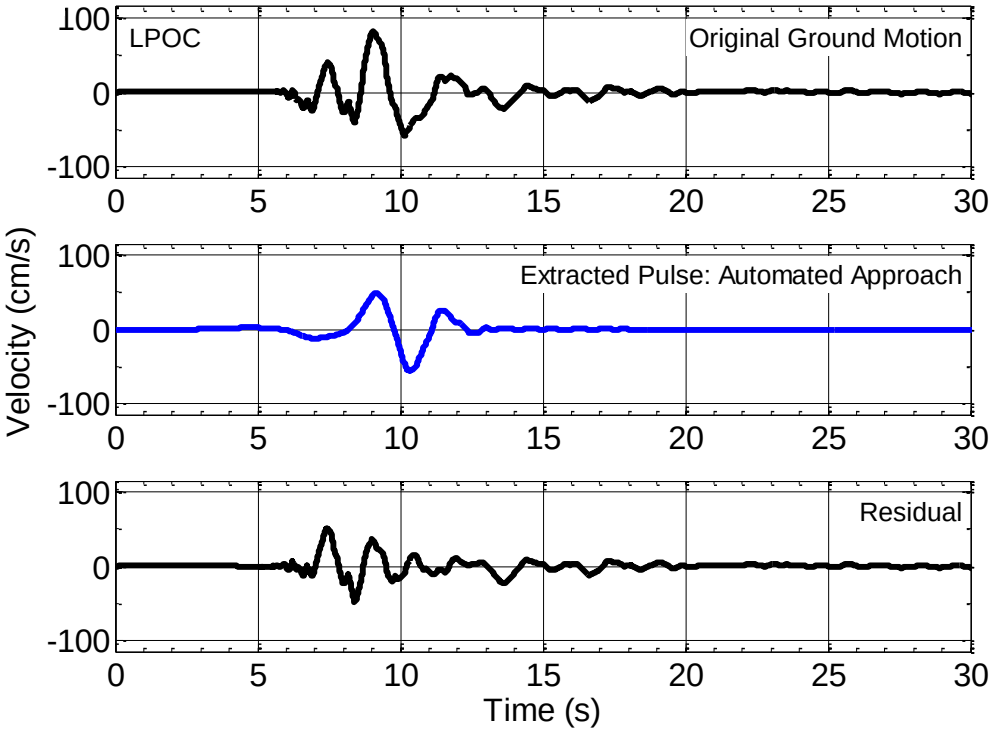
LPOC
Original Ground Motion
Extracted Pulse: Automated Approach
Residual
Velocity (cm/s)
Time (s)
100
0
-100
0
5
10
15
20
25
30

(b)

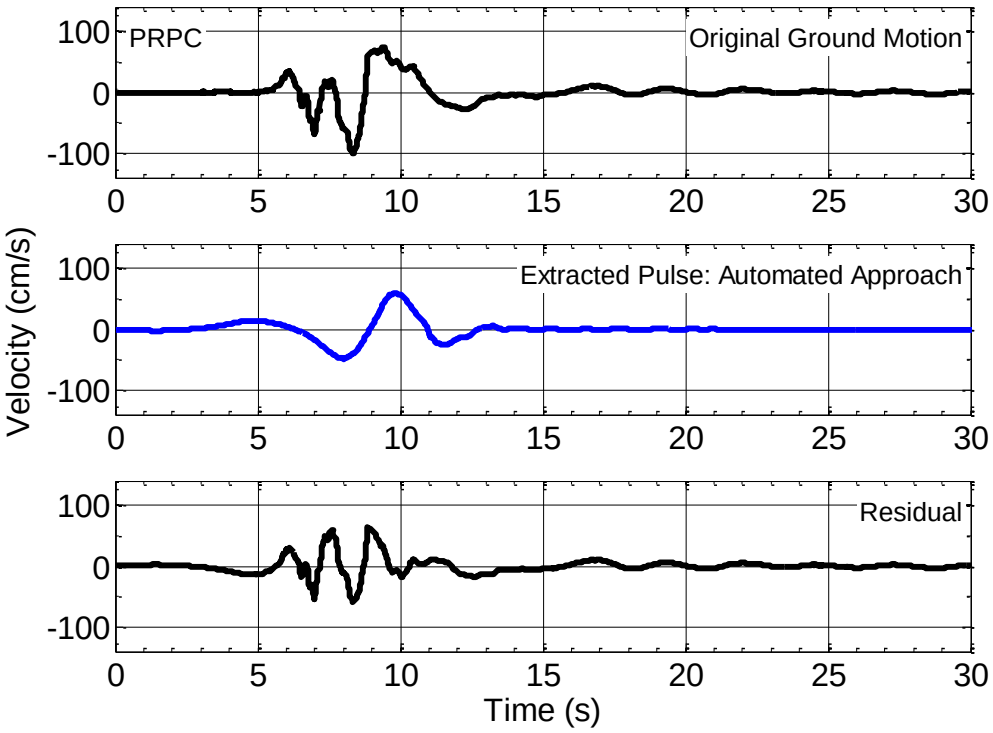
PRPC
Original Ground Motion
Extracted Pulse: Automated Approach
Residual
Velocity (cm/s)
Time (s)
100
0
-100
0
5
10
15
20
25
30

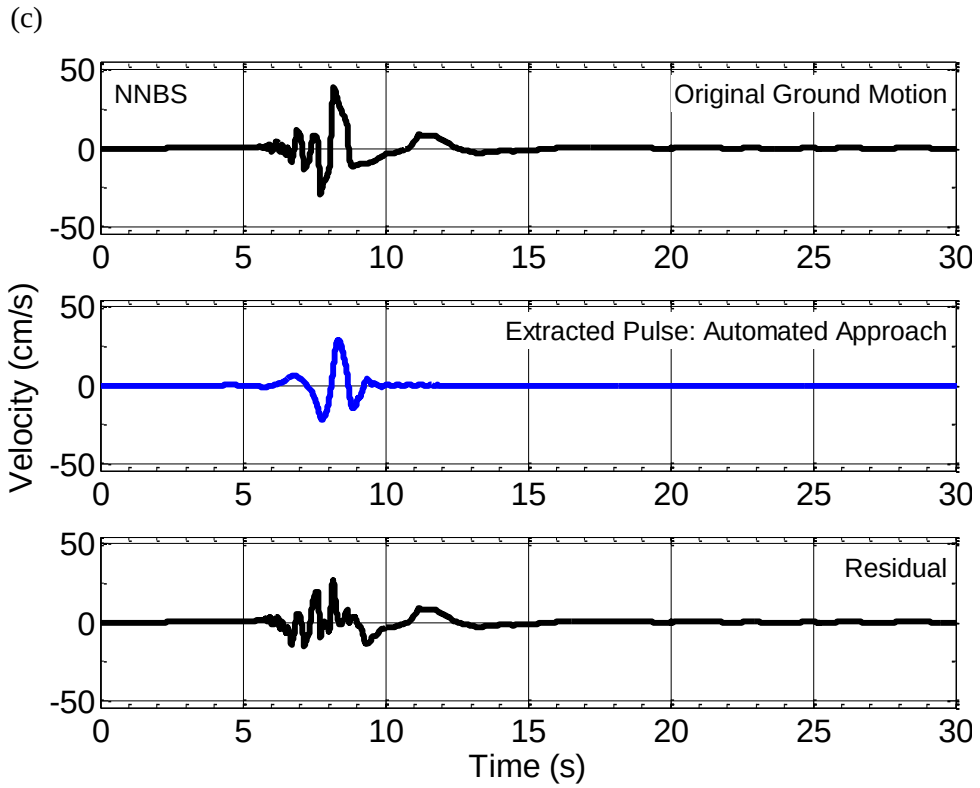

Figure 3.13: Ground motions observed at: (a) LPOC; (b) NBLC; and (c) PRPC in the 22 February 2011 M_w6.2 Christchurch earthquake, and identified as pulse-like using the automated Baker (2007) pulse classification algorithm.

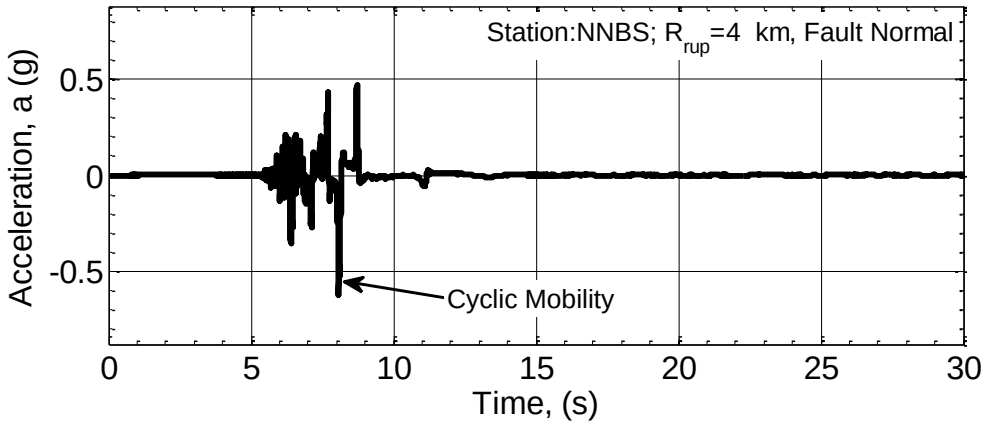

Figure 3.14: Evidence of liquefaction observed in the fault-normal acceleration time-series recorded at NNBS in the 22 February 2011 M_w6.2 Christchurch earthquake.

Based on the one-fault model developed by Beavan et al. (2011), directivity effects in the Christchurch earthquake should be significant over a small area around the surface exposure of the fault. This was initially highlighted by Bradley & Cubrinovski (2011) based on the misalignment of the slip direction and the inferred elliptical rupture front along the modelled fault plane. However, upon inspecting the horizontal velocity trajectory observed at Christchurch Hospital (CHHC), they found some evidence of directivity in the fault-parallel direction, thereby indicating a complex rupture process. In fact, as previously discussed in Chapter 2, a recently developed FFM by Beavan et al. (2012) includes three fault planes with different faulting mechanisms, which confirms the above claim. As a result, a modified approach was adopted to further investigate the presence of forward-directivity in orientations other than the inferred fault-normal direction. This approach is illustrated below using the CHHC ground motion as an example:

1. A time interval corresponding to the arrival of a potential directivity pulse (typically at the beginning of the velocity time-series) is identified based on a visual examination of the fault-parallel and fault-normal components of the velocity time-series as illustrated in Figure 3.15.

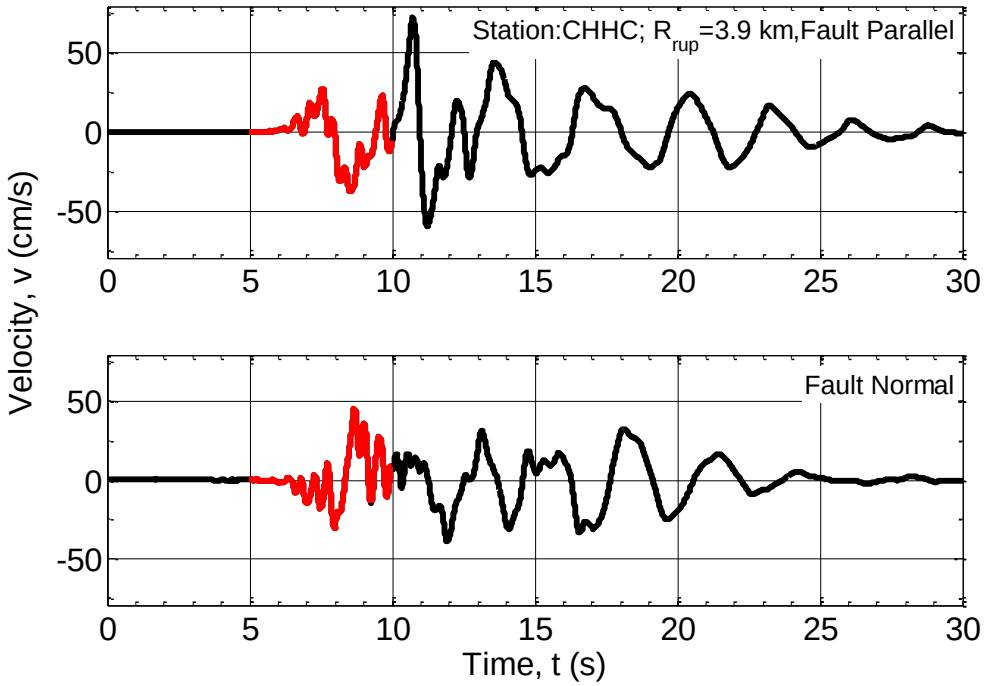

Figure 3.15: Illustration of the chosen time interval corresponding to the arrival of a potential directivity pulse using the two orthogonal velocity time-series recorded at Christchurch Hospital in the 22 February 2011 M_w6.2 Christchurch earthquake.

2. The record is subsequently rotated through all possible non-redundant orientations (0-180°) and the orientation corresponding to the maximum peak ground velocity (PGV) is identified as the 'pulse orientation'. This process is illustrated in Figure 3.16 and has been used in previous research (e.g. Howard et al. (2005)) on the basis that the amplitude of the directivity pulse typically coincides with the PGV of the ground motion record.

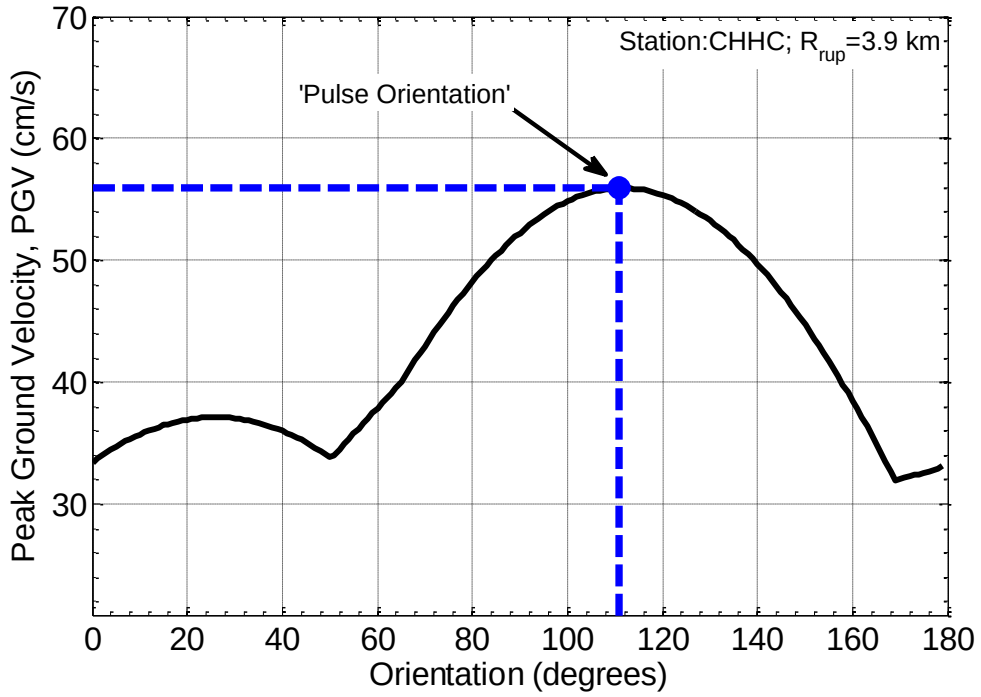

Figure 3.16: Identification of the 'pulse orientation' obtained after rotating a single component of the velocity time-series through all possible non-redundant orientations.

3. A polar plot corresponding to the azimuth identified in the previous step and its orthogonal component are obtained in order to identify whether the preferred direction of the horizontal trajectory corresponds to the 'pulse orientation', as illustrated in Figure 3.17.

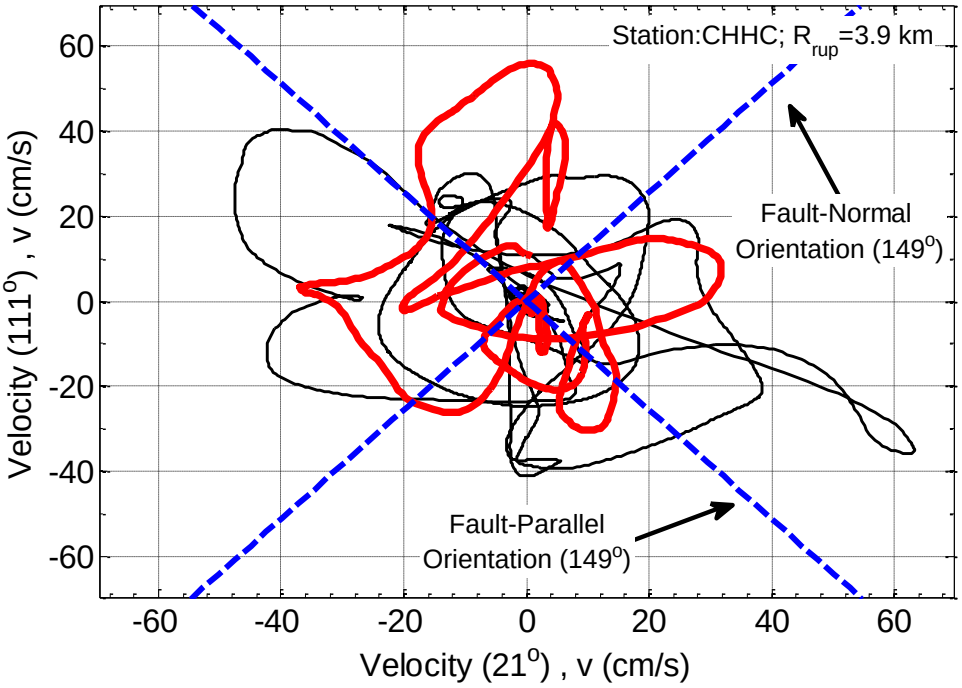

Figure 3.17: Illustration of the horizontal velocity trajectory corresponding to the 'pulse orientation' and its orthogonal component. The red and blue lines correspond to the initial directivity pulse and the remainder of the velocity time-series, respectively.

4. The B07 algorithm is subsequently applied to the velocity time-series corresponding to the 'pulse orientation' if the ground motion demonstrates some evidence of forward-directivity, as illustrated in Figure 3.18. A manual cut-off is applied, if necessary, to ensure appropriate pulse extraction.

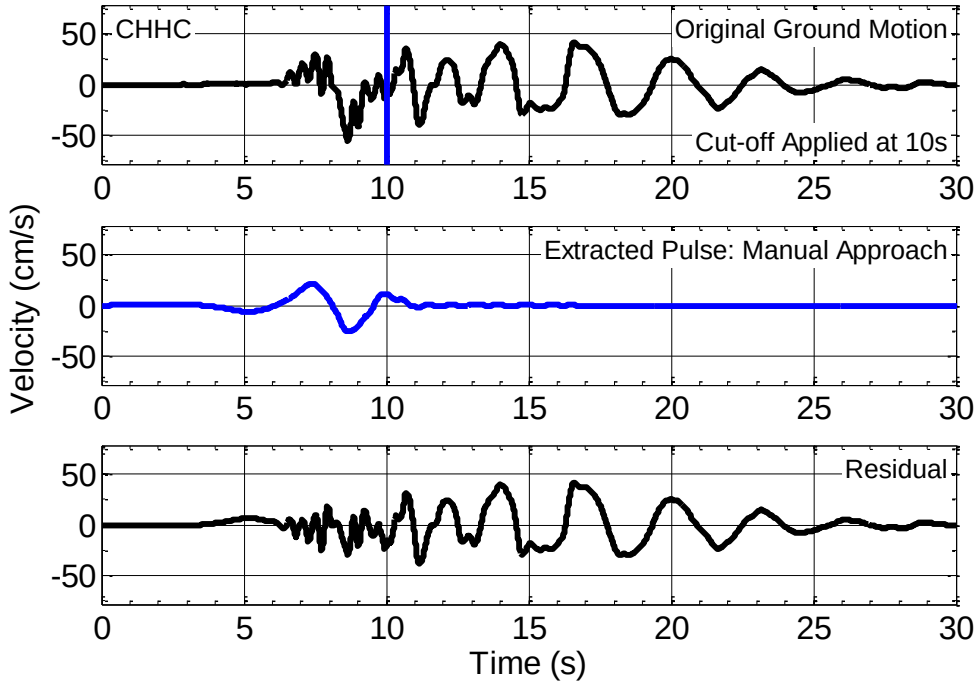

Figure 3.18: Illustration of the Baker (2007) algorithm applied to the velocity time-series (corresponding to the 'pulse orientation') recorded at Christchurch Hospital in the 22 February 2011 M_w6.2 Christchurch earthquake.

From an objective point of view, the second cycle of ground motion in the fault-parallel velocity time-series observed at CHHC (refer to Figure 3.15) can easily be misinterpreted as a directivity pulse. This pulse-like feature is observed due to a reduction in high frequency ground motion in the acceleration time-series and acceleration 'spikes' following several seconds of S-wave arrivals, which is indicative of liquefaction of the soils underlying the ground surface at the site (Bradley & Cubrinovski, 2011). In fact, liquefaction was severe in the Christchurch earthquake with nearly one third of the city being affected by this phenomenon (Cubrinovski et al., 2012). Evidence of liquefaction in the acceleration time-series recorded in the CBD and eastern suburbs has been previously documented by Bradley & Cubrinovski (2011) and Smyrou et al. (2011). In addition to applying the procedure described above, these ground motions were further examined to ensure appropriate identification of forward-directivity effects.

Figure 3.19 illustrates the application of the B07 algorithm to the 15 near-fault ground motions which showed evidence of forward-directivity effects in the M_w6.2 Christchurch earthquake. It is important to note that in each case, the algorithm was applied to the component of ground motion corresponding to the strongest directivity pulse. The results

effectively illustrate the prevalence of directivity effects in the Christchurch earthquake, particularly in the eastern suburbs and the CBD. For example, the largest velocity pulse is observed at Pages Road (PRPC) with a $PGV = 98.7$ cm/s. The large amplitude of this pulse can also be attributed to the proximity of the strong motion station to the slip asperity (with inferred slips of up to 2.5 m according to the one-fault model of Beavan et al. (2011)) and liquefaction effects (Bradley and Curbinovski, 2011; Beavan et al., 2011). In a similar manner, the large amplitude velocity pulse ($PGV = 91$ cm/s) observed at Heathcote Valley (HVSC) resulted from a combination of its proximity to the causative fault, directivity effects (due to its location on the hanging wall) and basin edge effects. The HVSC strong motion station is located at the edge of the Canterbury basin (near the outcropping Port Hills) which gives rise to the latter physical phenomenon where constructive interference of S-waves arriving through the underlying basin occurs with diffracted Rayleigh waves at the basin edge (Bradley, 2012). Hence, it is important to appreciate the complex interaction of source, path and site effects in producing the ground motions at the two sites described above, rather than one particular effect. This further emphasises the importance of applying user judgement in the identification and characterisation of forward-directivity ground motions.

Similar to the Darfield earthquake, several ground motions resulting from the Christchurch earthquake also showed evidence of basin-generated surface wave effects, as illustrated in Figure 3.19. For these cases, it can be observed that the 'manual' approach discussed previously has been applied to ensure correct pulse extraction. In addition, the pulse indicator scores in numerous cases are very low (refer to Table 3.6) because the moderate-long period waveforms (representing the surface waves and other physical phenomena such as liquefaction effects and non-linear soil response) remain in the residual motion after the directivity pulse has been extracted (refer to discussion in Section 3.3.1.1). From an engineering viewpoint, it is important to bear in mind that although forward-directivity on its own can be a damaging phenomenon, the resonant shaking following the arrival of the directivity pulse due to basin effects can potentially have cumulative effects on moderate-long period structures, both in terms of strength and stiffness degradation.

As an aside, it is important to note that the four-step approach described previously in this section to visually identify evidence of forward-directivity effects in orientations other than the inferred fault-normal direction, was also applied to the near-fault ground motions resulting from the M_w7.1 Darfield earthquake. In a majority of cases, due to the strike-slip

nature of the Greendale fault which ruptured bilaterally, the observed directivity pulses were strongly polarised towards the fault-normal orientations of either the western or central segments. A further discussion on the pulse orientations is provided in Section 3.5.1

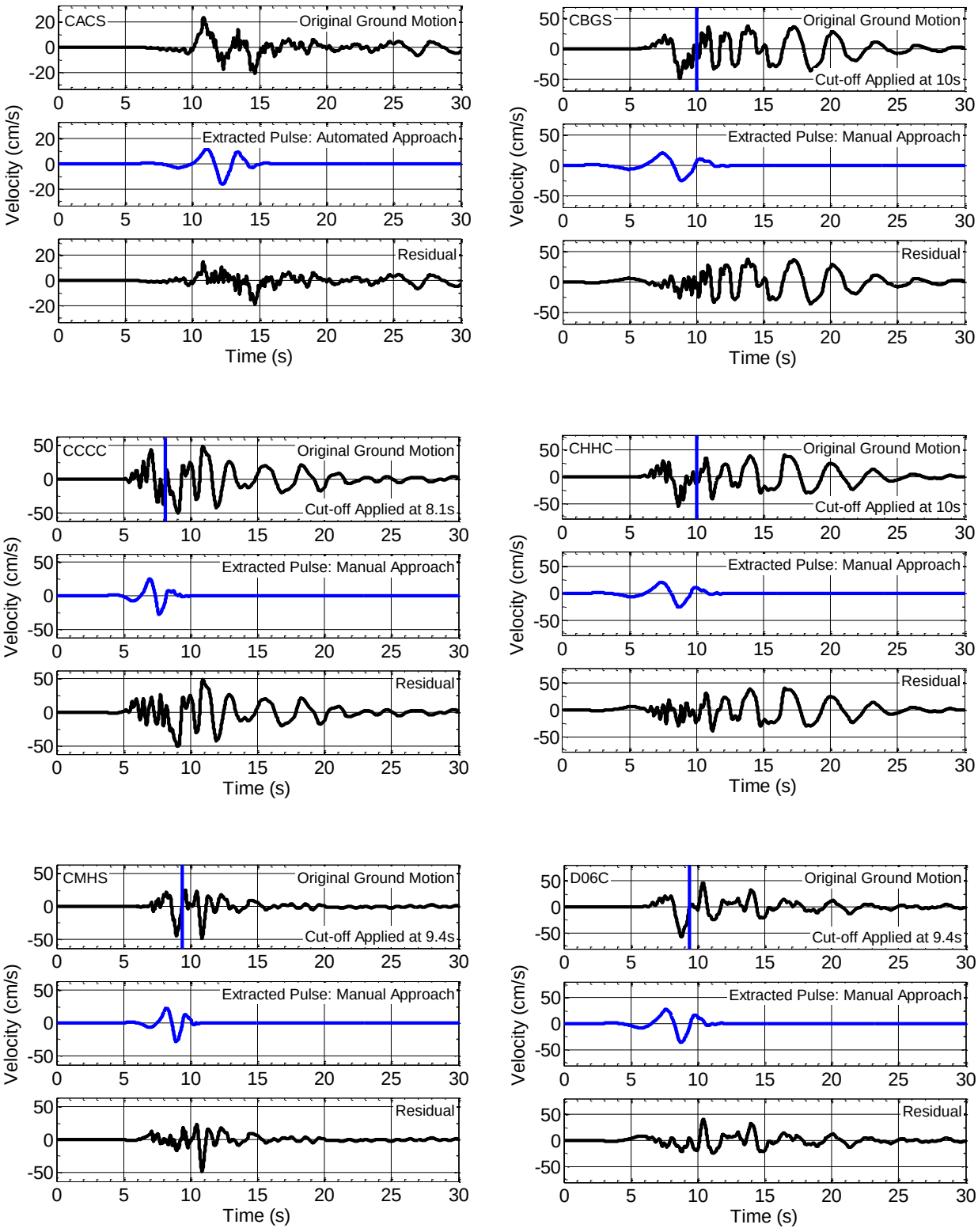

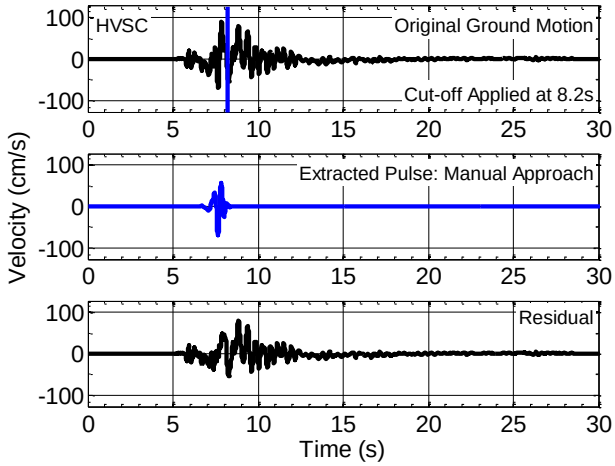
HVSC
Original Ground Motion
Cut-off Applied at 8.2s
Extracted Pulse: Manual Approach
Residual
Velocity (cm/s)
Time (s)

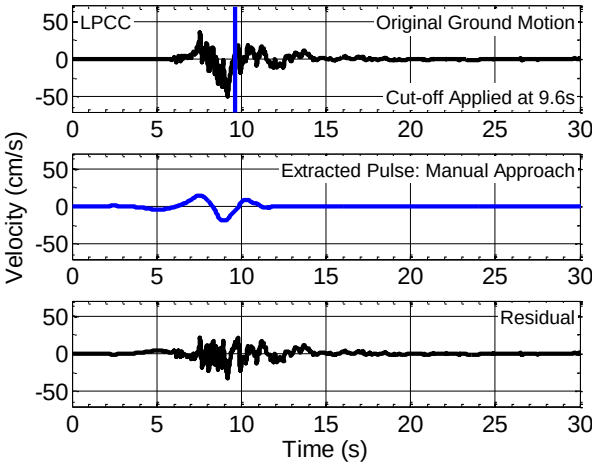
LPCC
Original Ground Motion
Cut-off Applied at 9.6s
Extracted Pulse: Manual Approach
Residual
Velocity (cm/s)
Time (s)

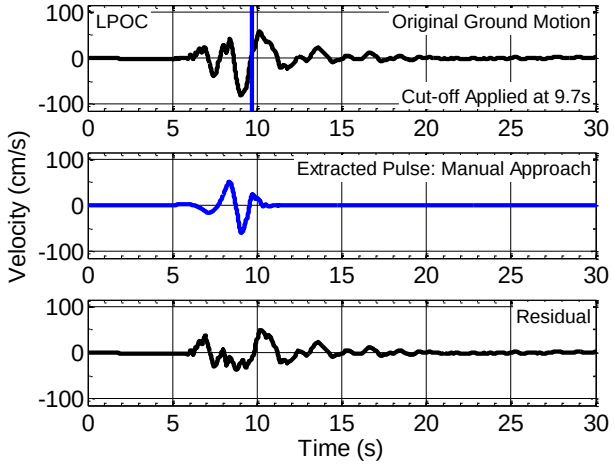
LPOC
Original Ground Motion
Cut-off Applied at 9.7s
Extracted Pulse: Manual Approach
Residual
Velocity (cm/s)
Time (s)

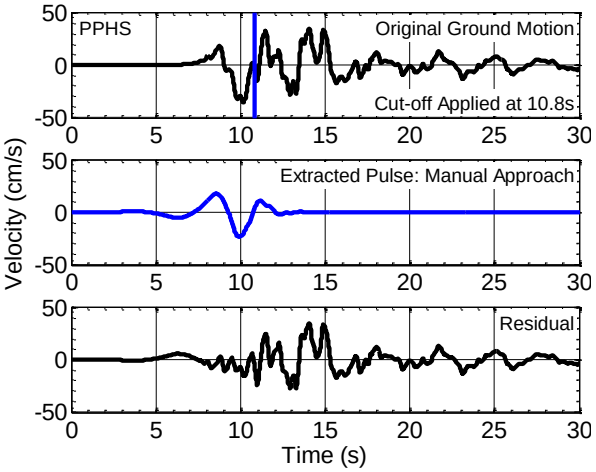
PPHS
Original Ground Motion
Cut-off Applied at 10.8s
Extracted Pulse: Manual Approach
Residual
Velocity (cm/s)
Time (s)

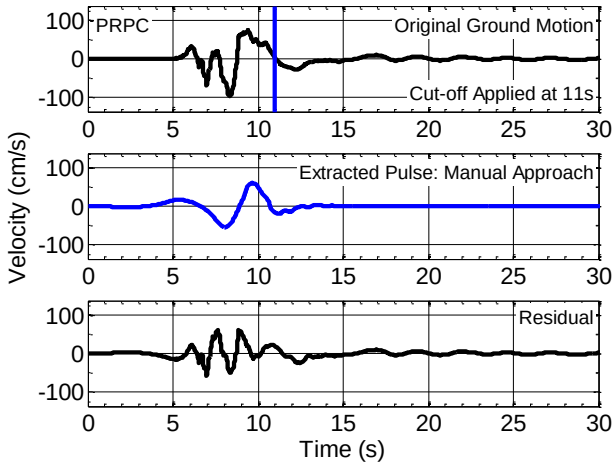
PRPC
Original Ground Motion
Cut-off Applied at 11s
Extracted Pulse: Manual Approach
Residual
Velocity (cm/s)
Time (s)

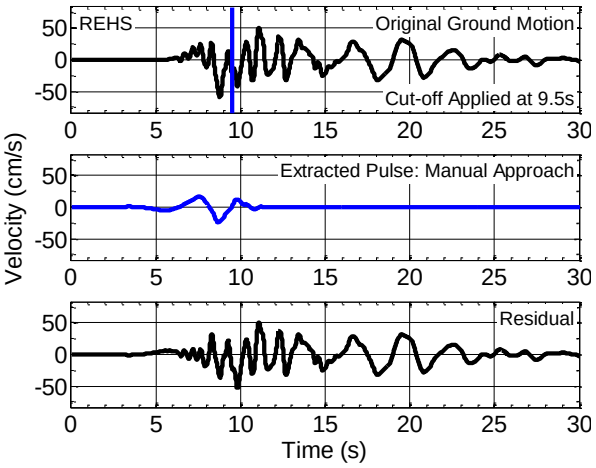
REHS
Original Ground Motion
Cut-off Applied at 9.5s
Extracted Pulse: Manual Approach
Residual
Velocity (cm/s)
Time (s)

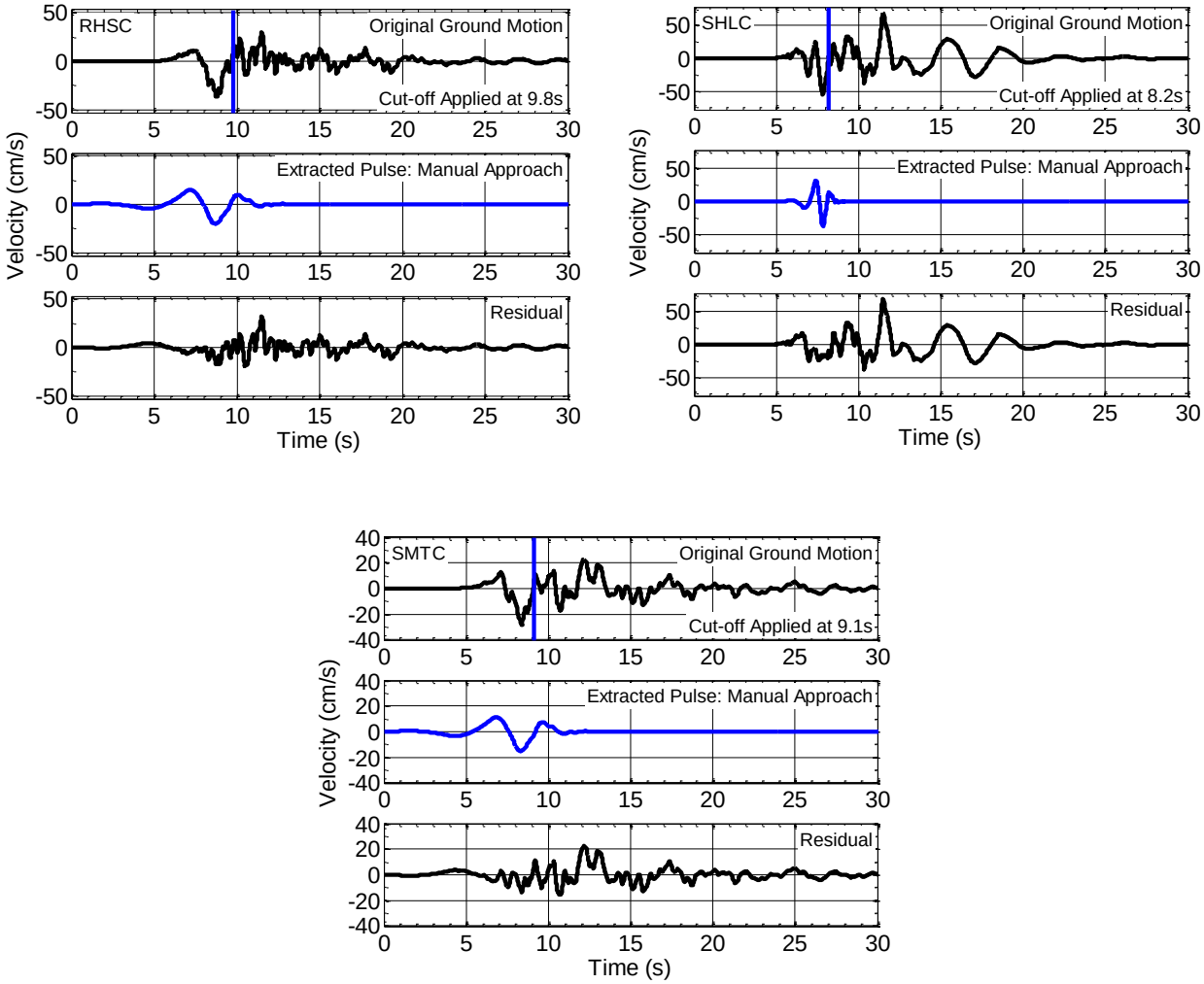

Figure 3.19: Identification of ground motions exhibiting evidence of forward-directivity effects in the 22 February 2011 M_w6.2 Christchurch earthquake using the Baker (2007) pulse classification algorithm.

Table 3.6 provides a summary of the forward-directivity ground motions from the 22 February 2011 event. This includes the orientations in which the principal directivity pulse was found and the results obtained from applying the B07 algorithm. The geographic locations of the recorded ground motions have been previously illustrated in Figure 3.3.

Table 3.6: Forward-directivity ground motions identified using the Baker (2007) wavelet analysis algorithm in the M_w6.2 Christchurch earthquake.

Station	Orientation[1] (degrees)	Cut-off Point[2] (s)	PGV (cm/s)	Pulse Period, T_p (s)	Pulse Indicator Score	Late Arrival	Pulse-Like Motion
CACS	136	-	23.9	3.1	0.30	No	Yes[4]
CBGS	113	10.0	49.6	3.6	0.01	No	Yes[4]
CCCC	145	8.1	44.2	1.6	0.00	No	Yes[4]
CHHC	111	10.0	55.9	3.3	0.01	No	Yes[4]
CMHS	73	9.4	45.6	1.7	0.02	No	Yes[4]
D06C	101	9.4	57.8	3.2	0.99	No	Yes[3]
HVSC	69	8.2	91.0	0.5	0.00	No	Yes[4]
LPCC	51	9.6	50.4	3.2	0.88	No	Yes[3]
LPOC	169	9.7	81.9	1.7	0.96	No	Yes[3]
PPHS	151	10.8	36.4	3.8	0.04	No	Yes[4]
PRPC	133	11	98.7	4.6	0.99	No	Yes[3]
REHS	140	9.5	59.8	1.4	0.00	No	Yes[4]
RHSC	83	9.8	37.8	3.7	0.33	No	Yes[4]
SHLC	14	8.2	55.9	1.2	0.00	No	Yes[4]
SMTC	156	9.1	28.7	2.9	0.04	No	Yes[4]

[1] The azimuth of the velocity time-series corresponding to the strongest directivity pulse.

[2] The symbol '-' indicates that the manual approach is not warranted as the automated approach extracts the initial directivity pulse correctly.

[3] As determined using the classification criteria proposed by Baker (2007)

[4] Classified as pulse-like based on visual examination of the velocity time-series, polar plot and source-to-site geometry.

3.3.1.3 13 June 2011 M_w5.3 earthquake

Before applying the B07 algorithm to the near-fault ground motions recorded in the 13 June 2011 M_w5.3 event, a sub-set of ground motions showing some evidence of forward-directivity was identified using the aforementioned visual methods (e.g. examination of velocity time-series). In doing so, the four-step approach described previously in the context of the Christchurch earthquake was applied. As described previously, this includes the application of the B07 algorithm to the velocity time-series in which the strongest directivity pulse (i.e. with the maximum PGV) is found. The fact that 17 out of 25 near-fault ground motions from this event feature an early-arriving velocity pulse is clearly indicative of rupture directivity effects. However, in general, the small amplitude of the velocity pulses (for example, 9 ground motions have PGVs less than 20 cm/s) implies that these motions have low engineering significance. Figure 3.20 illustrates the application of the B07 algorithm to 4 ground motions which demonstrate evidence of forward-directivity effects. Although the pulse indicator score in each case is greater than 0.85, only the ground motions

recorded at North New Brighton School (NNBS) and Pages Road (PRPC) are classified as pulse-like by the algorithm because their PGVs (33.2 cm/s and 36.6 cm/s respectively) are greater than the 30 cm/s threshold. In fact, these ground motions represent the strongest cases of directivity in the M_w5.3 event, which is consistent with the locations of the respective strong motion stations in relation to the causative strike-slip fault (refer to Figure 3.4) and the inferred direction of rupture propagation (i.e. along strike towards the eastern suburbs of Christchurch).

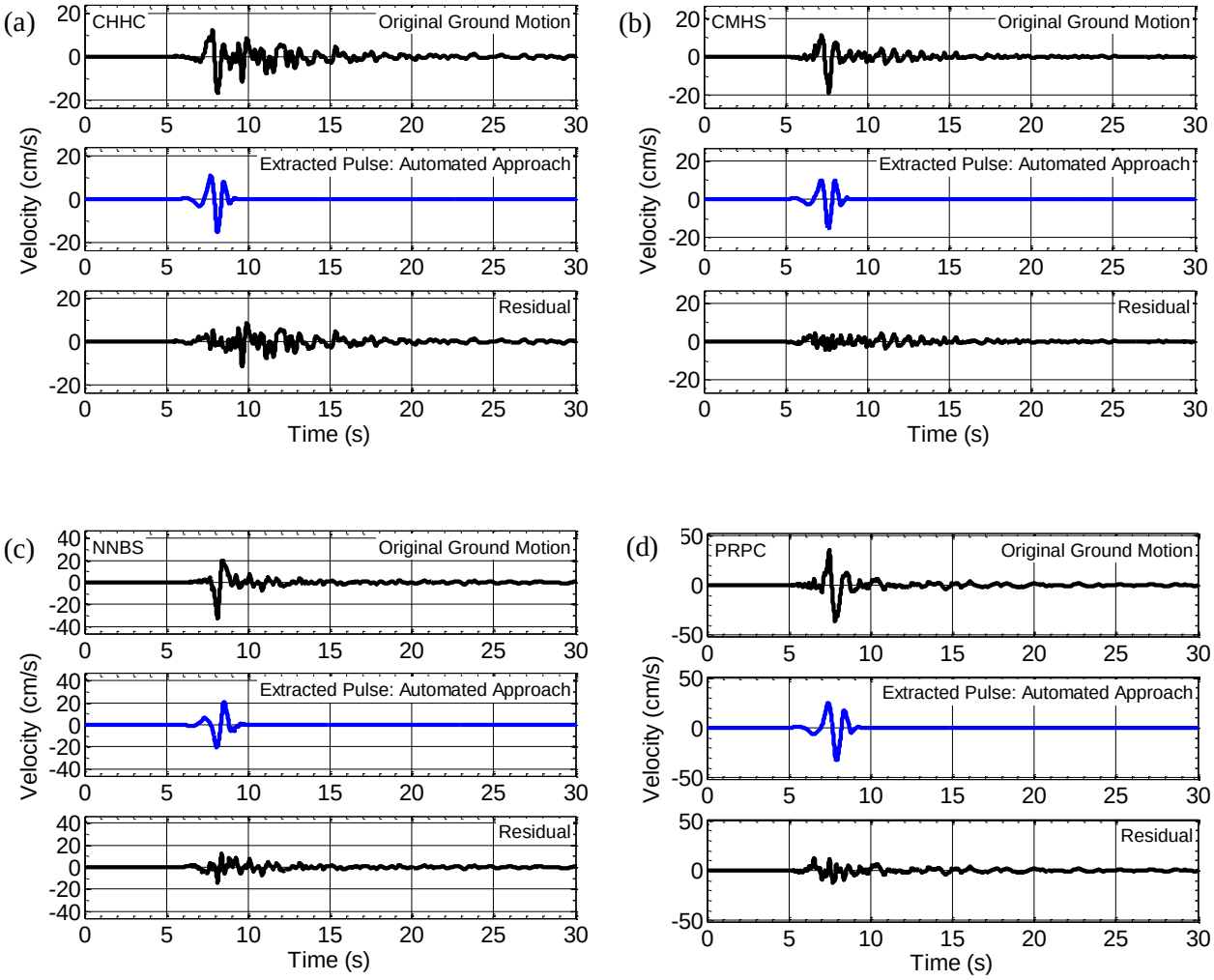

Figure 3.20: Evidence of forward-directivity effects observed in the ground motions recorded at: (a) CHHC; (b) CMHS; (c) NNBS; and (d) PRPC during the 13 June 2011 M_w5.3 earthquake.

3.3.1.4 13 June 2011 M_w6.0 earthquake

In order to identify and document the presence of forward-directivity effects in the near-fault ground motions resulting from the 13 June 2011 M_w6.0 earthquake, the procedure described in the previous section was applied. This was required primarily because the causative rupture, according to the FFM of Beavan et al. (2012), includes a left-lateral strike-slip fault and an oblique fault (with a mix of right-lateral and reverse faulting). Although the location of this event is very similar to the first M_w5.3 event (refer to Figure 3.4), the significance of directivity effects is clearly highlighted by the large amplitude velocity pulses extracted from the original ground motions using the B07 algorithm in Figure 3.21. For example, the observed PGVs at Godley Drive (GODS), Panorama Drive (PARS) and Pages Road (PRPC) are 155 cm/s, 116 cm/s and 91 cm/s, respectively. This is consistent with the proximity of the three strong motion stations to the causative rupture (2 km, 2.7 km and 3.1 km, respectively) and the larger magnitude of the event in relation to the first M_w5.3 event. In addition, the fact that the principal directivity pulse in these three cases was found in orientations very similar to the fault-normal direction of the strike-slip fault (63°) is indicative of strong rupture directivity resulting from the alignment of the rupture and inferred slip direction (from the FFM of Beavan et al. (2012)) along the fault plane. Conversely, pulse-like characteristics in several ground motions (e.g. CMHS, LPCC and NBLC) were found in orientations similar to the fault-normal direction of the oblique fault (159°). A further discussion of the orientations corresponding to the strongest directivity pulse observed in this event and others is provided in Section 3.5.

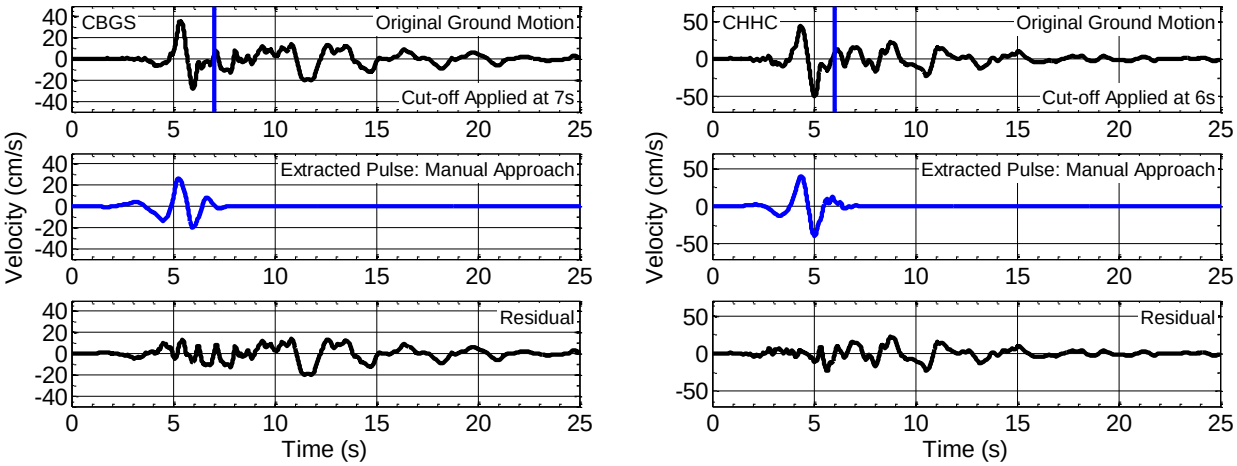

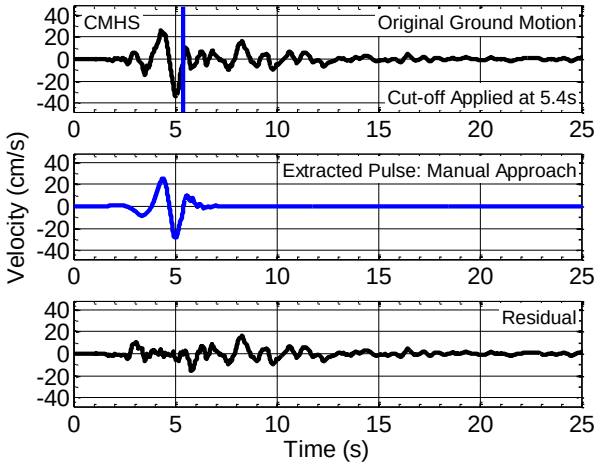
CMHS
Original Ground Motion
Cut-off Applied at 5.4s
Extracted Pulse: Manual Approach
Residual
Velocity (cm/s)
Time (s)

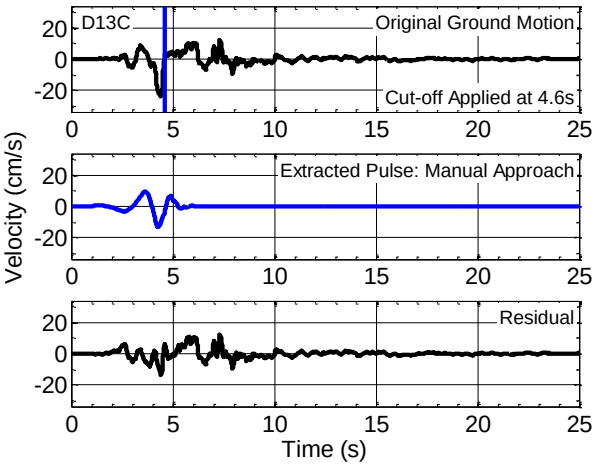
D13C
Original Ground Motion
Cut-off Applied at 4.6s
Extracted Pulse: Manual Approach
Residual
Velocity (cm/s)
Time (s)

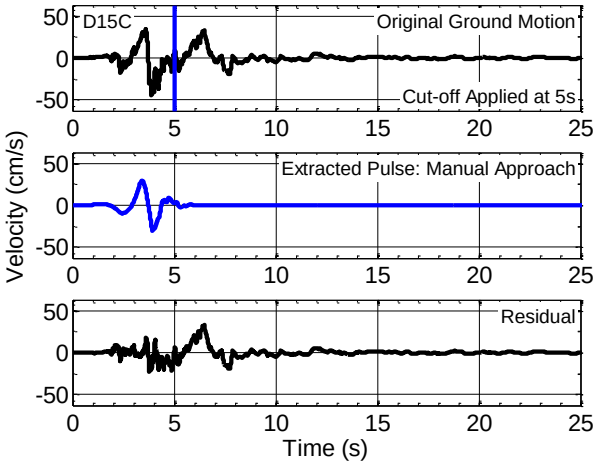
D15C
Original Ground Motion
Cut-off Applied at 5s
Extracted Pulse: Manual Approach
Residual
Velocity (cm/s)
Time (s)

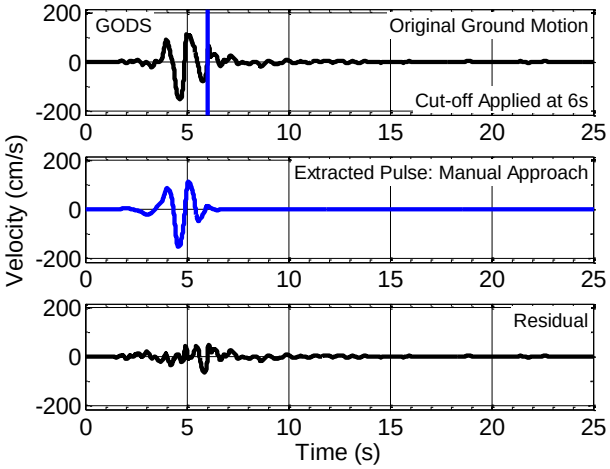
GODS
Original Ground Motion
Cut-off Applied at 6s
Extracted Pulse: Manual Approach
Residual
Velocity (cm/s)
Time (s)

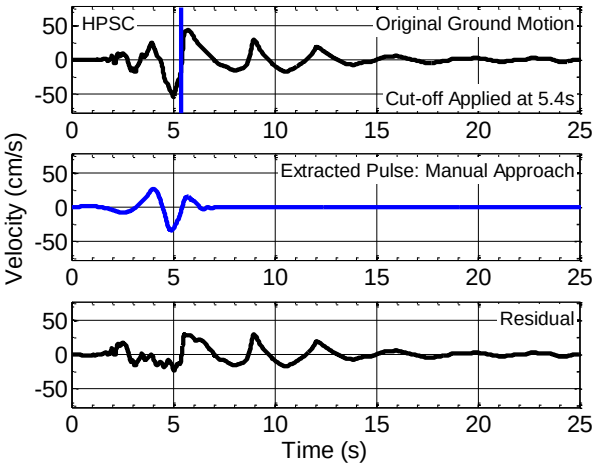
HPSC
Original Ground Motion
Cut-off Applied at 5.4s
Extracted Pulse: Manual Approach
Residual
Velocity (cm/s)
Time (s)

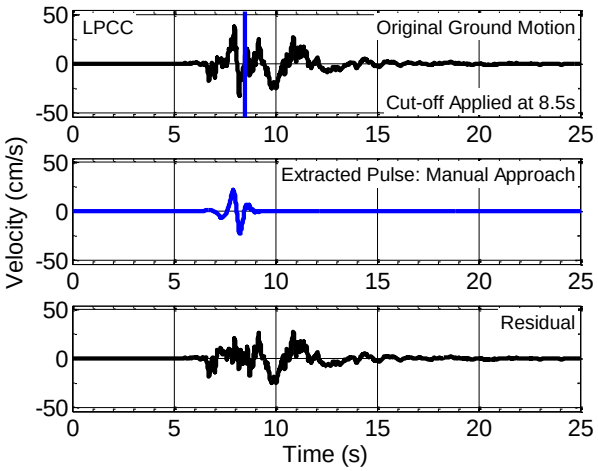
LPCC
Original Ground Motion
Cut-off Applied at 8.5s
Extracted Pulse: Manual Approach
Residual
Velocity (cm/s)
Time (s)

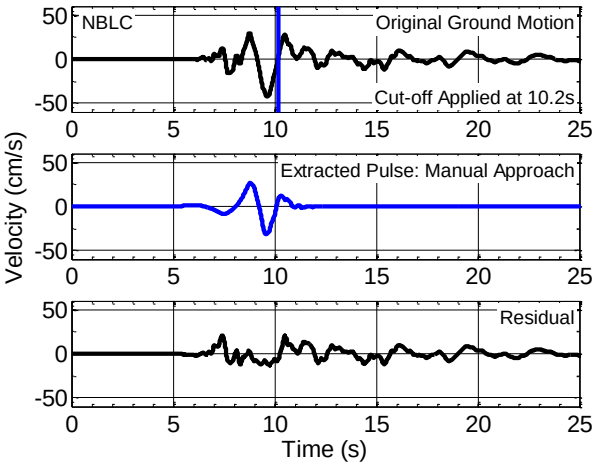
NBLC
Original Ground Motion
Cut-off Applied at 10.2s
Extracted Pulse: Manual Approach
Residual
Velocity (cm/s)
Time (s)

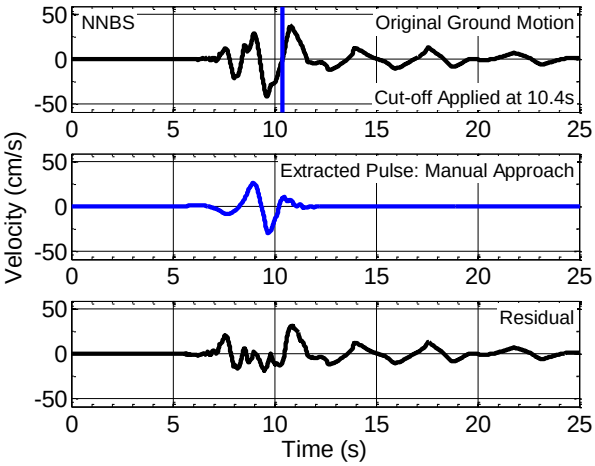
NNBS
Original Ground Motion
Cut-off Applied at 10.4s
Extracted Pulse: Manual Approach
Residual
Velocity (cm/s)
Time (s)

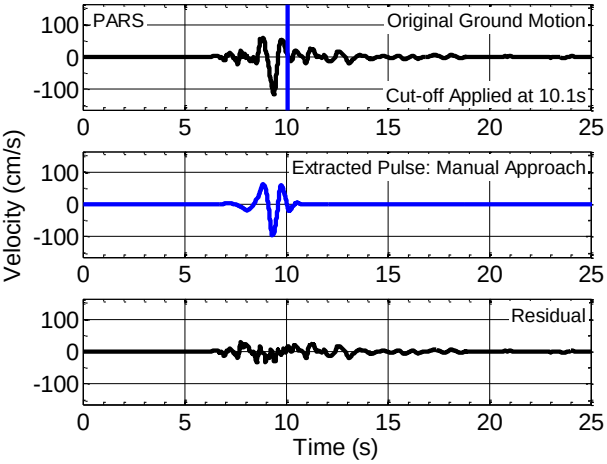
PARS
Original Ground Motion
Cut-off Applied at 10.1s
Extracted Pulse: Manual Approach
Residual
Velocity (cm/s)
Time (s)

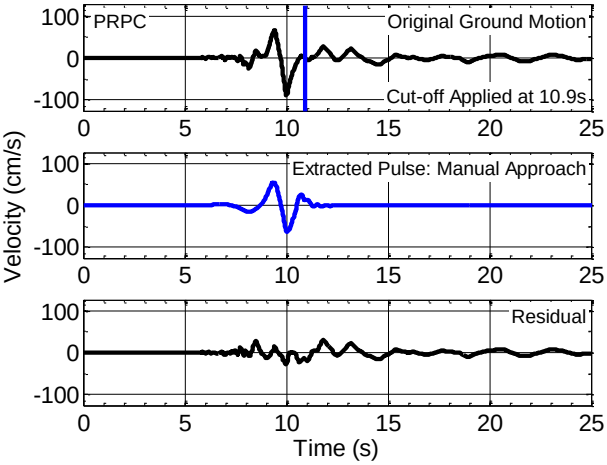
PRPC
Original Ground Motion
Cut-off Applied at 10.9s
Extracted Pulse: Manual Approach
Residual
Velocity (cm/s)
Time (s)

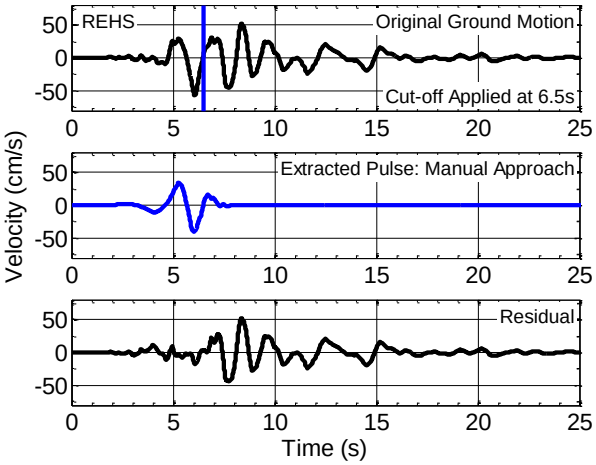
REHS
Original Ground Motion
Cut-off Applied at 6.5s
Extracted Pulse: Manual Approach
Residual
Velocity (cm/s)
Time (s)

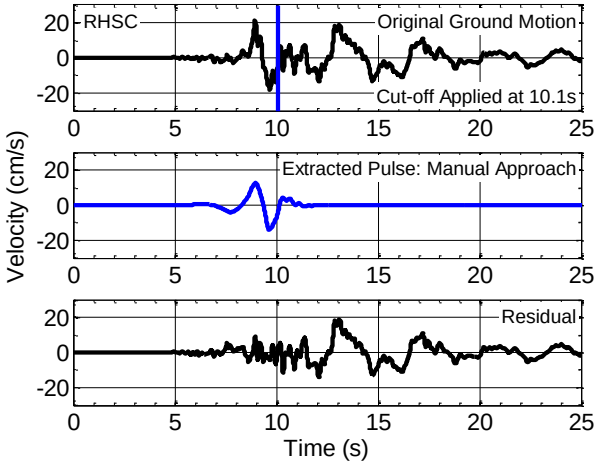
RHSC
Original Ground Motion
Cut-off Applied at 10.1s
Extracted Pulse: Manual Approach
Residual
Velocity (cm/s)
Time (s)

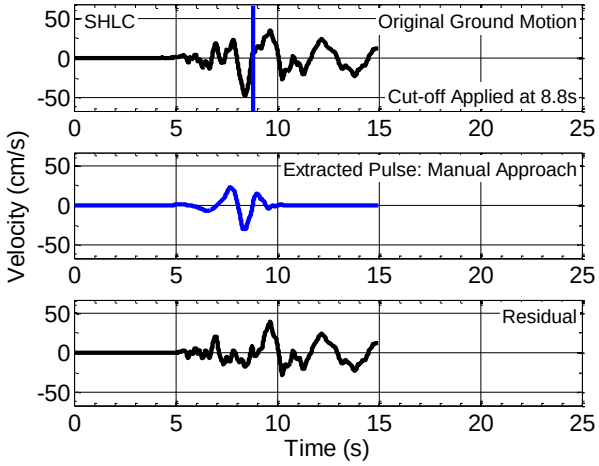

Figure 3.21: Identification of ground motions exhibiting evidence of forward-directivity effects in the 13 June 2011 M_w6.0 earthquake using the Baker (2007) pulse classification algorithm.

Table 3.7 provides a summary of the results obtained from applying the B07 algorithm to the forward-directivity ground motions. The locations of the recorded ground motions have been previously illustrated in Figure 3.4.

3.3.1.5 23 December 2011 M_w5.8 earthquake

Due to the off-shore location of the causative rupture in this event, forward-directivity effects were only significant in the eastern areas of Christchurch. Figure 3.22 shows the B07 algorithm applied to the velocity time-series recorded at New Brighton Library (NBLC) and Pages Road (PRPC). In each case, an early-arriving directivity pulse is extracted by the algorithm with PGVs of 37.4 cm/s and 41.1 cm/s, respectively. Although the ground motions recorded in areas such as the CBD also featured velocity pulses, their generally low amplitudes suggest that they do not warrant further attention, similar to the first M_w5.3 event on 13 June 2011.

Table 3.7: Forward-directivity ground motions identified using the Baker (2007) wavelet analysis algorithm in the M_w6.0 June, 2011 earthquake.

Station	Orientation[1] (degrees)	Cut-off Point[2] (s)	PGV (cm/s)	Pulse Period, T_p (s)	Pulse Indicator Score	Late Arrival	Pulse-Like Motion
CBGS	24	7.0	35.2	1.9	0.81	No	Yes[4]
CHHC	91	6.0	50.2	1.5	1.00	No	Yes[3]
CMHS	145	5.4	34.2	1.5	1.00	No	Yes[3]
D13C	146	4.6	24.3	1.5	0.93	No	Yes[3]
D15C	130	5.0	45.0	1.4	0.73	No	Yes[4]
GODS	56	6.0	154.7	1.4	1.00	No	Yes[3]
HPSC	133	5.4	55.1	2.2	0.97	No	Yes[3]
LPCC	152	8.5	38.8	0.8	0.07	No	Yes[4]
NBLC	164	10.2	43.0	2.1	1.00	No	Yes[3]
NNBS	79	10.4	42.6	1.8	0.70	No	Yes[4]
PARS	98	10.1	116.4	1.1	1.00	No	Yes[3]
PRPC	40	10.9	90.6	1.8	1.00	No	Yes[3]
REHS	16	6.5	57.4	1.7	0.02	No	Yes[4]
RHSC	8	10.1	21.4	1.7	0.00	No	Yes[4]
SHLC	98	8.8	47.5	1.7	0.06	No	Yes[4]

[1] The azimuth of the velocity time-series corresponding to the strongest directivity pulse.

[2] The symbol '-' indicates that the manual approach is not warranted as the automated approach extracts the initial directivity pulse correctly.

[3] As determined using the classification criteria proposed by Baker (2007).

[4] Classified as pulse-like based on visual examination of the velocity time-series, polar plot and source-to-site geometry.

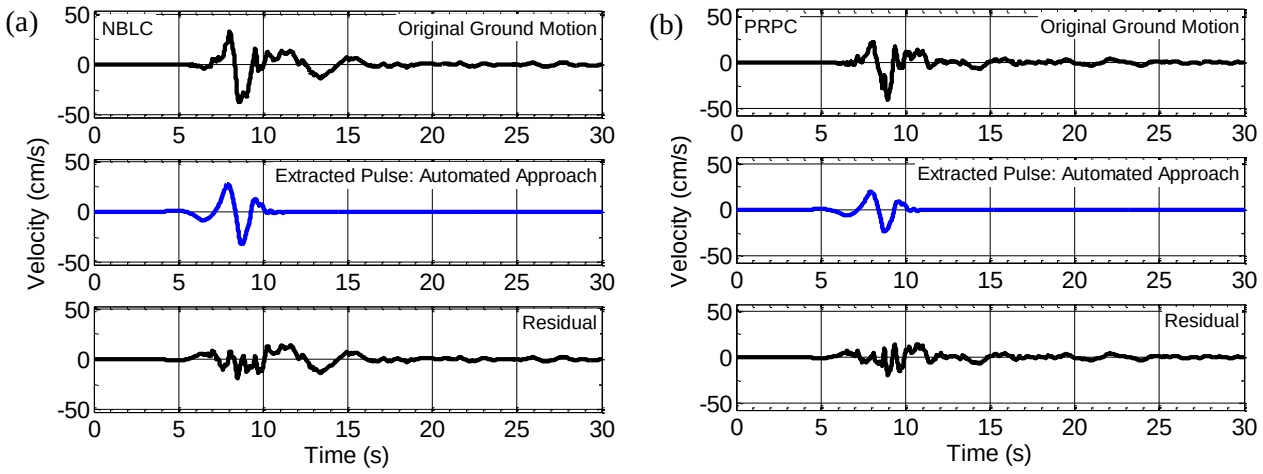

Figure 3.22: Evidence of forward-directivity effects observed in the ground motions recorded at: (a) NBLC; and (b) PRPC during the 23 December 2011 M_w5.8 earthquake.

3.3.1.6 23 December 2011 M_w5.9 earthquake

In a similar manner to the first event, the ground motions observed in the eastern suburbs of Christchurch demonstrated evidence of forward-directivity effects in the subsequent M_w5.9 event. The four-step approach described previously to find the strongest directivity pulse from a single component of the velocity time-series was applied to all near-fault ground motions from this event. Figure 3.23 illustrates the pulse extraction procedure for the ground motions exhibiting evidence of directivity effects using the B07 algorithm. Although some ground motions (e.g. CMHS and SMTC) exhibit low amplitude velocity pulses, it was decided to include these cases in the present study for the purposes of further empirical analysis in Chapters 4, 5 and 6.

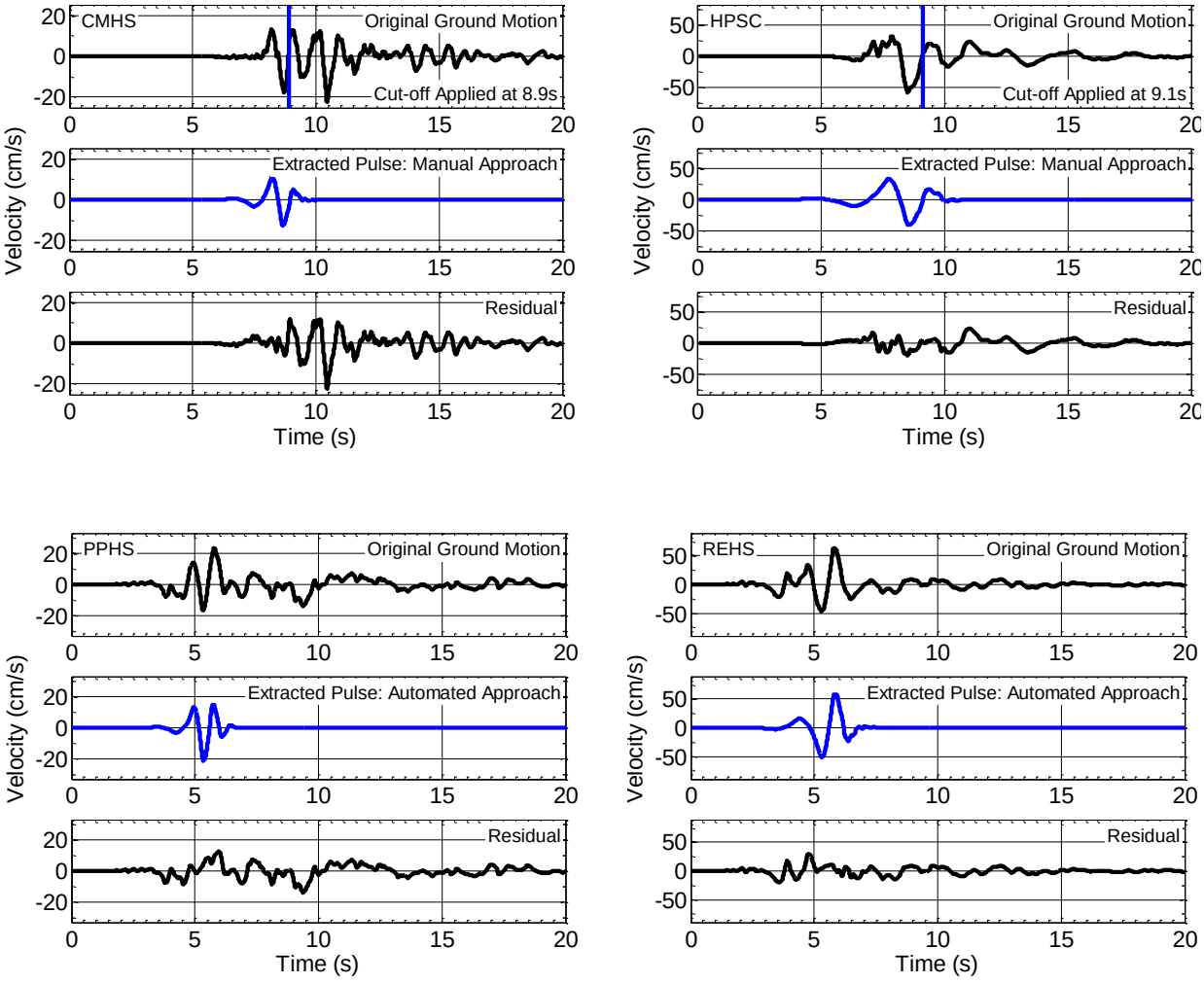

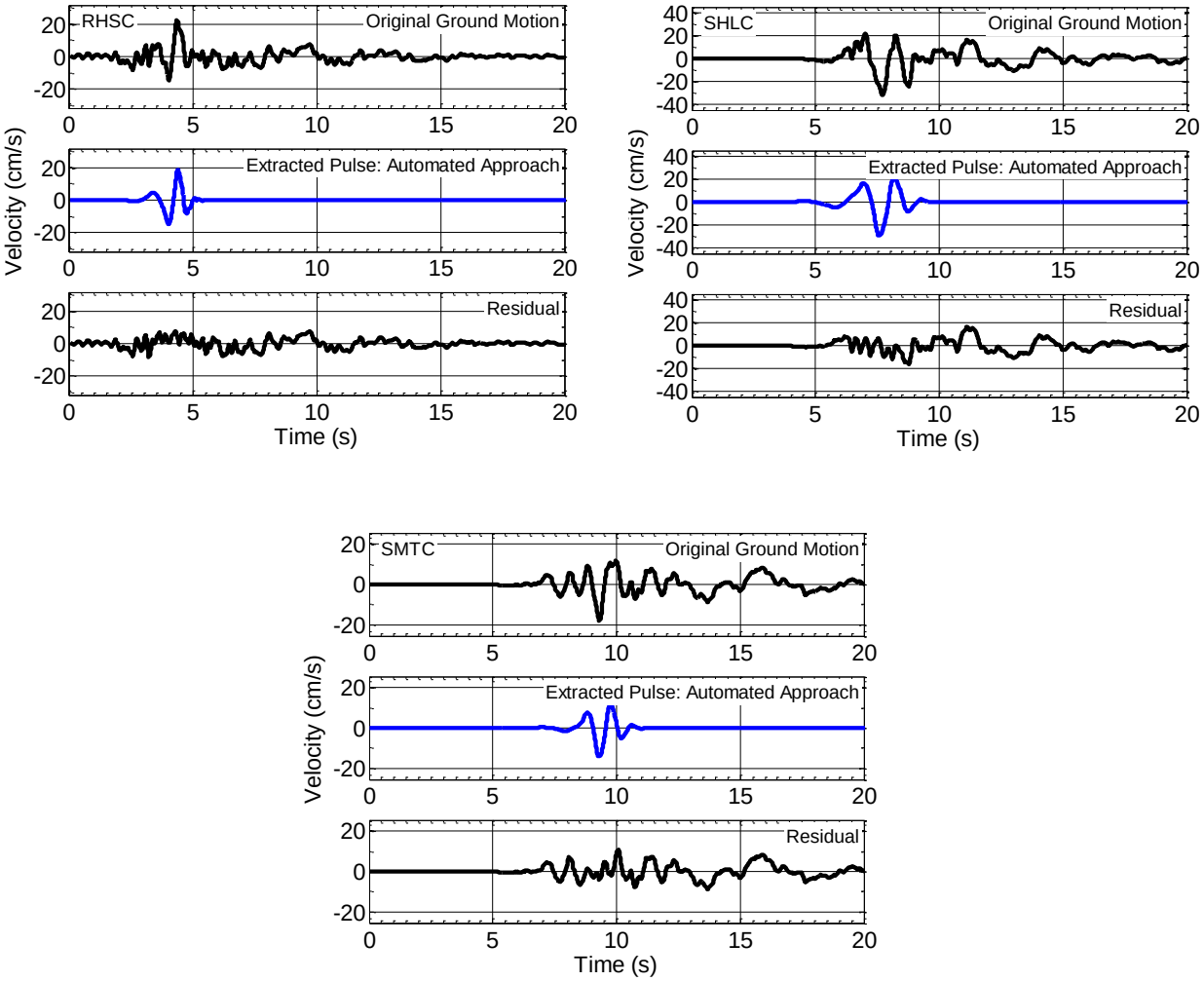

Figure 3.23: Identification of ground motions exhibiting evidence of forward-directivity effects in the 23 December 2011 M_w5.9 earthquake using the Baker (2007) pulse classification algorithm.

Table 3.8 provides a summary of the results obtained from applying the B07 algorithm to the seven identified forward-directivity ground motions in the 23 December 2011 M_w5.9 earthquake. It can be observed that the Resthaven (REHS) and Hulverston Drive (HPSC) motions represent the strongest cases of directivity in this event with PGVs of 64.2 cm/s and 58.4 cm/s.

Table 3.8: Forward-directivity ground motions identified using the Baker (2007) wavelet analysis algorithm in the 23 December 2011 M_w5.9 earthquake.

Station	Orientation[1] (degrees)	Cut-off Point[2] (s)	PGV (cm/s)	Pulse Period, T_p (s)	Pulse Indicator Score	Late Arrival	Pulse-Like Motion
CMHS	110	8.9	18.1	1.1	0.00	No	Yes[4]
HPSC	130	9.1	58.4	2.1	1.00	No	Yes[3]
PPHS	180	-	23.6	1.1	0.89	No	Yes[4]
REHS	126	-	64.2	1.3	1.00	No	Yes[3]
RHSC	149	-	22.6	0.91	1.00	No	Yes[4]
SHLC	160	-	32.1	1.6	1.00	No	Yes[3]
SMTC	150	-	18.1	1.3	0.66	No	Yes[4]

[1] The azimuth of the velocity time-series corresponding to the strongest directivity pulse.

[2] The symbol '-' indicates that the manual approach is not warranted as the automated approach extracts the initial directivity pulse correctly.

[3] As determined using the classification criteria proposed by Baker (2007).

[4] Classified as pulse-like based on visual examination of the velocity time-series, polar plot and source-to-site geometry.

3.3.1.7 Other events

In addition to the six events previously considered, the ground motions resulting from four other significant, but smaller magnitude earthquakes were also examined using the B07 algorithm. This includes the events which occurred on 19 October 2010 (M_w 4.8), 26 December 2010 (M_w4.7), 16 April 2011 (M_w5.0) and 21 June 2011 (M_w5.2). Although ground motions from certain events demonstrated evidence of forward-directivity, it was decided not to devote further attention to these cases mainly due to the low amplitude of the velocity pulses.

3.3.2 Shahi (2013) pulse classification algorithm

In an effort to overcome the issues associated with the Baker (2007) algorithm outlined in Chapter 2, Shahi (2013) developed a revised automated pulse classification algorithm (the 'S13 algorithm' hereafter) which is capable of identifying pulse-like characteristics in multi-component ground motions at arbitrary orientations. Specific details of the algorithm have been omitted herein for brevity and only the main steps of the classification procedure are summarised below:

1. The continuous wavelet transform (CWT) is performed for two orthogonal components of the velocity time-series to find the maximum wavelet coefficients at each scale[1] and location[2] over all non-redundant orientations.
2. Five potential pulses are selected to ensure that false-negative pulse-like ground motion classifications do not occur.
3. The velocity time-series is rotated to the orientations in which each of the five prospective pulses are found in Step 2.
4. The wavelet analysis procedure initially proposed by Baker (2007) (and repeated in Chapter 2) is applied to each velocity time-series in order to extract the pulse-like feature corresponding to the scale and location identified in Step 2.
5. The ground motion is classified as pulse-like if the pulse indicator score corresponding to any of the five velocity time-series is positive and the pulse-like feature arrives early (refer to Section 2.4.2 in Chapter 2 for further details).
6. If multiple pulse-like cases exist, the extracted pulse with the largest wavelet coefficient is chosen by the algorithm.

[1] The scale parameter (s) is used to transform the wavelet in the frequency domain which essentially involves stretching and dilating the wavelet (Shahi, 2013).

[2] The location parameter (l) is used to transform the wavelet in the time domain which essentially involves translating the wavelet shape on the time axis (Shahi, 2013).

3.3.2.1 4 September 2010 M_w7.1 Darfield earthquake

Figure 3.24 illustrates the application of the algorithm to the velocity time-series recorded at Templeton (TPLC) in the Darfield earthquake. It should be noted that the extracted pulses shown in blue and red correspond to velocity time-series identified as pulse-like and non-pulse-like, respectively. In this particular example, the first pulse is chosen by the algorithm because it has a larger wavelet coefficient compared to the second pulse. As discussed previously in Section 3.3.1.1, the second cycle of ground motion following the initial directivity pulse corresponds to basin-induced surface wave effects and hence, the 'pulse-like' classification is inappropriate for this case. Although the directivity pulse is correctly extracted in the second 'pulse-like' case, the subsequent full cycle of motion is also present in the extracted pulse. To some extent, this is unavoidable due to the shape of the Daubechies wavelet (refer to Baker (2007) and references therein) adopted in the algorithm for pulse extraction. While this issue can be overcome by adopting the 'manual' approach which was discussed extensively in Section 3.3.1.1, doing so would defeat the purpose of applying the automated S13 algorithm in this case because it is supposedly an improved version of its predecessor.

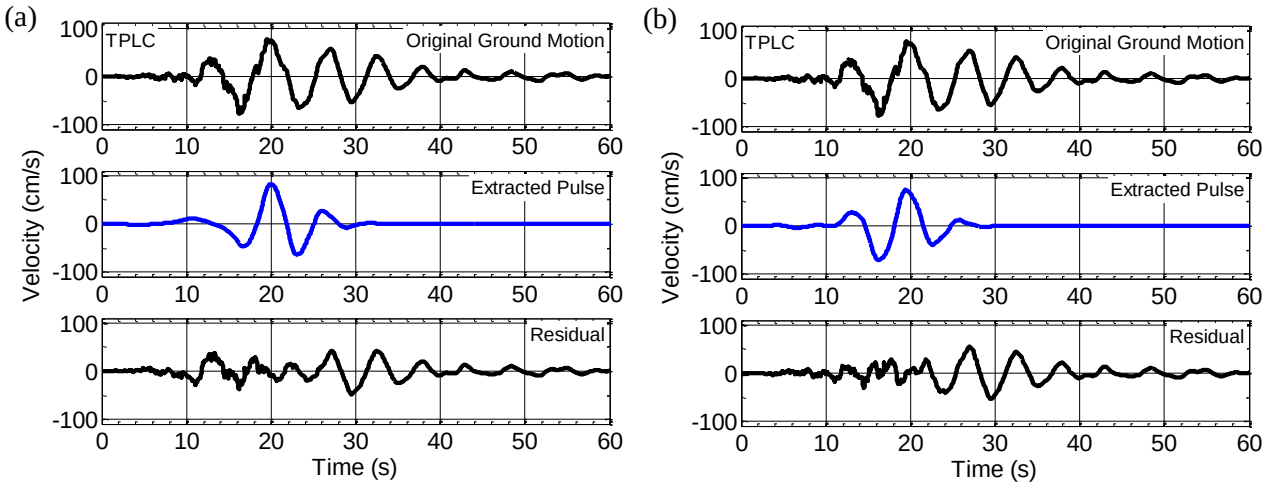

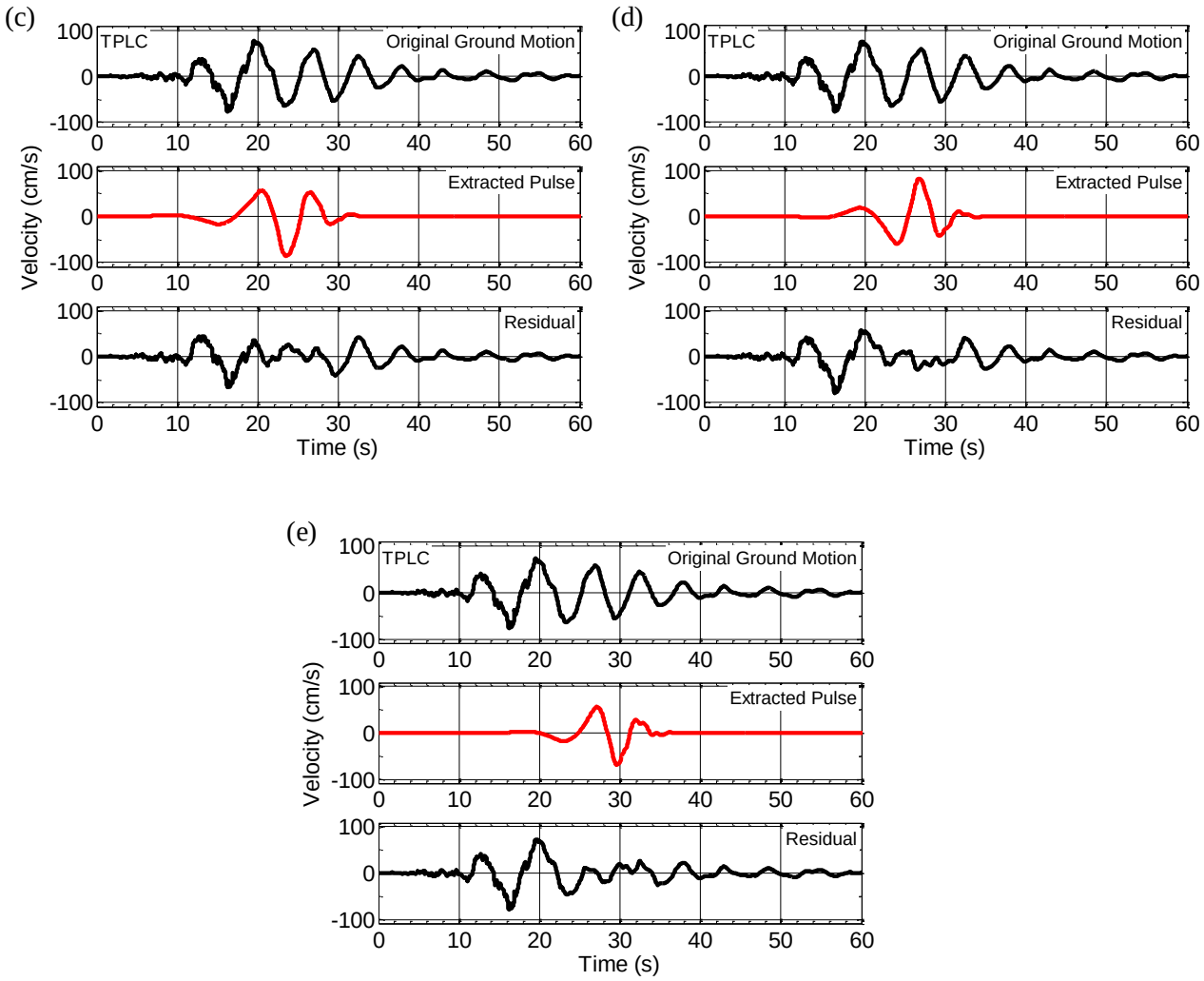

Figure 3.24: Illustration of the automated Shahi (2013) pulse classification algorithm applied to the ground motion recorded at Templeton (TPLC) in the M_w7.1 Darfield earthquake. Panels (a) to (e) show the extraction of the five largest pulses from the original ground motion. Note that the pulses shown in blue and red correspond to 'pulse-like' and 'non-pulse-like' classifications, respectively.

The remaining seven ground motions identified as pulse-like by the S13 algorithm are illustrated in Figure 3.25. It can be observed that three additional ground motions (CCCC, GDLC and SBRC) are correctly identified as pulse-like in comparison to the classifications obtained using the automated B07 algorithm previously in Figure 3.6. Although this is indicative of the improvements of the S13 algorithm, the results arguably still do not justify the use of stand-alone automated approaches in classifying pulse-like motions on an event-specific basis. In fact, it is obvious that both algorithms fail to classify ground motions where cycles of large amplitude and long period ground motion follow the main directivity pulse. In these cases, the use of other approaches (such as the 'manual' approach proposed in the present study for correct pulse extraction combined with visual examination of the velocity

time-series, polar plot and source-to-site geometry) in conjunction with the wavelet analysis algorithms appears warranted. It is worth re-iterating at this point that the present exercise is aimed towards extracting pulse-like features caused by forward-directivity effects only. Other important physical phenomena such as basin effects are considered in Chapter 5 by means of modifications to predicted acceleration response spectra. Further details can be found in the respective chapter.

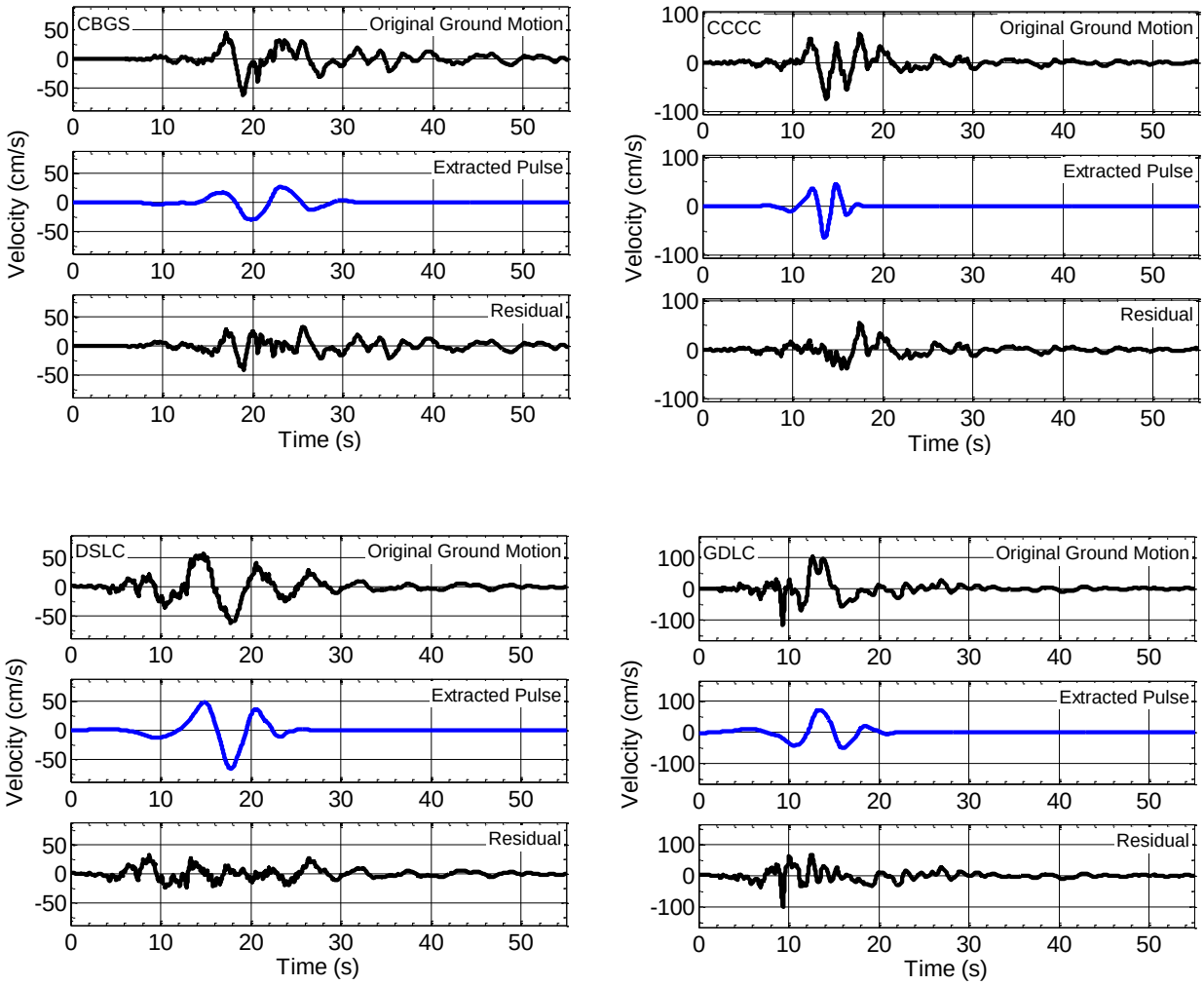

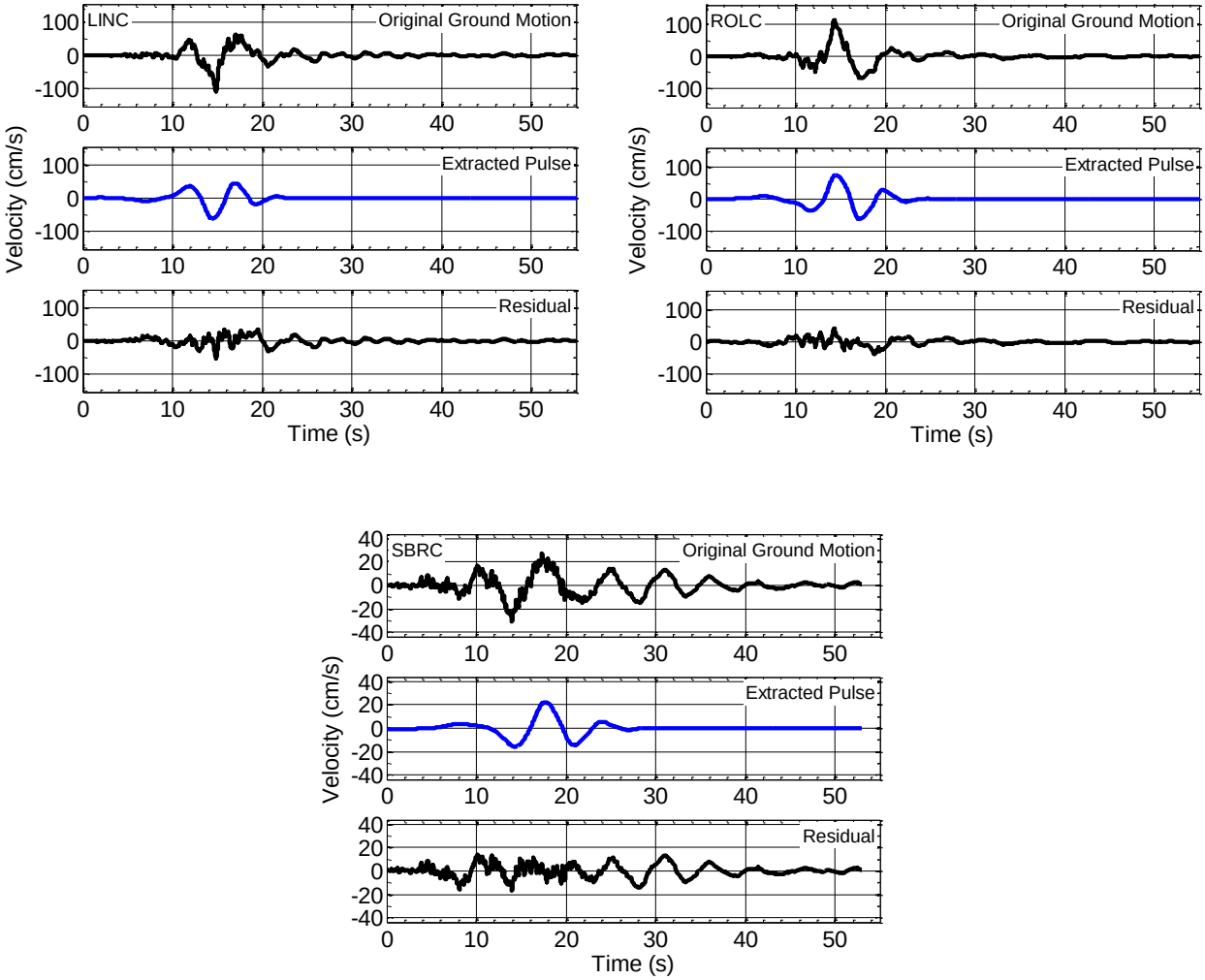

Figure 3.25: Ground motions identified as pulse-like using the automated Shahi (2013) pulse classification algorithm in the M_w7.1 Darfield earthquake.

3.3.2.2 22 February 2011 M_w6.2 Christchurch earthquake

The S13 algorithm was also applied to the near-fault ground motions resulting from the 22 February 2011 M_w6.2 Christchurch earthquake. For the purposes of clarity, 'correct' and 'incorrect' classifications of pulse-like ground motions using the automated algorithm are separately illustrated in Figure 3.26 and Figure 3.27, respectively. It is evident from both figures that the automated pulse classifications obtained using the B07 and S13 algorithms are similar. In addition, three ground motions (D06C, HPSC and LPCC) which were not classified as such by the B07 method are identified as pulse-like by the S13 method. However. the 'pulse-like' classifications of the motions observed at Hulverston Drive (HPSC) and North New Brighton School (NNBS) in Figure 3.27 are considered incorrect because: (i)

the pulse extracted by the S13 algorithm from the HPSC motion corresponds to the portion of the velocity time-series where failure of the ground occurred (and subsequent tilting of the recording instrument) due to liquefaction (Bradley, personal communication, 2012); and (ii) the pulse observed in the NNBS motion is a manifestation of the cyclic mobility 'spikes' in the acceleration time-series, as discussed previously (refer to Figure 3.14). In the cases of the Moorehouse Avenue (D06C) and Lyttelton Port (LPCC) motions, the 'pulse-like' classifications are considered appropriate because they clearly demonstrate evidence of forward-directivity effects.

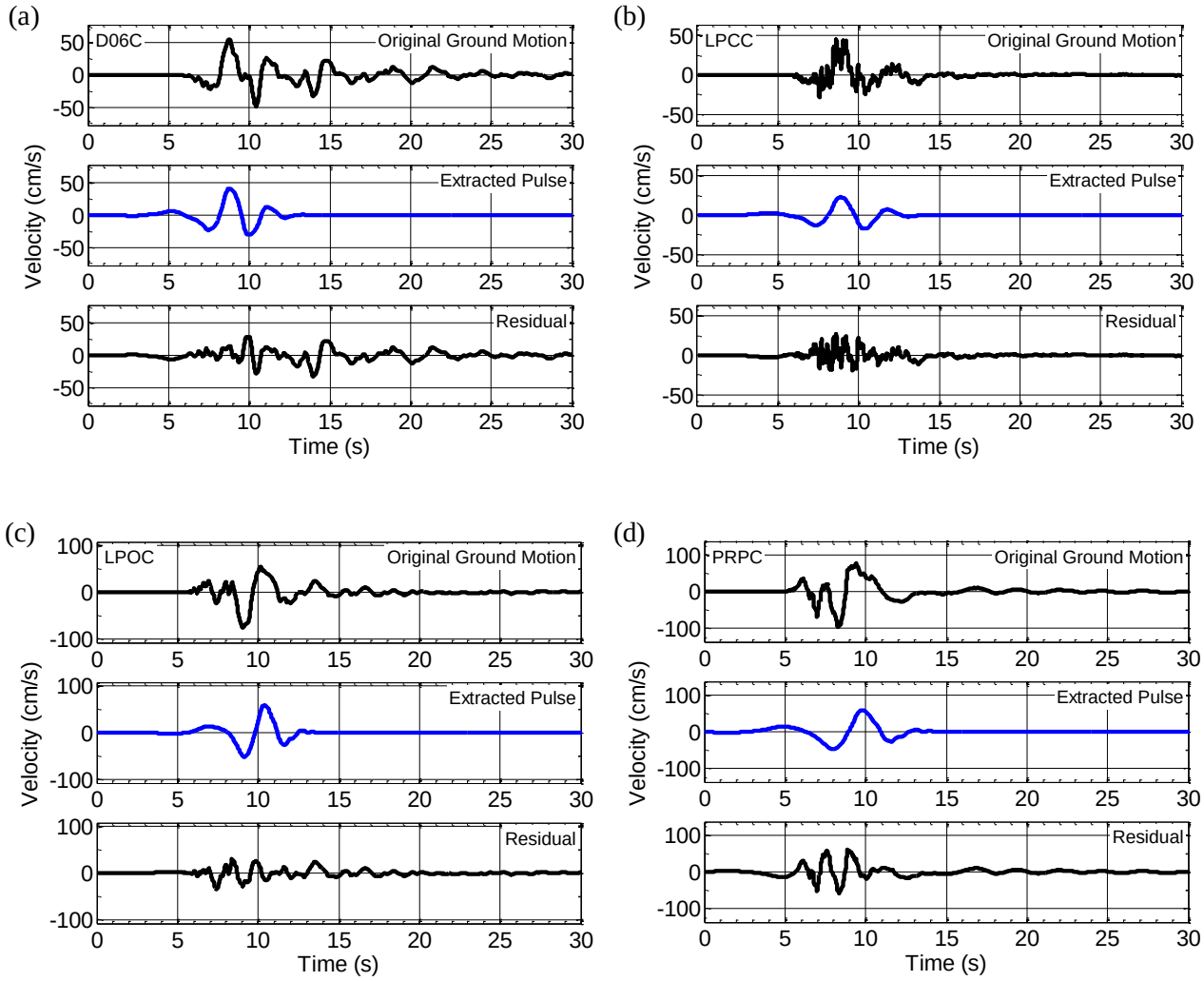

Figure 3.26: Correct classification of pulse-like ground motions observed at: (a) D06C; (b) LPCC; (c) LPOC; and (d) PRPC in the M_w6.2 Christchurch earthquake using the automated Shahi (2013) pulse classification algorithm.

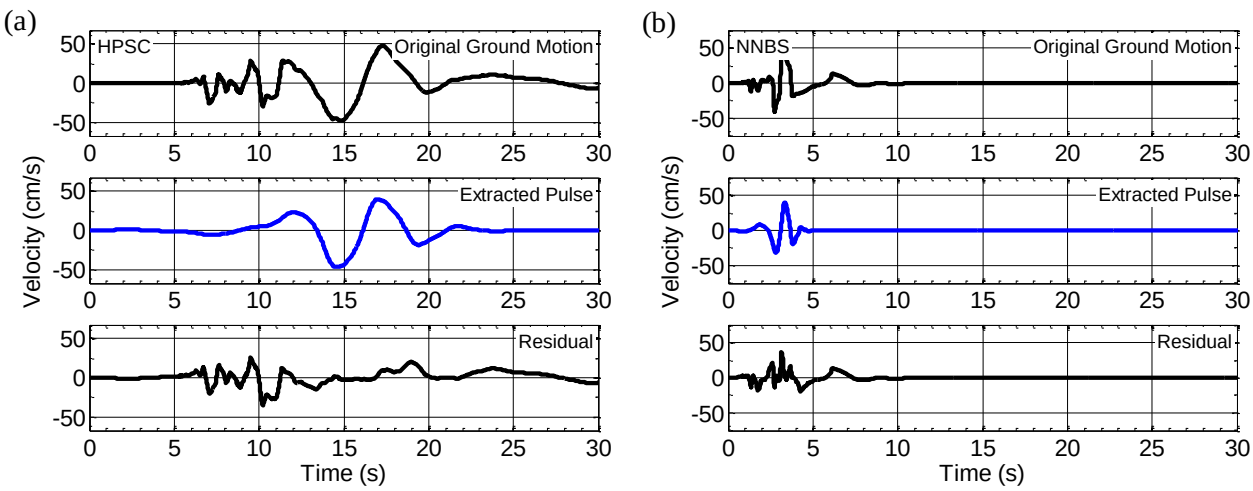

Figure 3.27: Examples of incorrect pulse-like classification of ground motions observed at (a) HPSC; and (b) NNBS in the M_w6.2 Christchurch earthquake using the automated Shahi (2013) pulse classification algorithm.

3.3.3 Comparison of pulse classification methods

The identification of ground motions exhibiting forward-directivity effects using the B07 algorithm (in conjunction with the 'manual' and visual approaches) in the Canterbury earthquakes was largely completed before the S13 algorithm was released in the public domain. Hence, the pulse classification exercise in the previous two sections was carried out purely to determine whether improved results could be obtained in relation to the B07 algorithm. It has been illustrated through several examples that the automated nature of both methods does not allow them to distinguish between early-arriving directivity pulses and pulse-like features due to other effects. In general, it was also evident that the improved classification criteria associated with the S13 algorithm did not provide superior pulse classification results for the two main events in the Canterbury earthquake sequence. Nonetheless, it should be noted that this method has several advantages over its predecessor, which have been addressed in Chapter 2. For example, according to Shahi (2013), several days of computation time can be saved using this algorithm in classifying large ground motion databases (e.g. NGA-West2) when compared to the B07 algorithm. Moreover, the use of both algorithms eliminates the need for an otherwise laborious and slow manual classification process, particularly when dealing with large strong motion datasets. Based on the previous comparisons in this chapter, the classification results obtained using the B07 algorithm (presented in Section 3.3.1) were adopted for the remainder of the present study.

3.4 Pulse period

The period of the directivity pulse has an important role in the response of structures subjected to pulse-like ground motions, as mentioned in Chapter 2. Several approaches have been proposed by researchers in the past to characterise the pulse period, including: (i) finding the period corresponding to the peak of the pseudo-velocity response spectrum (Alavi & Krawinkler, 2000); (ii) determining the time interval between zero-crossings of the directivity pulse (Bray & Rodriguez-Marek, 2004); (iii) the period corresponding to the dominant frequency of a pulse fitted using analytical models (Mavroeidis & Papageorgiou, 2003); and (iv) the period associated with the maximum Fourier amplitude of the pulse extracted using wavelet analysis from the original ground motion (Baker, 2007; Shahi, 2013). In this study, the first and fourth approaches were considered because they are fully automated and hence require no user judgement, unlike the other two methods. Figure 3.28 provides a comparison between the pulse periods obtained using these approaches for the forward-directivity ground motions from the Darfield and Christchurch earthquakes. In general, it can be observed that the pulse periods obtained using the B07 algorithm are higher than those associated with the peak of the pseudo-velocity response spectrum. Baker (2007) recommends that in cases where there is a significant difference between the periods provided by the two methods, the B07 approach is more robust because the period corresponds to the extracted pulse. Hence, the pulse periods corresponding to the forward-directivity ground motions from the Canterbury earthquakes obtained using wavelet analysis are adopted for the remainder of this study. Further analysis of the characteristics of the observed pulse periods in the Canterbury earthquakes is carried out in Chapter 6.

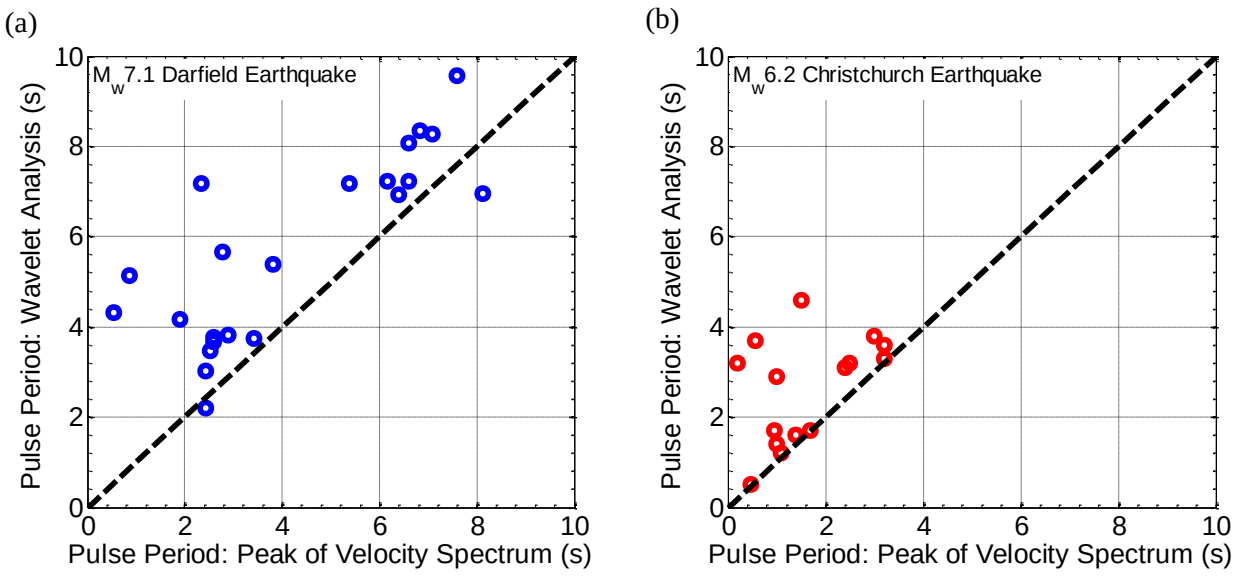

Figure 3.28: Comparison of the pulse periods obtained using the Baker (2007) wavelet analysis algorithm and pseudo-velocity response spectrum for the forward-directivity ground motions from: (a) 4 September 2010 M_w 7.1 Darfield; and (b) 22 February 2011 M_w6.2 Christchurch earthquakes.

3.5 Pulse orientation

Assuming that the conditions for rupture directivity are met (i.e. the direction of rupture and slip are aligned on the causative fault), seismological theory indicates that the S-waves travelling in the direction of rupture will be polarised in the fault-normal direction due to their radiation pattern (Somerville et al., 1997). Consequently, a large amplitude velocity pulse, which results from the constructive interference of S-waves travelling slightly ahead of the rupture front is also observed in the fault-normal component of horizontal ground motion, as discussed previously in Chapter 2. However, for complex earthquake ruptures involving multiple fault planes, a well-defined fault-normal direction does not exist. In such cases, it is useful to ascertain and compare the orientation corresponding to the strongest directivity pulse (if observed) to the fault-normal orientations of the causative fault planes. This involves rotating the horizontal components of the velocity time-series through all possible non-redundant orientations and finding the orientation corresponding to the maximum PGV (within the time interval in which the directivity pulse arrives). This approach was applied to the forward-directivity ground motions resulting from the Darfield, Christchurch and 13 June 2011 (M_w6.0) events (documented in Section 3.3.1), and the results are discussed in the following sections.

3.5.1 4 September 2010 M_w7.1 Darfield earthquake

Figure 3.29 illustrates the pulse orientations observed at strong motion stations located east and west of the central and eastern segments (a reminder that these segments are represented as a single fault plane in the FFM of Holden et al. (2011)) of the Greendale fault. Also shown are the directions normal to the strike of the three fault segments which comprise the Greendale fault. It can be seen that a majority of the pulses in the eastern locations exhibit strong polarity towards the fault-normal direction (176°) of the central and eastern segments. This can be explained by large slip amplitudes (approximately 5 m according to the slip distribution obtained by Beavan et al. (2012)) along the central segment of the Greendale fault which ruptured towards Christchurch. Similarly, the pulses observed at western locations such as HORC and DSLC are closely aligned with the fault-normal direction of the north-western Greendale fault segment (33°), with the only exception being the pulse observed at GDLC. In the latter case, the pulse orientation is comparable to the fault-normal direction of the central segment. This can possibly be attributed to its location (R_{rup} = 0.8 km) in relation to the bilateral rupture of the Greendale fault.

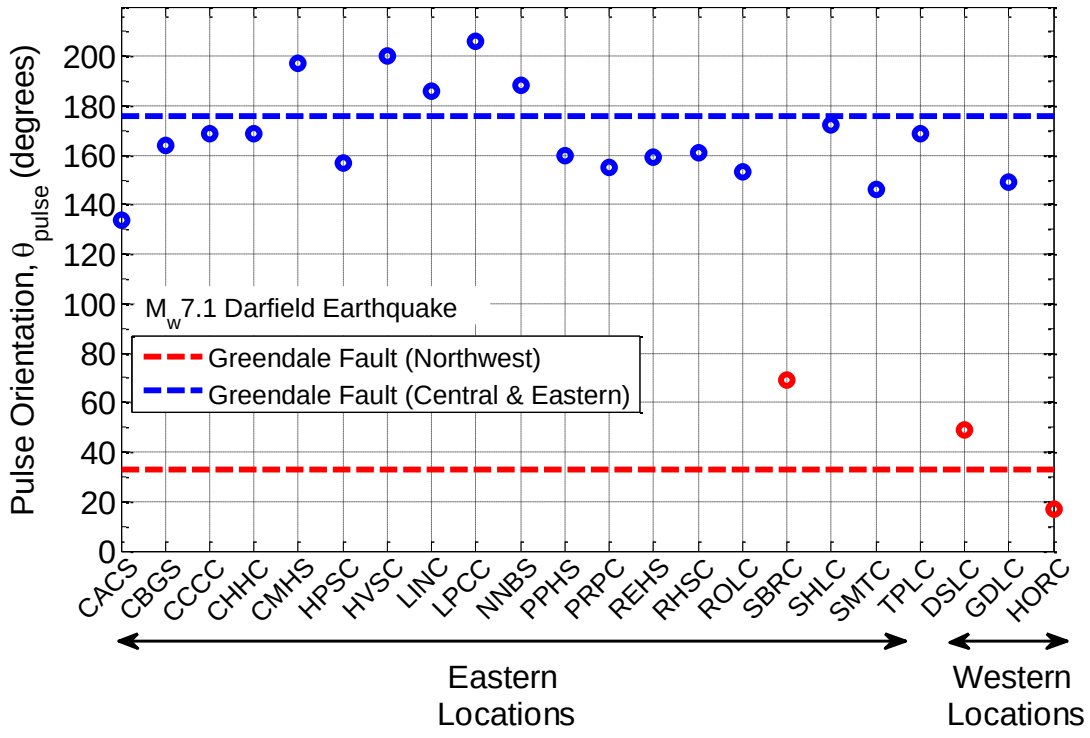

Figure 3.29: Comparison of observed pulse orientations in the M_w7.1 Darfield earthquake to the fault-normal orientations of the three segments of the strike-slip Greendale fault.

3.5.2 22 February 2011 M_w6.2 Christchurch earthquake

The pulse orientations observed in the Christchurch earthquake are illustrated in Figure 3.30 and are grouped together based on the locations of the corresponding stations with respect to the CBD. In addition, orientations normal to the fault segments from the one-fault model of Beavan et al. (2011) and three-fault model of Beavan et al. (2012) are shown for comparison. Generally, it can be observed that the orientations of the pulses observed in each group are similar and are well-aligned with at least one fault plane. For example, the pulse orientations in the northern locations are remarkably similar to the fault-normal directions of the right-lateral fault (157°), oblique fault (154°) and reverse thrust fault (149°). Given that the more recent FFM, which indicates a segmented rupture process and is considered to be superior in relation to the one-fault model (Beavan et al., 2012), it is likely that the pulses observed in the northern locations occurred due to rupture directivity along either or both of the two aforementioned fault segments. Nonetheless, this is difficult to confirm using kinematic finite fault models alone as they do not offer any information on the evolution of rupture with time.

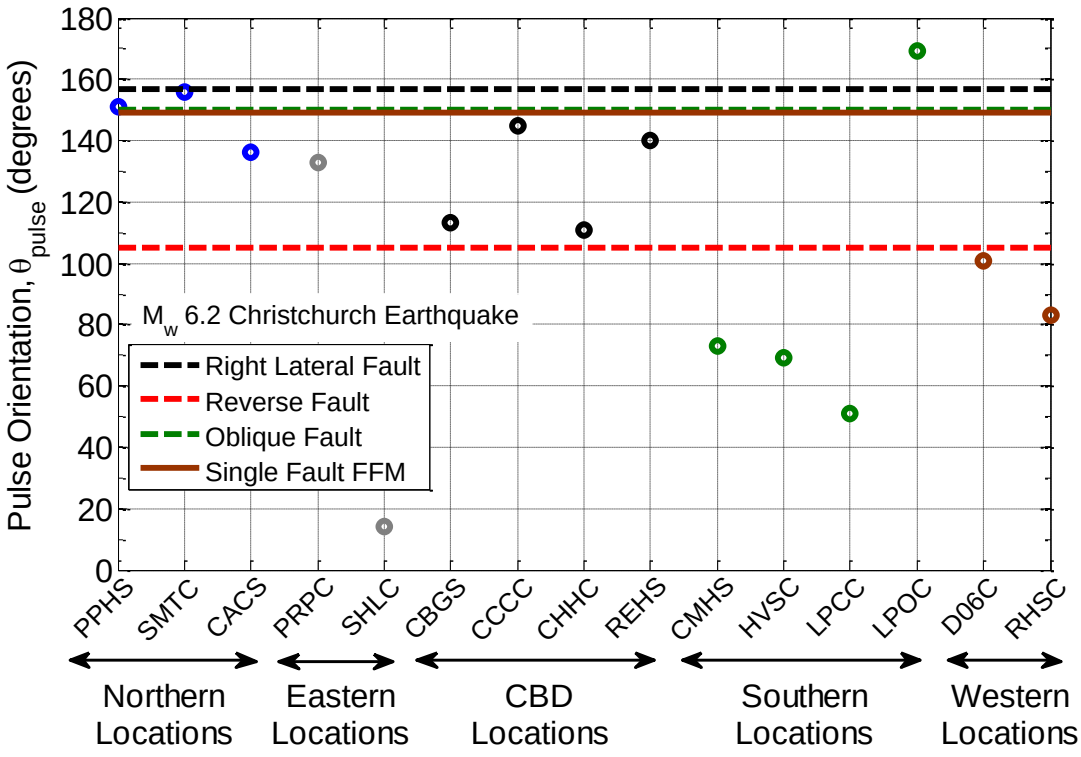

Figure 3.30: Comparison of observed pulse orientations in the M_w6.2 Christchurch earthquake to the fault-normal orientations of the causative fault planes.

It is interesting to note that the pulse orientations observed at the LPCC (51°) and LPOC (169°) stations in Lyttelton (south of the CBD) are significantly different despite being approximately 1 km apart. This can likely be attributed to the influence of local site effects on the incoming directivity pulse. While the LPCC station is situated on engineering bedrock (site class B), the LPOC station is located on a thin layer of colluvium (site class C), as mentioned in Chapter 2. Based on the horizontal velocity trajectory shown in Figure 3.31 (corresponding to the north and east components of the velocity time-series), it is obvious that the ground response is remarkably different at the two stations despite their close proximity. For example, in addition to the larger PGV observed at LPOC, it can be observed that the response is characterised by significantly lower high-frequency ground motion compared to LPCC. This has been inferred as being a result of the nonlinear response of surficial soils at the site (Bradley & Cubrinovski, 2011).

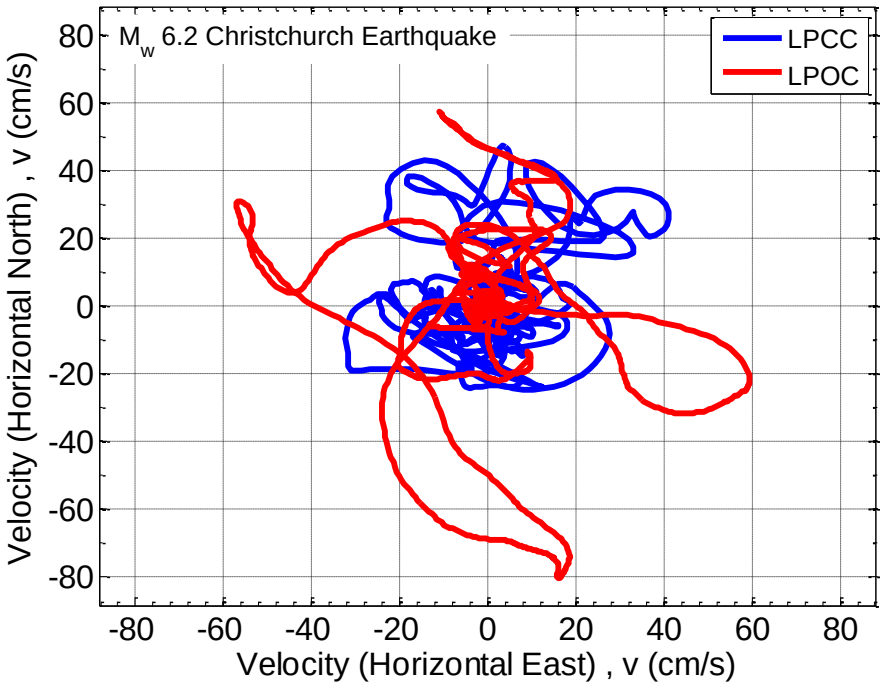

Figure 3.31: Comparison of the horizontal velocity trajectory observed at two stations in Lyttelton Port, one on rock (LPCC) and the other on soil (LPOC).

3.5.3 13 June 2011 M_w6.0 June earthquake

Similar to the Christchurch earthquake, the pulse orientations observed in the 13 June 2011 M_w6.0 event are also grouped according to the locations of the strong motion stations in Figure 3.32. The fault-normal directions corresponding to the two causative fault planes are shown for comparison. Unlike the two events discussed previously, the trends exhibited by the individual groupings are not immediately obvious. To some extent, this is a limitation of the simplified approach adopted in determining the pulse orientation. Nevertheless, by examining the results shown in Figure 3.32, some general trends can be identified. For example, apart from the GODS and PARS stations, the remaining southern stations have pulse orientations which are closely aligned with the oblique fault. Conversely, the orientations of the GODS and PARS stations are closer to the fault-normal direction of the strike-slip fault. This is likely due to the location of these stations within the surface projection of the latter fault segment (refer to Figure 3.4), where the rupture was initiated.

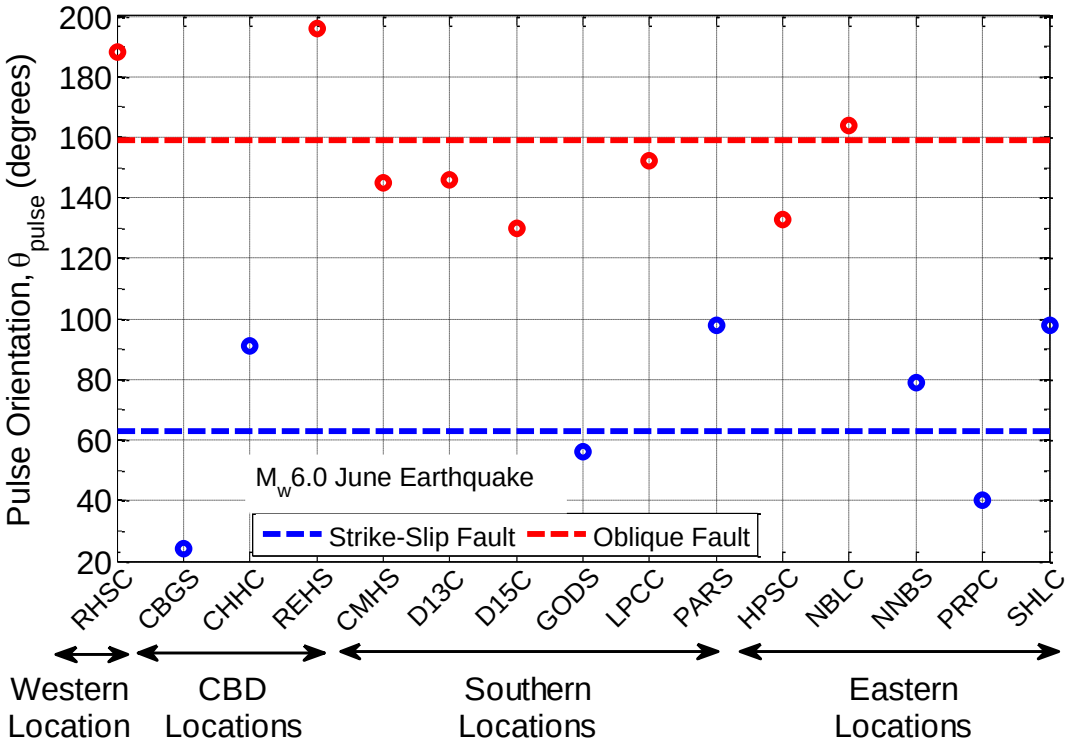

Figure 3.32: Comparison of observed pulse orientations in the M_w6.0 June event to the fault-normal orientations of the two causative fault planes.

3.6 References

Alavi, B., & Krawinkler, H. (2000). Consideration of near-fault ground motion effects in seismic design. In *Proceedings of the 12th World Conference on Earthquake Engineering*. Auckland, New Zealand. Retrieved from http://www.iitk.ac.in/nicee/wcee/article/2665.pdf

Baker, J. W. (2007). Quantitative classification of near-fault ground motions using wavelet analysis. *Bulletin of the Seismological Society of America*, **97**(5):1486–1501. doi:10.1785/0120060255

Bannister, S., & Gledhill, K. (2012). Evolution of the 2010–2012 Canterbury earthquake sequence. *New Zealand Journal of Geology and Geophysics*, **55**(3):295–304. doi:10.1080/00288306.2012.680475

Beavan, J., Fielding, E., Motagh, M., Samsonov, S., & Donnelly, N. (2011). Fault location and slip distribution of the 22 February 2011 Mw 6.2 Christchurch, New Zealand, Earthquake from geodetic data. *Seismological Research Letters*, **82**(6):789–799. doi:10.1785/gssrl.82.6.789

Beavan, J., Wallace, L., Samsonov, S., Ellis, S., Motagh, M., & Palmer, N. (2010). The Darfield (Canterbury) earthquake: geodetic observations and preliminary source model. *Bulletin of the New Zealand Society for Earthquake Engineering*, **43**(4):228.

Beavan, J., Motagh, M., Fielding, E. J., Donnelly, N., & Collett, D. (2012). Fault slip models of the 2010–2011 Canterbury, New Zealand, earthquakes from geodetic data and observations of postseismic ground deformation. *New Zealand Journal of Geology and Geophysics*, **55**(3):207–221. doi:10.1080/00288306.2012.697472

Bradley, B. A. (2012). Strong ground motion characteristics observed in the 4 September 2010 Darfield, New Zealand earthquake. *Soil Dynamics and Earthquake Engineering*, **42**, 32–46. doi:10.1016/j.soildyn.2012.06.004

Bradley, B. A., & Cubrinovski, M. (2011). Near-Source Strong Ground Motions Observed in the 22 February 2011 Christchurch Earthquake. *Bulletin of the New Zealand Society for Earthquake Engineering*, **44**(4):181–194.

Bray, J. D., & Rodriguez-Marek, A. (2004). Characterization of forward-directivity ground motions in the near-fault region. *Soil Dynamics and Earthquake Engineering*, **24**(11):815–828. doi:10.1016/j.soildyn.2004.05.001

Chiou, B., Darragh, R., Gregor, N., & Silva, W. (2008). NGA Project Strong-Motion Database. *Earthquake Spectra*, **24**(1):23–44. doi:10.1193/1.2894831

Cubrinovski, M., Pampanin, S., & Bradley, B. (2012). Geotechnical and Structural Aspects of the 2010-2011 Christchurch (New Zealand) Earthquakes. In *Earthquakes and Health Monitoring of Civil Structures* (1st ed., p. 337). Springer. Retrieved from http://canterbury.eblib.com.au.ezproxy.canterbury.ac.nz/patron/FullRecord.aspx?p=1083532&echo=1&userid=5Mh2J3e%2fCZk%3d&tstamp=1371262344&id=302BAD172B34A197FCEF5A6A7EC8CC620A5C8B0F

GeoNet. (2011). *GeoNet moment Tensor Solution Database 2011*. Retrieved May 5, 2013, from www.geonet.org.nz/resources/earthquake/

Holden, C., Beavan, J., Fry, B., Reyners, M., Ristau, J., Van Dissen, R., … Quigley, M. (2011). Preliminary source model of the Mw 7.1 Darfield earthquake from geological, geodetic and seismic data. In *Proceedings of the Ninth Pacific Conference on Earthquake Engineering: Building an Earthquake-Resilient Society* (pp. 14–16). Retrieved from http://www.nzsee.org.nz/db/2011/164.pdf

Kempton, J. J., & Stewart, J. P. (2006). Prediction Equations for Significant Duration of Earthquake Ground Motions Considering Site and Near-Source Effects. *Earthquake Spectra*, **22**(4):985–1013. doi:10.1193/1.2358175

Mavroeidis, G. P., & Papageorgiou, A. S. (2003). A mathematical representation of near-fault ground motions. *Bulletin of the Seismological Society of America*, **93**(3):1099–1131.

Ristau, J., Holden, C., Kaiser, A., Williams, C., Bannister, S., & Fry, B. (2013). The Pegasus Bay aftershock sequence of the Mw 7.1 Darfield (Canterbury), New Zealand earthquake. *Geophysical Journal International*. doi:10.1093/gji/ggt222

Shahi, S. K. (2013, January). *A probabilistic framework to include the effects of near-fault directivity in seismic hazard assessment*. Stanford University, Stanford.

Smyrou, E., Tasiopoulou, P., Bal, I. E., & Gazetas, G. (2011). Ground Motions versus Geotechnical and Structural Damage in the February 2011 Christchurch Earthquake. *Seismological Research Letters*, **82**(6):882–892. doi:10.1785/gssrl.82.6.882

Somerville, P. G., Smith, N. F., Graves, R. W., & Abrahamson, N. A. (1997). Modification of empirical strong ground motion attenuation relations to include the amplitude and duration effects of rupture directivity. *Seismological Research Letters*, **68**(1):199–222.

Standards New Zealand. (2004). *NZS1170.5:2004, Structural Design Actions, Part 5: Earthquake actions- New Zealand*. Wellington, New Zealand.

Stirling, M. W., Gerstenberger, M., Litchfield, N., McVerry, G. H., Smith, W. D., Pettinga, J. R., & Barnes, P. (2007). *Updated probabilistic seismic hazard assessment for the Canterbury Region*. Retrieved from

http://ecan.govt.nz/publications/Reports/canterbury-probabilistic-seismic-hazard-assessment-report.pdf

4 Probability of Pulse Occurrence

4.1 Overview

In this chapter, empirical models developed by several researchers for predicting the probability of pulse occurrence are reviewed and evaluated (in terms of bias and precision) using observations from four events in the Canterbury earthquake sequence. The evaluation procedure involves fitting logistic regression models to the pulse/non-pulse observations with predictions from the pulse probability models acting as the main predictor variable. In doing so, the most suitable pulse probability model is chosen for use in the subsequent examination of response spectra-based directivity models (Chapter 5) and New Zealand-specific probabilistic seismic hazard analyses incorporating near-fault directivity effects (Chapter 7). Finally, pulse probability contour maps are developed for the four events listed above and compared to observations of pulse-like and non-pulse-like ground motions at sites located within the near-fault region of the causative ruptures.

4.2 Pulse probability models

Evidence from numerous studies (refer to the detailed literature review in Chapter 2) has consistently shown that pulse-like ground motions place larger demands on structures located in the near-fault region when compared to ordinary ground motions. For example, it has been established that ground motions from the former category typically have larger elastic pseudo-spectral acceleration (*SA*) amplitudes in the vicinity of the pulse period than those from the latter category (e.g. Somerville (2003); Shahi & Baker (2011)). However, empirical evidence from previous earthquakes has also shown that pulse-like ground motions may not always be observed at near-fault sites where they are expected to occur (i.e. if the rupture and slip direction is aligned in the direction of a particular site). In these cases, the observed velocity time-series typically resembles a ground motion observed in the far-field region. More importantly, the response of structures to these so-called non-pulse-like ground motions is effectively similar to ordinary (or far-field) ground motions (Tothong & Luco, 2007).

Current empirical ground motion prediction models do not make any provision for the aforementioned amplification of *SA* amplitudes caused by pulse-like ground motion features. The application of these models in conventional probabilistic seismic hazard analysis (PSHA) therefore results in the underestimation of seismic hazard for a given near-fault site (Abrahamson, 2000; Shahi & Baker, 2011; Tothong et al., 2007). Based on this realisation, there has been a growing interest among researchers in the development of models that predict the occurrence of pulse probability. For example, Iervolino & Cornell (2008) developed the first empirical model to predict the pulse probability for strike-slip and non strike-slip events. Using a larger database of pulse-like ground motions from the NGA (Chiou et al., 2008) and NGA West2 (Ancheta et al., 2013) strong motion databases, respectively, Shahi & Baker (2010) and Shahi (2013) developed similar prediction models. In fact, as part of the former study, the authors successfully demonstrated that the use of such models provides a more representative estimate of the near-fault seismic hazard when used in conjunction with ground motion models which include the effect of pulse-like ground motions (e.g. using the broadband and narrowband directivity models discussed in Chapter 2)

Although forward-directivity is a well understood phenomenon, predicting its occurrence based solely on simple physical parameters is difficult due to the complexity of rupture and wave propagation phenomena (Iervolino & Cornell, 2008; Chioccarelli & Iervolino, 2012). Since the process of observing pulse-like ground motions is a binary process, it can be defined using an indicator (or random) variable (I) which has a value of 1 if a pulse is observed or 0 if no pulse is observed in the ground motion record (Iervolino & Cornell, 2008). In order to represent this categorical variable as a function of independent variables which have some explanatory power, logistic regression is most commonly used (Kutner et al., 2005). It has been ascertained in previous research (e.g. Somerville et al., 1997) that the variation in ground motion amplitude due to forward-directivity effects in the near-fault region is strongly dependent on the source-to-site geometry. Based on a detailed statistical analysis, Iervolino & Cornell (2008) found that the closest distance to the fault plane from the site (R_{rup} in units of kilometres); fault rupture length (s for strike-slip and d for non strike-slip events in units of kilometres); and the angle between the direction of rupture propagation and waves travelling from the fault to site (θ in units of degrees for strike-slip events measured from the epicentre to the site in the horizontal plane; and ϕ in units of degrees for non strike-slip events measured from the hypocentre to the site in the vertical plane) have the best predictive capabilities for the purposes of predicting pulse probability. These parameters are illustrated in Figure 4.1. The multivariate logistic regression equations developed by Iervolino & Cornell (2008) to predict the occurrence of pulse probability for strike-slip and non strike-slip events are shown in Equations (4.1) and (4.2), respectively:

$$P\left(pulse|R_{rup}, s, \theta\right) = \frac{e^{0.859-0.111R_{rup}+0.019s-0.044\theta}}{1+e^{0.859-0.111R_{rup}+0.019s-0.044\theta}} \tag{4.1}$$

$$P\left(pulse|R_{rup}, d, \phi\right) = \frac{e^{0.553-0.055R_{rup}+0.027s-0.27\phi}}{1+e^{0.553-0.055R_{rup}+0.027s-0.27\phi}} \tag{4.2}$$

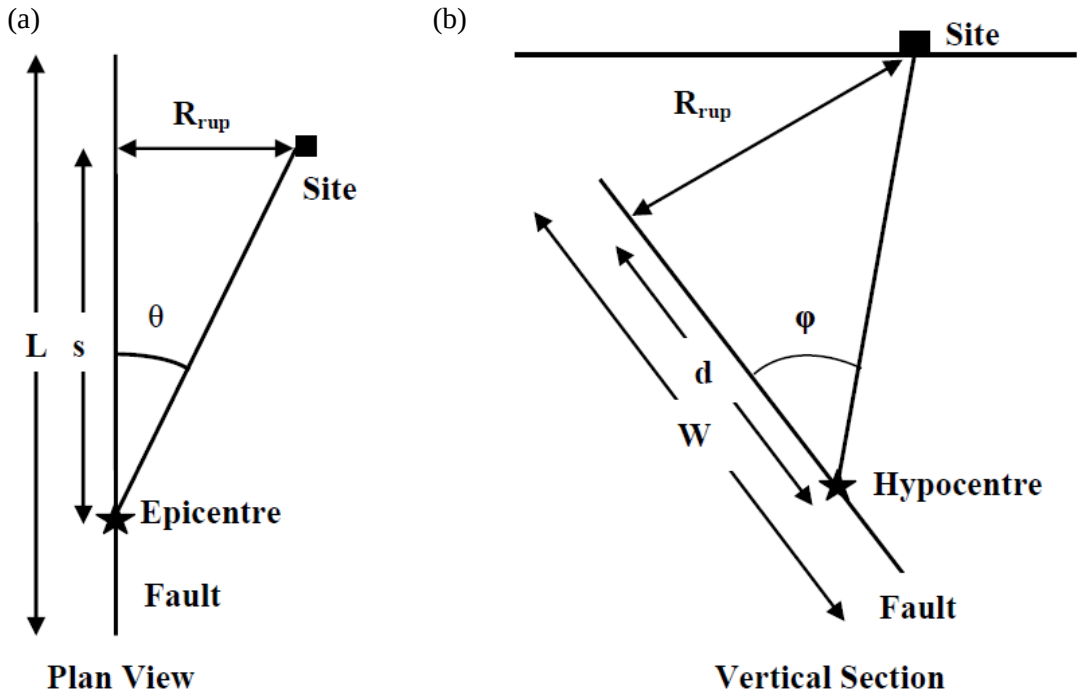

Figure 4.1: Source-to-site geometry illustrating the parameters used in the development of pulse probability prediction models for: (a) Strike-slip fault; and (b) Non strike-slip fault (modified from Somerville et al., 1997).

It is important to note that Iervolino & Cornell (2008) developed their pulse probability model (hereafter referred to as the IC08 model) using a database of 91 pulse-like ground motions classified by Baker (2007) using a wavelet-based pulse classification algorithm (refer to Chapters 2 and 3 for further details regarding the algorithm). Because these classifications were carried out only using the fault-normal component of the ground motions, Shahi & Baker (2010) reasoned that the IC08 model can only be used to predict the pulse probability in the fault-normal orientation. As a result, Shahi and Baker (2010) classified pulses using ground motions from the NGA database (Chiou et al., 2008) at arbitrary orientations. In essence, this involved rotating the ground motion though all non-redundant orientations and classifying the ground motion as pulse-like or non-pulse-like in each orientation using the wavelet analysis algorithm of Baker (2007). Using 169 identified pulse-like ground motions, Shahi & Baker (2010) developed a revised pulse probability model (hereafter referred to as the SB10 model) for strike-slip and non strike-slip events which are illustrated in Equations (4.3) and (4.4), respectively. It can be observed that θ does not feature in their model for strike-slip events because it was found that R_{rup} and s effectively define the geometry for a majority of the identified pulse-like cases (refer to Shahi & Baker (2010) for further details).

$$P(pulse|R_{rup}, s) = \frac{1}{1 + e^{0.642+0.167R_{rup}-0.075s}} \quad (4.3)$$

$$P(pulse|R_{rup}, d, \phi) = \frac{1}{1 + e^{0.128+0.055R_{rup}-0.061d+0.036\phi}} \quad (4.4)$$

Recently, Shahi (2013) argued that the two previously described IC08 and SB10 models were fit using databases that include ground motions with pulse-like features caused by phenomena other than forward-directivity effects. Thus, using a database of 145 forward-directivity ground motions identified by means of a revised pulse classification algorithm (refer to Chapters 2 and 3 for further details regarding the algorithm) from the NGA-West2 database (Ancheta et al., 2013), Shahi (2013) re-fit the logistic regression equations for both, strike-slip and non strike-slip events, as shown in Equations (4.5) and (4.6), respectively. It can be observed from both equations that the Shahi (2013) model (hereafter referred to as the S13 model) differs from its predecessors due to the square root dependence of the pulse probability on the fault rupture length. This functional form was justified by the fact that the IC08 and SB10 models predict high pulse probabilities for large values of s in strike-slip ruptures, which is due to the lack of data with long rupture lengths and also inconsistent with theoretical predictions (Shahi, 2013). More importantly, the model presented in Equation (4.5) provides a better extrapolation for longer rupture lengths in comparison to the model developed in the same study without the square root dependence. For non strike-slip events, the model presented in Equation (4.6) was chosen in relation to other possible functional forms based on the results of statistical analysis (refer to Shahi (2013) for further details).

$$P(pulse|R_{rup}, s, \theta) = \frac{1}{1 + e^{0.7897+0.1378R_{rup}-0.3533\sqrt{s}+0.020\theta}} \quad (4.5)$$

$$P(pulse|R_{rup}, d, \phi) = \frac{1}{1 + e^{1.483+0.124R_{rup}-0.688\sqrt{d}+0.022\phi}} \quad (4.6)$$

Figure 4.2 illustrates the scaling of the IC08, SB10 and S13 pulse probability models as a function of the source-to-site distance (R_{rup}) and fault rupture length (s and d for strike-slip and non strike-slip events , respectively). By examining the fault geometry in Figure 4.1, it is evident that the source-to-site angle dependence (θ and ϕ) of the models can also be captured by varying the two aforementioned geometric parameters (i.e. $\theta = \tan^{-1}(R_{rup}/s)$ and $\phi = \tan^{-1}(R_{rup}/d)$). In general, it can be observed from Figure 4.2 that the pulse

probability decreases with R_{rup} (and therefore with θ and ϕ for constant values of s and d, , respectively) and increases with the fault rupture length for both type of events.

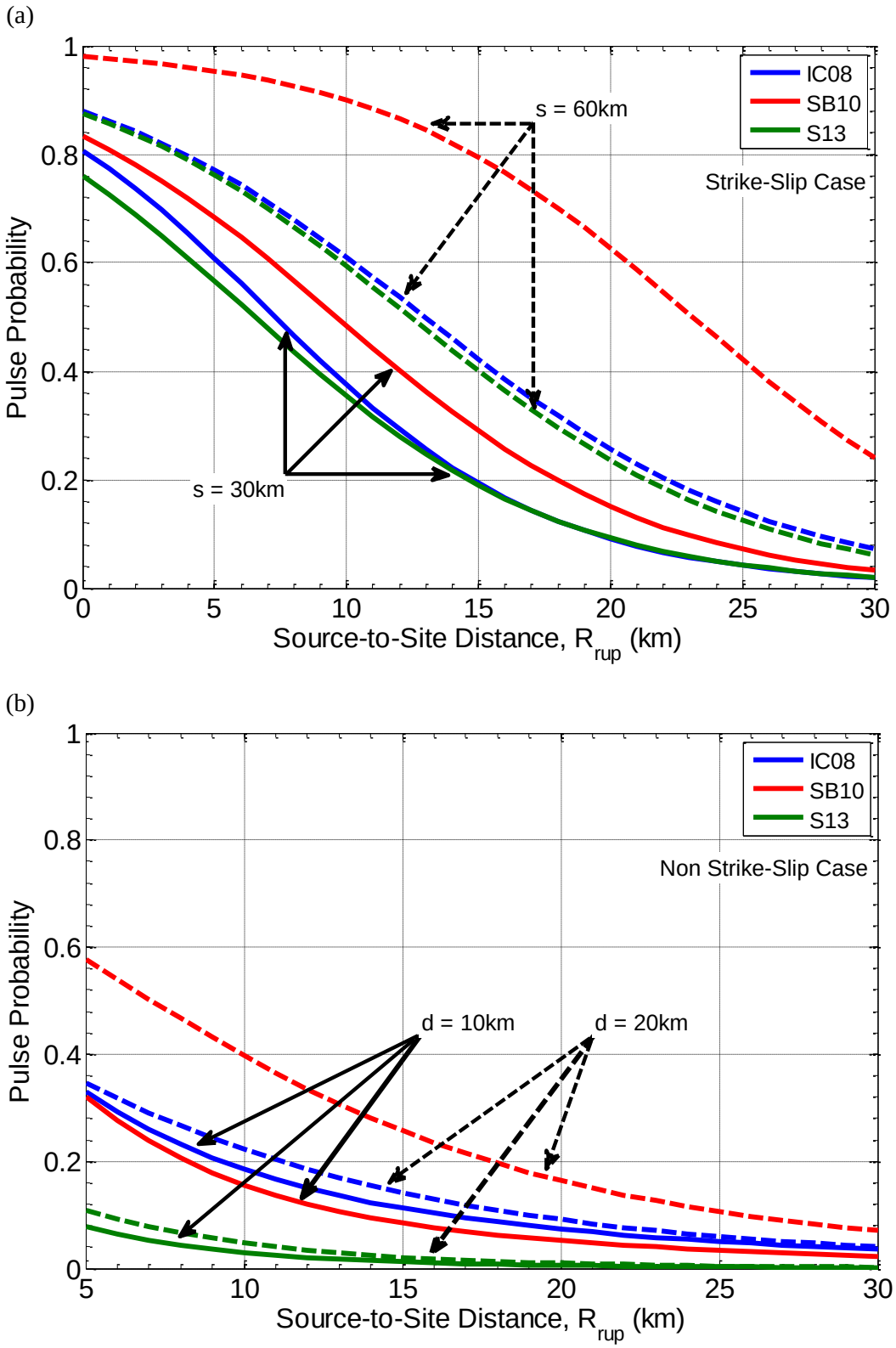

Figure 4.2: Source-to-site distance and fault rupture length scaling of the IC08, SB10 and S13 pulse probability models for (a) Strike-slip faults; and (b) Non strike-slip faults.

4.3 Evaluation of pulse probability models

The present study requires the use of pulse probability models for the purposes of assessing empirical models which capture the effect of directivity on acceleration response spectra and to carry out New Zealand-specific PSHA accounting for the directivity phenomenon (refer to Chapters 5 and 7, respectively). Observations from the 4 September 2010 M_w7.1 Darfield; 22 February 2011 M_w6.2 Christchurch; 13 June 2011 M_w6.0; and 23 December 2011 M_w5.9 earthquakes are used herein to evaluate the IC08, SB10 and S13 models described previously. The following sections outline this evaluation procedure and present the associated results.

4.3.1 Pulse probability predictions for the Canterbury earthquakes

Predictions of the pulse probabilities for sites located in the near-fault region of the causative faults in the four aforementioned events were obtained using the IC08, SB10 and S13 models. Although several events in the Canterbury earthquake sequence are characterised by complex ruptures involving multiple fault planes (refer to Chapters 2 and 3 for further details), the following assumptions were made in defining the source-to-site geometry:

- **4 September 2010**: The western and central segments of the Greendale fault from the finite fault model (FFM) of Holden et al. (2011) were used to define the source-to-site geometry in the M_w7.1 Darfield earthquake because the ground motion analysis in Chapter 3 indicated strong polarity of the observed directivity pulses towards the fault-normal orientations corresponding to these fault segments.
- **22 February 2011**: Although the more recent FFM of Beavan et al. (2012) includes three fault planes, the one-fault model of Beavan et al. (2011) was used to define the source-to-site geometry because guidelines on incorporating multiple fault planes in the calculations do not exist in previous research (as far as the author's knowledge is concerned).
- **13 June 2011**: Similar to the Christchurch earthquake, the rupture process in the M_w 6.0 June earthquake was characterised by a left-lateral strike-slip fault segment and an oblique fault segment according to the FFM of Beavan et al. (2012). For the purposes of defining the source-to-site geometry, the former fault

plane was used because the moment tensor solution indicated a strike-slip faulting mechanism and also due to the reason provided above.

- **23 December 2011**: The single fault model of Beavan et al. (2012), which indicates oblique faulting, was used to define the source-to-site geometry for the M_w5.9 December earthquake.

Based on an examination of the source-to-site geometry for generalised strike-slip and non-strike-slip faults in Figure 4.1, it is evident that the calculation of geometric parameters must be carried out in the horizontal and vertical planes, respectively. Although a consistent set of guidelines do not exist in literature for the calculation of geometric (or directivity) parameters (d and ϕ) in the case of non strike-slip events (which are three-dimensional in nature), a simplified approach recommended by Bradley (personal communication, 2013) and Shahi (personal communication, 2013) was adopted herein. In short, this approach involves calculating the source-to-site distance (R_{rup}) using three-dimensional geometry and the directivity parameters using two-dimensional geometry. The approach followed in the OpenSHA (Field et al., 2003) framework to incorporate the broadband directivity model of Abrahamson (2000) was employed herein to calculate the geometric (or directivity) parameters (s and θ) for strike-slip events. Table 4.1-Table 4.4 summarise the parameters which define the source-to-site geometry for all near-fault strong motions stations in the four events and the corresponding predicted pulse probabilities (using the IC08, SB10 and S13 models). In addition, it is also indicated whether or not a directivity pulse was observed at the near-fault sites in each event. It should be noted that only the Greendale fault and left-lateral strike-slip segment have been used to calculate the source-to-site distance for the Darfield and June events, respectively. This provides an explanation for the slight discrepancies between the R_{rup} values reported here and in Chapter 3 where all the fault planes were used.

Table 4.1: Summary of the geometric parameters, predicted pulse probabilities and observations of pulse occurrence corresponding to near-fault strong motion stations in the 4 September 2010 M_w7.1 Darfield earthquake.

Station	Distance[1], R_{rup} (km)	s (km)	θ (degrees)	Predicted Pulse Probability			Pulse Observed
				IC08	SB10	S13	
CACS	11.9	29.9	15.3	0.06	0.40	0.31	Yes
CBGS	14.4	29.9	6.2	0.04	0.31	0.28	Yes
CCCC	16.3	29.9	4.6	0.02	0.25	0.23	Yes
CHHC	14.8	29.9	5.2	0.03	0.30	0.27	Yes
CMHS	14.0	29.9	0.8	0.04	0.32	0.31	Yes
DFHS	11.0	1.0	90.0	0.01	0.09	0.03	No
DSLC	9.3	8.1	43.4	0.07	0.17	0.13	Yes
GDLC	0.9	0.0	90.0	0.04	0.31	0.06	Yes
HORC	1.8	10.0	4.5	0.49	0.45	0.50	Yes
HPSC	21.7	29.9	8.8	0.01	0.12	0.12	Yes
HVSC	20.8	29.9	1.3	0.01	0.13	0.15	Yes
KPOC	27.7	29.9	24.4	0.00	0.05	0.04	No
LINC	5.8	29.9	10.5	0.23	0.65	0.53	Yes
LPCC	22.4	29.9	4.8	0.01	0.11	0.12	Yes
LRSC	24.5	10.0	57.9	0.00	0.02	0.01	No
NNBS	23.2	29.9	9.3	0.01	0.09	0.10	Yes
OXZ	25.5	10.0	59.3	0.00	0.02	0.01	No
PPHS	15.4	29.9	11.8	0.03	0.28	0.23	Yes
PRPC	19.4	29.9	5.9	0.01	0.16	0.16	Yes
REHS	15.9	29.9	7.1	0.03	0.26	0.23	Yes
RHSC	10.0	29.9	5.9	0.10	0.48	0.41	Yes
RKAC	18.1	0.0	90.0	0.00	0.03	0.01	No
ROLC	2.0	23.0	4.5	0.50	0.68	0.63	Yes
SBRC	25.2	11.1	59.6	0.00	0.02	0.01	Yes
SHLC	18.7	29.9	8.9	0.01	0.18	0.17	Yes
SMTC	17.6	29.9	15.0	0.02	0.21	0.17	Yes
SPFS	23.9	10.0	42.6	0.00	0.02	0.02	No
TPLC	3.2	29.9	4.7	0.40	0.74	0.65	Yes
WSFC	43.1	10.0	59.3	0.00	0.00	0.00	No

[1] Note that the source-to-site distance has been calculated only using the Greendale fault segments from the finite fault model of Holden et al. (2011) and hence, the values reported here differ from those presented in Chapter 3 for several stations.

Table 4.2: Summary of the geometric parameters, predicted pulse probabilities and observations of pulse occurrence corresponding to near-fault strong motion stations in the 22 February 2011 M_w6.2 Christchurch earthquake.

Station	**Distance, R_{rup} (km)**	**d (km)**	**ϕ (degrees)**	**Predicted Pulse Probability**			**Pulse Observed**
				IC08	**SB10**	**S13**	
CACS	12.9	5.5	47.9	0.17	0.10	0.07	Yes
CBGS	4.8	5.5	28.2	0.35	0.26	0.25	Yes
CCCC	2.9	5.5	17.8	0.44	0.36	0.35	Yes
CHHC	3.9	5.5	23.6	0.39	0.30	0.29	Yes
CMHS	1.5	5.5	6.0	0.54	0.48	0.45	Yes
D06C	3.9	5.5	24.5	0.38	0.29	0.29	Yes
HPSC	4.1	5.5	24.5	0.38	0.29	0.29	No
HVSC	3.9	5.5	40.8	0.29	0.19	0.22	Yes
KPOC	17.5	5.5	52.7	0.12	0.07	0.04	No
LINC	13.5	5.5	13.4	0.33	0.27	0.14	No
LPCC	7.0	3.0	64.5	0.16	0.07	0.07	Yes
LPOC	6.6	4.0	62.1	0.17	0.08	0.09	Yes
NNBS	4.0	5.5	24.2	0.38	0.29	0.29	No
MQZ	14.0	1.0	85.4	0.07	0.02	0.01	No
PPHS	8.8	5.5	40.8	0.23	0.15	0.14	Yes
PRPC	2.6	5.5	15.9	0.46	0.38	0.37	Yes
REHS	4.9	5.5	28.4	0.35	0.25	0.25	Yes
RHSC	6.6	5.5	34.4	0.29	0.20	0.19	Yes
ROLC	19.5	5.5	40.5	0.15	0.09	0.04	No
SHLC	5.3	5.5	30.1	0.33	0.24	0.23	Yes
SLRC	26.9	5.5	21.4	0.16	0.12	0.02	No
SMTC	10.9	5.5	45.0	0.20	0.12	0.10	Yes
SWNC	25.2	5.5	57.2	0.07	0.04	0.01	No
TPLC	12.6	5.5	41.2	0.20	0.12	0.09	No

Table 4.3: Summary of the geometric parameters, predicted pulse probabilities and observations of pulse occurrence corresponding to near-fault strong motion stations in the 13 June 2011 M_w6.0 earthquake.

Station	Distance[1], R_{rup} (km)	s (km)	θ (degrees)	Predicted Pulse Probability			Pulse Observed
				IC08	SB10	S13	
CACS	18.7	2.5	5.4	0.01	0.03	0.05	No
CBGS	10.8	2.5	56.0	0.04	0.09	0.06	Yes
CHHC	10.2	2.5	58.5	0.04	0.10	0.06	Yes
CMHS	10.4	2.5	62.3	0.03	0.10	0.05	Yes
D13C	10.5	0.0	90.0	0.01	0.08	0.02	Yes
D14C	12.8	2.0	50.8	0.03	0.07	0.04	No
D15C	4.8	1.0	90.0	0.02	0.20	0.05	Yes
GODS	1.9	2.0	17.9	0.38	0.31	0.29	Yes
HPSC	6.6	2.5	51.9	0.08	0.17	0.10	Yes
HVSC	5.6	0.0	90.0	0.02	0.17	0.03	No
KPOC	19.8	2.5	44.3	0.01	0.02	0.02	No
LINC	22.8	2.5	49.7	0.00	0.01	0.01	No
LPCC	5.9	3.0	73.8	0.04	0.20	0.08	Yes
MQZ	14.7	7.5	42.7	0.02	0.07	0.06	No
NBLC	4.6	2.5	35.5	0.16	0.23	0.17	Yes
NNBS	6.2	2.5	41.7	0.11	0.18	0.13	Yes
PARS	2.6	0.0	90.0	0.03	0.25	0.05	Yes
PPHS	13.1	2.5	41.8	0.03	0.07	0.05	No
PRPC	6.5	2.5	59.8	0.06	0.18	0.09	Yes
REHS	10.0	2.5	62.5	0.03	0.11	0.05	Yes
RHSC	14.6	2.5	20.6	0.03	0.05	0.07	Yes
ROLC	28.5	2.5	39.6	0.00	0.01	0.01	No
SHLC	8.8	2.5	56.2	0.05	0.13	0.07	Yes
SMTC	14.2	2.5	45.6	0.03	0.06	0.04	No
SWNC	28.3	2.5	15.4	0.00	0.01	0.01	No
TPLC	21.2	2.5	29.0	0.01	0.02	0.02	No

[1] Note that the source-to-site distance has been calculated only using the left-lateral strike-slip fault segment from the finite fault model of Beavan et al. (2012) and hence, the values reported here differ from those presented in Chapter 3 for several stations.

Table 4.4: Summary of the geometric parameters, predicted pulse probabilities and observations of pulse occurrence corresponding to near-fault strong motion stations in the 23 December 2011 M_w5.9 earthquake.

Station	Distance, R_{rup} (km)	d (km)	ϕ (degrees)	Predicted Pulse Probability			Pulse Observed
				IC08	SB10	S13	
ASHS	27.0	5.5	56.9	0.07	0.03	0.01	No
CACS	15.1	5.5	40.4	0.18	0.11	0.07	No
CBGS	8.3	5.5	6.3	0.45	0.38	0.26	No
CCCC	6.8	5.5	9.1	0.45	0.38	0.29	No
CHHC	8.0	5.5	1.0	0.48	0.43	0.29	No
CMHS	3.9	5.5	26.3	0.37	0.28	0.28	Yes
CRLZ	10.9	5.5	33.6	0.25	0.17	0.12	No
D09C	7.4	5.5	0.3	0.50	0.45	0.31	No
D14C	16.0	3.0	69.7	0.09	0.03	0.02	No
D15C	9.0	3.0	67.3	0.14	0.05	0.05	No
HPSC	1.8	5.5	1.5	0.57	0.51	0.47	Yes
HVSC	8.5	4.0	61.9	0.15	0.07	0.07	No
LINC	23.9	5.5	18.2	0.20	0.15	0.04	No
LPCC	11.4	3.0	75.6	0.10	0.04	0.03	No
PPHS	8.9	5.5	28.6	0.30	0.21	0.17	Yes
REHS	6.9	5.5	7.3	0.46	0.39	0.29	Yes
RHSC	12.7	5.5	16.8	0.32	0.25	0.14	Yes
ROLC	28.7	5.5	26.4	0.13	0.09	0.02	No
SHLC	4.4	5.5	10.4	0.47	0.40	0.35	Yes
SMTC	9.2	5.5	35.8	0.26	0.17	0.14	Yes
STKS	12.7	4.0	61.8	0.13	0.06	0.05	No
SWNC	23.2	5.5	54.4	0.09	0.05	0.02	No
TPLC	20.3	5.5	28.4	0.19	0.13	0.05	No

4.3.2 Logistic regression of directivity pulse observations from the Canterbury earthquakes

As discussed previously, the probability of pulse occurrence can be represented using a random variable which assumes a value of 1 or 0 based on whether or not a directivity pulse is observed. This implies that logistic regression can be employed to regress on the binary pulse observation data (Kutner et al., 2005). Given that the scope of the present exercise is to compare the relative performance (in terms of bias and precision) of pulse probability models, the predictions from these models act as the main predictor variable. Equation (4.7) illustrates the cumulative distribution of the logistic random variable (pulse probability in this case):

$$P(pulse\ observation|prediction) = \frac{1}{1 + e^{-(\beta_0 + \beta_1 x_1)}} \tag{4.7}$$

where x_1 is the predicted pulse probability obtained from a particular model (for a given faulting style and source-to-site geometry), β_0 and β_1 represent the coefficients obtained from logistic regression. The 'glmfit' tool in the MATLAB (2010) package was used to carry out the regression for each event. Figure 4.3 illustrates the three logistic regression models fitted using the observed pulse data and predicted pulse probabilities from the M_w 7.1 Darfield earthquake. Note that the binary observations of directivity pulses (i.e. 0 or 1) are shown on the vertical axis and correspond to the predictions from the three empirical models on the horizontal axis. For clarity, the inset of the figure provides an illustration of the residual (ε), which represents the difference between the observations and fitted model predictions. The coefficients obtained from the logistic regression for all four events are summarised in Table 4.5

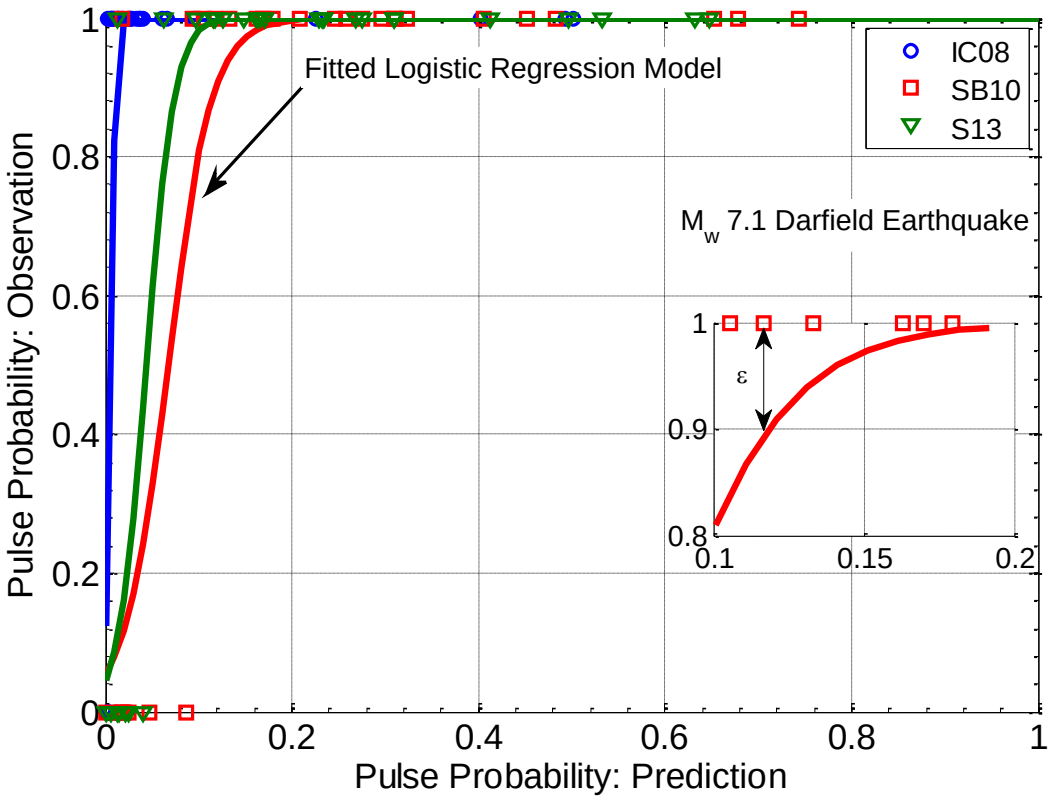

Figure 4.3: Logistic regression models fitted using the predicted pulse probabilities and pulse observation data from the 4 September 2010 M_w7.1 Darfield earthquake. The inset provides an illustration of the residual (ε) defined as the difference between the observations and fitted model predictions.

Table 4.5: Coefficients obtained using logistic regression of pulse observation data from the four considered events in the Canterbury earthquake sequence.

	M_w7.1 Darfield Earthquake			**M_w6.2 Christchurch Earthquake**			**M_w6.0 June Earthquake**			**M_w5.9 December Earthquake**		
	IC08	**SB10**	**S13**	**IC08**	**SB10**	**S13**	**IC08**	**SB10**	**S13**	**IC08**	**SB10**	**S13**
β_0	-2.0	-2.9	-3.1	-1.5	-0.79	-1.1	-3.9	-2.9	-3.5	-3.2	-2.4	-2.7
β_1	346	42.8	69.8	7.92	7.07	9.94	151	34.8	75.8	7.7	6.7	10.4

Figure 4.4 illustrates the logistic regression models fitted using observations and predictions corresponding to the Christchurch, June and December events:

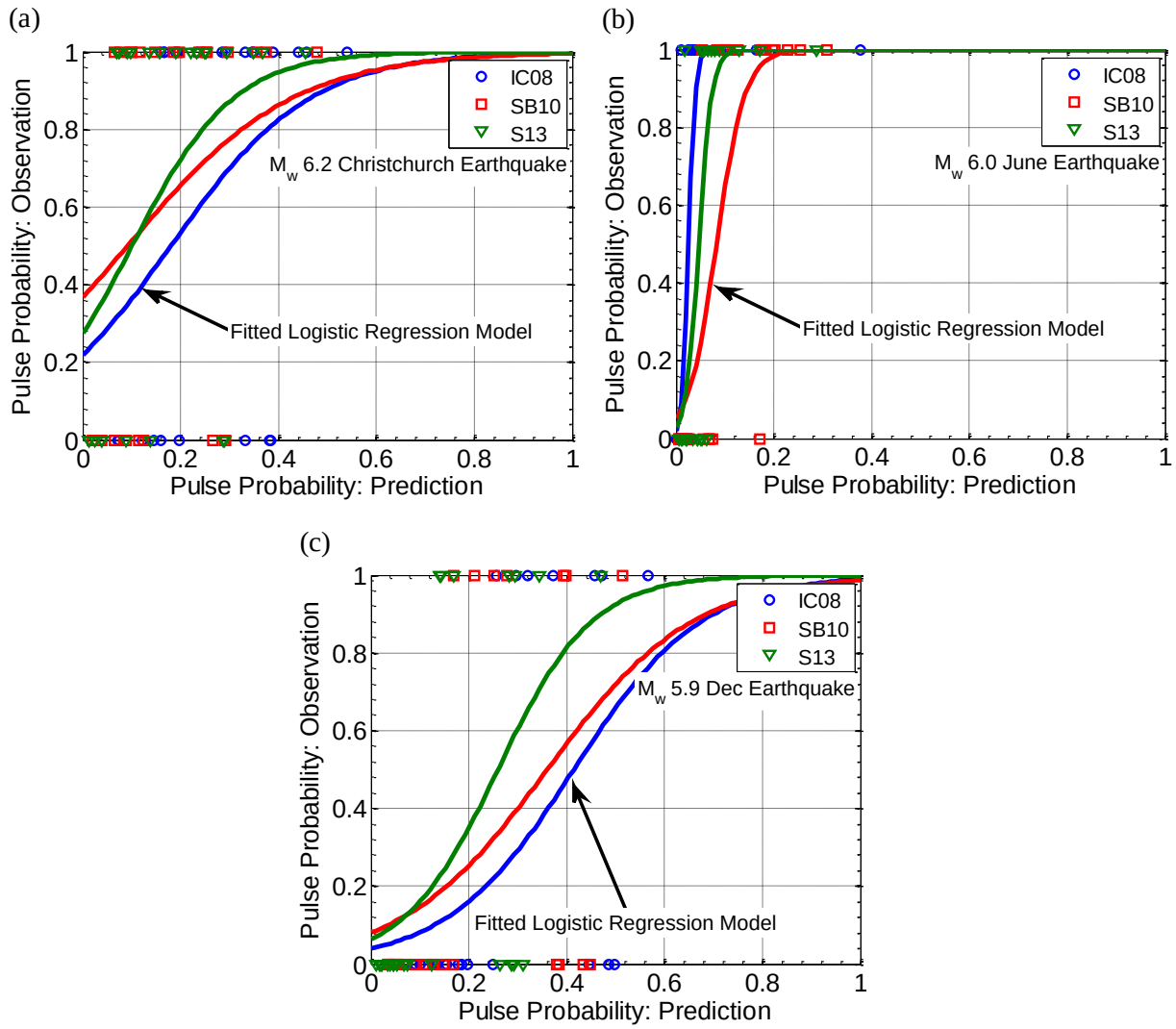

Figure 4.4: Logistic regression models fitted using the predicted pulse probabilities and pulse observation data from: (a) 22 February 2011 M_w6.2 Christchurch earthquake; (b) 13 June 2011 M_w6.0 June earthquake; and (c) 23 December 2011 M_w5.9 December earthquake.

In a manner analogous to ordinary least squares regression, the residual sum of squares ($RSS = \sum_{i=1}^{n} |\varepsilon_i|^2$ where n represents the number of observations) was used herein to assess the adequacy of the three pulse probability models. Typically, the model with the lowest *RSS* value is considered the tightest fit to the observed data (Ang & Tang, 2007). Figure 4.5 illustrates the *RSS* values associated with each logistic regression model for the four earthquakes considered. It can be observed that the logistic regression model fitted using predictions from the S13 pulse probability model has the lowest *RSS* values for the Darfield, Christchurch and December earthquakes. On the other hand, the *RSS* values associated with

logistic models fitted using the IC08 and SB10 pulse probability model predictions for the June earthquake are lower than the S13 model.

A comparison across the four events based on the RSS values illustrated in Figure 4.5 suggests that the pulse probability predictions for strike-slip earthquakes (i.e. Darfield and June events) are superior compared to non strike-slip earthquakes (i.e. February and December events). To some extent, this can be explained by the generally larger pulse probabilities predicted by the three models for strike-slip events in comparison to their non strike-slip counterparts (refer to Figure 4.2 for a visual comparison), which perhaps is also indicative of the 'cleaner' nature of the geometry and physics in the former case, according to Iervolino & Cornell (2008). In addition, it is also evident from Figure 4.5 that the empirical models provide the best predictions for the Darfield event. While this reinforces the idea that the model predictions are better for strike-slip cases, it could also be attributed to the fact that forward-directivity effects were observed in the Darfield event primarily due to the alignment of the rupture and slip direction along the strike-slip Greendale fault. On the other hand, contributions from fault planes other than those considered here may have been important for the Christchurch and June events, as discussed previously in Chapter 3. This could possibly explain the higher RSS values observed in the latter two events in comparison to the Darfield earthquake.

In interpreting the trends observed in Figure 4.5, it is also important to consider the uncertainty surrounding the location of the causative faults in each event, given that the pulse probability models solely depend on source-to-site geometry. The efficacy of finite fault models (FFM) is dependent upon the availability and quality of: (i) near-fault ground motion recordings; and (ii) geodetic and geological data. Due to a well-maintained network of strong motion instrumentation in the Canterbury plains, an unprecedented set of near-fault ground motions have been recorded in the four significant events from the Canterbury earthquake sequence considered herein. However, previous research (e.g. Beavan et al., 2010, 2011; Beavan et al., 2012; Holden et al., 2011; Holden, 2011) has largely focused on constraining the sources for the Darfield and Christchurch earthquake primarily because of their overall significance in the Canterbury earthquake sequence. In addition, due to the onshore location of the two events, the location and geometry of the modelled fault planes have been well constrained using geodetic data, including GPS (global positioning system) displacements and satellite radar data. For the Darfield earthquake in particular, the two segments of the

strike-slip Greendale fault in the finite fault models closely follow the surface rupture trace mapped by several researchers (e.g. Quigley et al., 2010; Villamor et al., 2012). On the other hand, the difficulty in obtaining a reliable solution for the M_w6.0 June earthquake due to offshore faulting and the subsequent lack of offshore geodetic data has been acknowledged by Beavan et al. (2012) in the development of their FFM. Similarly, the faulting in the M_w5.9 December earthquake occurred largely offshore, which resulted in a better constraint only for the western end of the modelled fault plane using the available onshore displacement data (refer to Figure 3 in Beavan et al. (2012)). Based on the above evidence, a larger weighting was placed on the *RSS* values corresponding to the Darfield and Christchurch earthquakes. As a result, the S13 model was deemed the most suitable for use in the chapters to follow.

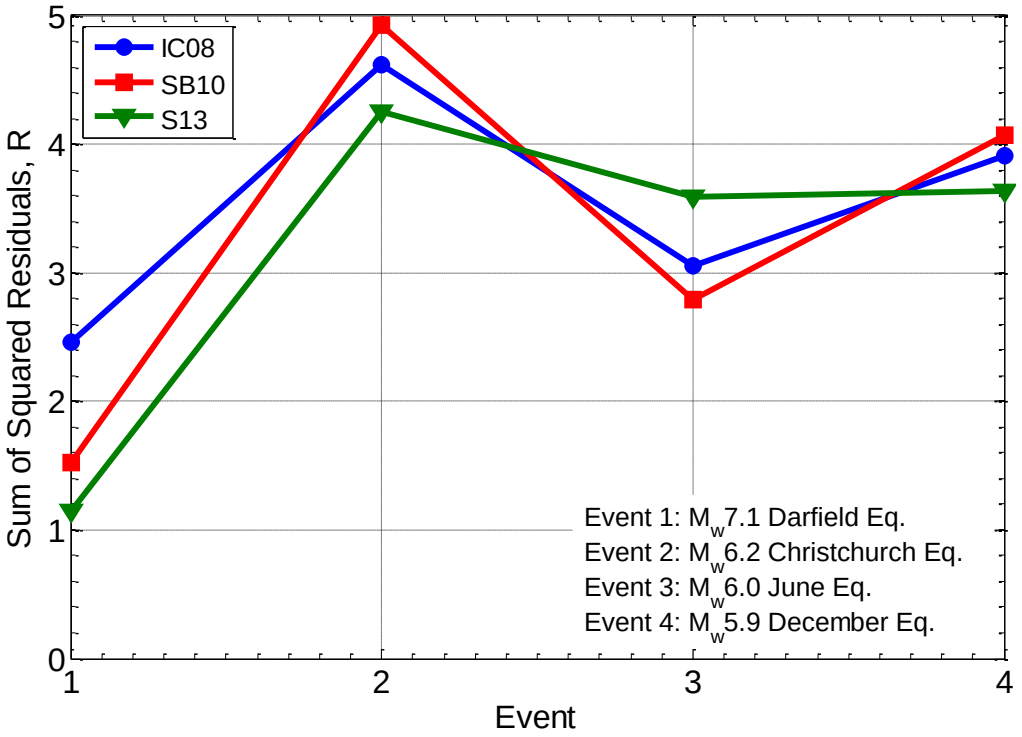

Figure 4.5: Residual sum of squares associated with the logistic regression models fitted using pulse probability model predictions for the four considered events in the Canterbury earthquake sequence.

4.4 Pulse probability contour maps for the Canterbury earthquakes

Figure 4.7 illustrates the pulse probability contour maps developed using the S13 model for the M_w 7.1 Darfield, M_w 6.2 Christchurch, M_w 6.0 June and M_w 5.9 December earthquakes. Also illustrated in these maps are observations of pulse-like and non-pulse-like ground motions from the four events. It is important to bear in mind that the pulses observed in these events were identified as being caused by forward-directivity effects (refer to Chapter 3 for further details on the identification and characterisation of forward-directivity ground motions). In general, it can be observed that the model predicts higher probabilities of pulse occurrence at sites where directivity pulses were observed. The following paragraphs provide some insight on the discrepancies between observations and predictions based on an examination of the contour maps for the four considered events.

Figure 4.7a indicates that the predictions of the S13 model for the Darfield earthquake are generally in good agreement with the observations, which explains the low corresponding RSS value observed previously in Figure 4.5. In particular, a significant number of directivity pulses observed in Christchurch and its surrounding suburbs (i.e. east of the Greendale fault) lie in between the 0.1 and 0.4 pulse probability contours. The only outlier from this event is the pulse observed at SBRC where the S13 model predicts an extremely low probability of occurrence (annotated in Figure 4.5). As stated earlier, the pulse classification algorithm of Shahi (2013) was used in classifying pulse-like ground motions for the development of the S13 model. The algorithm generally excludes pulse-like ground motions with low peak ground velocities (PGV < 30cm/s) due to the nature of the classification criteria. As a result, it is likely that the pulse probabilities obtained using the S13 model decrease with R_{rup} much quicker than would be expected with a model developed using a database which includes pulse-like motions with PGVs less than 30 cm/s. This explanation seems plausible considering that the SBRC station is located approximately 25km from the causative fault and has a PGV of 24 cm/s. On the other hand, the pulse observed at the station could also be a result of rupture directivity on the Charring Cross fault, which has not been considered in calculating the geometric parameters required by the S13 model.

The predicted pulse probability contours for the Christchurch earthquake illustrated in Figure 4.7b are larger in the vicinity of the fault surface exposure as expected. It can also be observed that larger probabilities are predicted for footwall sites in comparison to hanging wall sites. This can be attributed to the fact that for the same source-to-site distance, the up-dip rupture distance (d) will always be larger for sites located on the footwall, as illustrated in Figure 4.6. Although a probability of approximately 0.3 is predicted for two non-pulse observations in the eastern suburbs of Christchurch (HPSC and NNBS), complete failure of the ground and tilting of the recording instrument at these sites due to severe liquefaction (Bradley & Cubrinovski, 2011) made the identification of pulses from the velocity time-series extremely difficult. Nonetheless, it is likely that directivity effects were significant at the two sites according to the interpretation of the slip distribution (from the FFM of Beavan et al. (2011)) by Bradley & Cubrinovski (2011).

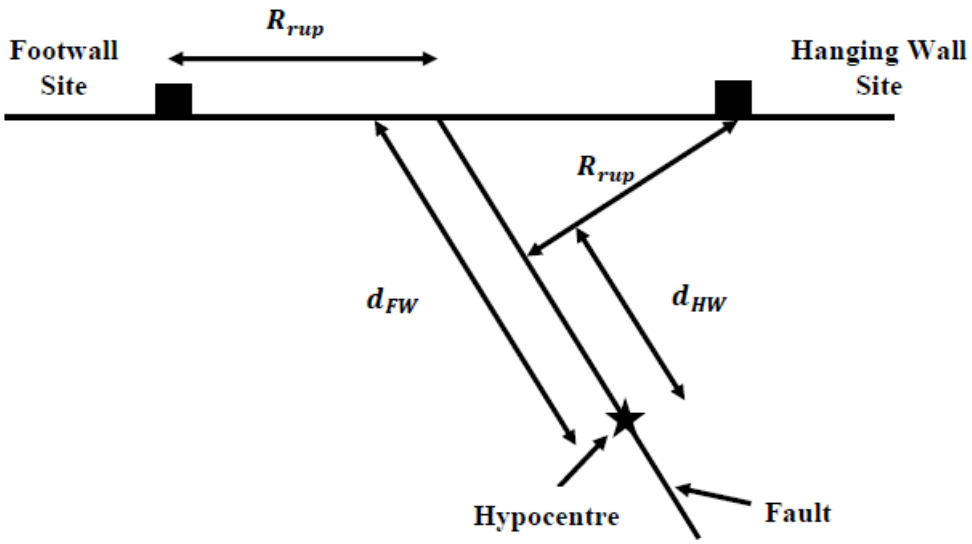

Figure 4.6: Illustration of the difference in the up-dip rupture distance (d) for sites with the same source-to-site distance (R_{rup}) on the footwall (d_{FW}) and hanging wall (d_{HW}).

Although the S13 model predicts extremely low probabilities (between 0 and 0.1) of pulse occurrence for the 6 pulse-like cases from the June event in Figure 4.7c, the detailed analysis in Chapter 3 clearly highlighted the presence of directivity pulses in these ground motions. It is worth bearing in mind that the pulse probability contour map for this event has been developed considering only the strike-slip segment of the FFM developed by Beavan et al. (2012). The rupture also involved an oblique fault which is likely to have contributed to the observed directivity effects at the aforementioned strong motion stations (refer to Section 3.5.3 in Chapter 3). This clearly highlights the limitation of the currently available approach used in determining the geometric parameters required as inputs in pulse probability models.

Hence, it is anticipated that future research will be directed towards developing guidelines for defining the source-to-site geometry in cases where multiple fault segments (with different faulting mechanisms) are involved in the rupture process.

In general, observations from the December event are consistent with the pulse probability contours illustrated in Figure 4.7d except for two notable discrepancies. Firstly, it can be observed that although the S13 model predicts moderate pulse probabilities (between 0.2 and 0.3) for a cluster of 5 sites in the Christchurch CBD, only the ground motion recorded at REHS was identified as pulse-like. A notable pulse-like feature did not exist in the velocity time-series corresponding to the other four cases (i.e. CBGS, CCCC, CHHC and D09C). This example is effective in highlighting the fact that the occurrence of directivity pulses is not purely dependent upon geometric parameters, but also the aforementioned physical phenomena related to source, wave propagation and local site effects. A similar situation exists further south from this cluster where two sites (CMHS and CRLZ) with effectively the same source-to-site geometry (and pulse probabilities as a result) are classified as pulse-like and non-pulse-like, respectively. Although a directivity pulse was present in both cases, the PGV associated with the pulse in the CRLZ velocity time-series was less than 5 cm/s, which prompted its removal from the pulse-like motion category in Chapter 3. The lower amplitude of the velocity pulse can be possibly be attributed to the fact that the CRLZ station is located on a rock site (site class B according to NZS1170.5:2004 (Standards New Zealand, 2004)), whereas the CMHS station is situated on soft soils (alluvial sand and silt according to Wood et al. (2011), and site class D according to NZS1170.5:2004 (Standards New Zealand, 2004)), thereby resulting in a larger amplitude pulse (PGV = 18.1 cm/s).

(a)

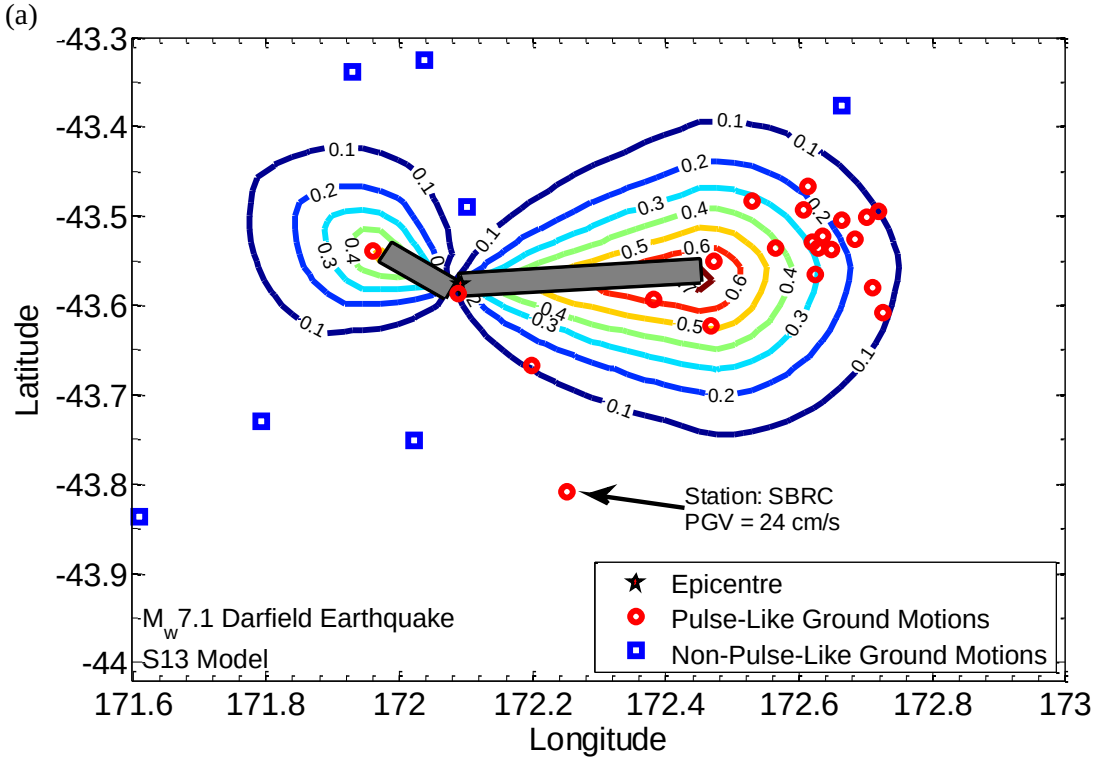
Latitude
Longitude
-43.3
-43.4
-43.5
-43.6
-43.7
-43.8
-43.9
-44
171.6
171.8
172
172.2
172.4
172.6
172.8
173
Station: SBRC
PGV = 24 cm/s
Epicentre
Pulse-Like Ground Motions
Non-Pulse-Like Ground Motions
M_w 7.1 Darfield Earthquake
S13 Model

(b)

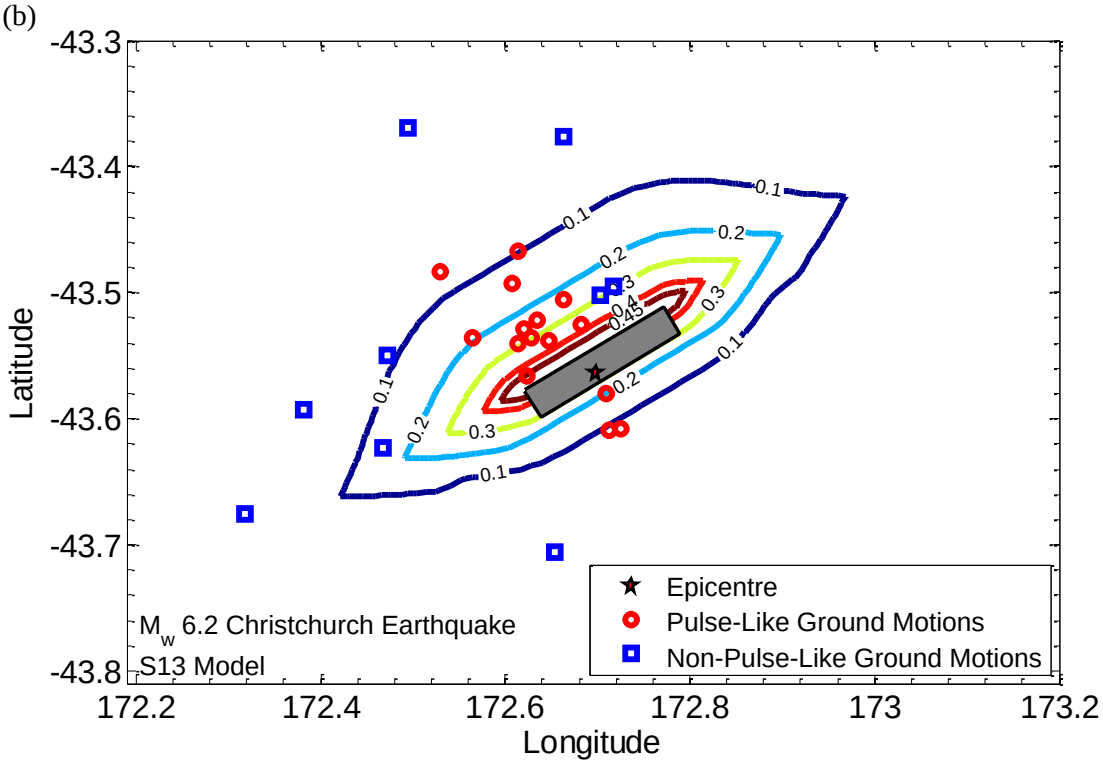
Latitude
Longitude
-43.3
-43.4
-43.5
-43.6
-43.7
-43.8
172.2
172.4
172.6
172.8
173
173.2
Epicentre
Pulse-Like Ground Motions
Non-Pulse-Like Ground Motions
M_w 6.2 Christchurch Earthquake
S13 Model

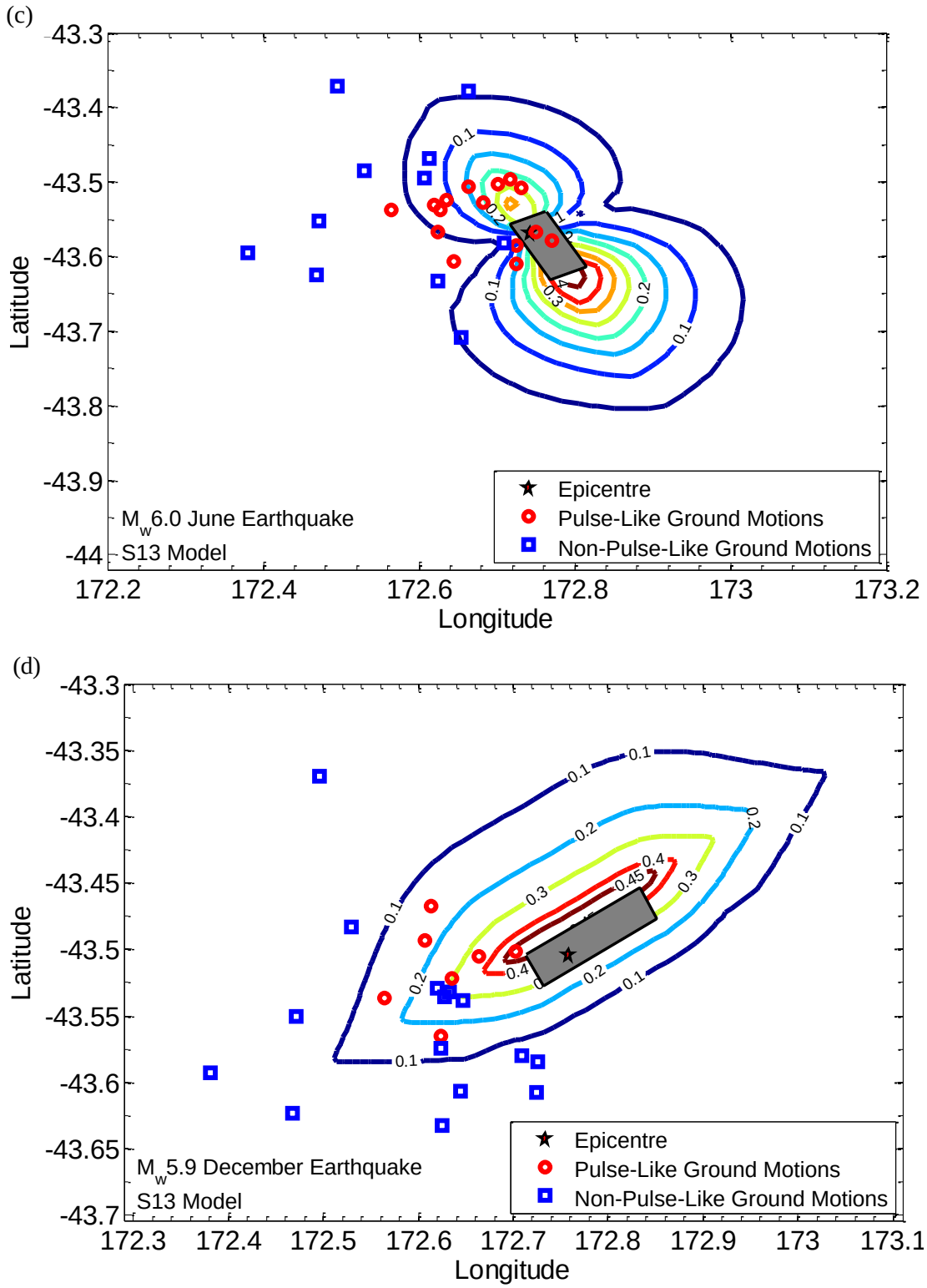

Figure 4.7: Contour maps of pulse probability developed using the S13 model for: (a) M_w7.1 Darfield earthquake; (b) M_w6.2 Christchurch earthquake; (c) M_w6.0 June earthquake; and (d) M_w5.9 December earthquake. Also illustrated are observations of pulse-like and non-pulse-like ground motions from each event.

4.5 Conclusions

This chapter has examined the predictive capabilities of models developed in previous research to determine the probability of pulse occurrence. In particular, models developed by Iervolino & Cornell (2008), Shahi & Baker (2010) and Shahi (2013) were assessed using observations from four significant events in the Canterbury earthquake sequence. The process of observing directivity pulses is binary in nature, thereby justifying the use of logistic regression in the evaluation of pulse probability models. Upon examining the results obtained using this procedure, it was found that the Shahi (2013) model provided the most adequate predictions in comparison to the two other models. Hence, this model is subsequently used in the examination of response spectra-based directivity models and to also carry out New Zealand-specific probabilistic seismic hazard analysis including the effects of forward-directivity in Chapters 5 and 7, respectively. Finally, pulse probability contour maps were developed for the four events considered using the Shahi (2013) model. Potential reasons for the discrepancies between observations and predictions were also provided.

4.6 References

Abrahamson, N. A. (2000). Effects of rupture directivity on probabilistic seismic hazard analysis. In *Proceedings of the 6th International Conference on Seismic Zonation*. Palm Springs, California.

Ancheta, T. D., Darragh, R. B., Stewart, J. P., Seyhan, E., Silva, W. J., Chiou, B. S., … Boore, D. M. (2013). *PEER NGA-West2 Database*. Retrieved from http://peer.berkeley.edu/publications/peer_reports/reports_2013/webPEER-2013-03-Ancheta.pdf

Ang, A. H.-S., & Tang, W. H. (2007). *Probability Concepts In Engineering* (2nd ed.). New York: Wiley.

Baker, J. W. (2007). Quantitative classification of near-fault ground motions using wavelet analysis. *Bulletin of the Seismological Society of America*, **97**(5):1486–1501. doi:10.1785/0120060255

Beavan, J., Fielding, E., Motagh, M., Samsonov, S., & Donnelly, N. (2011). Fault location and slip distribution of the 22 February 2011 Mw 6.2 Christchurch, New Zealand, Earthquake from geodetic data. *Seismological Research Letters*, **82**(6):789–799. doi:10.1785/gssrl.82.6.789

Beavan, J., Wallace, L., Samsonov, S., Ellis, S., Motagh, M., & Palmer, N. (2010). The Darfield (Canterbury) earthquake: geodetic observations and preliminary source model. *Bulletin of the New Zealand Society for Earthquake Engineering*, **43**(4):228–235.

Beavan, J., Motagh, M., Fielding, E. J., Donnelly, N., & Collett, D. (2012). Fault slip models of the 2010–2011 Canterbury, New Zealand, earthquakes from geodetic data and observations of postseismic ground deformation. *New Zealand Journal of Geology and Geophysics*, **55**(3):207–221. doi:10.1080/00288306.2012.697472

Bradley, B. A., & Cubrinovski, M. (2011). Near-source Strong Ground Motions Observed in the 22 February 2011 Christchurch Earthquake. *Seismological Research Letters*, **82**(6):853–865. doi:10.1785/gssrl.82.6.853

Chioccarelli, E., & Iervolino, I. (2012). Near-source seismic hazard and design scenarios. *Earthquake Engineering & Structural Dynamics*, n/a–n/a. doi:10.1002/eqe.2232

Chiou, B., Darragh, R., Gregor, N., & Silva, W. (2008). NGA Project Strong-Motion Database. *Earthquake Spectra*, **24**(1):23–44. doi:10.1193/1.2894831

Field, E. H., Jordan, T. H., & Cornell, C. A. (2003). OpenSHA: A developing community-modeling environment for seismic hazard analysis. *Seismological Research Letters*, **74**(4):406–419.

Holden, C. (2011). Kinematic Source Model of the 22 February 2011 Mw 6.2 Christchurch Earthquake Using Strong Motion Data. *Seismological Research Letters*, **82**(6):783–788. doi:10.1785/gssrl.82.6.783

Holden, C., Beavan, J., Fry, B., Reyners, M., Ristau, J., Van Dissen, R., … Quigley, M. (2011). Preliminary source model of the Mw 7.1 Darfield earthquake from geological, geodetic and seismic data. In *Proceedings of the Ninth Pacific Conference on Earthquake Engineering: Building an Earthquake-Resilient Society* (pp. 14–16). Retrieved from http://www.nzsee.org.nz/db/2011/164.pdf

Iervolino, I., & Cornell, C. A. (2008). Probability of occurrence of velocity pulses in near-source ground motions. *Bulletin of the Seismological Society of America*, **98**(5):2262–2277. doi:10.1785/0120080033

Kutner, M. H., Nachtsheim, C. J., Li, W., & Neter, J. (2005). *Applied linear statistical models* (5th ed.). Boston: McGraw-Hill Irwin.

MATLAB. (2010). Natick, Massachusetts: The MathWorks Inc.

Quigley, M., Van Dissen, R., Villamor, P., Litchfield, N., Barrell, D., Furlong, K., … Pedley, K. (2010). Surface rupture of the Greendale Fault during the Darfield (Canterbury)

Earthquake, New Zealand: Initial Findings. *Bulletin of the New Zealand Society for Earthquake Engineering*, **43**(4):236–242.

Shahi, S., & Baker, J. W. (2010). Regression models for predicting the probability of near-fault earthquake ground motion pulses, and their period. In *Proceeding of 11th International conference on applications of statistics and probability in civil engineering*. Retrieved from http://shreyshahi.com/papers/Shahi%20Baker%20(2010)%20ICASP.pdf

Shahi, S. K. (2013, January). *A probabilistic framework to include the effects of near-fault directivity in seismic hazard assessment*. Stanford University, Stanford.

Shahi, S. K., & Baker, J. W. (2011). An empirically calibrated framework for including the effects of near-fault directivity in probabilistic seismic hazard analysis. *Bulletin of the Seismological Society of America*, **101**(2):742–755. doi:10.1785/0120100090

Somerville, P. G. (2003). Magnitude scaling of the near fault rupture directivity pulse. *Physics of the Earth and Planetary Interiors*, **137**(1-4):201–212. doi:10.1016/S0031-9201(03)00015-3

Somerville, P. G., Smith, N. F., Graves, R. W., & Abrahamson, N. A. (1997). Modification of empirical strong ground motion attenuation relations to include the amplitude and duration effects of rupture directivity. *Seismological Research Letters*, **68**(1):199–222.

Standards New Zealand. (2004). *NZS1170.5:2004, Structural Design Actions, Part 5: Earthquake actions- New Zealand*. Wellington, New Zealand.

Tothong, P., Cornell, C. A., & Baker, J. W. (2007). Explicit directivity-pulse inclusion in probabilistic seismic hazard analysis. *Earthquake Spectra*, **23**(4):867–891. doi:10.1193/1.2790487

Tothong, P., & Luco, N. (2007). Probabilistic seismic demand analysis using advanced ground motion intensity measures. *Earthquake Engineering & Structural Dynamics*, **36**(13):1837–1860. doi:10.1002/eqe.696

Villamor, P., Litchfield, N., Barrell, D., Van Dissen, R., Hornblow, S., Quigley, M., … Grant, H. (2012). Map of the 2010 Greendale Fault surface rupture, Canterbury, New Zealand: application to land use planning. *New Zealand Journal of Geology and Geophysics*, **55**(3):223–230. doi:10.1080/00288306.2012.680473

Wood, C. M., Cox, B. R., Wotherspoon, L. M., & Green, R. A. (2011). Dynamic site characterization of Christchurch strong motion stations. *Bulletin of the New Zealand Society for Earthquake Engineering*, **44**(4):195–204.

5 Assessment of Response Spectrum Amplification due to Forward-Directivity Effects

5.1 Overview

Conventional ground motion prediction equations (GMPEs) generally do not account for the observed effects of rupture directivity on elastic pseudo-acceleration response spectral amplitudes (SA). Recent studies (e.g. Bradley, 2012a; Bradley & Cubrinovski, 2011) have also illustrated that NZ-specific GMPEs provide a notable under-prediction of long period SA amplitudes observed in the recent 4 September 2010 M_w7.1 Darfield and 22 February 2011 M_w6.2 Christchurch earthquakes, and that inclusion of specific models for directivity will improve ground motion predictions.

In this chapter, observations of forward-directivity ground motions resulting from the Canterbury earthquakes are used to assess the adequacy of several empirical models which account for the directivity amplification of acceleration response spectra. Broadband models, which form the basis of the near-fault factor in the New Zealand loadings standard, NZS1170.5 (Standards New Zealand, 2004) are firstly examined, followed by a more recent model developed by Shahi & Baker (2011), which accounts for the 'narrowband' characteristics of the directivity pulse. In the past, a lack of near-fault strong motion data has restricted this type of study in New Zealand. Moreover, the predictive capabilities of existing directivity models have not been scrutinised using a significant proportion of ground motions recorded on soft soils in previous research. Details of model applications are initially provided using specific examples from the Canterbury earthquakes. Residual analysis is subsequently carried out to measure any bias demonstrated by each of the directivity models. Finally, the contribution of basin-generated surface waves, as distinct from that due to forward directivity, to the observed amplification of long-period spectral ordinates in the Darfield and Christchurch earthquakes is investigated. Revised basin depths are adopted for

sites located above the Canterbury basin in an effort to determine whether improved long-period response spectral amplitude predictions can be obtained.

5.2 Effect of forward-directivity on elastic pseudo-acceleration response spectra

Near-fault ground motions which feature an early-arriving large-amplitude velocity pulse are typically caused by forward-directivity effects (as discussed extensively in Chapters 2 and 3), as a result of alignment of the rupture front and slip direction towards a given site. The resulting pulse-like feature (also known as the directivity pulse), typically observed in the fault-normal component of the velocity time-series, also causes larger fault-normal pseudo-acceleration response spectral amplitudes than so-called 'ordinary' ground motions. Somerville et al. (1997) noted that the effects of forward-directivity become significant at a vibration period of T = 0.6 s and increase monotonically for larger periods. However, as mentioned previously in Chapter 2, empirical evidence from major worldwide earthquakes prompted Somerville (2003) to highlight the fact that the directivity pulse is inherently 'narrowband' in nature, whose period increases with earthquake magnitude (M_w). As a result, it was also found that directivity amplification of spectral ordinates only occurs over a small/narrow range of vibration periods surrounding the pulse period (T_p). It is important to note that the level of amplification is also influenced by the earthquake magnitude, source-to-site geometry and local site effects.

Figure 5.1a and Figure 5.1b illustrate the response spectra of two forward-directivity ground motions from the 4 September 2010 M_w7.1 Darfield (LINC) and 22 February 2011 M_w6.2 Christchurch (PRPC) earthquakes, respectively. Also shown are the response spectra corresponding to the residual ground motion obtained after extracting the principal directivity pulse using the Baker (2007) pulse classification algorithm. In both cases, it is evident that the directivity amplification occurs in a narrow region surrounding the pulse period (T_p=7.2 s and T_p= 4.6 s, respectively), which has been highlighted in Figure 5.1 for clarity. It is worth remembering that the observed pulse periods were characterised previously in Chapter 3 using the Baker (2007) algorithm. Furthermore, the observed velocity time-series (both original and residual) at LINC and PRPC in the two events were also presented in the same chapter (refer to Figures 3.6 and 3.19, respectively).

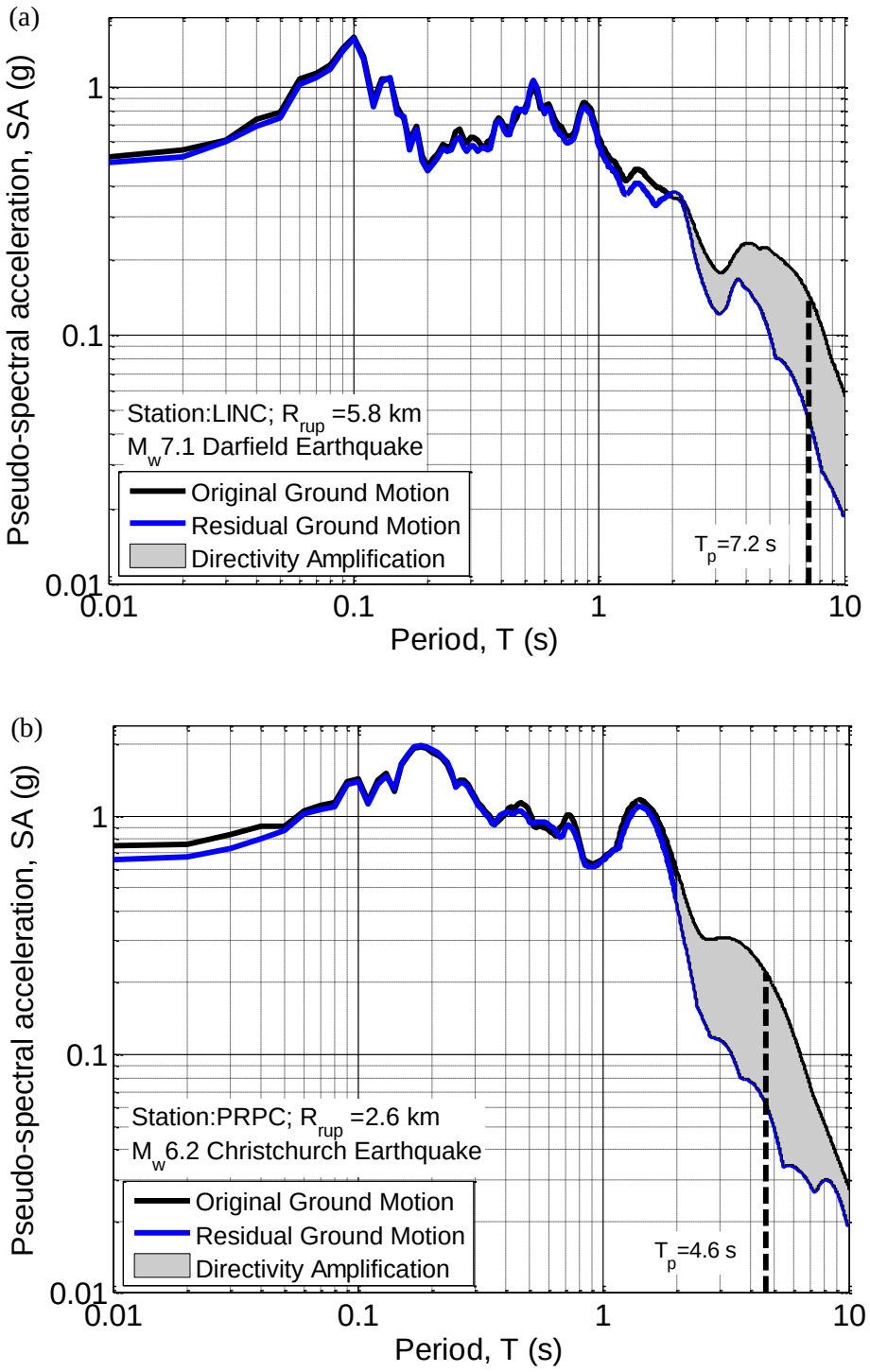

Figure 5.1: Illustration of the narrowband amplification of response spectra caused by the directivity pulse using examples of forward-directivity ground motions observed at (a) Lincoln School (LINC) in the 4 September 2010 M_w7.1 Darfield earthquake; and (b) Pages Road (PRPC) in the 22 February 2011 M_w6.2 Christchurch earthquake.

5.3 Empirical prediction of strong ground motion intensity measures

5.3.1 General background

Ground motion prediction equations (GMPEs) are frequently developed to estimate important scalar ground motion intensity measures, including, but not limited to, peak ground acceleration (PGA), pseudo-spectral acceleration (SA at 5% damping), peak ground velocity (PGV) and significant duration (Ds_{5-75} and Ds_{5-95}). Typically, their development involves the regression of a database of strong ground motion recordings from previous earthquakes. For the purpose of statistical robustness, the adopted database must include a large number of ground motions. Often, this may not be feasible for the geographic region of interest, thereby warranting the need to obtain ground motions from larger regions or various locations around the world (Bradley, 2013). This can be justified by the fact that ground motions recorded in geographic regions with similar tectonic regimes will generally possess similar characteristics (i.e. amplitude, frequency content and duration), as has been asserted previously by Douglas (2004, 2007). Moreover, for tectonic regions with limited empirical observations, the use of well-constrained ground motion models in estimating the intensity measure of interest is generally considered to be a reasonable alternative (Douglas, 2007). The aforementioned approach was adopted in the Next Generation Attenuation (NGA) project (Power et al., 2008), which utilised ground motions resulting from numerous worldwide active shallow crustal earthquakes in the development of GMPEs.

GMPEs are conventionally employed to quantify the seismic hazard at a given site within the probabilistic seismic hazard analysis (PSHA) framework. Due to the complexity of processes related to earthquake rupture, wave propagation and response of surficial soils beneath the site in question, predictions of intensity measures provided by these empirical relationships are highly uncertain (Bradley, 2012a). This uncertainty is well-represented by the lognormal distribution and hence, any percentile of the ground motion distribution can be calculated using Equation (5.1):

$$IM_x = IM_{50}\exp\left(z_x \sigma_{lnIM}\right) \tag{5.1}$$

where $IM_{50}$and σ_{lnIM} are the median and lognormal standard deviation of the distribution; and z_x is the normal variate (i.e. defines the number of standard deviations that the x^{th}

percentile is from the median). For example, if a GMPE provides a median prediction of 0.5g for PGA (for a given earthquake scenario and site) and has a standard deviation of 0.6 (values generally range between 0.23 and 0.92 (Strasser et al., 2009)), the 16th and 84th percentiles (i.e. $\pm\sigma_{lnIM}$) are 0.28 g and 0.91 g, respectively. This clearly highlights the large variability in the ground motion intensity provided by GMPEs and the need to account for the uncertainty associated with their predictions in seismic hazard assessment. Furthermore, because GMPEs are empirically calibrated, they should only be considered in ground motion modelling of earthquake scenarios which have adequate representation in the ground motion database employed in developing the prediction model. This can be problematic, especially in estimating ground motion intensity measures for moderate-to-large magnitude earthquakes at small source-to-site distances, which often have high contributions to the seismic hazard in active tectonic regions (Bradley, 2012), but occur infrequently. The issue is further exacerbated by the lower likelihood of strong motion instrumentation being located at closer distances to fault sources which are capable of producing such earthquakes, as discussed previously in Chapter 2.

Although GMPEs are empirical in nature, their functional forms are often guided based on simple seismological theory. The complexity of these empirical models has increased significantly in the last decade, owing mainly to the expanding database of worldwide strong ground motions, as well as advances made by the research community in understanding the aforementioned source, path and site effects. For example, a state-of-the-art GMPE developed by Campbell (1981) for PGA used an extremely simple logarithmic function involving only the earthquake magnitude and distance as the predictor variables. On the other hand, a more recent GMPE (for PGA, PGV and SA) developed as part of the NGA project by Chiou & Youngs (2008) (which utilised a subset of 3,551 ground motions from 173 active shallow crustal earthquakes), is a function of 12 predictor variables and includes 29 empirical constants. Despite the increased complexity and range of applicability associated with the newer prediction models, it is worth re-iterating that they do not aim to capture the complex physical processes which produce strong ground motions. In fact, the simplicity of GMPEs can be highlighted by comparing their predictor variables with physical factors which influence ground motions (Bradley, 2012a). This comparison is carried out below:

- The earthquake source is typically represented only by the moment magnitude (M_w) and faulting style (e.g. strike-slip, normal, reverse etc.) in the GMPE. It does not consider: (i) the hypocentre which represents the location of rupture initiation on the causative fault; (ii) the time evolution of rupture propagation over the fault; and (iii) the amplitude, direction (rake) and duration (rise time) of slip at each location on the fault (Bradley, 2012).
- The effects of wave propagation are represented by simple distance measures such as the closest distance from the fault plane to the site (R_{rup}) and/or the Joyner-Boore distance (R_{JB}), among others. No attempt is made to consider the reflections and refractions that seismic waves undergo as they travel through the various rock and soil mediums towards the site. The effects of deep sedimentary basins on the incoming seismic waves are often considered only using the basin depth.
- The effects of local site response are considered only using the shear wave velocity time-averaged over the top 30 m of the soil layers beneath the site ($V_{s,30}$) and depth to which the soil layers attain a specific shear wave velocity (e.g. $V_{s,30}$ = 1.0 km/s) (Bradley, 2012). In fact, no attempt is made to account for variability in soil layering and non-linear soil response, which becomes significant for larger levels of shaking (and is a function of the soil type and ground water level, among other factors).

5.3.2 NZ-specific pseudo-spectral acceleration ground motion prediction equations

Given that the scope of the present chapter is to assess the adequacy of several models which account for the directivity amplification of response spectra using observations from the Canterbury earthquakes, it is pertinent to review the available GMPEs for the New Zealand (NZ) active shallow crustal tectonic environment. The following paragraphs provide a brief overview of two GMPEs developed by McVerry et al. (2006) and Bradley (2010) (referred to as the McV06 and B10 GMPEs hereafter, respectively), which are routinely used in performing seismic hazard analyses for locations in NZ at present.

The McV06 GMPE was developed in several stages between 1997 and 2001 (despite being formally published in 2006) to predict the horizontal geometric mean and larger component (i.e. maximum value between two orthogonal components of ground motion) peak ground acceleration and pseudo-spectral acceleration for active shallow crustal and

subduction earthquakes in NZ. Due to the scarcity of recorded ground motions in NZ (among other reasons discussed by McVerry et al. (2006)), relationships for crustal and subduction earthquakes were developed based on the functional forms of models from Abrahamson & Silva (1997) and Youngs et al. (1997), respectively. The model development involved the use of 435 strong motion records from 49 earthquakes in NZ which were recorded between 1966 and 1995. In order to constrain the active shallow crustal model at short distances, 66 records from 17 overseas crustal earthquakes (recorded within 10 km of the source) with moment magnitudes ranging from 5.2 to 7.4 were included in the empirical database (McVerry et al., 2006). It should be noted that the elastic site hazard response spectra prescribed by the current earthquake loadings standard in NZ, commonly referred to as NZS1170.5:2004 (Standards New Zealand, 2004), were developed using results from seismic hazard analyses involving the McV06 GMPE.

The NZ strong ground motion database has grown significantly in the past decade (2,852 records from 213 events in the period 1973-2009 compiled by Bradley (2010)). Note that the magnitude-distance distribution of this database was presented in Chapter 3 (refer to Figure 3.1). Bradley (2010) initially used the expansion in the NZ database to justify the development of an updated GMPE for active shallow crustal and subduction zone earthquakes. Nonetheless, the development of a model to predict SA amplitudes based on NZ-specific data alone was not possible due to the lack of near-source ground motion recordings from moderate-to-large magnitude earthquakes. Hence, Bradley (2010) decided to determine the applicability of several foreign GMPEs for NZ with the updated database mentioned above. This included models developed by McVerry et al. (2006), Zhao et al. (2006) (Z06), Boore & Atkinson (2008) (BA08), Chiou & Youngs (2008) (CY08), and Chiou et al. (2010) (C10). The McV06 model was firstly examined to determine whether it could provide adequate predictions of the observed ground motions in the more recent NZ dataset, and also whether consideration of overseas GMPEs was necessary. Reasons for adopting the remaining four models are elaborated in Bradley (2010; 2013).

The applicability of the GMPEs above was assessed using a combination of: (i) qualitative comparison of predictor variable scaling; and (ii) goodness of fit as a function of predictor variables (refer to Bradley (2010; 2013) for further details). It was found that the McV06 and C10 models were the least and most applicable to the NZ database, respectively. Hence, Bradley (2010) adopted the functional form of the C10 model and appropriate

modifications were made to account for NZ-specific features. In doing so, it was ensured that the B10 model provided appropriate scaling of parameters which were not well-constrained by the data and also accounted for the characteristics of observed NZ ground motions.

5.3.3 Comparison of GMPE predictions with observed ground motions from the Canterbury earthquakes

As has been discussed previously in Chapters 2 and 3, the strong ground motions resulting from Canterbury earthquakes have significantly augmented the NZ strong motion database. In particular, an unparalleled number of near-fault strong ground motions were recorded due to a well-maintained network of strong motion instrumentation in the Canterbury plains. This provided an excellent opportunity to examine the efficacy of the two NZ-specific GMPEs developed by McVerry et al. (2006) and Bradley (2010). In this section, some of the key results from a previous study carried out by Bradley (2012a), which compared ground motion amplitudes from the 4 September 2010 M_w7.1 Darfield and 22 February 2011 M_w6.2 Christchurch earthquakes, with predictions from the McV06 and B10 GMPEs are presented (albeit with some modification). As will be observed in the figures to follow, the McV06 significantly over-predicts short period SA amplitudes, whereas the B10 GMPE provides significantly improved predictions of the observed ground motions for short and moderate period amplitudes on a consistent basis.

Figure 5.2 illustrates the observed response spectra associated with the ground motion recorded at Greendale, which is located approximately 0.9 km from the Greendale fault, in the M_w7.1 Darfield earthquake. The spectra are presented for the fault-parallel, fault-normal and average horizontal (or geometric mean) components of ground motion. For comparison, median predictions (50th percentile) of the McV06 and B10 GMPEs (also for the average horizontal component) are shown in Figure 5.2a and Figure 5.2b, respectively. In order to account for the uncertainty in the model predictions, the 16th and 84th percentiles are also illustrated in both figures. It is noted that the McV06 model is only applicable for vibration periods up to T = 3 s, whereas the B10 GMPE provides predictions for the period range 0.01 s $\leq T \leq$ 10 s. In general, it can be observed from Figure 5.2b that the median prediction of the B10 GMPE is similar to the observed average horizontal response spectra for all vibration periods of interest. The McV06 GMPE, on the other hand, severely under-predicts the observed spectral amplitudes at moderate-to-long-periods in Figure 5.2b; and also displays a

large peak at approximately T = 0.2 s, unlike the B10 model where the variation of SA with vibration period is relatively smooth.

The comparison in the previous paragraph was effective in highlighting the superior predictive capabilities of the B10 GMPE in relation to the McV06 GMPE. To further elucidate the improved nature of the former model, predictions (16^{th}, 50^{th} and 84^{th} percentiles) from both models are compared to observations from the Darfield event for four vibration periods ($T = 0.0$, 0.2, 1.0 and 3.0 seconds) of engineering interest in Figures 5.3 and 5.4. In each plot, the SA amplitudes are illustrated as a function of source-to-site distance (R_{rup}) and the observations are colour-coded according to the site classification prescribed by NZS1170.5:2004 (Standards New Zealand, 2004) for each instrument location. In order to determine whether the predictions are biased, mixed-effects regression was employed by Bradley (2012a) to calculate the normalised inter- and intra-event residuals (η and τ) for each period. The inset of each plot shows η, which effectively represents the average model bias with respect to the observations. For example, η = 0 implies no bias, whereas η = 1 indicates that the observations are one standard deviation above the median prediction, on average.

The results of Figure 5.3 indicate that the McV06 provides an accurate prediction of the observed PGA values from the Darfield earthquake (η = 0.01) but significantly over-predicts the short period (SA(0.2 s)) spectral amplitudes (η = -0.86). Furthermore, the model notably under-predicts the observed long-period ground motion (SA(1 s) and SA(3 s)) at short source-to-site distances. Similar trends were also observed upon comparing the McV06 model predictions with observations from the M_w 6.2 Christchurch earthquake (Bradley, 2012a).

Upon examining the results in Figure 5.4, Bradley (2012a) concluded that the B10 model is able to capture the source-to-site dependence of the observed ground motions with good accuracy (low bias) and precision (correct variability). More specifically, the model exhibits very low bias for periods of T= 0.0, 0.2 and 1.0 s, as indicated by the values of the normalised inter-event residuals (η = -0.09, 0.01 and 0.14 respectively). In contrast, the B10 GMPE notably under-predicts the SA(3 s) amplitudes (η = 0.46), especially at distances between 10 and 30 km. Although not illustrated here, congruent trends were also observed by Bradley (2012a) following a comparison between observations from the Christchurch event and predictions from the B10 model. Reasons for the under-prediction of long-period ground

motion in the two events can be attributed to forward-directivity effects, basin-generated surface waves and waveguide effects, as well as non-linear surficial soil response (Bradley, 2012a; Bradley & Cubrinovski, 2011). While conventional GMPEs account for the latter two phenomena (albeit in a simplified manner), the aforementioned effects of forward-directivity (refer to Section 5.2) on moderate-to-long-period SA amplitudes are not explicitly considered in their development. This provides an impetus to the present chapter, which examines the predictive capabilities of response spectra-based directivity models (reviewed in Chapter 2) using observations from the Canterbury earthquakes. Such an examination has not been possible in the past for NZ, primarily due to a lack of near-fault ground motion recordings, a fact which has been emphasised throughout this thesis. The B10 GMPE will be adopted herein based on the evidence presented in this section, which clearly showed that the model provides markedly improved predictions in comparison to the McV06 GMPE, especially for short-to-moderate vibration periods in the near-fault region.

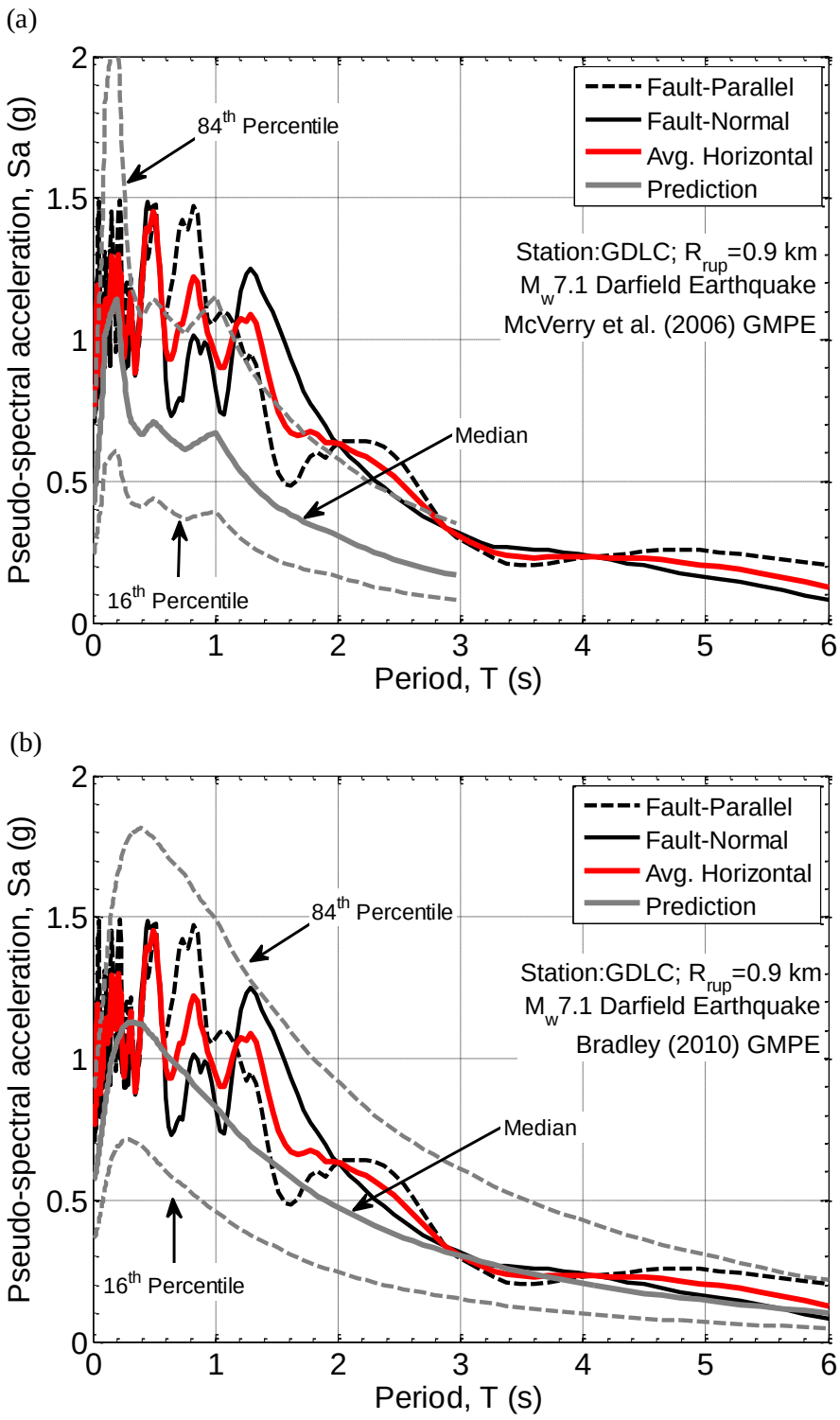

Figure 5.2: Comparison of the observed pseudo-acceleration response spectra at Greendale (GDLC) during the 4 September 2010 M_w7.1 Darfield earthquake (corresponding to the fault-parallel, fault-normal and average horizontal components of ground motion) with empirical predictions obtained using the NZ-specific models of: (a) McVerry et al. (2006); and (b) Bradley (2010) (modified from Bradley (2012a)).

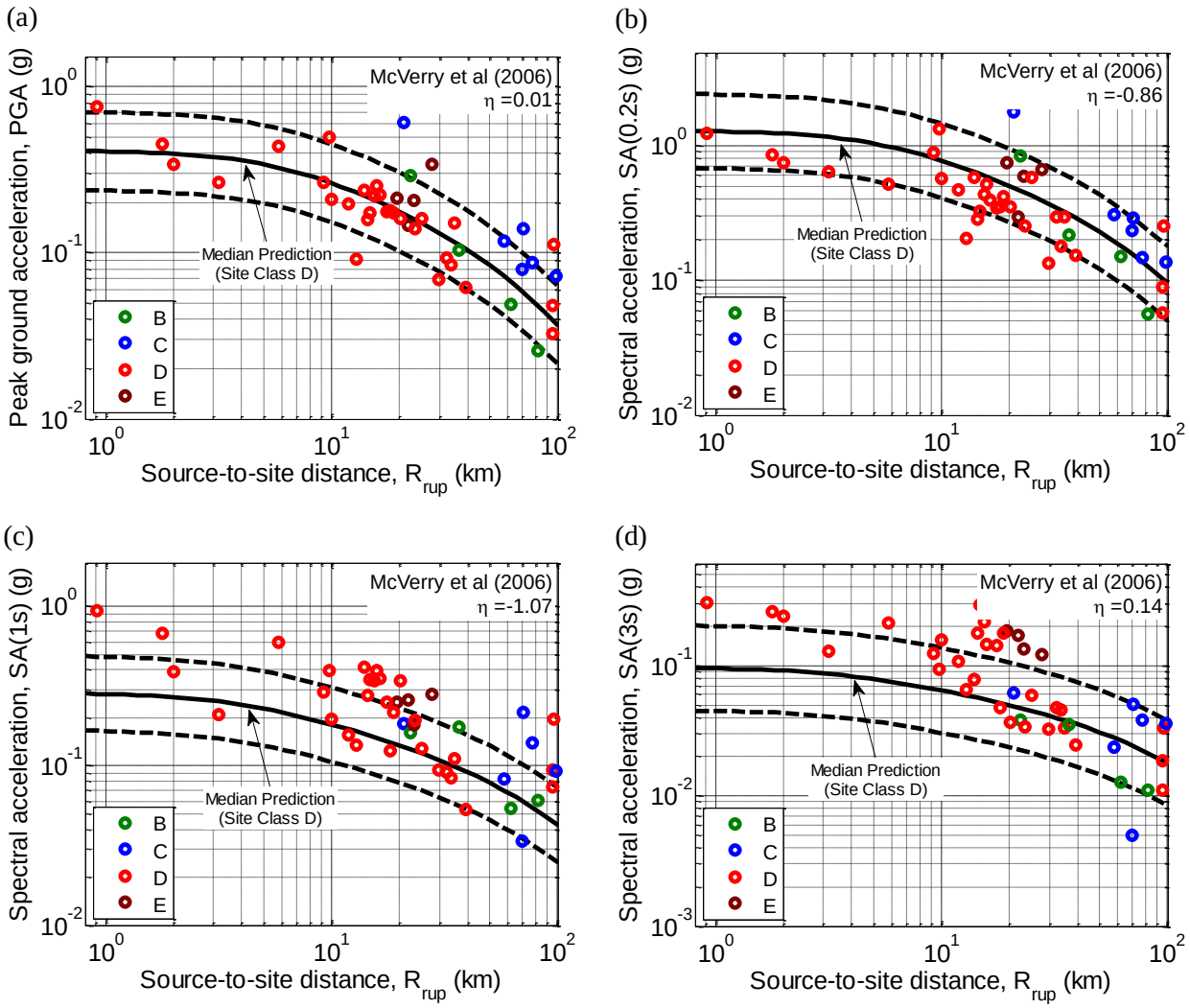

Figure 5.3: Comparison of observed pseudo-spectral acceleration amplitudes from the 4 September 2010 M_w7.1 Darfield earthquake for (a) T = 0.0 s; (b) T = 0.2 s; (c) T = 1.0 s; and (d) T = 3.0 s with predictions (the solid line illustrates the median whereas the 16th and 84th percentiles are given by the dotted lines) of the McVerry et al. (2006) GMPE for site class D (modified from Bradley (2012a)).

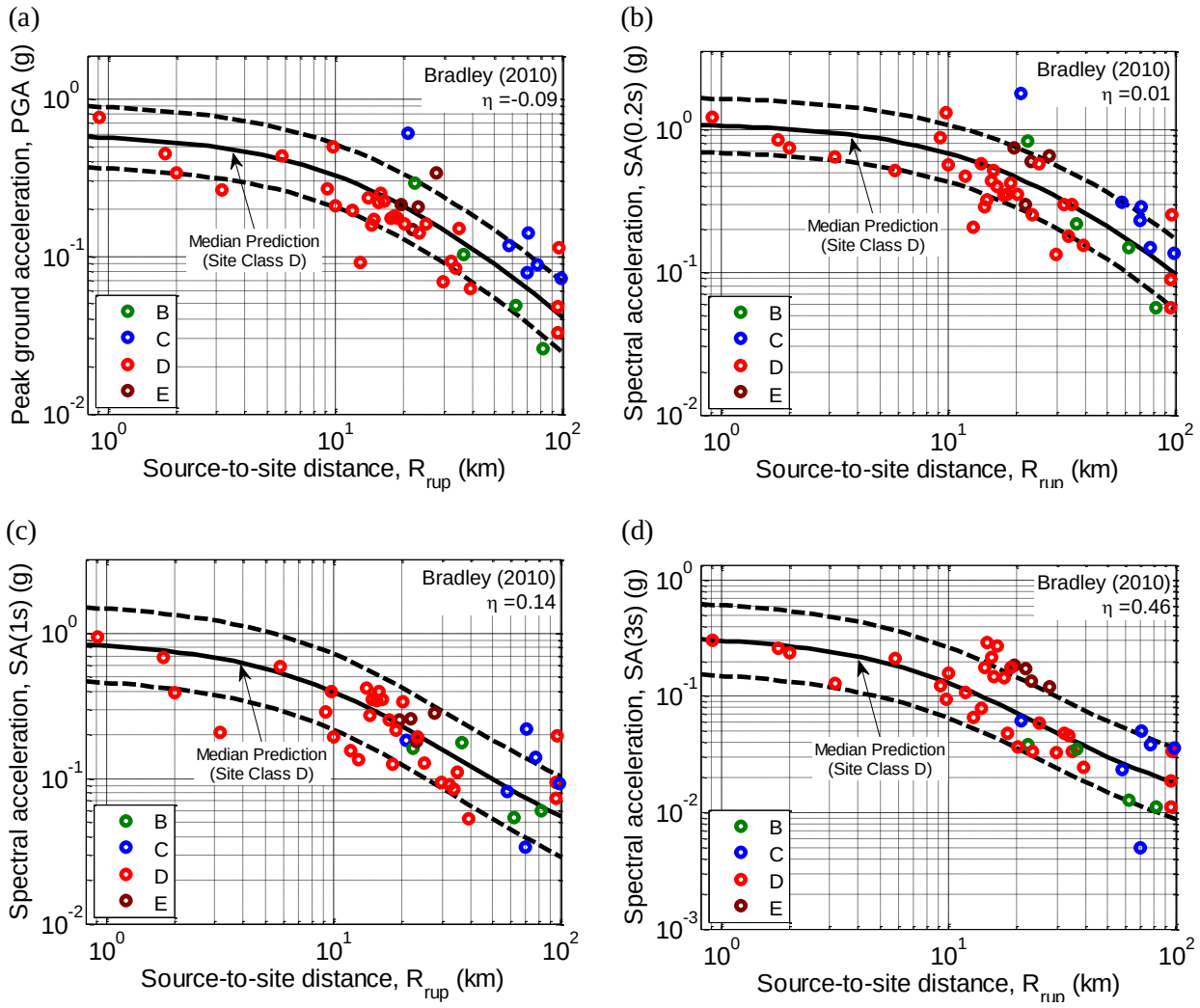

Figure 5.4: Comparison of observed pseudo-spectral acceleration amplitudes from the 4 September 2010 M_w7.1 Darfield earthquake for (a) T = 0.0 s; (b) T = 0.2 s; (c) T = 1.0 s; and (d) T = 3.0 s with predictions (the solid line illustrates the median whereas the 16th and 84th percentiles are given by the dotted lines) of the Bradley (2010) GMPE for site class D (modified from Bradley (2012a)).

5.3.4 Explanatory variables of the Bradley (2010) GMPE

It is important to correctly[1] define the predictor variables required by a ground motion prediction model in order to obtain reliable estimates of the response variable. Table 5.1 presents a summary of the explanatory variables used by the Bradley (2010) GMPE and the manner in which each variable was determined for this study:

[1] It should be appreciated that the predictor variables are likely to possess some uncertainty. For example, site-related parameters (e.g. $V_{s,30}$, $Z_{1.0}$ and $Z_{2.5}$) required by GMPEs are often very difficult to determine due to a lack of field testing data in the region of interest, and hence typically rely on surficial geology to be defined.

Table 5.1: Method of determination of the explanatory variables required by the Bradley (2010) ground motion prediction equation.

Explanatory Variable		
Symbol	**Definition**	**Method of Determination**
M_w	Moment magnitude	Obtained from the regional moment tensor solution (GeoNet, 2011)
R_{rup}	Closest distance to the fault rupture plane (km)	Calculated using the event-specific finite fault models discussed extensively in Chapters 2 and 3
R_{JB}	Joyner-Boore distance, also defined as the horizontal distance to the surface projection of the fault rupture plane (km)	Calculated using the event-specific finite fault models
R_X	Distance (km) from the surface projection of the updip edge of the fault rupture plane, measured perpendicular to the strike (positive in the down-dip direction)	Following the approach used in the OpenSHA framework (Field et al., 2003) to define source-to-site geometry in seismic hazard calculations
R_{TVZ}	Distance of wave propagation through the Taupo Volcanic Zone (TVZ) (km)	Since the Canterbury region does not form a part of the TVZ, R_{TVZ} = 0
F_{HW}	Hanging wall flag	1 if $R_X > 0$; 0 otherwise
δ	Fault dip angle (degrees)	Obtained from the event-specific finite fault models
Z_{TOR}	Depth to the top of the fault rupture plane (km)	Calculated using the event-specific finite fault models
F_{RV}	Reverse faulting flag	1 for rake angles $30^o \leq \lambda \leq 150^o$; 0 otherwise
F_{NM}	Normal faulting flag	1 for rake angles $-120^o \leq \lambda \leq -60^o$; 0 otherwise
$V_{s,30}$	Time-averaged shear wave velocity for the top 30 m of the site (m/s)	For strong motion stations where geophysical characterisation (consisting of active- and passive-source surface wave testing) was carried out by Wood et al. (2011), the $V_{s,30}$ values reported therein are used. For all other sites, the $V_{s,30}$ values based on the site classification of NZS1170.5:2004 (Standards New Zealand, 2004) are adopted as follows: • Site Class A: 1500 m/s • Site Class B: 800 m/s • Site Class C: 450 m/s • Site Class D: 250 m/s • Site Class E: 180 m/s
$Z_{1.0}$	Depth to shear wave velocity of 1.0 km/s (m)	Site-specific basin depths were not available at the time of writing and hence, the relationship proposed by Chiou & Youngs (2008) is utilised herein to calculate $Z_{1.0}$, unless reported otherwise.

5.4 Directivity models considered

In Chapter 2, the available empirical approaches for modelling the effects of forward-directivity on the pseudo-acceleration response spectrum were discussed in great detail. Nonetheless, this section serves to briefly describe the models considered in the present study and explain some of the assumptions made in their application to events from the Canterbury earthquake sequence.

5.4.1 Somerville et al. (1997)

The fact that conventional GMPEs do not account for the spatial variations of ground motion amplitude and duration due to rupture directivity effects prompted Somerville et al. (1997) to develop the first empirical directivity model (referred to as the S97 model hereafter). In particular, models were developed to modify: (i) the average horizontal spectral acceleration; (ii) average significant duration ($D_{s,5-75}$) of orthogonal horizontal acceleration time-series; and (iii) ratio of fault-normal (FN) and fault-parallel (FP) spectral acceleration. Essentially, models (i) and (ii) provide period-dependent scaling factors which can be applied to the median predictions obtained using GMPEs for spectral acceleration and significant duration, respectively. The level of predicted directivity amplification (or deamplification), as mentioned previously in Chapter 2, is dependent upon $Xcos(\theta)$ for strike-slip (SS) events and $Ycos(\phi)$ for non strike-slip (NSS) events; where X and Y represent the proportion of the total fault length which ruptures towards the given site; and θ and ϕ represent the source-to-site azimuth (refer to Figure 2.13 in Chapter 2 for further details). In contrast, Somerville et al. (1997) found that the FN/FP ratio is dependent only on the moment magnitude (M_w), source-to-site distance (R_{rup}) and azimuth ($\xi = \theta$ for SS events and ϕ for NSS events). It is worth noting at this point that only the amplitude-based models are considered herein (and not duration-based models). The directivity models were developed by correlating the above parameters to the ground motion residuals (i.e. difference between the logarithm of observed and predicted SA amplitudes) using the functional forms illustrated in Equations (5.2), (5.3) (for model (i)) and (5.4) (for model (iii)).

$$y = C_1 + C_2 X cos(\theta) \quad \text{(Strike-slip events; } M_w > 6.5\text{)} \tag{5.2}$$

$$y = C_1 + C_2 Y cos(\phi) \quad \text{(Non strike-slip events; } M_w > 6.5\text{)} \tag{5.3}$$

$$y = \cos(2\xi)\left[C_1 + C_2 \ln(R_{rup} + 1) + C_3(M_w - 6)\right] \quad (M_w > 6.0;\ \xi < 45°;\ y = 0 \text{ otherwise}) \tag{5.4}$$

where y represents the ground motion residual; C_1 , C_2 and C_3 are period-dependent coefficients obtained from regression analysis.

Figure 5.5 illustrates the period dependence of the S97 amplification factor for the average horizontal SA amplitudes obtained from ground motion prediction models. The dependence of the factor on $Xcos(\theta)$ (Figure 5.5a) for SS faults and $Ycos(\phi)$ (Figure 5.5b) for NSS faults is also shown. As expected, larger levels of amplification are predicted for increasing values of the geometric parameters. It can be observed that the model is 'broadband' in nature because the amplification of spectral ordinates occurs over a wide range of periods, starting at T = 0.6 s and increasing with period. In addition, the model also predicts a larger amplification for SS events in comparison to NSS events. For example, at T= 3 s under maximum directivity conditions, the amplification factors predicted by the SS and NSS models are approximately 2.1 and 1.3, respectively.

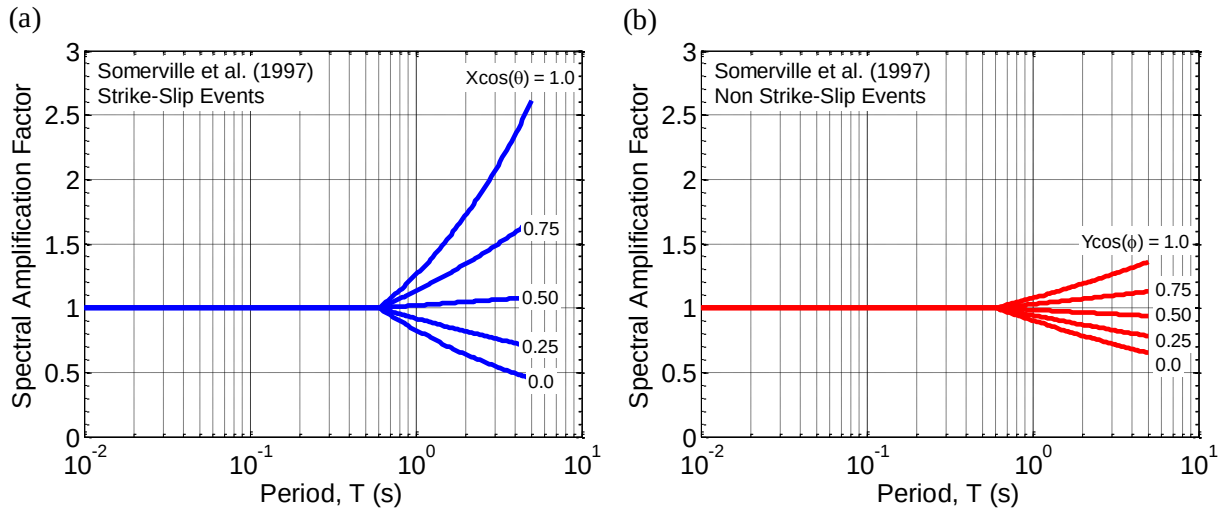

Figure 5.5: Period dependence of the spectral amplification factor predicted by the Somerville et al. (1997) broadband model for (a) Strike-slip (SS) events; and (b) Non strike-slip (NSS) events. Note that the amplification predicted by the model for varying levels of the directivity parameter ($Xcos(\theta)$ for SS events and $Ycos(\phi)$ for NSS events) is also illustrated (adapted from Somerville et al. (1997)).

Figure 5.6 illustrates the period dependence of the S97 model for the ratio of fault-normal to average horizontal spectral acceleration (defined as the square root of the FN/FP ratio (Somerville et al., 1997)). The dependence of this ratio on ξ is also shown for M_w = 7.0 and R_{rup} = 5 km. Similar to the spectral amplification factor, the fault-normal to average horizontal ratio increases with vibration period and is larger for sites with smaller values of ξ. Although the S97 model is only applicable for periods less than or equal to T = 5 s, this limitation is relaxed here and the factors prescribed by models (i) and (iii) for T = 5 s are also applied to larger vibration periods.

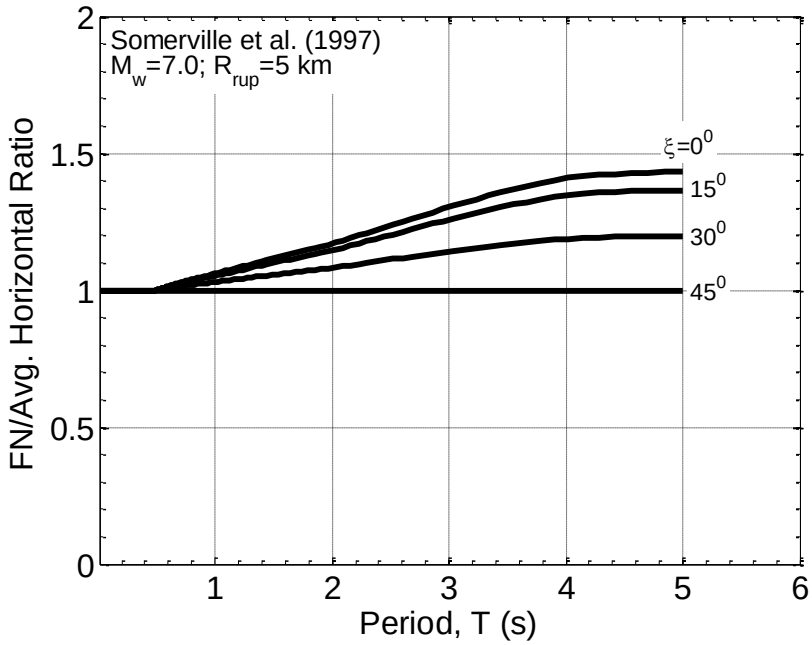

Figure 5.6: Period dependence of the fault-normal to average horizontal response spectra ratio for M_w = 7.0 and R_{rup} = 5 km. Note that the dependence of this ratio on the source-to-site azimuth is also illustrated (adapted from Somerville et al. (1997)).

5.4.2 Abrahamson (2000)

In an effort to ensure that the S97 directivity model could be applied to PSHA, Abrahamson (2000) applied magnitude- and distance-dependent taper functions to the model such that the effects of directivity (i.e. the period-dependent spectral amplification factor illustrated in Figure 5.5) become negligible for magnitudes less than 6.0 and distances greater than 60 km. Furthermore, it was also found that the original S97 model was poorly constrained for larger values of $Xcos(\theta)$. Hence, the functional form of the model was modified such that the maximum directivity amplification occurs at $Xcos(\theta)$ = 0.4 for strike-slip earthquakes, as illustrated in Figure 5.7 for T = 3 s. It is evident from the figure that the revised model (referred to as the AB00 model hereafter) predicts a lower amplification factor

(1.5) under maximum directivity conditions in comparison to the S97 model (2) at T = 3 s. Specific details of the AB00 model are omitted here and can be found in Abrahamson (2000).

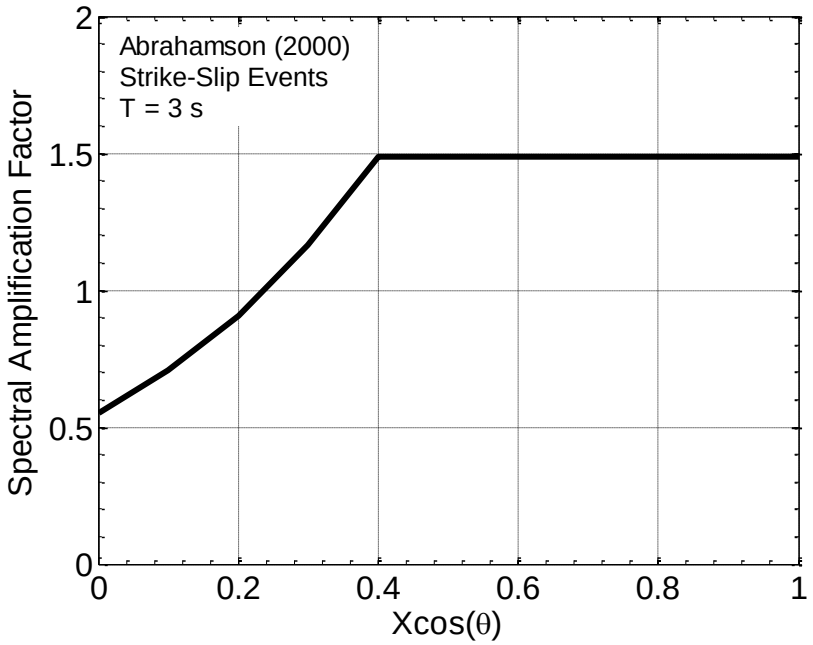

Figure 5.7: Illustration of the Somerville et al. (1997) broadband directivity model, as modified by Abrahamson (2000) to limit the level of directivity amplification at $Xcos(\theta)$ = 0.4. Note that the revised model is only applicable for strike-slip events and has been shown here for T = 3 s (adapted from Abrahamson (2000)).

5.4.3 Rowshandel (2010)

One of the main limitations of the S97 and AB00 models, as described previously in Chapter 2, is the fact that they do not account for the multi-directional nature of the fault rupture process. In order to address this issue, Rowshandel (2010) developed a broadband directivity model (referred to as the R10 model hereafter) which includes the geometric parameter illustrated in Equation (5.5):

$$\xi = \frac{\sum_{i=1}^{N} \zeta_i . \Delta A_i . \overrightarrow{r_1} . \overrightarrow{r_2}}{\sum_{i=1}^{N} \Delta A} = \frac{\sum_{i=1}^{N} \zeta_i . \Delta A_i . \cos\theta_{ij}}{\sum_{i=1}^{N} \Delta A} \tag{5.5}$$

where ΔA_i is an increment of the fault area which ruptures in the direction represented by the unit vector $\overrightarrow{r_1}$; $\overrightarrow{r_2}$ represents the unit vector which defines the direction from the rupturing area increment $\Delta A_i$to the site; N represents the total number of fault area increments; and ζ_i is a parameter which accounts for the heterogeneity of the rupture and can be assumed to be 1 when the focus is solely on modelling directivity effects (Rowshandel, 2010). An illustration of the relevant parameters from Equation (5.5) is provided in Figure 5.8. In essence, ξ can be

regarded as the effective proportion of the fault surface which ruptures towards a given site, and the level of directivity amplification for sites in the forward-directivity region saturates at approximately ξ = 0.5 (Rowshandel, 2010). Similar to the S97 model, the functional form of the directivity model was developed by correlating ground motion residuals with several important parameters including earthquake magnitude (M_w), faulting style, source-to-site distance (R_{rup}), vibration period (T) and ξ. However, it was found that only the latter 3 variables provided the strongest explanatory power in predicting directivity amplification of spectral acceleration. The final functional form of the model, which effectively provides a directivity correction factor for the median prediction of SA provided by GMPEs is given by Equation (5.6). Further details regarding model development are omitted here and can be found in Rowshandel (2010).

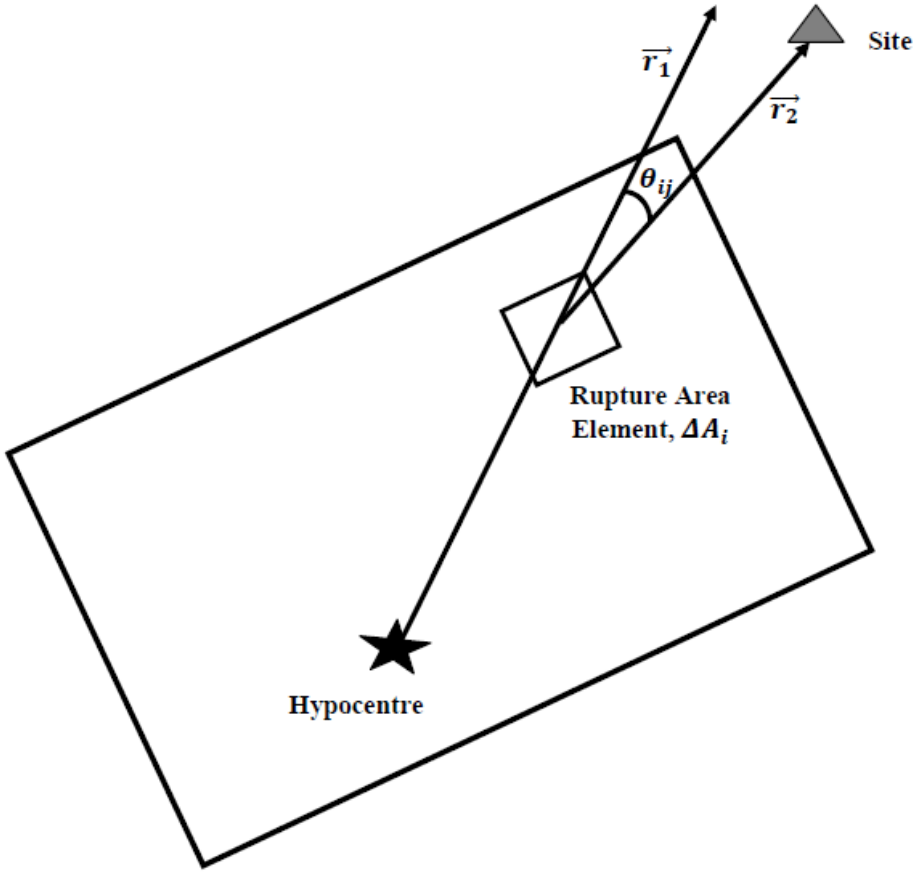

Figure 5.8: Illustration of the relevant parameters required to calculate the directivity parameter, ξ for a generalised source-to-site geometry (adapted from Rowshandel (2010)).

$$\ln \Delta SA\left(T, R_{rup}; \xi\right) = \left(0.5 \ln(T/R_{rup}) + 1.0\right) \xi \quad (5.6)$$
$$0.3 < T < 10\ (s);\ 0.3 < R_{rup} < R_{rup,max}\ (km);\ |\xi| < 0.5$$

where $\ln \Delta SA$ is the directivity amplification factor; and $R_{rup,max}$ represents the period dependent limiting distance prescribed by Rowshandel (2010).

5.4.4 Shahi & Baker (2011)

It is important to realise the fact that none of the three models described in the previous section account for the magnitude dependence of the pulse period (T_p), nor do they consider the probability of pulse occurrence in predicting the directivity amplification of pseudo-spectral acceleration. Shahi & Baker (2011) developed a directivity model (referred to as the SB11 model hereafter), which accounts for both features, as part of calibrating a framework for incorporating the effects of pulse-like ground motions in PSHA. In order to do so, the ratio of SA computed using the pulse-like ground motions identified from the NGA database, and their corresponding residual ground motions (refer to Section 5.2), were initially plotted as a function of the normalised period (T/T_p). As a result, the amplification due to the main pulse-like feature could be obtained. The average amplification exhibited a bell-shaped pattern with a peak close to T/T_p = 1, thereby highlighting the narrowband nature of the directivity pulse. Equation (5.7) displays the functional form of the model:

$$\mu_{lnAf|T_p} = \begin{matrix} 1.131 \exp\left(-3.11\ (\ln(T/T_p) + 0.127)^2\right) + 0.058 \ (\text{if } T \leq 0.88\ T_p) \\ 0.924 \exp\left(-2.11\ (\ln(T/T_p) + 0.127)^2\right) + 0.255 \ (\text{if } T > 0.88\ T_p) \end{matrix} \quad (5.7)$$

where μ_{lnAf} represents the mean amplification factor predicted by the SB11 model for a given vibration period and pulse period given by T and T_p, respectively. Figure 5.9, which provides an illustration of the empirical model, clearly highlights the trend mentioned above. Further details regarding model application are provided in Section 5.5.2

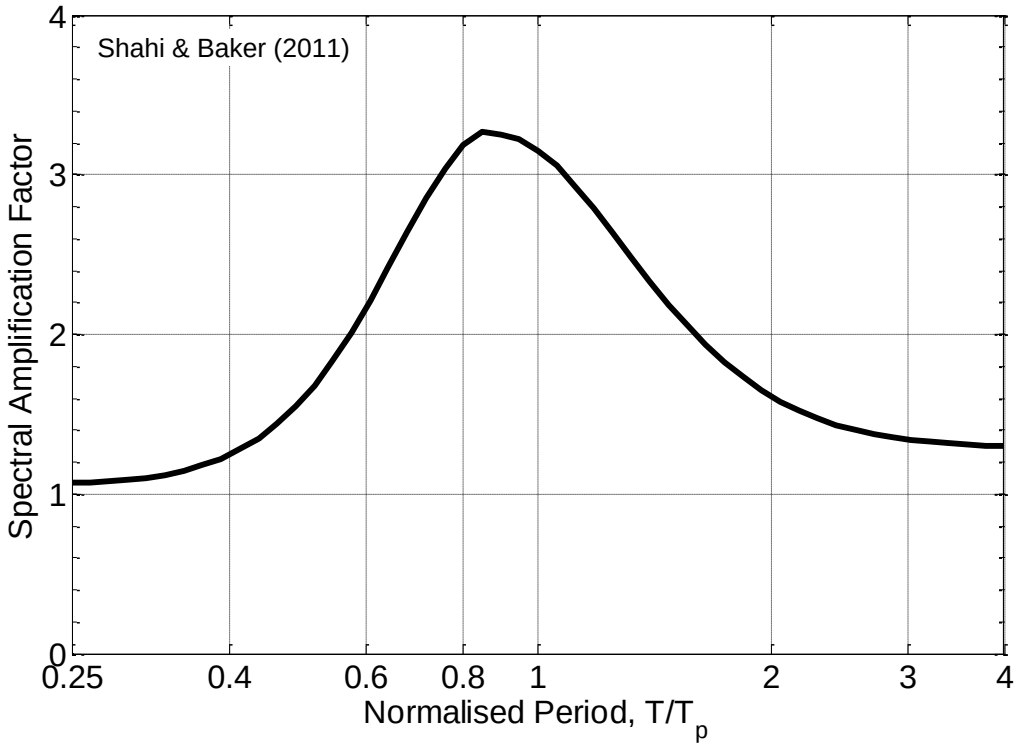

Figure 5.9: Illustration of the directivity amplification factor (plotted as a function of the normalised vibration period, T/T_p) predicted by the narrowband Shahi & Baker (2011) model (adapted from Shahi & Baker, 2011).

5.5 Application of directivity models to specific events from the Canterbury earthquakes

In this section, application of the directivity models described previously to the ground motions observed in the Canterbury earthquakes is illustrated using event-specific examples. Although these models have been calibrated using different ground motion prediction models (e.g. the S97 model was developed using the Abrahamson & Silva (1997) GMPE), their respective developers explicitly state that they are applicable for use with other well-developed GMPEs. Hence, it is considered appropriate for the directivity models to be applied in conjunction with the B10 GMPE for crustal earthquakes in NZ. For clarity, a brief description of the manner in which the directivity models are applied is also provided. The predictive capabilities of the empirical models will be assessed in the sections to follow.

5.5.1 Broadband models

The S97, AB00 and R10 models belong to the broadband model category because they systematically increase or decrease the median SA predictions obtained from conventional GMPEs over a wide period range. A reduction in the standard deviation associated with the GMPE predictions is also provided by the AB00 and R10 models to account for the directivity correction. Equations (5.8) and (5.9) illustrate the median estimate of SA ($\ln SA_{dir}$) and the associated uncertainty (σ_{dir}), respectively, obtained after correcting for directivity using the broadband models:

$$\ln SA_{dir}(Rup,T) = \ln SA(Rup,T) + \ln\big(SAF\ (Z,T)\big) \tag{5.8}$$

$$\sigma_{dir}(Rup,T) = \sigma(Rup,T) \cdot Rf(\mathrm{Z},T) \tag{5.9}$$

where $\ln SA(Rup,T)$ and $\sigma(Rup,T)$ are the median and lognormal standard deviation of spectral acceleration for a specific earthquake scenario (Rup i.e. M_w,R_{rup} etc.) and vibration period (T); $\ln\,(SAF(Z,T))$ represents the spectral amplification factor predicted by the directivity model, which is a function of model-specific directivity parameters (Z) and vibration period; and Rf is the reduction factor applied to the lognormal standard deviation.

5.5.1.1 Somerville et al. (1997)

Figure 5.10 illustrates the observed average horizontal response spectra at two near-fault sites: (i) Christchurch Hospital (CHHC) in the 4 September 2010 M_w 7.1 Darfield earthquake (strike-slip); and (ii) Pages Road (PRPC) in the 22 February 2011 M_w 6.2 Christchurch earthquake (reverse). In both cases, an amplification of the spectral ordinates in the region surrounding the pulse period (T_p = 3.7 s and 4.6 s) is clearly visible. The observations are compared to the prediction of the B10 GMPE (shown in blue) and the S97 broadband model. In the inset of each figure, the geometric parameters (X, Y, θ and ϕ) required by the model are also displayed. Note that these parameters were calculated as part of quantifying the probability of pulse occurrence in Chapter 4. The monotonic scaling of spectral amplitudes at periods greater than T = 0.6 s by the S97 model is evident from Figure 5.10. In both cases, it is obvious that the observed directivity amplification is notably under-predicted by the model. Although the directivity parameters are comparable for CHHC ($X\cos\theta$ = 0.75) and PRPC ($Y\cos\phi$ = 0.67), the level of amplification predicted in the latter case is significantly lower. Howard et al. (2005) suggest that the lower amplification predicted by the S97 model for non-strike-slip events is likely a result of low levels of

directivity amplification in the reverse-faulting records used by Somerville et al. (1997) in developing their model. On the other hand, Somerville et al. (1997) argue that the spatial variation of ground motion due to rupture directivity effects in the near-fault region of non strike-slip faults is presumably already included in the GMPE by means of the distance (R_{rup}) dependence. This seems plausible, considering that the source-to-site azimuth, ϕ is analogous to R_{rup} in predicting the variation of ground motion amplitude, according to the source-to-site geometry illustrated previously in Chapter 2 (refer to Figure 2.13).

Figure 5.11 illustrates the application of the S97 model which allows the fault-normal and fault-parallel components of response spectra to be computed from the predicted average horizontal response spectra with modifications to account for directivity effects. It is unsurprising that this model also under-predicts the directivity amplification observed in the fault-normal component (at approximately T = 2.5 s) at CHHC during the Darfield earthquake. This particular model will not be assessed further as the focus here is on the average horizontal component of ground motion, which is also typically considered in PSHA to represent the intensity of earthquake ground shaking in two orthogonal directions.

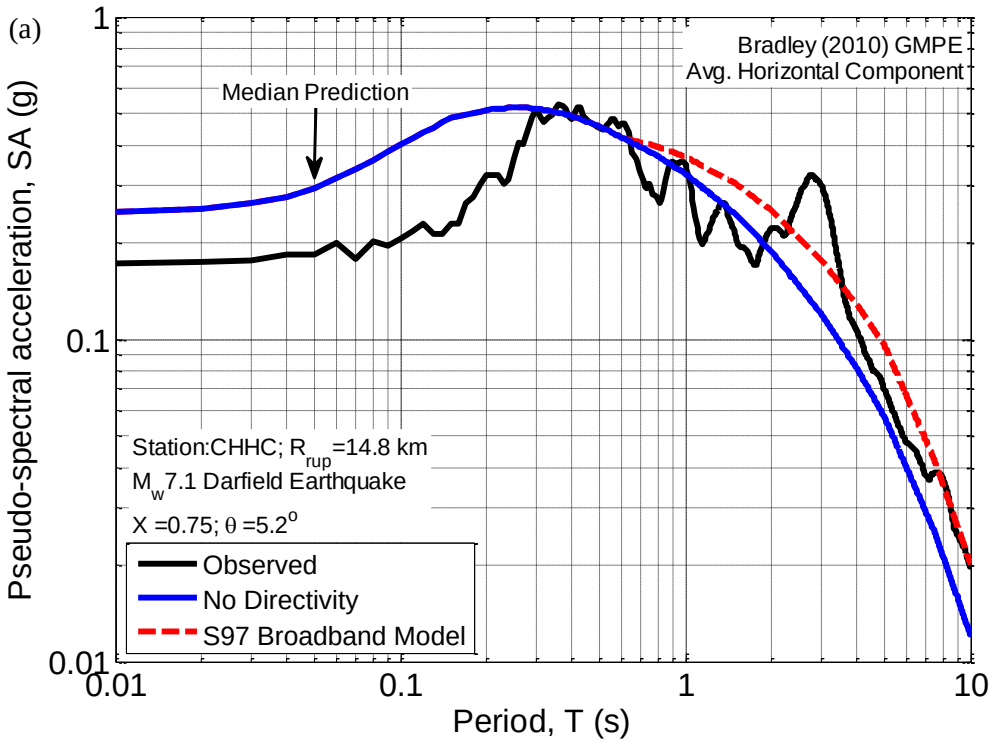

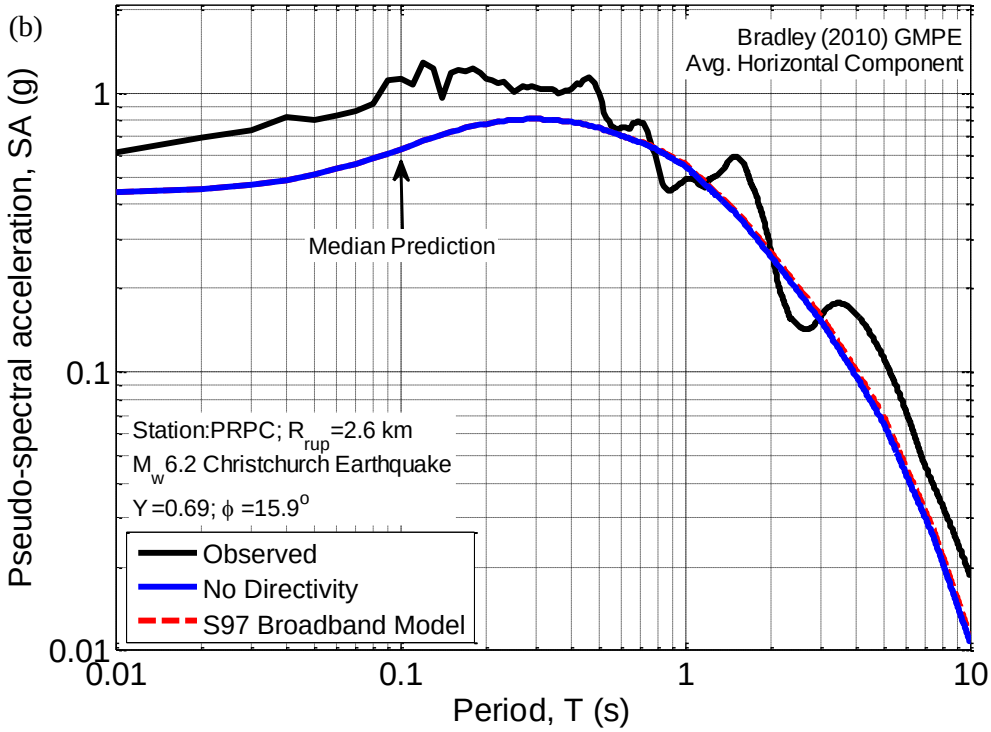

Figure 5.10: Amplification of the average horizontal response spectra due to forward-directivity effects predicted by the Somerville et al. (1997) broadband model for (a) Christchurch Hospital (CHHC) during the 4 September 2010 M_w7.1 Darfield earthquake; and (b) Pages Road (PRPC) during the 22 February 2011 M_w6.2 Christchurch earthquake.

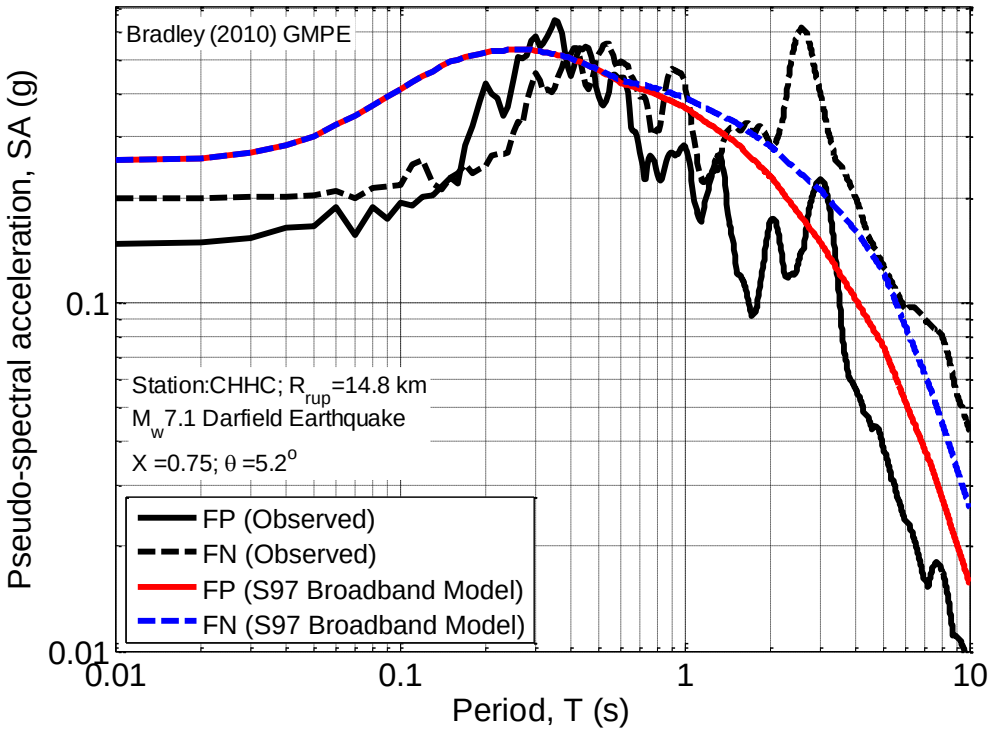

Figure 5.11: Comparison of the observed fault-normal and fault-parallel response spectra at Christchurch Hospital (CHHC) in the M_w7.1 Darfield earthquake with the corresponding predictions, obtained using the Somerville et al. (1997) model for the ratio of fault-normal and average horizontal response spectra.

5.5.1.2 Abrahamson (2000)

Figure 5.12 illustrates the application of the S97 model, as modified by Abrahamson (2000), using the CHHC ground motion from the Darfield event as an example. For comparison, the amplification calculated using the S97 model is also shown. It is evident from the figure that both models predict the same level of amplification for the median response spectra obtained using the B10 GMPE. The maximum directivity amplification predicted by the AB00 model saturates at $X\cos\theta$ = 0.40 over all applicable vibration periods for reasons mentioned previously, whereas the calculated directivity parameter ($X\cos\theta$) at the site is approximately 0.75. This provides an explanation for the same amplification predicted by both models.

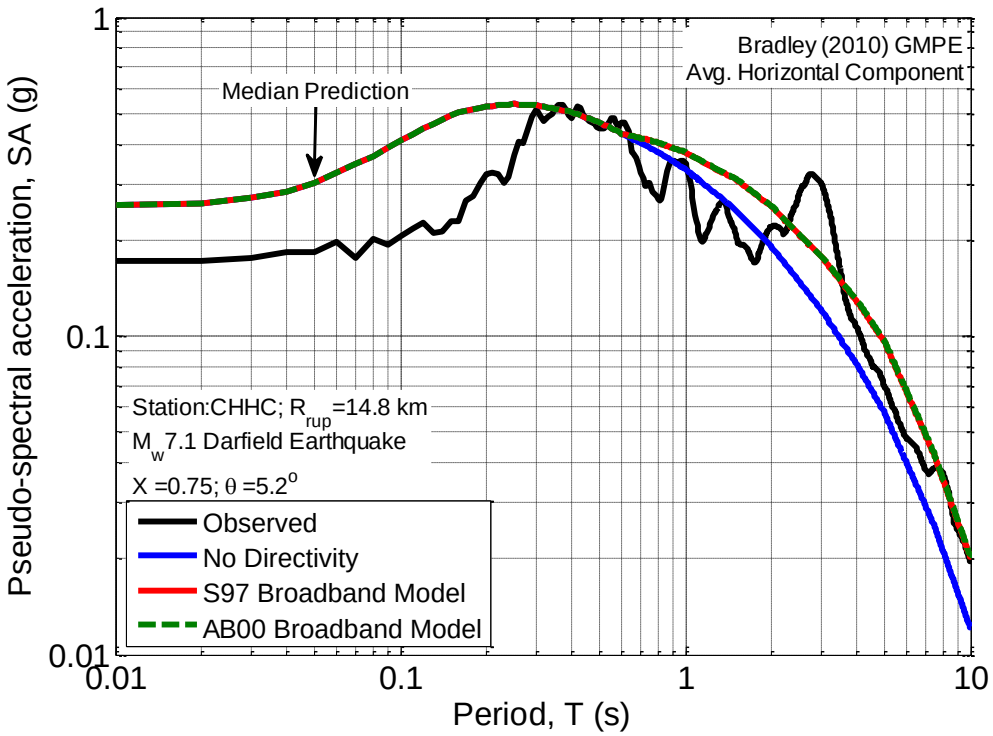

Figure 5.12: Amplification of the response spectra due to forward-directivity effects predicted by the Abrahamson (2000) broadband model for Christchurch Hospital (CHHC) during the 4 September 2010 M_w7.1 Darfield earthquake. The predicted amplification of the Somerville et al. (1997) model is also shown for comparison.

5.5.1.3 Rowshandel (2010)

Figure 5.13 compares the observed average horizontal response spectra at CHHC during the Darfield earthquake with the predicted response spectra after correcting for directivity using the R10 model. It should be noted that the directivity parameter, ξ was calculated using the strike-slip Greendale fault segments from the finite fault model of Holden et al. (2011). Similar to the S97 and AB00 models, the amplification of the predicted

spectral ordinates occurs over a wide range of periods. More importantly, the observed directivity amplification is severely under-estimated by the R10 model.

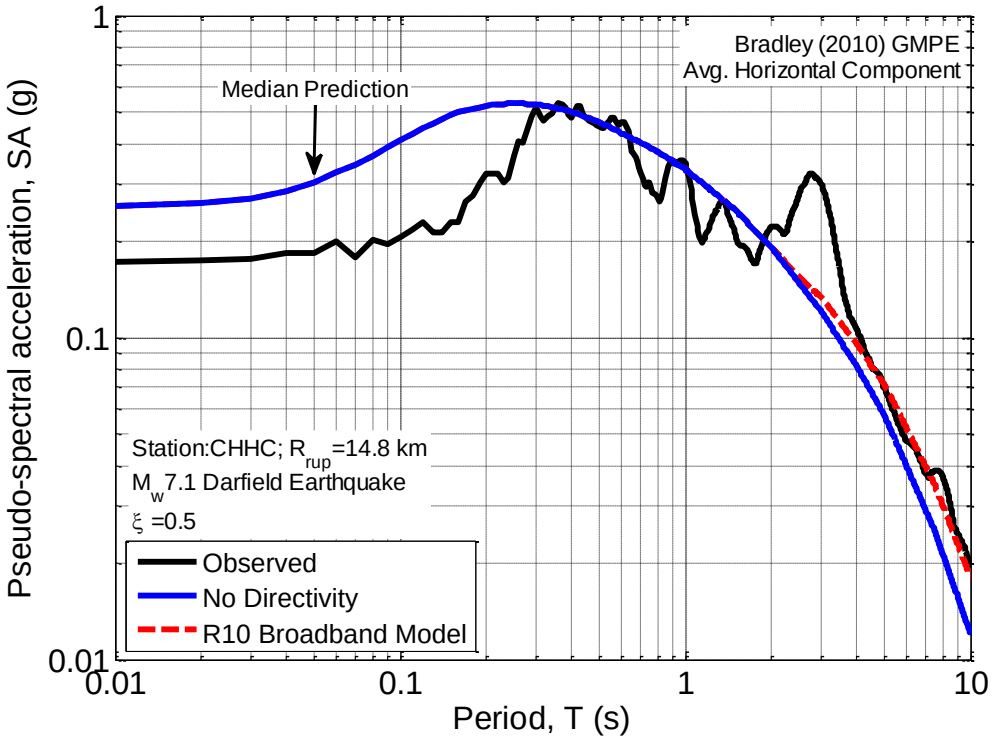

Figure 5.13: Amplification of the response spectra due to forward-directivity effects predicted by the Rowshandel (2010) broadband model for Christchurch Hospital (CHHC) during the 4 September 2010 M_w7.1 Darfield earthquake.

Unlike the S97 and AB00 models, the ξ parameter required in calculating the directivity amplification using the R10 model can be defined for earthquake ruptures with multiple causative faults. As a result, the one-fault model of Beavan et al. (2011) and three-fault model of Beavan et al. (2012) were utilised to calculate the directivity parameter for the Christchurch earthquake. Figure 5.14 illustrates the effect of using both models on the predicted directivity amplification for the PRPC ground motion. From the insets of Figure 5.14, it can be observed that ξ = -0.24 using the one-fault model and ξ = 0 using the three-fault model (note that positive values of ξ represent sites in front of the rupture direction, whereas negative values represent sites behind the rupture direction (Rowshandel, 2010)). Hence, this results in a deamplification of the spectral ordinates in Figure 5.14a and no amplification for the response spectra in Figure 5.14b. This trend was observed for a majority of the near-fault sites which demonstrated evidence of forward-directivity effects in the Christchurch event. Consequently, the three-fault model was adopted for the remainder of this study in quantifying the directivity correction using the R10 model.

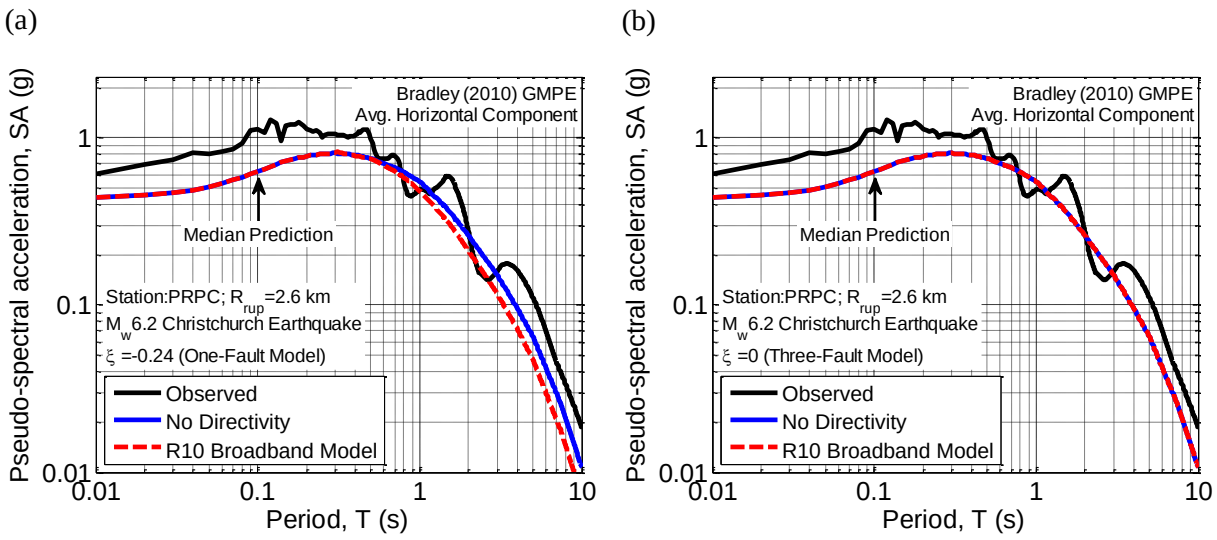

Figure 5.14: Effect of using: (a) the one-fault model of Beavan et al. (2011); and (b) the three-fault model of Beavan et al. (2012) in computing the ξ parameter required in determining the directivity amplification for the ground motion observed at Pages Road (PRPC) during the 22 February 2011 M_w6.2 Christchurch earthquake.

In qualitatively comparing the predictions of the broadband models with the observed response spectra from the examples illustrated previously, it is important to appreciate the contribution of other physical phenomena to the large observed SA amplitudes at longer vibration periods. For example, in the CHHC example, the large amplification of spectral ordinates between T = 2 and 3 seconds can be attributed to both forward-directivity effects and basin-generated surface waves (readers are referred back to Chapter 3 where this phenomenon was discussed extensively). Similarly, the 'bump' observed in the PRPC response spectra at T ≅ 4.5 seconds is likely the result of: (i) forward-directivity effects; and (ii) nonlinear site response including liquefaction (Bradley & Cubrinovski, 2011), especially considering the proximity of the site to the largest slip asperity on the causative fault (refer to Figure 5 in Beavan et al. (2011)) and characteristics of the underlying surficial soils (alluvial silt and sand according to Brown & Weeber (as cited in Wood et al. (2011)) and Site Class D according to NZS1170.5:2004 (Standards New Zealand, 2004)). These issues are further addressed in the sections to follow, where the performance of the directivity models is examined in a quantitative manner.

5.5.2 Narrowband model

The SB11 model represents the most recent attempt in capturing the narrowband characteristics of the directivity pulse. It was evident from Equation (5.7) that the spectral amplification factor predicted by the model is dependent upon the ratio of the vibration period and pulse period (T/T_p). Therefore, in order to carry out comparisons between the observed and predicted directivity amplification for a particular earthquake scenario and site, an estimate of the pulse period is required. This can be readily obtained using predictive relationships which relate T_p to the moment magnitude (M_w) of the earthquake (recall that the reasons for the magnitude dependence of the pulse period were previously outlined in Chapter 2). It should be noted that the uncertainty associated with the predicted pulse period is well represented using a lognormal distribution (Shahi & Baker, 2011). Because the pulse period is treated as a random variable, the mean directivity amplification ($\mu_{\ln(Af)}$) can be computed using the convolution integral displayed in Equation (5.10):

$$\mu_{\ln(Af)} = \int \mu_{\ln Af|T_p} f_{T_p} dT_p \tag{5.10}$$

where $\mu_{\ln(Af|T_p)}$ is the SB11 narrowband model from Equation (5.7) and f_{T_p} denotes the lognormal distribution of the pulse period for a given earthquake magnitude obtained from a prediction equation. As will be shown in Chapter 6, the pulse period equation developed by Shahi & Baker (2011) (SB11) provides the most improved predictions with respect to observations from the Canterbury earthquakes, among other models developed in previous research. Hence, this model will be adopted for the purposes of the present study.

Once the directivity amplification has been determined, it can be combined with the pulse occurrence probability and median prediction from a conventional GMPE to obtain the directivity corrected SA amplitudes (SA_{dir}), as illustrated in Equation (5.11):

$$\begin{aligned} SA_{dir}(Rup,T) = {} & SA(Rup,T) \cdot \exp\left(\mu_{\ln(Af)}\right) \cdot P(Pulse) \\ & + SA(Rup,T) \cdot \exp\left(\mu_{ln(Df)}\right) \cdot (1 - P(Pulse)) \end{aligned} \tag{5.11}$$

where $SA(Rup,T)$ is the median spectral acceleration for a specific earthquake scenario (Rup i.e. M_w,R_{rup} etc.) and vibration period (T); $P(Pulse)$ is the predicted pulse probability obtained using an empirical prediction model; and $\mu_{ln(Df)}$ represents the deamplification factor obtained using the Shahi & Baker (2011) model (not shown here for brevity) to account for the possibility of observing non-pulse-like ground motions at the site of interest.

The pulse probability model of Shahi (2013) (S13) will be utilised in this chapter based on the results of Chapter 4. A reduction factor (which is a function of the T/T_p ratio) for the lognormal standard deviation associated with the GMPE predictions is also included in the SB11 model and can be applied in a similar manner to Equation (5.11).

The results of the previous section were effective in highlighting the inadequacy of the broadband models in predicting the directivity amplification of response spectra, albeit in a qualitative manner. In an effort to determine whether improved predictions can be obtained using the SB11 model, examples of its application to ground motions from the M_w 7.1 Darfield, M_w6.2 Christchurch, M_w6.0 June and M_w5.9 December earthquakes are illustrated in Figure 5.15. The inset of each plot shows the geometric parameters required in calculating the pulse probability (refer to Chapter 4) and the vibration period corresponding to the directivity pulse. In all four cases, it can be observed that the predicted amplification has been obtained considering the pulse period as: (i) a random variable i.e. using the entire lognormal distribution of the pulse period; and (ii) a constant value i.e. using the pulse period associated with the ground motion obtained by means of wavelet analysis in Chapter 3. For the latter case, it is evident from the figure that the resulting amplification occurs over a small range of periods, thereby highlighting the narrowband nature of the SB11 model. On the other hand, the effect of treating T_p as a random variable results in an amplification over a wider range of periods. Nonetheless, it is important to realise that the SB11 model allows the amplification to be centred around the pulse period (which is consistent with theoretical considerations) unlike the broadband models which monotonically scale the spectral amplitudes within the moderate-to-long period range.

In general, it can be observed from Figure 5.15 that the SB11 model provides improved predictions in relation to its predecessors. This is particularly evident for the ground motion observed at PRPC and NBLC (New Brighton Library) in the Christchurch and June events, respectively. It can also be seen from Figure 5.15a that the predicted amplification for the PRPC response spectra obtained using the two different methods described previously occurs within distinct period ranges. This can be attributed to the differences in pulse period associated with the observed directivity pulse (T_p = 4.6 s) and median prediction (T_p = 1.6 s) obtained using the Shahi & Baker (2011) equation.

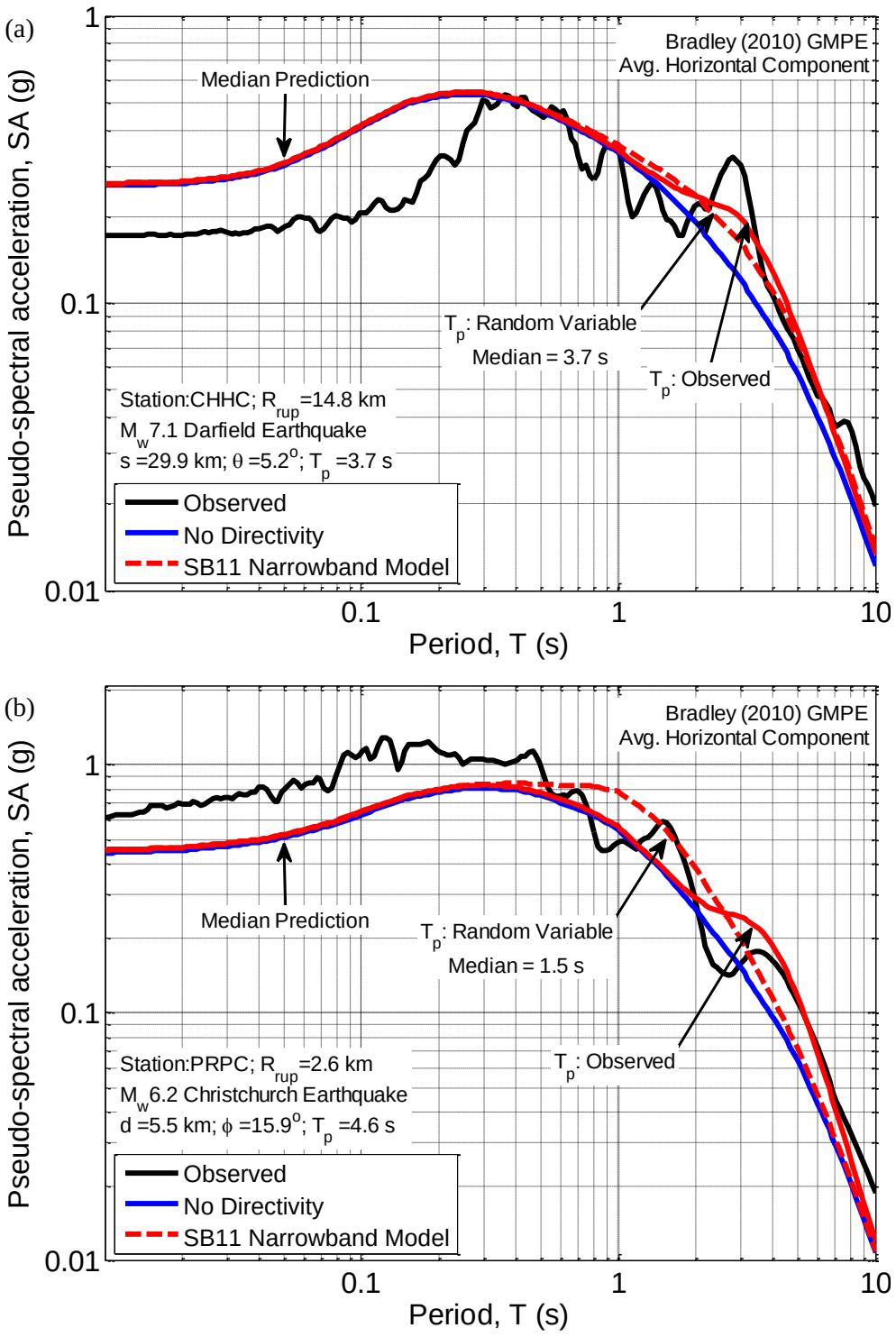
(a)
Pseudo-spectral acceleration, SA (g)
1
0.1
0.01
0.1
1
10
Period, T (s)
Bradley (2010) GMPE
Avg. Horizontal Component
Median Prediction
T_p: Random Variable
Median = 3.7 s
T_p: Observed
Station:CHHC; R_rup=14.8 km
M_w7.1 Darfield Earthquake
s =29.9 km; θ =5.2°; T_p =3.7 s
Observed
No Directivity
SB11 Narrowband Model
(b)
Pseudo-spectral acceleration, SA (g)
1
0.1
0.01
0.1
1
10
Period, T (s)
Bradley (2010) GMPE
Avg. Horizontal Component
Median Prediction
T_p: Random Variable
Median = 1.5 s
T_p: Observed
Station:PRPC; R_rup=2.6 km
M_w6.2 Christchurch Earthquake
d =5.5 km; ϕ =15.9°; T_p =4.6 s
Observed
No Directivity
SB11 Narrowband Model

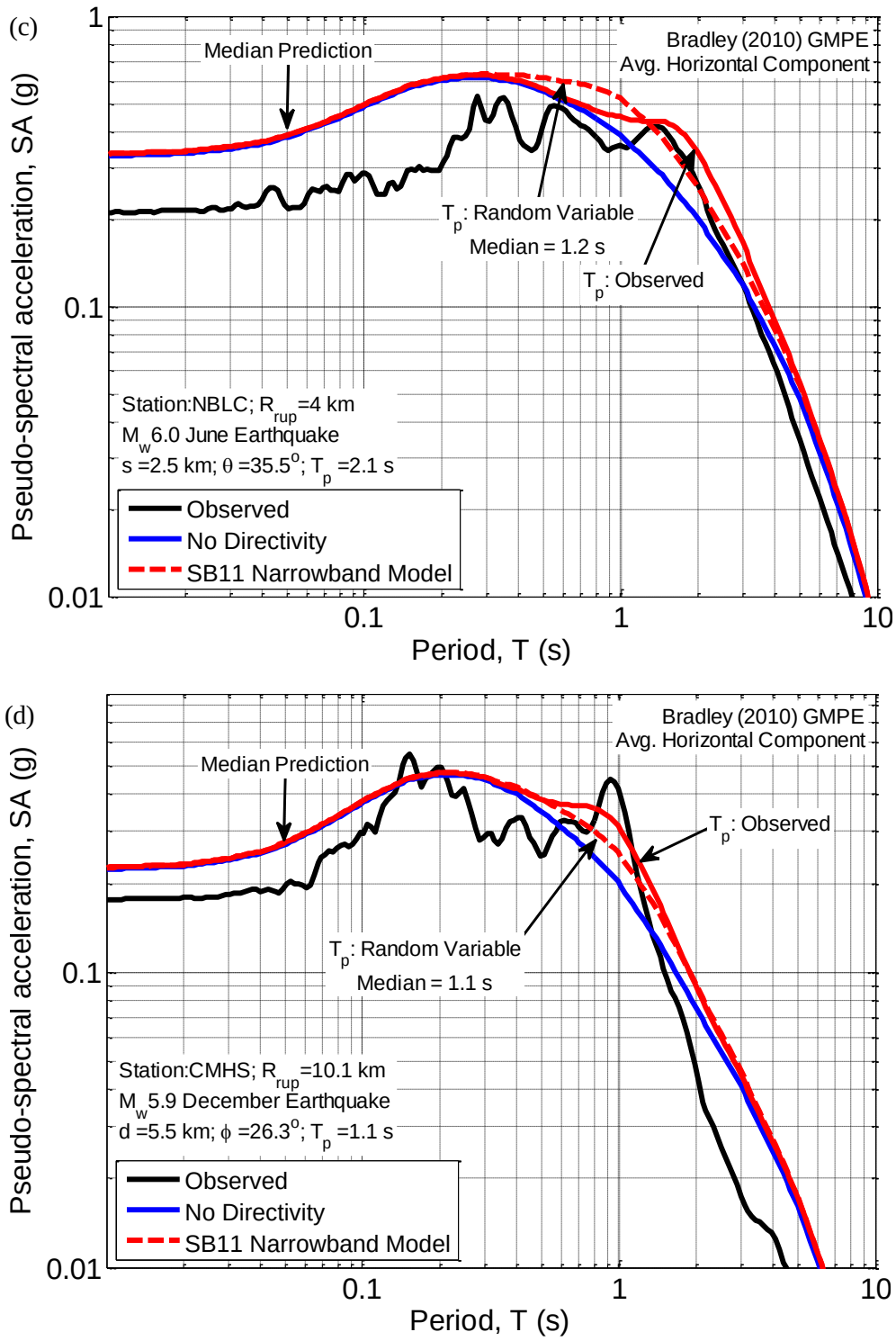

Figure 5.15: Amplification of the average horizontal response spectra due to forward-directivity effects predicted by the Shahi & Baker (2011) narrowband model for (a) Christchurch Hospital (CHHC) during the 4 September 2010 M_w7.1 Darfield earthquake; (b) Pages Road (PRPC) during the 22 February 2011 M_w6.2 Christchurch earthquake; (c) New Brighton Library (NBLC) during the 13 June 2011 M_w6.0 earthquake; and (d) Cashmere High School (CMHS) during the 23 December 2011 M_w5.9 earthquake. Note that the amplification in each case has been calculated considering the directivity pulse period (T_p) as a random variable (i.e. using the entire lognormal distribution obtained from the Shahi & Baker (2011) empirical equation) and as a constant value (i.e. using the pulse period corresponding to the observed directivity pulse).

5.6 Direct comparison of observed and predicted directivity amplification

As will be made evident in the following sections, discrepancies between the observed spectral amplitudes of forward-directivity ground motions in the Canterbury earthquakes and predictions provided by several directivity models can also be attributed to other salient physical phenomena (i.e. basin-generated surface waves and non-linear surficial soil response for example). Hence, a robust method of determining the efficacy of the directivity models considered in this chapter is to directly compare the amplification of response spectra caused by the directivity pulse, with the amplification prescribed by the models. The observed amplification can be computed using the two-step process outlined below:

1. Extract the directivity pulse from the observed velocity time-series using a wavelet analysis algorithm (e.g. Baker, 2007; Shahi, 2013), which allows the residual ground motion to be obtained (i.e. difference between the original ground motion and extracted pulse).
2. Compute the observed directivity amplification using Equation (5.12) for each vibration period of interest:

$$Directivity\ Amplification = \frac{SA_{original}}{SA_{residual}} \tag{5.12}$$

where $SA_{original}$ and $SA_{residual}$ represent the response spectra corresponding to the original and residual ground motions, respectively.

5.6.1 Broadband model comparisons

The observed mean directivity amplification with vibration period in the four considered events (i.e. M_w 7.1 Darfield, M_w 6.2 Christchurch, M_w 6.0 June and M_w 5.9 December earthquakes) from the Canterbury earthquakes is compared with the mean amplification predicted by the S97 and R10 broadband models in Figure 5.16. It is noted that the AB00 model is not considered in this comparison as it is only applicable for strike-slip events and its predictions are similar to the S97 model, as highlighted previously in Section 5.5.1. The thin grey lines represent the directivity amplification observed in individual ground motions from a particular event. For clarity, the amplification values predicted by the

models for individual sites are not shown in the figure. It is immediately obvious from the figure that the observed mean amplification in each event becomes notable for periods greater than approximately T = 0.6 s, which is consistent with the findings of Somerville et al. (1997). The period range corresponding to the largest observed mean amplification appears to gradually decrease as the earthquake magnitude reduces. For example, the period ranges corresponding to significant directivity amplification in the M_w 7.1 Darfield and M_w 6.2 Christchurch events are 4 s $\leq T \leq$ 9 s and 2 s $\leq T \leq$ 5 s, respectively. This is clearly indicative of the magnitude scaling of the directivity pulse (Somerville, 2003).

The results of Figure 5.16 also confirm that the predictions of the S97 and R10 broadband models are inadequate in general. In particular, it can be seen that either no amplification or varying levels of deamplification are predicted by the two models for the Christchurch, June and December earthquakes. Although the R10 model under-predicts the amplification in the Darfield event for all vibration periods, the S97 model predictions are reasonably consistent with the observations for $T \leq$ 3s.

In Figure 5.17a, a comparison between the mean observed and predicted (i.e. using the S97 and R10 models) directivity amplification considering all four events is carried out. The dotted black lines indicate the 16th and 84th percentile values of the observations for each vibration period. It can be seen that, on average, the levels of predicted amplification are negligible over the entire period range, whereas, the observed median amplification ranges between 1.1 and 1.6 for 0.6 s $\leq T \leq$ 10 s. For each vibration period, the standard deviation (σ_{res}) of the residuals (defined as the difference between the observed and predicted amplification) are shown in Figure 5.17b. As expected, notably large σ_{res} values are observed for periods greater than T = 1s due to the significant under-predictions provided by the broadband models.

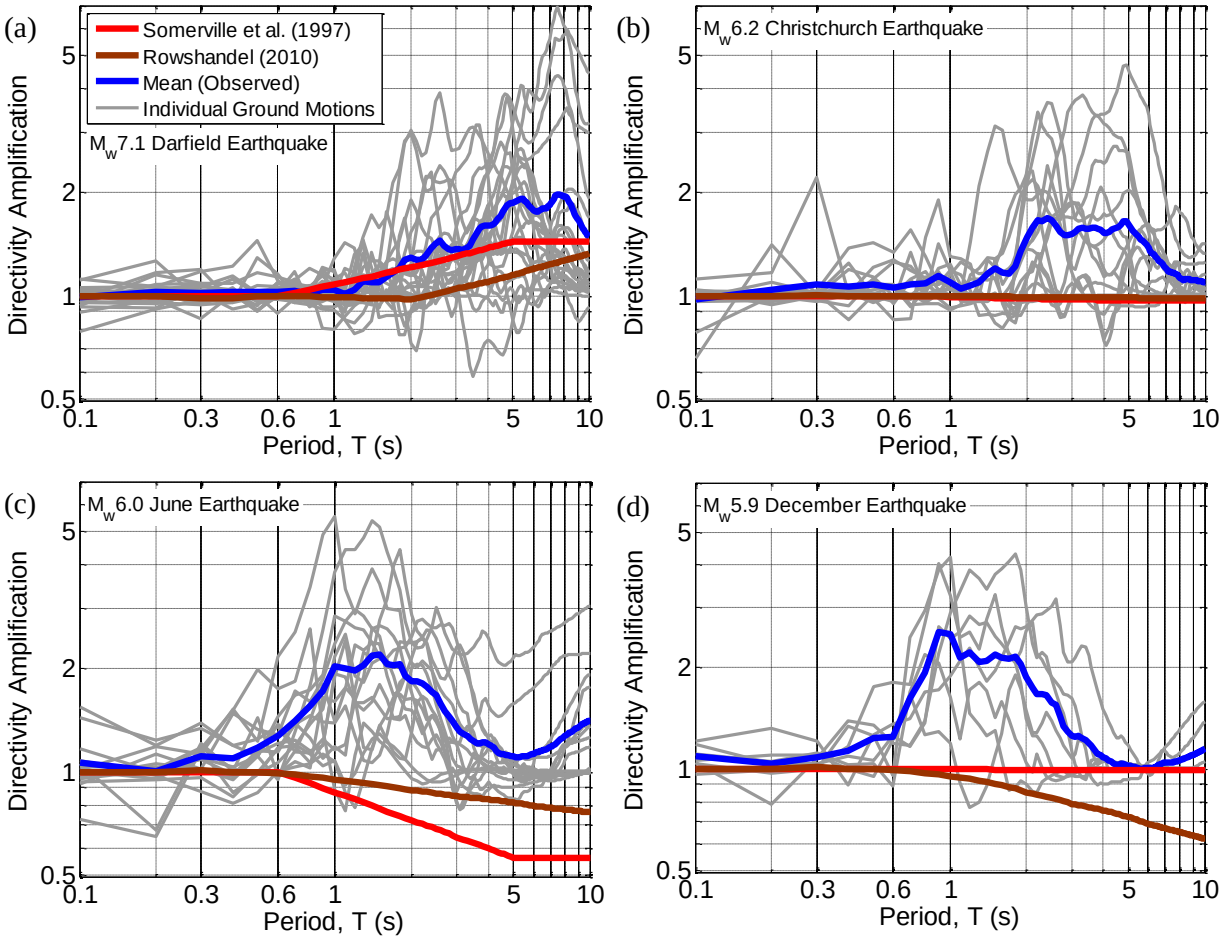

Figure 5.16: Direct comparison of the mean amplification predicted by the Somerville et al. (1997) and Rowshandel (2010) broadband directivity models with the mean directivity amplification of spectral ordinates observed in (a) 4 September 2010 M_w7.1 Darfield earthquake; (b) 22 February 2011 M_w6.2 Christchurch earthquake; (c) 13 June 2011 M_w6.0 earthquake; and (d) 23 December 2011 M_w5.9 earthquake.

5.6.2 Narrowband model comparison

Figure 5.18 provides a comparison between the mean directivity amplification observed in the M_w7.1 Darfield, M_w6.2 Christchurch, M_w6.0 June and M_w5.9 December earthquakes and the narrowband model SB11 model, plotted as a function of the normalised vibration period (T/T_p). The amplification associated with the individual ground motions is also shown using the thin grey lines. As expected from previous experience (e.g. Shahi & Baker, 2011), the observed mean amplification curves in each event form a bell-shaped pattern with peaks close to T/T_p = 1, thereby reinforcing the fact that the directivity pulse is inherently narrowband in nature. It can also be seen that, on average, the amplification resulting from forward-directivity effects in all four events is lower than that predicted by the SB11 model. This is discussed further in Section 5.7.4 where the effect of directly applying the model to conventional GMPE predictions is examined.

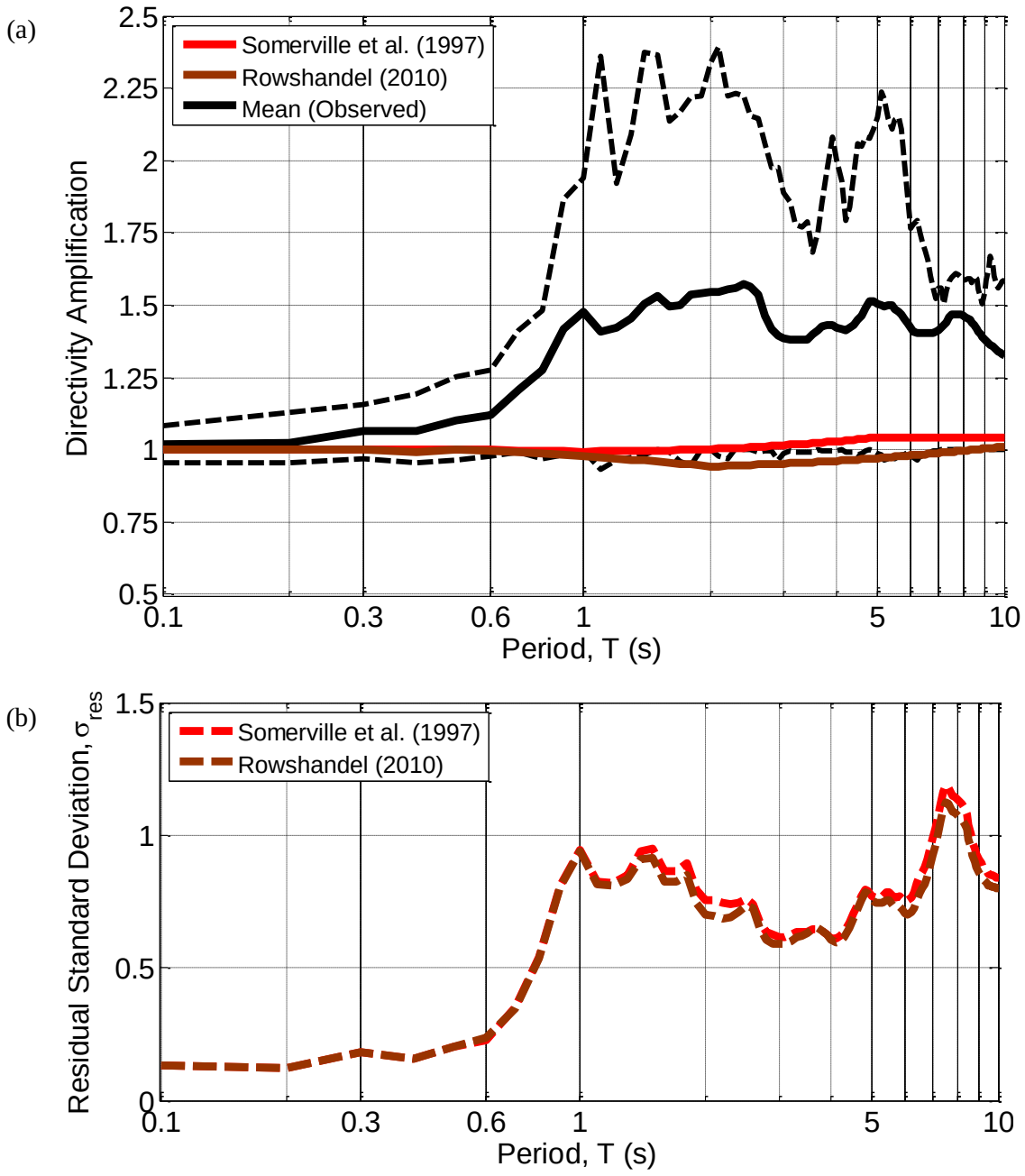

Figure 5.17: Panel (a) Comparison of the mean directivity amplification associated with observations from the four considered events in the Canterbury earthquake sequence with the mean amplification of the Somerville et al. (1997) and Rowshandel (2010) broadband models. Note that the dotted black lines represent the 16th and 84th percentiles of the observed amplification. Panel (b) Standard deviation associated with the residual (calculated as the difference between the observed and predicted directivity amplification) plotted as a function of vibration period.

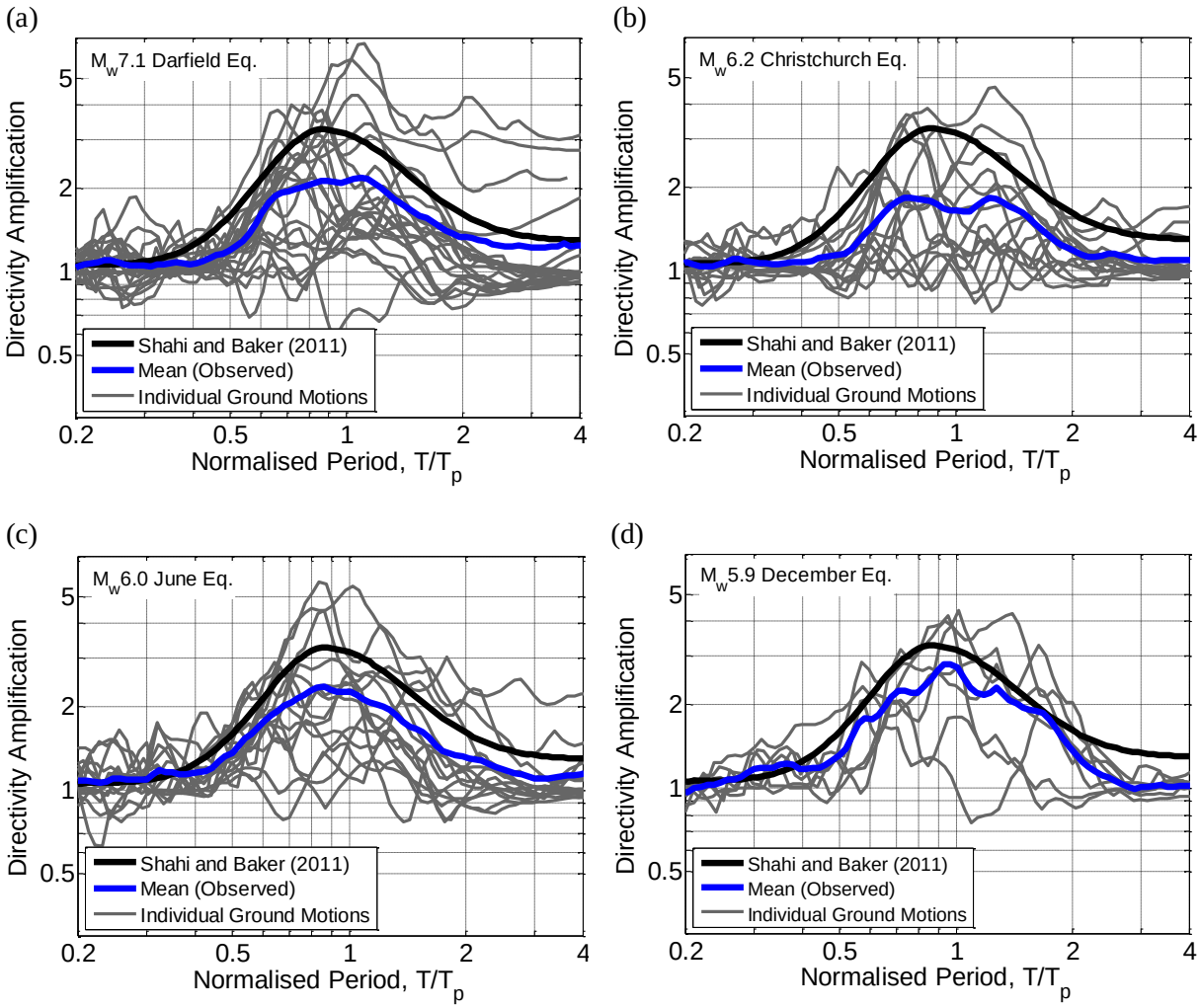

Figure 5.18: Direct comparison of the empirical amplification of the Shahi & Baker (2011) narrowband model with the mean directivity amplification of spectral ordinates observed in (a) 4 September 2010 M_w7.1 Darfield earthquake; (b) 22 February 2011 M_w6.2 Christchurch earthquake; (c) 13 June 2011 M_w6.0 earthquake; and (d) 23 December 2011 M_w5.9 earthquake.

To further elucidate the observations in Figure 5.18, the mean directivity amplification considering all four events from the Canterbury earthquake sequence is compared with the SB11 model prediction in Figure 5.19a. The dotted lines represent the 16th and 84th percentiles of the observations, and the amplification associated with individual ground motions is indicated by grey lines.

Similar to the broadband models examined previously, the standard deviation of the amplification residuals is illustrated as a function of the normalised vibration period in Figure 5.19b. Given that the largest over-prediction of the observed amplification in Figure 5.19a occurs in the range, $0.75 \leq T/T_p$ 1.25 , it is unsurprising that the largest σ_{res} values also correspond to the same normalised periods.

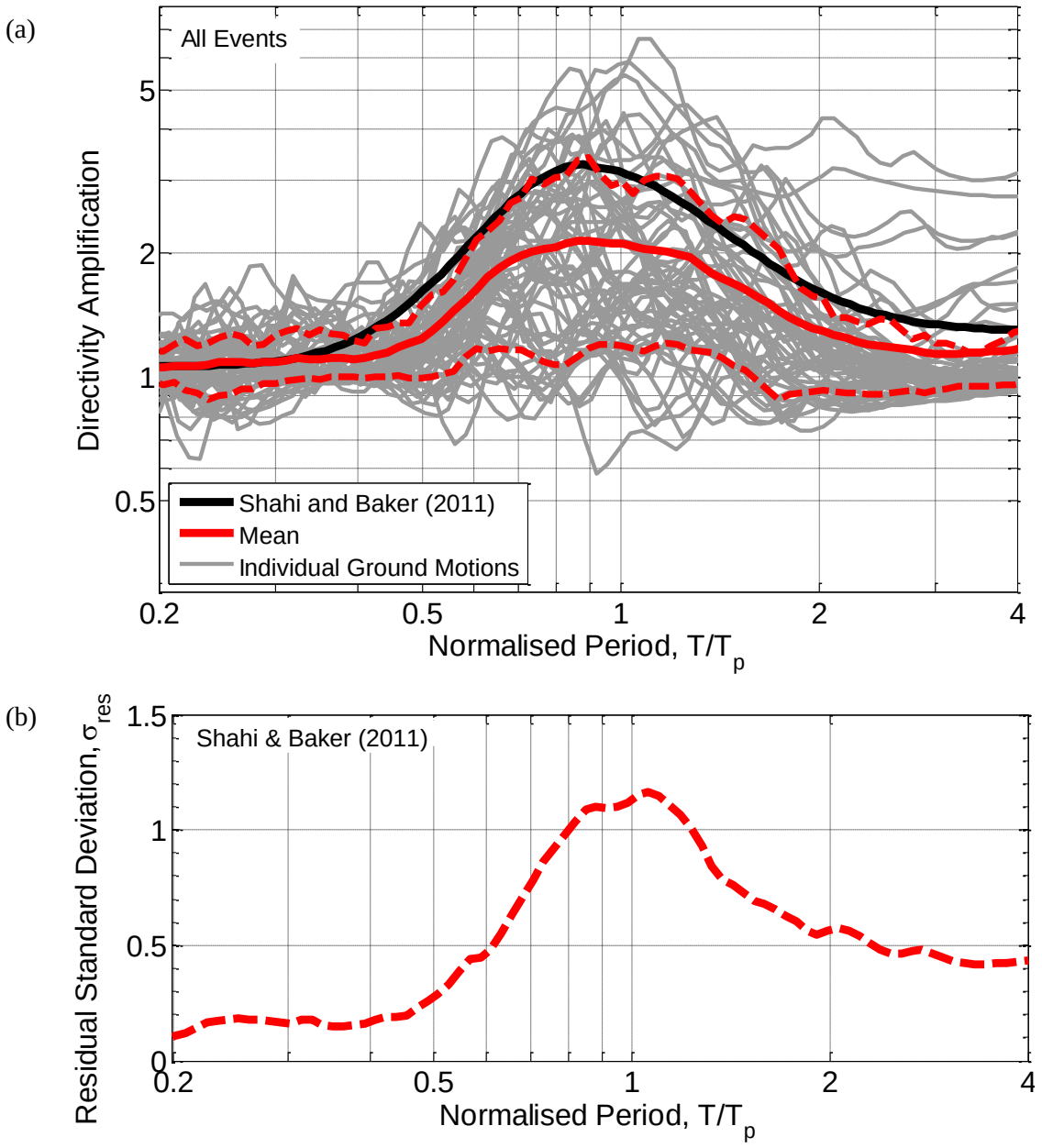

Figure 5.19: Panel (a) Comparison of the mean directivity amplification associated with observations from the four considered events in the Canterbury earthquake sequence compared with the empirical amplification of the Shahi & Baker (2011) narrowband model. Note that the dotted red lines represent the 16th and 84th percentiles of the observed amplification. Panel (b) Standard deviation associated with the residual (calculated as the difference between the observed and predicted directivity amplification) plotted as a function of the normalised vibration period.

5.7 Residual analysis

The deviation of observed spectral ordinates from GMPE predictions can be quantified by the normalised total residual (ε), which is computed using Equation (5.13):

$$\varepsilon = \frac{\ln SA(T) - \mu_{\ln SA(T)}}{\sigma_{\ln SA(T)}} \tag{5.13}$$

where $SA(T)$ is the observed spectral acceleration for a particular vibration period; $\mu_{\ln SA(T)}$ and $\sigma_{\ln SA(T)}$ are the logarithmic mean and standard deviation values of $SA(T)$ obtained from a GMPE. In essence, ε measures the number of standard deviations by which an observed ground motion deviates from the predicted SA value, and hence provides a measure of bias. A value of ε = 0 indicates no bias whereas a value of ε = 1 indicates that the observations are one standard deviation above the median predictions on average. Hence, in order to assess the adequacy of the directivity models examined previously, the total residuals were computed for all ground motions showing evidence of forward-directivity effects in the four events from the Canterbury earthquake sequence. It is noted that the component of ground motion exhibiting the strongest directivity pulse was used in computing the residuals. The following sections summarise the results obtained from the residual analysis.

5.7.1 Broadband models

The two previous sections, to a large extent, have established that the broadband models considered in this study do not provide adequate predictions of the observed directivity amplification. As a result, the residual analysis in this section is restricted to the two main events from the Canterbury earthquake sequence i.e. M_w7.1 Darfield and M_w6.2 Christchurch earthquakes. Figure 5.20 illustrates the mean value of all of the total residuals as a function of vibration period for the two events. In each case, the mean residuals corresponding to the B10 GMPE and S97 broadband directivity model are shown. The uncertainty in the mean residual for each vibration period is indicated using the standard error. It should be noted that the thin dotted blue lines and shaded grey area correspond to the GMPE and directivity model, respectively. A solid black line is also included to indicate ε = 0 i.e. no bias.

The results of Figure 5.20a illustrate that the use of a conventional GMPE without any directivity amplification results in a notable under-prediction ($\varepsilon > 0.5$) of spectral ordinates at longer periods ($T > 4$ s) for the Darfield event. These observations are consistent with the findings of Bradley (2012a), which were summarised previously. Upon adjusting the median prediction of the B10 GMPE using the S97 directivity model, a systematic reduction in the mean residuals for all periods greater than $T = 0.6$ s is observed for the Darfield earthquake. For the period range 0.6 s $\leq T \leq$ 2.5 s in particular, it can be seen that the over-prediction (indicated by the negative mean residuals) of the B10 model becomes significant upon applying the S97 model. Between periods of 2.5 s and 5 s however, there appears to be no significant bias in the mean residuals. Despite the reduction in the residuals associated with the broadband model for periods greater than 5 s, it is evident that a notable positive bias still remains. This observation is consistent with the trends observed in the previous sections.

In the Christchurch event, neglecting the directivity amplification results in a nearly constant positive bias ($\varepsilon_{mean} \cong 0.5$) for $T \geq 0.6$ s, as illustrated in Figure 5.20b. The S97 model predicts a deamplification of spectral ordinates for several sites in the Christchurch event, which is also highlighted by the slight increase in the mean residuals obtained after correcting for directivity. This is clearly indicative of the weaker predictive capabilities of the S97 model for non strike-slip events, a trend which has also been observed by Howard et al. (2005), and discussed previously. Although directivity effects were significant in the Christchurch earthquake, the observed positive bias ($\varepsilon \geq 0.5$) for long-period SA amplitudes relative to the B10 GMPE can also possibly be attributed to the large amplitude and long period ground motion resulting from basin-generated surface waves, as well as nonlinear soil response, as noted by Bradley and Cubrinovski (2011). For example, the spectral amplification at periods greater than $T = 2$ s at four sites located in the Christchurch CBD (CBGS, CCCC, CHHC and REHS) was attributed to liquefaction by Smyrou et al. (2011). These observations were subsequently supported using one-dimensional effective stress analyses. Although the effects of local site response are considered by the B10 GMPE, it is acknowledged by Bradley (2013) that it does so in a highly simplified manner and that empirical strong motion databases (used in model development) do not adequately represent ground motions recorded on soft soils.

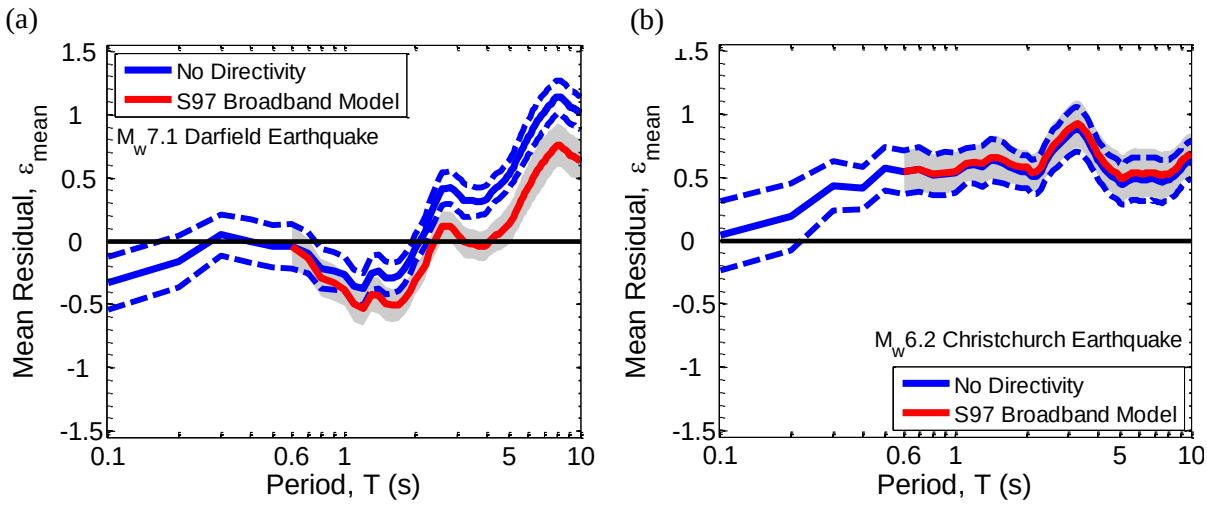

Figure 5.20: Mean residuals associated with the Bradley (2010) GMPE and the Somerville et al. (1997) broadband model predictions for (a) 4 September 2010 M_w7.1 Darfield earthquake; (b) 22 February 2011 M_w6.2 Christchurch earthquake. Note that the thinner dotted lines and shaded area represent the uncertainty in the mean residual obtained using the GMPE and directivity model, respectively.

The mean residuals calculated using observations from the Darfield earthquake and predictions obtained from the B10 GMPE and AB00 directivity model are illustrated in Figure 5.21. As previously noted, the latter model is a modified version of the S97 directivity model for strike-slip events. An examination of the residuals reveals that the trends described previously with respect to the S97 model also apply to the AB00 model.

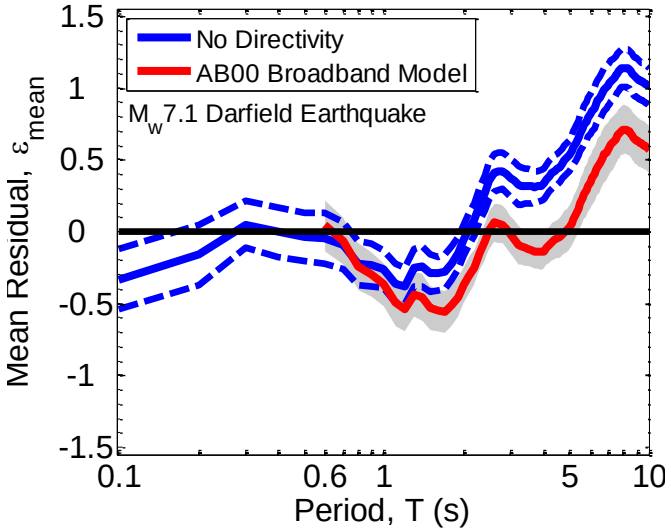

Figure 5.21: Mean residuals associated with the Bradley (2010) GMPE and the Abrahamson (2000) broadband model predictions for the 4 September 2010 M_w7.1 Darfield earthquake. Note that the thinner dotted lines and shaded area represent the uncertainty in the mean residual obtained using the GMPE and directivity model, respectively.

The mean residuals associated with the R10 directivity model are displayed along with the standard error for the Darfield and Christchurch earthquakes in Figure 5.22. In the case of the Darfield event, the model has no effect on the predicted spectral amplitudes in the periods range 0.3 s $\leq T \leq$ 3 s, as indicated by the similarities in the mean residuals corresponding to the B10 and R10 models. Although there is a systematic reduction of the mean residual for periods greater than 4 s, it can be seen that the observed spectral ordinates remain significantly under-predicted on average. These trends are consistent with those identified previously in Sections 5.5 and 5.6. The residuals corresponding to the Christchurch event in Figure 5.22b illustrate that correcting for directivity using the R10 model has no effect on the predictions. This can be attributed to the fact that the parameter, ξ, required in computing the directivity correction factor is effectively zero for a number of sites where forward-directivity effects were observed.

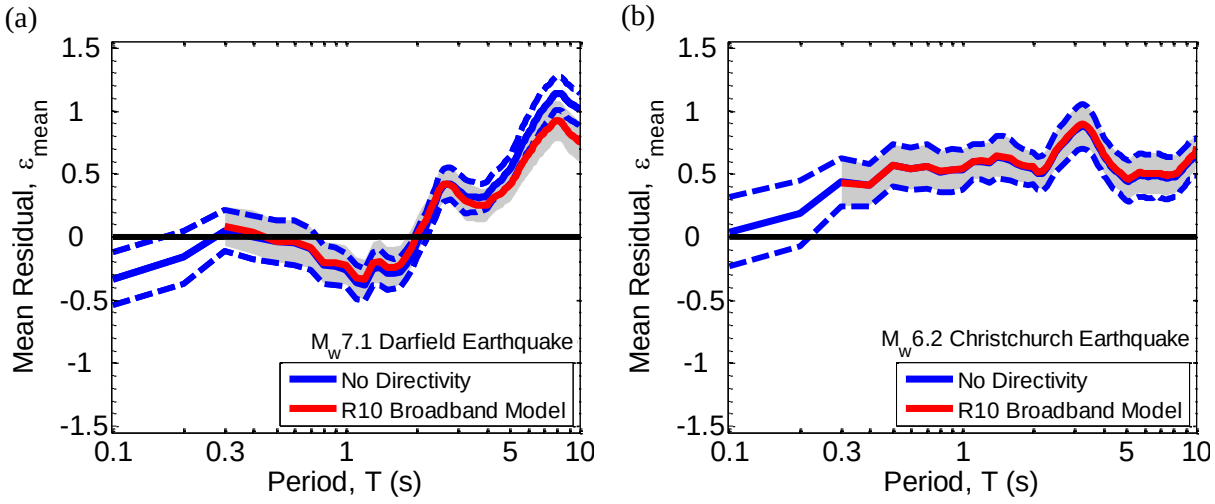

Figure 5.22: Mean residuals associated with the Bradley (2010) GMPE and the Rowshandel (2010) broadband model predictions for (a) 4 September 2010 M_w7.1 Darfield earthquake; (b) 22 February 2011 M_w6.2 Christchurch earthquake. Note that the thinner dotted lines and shaded area represent the uncertainty in the mean residual obtained using the GMPE and directivity model, respectively.

5.7.2 Narrowband model

In a manner similar to the broadband models, Figure 5.23 illustrates the mean residuals associated with the B10 GMPE and SB11 narrowband directivity model as a function of vibration period. These residuals are presented for the M_w7.1 Darfield, M_w6.2 Christchurch, M_w6.0 June and M_w5.9 December earthquakes. For each event, the mean residuals corresponding to the SB11 model are shown considering the pulse period both as a random variable and constant value. It should be recalled that the SB11 amplification function depends only on T/T_p and that the level of predicted directivity amplification is

governed by the probability of observing a pulse at the site under consideration (refer to Equation (5.11)).

Despite applying the SB11 in two different ways (i.e. T_p known or T_p unknown), it can be observed from Figure 5.23 that the mean residuals from each event display similar trends. Similar to its broadband counterparts, the mean residuals associated with the SB11 model do not demonstrate any significant bias for periods less than T= 4 s in the Darfield event. At longer periods, a marginal reduction in the mean residuals occurs, but there is still notable bias, indicating other important factors. The remaining significant positive bias can likely be attributed to (i) the lower levels of amplification predicted by the SB11 model due to low probabilities of pulse occurrence (recall from Chapter 4 that the predicted pulse probabilities ranged between 0.2 and 0.3 for a majority of sites where forward-directivity effects were prevalent); and (ii) the effect of long-period basin-generated surface waves which were significant at numerous locations in the western, central and northern areas of Christchurch (refer to Appendix B). Hence, it is expected (and demonstrated in Figure 5.8) that the large spectral amplification at periods greater than 5 s resulted from both forward-directivity and basin effects (i.e. directivity-basin coupling). In certain cases, (e.g. at the Templeton (TPLC)), basin waves feature in both orthogonal directions of horizontal ground motion, which obviously results in larger geometric mean SA amplitudes at longer periods. It is pertinent to note at this point that the positive bias exhibited by the residuals associated with the broadband S97, AB00 and R10 models at longer periods could also be attributed to the additional amplification caused by basin effects.

Although the B10 GMPE allows the effect of basin depth on surface waves to be considered by means of the parameter $Z_{1.0}$ (refer to Table 5.1), a seismic velocity model for the Canterbury region is presently not available to provide accurate values of $Z_{1.0}$. Hence, in lieu of specific data, the empirical equation of Chiou & Youngs (2008) (CY08) was used to calculate $Z_{1.0}$ from $V_{s,30}$. Previous research (e.g. Bradley (2012b)) has shown that the depth of gravel layers exceeds 500 m in the Canterbury region, which implies that the value of $Z_{1.0}$ is also likely to be greater than 500 m. However, the CY08 equation gives a value of $Z_{1.0}$ = 332 m for site class D conditions (recall that a majority of the strong motion stations in Christchurch belong to this site class category i.e. $V_{s,30}$.= 250 m/s), which results in a notable under-prediction of long-period spectral ordinates, as observed in Figure 5.23a for the

Darfield event. The effect of increasing the $Z_{1.0}$ parameter to more appropriately account for basin effects (in conjunction with directivity effects) is considered in a subsequent section.

In contrast to the broadband models, the SB11 model offers improved predictions for the Christchurch earthquake as highlighted by the reduction in mean residuals in Figure 5.23b between T = 0.6 s and T = 3 s. A qualitative examination of the observed and predicted response spectra (e.g. Figure 5.15b) highlighted the fact that the largest predicted amplification occurs in the vicinity of the predicted pulse period (median of 1.6 s for the Christchurch earthquake using the SB11 equation), and hence very low levels of amplification are predicted (considering T_p as a random variable) at longer periods. This also applies to the amplification obtained using the observed pulse period (which range between 0.5 s and 4.6 s in the Christchurch event). Based on this evidence, and also taking into account the additional amplification of long-period spectral ordinates due to basin effects and significant nonlinear soil response at a number of sites in Christchurch, it is unsurprising that the mean residual remains positively biased for $T \geq 4$ s after applying the SB11 model.

The results of Figure 5.23c indicate that the B10 GMPE significantly under-predicts the directivity amplification of spectral ordinates for the period range 0.7 s ≤ T ≤ 4 s in the M_w6.0 June earthquake. Upon correcting for directivity using the SB11 model, a small reduction in the mean residuals within the same period range is observed. This can likely be attributed to: (i) the significant directivity amplification demonstrated by the ground motions, particularly those recorded within R_{rup} = 10 km of the causative rupture; and (ii) low levels of amplification obtained using the SB11 model, which is a direct result of low pulse probabilities predicted by the S13 equation for a majority of sites where directivity effects were observed (refer to Figure 4.6c in Chapter 4 and discussion therein). As expected, the largest reduction in the mean residuals occurs in the region surrounding the pulse period (i.e. T_p = 1.2 s using the SB11 equation, and observed pulse periods ranging between 0.8 s and 2.2 s). While basin-generated surface waves were observed in several ground motions in this event, their amplitude relative to the main directivity pulse was small (on the order of 20 cm/s). Hence, the effect of these waves on the amplification of spectral ordinates in the aforementioned period range is also likely to be small in general. However, it is speculated that the significant nonlinear response of surficial soils (including liquefaction), particularly at sites located in the eastern suburbs of Christchurch (e.g. HPSC, NBLC, NNBS and PRPC) could have also contributed to the large positive bias exhibited by the mean residuals at

longer periods (i.e. 1 s $\leq T \leq$ 3 s). This is plausible, considering that a notable earthquake (M_w5.3) occurred 80 minutes prior to this event and likely lead to non-zero pore pressures at many sites.

For the M_w5.9 December event, the B10 GMPE generally provides an over-prediction of the observed SA amplitudes with the only exception being an under-prediction in the period range 0.6 $\leq T \leq$ 2 s due to the amplification caused by forward-directivity, as illustrated in Figure 5.23d. It is also evident from the figure that correcting for directivity using the SB11 model results in a reduction of the mean residuals in the above period range. In fact, the model over-predicts the observed spectral amplitudes on average with ε_{mean} ranging between 0.1 and -1. Nonetheless, it is worth noting that a relatively smaller number of ground motions demonstrated evidence of directivity effects in comparison to the other three events, which could possibly be attributed to its smaller magnitude and offshore location of the causative oblique fault.

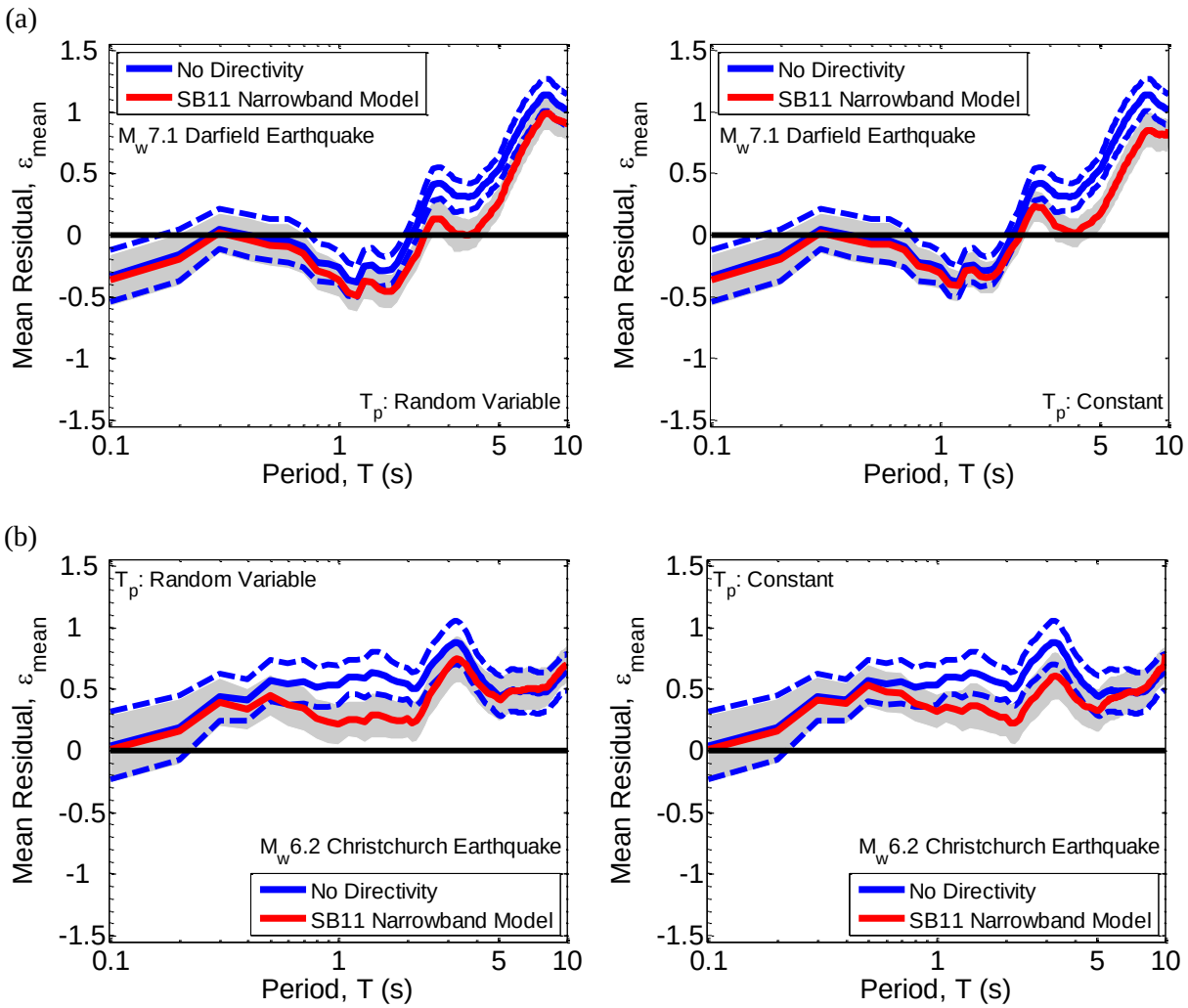

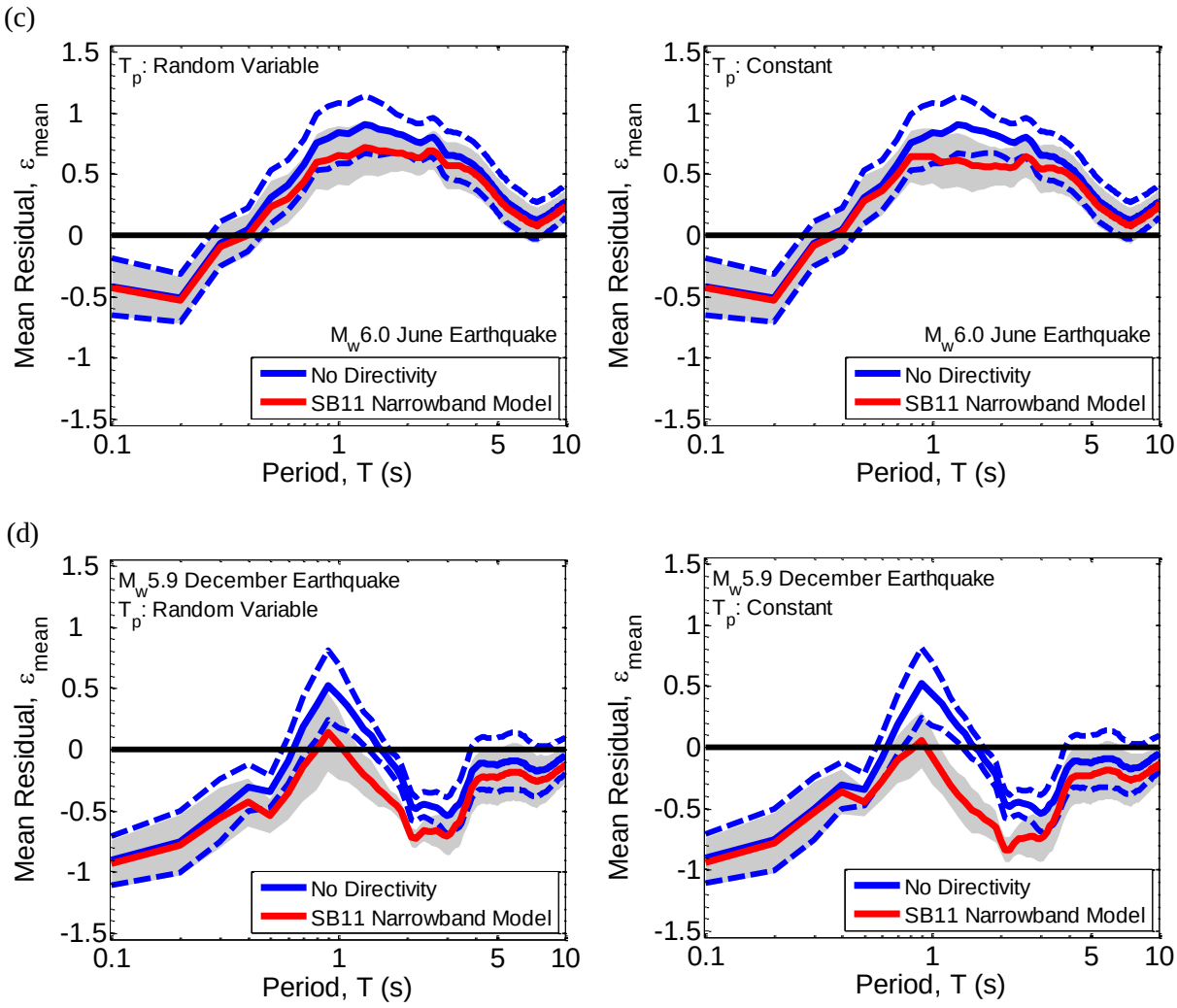

Figure 5.23: Mean residuals associated with the Bradley (2010) GMPE and the Shahi & Baker (2011) narrowband model predictions for (a) 4 September 2010 M_w7.1 Darfield earthquake; (b) 22 February 2011 M_w6.2 Christchurch earthquake; (c) 13 June 2011 M_w6.0 June earthquake; (d) 23 December 2011 M_w5.9 June earthquake. For each event, the model has been applied by treating the pulse period as a random variable and by using the exact value corresponding to the observed directivity pulse Note that the thinner dotted lines and shaded area represent the uncertainty in the mean residual obtained using the GMPE and directivity model, respectively.

5.7.3 Comparison of all models

It is worthwhile to collectively examine the mean residuals corresponding to all directivity models considered in the present study, as illustrated in Figure 5.24 for the Darfield and Christchurch earthquakes. The results of Figure 5.24a indicate that the S97, AB00 and SB11 models provide similar levels of directivity amplification for moderate-to-long period (0.6 s $\leq T \leq$ 3 s) average horizontal SA amplitudes in the Darfield event. However, the fact that S97/AB00 models monotonically increase or decrease spectral amplitudes for periods greater than T = 0.6 s is not consistent with empirical evidence from past earthquakes. The SB11 model is more appropriate because it allows directivity

amplification to be centred around the pulse period, which is consistent with the magnitude scaling of the directivity pulse initially observed by Somerville (2003). It is also clear from Figure 5.24a that the effect of the recently developed R10 model is notable only for longer periods in the Darfield earthquake (T > 4 s) and negligible for the Christchurch earthquake. At periods greater than T = 5 s, the residuals corresponding to each model show significant positive bias ($\varepsilon_{mean} \geq 0.5$) for reasons discussed previously.

The inadequacy of the broadband models for non-strike-slip events is clearly highlighted by the mean residuals associated with the Christchurch earthquake in Figure 5.24b. While the R10 model does not offer improved predictions, the S97 model predicts a deamplification of spectral ordinates for several sites, thereby resulting in slightly larger under-prediction in comparison to the B10 GMPE. Conversely, the SB11 model gives slightly improved predictions particularly in the vicinity of the pulse period (i.e. median T_p = 1.6 s obtained using the SB11 equation)

(a)

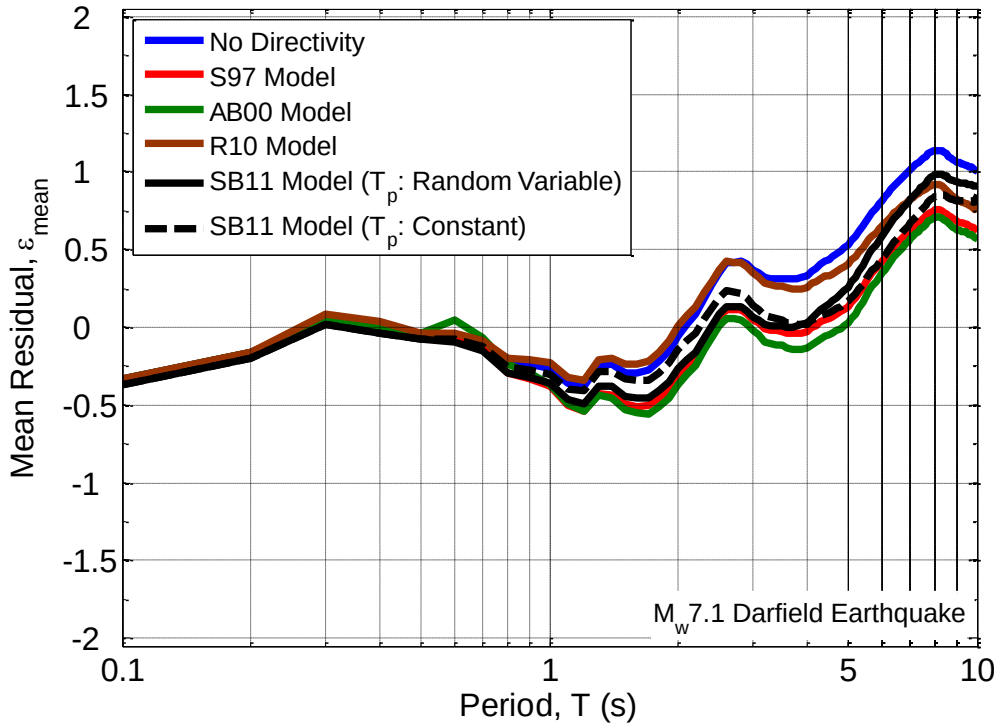

(b)

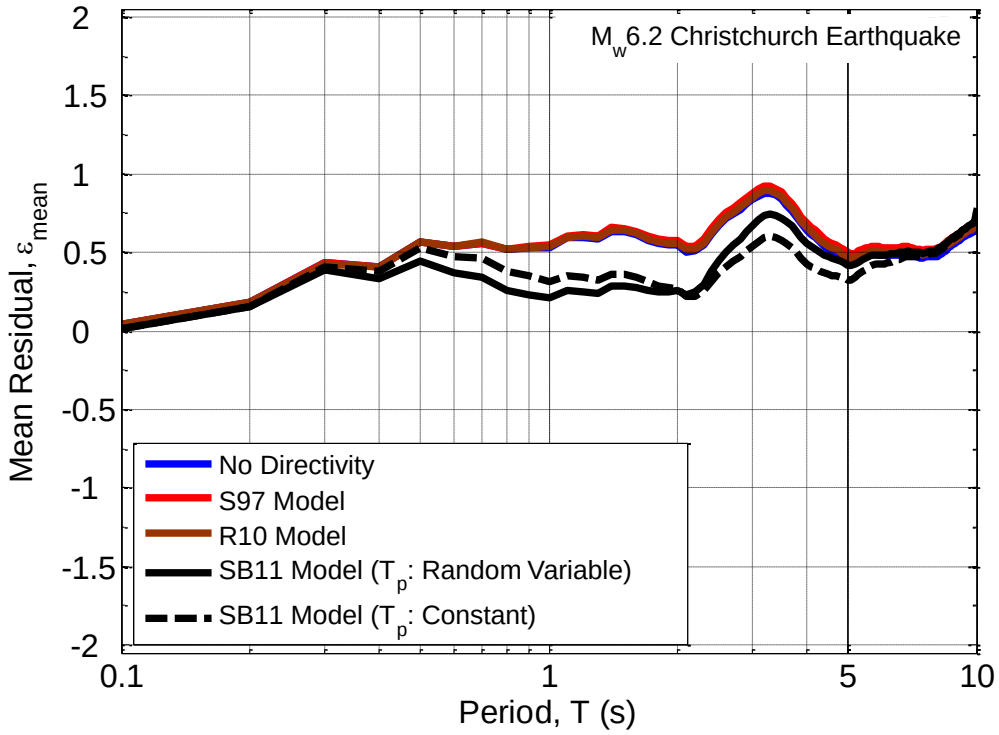

Figure 5.24: Comparison of the mean residuals associated with the Bradley (2010) GMPE with and without directivity modifications using broadband and narrowband model predictions for (a) 4 September 2010 M_w7.1 Darfield earthquake; and (b) 22 February 2011 M_w6.2 Christchurch earthquake.

5.7.4 Direct application of narrowband model

Thus far, the SB11 model has been used to obtain 'blind' predictions of the directivity amplification by treating the pulse period and pulse probability as random variables. Given that observations of forward-directivity from the Canterbury earthquakes were identified and documented in Chapter 3, it is possible to directly apply the SB11 model by setting the pulse probability to 1 and using the period associated with the observed pulse in Equation (5.8). Shahi (2013) also mentions that the occurrence of a particular pulse can be assumed when calculating the directivity-corrected *SA* amplitudes for specific earthquake scenarios. Such an approach is adopted here primarily to illustrate the adequacy of the SB11 model. Figure 5.25 shows the direct application of the SB11 to the ground motion observed at CHHC in the Darfield event. Also shown is the model prediction for the case where uncertainties in pulse occurrence and pulse period are taken into account. It is clear that the model is able to accurately predict the narrowband directivity amplification observed at the site.

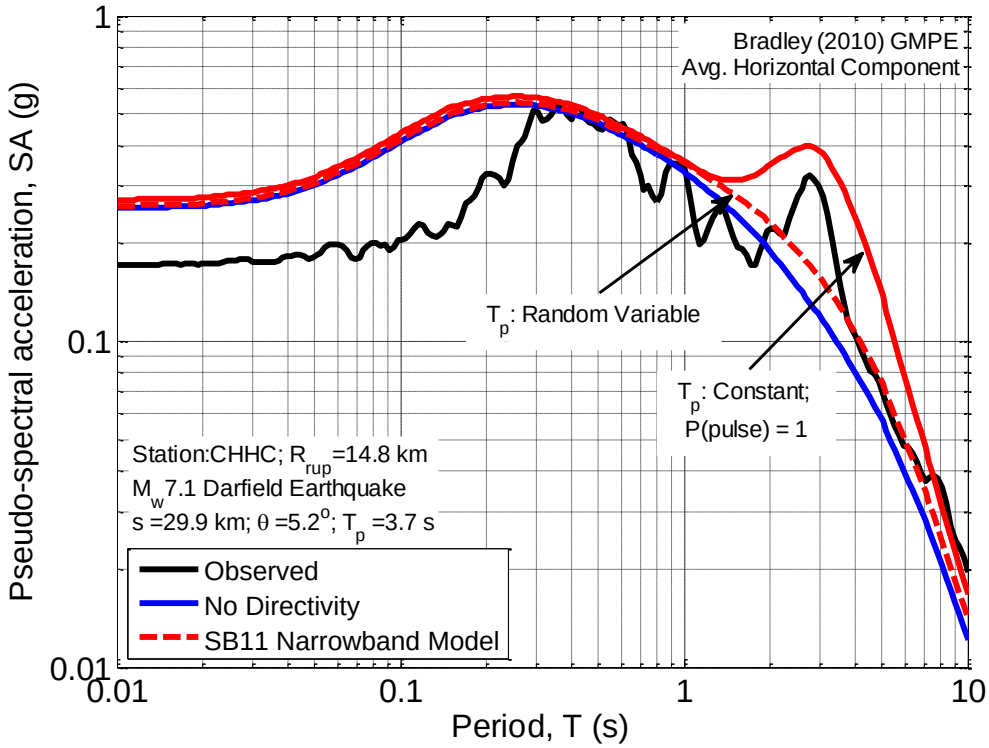

Figure 5.25: Direct application of the Shahi & Baker (2011) narrowband model to the median response spectra predicted by the Bradley (2010) GMPE for the Christchurch Hospital (CHHC) site in the 4 September 2010 M_w7.1 Darfield earthquake. Also shown for comparison is the observed average horizontal response spectra and application of the directivity model considering the pulse period and pulse probability as random variables.

Figure 5.26 provides a comparison of the mean residuals associated with each directivity model for the Darfield and Christchurch earthquakes. As expected, direct application of the SB11 model results in a significant reduction of the mean residuals in relation to those obtained using the B10 GMPE. For example, the model provides an over-prediction of the observed amplification between vibration periods of T = 1 s and T = 6 s in both events. Similar trends were evident in Section 5.6 where a direct comparison of the observed and predicted directivity amplification for the four considered events in the Canterbury earthquakes was carried out. From the point-of-view of predicting directivity amplified response spectral amplitudes for a future earthquake scenario (e.g. in PSHA calculations), it should be appreciated that the amplification predicted by the SB11 model will always occur over a wide range of periods as a result of considering the uncertainty in the expected pulse period and likelihood of pulse occurrence

(a)

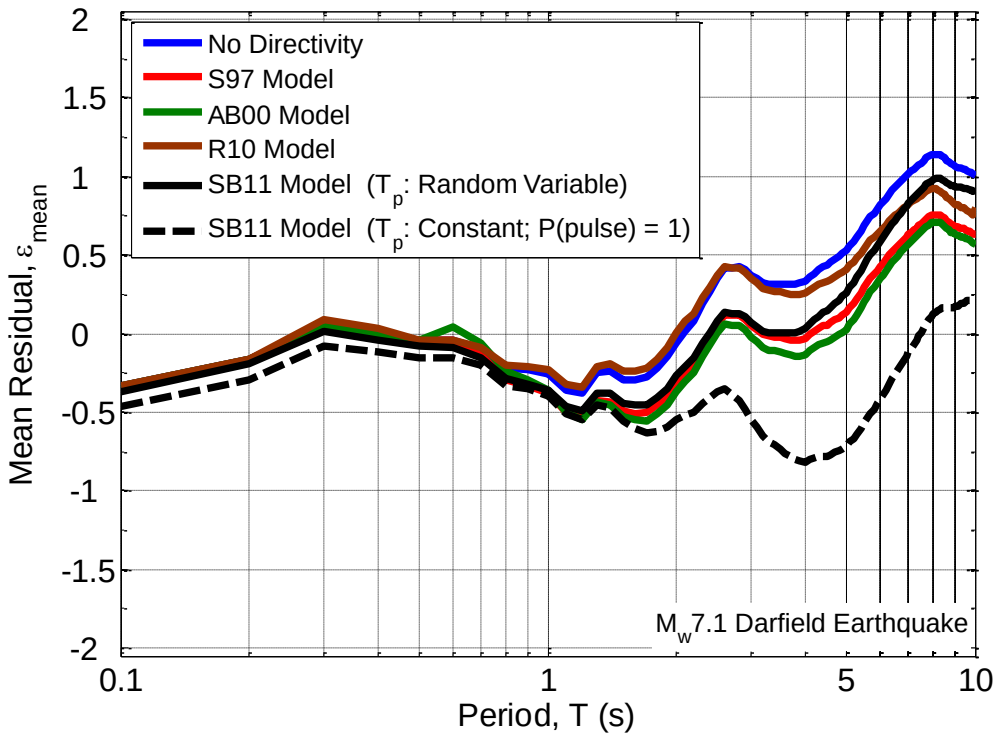

(b)

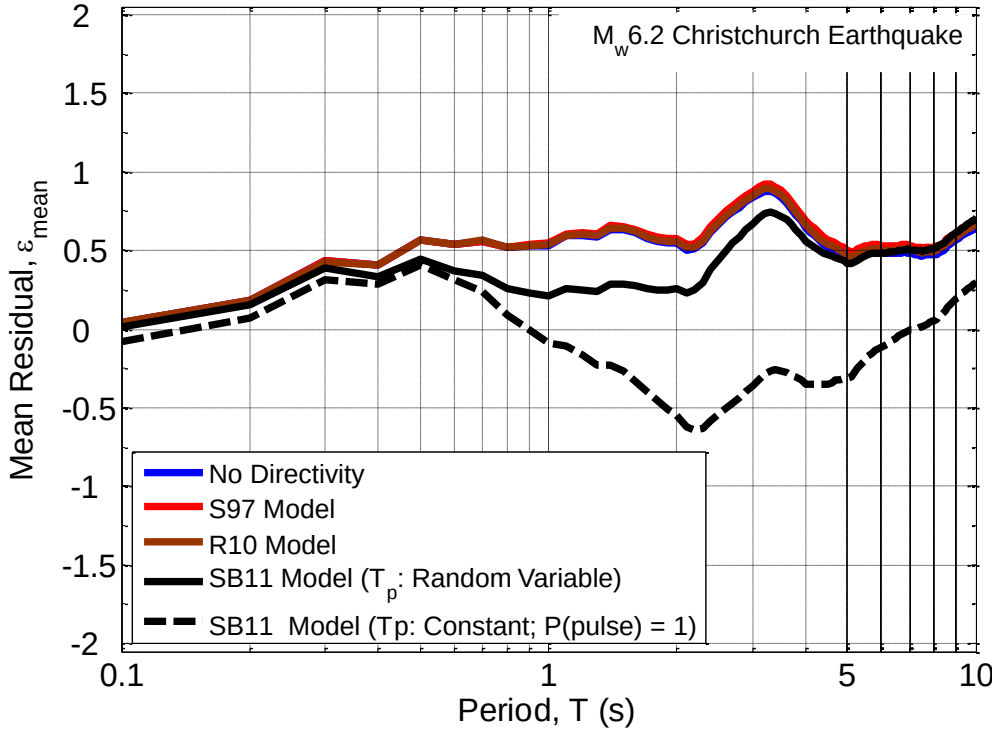

Figure 5.26: Mean residuals obtained upon directly applying the Shahi & Baker (2011) narrowband model for (a) 4 September 2010 M_w7.1 Darfield earthquake; and (b) 22 February 2011 M_w6.2 Christchurch earthquake. Also shown for comparison are the mean residuals associated with the Bradley (2010) GMPE, broadband models and narrowband model considering the pulse period as a random variable.

It should be recalled from Chapter 2 that forward-directivity effects are accounted for in the NZ design code response spectra by the near-fault factor (Standards New Zealand, 2004), which is based on the S97 broadband model. The inadequacy of this factor has been highlighted in previous research (e.g. Bradley, 2012a) and has been further exemplified in this study, albeit in an indirect manner. The results of this section also indicate that changes to the near-fault factor can be achieved by incorporating the more appropriate narrowband models in seismic hazard analyses that form the basis of design response spectra.

5.8 Consideration of basin effects

Although research efforts (e.g. Lee et al., 2013) are currently underway in developing a detailed seismic velocity model for the Canterbury basin, site-specific basin depths required for ground motion prediction were not available at the time of writing. As mentioned previously, an approximate contour map illustrating the basement rock depths in the Canterbury region (Bradley, 2012a; Hicks, 1989) indicates that the depth to gravel layers is greater than 500 m, with the greatest depths to basement rock being on the order of 2 km at several locations. Figure 5.27a effectively highlights the effects of the large basin depth at TPLC (approximately 1 km based on examining the contour map mentioned above) where the arrival of the directivity pulse in the fault-normal velocity time-series is followed by several significant cycles of long-period (approximately 6 seconds) Love waves (on the order of 50-80 cm/s). Although smaller in amplitude (on the order of 30 cm/s), surface waves are also observed in the fault-parallel component. Examination of the response spectra presented in Figure 5.27b shows large amplification of fault-normal SA amplitudes at long periods (note the peak at approximately T = 7 s), which can be attributed to the coupling effect of the directivity pulse and basin-induced Love waves.

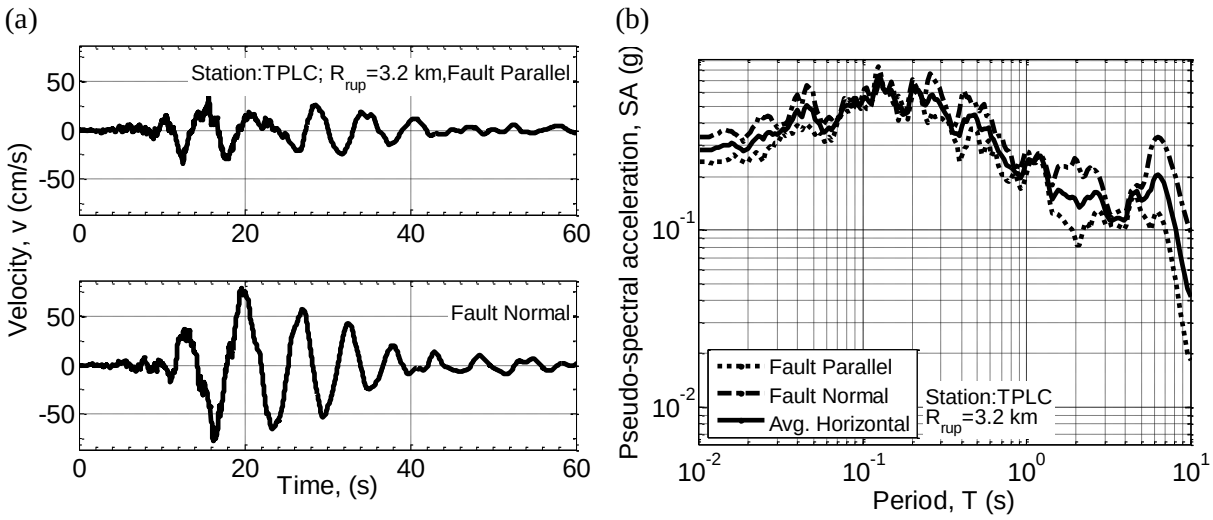

Figure 5.27: Illustration of the significant basin-generated surface waves observed at Templeton (TPLC) during the 4 September 2010 M_w7.1 Darfield earthquake using (a) the velocity time-series; and (b) the acceleration response spectra.

To further visualise the contribution of basin waves to the observed amplification at TPLC in Figure 5.27b, the average horizontal response spectra corresponding to (i) the original (i.e. observed) ground motion; (ii) the first 18 s of the ground motion (i.e. arrival of directivity pulse); (iii) and the residual ground motion obtained after extracting the directivity pulse using the Baker (2007) pulse classification algorithm are plotted in Figure 5.28. It is clear from the figure that the spectral amplitudes of the residual ground motion are very similar to those corresponding to the original ground motion for all vibration periods. Hence, the TPLC example is an excellent illustration of the fact that generally speaking, the effect of forward-directivity on moderate-to-long period spectral ordinates is less pronounced when the initial directivity pulse is followed by several significant cycles of ground motion resulting from basin effects. However, it should also be noted that such significant basin effects due to directivity-basin coupling cannot occur without the occurrence of rupture directivity effects.

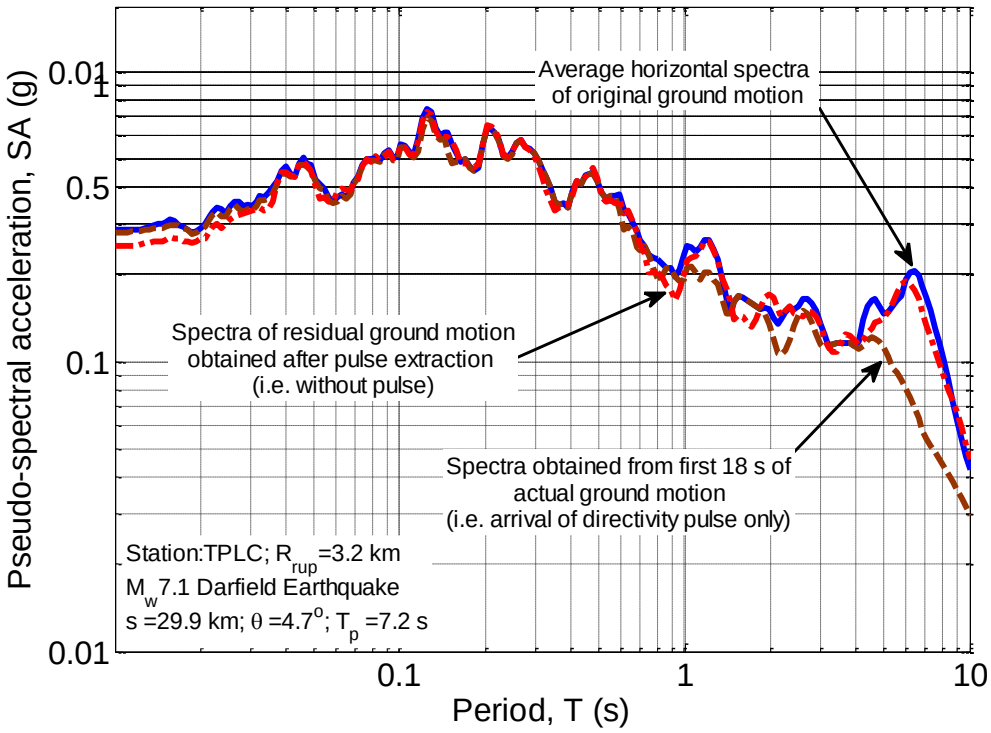

Figure 5.28: Effect of directivity-basin coupling on the observed response spectral amplitudes at Templeton (TPLC) during the 4 September 2010 M_w7.1 Darfield earthquake.

In a previous study, Bradley & Cubrinovski (2011) demonstrated that increasing $Z_{1.0}$, which is used as a proxy for the basin depth in the B10 GMPE, to a more representative value of 1000 m results in significantly improved predictions of long-period SA amplitudes, using the ground motion observed at CHHC during the Christchurch earthquake as an example. Figure 5.29 provides a similar illustration using the TPLC ground motion in the Darfield earthquake. The observed response spectra (for the fault-parallel, fault-normal and average horizontal components) is firstly compared with the median response spectra predicted by the B10 GMPE with and without directivity modifications for the default $Z_{1.0}$ value of 332 m associated with site class D conditions. As discussed previously, the default value fails to provide adequate predictions of the significant amplification of SA caused primarily by basin effects at the site for $T \geq 4$s. Upon increasing $Z_{1.0}$ to 1000 m, there is a marked improvement in the empirical prediction at longer periods, consistent with the observed amplitudes. An obvious drawback of adopting a larger basin depth is the significant increase in predicted spectral amplitudes at short-to-moderate periods, thereby resulting in a notable over-prediction of the observed SA values at these periods. These results, in addition to those in Bradley and Cubrinovski (2011), clearly illustrate the current limitations of basin-effects modelling in empirical GMPEs. This is exacerbated by the fact that such effects are

ultimately highly region-specific (depending on the specific 3D basin geometry of the region in question), and also event-specific (depending on the source location relative to the basin).

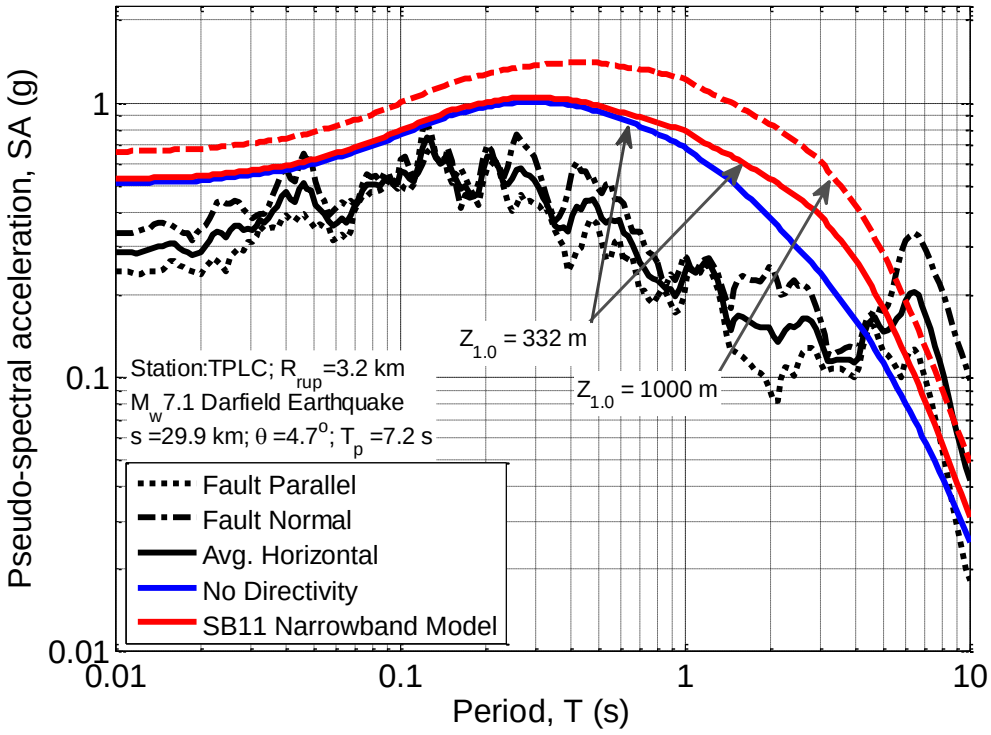

Figure 5.29: Effect of basin depth on the predicted median response spectra obtained using the Bradley (2010) GMPE for the Templeton (TPLC) site in the 4 September 2010 M_w7.1 Darfield earthquake. Note that the predictions are shown with and without directivity modifications predicted by the Shahi & Baker (2011) model for the two basin depths considered. Also shown for comparison is the observed response spectra at the site.

To more systematically quantify the effect of increasing $Z_{1.0}$ on the predicted SA amplitudes, ground motions demonstrating evidence of basin effects (in addition to directivity effects) in the Darfield and Christchurch earthquakes were identified, and the $Z_{1.0}$ values corresponding to their strong motion stations were subsequently updated to 1000 m. Figure 5.30 illustrates the mean residuals associated with the B10 GMPE and SB11 model obtained using the default and updated $Z_{1.0}$ values. In both events, there is a notable reduction of the mean residuals at all vibration periods. For the Darfield earthquake, the previously discussed positive bias exhibited by the residuals using the default $Z_{1.0}$ value at periods greater than T = 4 s is approximately halved. At other periods, using the updated basin depth causes significant over-prediction of the observed SA amplitudes with ε_{mean} less than -0.5 for $0.1 \leq T \leq 2$ s. In the Christchurch earthquake, however, the reduction in mean residuals as a result of including directivity corrections and increased $Z_{1.0}$ values effectively results in unbiased predictions for all vibration periods. It is anticipated that ongoing efforts to characterise the geometric and mechanical properties of the Canterbury basin will provide more accurate site-

specific basin depths, which can ultimately be used to obtain reliable ground motion predictions in seismic hazard assessments of the Canterbury region.

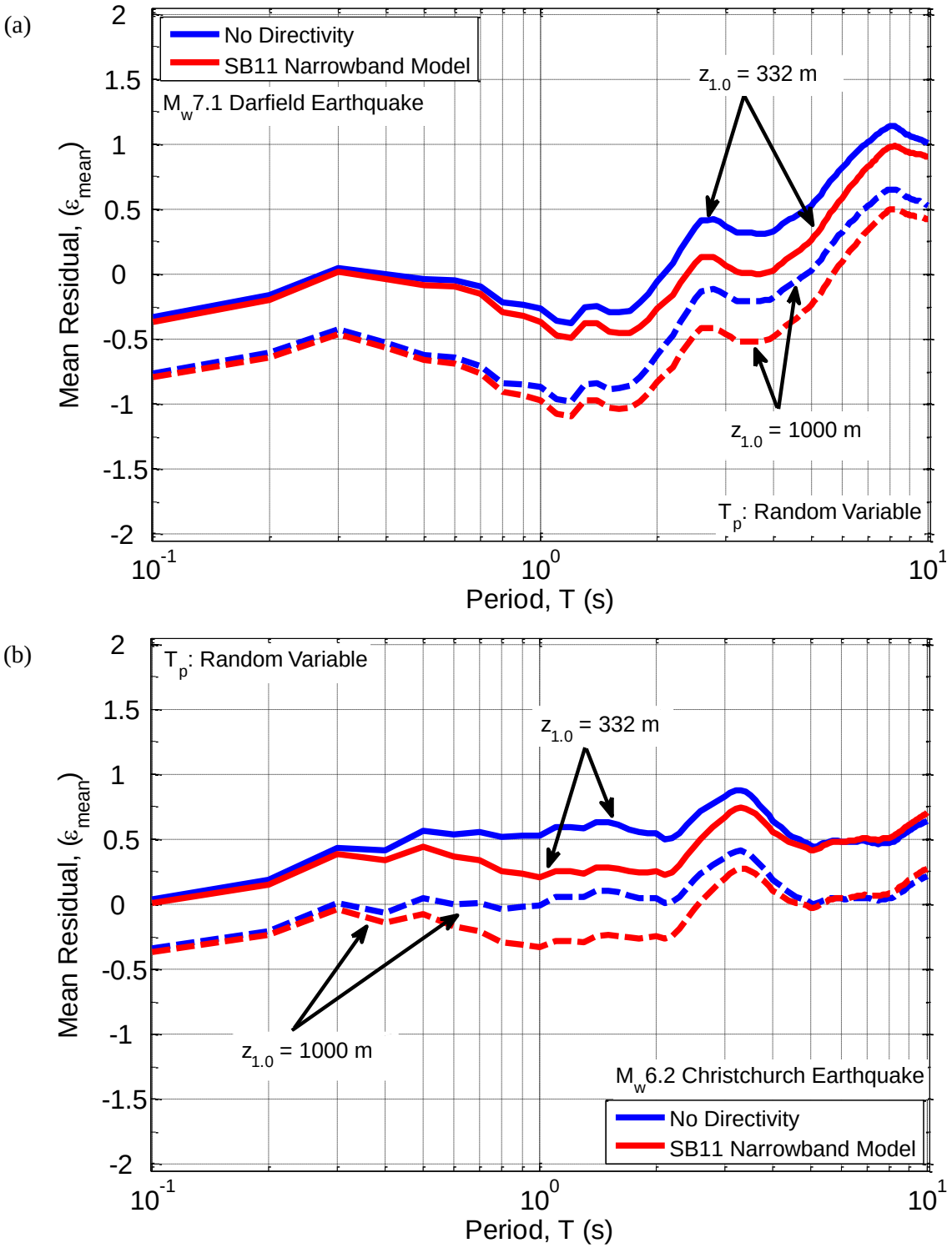

Figure 5.30: Effect of basin depth on the mean residuals obtained using the Bradley (2010) GMPE with and without directivity modifications predicted by the Shahi & Baker (2011) narrowband model for (a) 4 September 2010 M_w7.1 Darfield earthquake; and (b) 22 February 2011 M_w6.2 Christchurch earthquake.

5.9 Effect of directivity and basin-generated surface waves on significant duration of observed ground motions

It is worth recalling that the severity of a ground motion is, in general, a function of its amplitude, frequency content and duration. This chapter has largely focussed on the former two characteristics of ground motion by means of the acceleration response spectrum. The duration of a ground motion can be especially important if its amplitude is significant enough to cause non-linear soil and structural response. For example, Hancock & Bommer (2007) used spectral matching techniques to scale 30 ground motions with different durations to almost identical spectral ordinates. Upon applying these scaled ground motions to model the response of a reinforced concrete structure, it was found that the duration of the motion strongly influences the inelastic response if cumulative damage measures such as absorbed hysteretic energy are utilised. In addition to the large amplitude and long-period ground motion generated by the multiple wave reflections which occur in a three-dimensional basin structure, it is worth noting that these effects also result in longer ground motion duration. For the Darfield event in particular, it was noted previously that basin effects were significant in the western, central and northern areas of Christchurch. This can be attributed to the waveguide effect, which according to Bradley (2012b) occurred due to the directivity of rupture propagation (i.e. along the Greendale fault) and geometry of the Canterbury basin.

The 5-95% significant duration (Ds_{5-95}), represents the duration of strong ground motion corresponding to the arrival of both body and surface waves (Bommer et al., 2009). Figure 5.31 illustrates the observed average horizontal Ds_{5-95} in the Darfield event for stations located within 30 km of the causative rupture. The observed values are colour-coded according to their site classification. Also shown for comparison is the median prediction ($\pm$ one standard deviation) of the Bommer et al. (2009) GMPE. The following points of note are made after examining the figure:

- The observations are under-predicted by the GMPE on average, as indicated by the positive inter-event residual, η = 0.23, which according to Bradley (2012b) can be attributed to the complex rupture process involving multiple fault planes.

- Stations which only demonstrate evidence of forward-directivity effects (i.e. HORC, HVSC, LINC, LPCC and ROLC) have significantly smaller durations than the median prediction, and are similar to the 16th percentile values of the GMPE. This is consistent with the arrival of a majority of the radiated seismic energy in the form of a single velocity pulse.
- Stations which demonstrate both forward-directivity and significant basin effects (northern locations: CACS, PPHS and SMTC; western location: TPLC) have notably longer durations as expected, and are similar to the 84th percentile values of the GMPE.

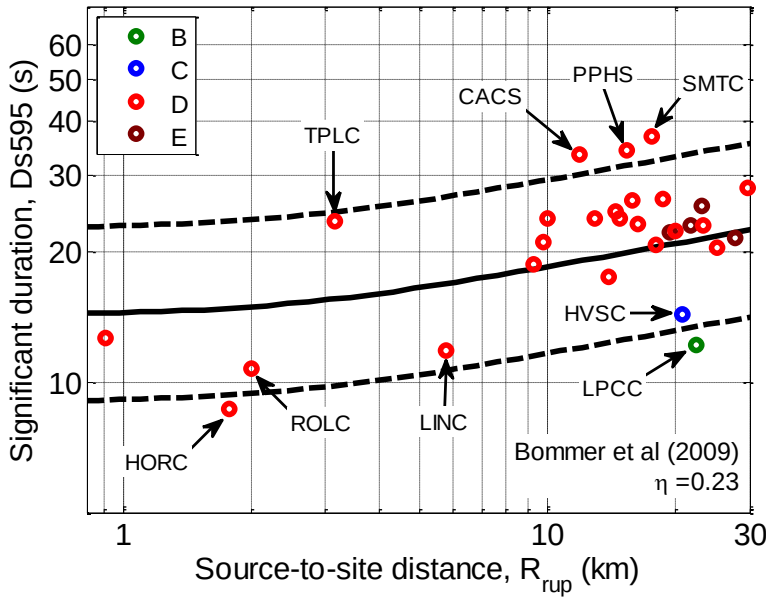

Figure 5.31: Effects of forward-directivity and basin-generated surface waves on the observed 5-95% significant durations (Ds_{5-95}) in the 4 September 2010 M_w7.1 Darfield earthquake. For comparison, the prediction of the Bommer et al. (2009) GMPE is also provided for the average horizontal component (modified from Bradley (2012b)).

5.10 Conclusions

Evidence from earthquakes worldwide has consistently demonstrated that near-fault directivity pulses cause heightened elastic pseudo-spectral acceleration amplitudes at moderate-to-long vibration periods. More importantly, empirical models have been developed by several researchers in the past to predict the directivity amplification of response spectra obtained using conventional ground motion predictions equations. Models which monotonically scale the predicted spectral amplitudes over a wide range of periods are classified as 'broadband', whereas the term 'narrowband' is reserved for models which predict

an amplification of spectral ordinates in the region surrounding the directivity pulse period. This chapter has examined the efficacy of (i) broadband directivity models developed by Somerville et al. (1997) (S97), Abrahamson (2000) (AB00) and Rowshandel (2010) (R10); and (ii) a recently developed narrowband directivity model developed by Shahi & Baker (2011) (SB11) using observations of forward-directivity ground motions from the Canterbury earthquakes. Such an examination has previously not been possible in a New Zealand context, mainly due to a lack of recorded near-fault strong ground motions resulting from moderate-to-large magnitude earthquakes.

A direct comparison of the observed directivity amplification in the Canterbury earthquakes with the S97, R10 and SB11 model predictions was initially carried out. The results of this comparison were effective in highlighting that: (i) the broadband models, which form the basis of the near-fault factor in New Zealand loadings standard, NZS1170.5:2004 (Standards New Zealand, 2004) do not provide accurate estimates of the observed directivity amplification of moderate-to-long period spectral ordinates; and (ii) the SB11 model, which accounts for the narrowband nature of the directivity pulse offers improved predictions, but was higher than the observed amplification.

Residual analysis was utilised as a primary means of determining any bias exhibited by the four models on an event-specific basis. The results of this analysis confirmed the trends observed from the direct comparison above. For example, the non-strike-slip version of the S97 model predicted a deamplification of spectral ordinates for several sites in the 22 February 2011 M_w 6.2 Christchurch earthquake, thereby offering no improvement in prediction compared with the NZ-specific Bradley (2010) (B10) GMPE. Examination of the mean residuals associated with the R10 model revealed its inadequacy in capturing the observed directivity amplification, which was attributed primarily to its inherent broadband nature. Specifically, the predicted amplification for the 4 September 2010 M_w7.1 Darfield earthquake was notable only for periods greater than 4 s. The SB11 narrowband model generally provided similar or improved predictions in relation to its broadband counterparts. Moreover, it was found that the greatest reduction in mean residuals occurred in the vicinity of the pulse period upon applying the model to the four main events in the Canterbury earthquake sequence. The effects of explicitly including the more appropriate narrowband model in seismic hazard analyses for NZ are examined in Chapter 7.

In addition to forward-directivity effects, it was inferred that the positive bias exhibited by all models at longer periods (T > 5 s) was likely due to the additional amplification of *SA* amplitudes caused by basin-generated surface waves and non-linear soil response in the Darfield and Christchurch events. Although the B10 GMPE allows the effect of basin depth on surface waves to be considered by means of the $Z_{1.0}$ parameter, accurate site-specific values could not be obtained due to the absence of a seismic velocity model for the Canterbury region. This required the use of an empirical relationship developed by Chiou & Youngs (2008), which notably under-predicted the observed long-period SA amplitudes. By increasing the $Z_{1.0}$ values of sites where basin effects were observed, significantly improved predictions of spectral amplitudes at longer periods were obtained, and generally in line with the observed amplitudes.

5.11 References

Abrahamson, N. A. (2000). Effects of rupture directivity on probabilistic seismic hazard analysis. In *Proceedings of the 6th International Conference on Seismic Zonation*. Palm Springs, California.

Abrahamson, N. A., & Silva, W. J. (1997). Empirical response spectral attenuation relations for shallow crustal earthquakes. *Seismological Research Letters*, **68**(1):94–127.

Baker, J. W. (2007). Quantitative classification of near-fault ground motions using wavelet analysis. *Bulletin of the Seismological Society of America*, **97**(5):1486–1501. doi:10.1785/0120060255

Beavan, J., Fielding, E., Motagh, M., Samsonov, S., & Donnelly, N. (2011). Fault location and slip distribution of the 22 February 2011 Mw 6.2 Christchurch, New Zealand, Earthquake from geodetic data. *Seismological Research Letters*, **82**(6):789–799. doi:10.1785/gssrl.82.6.789

Beavan, J., Motagh, M., Fielding, E. J., Donnelly, N., & Collett, D. (2012). Fault slip models of the 2010–2011 Canterbury, New Zealand, earthquakes from geodetic data and observations of postseismic ground deformation. *New Zealand Journal of Geology and Geophysics*, **55**(3):207–221. doi:10.1080/00288306.2012.697472

Bommer, J. J., Stafford, P. J., & Alarcon, J. E. (2009). Empirical Equations for the Prediction of the Significant, Bracketed, and Uniform Duration of Earthquake Ground Motion. *Bulletin of the Seismological Society of America*, **99**(6):3217–3233. doi:10.1785/0120080298

Boore, D. M., & Atkinson, G. M. (2008). Ground-Motion Prediction Equations for the Average Horizontal Component of PGA, PGV, and 5%-Damped PSA at Spectral Periods between 0.01 s and 10.0 s. *Earthquake Spectra*, **24**(1):99–138. doi:10.1193/1.2830434

Bradley, B. A. (2012a). *Ground Motion and Seismicity Aspects of the 4 September 2010 and 22 February 2011 Christchurch Earthquakes* (Technical report prepared for the Canterbury Royal Commission) (p. 62). Department of Civil and Natural Resources Engineering, University of Canterbury.

Bradley, B. A. (2012b). Strong ground motion characteristics observed in the 4 September 2010 Darfield, New Zealand earthquake. *Soil Dynamics and Earthquake Engineering*, **42:**32–46. doi:10.1016/j.soildyn.2012.06.004

Bradley, B. A. (2013). A New Zealand-Specific Pseudospectral Acceleration Ground-Motion Prediction Equation for Active Shallow Crustal Earthquakes Based on Foreign Models. *Bulletin of the Seismological Society of America*, **103**(3):1801–1822. doi:10.1785/0120120021

Bradley, B. A., & Cubrinovski, M. (2011). Near-source Strong Ground Motions Observed in the 22 February 2011 Christchurch Earthquake. *Seismological Research Letters*, **82**(6):853–865. doi:10.1785/gssrl.82.6.853

Bradley, B. A. (2010). *NZ-Specific Pseudo-Spectral Acceleration Ground Motion Prediction Equations Based on Foreign Models* (Research Report No. 2010-03) (p. 316). Department of Civil and Natural Resources, University of Canterbury.

Bradley, B. A., & Cubrinovski, M. (2011). Near-Source Strong Ground Motions Observed in the 22 February 2011 Christchurch Earthquake. *Bulletin of the New Zealand Society for Earthquake Engineering*, **44**(4):181–194.

Campbell, K. W. (1981). Near-source attenuation of peak horizontal acceleration. *Bulletin of the Seismological Society of America*, **71**(6):2039–2070.

Chiou, B., Youngs, R., Abrahamson, N., & Addo, K. (2010). Ground-Motion Attenuation Model for Small-To-Moderate Shallow Crustal Earthquakes in California and Its Implications on Regionalization of Ground-Motion Prediction Models. *Earthquake Spectra*, **26**(4):907–926. doi:10.1193/1.3479930

Chiou, B.-J., & Youngs, R. R. (2008). An NGA Model for the Average Horizontal Component of Peak Ground Motion and Response Spectra. *Earthquake Spectra*, **24**(1):173–215. doi:10.1193/1.2894832

Douglas, J. (2004). An investigation of analysis of variance as a tool for exploring regional differences in strong ground motions. *Journal of Seismology*, **8**(4):485–496.

Douglas, J. (2007). On the regional dependence of earthquake response spectra. *ISET Journal of Earthquake Technology*, **44**(1):71–99.

Field, E. H., Jordan, T. H., & Cornell, C. A. (2003). OpenSHA: A developing community-modelling environment for seismic hazard analysis. *Seismological Research Letters*, **74**(4):406–419.

GeoNet. (2011). *GeoNet moment Tensor Solution Database 2011*. Retrieved May 5, 2013, from www.geonet.org.nz/resources/earthquake/

Hancock, J., & Bommer, J. J. (2007). Using spectral matched records to explore the influence of strong-motion duration on inelastic structural response. *Soil Dynamics and Earthquake Engineering*, **27**(4):291–299. doi:10.1016/j.soildyn.2006.09.004

Hicks, S. R. (1989). *Structure of the Canterbury Plains, New Zealand from gravity modelling*. Wellington, New Zealand: GeoPhysics Division, Department of Science and industrial Research.

Holden, C., Beavan, J., Fry, B., Reyners, M., Ristau, J., Van Dissen, R., … Quigley, M. (2011). Preliminary source model of the Mw 7.1 Darfield earthquake from geological, geodetic and seismic data. In *Proceedings of the Ninth Pacific Conference on Earthquake Engineering: Building an Earthquake-Resilient Society* (pp. 14–16). Retrieved from http://www.nzsee.org.nz/db/2011/164.pdf

Howard, J. K., Tracy, C. A., & Burns, R. G. (2005). Comparing Observed and Predicted Directivity in Near-Source Ground Motion. *Earthquake Spectra*, **21**(4):1063–1092. doi:10.1193/1.2044827

Lee, R. L., Bradley, B. A., Pettinga, J. R., Hughes, M., & Graves, R. W. (2013). A 3D seismic velocity model of Canterbury, New Zealand for broadband ground motion simulation. Presented at the 2013 Southern California Earthquake Centre (SCEC) Annual Meeting, Palm Springs, California, USA.

McVerry, G. H., Zhao, J. X., Abrahamson, N. A., & Somerville, P. G. . (2006). New Zealand acceleration response spectrum attenuation relations for crustal and subduction zone earthquakes. *Bulletin of the New Zealand Society for Earthquake Engineering*, **39**(4):1–58.

Power, M., Chiou, B., Abrahamson, N., Bozorgnia, Y., Shantz, T., & Roblee, C. (2008). An Overview of the NGA Project. *Earthquake Spectra*, **24**(1):3–21. doi:10.1193/1.2894833

Rowshandel, B. (2010). Directivity Correction for the Next Generation Attenuation (NGA) Relations. *Earthquake Spectra*, **26**(2):525–559. doi:10.1193/1.3381043

Shahi, S. K. (2013, January). *A probabilistic framework to include the effects of near-fault directivity in seismic hazard assessment*. Stanford University, Stanford.

Shahi, S. K., & Baker, J. W. (2011). An empirically calibrated framework for including the effects of near-fault directivity in probabilistic seismic hazard analysis. *Bulletin of the Seismological Society of America*, **101**(2):742–755. doi:10.1785/0120100090

Smyrou, E., Tasiopoulou, P., Bal, I. E., & Gazetas, G. (2011). Ground Motions versus Geotechnical and Structural Damage in the February 2011 Christchurch Earthquake. *Seismological Research Letters*, **82**(6):882–892. doi:10.1785/gssrl.82.6.882

Somerville, P. G. (2003). Magnitude scaling of the near fault rupture directivity pulse. *Physics of the Earth and Planetary Interiors*, **137**(1-4):201–212. doi:10.1016/S0031-9201(03)00015-3

Somerville, P. G., Smith, N. F., Graves, R. W., & Abrahamson, N. A. (1997). Modification of empirical strong ground motion attenuation relations to include the amplitude and duration effects of rupture directivity. *Seismological Research Letters*, **68**(1):199–222.

Standards New Zealand. (2004). *NZS1170.5:2004, Structural Design Actions, Part 5: Earthquake actions- New Zealand*. Wellington, New Zealand.

Strasser, F. O., Abrahamson, N. A., & Bommer, J. J. (2009). Sigma: Issues, Insights, and Challenges. *Seismological Research Letters*, **80**(1):40–56. doi:10.1785/gssrl.80.1.40

Wood, C. M., Cox, B. R., Wotherspoon, L. M., & Green, R. A. (2011). Dynamic site characterization of Christchurch strong motion stations. *Bulletin of the New Zealand Society for Earthquake Engineering*, **44**(4):195–204.

Youngs, R. R., Chiou, S.-J., Silva, W. J., & Humphrey, J. R. (1997). Strong ground motion attenuation relationships for subduction zone earthquakes. *Seismological Research Letters*, **68**(1):58–73.

Zhao, J. X., Zhang, J., Asano, A., Ohno, Y., Oouchi, T., Takahashi, T., … Fukushima, Y. (2006). Attenuation Relations of Strong Ground Motion in Japan Using Site Classification Based on Predominant Period. *Bulletin of the Seismological Society of America*, **96**(3):898–913. doi:10.1785/0120050122

6 Empirical Characterisation of Directivity Pulse Period and Amplitude

6.1 Overview

The period, amplitude and number of half-cycles associated with the directivity pulse have been identified as key parameters in characterising the performance of structures located in the near-fault region. This evidence has prompted the development of several empirical relationships for the former two parameters in previous studies. In this chapter, observations from the Canterbury earthquakes are used to determine whether existing models provide adequate predictions. Following this, a mixed-effects model is adopted to carry out regression analyses of the pulse periods and amplitudes (represented by the peak ground velocity, PGV) in the most up-to-date NGA (Next Generation Attenuation)-West 2 pulse-type ground motion database. The models developed based on this recent dataset are subsequently used to determine whether improved predictions of both parameters can be obtained.

6.2 Background

Although the response spectrum is used by seismic design guidelines around the world to prescribe design ground motions, its inability to adequately characterise near-fault ground motions has been widely recognised. For example, response spectrum reduction factors utilised to account for nonlinear seismic response are typically computed on the basis of 'ordinary' ground motions and may be notably different for ground motions with significant directivity effects. Nonetheless, the results of numerous studies (refer to Chapter 2) have highlighted that the response of structures subjected to near-fault pulse-like ground motions (which are typically caused by rupture directivity effects) is governed by the amplitude, period and number of half-cycles in the respective velocity time-series. Hence, Somerville (1998) recommended that these parameters should also be provided by seismic design codes in conjunction with the design response spectra.

Based on the above findings, several researchers have focussed their efforts on developing predictive relationships for the amplitude and period of near-fault pulses. Such models have been typically developed to characterise simplified pulse shapes intended to be representative of actual observed velocity pulses. As mentioned in Chapter 2, Alavi & Krawlinker (2000) and Sasani & Bertero (2000), among others, found that these simplified representations of near-fault ground motions are able to sufficiently capture the salient aspects of structural response. Given that the response spectrum amplification due to directivity effects occurs in a small range of periods in the vicinity of the pulse period (refer to Chapter 5 for further details), models which predict the pulse period (T_p) also form an integral part of seismic hazard calculations (e.g. Shahi & Baker, 2011).

The number of half-cycles in a velocity time-series also plays an important role in the inelastic response of structures, and has been quantitatively defined in the past as the number of half-cycle velocity pulses which have an amplitude of at least 50% of the PGV (Bray & Rodriguez-Marek, 2004). Somerville (1998) indicated that the number of half-cycle pulses could be associated with the number of asperities on a fault, which is difficult to predict. This complexity has precluded the development of an empirical relationship for the number of half cycles to date. Nonetheless, based on an examination of 68 forward-directivity ground motions from 17 events, Bray et al. (2009) suggest that the directivity pulse sequence is unlikely to exceed two full cycles of significant ground motion.

6.3 Models developed in previous research

In this section, empirical models developed by researchers in the past to characterise the period and amplitude of the directivity pulse are briefly reviewed. The predictive capabilities of these models are subsequently examined using observations from the Canterbury earthquakes.

6.3.1 Pulse period

Somerville (1998) (S98) developed the first empirical model which related the logarithm of the directivity pulse period to the moment magnitude of the causal rupture. A self-similar relationship [1] was developed between the two parameters using regression analysis involving 15 recorded and 12 simulated ground motions (with moment magnitudes (M_w) ranging between 6.2 and 7.5, and source-to-site distances of 0 to 10 km), as illustrated in Equation (6.1):

$$\log_{10}(T_p) = -3.0 + 0.5M_w \tag{6.1}$$

where T_p is the period corresponding to the largest cycle of the fault-normal velocity waveform (Somerville, 1998). It was also found that the pulse period is strongly related to the rise time, T_R(i.e. duration of slip at a particular point on the fault) and fault dimensions, which generally increase with magnitude. In fact, Somerville et al. (1999) developed a self-similar relationship between rise time and magnitude. This allowed Somerville (1998) to demonstrate that the period of the pulse is approximately twice the rise time of slip on the fault and that the rise time effectively represents a lower bound for the pulse period. The use of a linear relationship between the logarithm of pulse period and moment magnitude was therefore justified by the linear dependence of the logarithm of rise time on magnitude.

Upon developing simple pulse shapes to capture the response of structures subjected to forward-directivity ground motions, it was noted by Alavi & Krawlinker (2000) (AK00) that the pseudo-velocity spectrum of the synthetic pulse demonstrates a peak at a normalised period of T/T_p = 1, where T_p represents the duration of a complete velocity cycle. As a result, they decided to define the pulse period such that the peak of the pseudo-velocity spectrum

[1] According to Somerville et al. (1999), constraining the relationship between pulse period and moment magnitude to be self-similar implies that both parameters are allowed to grow in proportion to the fault dimensions.

associated with synthetic pulse and recorded ground motion occurred at approximately the same vibration period. The dataset initially compiled by Somerville (1998) was used to develop an empirical relationship for the pulse period as shown in Equation (6.2):

$$\log_{10}(T_p) = -1.76 + 0.31M_w \tag{6.2}$$

Mavroeidis & Papageorgiou (2003) (MP03) followed a similar approach to Alavi & Krawlinker (2000) to define the pulse periods of the directivity ground motions in their adopted empirical database (36 motions with earthquake magnitudes ranging between $5.56 \leq M_w \leq 7.6$). In doing so, they developed a self-similar scaling relationship for the pulse period as illustrated in Equation (6.3):

$$\log_{10}(T_p) = -2.9 + 0.5M_w \tag{6.3}$$

The models discussed thus far do not make any provision to account for the uncertainty associated with the predictions of pulse period. Moreover, they do not examine the effects of local site response on the incoming directivity pulse. In an effort to address both issues, Bray & Rodriguez-Marek (2004) (BR04) decided to develop improved relationships using a significantly larger database of 54 forward-directivity ground motions resulting from crustal earthquakes in active tectonic regions, with magnitudes ranging between $6.1 \leq M_w \leq 7.6$ and source-to-site distances less than 20 km. While the aforementioned models had been developed using least-squares regression, Bray & Rodriguez-Marek (2004) used the random effects model as presented in Abrahamson & Youngs (1992) to develop relationships between the pulse period and magnitude. In essence, this allows the standard error to be partitioned into an inter-event term and intra-event term. More importantly, the random effects model ensures that the predictions from the regression equation are not heavily influenced by events with larger number of recordings (Bray & Rodriguez-Marek, 2004). Regression analyses were performed to develop empirical equations for the pulse period using the entire dataset as well as separate subsets containing rock and soil motions. In each case, the relationship has the functional form displayed in Equation (6.4):

$$\ln(T_p)_{ij} = a + bM_w + \eta_i + \varepsilon_{ij} \tag{6.4}$$

where $(T_p)_{ij}$ is the pulse period corresponding to the j^{th} recording from the i^{th} event; a and b are the model coefficients obtained from regression analysis; η_i represents the inter-event error (with a standard deviation, τ); and ε_{ij} represents the intra-event error (with a standard deviation, σ). It should be noted that the pulse periods in this case were defined as either: (i)

the zero crossing time; or (ii) the time at which the velocity is equal to 10% of the peak velocity of the pulse (Bray & Rodriguez-Marek, 2004). Table 6.1 summarises the relevant parameters associated with the three models. Upon comparing these models, it was found that the soil relation predicts larger pulse periods in comparison to the rock relation and was attributed to the effects of local site response. However, the difference in predictions of both model reduces for larger magnitudes.

Table 6.1: Parameters associated with the empirical models for the directivity pulse period developed by Bray & Rodriguez-Marek (2004).

Dataset	a	b	σ	τ	σ_{total}
All	-6.37	1.03	0.38	0.42	0.57
Rock	-8.60	1.32	0.27	0.30	0.40
Soil	-5.60	0.93	0.33	0.47	0.58

Bray et al. (2009) (BR09) updated the pulse period models summarised in Table 6.1 by adding 14 forward-directivity ground motions which resulted from 4 earthquakes (1986 Palm Spring, 2002 Denali, 2003 Bam and 2004 Parkfield earthquakes) to the aforementioned empirical database used by Bray & Rodriguez-Marek (2004). The model parameters are displayed in Table 6.2:

Table 6.2: Parameters associated with the empirical models for the directivity pulse period developed by Bray et al. (2009).

Dataset	a	b	σ	τ	σ_{total}
All	-4.42	0.75	0.41	0.38	0.56
Rock	-6.37	1.00	0.46	0.29	0.55
Soil	-3.71	0.65	0.35	0.37	0.51

More recently, Shahi & Baker (2011) compiled a set of 179 pulse-like ground motions from the NGA database (Chiou et al., 2008) using the pulse classification algorithm of Baker (2007). While previous models have focussed primarily on directivity pulses observed in the fault-normal direction, Shahi & Baker (2011) included ground motions which were classified as pulse-like at arbitrary orientations. Based on an examination of the velocity time-series of such ground motions, they concluded that directivity effects were the primary cause for a majority of the observed pulses The least-squares regression model of the pulse period is illustrated in Equation (6.5):

$$\ln(T_p) = -5.73 + 0.99M_w;\ \sigma = 0.56 \tag{6.5}$$

where T_p is the period corresponding to the maximum Fourier amplitude of the pulse extracted from the original velocity time-series using the pulse classification algorithm; and σ represents the total standard deviation. The residuals (i.e. difference between observations

and predictions) from this model fitted a normal distribution and hence, it can be assumed that the pulse period is log-normally distributed (or $\ln(T_p)$ is log-normally distributed) (Shahi & Baker, 2011). Despite including a significantly larger number of observations than Bray & Rodriguez-Marek (2004) and Bray et al. (2009), it is interesting to note that the standard deviation associated with Shahi & Baker (2011) model essentially remains unchanged.

Figure 6.1 provides an illustration of the median predictions associated with the pulse period models described above. Based on the above statement that the standard deviation associated with all models are similar, the 16th and 84th percentile predictions are shown for only the more recent SB11 model. In the case of the BR04 and BR09 models, the predictions shown correspond to the relationship developed for soil sites.

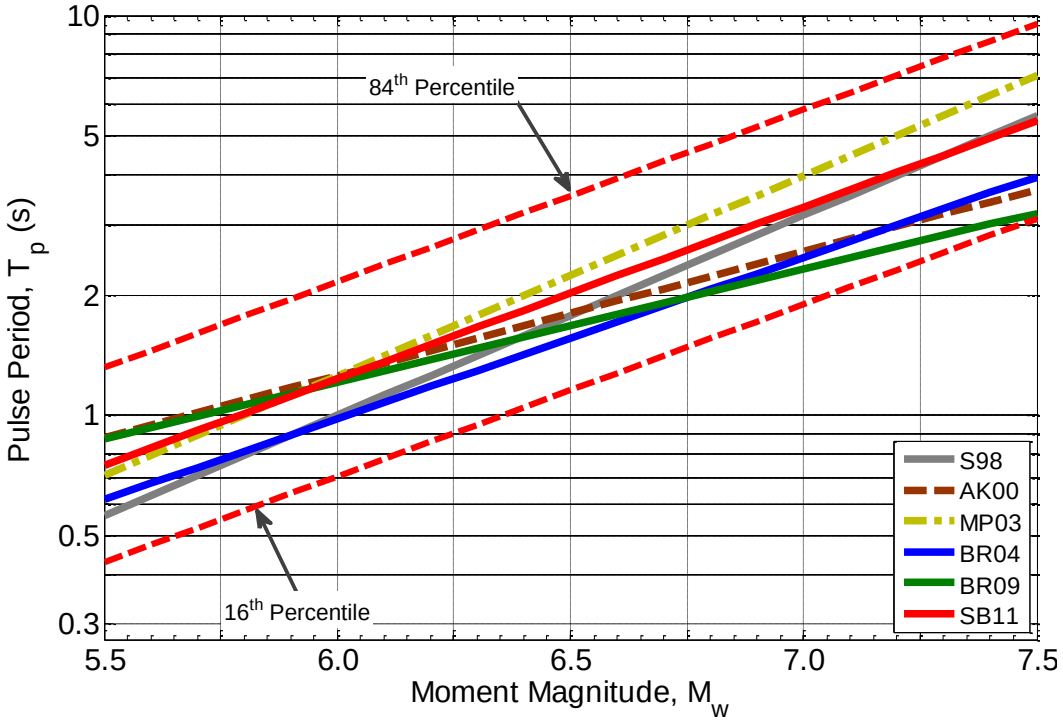

Figure 6.1: Comparison of the magnitude scaling demonstrated by several existing empirical relationships for the pulse period considered in the present study.

6.3.2 Pulse amplitude

The amplitude of the directivity pulse can be adequately characterised by the peak ground velocity (PGV) (Alavi & Krawinkler, 2000; Mavroeidis & Papageorgiou, 2003). Conventional ground motion prediction equations for PGV (e.g. Chiou & Youngs, 2008) are typically developed using large empirical databases containing both near- and far-fault ground motions, and can hence be applied over a wide range of source-to-site distances and earthquake magnitudes. In addition, the functional forms of these GMPEs are usually complex and related to various source, path and site parameters, as discussed previously in Chapter 5. Empirical models for PGV developed specifically for the near-fault region have been proposed by several researchers in the past, including Somerville (1998), Alavi & Krawlinker (2000), Bray & Rodriguez-Marek (2004) and Bray et al. (2009). In each case, the pulse amplitude is related to the moment magnitude (M_w) and source-to-site (R_{rup}) distance using simplified functional forms. Furthermore, the datasets used in the development of the respective pulse period models were also adopted in developing the PGV relationships by the above researchers.

Equations (6.6) and (6.7) provide the empirical models developed by Somerville (1998) and Alavi & Krawlinker (2000), respectively. In order to avoid unexpectedly large predictions of PGV at short distances, both models include a distance cut-off of 3 km (i.e. R_{rup} = max[R_{rup}, 3 km]).

$$\log_{10}(PGV) = -1.0 + 0.5M_w - 0.5\log_{10}(R_{rup}) \tag{6.6}$$

$$\log_{10}(PGV) = -2.22 + 0.69M_w - 0.58\log_{10}(R_{rup}) \tag{6.7}$$

Similar to their pulse period counterparts, the models above do not account for the uncertainty in model predictions nor do they consider the effects of local site response. This prompted Bray & Rodriguez-Marek (2004) and Bray et al. (2009) to develop PGV equations using their updated dataset, as well as subsets containing rock and soil motions only. In both studies, the functional form of the models is as follows:

$$\ln(PGV)_{ij} = a + bM_w + c\ln({R_{rup}}^2 + d^2) + \eta_i + \varepsilon_{ij} \tag{6.8}$$

where $(PGV)_{ij}$ is the peak ground velocity (in units of cm/s) of the j^{th} recording from the i^{th} event; a, b, c and d are the model coefficients obtained from regression analysis; η_i represents the normalised inter-event residual, common to all j recordings from the i^{th} event

(with a standard deviation, τ); and ε_{ij} represents the normalised intra-event error (with a standard deviation, σ). It should be noted that the inter-event and intra-event residual terms follow a normal distribution, which implies that $\ln(PGV)$ is also normally distributed (or PGV is log-normally distributed). Also, the models are applicable for $R_{rup} \leq 20$ km. The relevant parameters associated with models developed in both studies are summarised in Table 6.3 and Table 6.4, respectively. In both studies, it was found that the soil relation predicts larger pulse periods in comparison to the rock relation and was attributed to the effects of local site response. Furthermore, this difference became more pronounced at longer source-to-site distances.

Table 6.3: Parameters associated with the empirical models for the directivity pulse amplitude developed by Bray & Rodriguez-Marek (2004).

Dataset	a	b	c	d	σ	τ	σ_{total}
All	4.51	0.34	-0.57	7.00	0.45	0.20	0.49
Rock*	4.46	0.34	-0.58	7.00	-	-	0.39
Soil	4.58	0.34	-0.58	7.00	0.42	0.25	0.49

Table 6.4: Parameters associated with the empirical models for the directivity pulse amplitude developed by Bray et al. (2009).

Dataset	a	b	c	d	σ	τ	σ_{total}
All	2.05	0.55	-0.39	5.00	0.37	0.24	0.44
Rock*	1.86	0.55	-0.39	5.00	-	-	0.40
Soil	2.11	0.55	-0.39	5.00	0.33	0.30	0.44

* The rock relationship could not be constrained using the random effects model, so maximum likelihood was used to obtain model parameters (Bray & Rodriguez-Marek, 2004; Bray et al., 2009).

Figure 6.2 illustrates the magnitude and source-to-site distance dependence of the existing empirical models for pulse amplitude described above. In particular, it is noted that: (i) the predictions are shown for a M_w6.5 and M_w7.0 strike-slip event; (ii) the predictions of the BR04 and BR09 model correspond to the soil relationship; and (iii) the CY08 model predictions are shown for site class D conditions (i.e. average shear wave velocity, $V_{s,30}$ = 250 m/s).

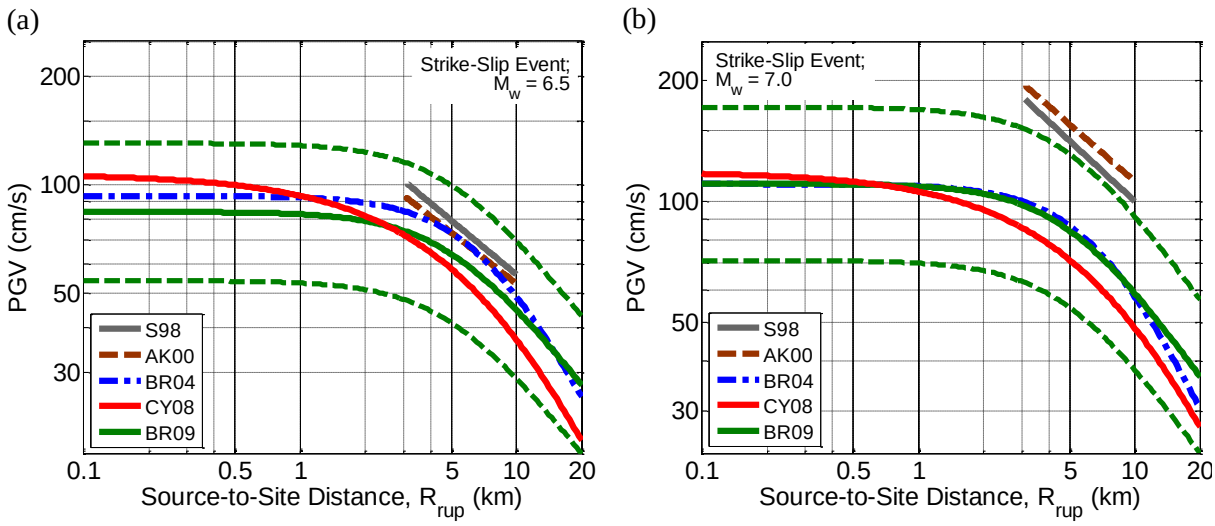

Figure 6.2: Comparison of the source-to-site dependence of several existing empirical relationships for the pulse amplitude (defined by the peak ground velocity) for a strike-slip event with (a) M_w6.5; and (b) M_w7.0.

6.3.3 Assessment of existing model predictions using observations from the Canterbury earthquakes

Observations of forward-directivity effects in the Canterbury earthquakes, as identified in Chapter 3, provide an excellent means of assessing the efficacy of the models for the directivity pulse period (T_p) and amplitude (PGV) examined in the previous two sections. It should be noted that the period and amplitude associated with the observed pulses of ground motions in the Canterbury earthquakes were characterised using the pulse classification algorithm of Baker (2007). Therefore, strictly speaking, comparisons of the observed pulse periods with the models developed by Somerville (1998) (S98), Alavi & Krawlinker (2000) (AK00), Mavroeidis & Papageorgiou (2003) (MP03), Bray & Rodriguez-Marek (2004) (BR04) and Bray et al. (2009) (BR09) are not appropriate because of the differences in adopted pulse period definitions. However, it is expected that the pulse periods obtained using the algorithm of Baker (2007) will be similar to those provided by the approaches of the above researchers. For example, Baker (2007) demonstrated that the period associated with the maximum Fourier amplitude of the pulse extracted using wavelet analysis (used herein and also by Shahi & Baker (2011) (SB11)) is generally in good agreement with the period corresponding to the peak pseudo-spectral velocity (used in the AK00 and MP03 models). Similar trends were also identified by Bray & Rodriguez-Marek (2004) who used the dominant period of the velocity time-series in characterising directivity pulses for their model. Hence, it was deemed suitable to carry out the aforementioned comparisons between pulse period observations and predictions provided by the existing empirical models.

Figure 6.3 provides a comparison between the pulse periods observed in the 4 September 2010 M_w 7.1 Darfield, 22 February 2011 M_w 6.2 Christchurch, 13 June 2011 M_w6.0 and 23 December 2011 M_w5.9 earthquakes, and the median predictions of existing empirical models. It is evident from the figure that there is significant variability in the observed pulse periods for a given event and hence, the median pulse periods from each event are indicated using solid lines. For purposes of clarity, models which do not account for the uncertainty in the predictions (S98, AK00 and MP03) are shown separately in Figure 6.3a, while Figure 6.4b illustrates the median predictions associated with the BR04[2], BR09[2] and SB11 models. Although the latter models account for the uncertainty in the predicted pulse periods, the 16th and 84th percentiles associated with only the more recent SB11 model are shown for clarity. It should be noted that certain relaxations have been made regarding the applicability of the above models. For example, while the BR04 model was developed using ground motions from earthquakes with M_w > 6.0, the model predictions have been extrapolated to lower magnitudes herein to allow a comparison with observed data.

The median observed pulse periods corresponding to the four events from the Canterbury earthquake sequence are 5.6 s (M_w 7.1 Darfield earthquake), 3.1 s (M_w 6.2 Christchurch earthquake), 1.7 s (M_w 6.0 June earthquake) and 1.3 s (M_w 5.9 December earthquake). Figure 6.3a indicates that the MP03 model consistently provides larger predictions compared to the S98 and AK00 models for magnitudes greater than 6.0, which is likely the result of including a larger empirical database in model development. It can be observed that all models under-predict the median observed pulse periods from the four events. In particular, observations from the Christchurch earthquake demonstrate the largest deviation from self-similar scaling with a median pulse period notably larger than the similar magnitude June and December events.

The results of Figure 6.4b highlight that the BR04 model consistently predicts smaller pulse periods for all magnitudes when compared to the BR09 and SB11 models. Because of the smaller magnitude scaling term of the BR09 model (refer to Table 6.2), it can be observed that larger pulse periods are predicted for magnitudes approximately less than M_w = 6.5 in relation to the BR04 relationship. The SB11 model provides larger estimates of the pulse periods for M_w > 6.0 compared to the BR04 and BR09 models. Moreover, this difference

[2] Given that a majority of the strong motion stations in the Canterbury region are classified as Site Class D or E, only the predictions associated with the soil relation are considered.

appears to increase with magnitude. Upon further examining Figure 6.3b, the following observations are deduced:

- The BR04 model significantly under-predicts the observed pulse periods from all four events, similar to the S98 model.
- The BR09 predictions are in reasonable agreement with the observed median pulse periods from the June and December events, similar to the AK00 and MP03 models. On the other hand, predictions for the Darfield and Christchurch events are inadequate.
- Similar to the AK00 and MP03 models, the SB11 model provides satisfactory estimates of the observed median pulse periods in the June and December events but a marked under-prediction can be seen for the Darfield and Christchurch events. Nonetheless, predictions for the two latter events are larger in relation to the BR04 and BR09 models due to the improved nature of the model.
- While the aforementioned variability in the observed data is relatively well-captured by the 16^{th} and 84^{th} percentile values of the SB11 model predictions for the June and December events, the same does not apply to the Darfield and Christchurch events, where several observations exceed the 84^{th} percentile values.

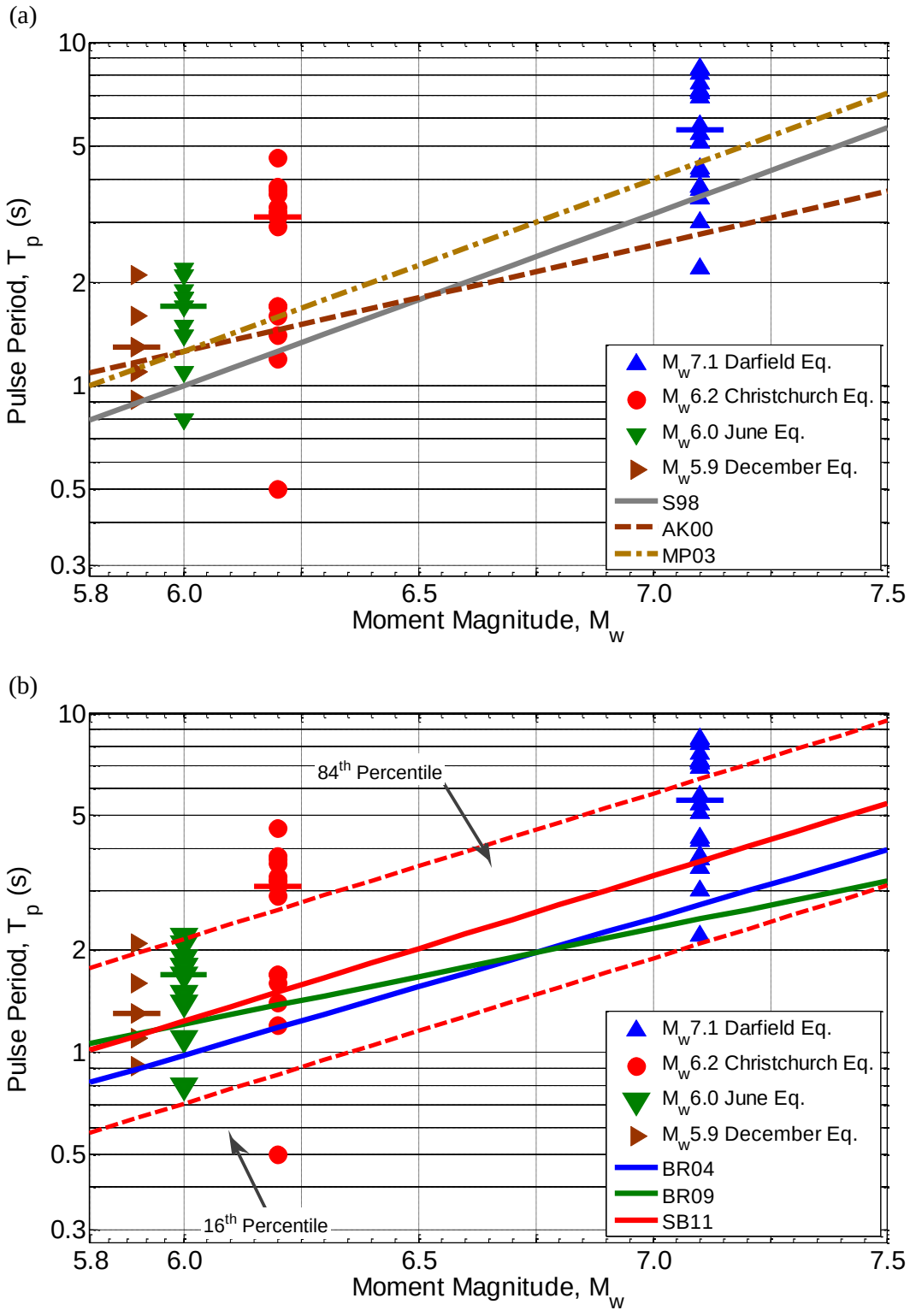

Figure 6.3: Comparison of the observed directivity pulse periods in the Canterbury earthquakes with the median predictions of existing empirical models developed by (a) Somerville (1998), Alavi & Krawlinker (2000) and Mavroeidis & Papageorgiou (2003); and (b) Bray & Rodriguez-Marek (2004) (soil model), Bray et al. (2009) (soil model) and Shahi & Baker (2011). Also shown in Panel (b) are the 16th and 84th percentiles of the pulse periods predicted by the Shahi & Baker (2011) model.

As mentioned previously, the pulse period is well-defined by the lognormal distribution, similar to other ground motion intensity measures (e.g. pseudo-spectral acceleration). Hence, it is useful to compare the cumulative distribution function (CDF) of existing empirical relationships with the empirical CDFs corresponding to the observed pulse periods in the Canterbury earthquakes. Since the S98, AK00 and MP03 models do not provide a lognormal standard deviation, they cannot be included in the comparisons which follow. Figure 6.4 illustrates the lognormal cumulative distributions associated with the BR04, BR09 and SB11 models, compared to the empirical distributions of the observations from the four considered events. The median pulse periods from each event are also annotated in the figure. For a large magnitude earthquake (i.e. M_w7.1 Darfield earthquake), it can be seen that the SB11 model provides appreciably larger pulse periods relative to the other models, as mentioned previously. The difference between the models becomes less significant for smaller magnitude events. It is also evident from the CDFs in Figure 6.4a and Figure 6.4b that the observed median pulse periods in the Darfield (T_p = 5.6 s) and Christchurch (T_p = 3.1 s) events are significantly greater than those predicted by the BR04 (2.7 s and 1.2s, respectively), BR09 (2.5 s and 1.4 s) and SB11 (3.7 s and 1.4 s) models. The inadequacy of the predictions is further highlighted by the fact that the empirical distributions from both events are notably further 'right' than the prediction CDFs. In contrast, the empirical distributions corresponding to the June and December events are reasonably consistent with the CDFs associated with the BR09 and SB11 models. For example, the median observed values of 1.7 s and 1.3 s in these events, respectively, are similar to the median predictions of 1.2 s and 1.1 s for both models. However, the BR04 model under-predicts the observed values with median predictions of 0.98 s and 0.89 s, respectively.

Empirical evidence from previous earthquakes (e.g. the 1989 M_w7.0 Loma Prieta earthquake) has consistently shown that pulse periods from forward-directivity ground motions recorded on soil sites are higher in relation to rock sites due to the effects of local site response. This has been further illustrated analytically by Rodriguez-Marek & Bray (2006) using seismic site response analyses involving forward-directivity ground motions. For example, it was illustrated that site response can increase the pulse period of forward-directivity motions if the input pulse period (i.e. period of pulse introduced at the base of the soil column in the site response analysis) is shorter than the degraded site period (defined as $T = 4H/V_s'$, where H is the soil depth and V_s' is the effective shear wave velocity of the soil

deposit). The above argument is based on the view that strain-degradation occurs during that cycle to the peak response.

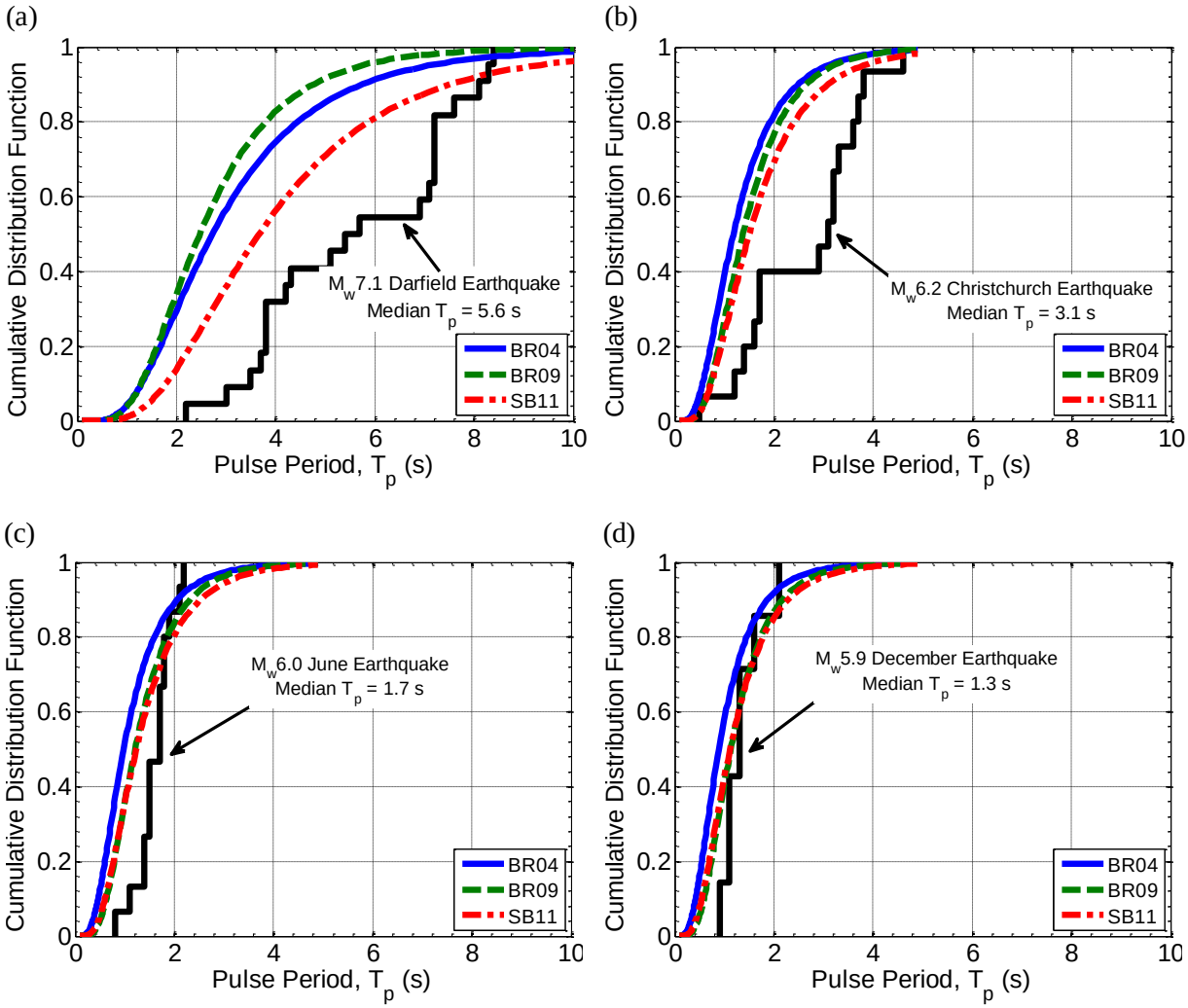

Figure 6.4: Comparison of the cumulative distribution functions associated with the observed directivity pulse periods from (a) 4 September 2010 M_w7.1 Darfield earthquake; (b) 22 February 2011 M_w6.2 Christchurch earthquake; (c) 13 June 2011 M_w6.0 earthquake; and (d) 23 December 2011 M_w5.9 earthquake with existing empirical models developed by Bray & Rodriguez-Marek (2004), Bray et al. (2009) and Shahi & Baker (2011).

Based on the above evidence, the observed pulse period elongation in the Darfield and Christchurch earthquakes could be attributed to: (i) nonlinear soil response; and (ii) the influence of the Canterbury basin. The effects of nonlinear site response on the recorded ground motions were more pronounced in the Christchurch earthquake, particularly in the CBD (CBGS, CCCC, CHHC, D06C and REHS) and eastern suburbs (PRPC) due to the severity of the recorded ground shaking (with horizontal geometric mean peak ground accelerations ranging between 0.43 g and 0.63 g (Bradley & Cubrinovski, 2011)), thereby resulting in pulse periods (3.2 s $\leq T_p \leq$ 4.6 s) which exceed the 84th percentile prediction of the more recent SB11 model (refer to Figure 6.3). As mentioned previously in Chapter 5, the

directivity of the rupture propagation in conjunction with basin geometry acted together to create a waveguide effect in the Darfield earthquake (Bradley, 2012).This provides a likely explanation for the long pulse periods (5.7 s $\leq T_p \leq$ 7.2 s) observed at strong motion stations located in the western (CACS, LINC, ROLC, SMTC and TPLC), central (CBGS) and northern (SMTC) areas of Christchurch. In an effort to determine whether improved predictions can be obtained, a subsequent section is dedicated to the development of pulse period models incorporating the most up-to-date NGA-West2 (Ancheta et al., 2013) database of pulse-like ground motions.

Further insight into the effects of site response on the directivity pulse period can be gained by examining paired ground motions from the same event at rock and soil sites situated within close proximity to each other (Bray & Rodriguez-Marek, 2004) - there is only one such pair of strong motion stations in the Canterbury region, located south-east of the Christchurch CBD in Lyttelton (refer to Figure 3.3 in Chapter 3). The LPCC station, which is located on engineering bedrock (site class B) is within 1 km of the LPOC site, located near the edge of the Port Hills outcrop (site class C). Figure 6.5 illustrates the velocity time-series and pseudo-velocity response spectra observed at both stations in the M_w6.2 Christchurch earthquake. In each case, it should be noted that the ground motion corresponds to the orientation in which the principal directivity pulse was observed (refer to Chapter 3 for further details). The influence of the site conditions is clearly visible in the velocity time-series observed at both stations in Figure 6.5a. For example, it can be seen that the LPOC ground motion has a larger peak ground velocity and longer duration, inferred as a result of nonlinear response of surficial soils at the site (Bradley & Cubrinovski, 2011). The pulse period, which corresponds to the peak value of pseudo-spectral velocity (only for the purposes of the present discussion), is significantly longer at the soil site (T_p = 1.7 s) in comparison to the rock site (T_p = 0.2 s) as a result. As Bray & Rodriguez-Marek (2004) note, differences in pulse periods observed at rock and soil sites can lead to different design considerations, especially when dealing with near-fault ground motions.

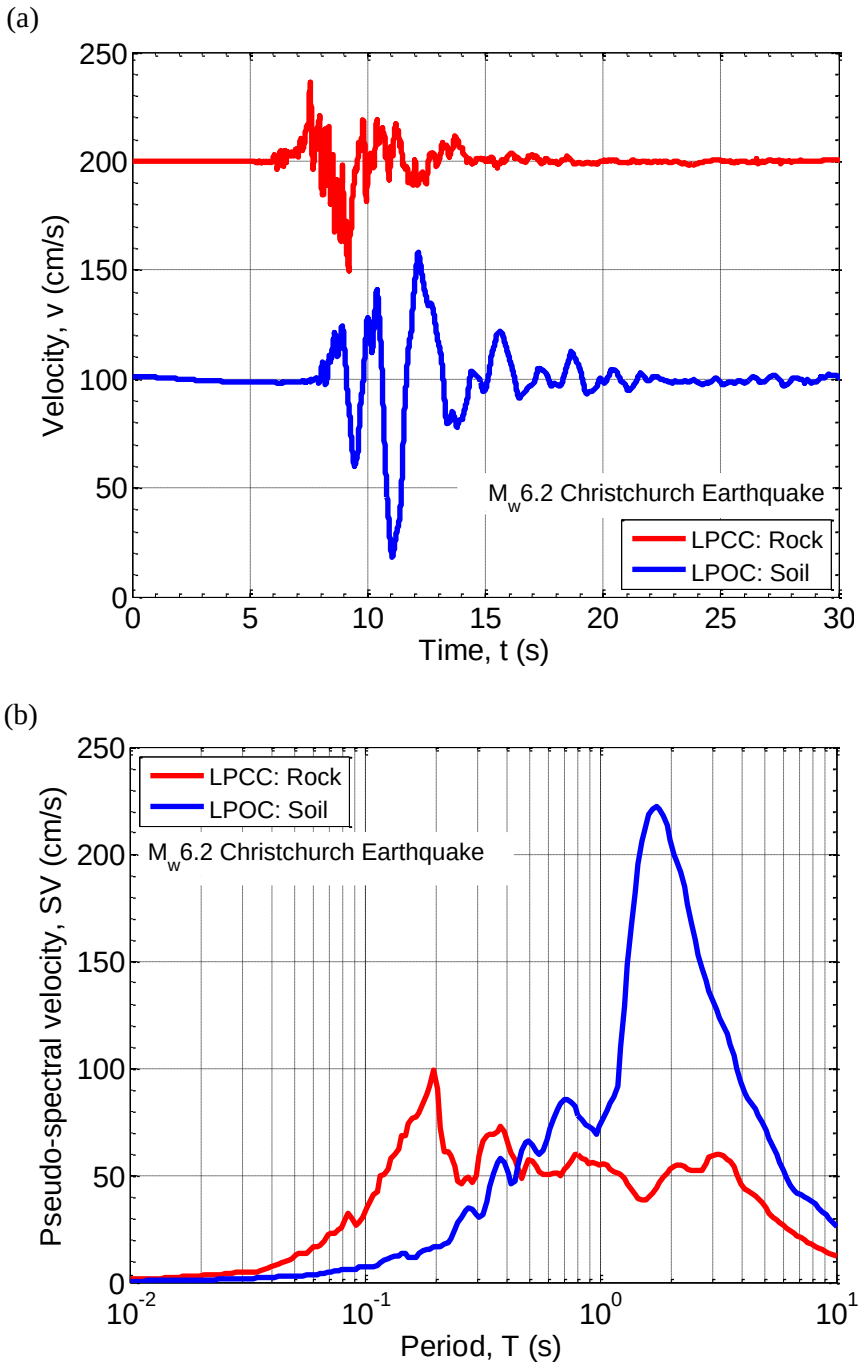

Figure 6.5: Illustration of the effects of local site response on the directivity pulse period by means of: (a) the velocity time-series (note the two records do not have the same absolute time); and (b) pseudo-velocity response spectra observed at two paired stations in Lyttelton (LPCC (rock) and LPOC (soil)) during the 22 February 2011 M_w6.2 Christchurch earthquake.

Figure 6.6 illustrates the peak velocities of the observed directivity pulses in the Canterbury earthquakes. For comparison, median predictions of the existing empirical models developed for the near-fault region are shown as a function of source-to-site distance. In addition, the predictions associated with a 'conventional' GMPE developed by Chiou & Youngs (2008)[3] (CY08) using a large database of near-fault and far-fault ground motions are also illustrated. It should also be noted that predictions associated with site class D ($V_{s,30}$ = 250 cm/s) are shown for the latter model on the basis that a majority of the observations correspond to the same site class. The 16th and 84th percentiles of only the more recent BR09 model are shown for the purposes of clarity. Based on the previous description of the models considered, it is known that the S98 and AK00 models are applicable for $R_{rup} \leq 10$ km, whereas the BR04[4] and BR09[4] models are applicable for $R_{rup} \leq 20$ km. In order to carry out comparisons with the observed data, predictions from these models have been extrapolated to larger distances.

Before comparing the amplitudes of the observed directivity pulses in the Canterbury earthquakes with empirical predictions, it is useful to examine the magnitude scaling of the models discussed previously. It is evident from Figure 6.6 that the variation of PGV with magnitude is stronger for the S98 and AK00 models in relation to its successors. Bray & Rodriguez-Marek (2004) have previously highlighted that the variation cannot be attributed to the inclusion of simulated ground motions in the database used by Somerville (1998) and Alavi & Krawlinker (2000). This can be explained by the fact that the PGVs of recorded ground motions increase more quickly than simulated ground motions (Somerville, 1998). A likely explanation for the differences in magnitude scaling, as highlighted by Bray & Rodriguez-Marek (2004), is the inclusion of a larger database in the development of the BR04 and BR09 models providing more constraint in the regression analyses.

[3] The Chiou & Youngs (2008) GMPE predicts the orientation-independent ground motion measure known as GMRotI50, where 'GM' represents the horizontal geometric mean; 'Rot' indicates that rotations over all non-redundant angles are used; and 50 represents the median value (Boore, 2006). Considering that the observed peak ground velocities from the Canterbury earthquakes represent the maximum values over all non-redundant orientations, the predictions from the above GMPE were multiplied by a ratio of 1.25 prescribed by Beyer & Bommer (2006) to obtain the MaxD ground motion measure. The latter represents the maximum value over all orientations.

[4] Given that a majority of the strong motion stations in the Canterbury region are classified as Site Class D or E, only the predictions associated with the soil relation are considered.

A large majority of the observed directivity pulse amplitudes in M_w 7.1 Darfield earthquake are at distances greater than 10 km, as shown in Figure 6.6a. In contrast, the observed PGVs in the M_w6.2 Christchurch, M_w6.0 June and M_w5.9 December earthquakes in Figure 6.6b-Figure 6.6d lie between distances of 1 km and 10 km. The results of Figure 6.7 indicate that the BR04, CY08 and BR09 models are able to accurately predict the observed peak velocities between source-to-site distances of 1 km and 10 km in general. Similar trends are also observed with respect to the S98 models, but only for the three moderate magnitude earthquakes. The AK00 model, on the other hand, appears to provide a notable under-prediction, particularly for the Christchurch and June events. For reasons identified previously, the S98 and AK00 models significantly over-predict the observed peak velocities between $3 \leq R_{rup} \leq 20$ km for the Darfield event. At distances greater than 10 km, the BR04, CY08 and BR09 models predict larger attenuation of the pulse amplitude, thereby resulting in an under-prediction of the observed PGV values which becomes significant for $R_{rup} \geq 15$ km. For example, it is evident from Figure 6.6a that the peak velocities corresponding to several sites located at $R_{rup} \geq 10$ km are very similar to the 84th percentile values of the BR09 model. The lack of empirical data in the databases adopted for the development of the BR04 and BR09 models at distances greater than 10km is a likely reason for the faster attenuation of PGV predicted by the models. Similar to the pulse period, the larger observed PGVs at greater source-to-site distances could possibly be due to the influence of local site response.

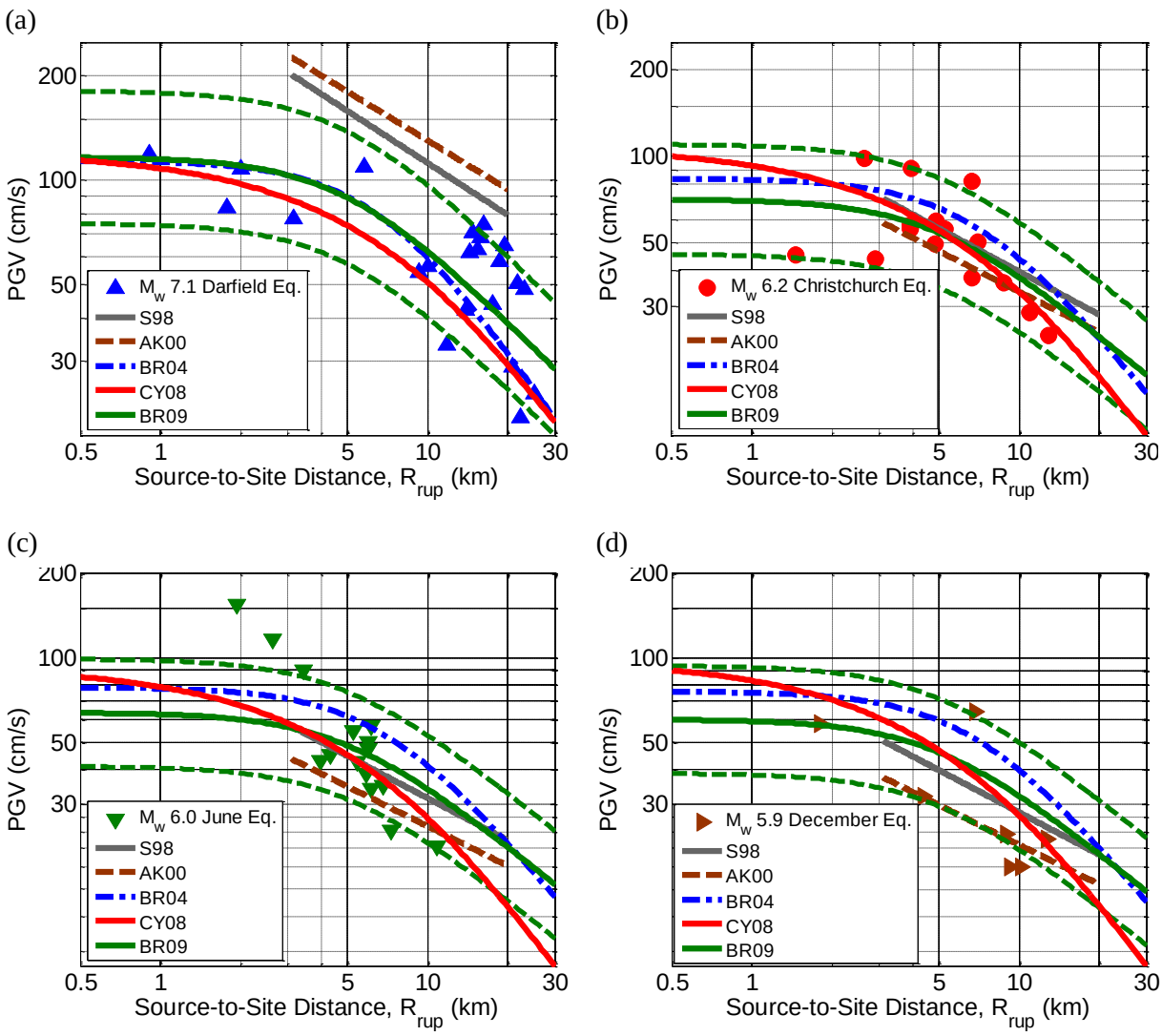

Figure 6.6: Comparison of the observed values of PGV in forward-directivity ground motions from: (a) 4 September 2010 M_w7.1 Darfield earthquake; (b) 22 February 2011 M_w6.2 Christchurch earthquake; (c) 13 June 2011 M_w6.0 earthquake; and (d) 23 December 2011 M_w5.9 earthquake with the median predictions from existing empirical models developed by Somerville (1998), Alavi & Krawlinker (2000), Bray & Rodriguez-Marek (2004) (soil model), Chiou & Youngs (2008) (site class D prediction) and Bray et al. (2009) (soil model). Note that the PGVs are plotted as a function of source-to-site distance. Also shown in the four plots are the 16th and 84th percentiles of the PGVs predicted by the Bray et al. (2009) model.

In addition to the qualitative comparison carried out between observed and predicted PGVs in Figure 6.6, it is useful to examine the residuals as a function of predictor variables used by the empirical models considered herein. Figure 6.7 illustrates the observed normalised intra-event residuals (ε_{ij}) for PGV from the Canterbury earthquakes with the BR04, BR09 and CY08 models, as a function of source-to-site distance. To illustrate the key trends, the mean residual and its 98% confidence interval are also plotted (shown by solid and dashed lines respectively) in the figure using non-parametric regression (Ruppert et al., 1995; Wasserman, 2006). The results of Figure 6.7 indicate that there is negligible bias in the intra-event residuals for $R_{rup} \leq 10$ km. Although the mean residual appears to be positively biased

for larger distances in the case of the BR04 and CY08 models, it is evident that the confidence interval generally includes zero, thereby implying that the models are, on average, unbiased with respect to all source-to-site distances. However, the previous qualitative comparisons clearly indicated that the predictions for the Darfield earthquake at larger distances are inadequate. An updated model is developed in Section 6.4 for the pulse amplitude based on the previously mentioned NGA-West2 strong motion database, particularly to determine whether improved predictions at larger source-to-site distances can be obtained.

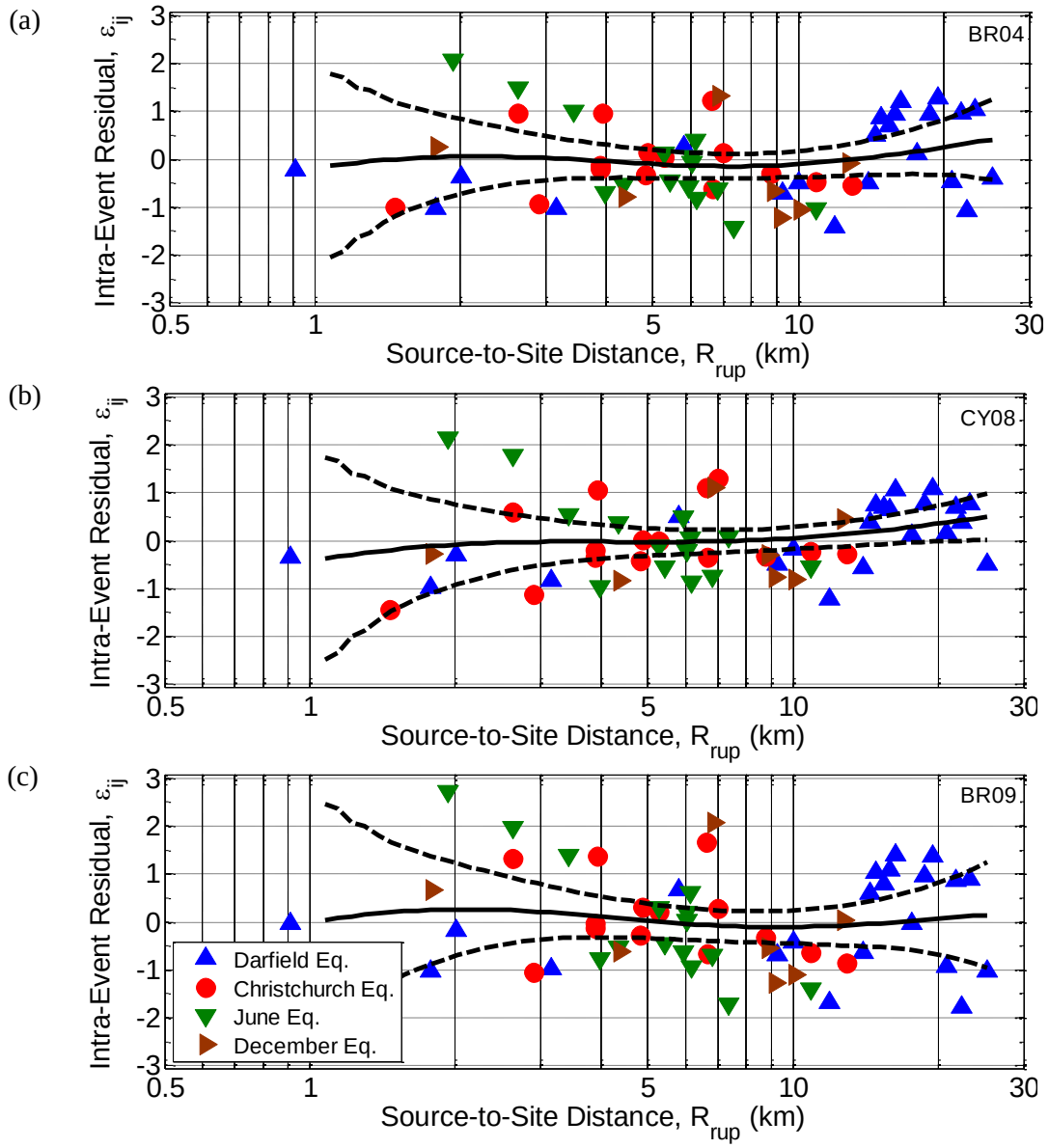

Figure 6.7: Intra-event residuals of *PGV* associated with forward-directivity ground motions in the Canterbury earthquakes as a function of source-to-site distance using existing empirical models: (a) Bray & Rodriguez-Marek (2004); (b) Chiou & Youngs (2008); and (c) Bray et al. (2009).

The normalised inter-event term (η_i), which can be viewed as an average bias of the predicted PGVs relative to those observed, are illustrated in Figure 6.8 using the BR04, CY08 and BR09 models as function of the magnitude associated with the four considered events. It is evident that the BR09 model has either marginal or no bias for the Darfield (M_w = 7.1), Christchurch (M_w = 6.2) and June (M_w = 6.0) events, but provides a notable over-prediction (η_i = -0.69) for the December (M_w = 5.9) event. On the other hand, the BR04 model is negatively biased for the smaller events and positively biased for the Darfield event. While the CY08 model provides similar predictions to the BR09 model for the Christchurch and December earthquakes, it can be observed from Figure 6.8 that it exhibits significant positive bias for the Darfield and June events. Hence, these comparisons clearly indicate that the BR09 predictions are superior on a consistent basis.

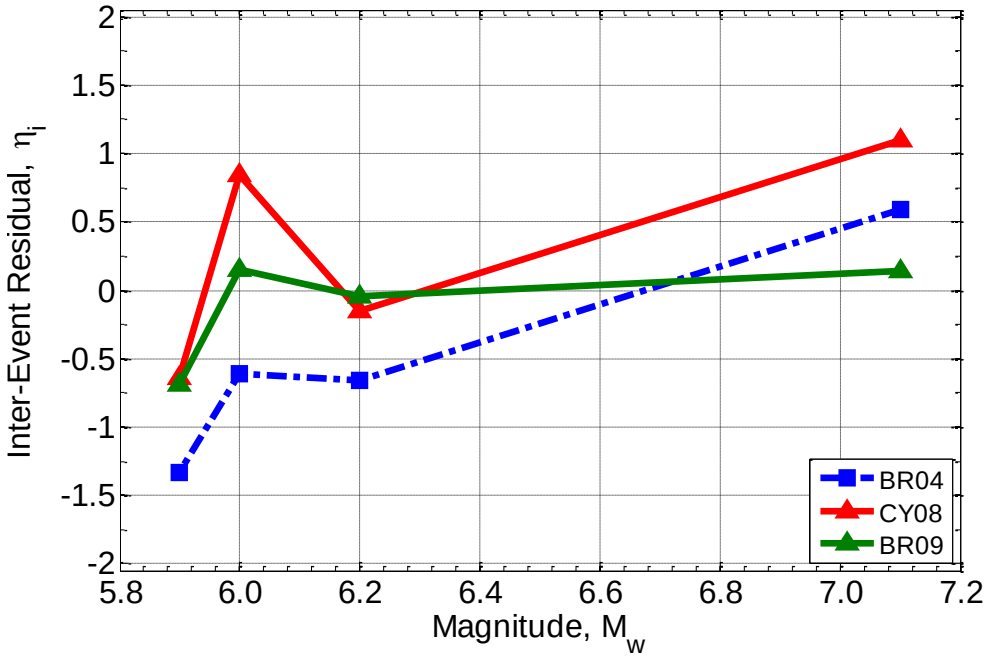

Figure 6.8: Inter-event residuals of PGV associated with the 4 September 2010 M_w7.1 Darfield; 22 February 2011 M_w6.2 Christchurch; 13 June 2011 M_w6.0; and 23 December 2011 M_w5.9 earthquakes using existing empirical models developed by Bray & Rodriguez-Marek (2004), Chiou & Youngs (2008) and Bray et al. (2009).

6.4 Models developed in the present study

As part of the NGA-West2 project, Shahi (2013) identified a total of 244 ground motions which featured an early-arriving pulse using an automated pulse classification algorithm (see Chapter 3). These 244 ground motions include those from the M_w7.1 Darfield and M_w6.2 Christchurch earthquakes. The motions were manually filtered to identify 145

motions which were likely caused by directivity effects (further details on this filtering process can be found in Shahi (2013)), with the remaining 99 inferred to be due to other salient ground motion phenomena. Figure 6.9 illustrates the magnitude-distance distribution of the 244 pulse-like and 145 directivity ground motions in the NGA-West2 (NGAW2 hereafter) database. It is noted that the ground motions in the database result from earthquake magnitudes ranging between $5.0 \leq M_w < 8.0$ with source-to-site distances of $0.1 \leq R_{rup} < 100$ km. In addition, the period and amplitude of the pulses have also been characterised by Shahi (2013) using the algorithm mentioned above. Because the models considered previously in this chapter are based on a deprecated NGA ground motion database, in the ensuing sections, models for the pulse period and amplitude are developed using the updated NGA-West2 dataset to determine whether improved predictions can be obtained (i.e. with respect to observations from the Canterbury earthquakes).

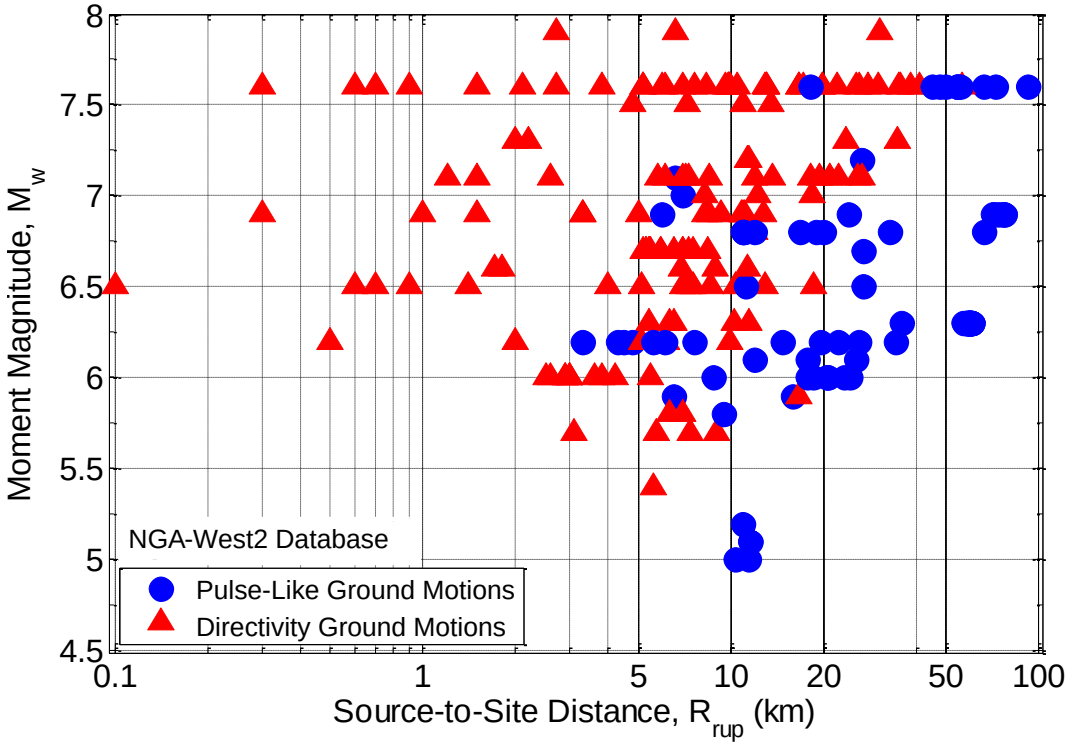

Figure 6.9: Magnitude-distance distribution of pulse-like ground motions in the NGA-West2 database compiled by Shahi (2013) using an automated pulse classification algorithm. Note that the forward-directivity ground motions are shown in red and the remaining pulse-like ground motions are highlighted in blue.

6.4.1 Mixed-effects regression model

A mixed-effects model of the mathematical form given in Equation (6.9) (Abrahamson & Youngs, 1992) and commonly used in the development of empirical GMPEs (Bradley, 2010) is adopted in developing the models for pulse period and pulse amplitude:

$$\ln y_{i,j} = f\left(\boldsymbol{\theta_{ij}}|\boldsymbol{\beta}\right) + \eta_i\tau + \varepsilon_{i,j}\sigma \tag{6.9}$$

where $y_{i,j}$ is the j^{th} observed ground motion intensity measure (e.g. peak ground acceleration) from the i^{th} event; $f\left(\boldsymbol{\theta_{ij}}|\boldsymbol{\beta}\right)$ is the predicted median value of the intensity measure, which is a function of a vector of predictor variables $\boldsymbol{\theta_{ij}}$ (e.g. M_w, R_{rup} etc.); and model coefficients, $\boldsymbol{\beta}$; η_i is the normalised inter-event residual common to all j recordings from the i^{th} event; $\varepsilon_{i,j}$ is the normalised intra-event residual for the j^{th} recording from the i^{th} event; and τ and σ represent the standard deviations of the inter- and intra-event errors, respectively. It should be noted that both η_i and $\varepsilon_{i,j}$ are independent normally distributed random variables with zero mean and unit variance (Bradley, 2010). The total standard deviation associated with the median prediction of the intensity measure of interest can be calculated using Equation (6.10):

$$\sigma_{total} = \sqrt{\tau^2 + \sigma^2} \tag{6.10}$$

As mentioned in Abrahamson & Youngs (1992), the inter- and intra-event residuals can be computed using Equations (6.11) and (6.12), respectively:

$$\eta_i = \frac{1}{\tau}\frac{\sigma^2}{N_{j,i}\sigma^2 + \tau^2}\sum_{j}^{N_{j,i}}\left(\ln y_{i,j} - f\left(\boldsymbol{\theta_{ij}}|\boldsymbol{\beta}\right)\right) \tag{6.11}$$

$$\varepsilon_{i,j} = \frac{\ln y_{i,j} - \left\{f\left(\boldsymbol{\theta_{ij}}|\boldsymbol{\beta}\right) + \eta_i\tau\right\}}{\sigma} \tag{6.12}$$

where $N_{j,i}$ is the number of recordings for event i. The manner in which the total residual is apportioned to the inter- and intra-event error terms can be observed in Equation (6.11). For example, if $N_{j,i}$ = 1 (i.e. an event with one recording), then the proportion of the total residual allocated to the inter-event term is governed by the ratio, $\sigma^2/\tau(\sigma^2 + \tau^2)$. Conversely, for events with a large number of recordings (i.e. $N_{j,i}$ >> 1), the quotient in Equation (6.11) approaches $1/\tau N_{j,i}$, which implies that the inter-event term is effectively equal to the average of the total normalised residuals for event i. Hence, it can be appreciated that the mixed-

effects model ensures that events with relatively large number of recordings do not control the regression analysis. In the present study, the non-linear mixed-effects tool ('nlmefit') in the MATLAB (2010) package is adopted to perform the required regression analyses.

6.4.2 Pulse period

In defining the periods of the identified pulses in the NGAW2 database, Shahi (2013) adopted the period associated with the maximum Fourier amplitude of the pulses extracted from the original motions, similar to Shahi & Baker (2011). The aim of this section is to develop empirical relationships for the pulse period (T_p) considering: (i) earthquake magnitude (M_w) dependence only; (ii) magnitude and rake angle (λ) dependence (i.e. in order to represent the dependence of pulse period on fault type); and (iii) magnitude, rake angle and site class dependence to examine the effects of site response on pulse period. It is worth noting that the 21 pulse-like ground motions from the Canterbury earthquakes in the NGAW2 database have been excluded on the basis that they are used in the assessment of all models in Section 6.4.4.

6.4.2.1 Magnitude dependence only

As mentioned previously, the linear dependence of the logarithm of pulse period on earthquake magnitude can be justified based on theoretical considerations (e.g. Somerville, 1998). A relationship using the mixed-effects model described previously is developed here using 222 pulse-like ground motions from the NGAW2 database. The functional form of the model obtained from regression analysis is given by:

$$\ln\left(T_{p_{i,j}}\right) = -5.52 + 0.95M_w + \eta_i + \varepsilon_{i,j} \qquad (6.13)$$

$$\sigma_{total} = 0.49; \sigma = 0.36; \tau = 0.33$$

Figure 6.10 illustrates the median prediction $\pm$ one standard deviation of the pulse periods predicted by the model shown in Equation (6.13), as a function of earthquake magnitude. The observed pulse periods used in model development are also presented in the same manner as the magnitude-distance distribution in Figure 6.9.

Figure 6.11a and Figure 6.11b show the inter- and intra-event residuals plotted as a function of magnitude, respectively. In order to identify any trends in the observed residuals, the non-parametric mean (Wasserman, 2006) and its 98% confidence interval are also

illustrated using the solid and dashed lines, respectively. In both cases, it can be appreciated that there are no obvious trends that depart from the ideal case of zero mean. The cumulative distribution of the inter- and intra-event residuals is examined in Figure 6.11 using the Kolmogorov-Smirnov (K-S) goodness-of-fit test (Ang & Tang, 2007). This test allows the empirical distribution (EDF) of the residuals to be compared with the cumulative distribution (CDF) of the assumed distribution. From a graphical viewpoint, if the EDF intersects the K-S test-statistic 'bounds' as indicated by the dotted lines, then the null hypothesis that the residuals follow a standard normal distribution should be rejected (Ang & Tang, 2007). Given that the EDFs of the inter- and intra-event residuals are within the bounds in Figure 6.11, the null hypothesis cannot be rejected. Therefore, the assumption that the pulse period is log-normally distributed (or $\ln(T_p)$ is normally distributed) is also valid.

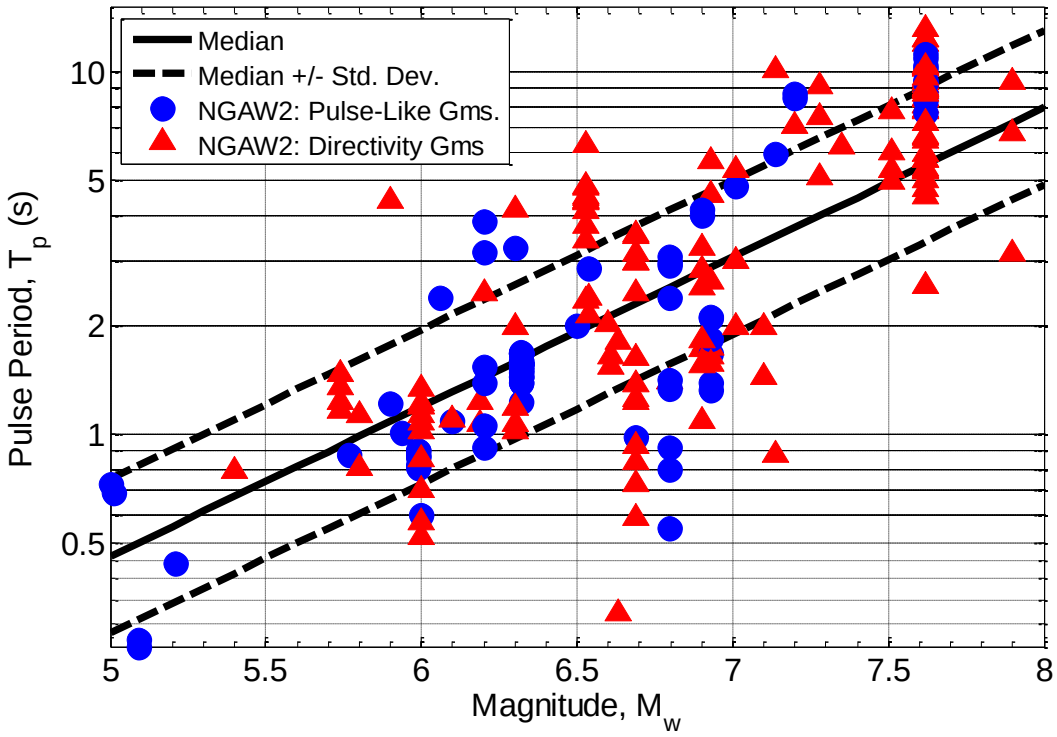

Figure 6.10: Magnitude scaling of the empirical model developed for pulse period using the pulse-like ground motions from the NGA-West2 database. Note that the dotted lines represent the median $\pm$ one standard deviation.

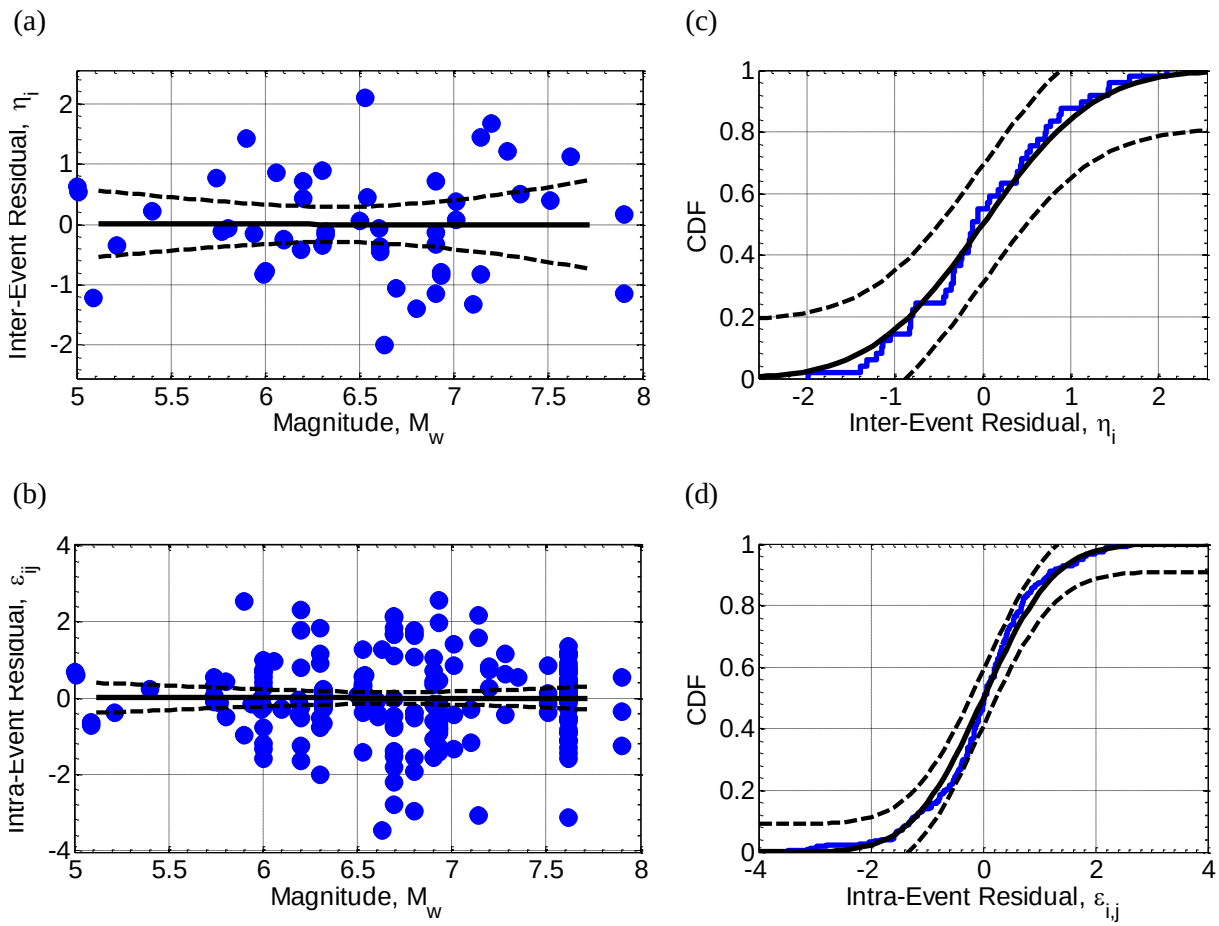

Figure 6.11: Residuals associated with the empirical model for pulse period developed using pulse-like ground motions from the NGA West2 database: (a) & (b) inter- and intra-event residuals plotted as a function of magnitude, respectively as well as the non-parametric mean and its 98% confidence interval. Panels (c) and (d) illustrate the Kolmogorov-Smirnov goodness-of-fit test to validate the assumption that the residuals are normally distributed.

It could be argued that the influence of pulse-like ground motions in the NGAW2 database resulting from physical phenomena other than forward-directivity effects could have a significant influence on the predictions of the model illustrated in Figure 6.10. To further investigate this issue, the regression analysis was repeated using only the subset of 133 (excluding observed pulse periods in the Darfield and Christchurch earthquakes from a total of 145 observations) directivity ground motions from the original database. In doing so, the relationship given by Equation (6.14) between the pulse period and earthquake magnitude is obtained:

$$\ln\left(T_{p_{i,j}}\right) = -4.88 + 0.85M_w + \eta_i + \varepsilon_{i,j} \tag{6.14}$$

$$\sigma_{total} = 0.53; \sigma = 0.38; \tau = 0.36$$

Figure 6.12 provides a comparison between the median predictions of the model developed using all pulse-like ground motions from the NGAW2 dataset and the subset

which includes directivity motions only. It can be observed that the former relationship provides smaller predictions of the pulse period at lower magnitudes and larger predictions at higher magnitudes. Because the observed differences between the predictions of the two relationships are not significant, it was decided that the pulse period model developed using all 222 pulse-like motions would be adopted for the purposes of the present study.

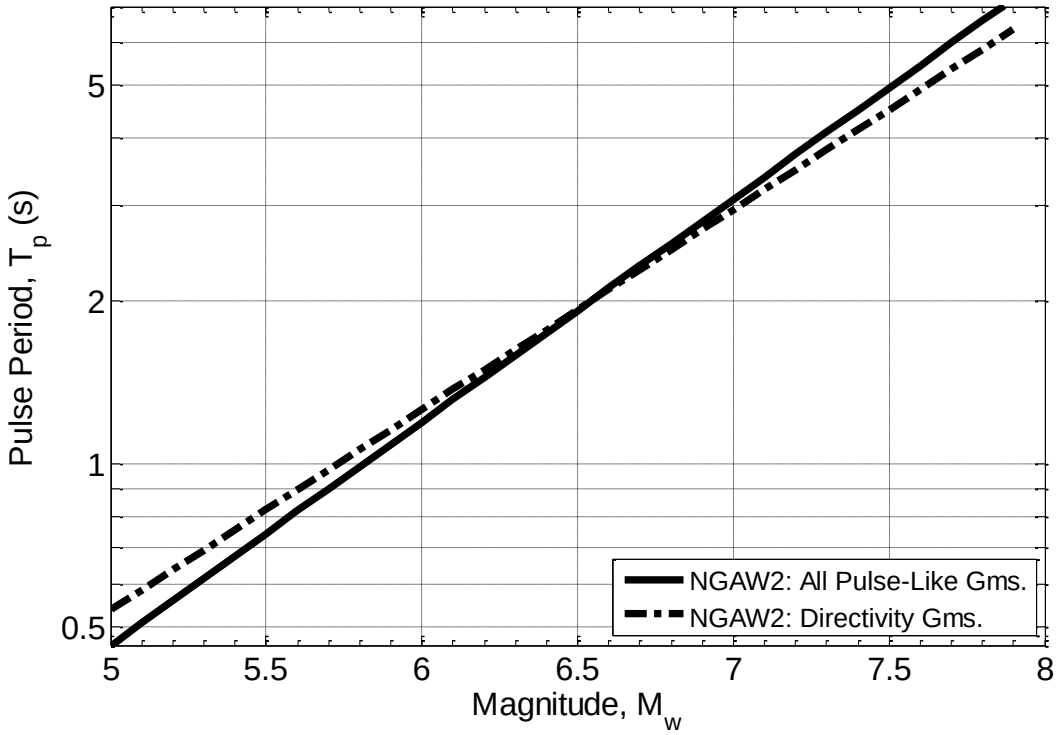

Figure 6.12: Comparison of the median predictions provided by the model for pulse period obtained using all pulse-like ground motions in the NGAW2 database and a subset of forward-directivity ground motions only.

6.4.2.2 Magnitude and rake angle dependence

As previously noted, the pulse period is known to be related to the earthquake magnitude, which in turn is related to rise time (Somerville et al., 1999). Since rise time is a function of stress drop, and stress drops systematically vary for different faulting mechanisms (Wells & Coppersmith, 1994), then it would be expected that the pulse period is also a function of faulting mechanism (Bradley & Somerville, personal communication, 2013). Previous research (e.g. Mavroeidis & Papageorgiou, 2003) has demonstrated empirically that the pulse periods produced by strike-slip earthquakes are, on average, larger than those observed in reverse-faulting earthquakes. This is consistent with the fact that reverse earthquakes have, on average, larger stress drops than strike slip earthquakes (and in turn, normal-faulting earthquakes). The only available relationship in published literature which considers the effect of fault type on pulse period was developed by Shahi & Baker (2010)

(SB10), who proposed separate relationships for strike-slip and non strike-slip events. The aim herein is to develop a rational relationship for the pulse period which is a continuous function of the earthquake magnitude and a representative predictor variable for the fault mechanism of interest. A commonly used variable in ground motion prediction to classify faults is the rake angle[5]. Table 6.5 summarises the classification scheme used in the NGA-West2 database (Ancheta et al., 2013) to identify the faulting mechanism:

Table 6.5: Classification scheme used in the NGA-West2 database to identify faulting mechanisms (after Ancheta et al. (2013)).

Faulting Mechanism	**Rake Angles, λ (degrees)**
Strike-Slip	$-180 < \lambda < -150$ $-30 < \lambda < 30$ $150 < \lambda < 180$
Normal	$-120 < \lambda < -60$
Reverse	$60 < \lambda < 120$
Reverse-Oblique	$30 < \lambda < 60$ $120 < \lambda < 150$
Normal-Oblique	$-150 < \lambda < -120$ $-60 < \lambda < -30$

The chosen functional form of the pulse period relationship included a $\cos(\lambda + \frac{\pi}{2})$ dependence in an effort to ensure that the aforementioned pulse period hierarchy could be maintained (i.e. $T_{p,Reverse} < T_{p,Strike-Slip} < T_{p,Normal}$) based on the rise time-stress drop relationship. Upon carrying out the regression analysis using a mixed-effects model with the pulse-like ground motions from the NGAW2 database, the relationship illustrated in Equation (6.15) was obtained:

$$\ln\left(T_{p_{i,j}}\right) = -5.57 + 0.96M_w + 0.14\cos\left(\lambda + \frac{\pi}{2}\right) + \eta_i + \varepsilon_{i,j} \qquad (6.15)$$

$$\sigma_{total} = 0.48; \sigma = 0.36; \tau = 0.32$$

Although the rake angle predictor variable has a non-zero coefficient in Equation (6.15), it is important to use a statistical test to determine its significance. Because it is assumed that the observations ($\ln T_p$) are normally distributed in the regression analysis, and since there are only a finite number of observations, it follows that the coefficient of the $\cos(\lambda + \frac{\pi}{2})$ predictor variable has a Student's t-distribution (Ang & Tang, 2007). A Student's t-test can hence be performed to obtain the t-statistic (t) and the associated p-value (p) used to assess the null hypothesis that the above regression coefficient is zero. A large t (> + 2.0 or < - 2.0)

[5] The angle measured on the fault plane anti-clockwise from the reference strike direction to the average slip direction (Chiou, 2005).

and small p (< 0.05) imply that the null hypothesis can be rejected (Kutner et al., 2005), thereby allowing one to assert that the coefficient is not zero. In this case, t = 1.312 and p = 0.191, which indicates that the null hypothesis cannot be rejected. As will be illustrated in Figure 6.13, the predictions of the model are consistent with theoretical considerations described previously, which implies that the rake angle is an important predictor in the pulse period relationship shown in Equation (6.15). Hence, it was considered appropriate to retain the rake angle dependence.

For the purposes of comparison with Equation 6.15, two regression analyses were conducted using subsets of the NGAW2 database containing pulse-like motions resulting from strike-slip and non strike-slip events, respectively. It should be noted that the strike-slip dataset contains 64 records from 23 events, whereas the non strike-slip dataset contains 158 records from 26 events. Equations (6.16) and (6.17) illustrate the equations obtained from regression analysis in both cases, respectively. Due to the paucity of observations resulting from normal-faulting earthquakes (i.e. only 7 out of 222 records), separate regression analyses using subsets of reverse- and normal-faulting events could not be conducted.

Strike-Slip

$$\ln\left(T_{p_{i,j}}\right) = -4.76 + 0.85M_w + \eta_i + \varepsilon_{i,j} \quad (6.16)$$

$$\sigma_{total} = 0.63; \sigma = 0.53; \tau = 0.33$$

Non Strike-Slip

$$\ln\left(T_{p_{i,j}}\right) = -6.38 + 1.06M_w + \eta_i + \varepsilon_{i,j} \quad (6.17)$$

$$\sigma_{total} = 0.69; \sigma = 0.62; \tau = 0.30$$

Figure 6.13 compares the median predictions provided by the model with magnitude and rake angle dependence (M_w-λ) (i.e. Equation 6.15), with the predictions of the two models for strike-slip (SS) and non strike-slip (NSS) events (i.e. Equations 6.16 and 6.17, respectively). The predictions are shown for three cases: (i) a strike-slip (SS) earthquake with λ = 0; (ii) a reverse-faulting (RV) earthquake with λ = 90°; and (iii) a normal-faulting (NM) earthquake with λ = -90°. The observed data is also overlaid and has been colour-coded based on fault-type. It can be seen that the M_w-λ model provides systematically larger predictions for the normal-faulting event followed by the strike-slip- and reverse-faulting events. Although this trend agrees with the rise time-stress drop relationship, the lack of normal-faulting events in the NGAW2 database does not allow the trend to be rigorously validated empirically. Nonetheless, the longer pulse periods predicted by the model for SS earthquakes

in comparison to RV earthquakes is consistent with empirical observations from previous research (Mavroeidis & Papageorgiou, 2003; Shahi & Baker, 2010). While the predictions of the M_w-λ model are notably larger than the NSS relationship for the NM event, comparable predictions are observed for the RV and SS events. It can also be observed from Figure 6.13 that the difference between the SS and NSS model predictions reduces with magnitude, and is essentially negligible for M_w > 7.5.

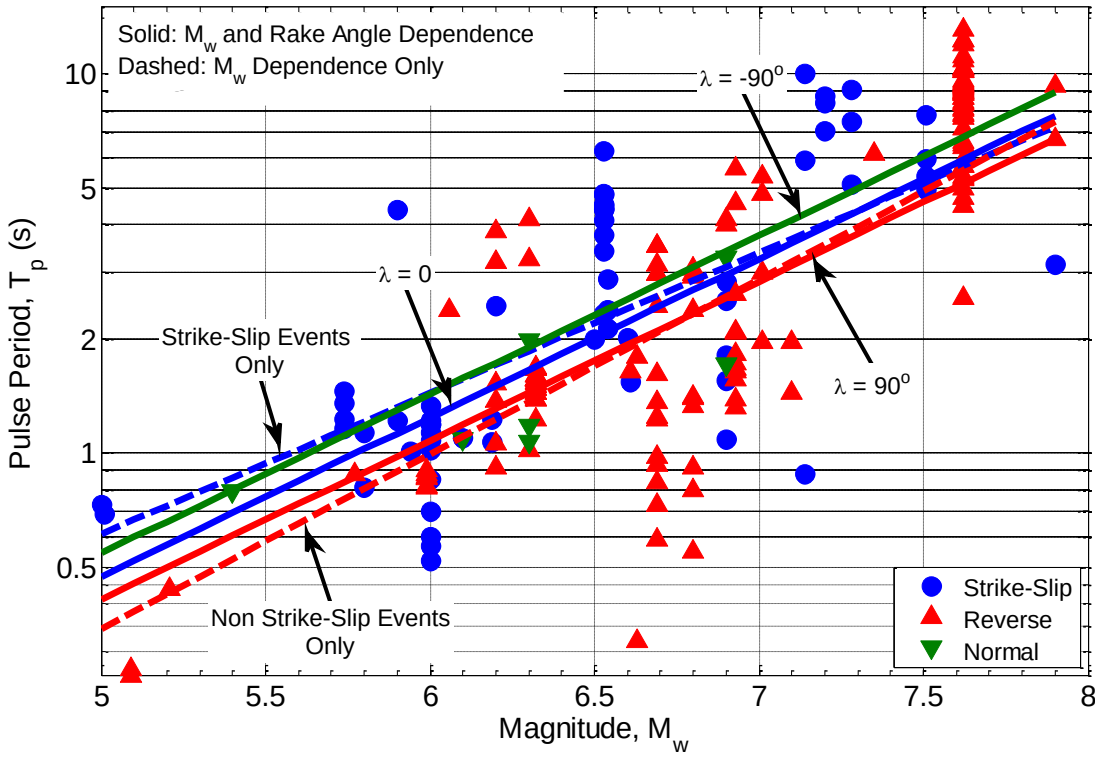

Figure 6.13: Comparison of the median predictions for pulse period provided by empirical models developed using: (i) earthquake magnitude and rake angle dependence for the pulse-like ground motions in the NGAW2 database; (ii) subsets of strike-slip and non strike-slip (reverse and normal) events from the NGAW2 database considering only magnitude dependence. Note that the blue, red and green markers represent the observed pulse periods in strike-slip, reverse and normal faulting events, respectively.

Figure 6.14 provides a comparison between the median predictions of all models developed for pulse period thus far in the present study. In relation to the M_w-dependent model developed using all pulse-like ground motions in the NGAW2 database, the M_w-λ model provides slightly larger and smaller estimates of the pulse period for strike-slip and reverse events, respectively. For the normal event, however, the M_w-dependent model gives notably lower predictions when compared to the M_w-λ model. Similar trends are also demonstrated by the SS and NSS relations in carrying out comparisons with the M_w-dependent model, but the differences in prediction diminish with increasing magnitude, as shown in Figure 6.14a and Figure 6.14b, respectively. Based on the above evidence, it is apparent that more robust and empirically consistent estimates of the pulse period can be

obtained for different faulting mechanisms by including the rake angle as an additional predictor variable in the model. Hence, the M_w-λ model is preferred in the assessment of model predictions (refer to Section 6.4.4), in addition to the M_w-dependent model.

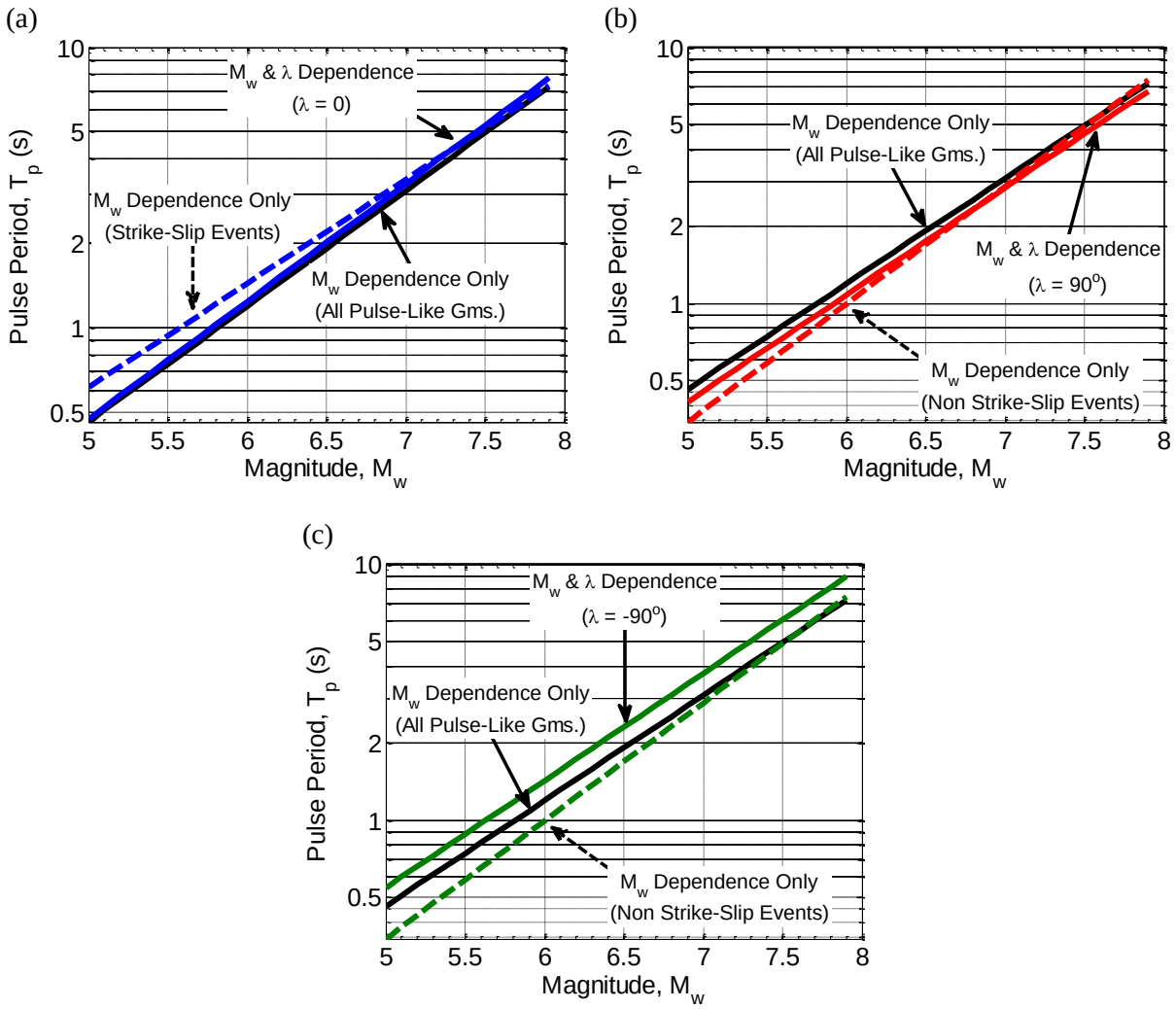

Figure 6.14: Comparison of the median predictions of pulse period provided by several models developed using the NGAW2 database for (a) strike-slip; (b) reverse-faulting; and (c) normal-faulting events.

In order to determine if the residuals of the models developed thus far exhibit any trends with respect to the main predictor variables, Figure 6.15 and Figure 6.16 plot the intra-event residuals as a function of earthquake magnitude and rake angle, respectively. It should be recalled that the residuals associated with the pulse period model with M_w only dependence were previously illustrated in Figure 6.16. Although three of the four models do not explicitly consider the rake angle in their functional form, it is a useful exercise to determine if they are biased with respect to rake angle. It is noted that the non-parametric mean and its confidence interval are employed only in Figure 6.15 to identify any trends in the residuals with respect to M_w. Due to the discrete groupings of the residuals plotted as a

function of rake angle (i.e. $\cos(\lambda + \frac{\pi}{2})$) in Figure 6.16, the mean and standard error are illustrated for each group. Both figures indicate that all models are unbiased with respect to earthquake magnitude and rake angle. The only exception to the above statement is the negative bias shown by the mean residual associated with the M_w-λ model for normal-faulting earthquakes. Although there is an indication that the model provides an over-prediction, it is difficult to scrutinise this trend at present based on the small number of recordings from normal events in the NGAW2 dataset. The fact that the seven pulse-like motions were recorded on stiff soil sites (site class C according to the NEHRP classification scheme outlined in Table 6.6) provides a plausible explanation for the lower than expected pulse periods (refer to the discussion in Section 6.3.3 on pulse periods at soft vs. stiff soil sites).

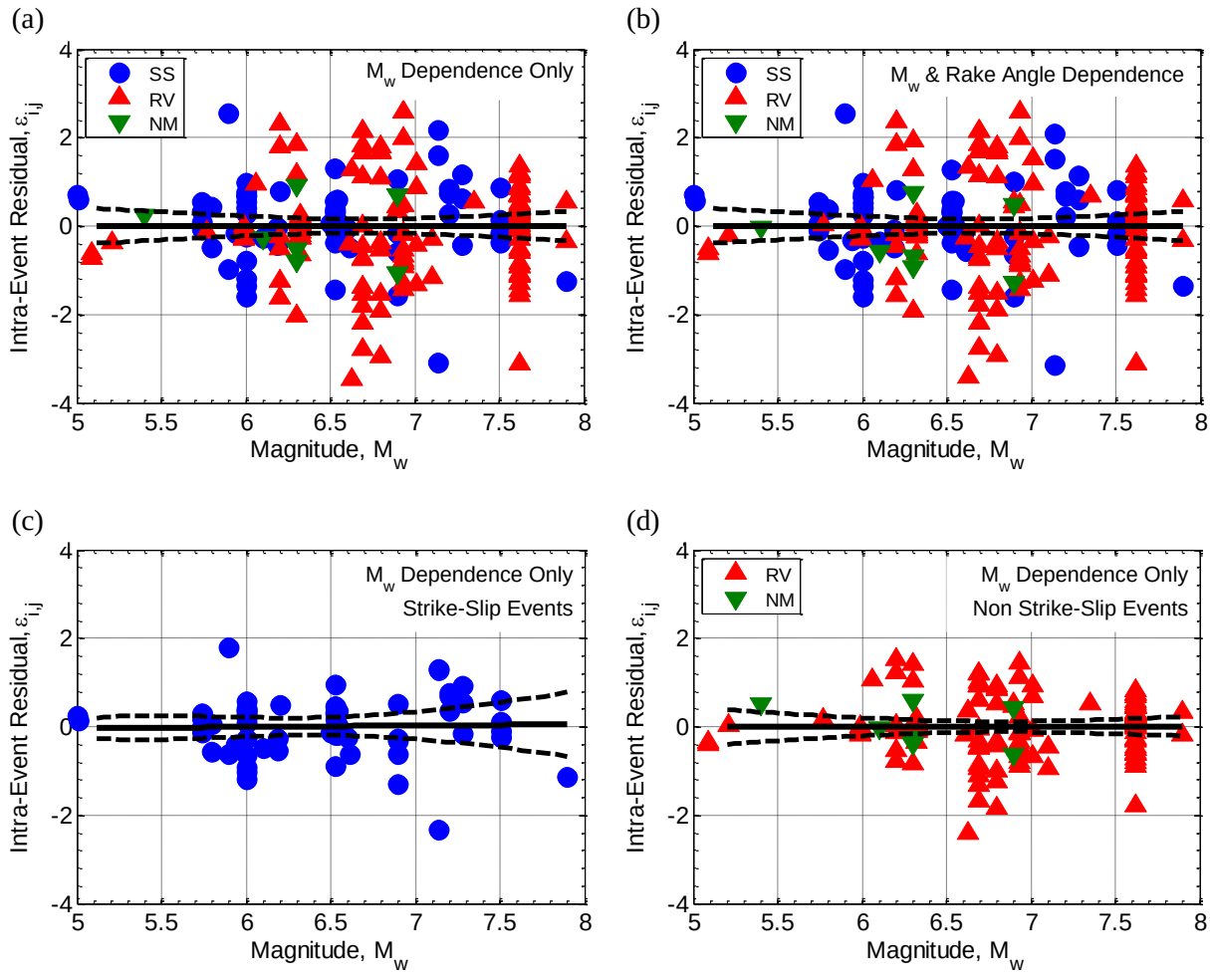

Figure 6.15:Intra-event residuals as a function of earthquake magnitude for pulse period using NGAW2 empirical models considering: (a) all pulse-like ground motions with magnitude dependence only; (b) all pulse-like ground motions with magnitude and rake angle dependence; (c) pulse-like motions from strike-slip events with magnitude dependence only; and (d) pulse-like motions from non strike-slip events with magnitude dependence only.

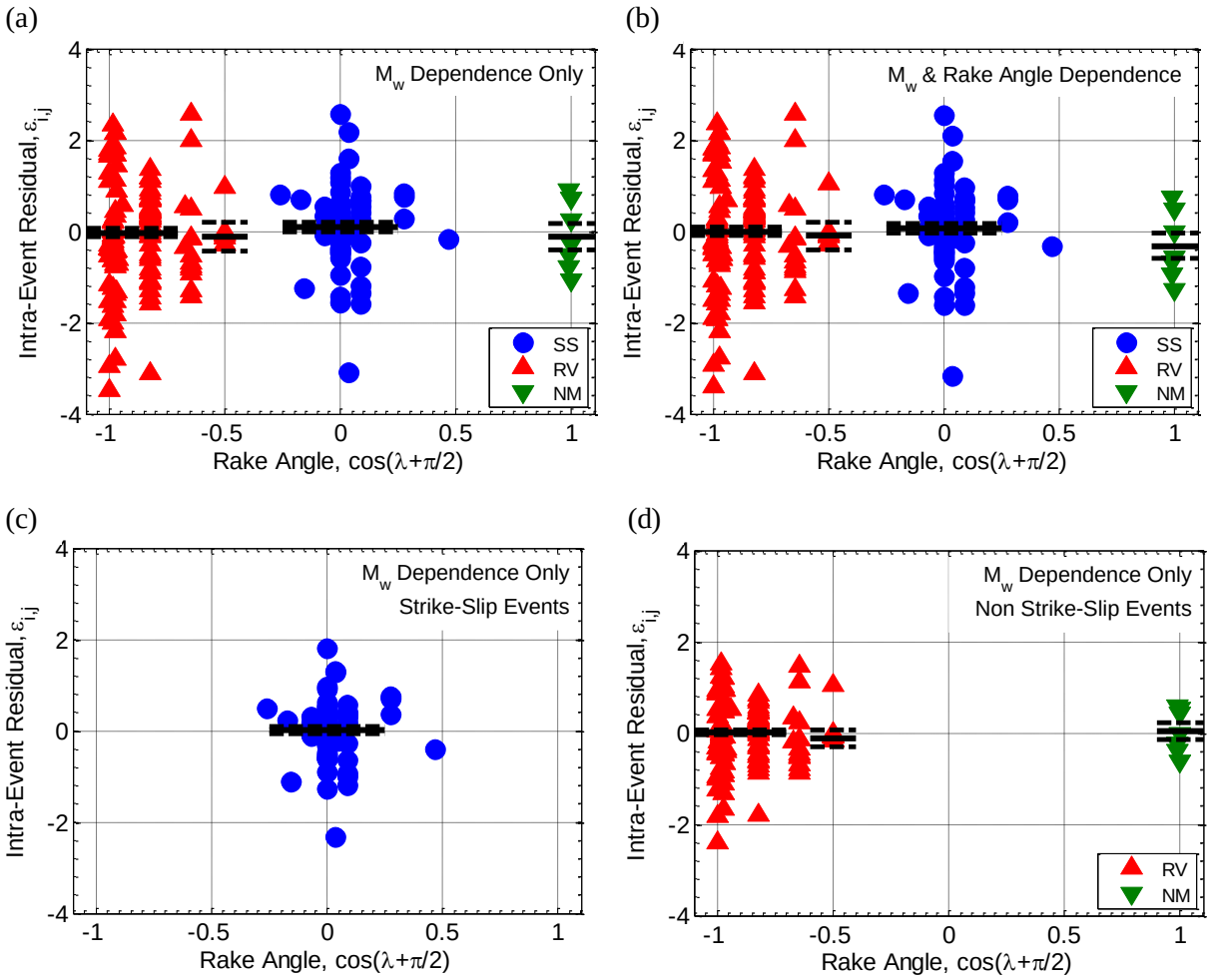

Figure 6.16: Intra-event residuals as a function of rake angle for pulse period using NGAW2 empirical models considering: (a) all pulse-like ground motions with magnitude dependence only; (b) all pulse-like ground motions with magnitude and rake angle dependence; (c) pulse-like motions from strike-slip events with magnitude dependence only; and (d) pulse-like motions from non strike-slip events with magnitude dependence only. Note that the residuals are colour-coded based on fault-type i.e. strike-slip (SS), reverse (RV) and normal (NM).

Given that the pulse period models developed using the NGAW2 database do not explicitly consider the effects of local site response, it is prudent to also examine the residuals with respect to site class. The NEHRP site classification scheme, which relies on the average shear-wave velocity to a depth of 30 m ($V_{s,30}$), is adopted herein to identify the site class and is summarised in Table 6.6:

Table 6.6: NEHRP site classification scheme (after Ancheta et al., 2013).

NEHRP Site Classification	**Average Shear-Wave Velocity, $V_{s,30}$ (m/s)**
A	> 1500
B	760 - 1500
C	360 - 760
D	180 - 360
E	< 180

Figure 6.17 illustrates the intra-event residuals as a function of site class for both, the M_w-dependent model and the M_w-λ model. In order to differentiate between residuals corresponding to rock and soil sites, strong motion stations with site classes A and B are classed as 'rock' sites, whereas those with site classes C, D and E are classed as 'soil' sites. The mean and standard error of the residuals from the two groupings are also indicated using solid and dashed lines, respectively. While there is some indication that both models provide an over- and under-prediction for rock and soil sites, respectively, the fact that the uncertainty bounds include the assumed mean of zero implies that the models are unbiased.

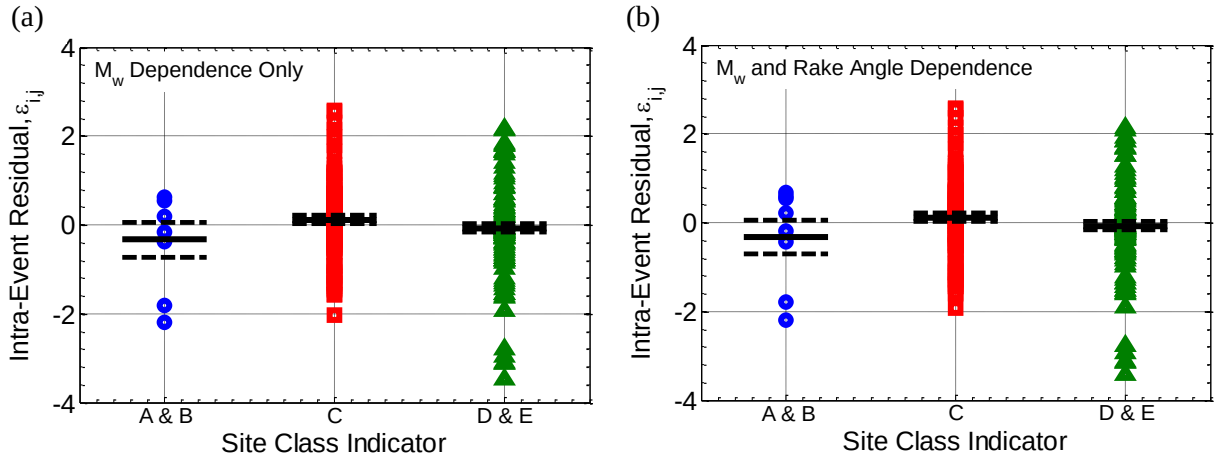

Figure 6.17: Intra-event residuals as a function of site class for pulse period using NGAW2 empirical models considering: (a) all pulse-like ground motions with magnitude dependence only; and (b) all pulse-like ground motions with magnitude and rake angle dependence.

6.4.2.3 Magnitude, rake angle and site class dependence

While the previous sections have demonstrated that the pulse period depends on moment magnitude and faulting mechanism, it is useful to consider the effects of site response on the pulse period following the findings of previous research (e.g. Bray & Rodriguez-Marek, 2004; Rodriguez-Marek & Bray, 2006). Using the definitions in the NEHRP classification scheme, strong motion stations with site classes A and B were classed as 'rock' sites, whereas those with site classes C, D and E were classed as 'soil' sites. Note that no distinction was made between site class C, D, or E sites because of the similarity of the residuals shown in Figure 6.17. In addition, only 8 out of the 222 ground motions were recorded on rock sites, which implies that the dataset is dominated by pulse periods recorded on shallow and deep soil sites. Rather than developing separate relationships for rock and soil sites (an approach followed by Bray & Rodriguez-Marek (2004), as discussed previously), a dummy variable, S, is included in the regression equation which takes on values of 0 for rock

and 1 for soil sites. Equations (6.18) provides the functional form of the model obtained using mixed-effects regression:

$$\ln\left(T_{p_{i,j}}\right) = -6.11 + 0.98M_w + 0.14\cos\left(\lambda + \frac{\pi}{2}\right) + 0.40S + \eta_i + \varepsilon_{i,j} \quad (6.18)$$

$$\sigma_{total} = 0.47; \sigma = 0.36; \tau = 0.31$$

Figure 6.18 illustrates the magnitude scaling of the relationship for both rock and soil sites, in addition to the observed pulse periods grouped according to their site class. For comparison, the predictions for soil and rock sites are shown for a strike-slip faulting event i.e. λ = 0. An examination of the figure indicates that the pulse periods predicted by the model for soil sites are systematically higher for all magnitudes, consistent with empirical observations from past earthquakes. A Student's t-test can again be employed to determine the statistical significance of the regression coefficient associated with site class dummy variable, S. As mentioned previously, the null hypothesis (that the regression coefficient is equal to zero) can be typically rejected for t > 2.0 and p < 0.05. Based on the calculated values of t = 2.37 and p = 0.0184 the null hypothesis can be rejected, thereby allowing the site class dependence to be retained. Note that the '0.40' coefficient of the dummy variable S implies that soil sites have, on average, a pulse period which is $\exp(0.40) \approx 1.5$ times that on rock sites. Clearly, further pulse-like ground motions corresponding to site classes A and B will assist in more robustly constraining the influence of soil response on pulse period in the future.

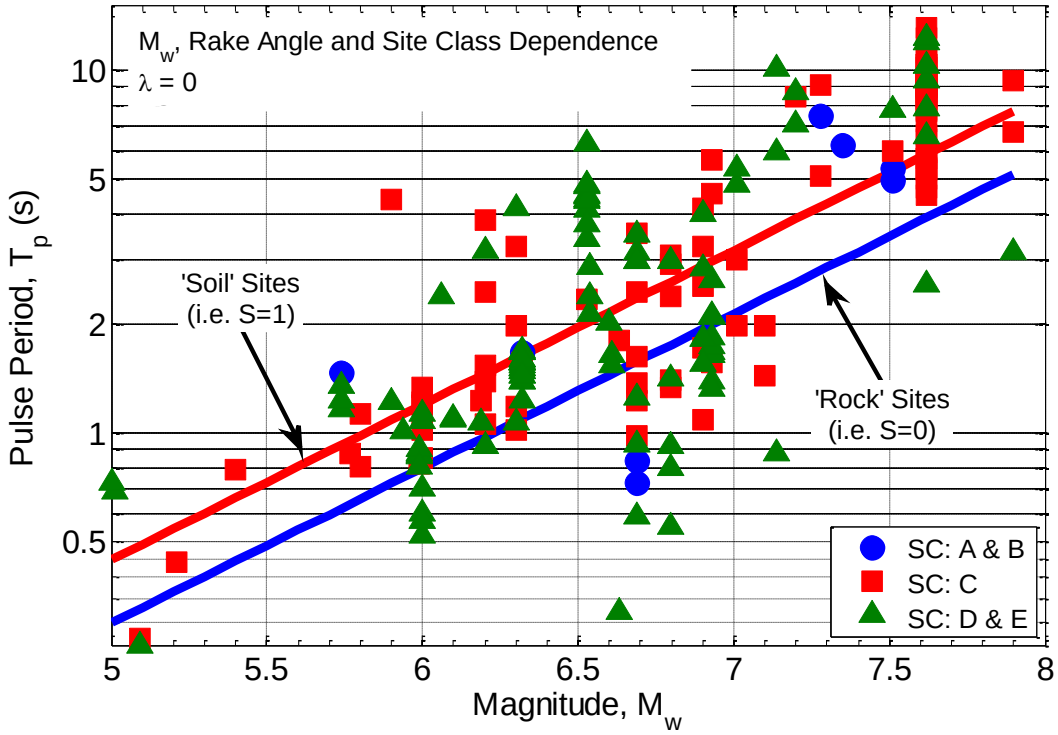

Figure 6.18: Comparison of median predictions provided by the pulse period model developed using magnitude, rake angle and site class dependence for both rock (site classes A and B) and soil (site classes C, D and E) sites. Pulse period observations from the NGAW2 database used in the regression are also shown and colour-coded based on the NEHRP site classification scheme.

6.4.3 Pulse amplitude

As discussed previously, the peak ground velocity (PGV) provides an adequate representation of the directivity pulse amplitude. The use of a simplified relationship to obtain estimates of the PGV in the near-fault region has been justified by several researchers (refer to Section 6.3.2) on the basis that the empirical data is often constrained to distances within 20 km. Similar to the previous section, the aim here is to develop an empirical prediction equation for the pulse amplitude based on near-fault ($R_{rup} \leq 20$ km) pulse-like ground motions in the more recent NGAW2 database. The magnitude-distance distribution of the 148 pulse-like ground motions (from 45 events) used in developing the PGV model is illustrated in Figure 6.19. It is evident that a majority of the pulse-like ground motions in the dataset are caused by forward-directivity effects.

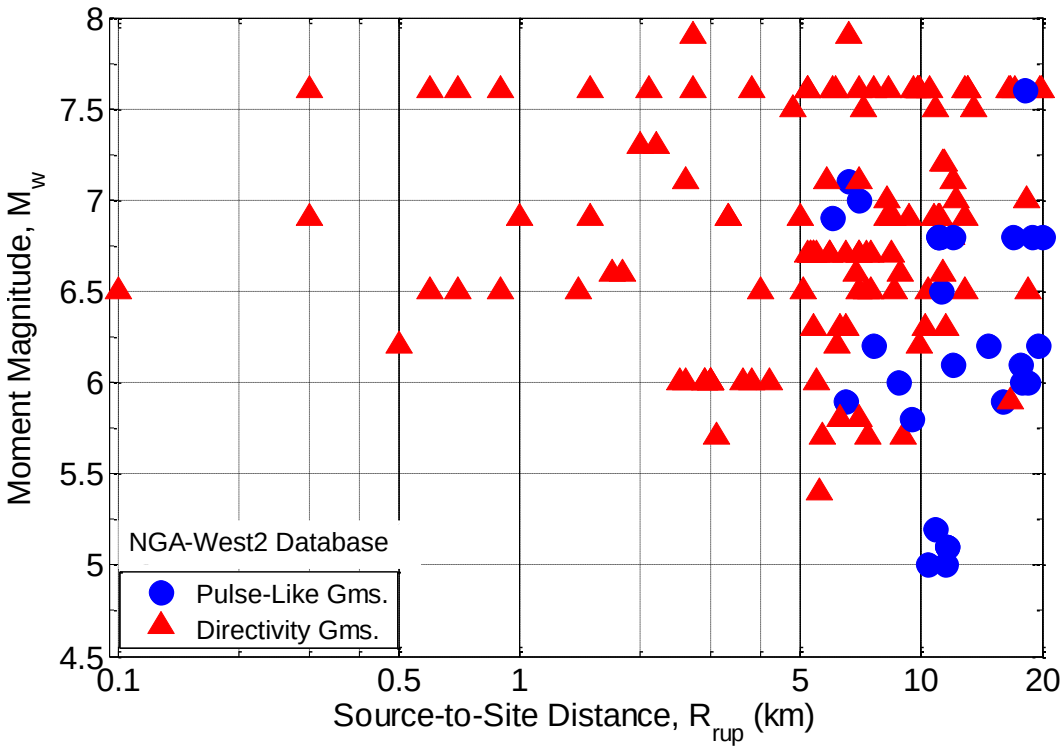

Figure 6.19: Magnitude-distance distribution of near-fault pulse-like ground motions from the NGAW2 database used in the development of an empirical model for the pulse amplitude. Note that the forward-directivity ground motions are shown in red and the remaining pulse-like ground motions are highlighted in blue.

Given that the wider scope of this chapter is to examine the differences in model prediction based on a current dataset, it is considered reasonable to adopt the functional form used by Bray & Rodriguez-Marek (2004) and Bray et al. (2009) (shown in Equation (6.8)). Upon carrying out a regression analysis using the mixed-effects model, the relationship illustrated in Equation (6.19) is obtained:

$$\ln(PGV)_{ij} = 2.34 + 0.35M_w - 0.14\ln({R_{rup}}^2 + 0.34^2) + \eta_i + \varepsilon_{ij} \qquad (6.19)$$

$$\sigma_{total} = 0.35; \sigma = 0.28; \tau = 0.21$$

Figure 6.20 illustrates the source-to-site dependence of the relationship for M_w = 6.0 and M_w = 7.0. It can be observed that the chosen functional form has a nearly zero slope at small distances, and becomes linear at larger distances (Bray & Rodriguez-Marek, 2004). The dotted lines represent the median prediction $\pm$ one standard deviation. Due to the scarcity of data at distances less than 3 km, as shown in Figure 6.19, the distance scaling term of the equation is controlled by data at longer distances. As will be seen in the following section, this results in relatively larger pulse amplitudes at small source-to-site distances when compared to the models developed in previous research for large magnitude events. Although

provisions can be made to account for magnitude saturation effects, such considerations are left for future research.

(a)

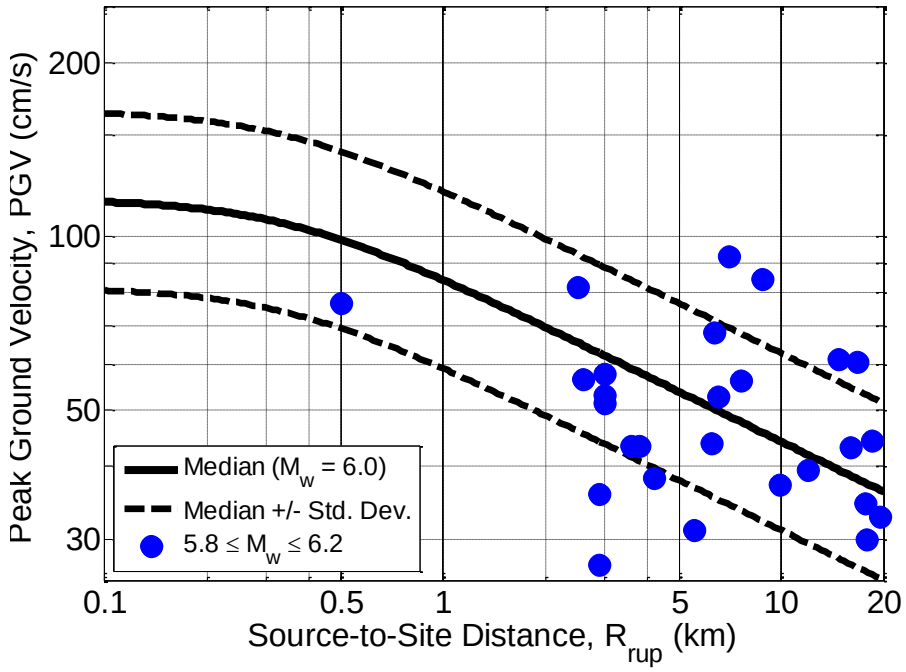

(b)

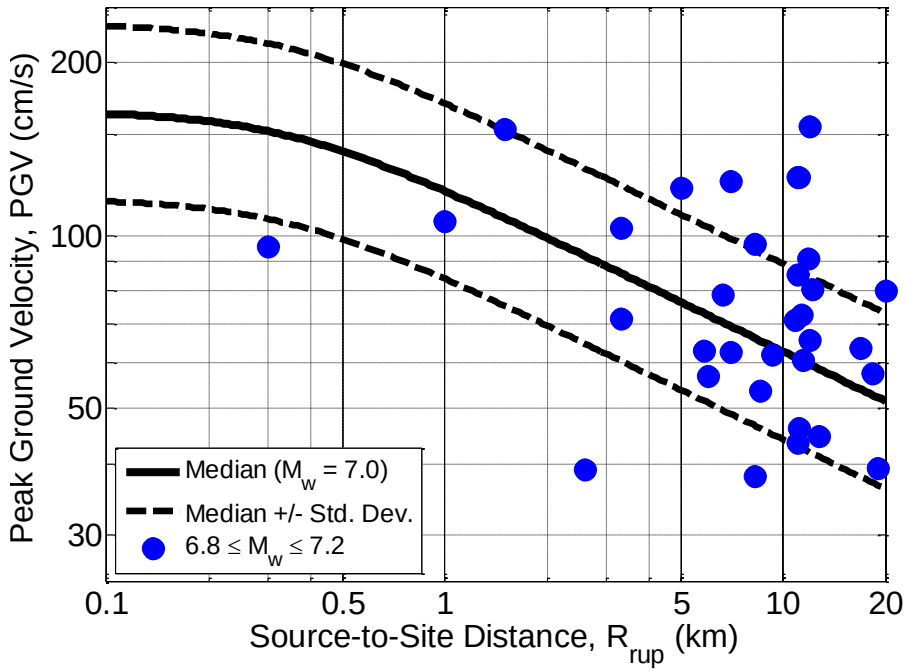

Figure 6.20: Illustration of the source-to-site distance dependence of the empirical model developed for pulse amplitude (PGV) using pulse-like motions in the NGAW2 database. Panels (a) and (b) illustrate the 16th, 50th and 84th percentiles of the prediction for M_w = 6.0 and M_w = 7.0, respectively. The observed pulse amplitudes from appropriate magnitude ranges are also shown in both panels.

Figure 6.21a and Figure 6.21b show the inter- and intra-event residuals plotted as a function of magnitude, respectively. The non-parametric mean (solid lines) and its 98% confidence interval (dashed lines) indicate that there is no variation in the residuals from the assumed zero mean with respect to magnitude. By means of the K-S goodness-of-fit test, Figure 6.21c and Figure 6.21d explicitly illustrate that the distribution of the residuals are consistent with the standard normal distribution. Similar to the pulse period, the assumption that the pulse amplitude follows a log-normal distribution (or $\ln(PGV)$ is normally distributed) is valid as a consequence. The results of Figure 6.21e are effective in highlighting the fact that the intra-event residuals are also unbiased with respect to source-to-site distance.

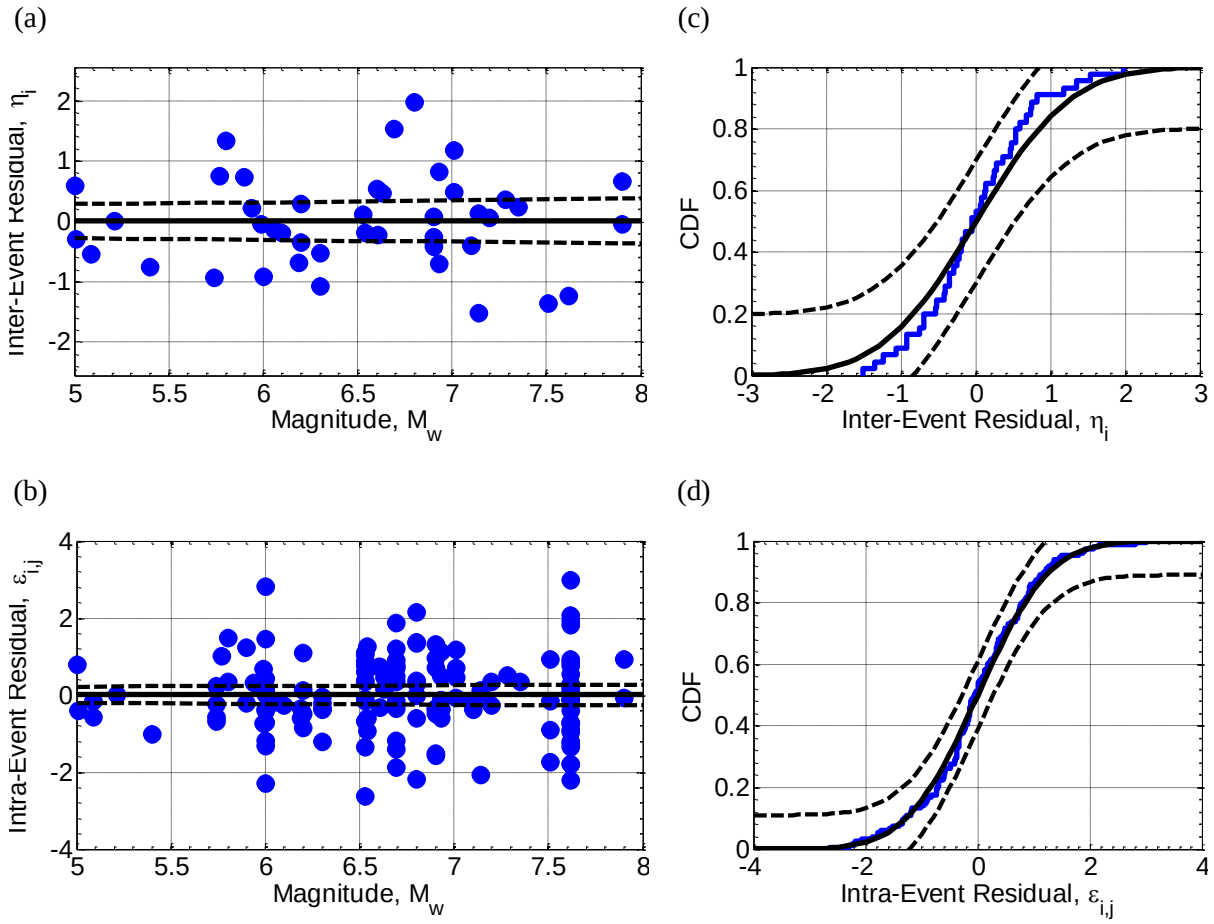

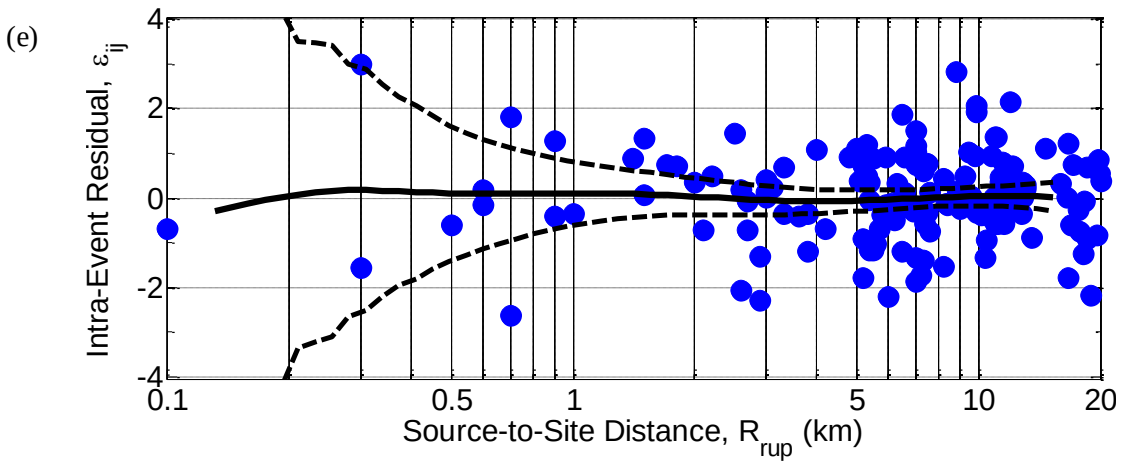

Figure 6.21: Residuals associated with the empirical model for pulse amplitude developed using pulse-like ground motions from the NGA West2 database: (a) & (b) inter- and intra-event residuals plotted as a function of magnitude, respectively; (c) & (d) graphical illustration of the Kolmogorov-Smirnov goodness-of-fit test to validate the assumption that the residuals are normally distributed; and (e) intra-event residuals plotted as a function of source-to-site distance.

Similar to the pulse period models developed previously, the pulse amplitude model developed in this section using does not account for the effects of local site response. Hence, it is appropriate to identify whether the residuals exhibit any trends with respect to site conditions. Figure 6.22 illustrates the intra-event residuals obtained using the model as a function of site class (identified using the NEHRP classification scheme). The mean and standard error of the residuals for the three site class groupings are also indicated using solid and dashed lines, respectively. It can be observed from the figure that the residuals do not demonstrate any bias with respect to site classes A, B and C. Although the mean residual for soil sites (site class D and E) indicates a marginal under-prediction of the pulse amplitude, the uncertainty bounds include the assumed mean of zero, thereby implying that the model is unbiased.

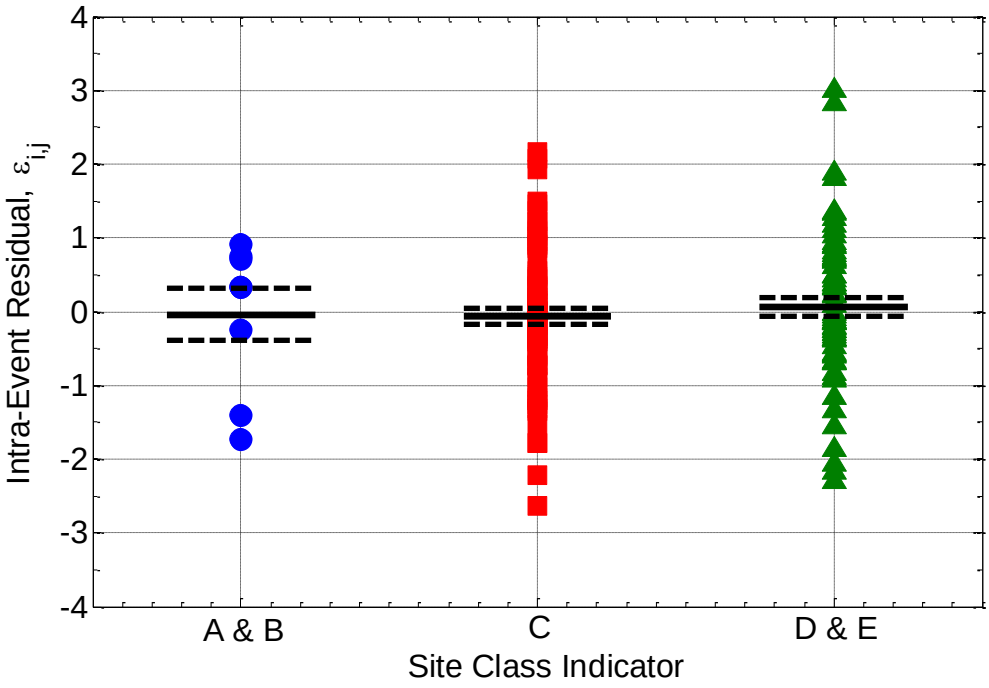

Figure 6.22:Intra-event residuals as a function of site class for the pulse amplitude using the empirical model developed using near-fault pulse-like ground motions from the NGA-West2 database.

Figure 6.23 shows a comparison between predictions of PGV provided by the NGAW2 model developed in this study and several existing models considered previously in this chapter. It is noted that the median predictions of all models are shown for two strike-slip events with M_w = 6.5 and M_w= 7.0 in Figure 6.23a and Figure 6.23b, respectively. Although the functional form of the NGAW2 model is based on the BR04 and BR09 models, the former model retains a nearly zero slope for source-to-site distances only less than 0.5 km. Conversely,. the functional form of the latter models becomes linear for R_{rup} > 3 km. A comparison of the median predictions of all models indicates that they are similar for 1 ≤ R_{rup} ≤ 10 km. For other distances, the NGAW2 model provides notably larger predictions in relation to its predecessors.

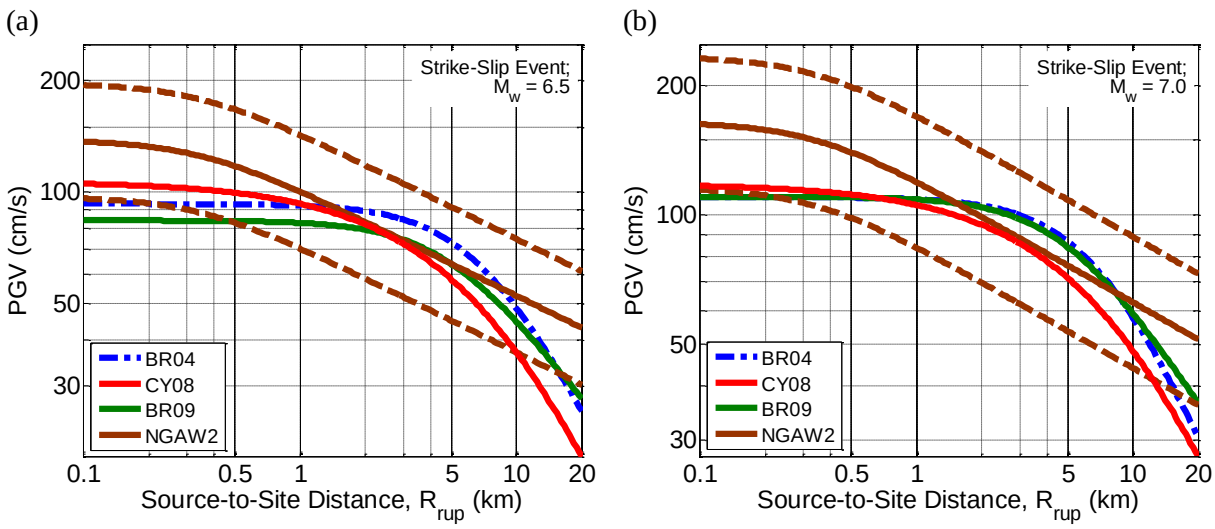

Figure 6.23: Comparison of the source-to-site dependence of several existing empirical relationships and the NGAW2 model developed in the present study for the pulse amplitude (defined by the peak ground velocity) for a strike-slip event with (a) M_w6.5; and (b) M_w7.0. The dotted brown lines represent the 16th and 84th percentile predictions of the NGAW2 model.

6.4.4 Assessment of all model predictions using observations from the Canterbury earthquakes

In the present section, the efficacy of empirical models developed using the NGAW2 database for the pulse period and amplitude are examined in conjunction with models developed in previous research. Once again, observations from the Canterbury earthquakes form the basis of this validation process.

Figure 6.24 illustrates a qualitative comparison between the pulse periods observed in the four events considered, and the median predictions of the BR04, BR09, SB11 (developed in previous research) models and the NGAW2 relationship considering only magnitude dependence (developed in the present study). The 16th and 84th percentiles corresponding to the latter model are also illustrated by the dashed lines. Similar to Figure 6.3, the median pulse periods observed in the four events are indicated using solid lines. It can be observed from the figure that the NGAW2 model provides extremely similar estimates of the pulse period in relation to the more recent SB11 model. In fact, it is evident that the NGAW2 predictions are slightly lower than the SB11 model and the difference increases with magnitude. The use of a larger database is the most likely reason for the improved predictions of both models in relation to the BR04 and BR09 models. Although the variability in pulse periods from the June and December is reasonably well-captured by the $\pm$ standard deviation

bands of the NGAW2 model, observations from the Darfield and Christchurch events remain notably under-predicted, with many exceeding the predicted 84th percentile values.

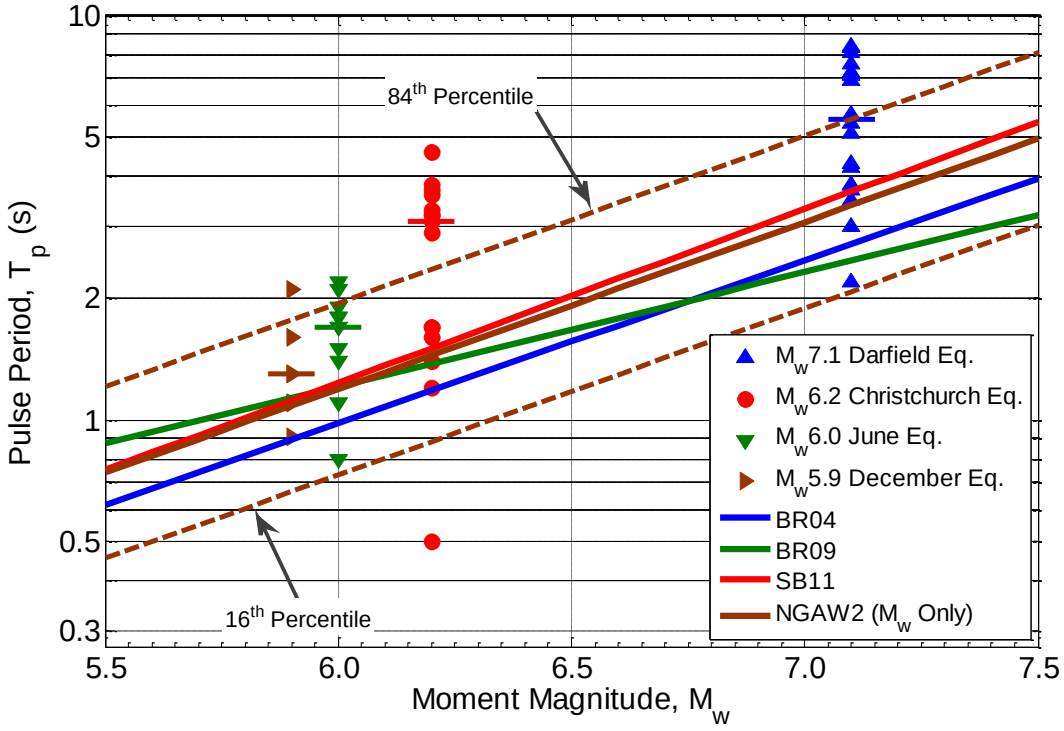

Figure 6.24: Comparison of the observed directivity pulse periods in the Canterbury earthquakes with the median predictions of models developed in both, previous (BR04, BR09 and SB11) and present (NGAW2) studies.

Table 6.7 provides a summary of the predicted and observed median pulse periods corresponding to all events:

Table 6.7: Summary of the median directivity pulse periods observed in four events from the Canterbury earthquake and the corresponding predictions from several empirical models from both, previous and present studies.

Median Pulse Period, T_p (s)						
Event	**Observed Median**	**BR04**	**BR09**	**SB11**	**NGAW2 (M_w only)**	**NGAW2 (M_w and λ only)**
04/09/2010	5.6	2.7	2.5	3.7	3.4	3.9
22/02/2011	3.1	1.2	1.4	1.5	1.4	1.5
13/06/2011	1.7	1.0	1.2	1.2	1.2	1.4
23/12/2011	1.3	0.9	1.1	1.1	1.1	1.1

In a manner similar to Figure 6.4, the lognormal CDF associated with all models is compared with the EDFs of the observed pulse period in Figure 6.25. It should be noted that the distributions corresponding to the NGAW2 model developed considering magnitude and rake angle dependence are also included in the comparisons. The trends discussed above are further elucidated with: (i) similarities between the predictions of the NGAW2 and SB11 models; and (ii) significant under-prediction of the observed pulse periods in the Darfield and

Christchurch events being the two outstanding features. The fact that improved predictions cannot be obtained using an up-to-date larger database for the latter events is effective in highlighting the importance of region-specific features on directivity characteristics.

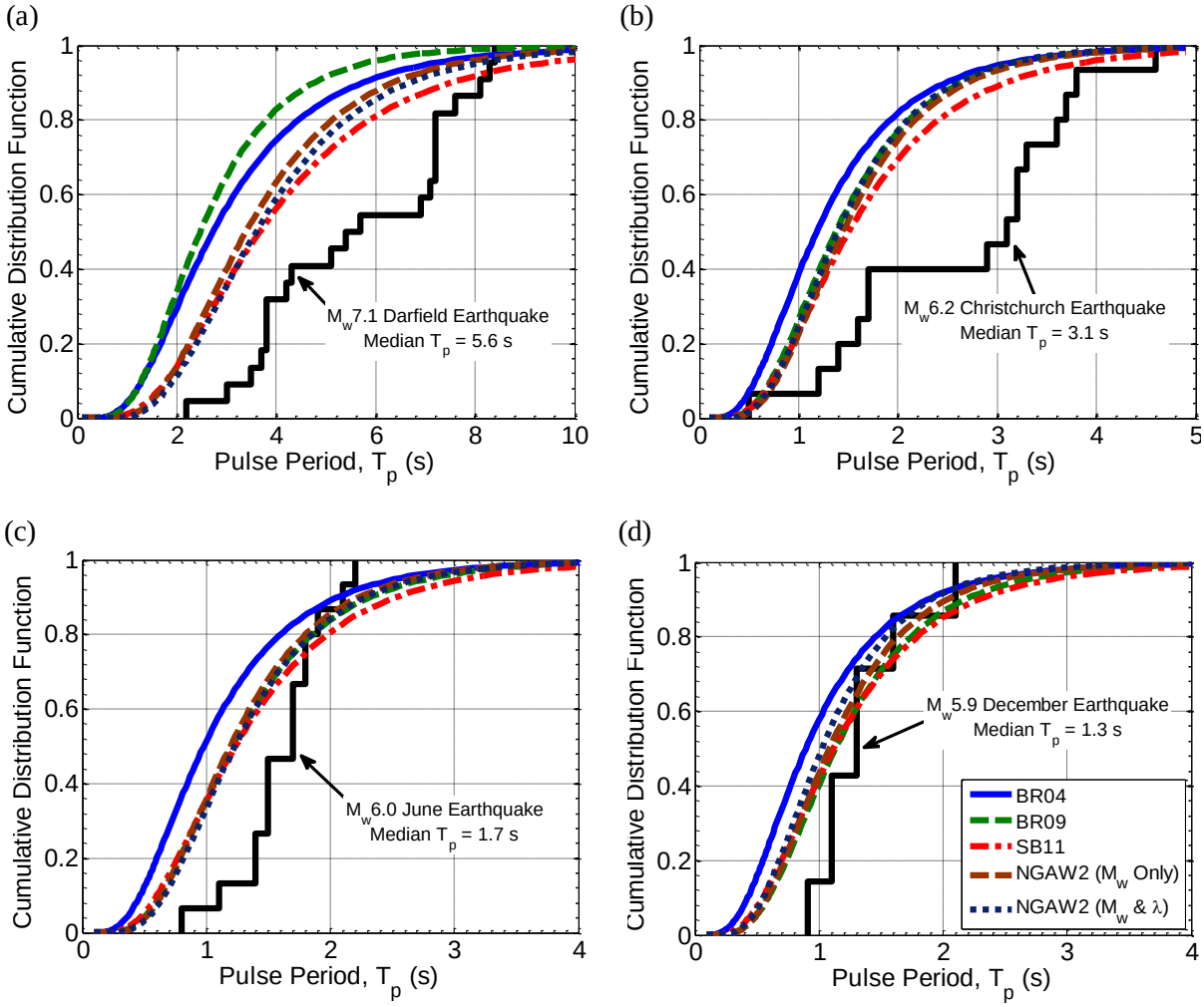

Figure 6.25: Comparison of the cumulative distribution functions associated with the observed directivity pulse periods from (a) 4 September 2010 M_w7.1 Darfield earthquake; (b) 22 February 2011 M_w6.2 Christchurch earthquake; (c) 13 June 2011 M_w6.0 earthquake; and (d) 23 December 2011 M_w5.9 earthquake with empirical models developed in both, previous (BR04, BR09 and SB11) and present (NGAW2) studies.

A qualitative comparison between the PGVs associated with forward-directivity ground motions in the Canterbury earthquakes and median predictions associated with the models developed in previous research, as well as the NGAW2 model developed in the present study is carried out in Figure 6.26. The S98 and AK00 models are excluded on the basis that they are outdated and not appropriate for distances greater than 10 km. For the purposes of clarity, the 16th and 84th percentiles of only the NGAW2 model are shown. It is worth recalling from the previous discussion that the BR04, CY08 and BR09 model capture the short-moderate source-to-distance dependence with good accuracy. However, due to the

faster attenuation of the predicted amplitudes with distance, the peak velocities in the Darfield earthquake remain notably under-predicted. The NGAW2 model provides similar predictions of PGV to its predecessors between $1 \leq R_{rup} \leq 10$ km. Due to the more gradual attenuation of pulse amplitudes at larger distances, especially for R_{rup} > 15 km, better estimates of the observed peak velocities are obtained using the NGAW2 model.

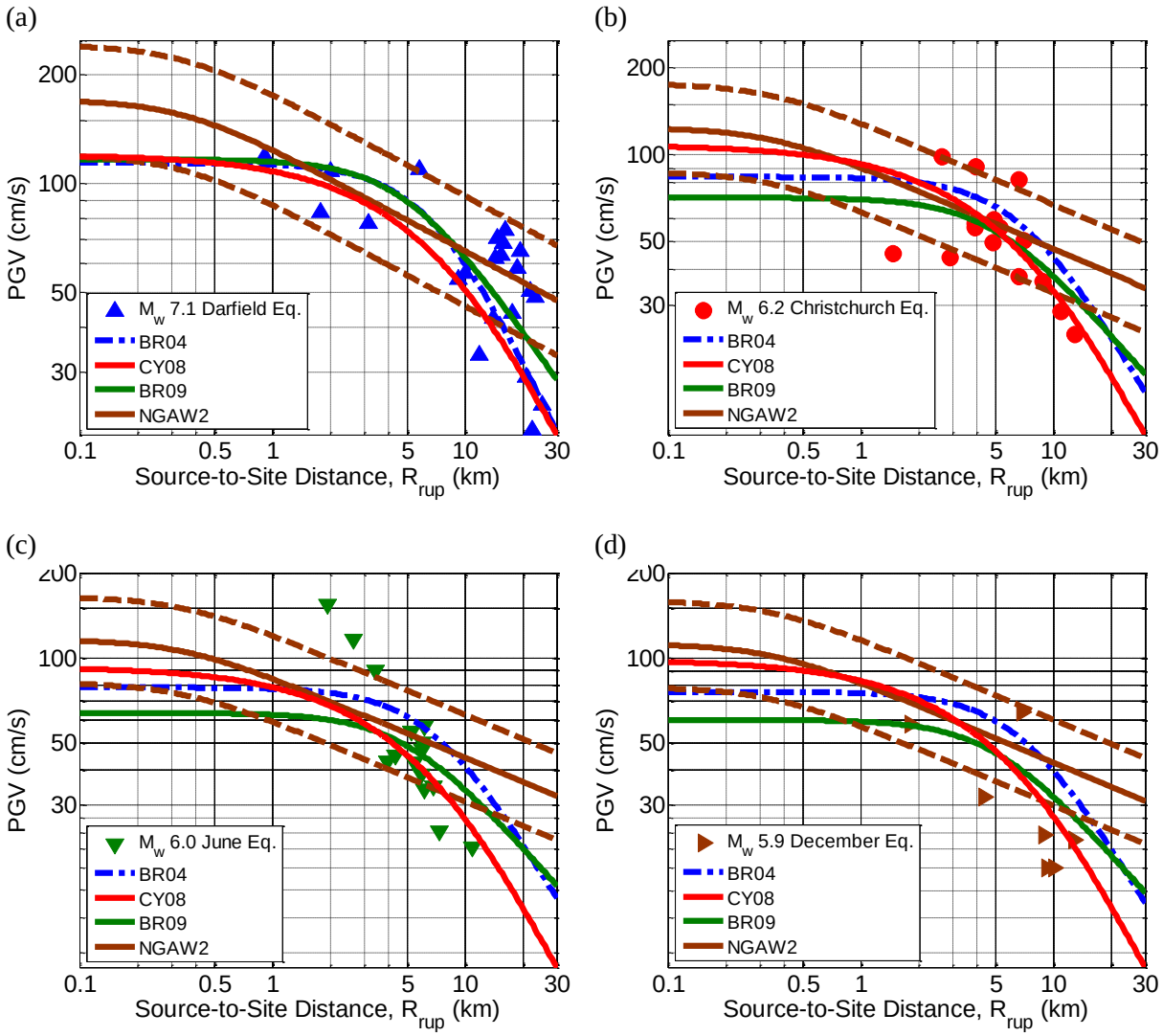

Figure 6.26: Comparison of the observed values of PGV in forward-directivity ground motions from (a) 4 September 2010 M_w7.1 Darfield earthquake; (b) 22 February 2011 M_w6.2 Christchurch earthquake; (c) 13 June 2011 M_w6.0 earthquake; and (d) 23 December 2011 M_w5.9 earthquake with the median predictions from empirical models developed in both, previous (BR04, CY08 and BR09) and present (NGAW2) studies. Note that the PGVs are plotted as a function of source-to-site distance. Also shown in the four plots are the 16th and 84th percentiles of the PGVs predicted by the NGAW2 model.

The intra-event residuals for the observed pulse amplitudes using all models are illustrated as a function of source-to-site distance in Figure 6.27. As before, the non-parametric mean and 98% confidence interval are employed to identify statistically significant biases in the prediction models. The BR04, CY08 and BR09 models do not demonstrate any notable trends with respect to distance, as discussed previously in Section 6.3.3. On the other hand, the mean residual using the NGAW2 model in Figure 6.27d demonstrates a positive bias for $R_{rup} \leq 5$ km and a negative bias (i.e. over-prediction) at greater distances. Since the confidence interval of the mean residual includes the zero mean for all distances, it can be deduced that the model is effectively unbiased over the entire distance range. Moreover, it can be appreciated from Figure 6.26 that the slower attenuation of the observed peak velocities is well-predicted by the NGAW2 model.

Figure 6.28 illustrates the normalised inter-event term (η_i) obtained using the BR04, CY08, BR09 and NGAW2 models as a function of M_w corresponding to the four considered events. It should be recalled that η_i essentially represents the overall bias of the empirical models with respect to the observations. The trends with respect to the models developed in previous research were discussed in Section 6.3.3. It can be observed from Figure 6.28 that the NGAW2 model provides over-predictions for all four events. This can be partly attributed to the slower attenuation of PGV predicted by the model. While the inter-event terms using the NGAW2 model are systematically lower for all events in relation to the BR09 and CY08 models, they are comparable to those obtained using the BR04 model for the Christchurch, June and December earthquakes.

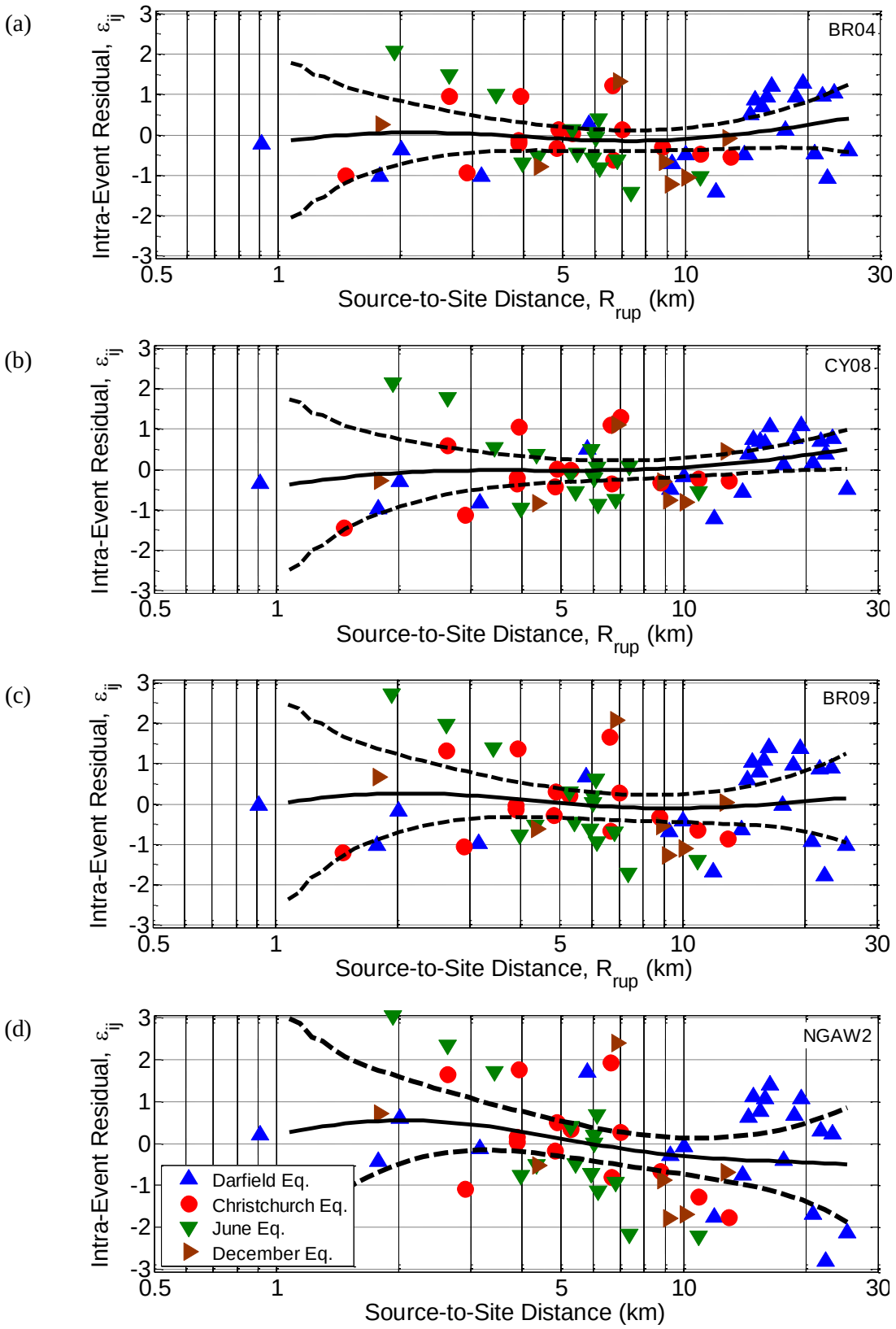

Figure 6.27: Intra-event residuals of PGV associated with forward-directivity ground motions in the Canterbury earthquakes as a function of source-to-site distance using models developed in: (a)-(c) previous research (BR04, CY08 and BR09); and (d) the present study using pulse-like ground motions in the NGA-West2 database.

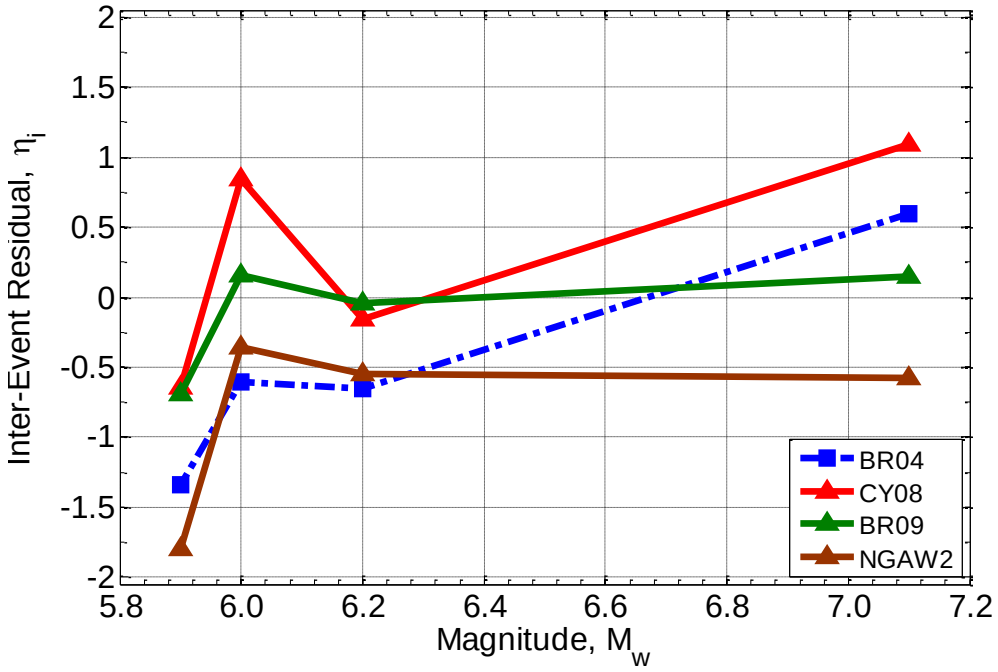

Figure 6.28: Inter-event residuals of PGV associated with the 4 September 2010 M_w7.1 Darfield; 22 February 2011 M_w6.2 Christchurch; 13 June 2011 M_w6.0; and 23 December 2011 M_w5.9 earthquakes using both, existing empirical models (BR04, CY08 and BR09) and the NGAW2 model developed in the present study..

6.5 Conclusions

This chapter has examined the predictive capabilities of several existing empirical models for the pulse period and amplitude (defined by the peak ground velocity, PGV) using observations from the Canterbury earthquakes. Although favourable comparisons between observed and predicted pulse periods were obtained for the 13 June 2011 M_w6.0 and 23 December 2011 M_w 5.9 earthquakes, significant under-predictions resulted for the 4 September 2010 M_w7.1 Darfield and 22 February 2011 M_w6.2 Christchurch events. The elongation in observed pulse periods was inferred as being a result of both, the effect of nonlinear site response and influence of the Canterbury basin. In contrast, the empirical equations for PGV generally provided accurate predictions for source-to-site distances between 1 km and 10 km, but notable under-predictions were seen at greater distances.

In an effort to determine whether improved predictions of the pulse period and amplitude could be obtained using a larger dataset, pulse-like ground motions from the up-to-date NGA West2 (NGAW2) database were utilised to develop revised empirical models. For the pulse period, models were developed considering: (i) earthquake magnitude dependence only; (ii) magnitude and rake angle dependence and (iii) magnitude, rake angle and site class

dependence. Model (ii), in particular, is a novel contribution because the effect of fault type on pulse period is explicitly modelled in the relationship. More importantly, predictions of the model were found to be consistent with observations from previous earthquakes, with estimates of pulse periods for strike-slip events being larger than reverse-faulting events. Similarly, predictions provided by model (iii) were also consistent with empirical observations, with pulse periods for soil sites being higher than those for rock sites. A model for PGV using a simple functional form (with magnitude and distance dependence only), initially proposed by Bray & Rodriguez-Marek (2004), was also developed using NGAW2 pulse-like ground motions recorded within source-to-site distances of 20 km.

Upon comparing the predictions of the revised models with observations from the Canterbury earthquakes, it was found that the use of a larger database does not necessarily translate to better estimates of the pulse periods, especially for the Darfield and Christchurch earthquakes. On a positive note, the NGAW2 model for PGV provided a more appropriate attenuation of the pulse amplitude in comparison to its predecessors, thereby resulting in improved predictions at distances greater than 10 km for the Darfield event.

6.6 References

Abrahamson, N. A., & Youngs, R. R. (1992). A stable algorithm for regression analyses using the random effects model. *Bulletin of the Seismological Society of America*, **82**(1):505–510.

Alavi, B., & Krawinkler, H. (2000). Consideration of near-fault ground motion effects in seismic design. In *Proceedings of the 12th World Conference on Earthquake Engineering*. Auckland, New Zealand. Retrieved from http://www.iitk.ac.in/nicee/wcee/article/2665.pdf

Ancheta, T. D., Darragh, R. B., Stewart, J. P., Seyhan, E., Silva, W. J., Chiou, B. S., … Boore, D. M. (2013). *PEER NGA-West2 Database*. Retrieved from http://peer.berkeley.edu/publications/peer_reports/reports_2013/webPEER-2013-03-Ancheta.pdf

Ang, A. H.-S., & Tang, W. H. (2007). *Probability Concepts In Engineering* (2nd ed.). New York: Wiley.

Baker, J. W. (2007). Quantitative classification of near-fault ground motions using wavelet analysis. *Bulletin of the Seismological Society of America*, **97**(5):1486–1501. doi:10.1785/0120060255

Beyer, K., & Bommer, J. J. (2006). Relationships between Median Values and between Aleatory Variabilities for Different Definitions of the Horizontal Component of Motion. *Bulletin of the Seismological Society of America*, **96**(4A):1512–1522. doi:10.1785/0120050210

Boore, D. M. (2006). Orientation-Independent Measures of Ground Motion. *Bulletin of the Seismological Society of America*, **96**(4A):1502–1511. doi:10.1785/0120050209

Bradley, B. A. (2012). Strong ground motion characteristics observed in the 4 September 2010 Darfield, New Zealand earthquake. *Soil Dynamics and Earthquake Engineering*, **42:**32–46. doi:10.1016/j.soildyn.2012.06.004

Bradley, B. A., & Cubrinovski, M. (2011). Near-source Strong Ground Motions Observed in the 22 February 2011 Christchurch Earthquake. *Seismological Research Letters*, **82**(6):853–865. doi:10.1785/gssrl.82.6.853

Bradley, Brendon A. (2010). *NZ-Specific Pseudo-Spectral Acceleration Ground Motion Prediction Equations Based on Foreign Models* (Research Report No. 2010-03) (p. 316). Department of Civil and Natural Resources, University of Canterbury.

Bray, J. D., & Rodriguez-Marek, A. (2004). Characterization of forward-directivity ground motions in the near-fault region. *Soil Dynamics and Earthquake Engineering*, **24**(11):815–828. doi:10.1016/j.soildyn.2004.05.001

Bray, J. D., Rodriguez-Marek, A., & Gillie, J. L. (2009). Design ground motions near active faults. *Bulletin of the New Zealand Society for Earthquake Engineering*, **42**(1):1–8.

Chiou, B., Darragh, R., Gregor, N., & Silva, W. (2008). NGA Project Strong-Motion Database. *Earthquake Spectra*, **24**(1):23–44. doi:10.1193/1.2894831

Chiou, B. S. J. (2005). NGA Flatfile Documentation.

Chiou, B.-J., & Youngs, R. R. (2008). An NGA Model for the Average Horizontal Component of Peak Ground Motion and Response Spectra. *Earthquake Spectra*, **24**(1):173–215. doi:10.1193/1.2894832

Kutner, M. H., Nachtsheim, C. J., Li, W., & Neter, J. (2005). *Applied linear statistical models* (5th ed.). Boston: McGraw-Hill Irwin.

MATLAB (Version 7.10.0). (2010). Natick, Massachusetts: The MathWorks Inc.

Mavroeidis, G. P., & Papageorgiou, A. S. (2003). A mathematical representation of near-fault ground motions. *Bulletin of the Seismological Society of America*, **93**(3):1099–1131.

Rodriguez-Marek, A., & Bray, J. D. (2006). Seismic site response for near-fault forward directivity ground motions. *Journal of geotechnical and geoenvironmental engineering*, **132**(12):1611–1620.

Ruppert, D., Sheather, S. J., & Wand, M. P. (1995). An effective bandwidth selector for local least squares regression. *Journal of the American Statistical Association*, **90**(432):1257–1270.

Sasani, M., & Bertero, V. V. (2000). Importance of severe pulse-type ground motions in performance-based engineering: historical and critical review. In *Proceedings of the 12th World Conference on Earthquake Engineering*. Auckland, New Zealand. Retrieved from http://www1.coe.neu.edu/~sasani/pubs/C2.pdf

Shahi, S., & Baker, J. W. (2010). Regression models for predicting the probability of near-fault earthquake ground motion pulses, and their period. In *Proceeding of 11th International conference on applications of statistics and probability in civil engineering*. Retrieved from http://shreyshahi.com/papers/Shahi%20Baker%20(2010)%20ICASP.pdf

Shahi, S. K. (2013, January). *A probabilistic framework to include the effects of near-fault directivity in seismic hazard assessment*. Stanford University, Stanford.

Shahi, S. K., & Baker, J. W. (2011). An empirically calibrated framework for including the effects of near-fault directivity in probabilistic seismic hazard analysis. *Bulletin of the Seismological Society of America*, **101**(2):742–755. doi:10.1785/0120100090

Somerville, P. (1998). Development of An Improved Representation of Near-Fault Ground Motions. In *SMIP98 Seminar on Utilization of Strong-Motion Data* (pp. 1–20). Woodward-Clyde, Pasadena, California.

Somerville, P., Irikura, K., Graves, R., Sawada, S., Wald, D., Abrahamson, N., … Kowada, A. (1999). Characterizing crustal earthquake slip models for the prediction of strong ground motion. *Seismological Research Letters*, **70**(1):59–80.

Wasserman, L. (2006). *All of Non-Parametric Statistics*. New York: Springer.

Wells, D. L., & Coppersmith, K. J. (1994). New empirical relationships among magnitude, rupture length, rupture width, rupture area, and surface displacement. *Bulletin of the Seismological Society of America*, **84**(4):974–1002.

7 Explicit Consideration of Near-Fault Directivity Effects in NZ-specific Probabilistic Seismic Hazard Analysis

7.1 Overview

Conventional probabilistic seismic hazard analysis (PSHA) does not explicitly account for the effects of pulse-like ground motions, which are usually observed in the near-fault region and typically caused by forward-directivity effects. The incorporation of this physical phenomenon in the PSHA framework has been considered in the past by several researchers. A brief review of the proposed approaches is firstly carried out in this chapter. This is followed by a detailed description of the adopted approach to account for directivity effects in NZ-specific PSHA. Example applications of the procedure are used to quantify the directivity amplification of SA for wide range of periods and at several exceedance probabilities. In particular, generic locations in Christchurch and Otira with different site class conditions are considered, and the implications of the directivity phenomenon for each region are addressed in detail.

7.2 Tectonic setting of New Zealand

New Zealand lies on the boundary of the Pacific and Australian plates, as illustrated in Figure 7.1. Its active tectonics are summarised as follows (Bradley & Cubrinovski, 2011; Gledhill et al., 2011):

- Oblique subduction of the Pacific plate beneath the Australian plate along the Hikurangi trough in the North Island.
- Oblique subduction of the Australian plate beneath the Pacific plate along the Puysegur trench in the southwest of the South Island.
- The plate boundary between the two subduction zones is characterised by continental convergence. At the surface, this boundary is demarcated by the 650-km long right-lateral strike-slip Alpine fault, which accommodates ~70-75% of the ~40 mm/yr plate motion (DeMets et al., 2010)
- Oblique, right-lateral slip along numerous other crustal faults of the axial tectonic belt between the Fiordland and Hikurangi subduction zones.

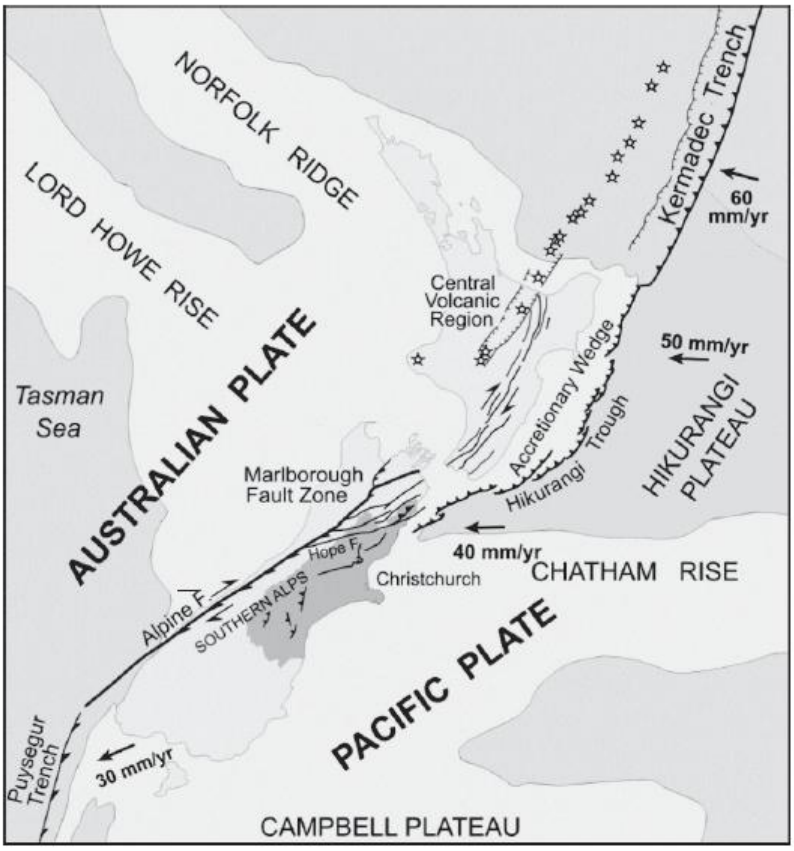

Figure 7.1: Tectonic setting of New Zealand (after Bradley & Cubrinovski, 2011).

Although the seismicity of NZ is dominated by the two subduction zones and the Alpine fault, it is noted that there are over 500 identified active[1] faults which pose varying levels of hazard. A number of significant earthquakes have occurred along these active faults since European settlement including the 1855 M_w 8.2 Wairarapa (Wairarapa Fault), 1888 M_w 7.1 North Canterbury (Hope Fault), 1929 M_w 7.0 Arthur's Pass (Poulter Fault), 1968 M_w 7.1 Inangahua (Glasgow-Inangahua Fault and Rotokohu Fault traces), and more recently, the 2010-11 Canterbury earthquakes (refer to Chapter 3 and references therein for further details), among many others (GeoNet, 2011).

7.3 NZ earthquake rupture forecast

The consideration of seismic hazard at a given site requires: (i) an earthquake rupture forecast (ERF) or seismicity model; and (ii) a ground motion prediction model which provides the expected level of ground motion (albeit with uncertainty) due to the occurrence of an earthquake (Kramer, 1996; McGuire, 2004). In particular, an ERF provides the geographic location, characteristics (i.e. fault geometry, faulting style, magnitude, slip distribution), and frequency of occurrence of all earthquakes in the region of interest. This section provides a brief description of the updated ERF for NZ developed by a multi-disciplinary team of earthquake geologists, seismologists and engineering seismologists in 2010. The results of this update were recently published by Stirling et al. (2012) and the ERF has been included by Bradley et al. (2012) in the OpenSHA framework (Field et al., 2003), an open-source code for seismic hazard analysis which is also used herein.

The seismicity of NZ is represented in the ERF using a combination of fault-based sources and distributed seismicity. Figure 7.2 provides a comparison between the distribution of fault sources in the previous (i.e. Stirling et al., 2002) and current versions of the ERF. According to Stirling et al. (2012), over 200 new onshore and offshore fault sources have been added to the updated ERF, based on paleoearthquake information collected using trenching and seismic-reflection profiles, respectively. It is noted that a total of 536 fault sources exist in the current ERF.

[1] A fault which has moved one or more times in the last 10,000 years and is likely to move in the future (USGS, 2012). There are several other definitions for an active fault which have been proposed in the past by various institutions and researchers. Interested readers are referred to Kramer (1996) and references therein for further information.

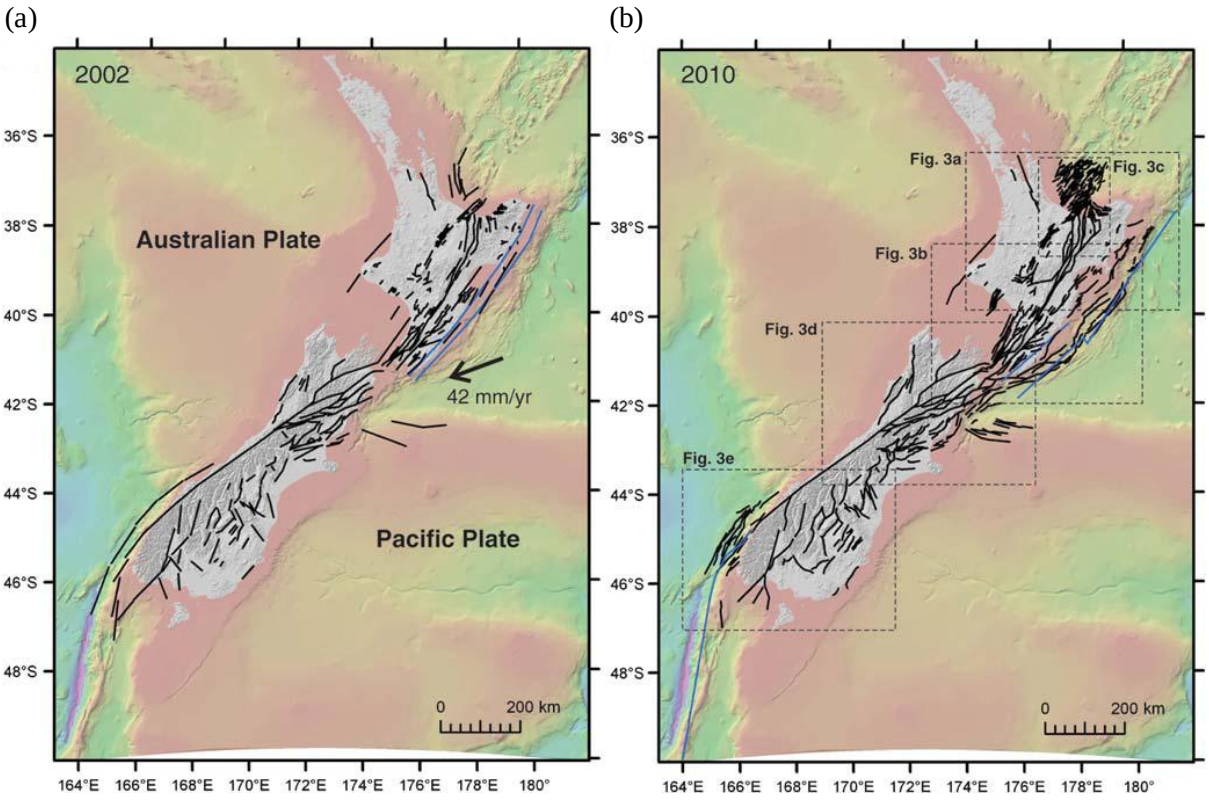

Figure 7.2: Comparison of the active fault sources in the older and more recent versions of the New Zealand Earthquake Rupture Forecast published by: (a) Stirling et al. (2002); and (b) Stirling et al. (2012), respectively (after Stirling et al., 2012).

Several important aspects of the fault-based seismicity model are listed below and a more detailed discussion can be found in Stirling et al. (2012):

- All fault sources are modelled as discrete fault planes characterised by geometric parameters (including the length (L), top of rupture extent (D_{top}), bottom of rupture extent (D_{bottom}) and dip angle (δ)) and deformation parameters (slip rate ($\dot{s}$) and coupling coefficient (c)).
- The characteristic earthquake recurrence law (Schwartz & Coppersmith, 1984; Youngs & Coppersmith, 1985) is used to model the fault sources. This model is based on the hypothesis that individual faults repeatedly generate earthquakes of similar (within about one-half magnitude units) size, also known as 'characteristic earthquakes', at or near their maximum magnitude (M_{max}) (Schwartz & Coppersmith, 1984).
- The maximum magnitude (M_{max}) of the fault sources is calculated using moment magnitude-area ($M_w - A$) scaling relationships developed by Hanks & Bakun (2002) (global plate boundary strike-slip faults i.e. Alpine Fault),

Villamor et al. (2007) (volcanic and rift environments), Stirling et al. (2007) (all other crustal faults) and Strasser et al. (2010) (subduction interface events).

For a known fault source, the fault-based model utilises the dimensions and slip rate to define the magnitude (i.e. M_{max}) and frequency (λ) of the characteristic earthquake. The occurrence of earthquakes with magnitudes smaller than the characteristic magnitude is assumed to be modelled appropriately by distributed background sources (Stirling et al., 2012).

It is important to realise the fact that the fault-based seismicity model only accounts for faults capable of producing large magnitude ($M_w \geq 7.0$) earthquakes. Such faults typically have high slip rates and are easily identified using techniques such as field mapping and paleoseismic trenching (Kramer, 1996, p. 109). However, faults which are only capable of producing smaller magnitude earthquakes ($M_w < 6.5$) may not have a surface expression, and hence cannot be mapped based on conventional methods (Stirling et al., 2007). Similarly, faults with relatively slower slip rates (e.g. the Greendale fault which was previously unknown and ruptured in the 4 September 2010 M_w7.1 Darfield earthquake has a minimum recurrence interval of 16,000 years, according to Stirling et al. (2012)) may not have ruptured in the historical settlement time of a region. As a result, the background seismicity model forms an integral part of the ERF in accounting for the possible occurrence of earthquakes on unknown faults.

The magnitude-frequency estimates for the background seismicity model in the NZ ERF are based on the Gutenberg-Richter (Gutenberg & Richter, 1944) distribution of historical seismicity (Stirling et al., 2012). All background sources are treated as point-sources located at depths of 10, 30, 50, 70 and 90 km. The background seismicity model accounts for the possibility of moderate-to-large magnitude earthquakes in regions between mapped faults, as illustrated in Figure 7.3. A minimum magnitude of M_w = 5.0 is assigned to each point-source and a uniform maximum magnitude of M_{cutoff} = 7.2 is applied to all regions, except the Taupo Volcanic Zone where M_{cutoff} = 6.5.

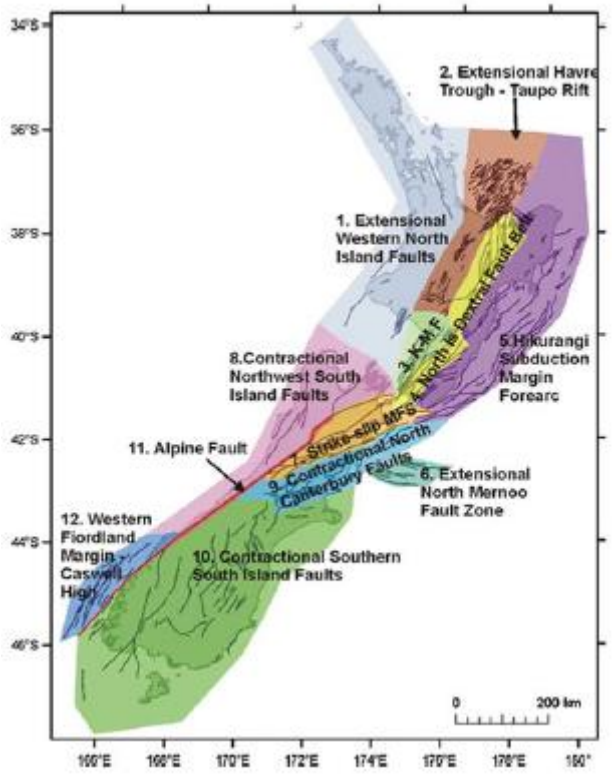

Figure 7.3: Seismotectonic background seismicity regions in the 2010 New Zealand earthquake rupture forecast (after Stirling et al., 2012).

The probability of earthquake occurrence over a given time period is calculated using the Poisson distribution (Ang & Tang, 2007) and is adopted due to its simplicity in the NZ ERF. This implies that the occurrence of earthquakes is a random process, which is clearly inconsistent with the implications of elastic rebound theory. The latter theory suggests that the occurrence of future earthquakes on a fault or fault segment should not be independent of past seismicity (Kramer, 1996). Since earthquakes occur to release strain energy which builds up over an extended period of time, then the occurrence of a large magnitude earthquake should significantly reduce the probability of another large earthquake occurring from the same source immediately thereafter. The Poisson model, however, does not have a 'memory' of the time, size, or location of any past seismicity. Time-dependent (i.e. non-Poissonian) models could be used as an alternative to account for the temporal occurrence of earthquakes on fault sources. Such models are useful in characterising the distribution of earthquake recurrence for large faults with high slip rates (e.g. Alpine Fault in NZ or the San Andreas Fault in California, USA which are major plate boundaries), as these type of faults are likely to behave largely in isolation, due to their relative dominance of the overall plate deformation slip budget (Berryman et al., 2012), and hence follow the basic principles of elastic rebound theory. Minor faults in a fault system are more likely to rupture due to stress transfer from

previous earthquakes. For example, the 4 September 2010 M_w7.1 Darfield earthquake caused a stress transfer to the wider Canterbury region, thereby triggering notable smaller magnitude events such as the 22 February 2011 M_w6.2 Christchurch earthquake (Bradley, personal communication, 2012). Another limitation of the use of time-dependent models is that the last rupture date may not be known for many faults. Hence, the Poisson model is more practical for routine seismic hazard assessments (Kramer, 1996).

7.4 Review of conventional probabilistic seismic hazard analysis

The main purpose of carrying out a probabilistic seismic hazard analysis (PSHA) is to estimate the annual rate of exceedance of a certain ground motion intensity measure, $\lambda(IM > im)$ at the site of interest (Kramer, 1996; McGuire, 2004). The analysis is conducted by combining: (i) all potential earthquake sources and their likelihood of occurrence (i.e. from the ERF); and (ii) the distribution of ground motion produced by the earthquake sources should they occur (i.e. from the ground motion prediction model). A summary of the main steps required in calculating the mean annual rate of exceeding a given intensity measure ($IM = im$) within the PSHA framework are given below:

1. For each potential earthquake rupture (Rup_i i.e. magnitude, source-to-site distance etc.), the corresponding rate of exceedance is obtained from the magnitude-frequency distribution corresponding to the respective earthquake source in the ERF.
2. The distribution of the ground motion intensity measure under consideration is computed for each earthquake rupture scenario, $f(IM|Rup_i)$, using a ground motion prediction equation (GMPE). From the distribution, the probability that $IM > im$, $P(IM > im|Rup_i)$, can then be obtained.
3. The mean annual rate of occurrence of the earthquake rupture scenario, $\lambda(Rup_i)$, is multiplied with $P(IM > im|Rup_i)$ to obtain the mean annual rate at which Rup_i occurs and produces ground motion with $IM > im$.
4. By considering all possible earthquake ruptures in the ERF, N_{rup}, the total rate of $IM > im$ can be obtained using Equation (7.1):

$$\lambda(IM > im) = \sum_{i=1}^{N_{rup}} P(IM > im|Rup_i)\, \lambda(Rup_i) \tag{7.1}$$

In the PSHA methodology outlined above, it is assumed that each earthquake rupture is independent, thereby allowing the summation of the mean annual rate of $IM > im$ over all potential earthquake ruptures (McGuire, 2004). By repeating the four steps for a range of IM values, a seismic hazard curve can be constructed, as illustrated in Figure 7.4 for peak ground acceleration (PGA):

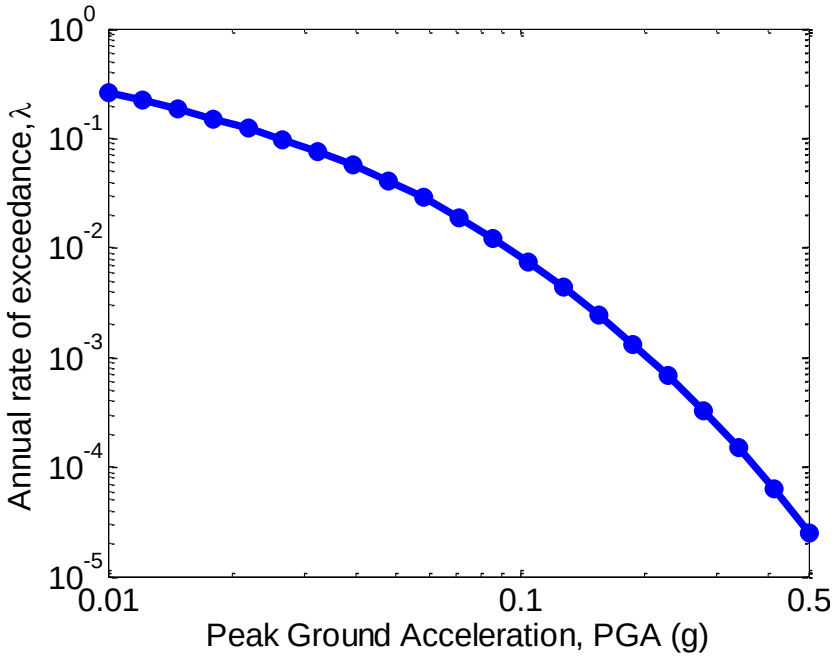

Figure 7.4: Example seismic hazard curve for peak ground acceleration, PGA.

As mentioned previously, it is conventional to assume that earthquake occurrence follows a Poisson process. This allows the probability of exceedance of a ground motion intensity measure, $P(IM > im)$, to be computed from the mean annual rate of exceedance using Equation (7.2) (Ang & Tang, 2007) for a given time period, T:

$$P(IM > im) = 1 - \exp(-\lambda T) \tag{7.2}$$

where exp () is the exponential function. Hence, if a structure is to be designed for a probability of exceedance of 10% in 50 years (a value typically specified by seismic design standards such as NZS1170.5:2004 (Standards New Zealand, 2004) for ordinary structures), the equivalent annual rate of exceedance, $\lambda = 2.1*10^{-3}$. It is important to note that the recurrence interval or return period, R, is also commonly used to quantify the likelihood of occurrence, as shown in Equation (7.3):

$$R(IM > im) = 1/\lambda(IM > im) \tag{7.3}$$

For example, a return period of 500 years corresponds to an annual rate of exceedance of $\lambda(IM > im)$ = 0.002. From the example seismic hazard curve in Figure 7.4, this value corresponds to a PGA = 0.165g.

Another useful way to interpret and visualise the results of PSHA is to construct a response spectrum with the value of each spectral ordinate having the same exceedance probability, commonly referred to as the uniform hazard spectrum (UHS). The procedure is outlined below and illustrated in Figure 7.5:

1. The PSHA procedure described previously is repeated for pseudo-spectral acceleration (SA) at several vibration periods. Figure 7.5a and Figure 7.5b illustrate example seismic hazard curves obtained for SA(0.2 s) and SA(1 s).
2. For the annual exceedance rate of interest ($\lambda = 2.1*10^{-3}$ or R = 475 years for the example in Figure 7.5), the corresponding SA values are obtained from the seismic hazard curves and plotted as a function of their respective vibration periods, as shown in Figure 7.5c.

An important point to note is the fact that each point on the UHS is obtained from separate seismic hazard analyses that are independent from each other. As will be demonstrated subsequently, using a process known as deaggregation, the earthquake rupture scenarios which dominate the seismic hazard vary from one vibration period to another. This implies that SA values on the UHS have different dominant earthquakes and hence, a single earthquake rupture should not be expected to produce a ground motion similar to the UHS over a wide range of periods (Bradley, 2012).

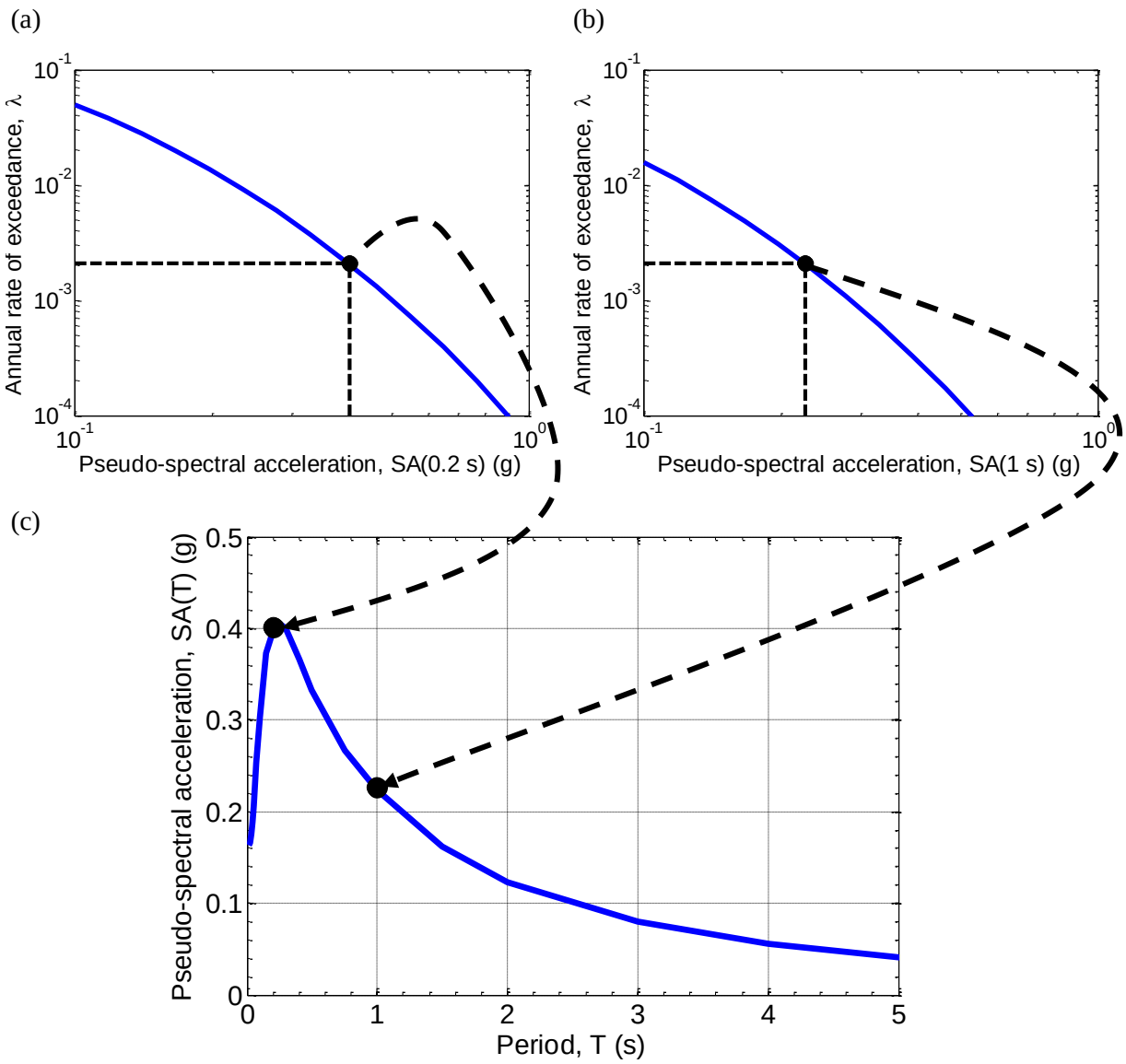

Figure 7.5: Construction of the uniform hazard curve based on the results of probabilistic seismic hazard analysis for a return period of 475 years. Panels (a) and (b) illustrate the seismic hazard curve for SA(0.2 s) and SA(1 s), respectively. Panel (c) shows the uniform hazard spectrum generated based on a number of hazard analyses similar to (a) and (b) for various vibration periods.

One of the main advantages of PSHA is the fact that it considers all possible earthquake sources in computing the seismic hazard for a particular site. Since the seismic hazard curve represents a probability-based weighted aggregate of all potential earthquake rupture scenarios, an obvious question to ask is: "which earthquake rupture scenario is most likely to cause $IM > im$?" (Baker, 2008). A procedure known as deaggregation (or disaggregation) (e.g. Bazzurro & Cornell, 1999) can be used to determine the percentage contribution of each earthquake source to the total hazard. More importantly, information regarding the dominant earthquake scenarios can be obtained through the procedure.

Equation (7.4) illustrates the application of Bayes Theorem (Ang & Tang, 2007) to carry out the deaggregation:

$$P(Rup_i|IM > im) = \frac{\lambda(IM > im|Rup_i)}{\lambda(IM > im)} = \frac{P(IM > im|Rup_i)\lambda(Rup_i)}{\sum_{i=1}^{N_{rup}} P(IM > im|Rup_i)\lambda(Rup_i)} \quad (7.4)$$

where $P(Rup_i|IM > im)$ represents the probability of Rup_i causing a ground motion with $IM > im$ at the site, and the three terms on the right-hand side of Equation (7.4) were previously described. Deaggregation plots are typically used to depict the percentage contribution of each earthquake source (represented by moment magnitude and source-to-site distance) to the seismic hazard. Figure 7.6 provides an example of such plots for Christchurch at a return period of 475 years for SA(0.2 s) and SA(1 s). It can be observed that the sources which contribute the most to the hazard are markedly different for the two intensity measures, as asserted previously. The 475-year SA(0.2 s) is largely controlled by small-to-moderate magnitude earthquakes at distances less than 50 km. In the case of SA(1.0 s), the hazard is dominated by moderate-to-large magnitude earthquakes which occur over a wide range of distances. It should also be noted that the results of deaggregation are commonly used in ground motion selection procedures (e.g. Baker, 2011; Bradley, 2012).

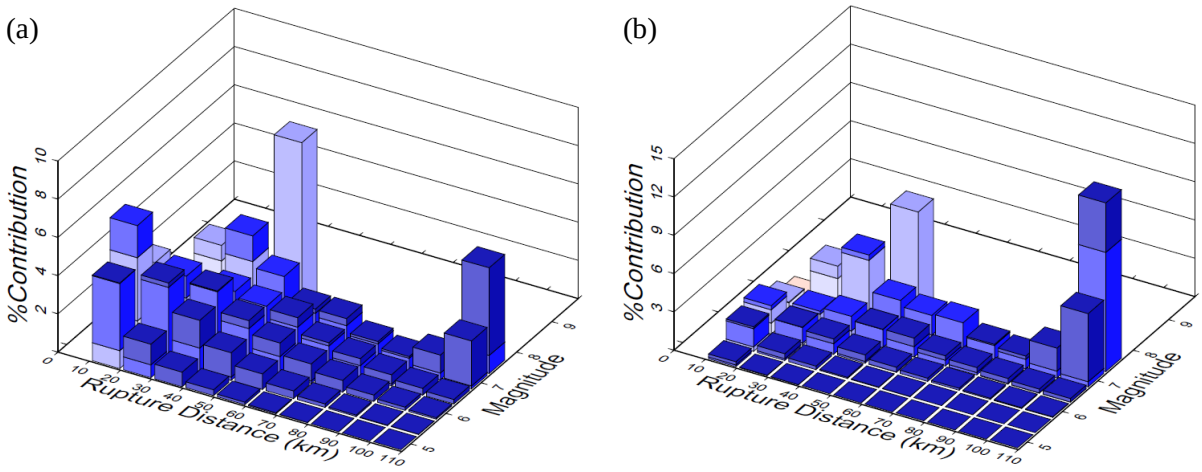

Figure 7.6: Illustration of the seismic hazard deaggregation for Christchurch (return period of 475 years): (a) SA(0.2 s); and (b) SA (1 s). Note that the deaggregation is dependent on the intensity measure and annual probability of exceedance (10% in 50 years in this case).

7.5 Framework for incorporating directivity effects in PSHA

It is important to recall that the directivity pulse, which is typically observed in the fault-normal component of the velocity time-series, causes an amplification of SA within a narrow range of periods surrounding the pulse period (T_p). As discussed previously in Chapter 5, conventional GMPEs used to perform PSHA do not explicitly account for the effects of pulse-like ground motions. This could result in an under-estimation of the seismic hazard at near-fault sites where directivity effects are expected to occur. Based on this realisation, researchers have focused their efforts on developing empirical directivity models which can be used to modify the predictions of GMPEs. In particular, models which monotonically scale the predicted spectral amplitudes over a wide range of periods are classified as 'broadband' (e.g. Rowshandel, 2010; Somerville et al., 1997; Spudich & Chiou, 2008), whereas those which predict an amplification in the vicinity of the pulse period are classified as 'narrowband' (e.g. Shahi & Baker, 2011; Somerville, 2003). These models form the basis of approaches which have been proposed in the past to incorporate the effects of near-fault directivity in PSHA calculations. The following sections provide a brief overview of these approaches followed by a description of the methodology adopted herein for NZ-specific PSHA.

7.5.1 Proposed approaches in previous research

7.5.1.1 Abrahamson (2000)

As mentioned in Chapter 2, the importance of including near-fault directivity in conventional PSHA was first highlighted by Abrahamson (2000). A modified version of the broadband model of Somerville et al. (1997) was adopted to quantify the effects on the average horizontal (geometric mean) and fault-normal components of SA. It should be noted that the level of amplification/de-amplification predicted by the model is solely dependent on the source-to-site geometry, thereby requiring the location of the hypocentre location on the causative fault to be known *a priori*. Since this is not possible, Abrahamson (2000) assigned a uniform probability distribution (i.e. the probability of rupture initiation on any given fault location is assumed to be equal) to the hypocentre location. Thus, for each fault source, the summation of the mean annual rate over all possible earthquake rupture scenarios (refer to Equation (7.1)) includes the hypocentre location in addition to typical parameters such as magnitude and source-to-site distance, among others. Although the proposed framework was

developed only for strike-slip faults, its extension to non strike-slip faults is similar in principle.

7.5.1.2 Shahi & Baker (2011)

In a recent study, Shahi & Baker (2011) considered the effects of pulse-like ground motions in PSHA by extending a framework initially proposed by Tothong et al (2007) and Iervolino & Cornell (2008). The first step in their approach involves sub-dividing the mean annual rate of exceeding a given level of SA into two terms, as illustrated in Equation (7.5):

$$\lambda(SA > sa) = \lambda(SA > sa)_{NF} + \lambda(SA > sa)_{FF} \tag{7.5}$$

where $\lambda(SA > sa)_{NF}$ and $\lambda(SA > sa)_{FF}$ represent the relative contributions from the near-fault and far-fault sources to the overall seismic hazard at the site. The conventional PSHA procedure can be used to compute $\lambda(SA > sa)_{FF}$, whereas $\lambda(SA > sa)_{NF}$ requires a modified approach. Since pulse-like ground motions may not always be observed at sites located in the near-fault region (i.e. source-to-site distance, $R_{rup} \leq 20$ km), it is necessary to consider the probability of pulse occurrence. In order to do so, $\lambda(SA > sa)_{NF}$ is subdivided into two additional terms, as shown in Equation (7.6):

$$\lambda(SA > sa)_{NF} = \lambda(SA > sa)_{NF,Pulse} + \lambda(SA > sa)_{NF,No\ Pulse} \tag{7.6}$$

The evaluation of $\lambda(SA > sa)_{NF}$ requires empirical models which: (i) predict the pulse probability and (ii) quantify the effect of pulse-like ground motions on SA amplitudes obtained from GMPEs. The pulse probability model developed by Shahi & Baker (2011) is a function of source-to-site geometry (refer to Chapter 4) and the directivity amplification of spectral ordinates predicted by their model is a function of the pulse period (refer to Chapter 5). This implies that a probability distribution for the hypocentre location must also be defined in the hazard calculations, similar to Abrahamson (2000). Further details pertaining to the calculation of near-fault hazard can be found in Shahi & Baker (2011) and are suppressed herein for brevity.

7.5.2 Adopted approach in present study

7.5.2.1 Inclusion of narrowband directivity model in Bradley (2010) GMPE

The results of Chapter 5 clearly demonstrated that the narrowband model of Shahi & Baker (2011) (SB11) provides accurate and theoretically consistent predictions of the

response spectral amplification caused by the directivity pulse. Hence, the model is also used in this chapter for the purposes of carrying out NZ-specific PSHA. The approach adopted here to incorporate directivity effects in the PSHA framework is slightly different when compared to the procedure of Shahi & Baker (2011). Rather than subdividing the total mean annual rate into near- and far-fault terms, the conventional PSHA procedure is used, with the explicit inclusion of the narrowband SB11 model in the Bradley (2010) GMPE being the main difference. The functional form of the directivity amplification model is given by Equation (7.7).

$$\mu_{ln(Af|T_p} = \begin{matrix} 1.131 \exp\left(-3.11\left(\ln(T/T_p) + 0.127\right)^2\right) + 0.058 \text{ (if } T \leq 0.88\, T_p) \\ 0.924 \exp\left(-2.11\left(\ln(T/T_p) + 0.127\right)^2\right) + 0.255 \text{ (if } T > 0.88\, T_p) \end{matrix} \quad (7.7)$$

where μ_{lnAf} represents the mean amplification factor for a given vibration period and pulse period given by T and T_p, respectively. Since the model is a function of T_p, which in turn is related to earthquake magnitude (M_w) and well-represented by a lognormal distribution, it is logical to employ a convolution integral to calculate the mean directivity amplification for a given M_w, as shown in Equation (7.8):

$$\mu_{\ln(Af)} = \int \mu_{\ln Af|T_p} f_{T_p} dT_p \quad (7.8)$$

where f_{T_p} denotes the distribution of the pulse period for a given earthquake magnitude obtained from a prediction equation. The SB11 pulse period model is used on the basis of its improved predictive capabilities (as determined in Chapter 6) and is given by Equation (7.9):

$$\ln(T_p) = -5.73 + 0.99M_w;\ \sigma_{\ln(T_p)} = 0.56 \quad (7.9)$$

where $\ln(T_p)$ and $\sigma_{\ln(T_p)}$ represent the mean and standard deviation of the pulse period. To account for the probability of observing a pulse at the site of interest, the empirical model of Shahi (2013) (S13) is used based on the results of Chapter 4. Equations (7.10) and (7.11) illustrate the logistic regression models developed for strike-slip (SS) and non strike-slip (NSS) events, respectively. The geometric parameters which act as the main predictor variables are also illustrated in Figure 7.7 and were defined previously in Chapters 2 and 4.

$$P(pulse|R_{rup}, s, \theta) = \frac{1}{1 + e^{0.7897 + 0.1378R_{rup} - 0.3533\sqrt{s} + 0.020\theta}} \quad (7.10)$$

$$P(pulse|R_{rup}, d, \phi) = \frac{1}{1 + e^{1.483 + 0.124R_{rup} - 0.688\sqrt{d} + 0.022\phi}} \quad (7.11)$$

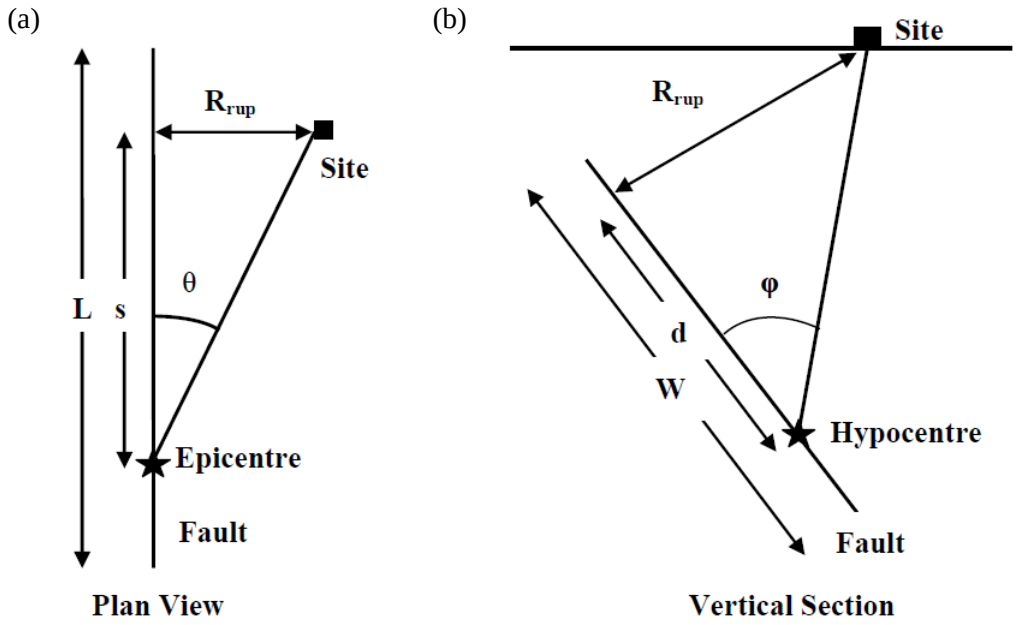

Figure 7.7: Source-to-site geometry illustrating the parameters used in the development of pulse probability prediction models for: (a) Strike-slip fault; and (b) Non strike-slip fault (modified from Somerville et al., 1997).

Based on the above information, it is now possible to evaluate the directivity corrected SA amplitudes (SA_{dir}) for the earthquake rupture scenario (Rup_i) and vibration period of interest (T), as shown in Equation (7.12):

$$SA_{dir}(Rup_i, T) = SA(Rup_i, T) \cdot \exp\left(\mu_{\ln(Af)}\right) \cdot P(Pulse) + SA(Rup_i, T) \cdot \exp\left(\mu_{ln(Df)}\right) \cdot (1 - P(Pulse)) \quad (7.12)$$

where $SA(Rup_i, T)$ represents the median GMPE prediction of the horizontal geometric mean SA ; $P(Pulse)$ is the predicted pulse probability; and $\mu_{ln(Df)}$ represents the deamplification factor obtained using the Shahi & Baker (2011) model (as shown in Equations (7.13) and (7.14) for SS and NSS events, respectively) to account for the possibility of observing non-pulse-like ground motions at the site of interest.

SS $$\mu_{\ln(Df)} = \max\left(-0.0905 \ln(T)\, g_M\, g_R, -0.0905 \ln(2)\, g_M\, g_R\right) \quad (7.13)$$

NSS $$\mu_{\ln(Df)} = -0.029 \ln(T)\, g_M\, g_R \quad (7.14)$$

where

$$g_M = \begin{cases} 0 & \text{if } M_w < 6 \\ (M_w - 6)/0.5 & \text{if } 6 \le M_w \le 6.5 \\ 1 & \text{if } M_w > 6.5 \end{cases} \quad (7.15)$$

and

$$\begin{aligned} g_R &= 10 - R_{JB} && \text{if } R_{JB} \leq 10\ km \\ &= 0 && \text{if } R_{JB} > 10\ km \end{aligned} \tag{7.16}$$

where R_{JB} is the Joyner-Boore distance (closest distance to the site from the surface projection of the fault).

A reduction factor (R_f) for the lognormal standard deviation associated with the GMPE ($\sigma_{\ln(SA)}$), is also prescribed by the SB11 model and is illustrated in Equation (7.17). This factor serves to account for the reduction in uncertainty of the predictions as a result of accounting for the effects of pulse-like ground motions. It is noted that the reduction factor can be applied in a manner similar to Equation (7.12).

$$\begin{aligned} R_f = 1 - 0.2 \exp\left(-0.96\ (\ln(T/T_p) + 1.56)^2\right)\ \ (\text{if } T \leq 0.21\ T_p) \\ 1 - 0.21 \exp\left(-0.24\ (\ln(T/T_p) + 1.56)^2\right)\ \ (\text{if } T > 0.21\ T_p) \end{aligned} \tag{7.17}$$

The procedure described above was incorporated in the OpenSHA framework (Field et al., 2003) and the resulting ground motion model predictions were verified independently using codes developed in MATLAB (*MATLAB*, 2010). In the seismic hazard calculations, it was considered appropriate to ignore the effects of near-fault directivity for R_{rup} > 50 km. This can be justified by the fact that the S13 model predictions for pulse probability are essentially negligible for distances greater than 30 km.

An example application of the Bradley (2010) (B10) GMPE with and without considering the effects of near-fault directivity is illustrated in Figure 7.9 (represented by solid and dashed lines, respectively). A strike-slip fault capable of producing M_w 7.0 earthquakes is considered and a length of 43 km is assigned based on the median prediction of the magnitude-scaling relation developed by Wells & Coppersmith (1994), as shown in Figure 7.8. The sites considered are assumed to have an average shear-wave velocity of $V_{s,30}$ = 250 m/s. In particular, Figure 7.8a considers the case where the location of the epicentre (or hypocentre) is varied while keeping the site location constant (i.e. varying rupture length, s and constant source-to-site azimuth, θ). The corresponding predictions of SA are illustrated in Figure 7.9a. As expected, increasing levels of amplification are predicted by the SB11 model for larger s values in the vicinity of the pulse period (T_p = 3.3 s). For the case where the location of the epicentre and site coincide, the model predicts a de-amplification of spectral ordinates to account for the possibility of observing non-pulse-like ground motions. In

addition, the narrowband nature of the model is most clearly visible when a scenario-based approach is used to apply the model i.e. by assuming the occurrence of a pulse at the site (P_{pulse} = 1). Similarly, Figure 7.8b considers the case where the hypocentre location is kept constant and the site location relative to the fault is varied (i.e. constant rupture length, s and varying source-to-site azimuth, θ). From the source-to-site geometry, it is evident that as R_{rup} increases, so does θ. This has two important implications as shown in Figure 7.9b: (i) there is a systematic reduction in spectral amplitudes predicted by the B10 GMPE due to the effects of geometric spreading and anelastic attenuation; and (ii) the level of directivity amplification predicted by the SB11 model decreases due to a reduction in the predicted probability of pulse occurrence. At a distance of 30 km (θ = 45°), the effect of directivity is essentially negligible.

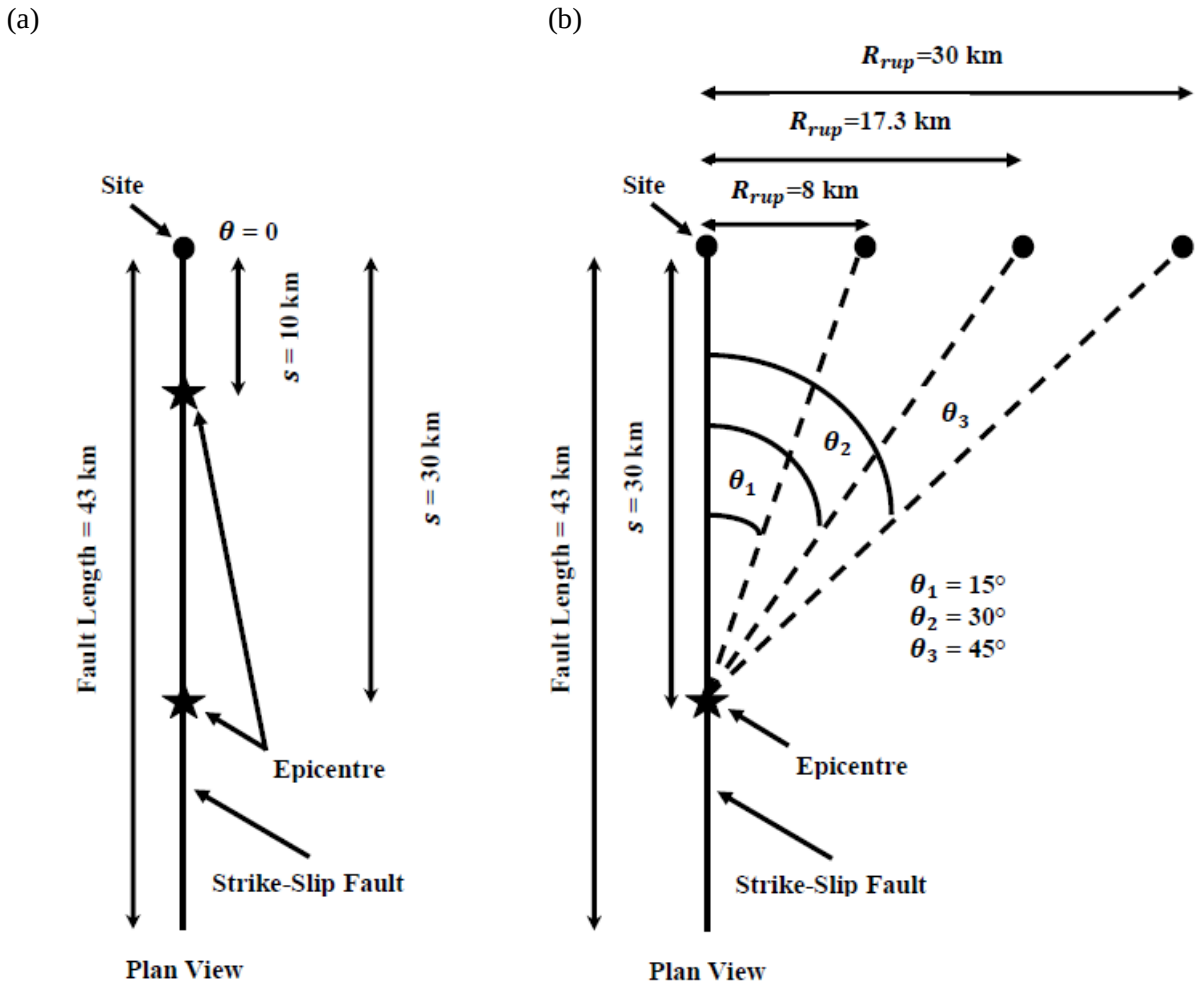

Figure 7.8: Source-to-site geometry for a hypothetical strike-slip fault capable of producing M_w7.0 earthquakes. Panel (a): effect of epicentre location on the proportion of the fault which ruptures towards a site located directly in the path of rupture propagation i.e. source-to-site azimuth of θ = 0. Panel (b): effect of site location on the source-to-site distance and azimuth for a fixed fault rupture length.

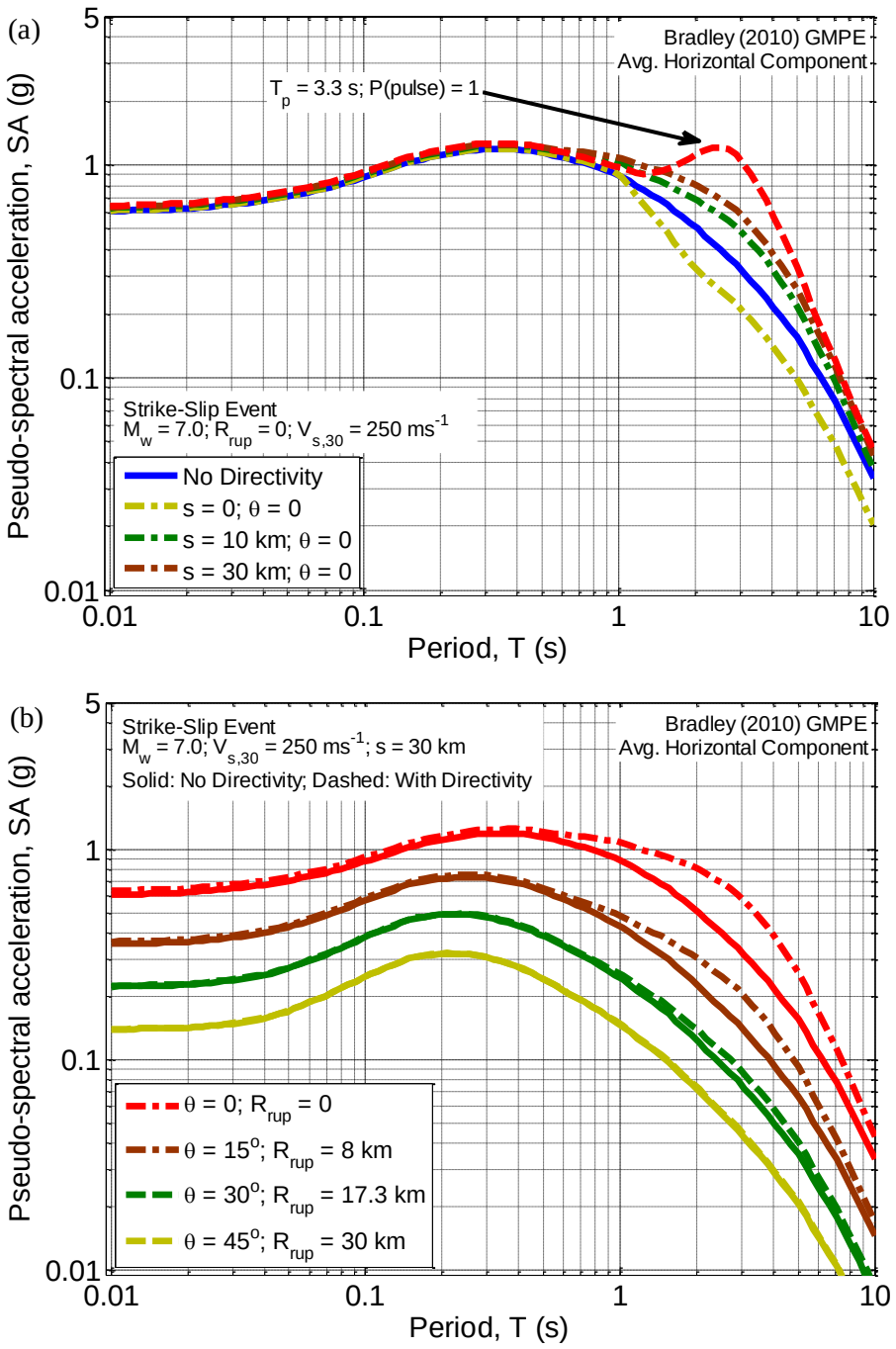

Figure 7.9: Effect of the narrowband directivity model of Shahi & Baker (2011) on the predicted response spectra obtained using the Bradley (2010) GMPE for a M_w7.0 strike-slip earthquake. Panel (a): predicted response spectra for a site located in the direction of rupture propagation but with varying epicentre locations. Panel (b): predicted response spectra for sites located at increasing source-to-site distances but with the epicentre location held constant. Note that the predictions are also shown without correcting for directivity in both cases.

As mentioned previously, it is essential to define the hypocentre location on the causative fault to account for directivity effects in PSHA. For the purposes of computational efficiency, it was considered reasonable to define hypocentres at three evenly distributed locations along-strike, as illustrated in Figure 7.10. The down-dip location of $0.6W$ was

assigned based on the results of an extensive statistical study carried out by Mai et al. (2005) on hypocentre locations in finite-fault models.

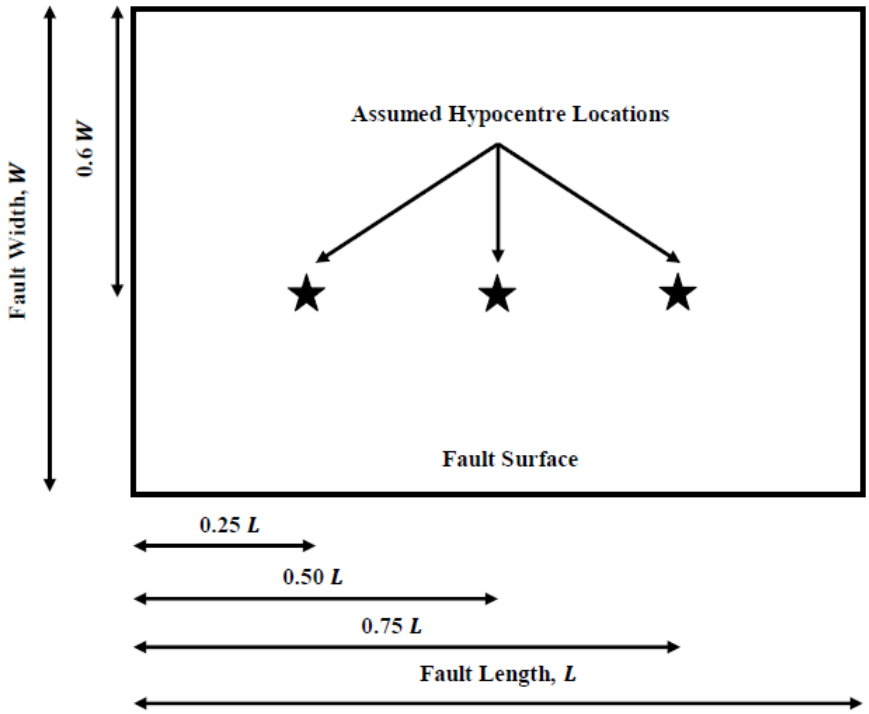

Figure 7.10: Illustration of the assumed hypocentre locations required in carrying out PSHA including near-fault directivity effects.

7.5.2.2 Consideration of point-sources as fault sources

The possibility of earthquake occurrence on unknown faults is accounted for by the background seismicity model in the NZ ERF (Stirling et al. 2002; Stirling et al., 2012). It was stated previously that the background earthquakes are modelled as point-sources located at depths ranging between 10 km and 90 km. This type of representation can result in unconservative estimates of the predicted surface ground motion in seismic hazard calculations, as illustrated by Bradley (2012) in the process of scrutinising the consistency of the current NZ background seismicity model with observed ground motions from the recent 2010-11 Canterbury earthquake sequence. It should be recalled that the causative faults in these events do not form part of the fault-based seismicity model, thereby providing the impetus for the study carried out by Bradley (2012).

Figure 7.11 provides an excellent example of the aforementioned unconservatism resulting from the point-source assumption for background sources and the minimum depth of 10 km. In particular, the predicted median SA amplitudes using the Bradley (2010) (B10) GMPE at Christchurch Hospital in the 4 September 2010 M_w7.1 Darfield (Figure 7.11a), and

22 February 2011 M_w6.2 Christchurch (Figure 7.11b) earthquakes are shown. The predictions have been calculated assuming: (i) that the earthquake is a point-source and has a depth of 10 km (i.e. presently the manner in which background sources are considered in the NZ seismicity model); (ii) an earthquake depth corresponding to the event-specific centroid depths (both of which are less than the minimum background depth of 10 km) but still considering the earthquakes as point-sources; and (iii) the correct finite-fault representation of the earthquake geometry (Bradley, 2012). The results of the figure clearly indicate that approaches (i) and (ii) provide significantly lower estimates of ground motion amplitudes in relation to the more consistent finite-fault representation of earthquake sources in seismicity models. Using the same example, Bradley (2012) found that the point-source representation results in SA amplitudes which are up to 60% less than those obtained using the latter approach. The differences stem from the different source-to-site distances, R_{rup} (annotated in Figure 7.11), with finite-fault source-to-site distances always being lower than the point-source-to-site distances.

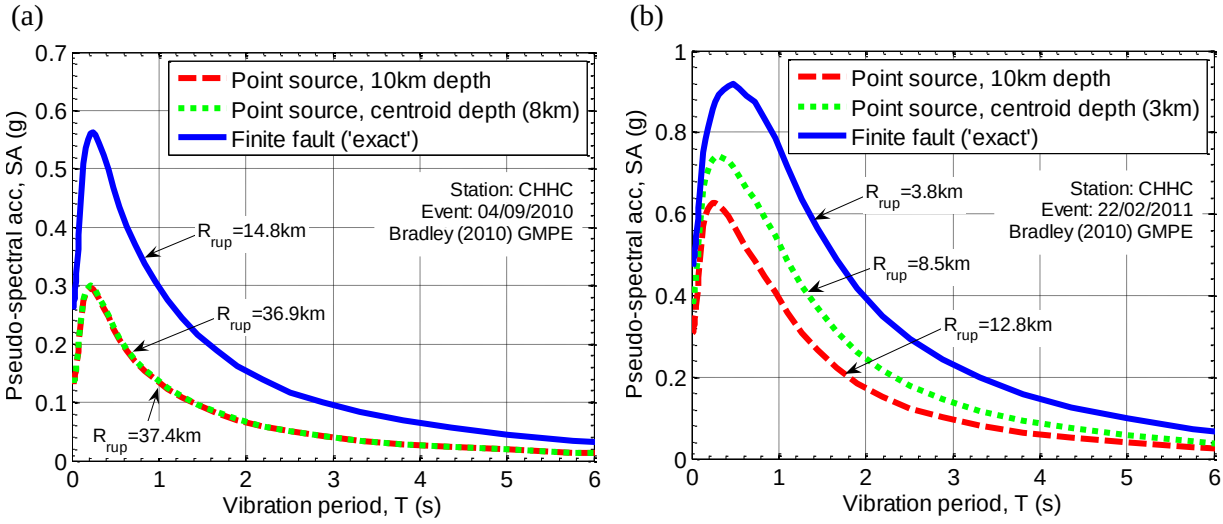

Figure 7.11: Effect of minimum earthquake depth of 10km and point-source approximation in seismicity modelling on median response spectral amplitudes predicted at Christchurch hospital (CHHC) during: (a) 4 September 2010 M_w7.1 Darfield; and (b) 22 February 2011 M_w6.2 Christchurch earthquakes. Note that the 'finite-fault' prediction represents the correct prediction in terms of consistency between seismicity and ground motion modelling (after Bradley, 2012)

The above findings imply that significant under-estimation of the seismic hazard is likely to occur using the conventional point-source representation of background sources, especially for regions such as Christchurch where the background seismicity provides a major contribution to the overall seismic hazard (Bradley, 2012; Stirling et al., 2007). As a result, background point-sources in the NZ ERF are represented as equivalent finite-faults in the present study. More importantly, this allows for the effects of near-fault directivity to be

addressed in an appropriate manner. Table 7.1 summarises the important parameters required in the point-source to finite-fault conversion, and the manner in which they were determined.

Table 7.1:Description of the parameters required in representing point-sources in the NZ background seismicity model as equivalent finite-faults.

Parameter	Method of Determination
Point-source location	Specified in the NZ ERF and used to represent the centroid of the equivalent finite-fault.
Strike	A strike of 45° is assumed for all point-sources and acts as a practical compromise between assigning multiple strike values (e.g. 0° and 90°), which would significantly increase the computational demand in PSHA calculations.
Dip angle, δ	Specified in the NZ ERF and used to define the finite-fault dip angle.
Rake angle, λ	Specified in the NZ ERF and used to distinguish between different faulting mechanisms.
Moment magnitude, M_w	Obtained from the Gutenberg-Richter distribution assigned to each point-source with M_{min} = 5.0 and M_{cutoff} = 7.2 (except for TVZ where M_{cutoff} = 6.5).
Finite-fault length, L	Using the Wells & Coppersmith (1994) magnitude-scaling relations.
Finite-fault width, W	Using the Wells & Coppersmith (1994) magnitude-scaling relations.

7.6 Application of PSHA including directivity effects

This section summarises the results associated with the application of the previously described PSHA procedure incorporating the effects of near-fault directivity to locations in New Zealand. Generic locations in Christchurch and Wellington have been typically considered in previous studies (Bradley et al., 2012; Stirling et al., 2012; Stirling et al., 2002) mainly because: (i) they represent two of NZ's largest cities; and (ii) fault-based seismicity dominates the hazard in Wellington, whereas in Christchurch, background seismicity provides a significant contribution to the overall seismic hazard at the 475-year return period. While the above reasoning indicates that it would be prudent to consider these two locations in the present study, it is noted that the Hikurangi subduction interface sources (with M_w8.1, 8.4 and 9.0 at 23 km) provide a notable contribution ($\cong$ 20%) to the long-period (SA = 1 s) ground motion hazard in Wellington (Stirling et al., 2012). Since the models considered herein to account for directivity effects have been calibrated using observations from active shallow crustal earthquakes alone, it is not appropriate to extrapolate their predictions to other tectonic regimes without specific examination of their appropriateness. As far as the author's

knowledge is concerned (and also highlighted by Shahi (2013)), such models do not exist for subduction interface and subduction slab earthquakes. In light of this issue, the township of Otira in the central South Island of NZ was selected as a location dominated by modelled faults (in close proximity to major sources of seismicity such as the Alpine, Kelly and Hope faults). This is clearly reflected by the hazard factor, Z = 0.6 in the seismic design standard, NZS1170.5:2004 (Standards New Zealand, 2004), which is significantly higher than the factors of 0.22[2] and 0.40 assigned to Christchurch and Wellington, respectively.

7.6.1 Example 1: Christchurch

In order to examine the effect of near-fault directivity on the expected seismic hazard for Christchurch, a generic location (latitude: -43.5300°; longitude: 172.6300°) corresponding to site class D (deep soil) conditions, as defined in NZS1170.5:2004 (Standards New Zealand, 2004) is considered. An exposure period of 50 years is adopted for all seismic hazard analyses whose results are presented herein. Based on the aforementioned importance of background seismicity for the Christchurch region, it is important to firstly quantify the effects of using point-source and finite-fault based representations of the background earthquake sources. Figure 7.12 illustrates the seismic hazard curves for five intensity measures to reflect short (PGA, SA(0.2 s)), moderate (SA (0.5 s)) and long period (SA (1 s), SA (3 s)) ground motion intensities. The hazard curves have first been obtained considering only background sources, which are defined as: (i) point-sources (i.e. as defined in the NZ ERF); (ii) finite-faults with dimensions that are consistent with the M_w of each possible event in the source's G-R distribution (i.e. 'exact' representation); and (iii) finite-faults with dimensions corresponding to the maximum magnitude (M_{max}) from the G-R distribution associated with each point-source. The latter form of representation was considered for reasons which will become apparent in the discussion to follow. Also shown in Figure 7.12 is a so-called 'error ratio', which is defined as the ratio of the intensity measure obtained using methods (i) and (iii) normalised by the value obtained using the 'exact' approach (ii) for each exceedance probability. An error ratio less than 1 indicates under-estimation whereas a ratio greater than 1 implies over-estimation of the seismic hazard. The grey lines in Figure 7.12 highlight the 50%,10%, and 2% in 50-year exceedance probabilities (PE) typically used in seismic design; each corresponding to return periods of 72, 475 and 2475 years, respectively.

[2] The hazard factor for Christchurch was revised to 0.30 following the 2010-11 Canterbury earthquakes (McVerry et al., 2012).

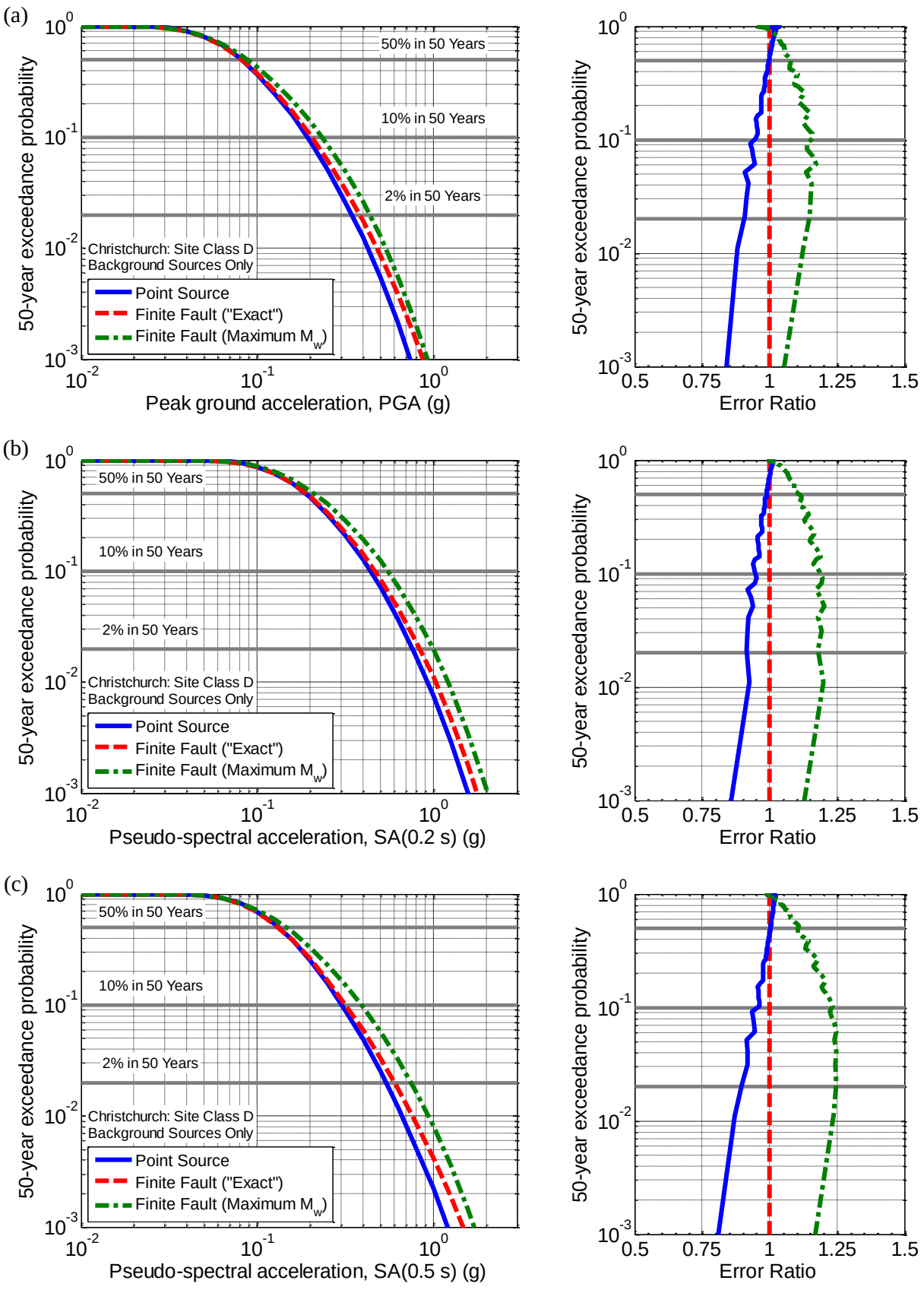
(a)
50-year exceedance probability
50% in 50 Years
10% in 50 Years
2% in 50 Years
Christchurch: Site Class D
Background Sources Only
Point Source
Finite Fault ("Exact")
Finite Fault (Maximum M_w)
Peak ground acceleration, PGA (g)
Error Ratio
(b)
Pseudo-spectral acceleration, SA(0.2 s) (g)
Error Ratio
(c)
Pseudo-spectral acceleration, SA(0.5 s) (g)
Error Ratio

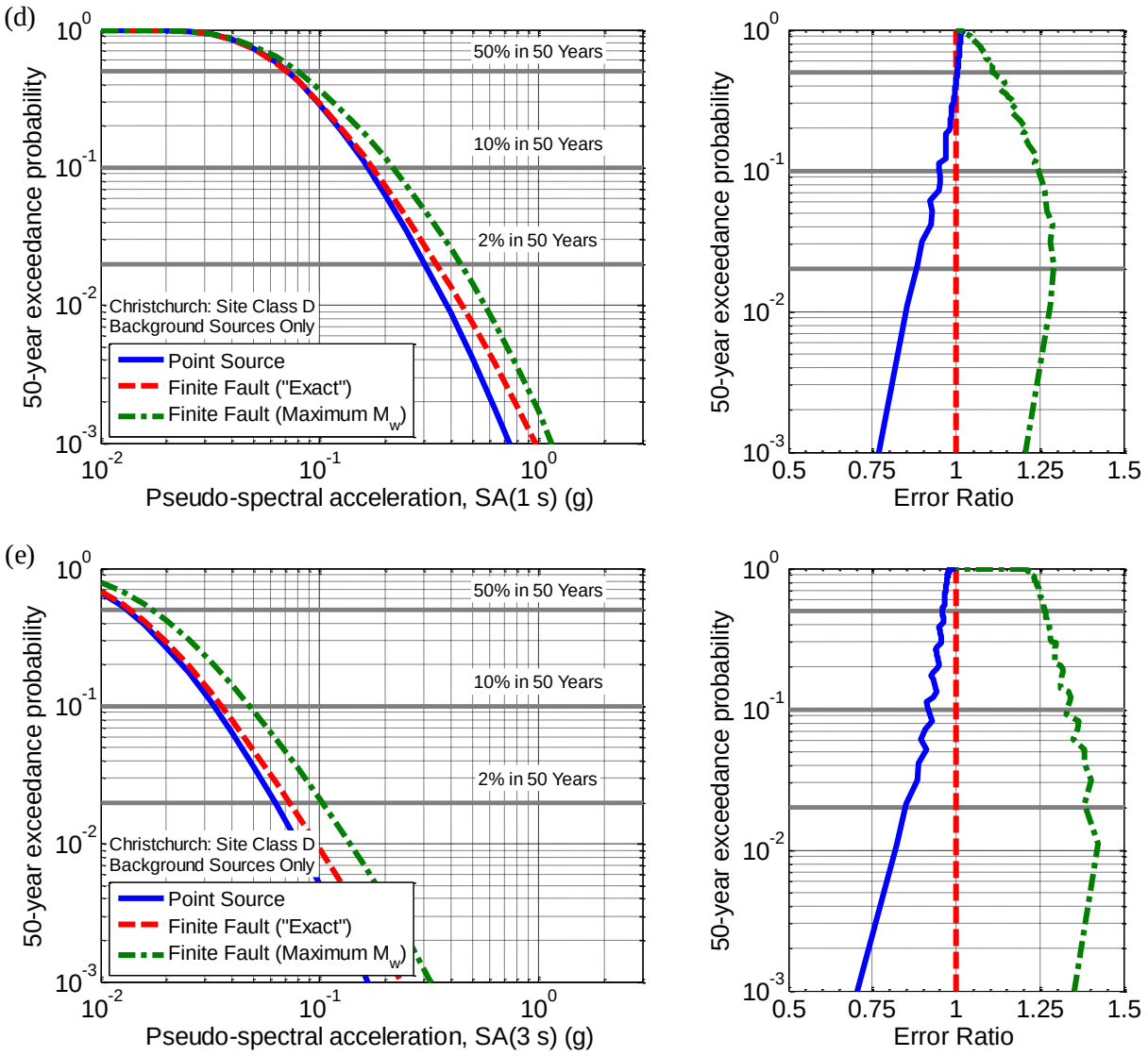

Figure 7.12: Importance of characterising background earthquake sources using the 'exact' finite-fault geometry illustrated using seismic hazard curves calculated for a site in Christchurch and for various IMs including: (a) PGA; (b) SA(0.2 s); (c) SA(0.5 s); (d) SA(1 s); and (e) SA(3 s). The plots on the right-hand side of each panel illustrate an 'error ratio' to demonstrate (i) the under-estimation of hazard resulting from the point-source approximation; and (ii) over-estimation of the hazard resulting from the use of fault geometry corresponding to the maximum M_w in the magnitude-frequency distribution.

As expected, the results of Figure 7.12 illustrate that the point-source representation of background earthquakes results in an under-estimation of all IMs at 10% and 2% in 50-year PEs. In particular, the error ratios indicate that the under-estimation ranges between 5-10% and 10-15% for the two PEs, respectively. However, for the 50% in 50-year PE, there is either marginal (< 5%) or no under-estimation for all IMs. The importance of using the 'exact' geometry in defining the finite-faults is clearly illustrated by the hazard curves and error ratios corresponding to the maximum M_w fault representation of each point-source. For the 10% and 2% in 50-year PE, it can be observed that using the finite-fault-based approach results in an over-estimation of the hazard for all IMs. Specifically, the level of over-

estimation ranges between 15-35% (10% in 50-year PE) and 15-40% (2% in 50-year PE), with the lower and upper limits of these ranges corresponding to the PGA and $SA(3\text{ s})$, respectively. This can be attributed to smaller source-to-site distances (R_{rup}) obtained using the larger fault geometry associated with the maximum M_w for each background source. Similarly, in the case of the 50% in 50-year PE, the hazard over-estimation becomes notable for long-period ground motion.

The previous discussion was effective in emphasising the significance of correctly defining the fault geometry for background sources. It is also useful to examine the relative contribution from the background and fault sources to the total hazard for the IMs considered. Figure 7.13 illustrates the seismic hazard curves for the aforementioned location in Christchurch considering: (i) background sources only; (ii) fault sources only; and (iii) both types of sources. The plots on the left- and right-hand side of the figure show the hazard curves for point-source and finite-fault representations of background earthquakes, respectively. Once again, the 50%, 10% and 2% in 50-year PE are indicated using grey lines. Upon examining the figure, it is apparent that the background seismicity dominates the hazard for short vibration periods (PGA and $SA(0.2\text{ s})$) and that the fault-based seismicity dominates the hazard for long vibration periods ($SA(3\text{ s})$). For the 50% and 10% PE, it can be observed that a cross-over between the hazard curves corresponding to the background and fault sources (i.e. their individual contributions) occurs at $SA(0.5\text{ s})$. Nonetheless, at lower exceedance probabilities, the contribution of the background sources is notably larger in relation to the fault sources, as highlighted by the gentler slopes of the hazard curves in Figure 7.13c and Figure 7.13d. Since background sources are capable of producing only small-to-moderate magnitude earthquakes and the standard deviation model of the B10 GMPE demonstrates a reduction in standard deviation with magnitude (Bradley, 2010), it is likely that the uncertainties in ground motion prediction are the main reason for the above observation. In fact, it can be observed that the hazard curve associated with background fault sources for $SA(1\text{ s})$ in Figure 7.13d also has a gentler slope for low exceedance probabilities. Nonetheless, at longer periods (e.g. $SA(3\text{ s})$), the hierarchy of the relative contribution from background and fault sources agrees with intuition.

(a)

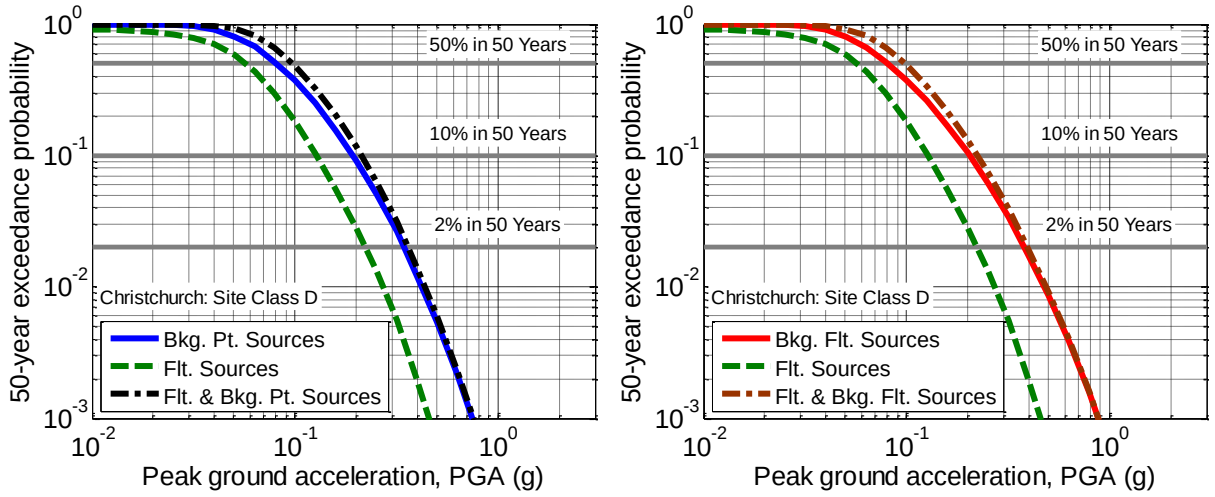
50-year exceedance probability
50% in 50 Years
10% in 50 Years
2% in 50 Years
Christchurch: Site Class D
Bkg. Pt. Sources
Flt. Sources
Flt. & Bkg. Pt. Sources
Peak ground acceleration, PGA (g)
Bkg. Flt. Sources
Flt. Sources
Flt. & Bkg. Flt. Sources
Peak ground acceleration, PGA (g)

(b)

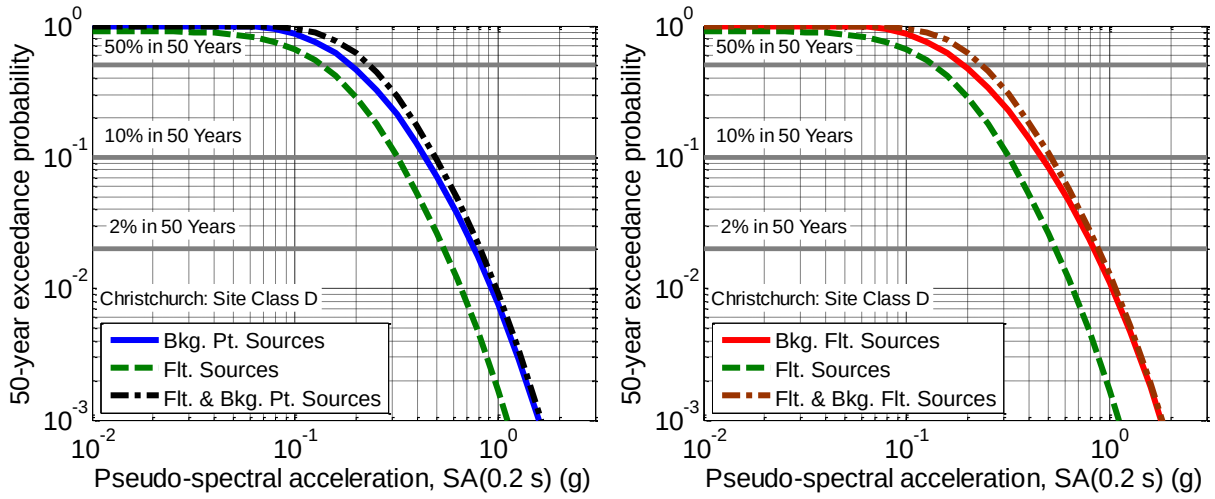
50-year exceedance probability
50% in 50 Years
10% in 50 Years
2% in 50 Years
Christchurch: Site Class D
Bkg. Pt. Sources
Flt. Sources
Flt. & Bkg. Pt. Sources
Pseudo-spectral acceleration, SA(0.2 s) (g)
Bkg. Flt. Sources
Flt. Sources
Flt. & Bkg. Flt. Sources
Pseudo-spectral acceleration, SA(0.2 s) (g)

(c)

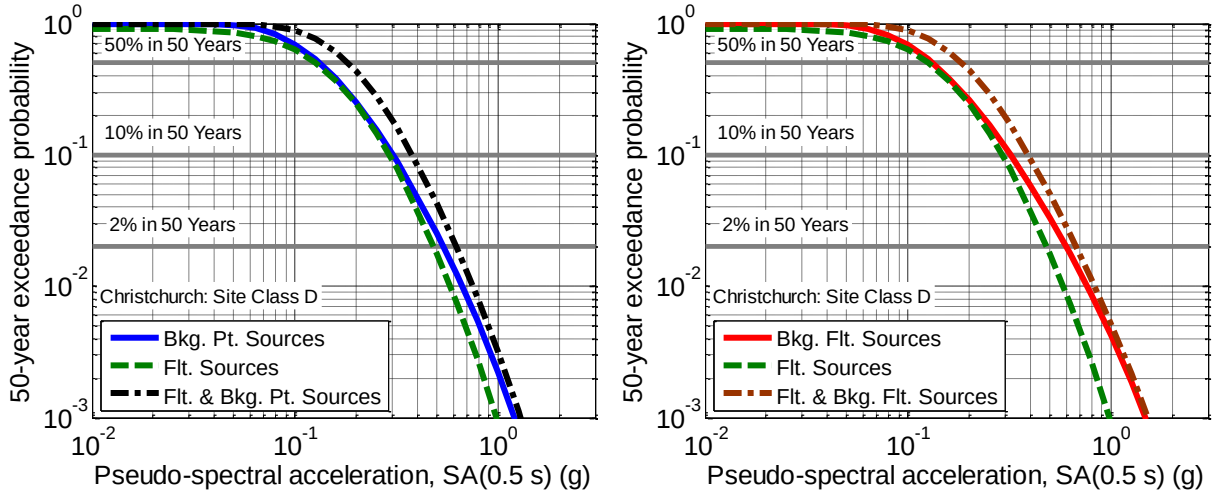
50-year exceedance probability
50% in 50 Years
10% in 50 Years
2% in 50 Years
Christchurch: Site Class D
Bkg. Pt. Sources
Flt. Sources
Flt. & Bkg. Pt. Sources
Pseudo-spectral acceleration, SA(0.5 s) (g)
Bkg. Flt. Sources
Flt. Sources
Flt. & Bkg. Flt. Sources
Pseudo-spectral acceleration, SA(0.5 s) (g)

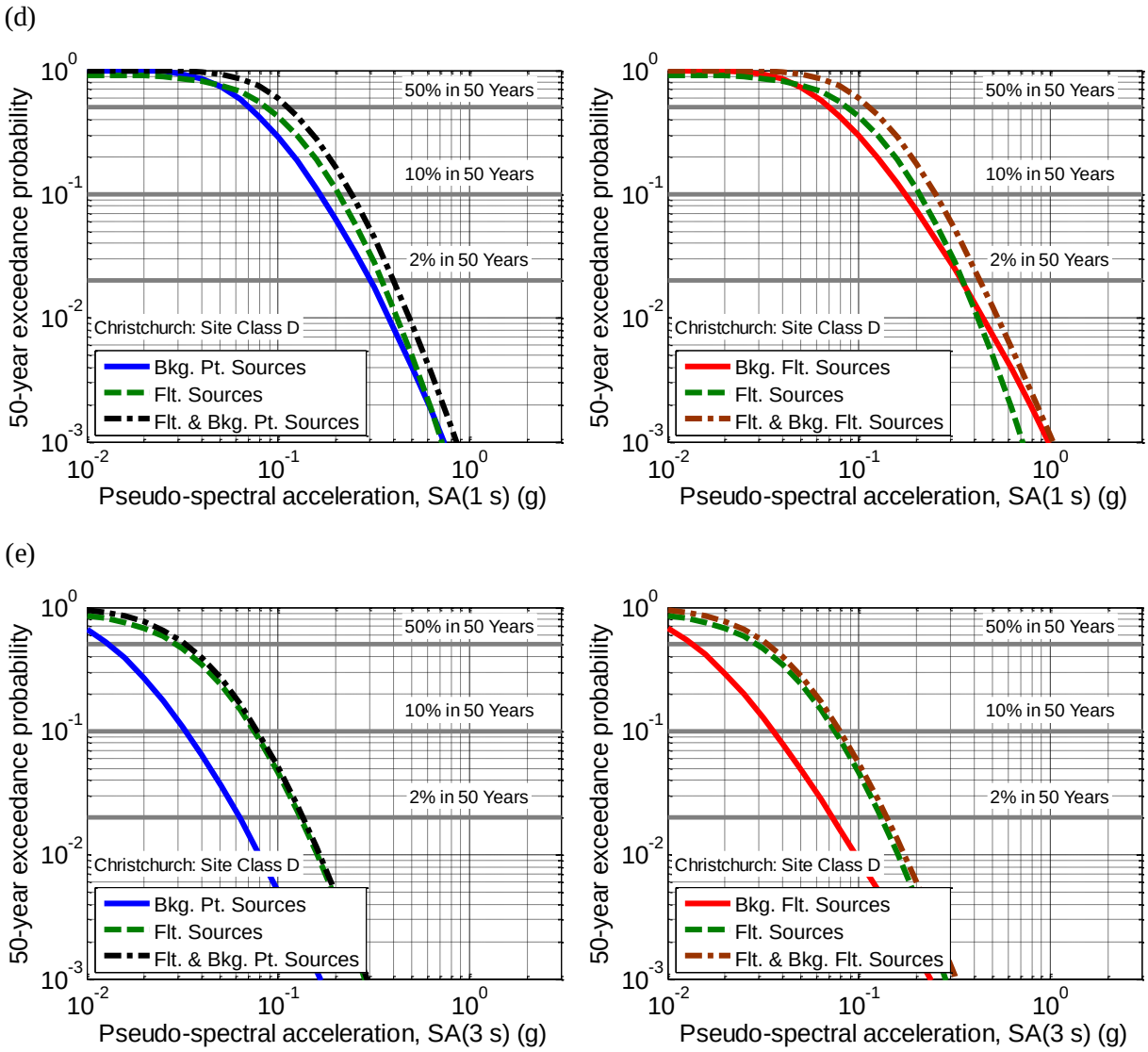

Figure 7.13: Comparison of the seismic hazard curves calculated for a typical site in Christchurch and for various IMs including: (a) PGA; (b) SA(0.2 s); (c) SA(0.5 s); (d) SA(1 s); and (e) SA(3 s). The hazard curves are shown considering: (i) background sources only (left panel: point-source representation; right panel: finite-fault representation); (ii) fault sources only; and (iii) a combination of both background and fault-based seismicity.

To further elucidate the trends described in Figure 7.13, uniform hazard spectra (UHS) corresponding to exceedance probabilities of 50%, 10% and 2% in 50 years are illustrated in Figure 7.14. Also shown is an 'error ratio' in Figure 7.14d, which is defined as the ratio of the UHS representing the total hazard considering background earthquakes as point-sources and finite-faults (i.e. $UHS_{(Flt.\ \&\ Bkg.\ Pt.)}$ / $UHS_{(Flt.\ \&\ Bkg.\ Flt.)}$). The results of Figure 7.14d, in particular, indicate that the error resulting from the point-source representation currently adopted in the NZ ERF is notable for short vibration periods. For example, an under-estimation between 2.5-5% and 5-10% is observed for periods less than 1.5 s at exceedance probabilities of 10% and 2% in 50 years, respectively. While the error ratio may be expected to approach 1 at longer periods (because of the dominance of fault-based

sources), this is clearly not the case as a result of the importance of finite-fault representation in the background sources for long periods (i.e. the dependence of SA with source-to-site distance is notably greater for long periods).For the 50% in 50-year PE, the under-estimation is negligible with error ratios ranging between 0.98 and 1 for all periods.

(a)

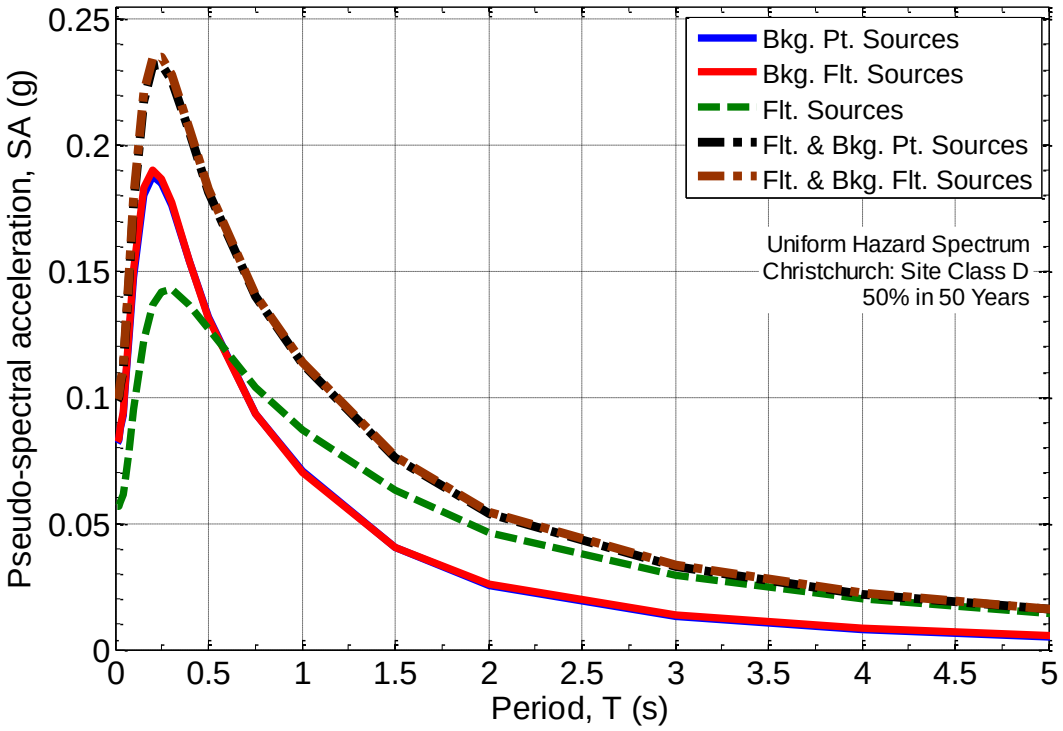

(b)

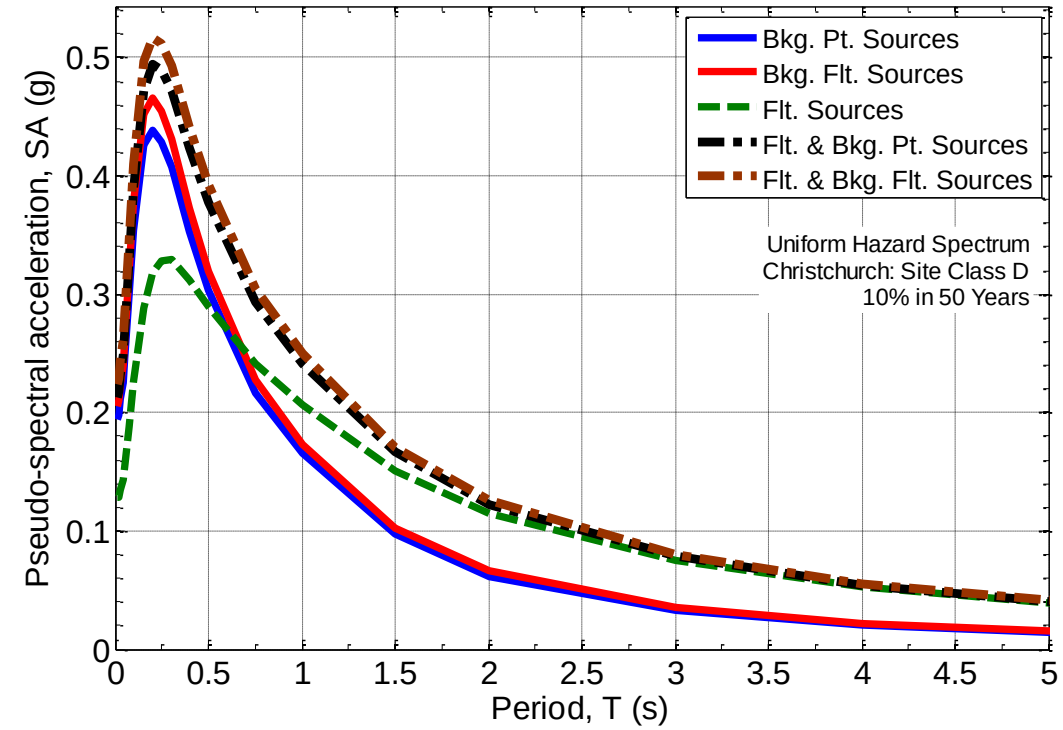

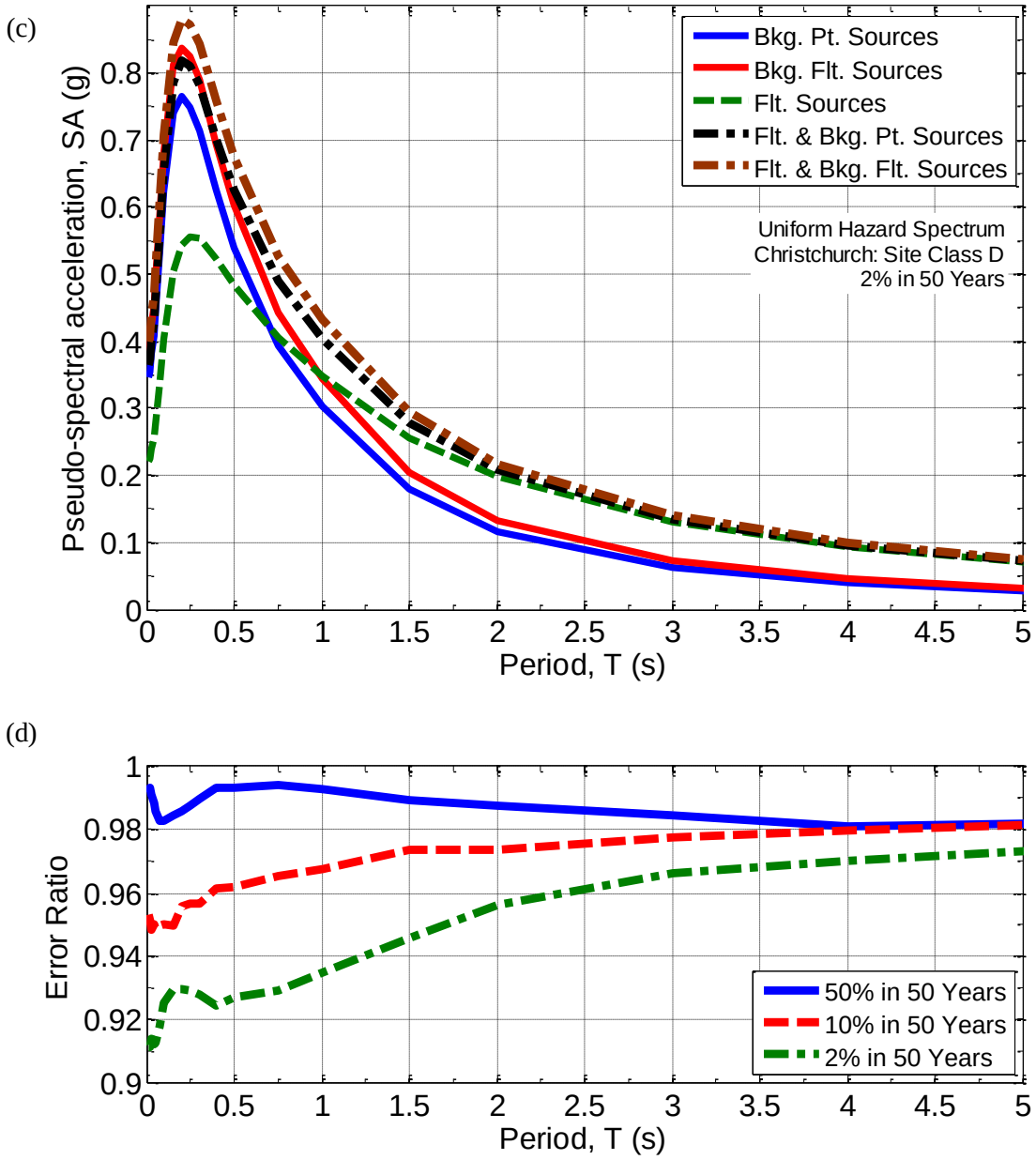

Figure 7.14: UHS corresponding to a typical site in Christchurch for exceedance probabilities of: (a) 50% in 50 years; (b) 10% in 50 years; and (c): 2% in 50 years. Panel (d): 'error ratio' defined as the ratio of UHS considering background point and fault sources and UHS considering background fault and fault sources. The hazard spectra are shown considering: (i) background sources only; (ii) fault sources only; and (iii) a combination of both background and fault-based seismicity.

The seismic hazard analyses discussed previously for Christchurch were repeated considering the effects of near-fault directivity, using the approach described in Section 7.5.2. For the purposes of comparison, the analyses were conducted using both point-source and 'exact' finite-fault representations of the background sources. When background sources were treated as point-sources, no directivity could be considered for these sources. Each of the three figures (Figure 7.15-Figure 7.17) which follow correspond to a single *PE* and illustrate: (i) uniform hazard spectra with and without accounting for directivity effects; and (ii) a so-

called 'hazard ratio' defined as the ratio of all UHS normalised by the base case i.e. UHS considering fault and background point-sources without directivity.

In an overall sense, it can be concluded that directivity effects are not significant for Christchurch based on the results of Figure 7.15-Figure 7.17. Specifically, the contribution of fault sources to the directivity amplification is negligible. This statement can be validated by the hazard ratio, which effectively remains unchanged at all periods after accounting for directivity using fault sources only (i.e. since the calculation of directivity amplification is not possible for background point-sources). Upon considering the background earthquakes as finite-faults in the seismicity model, it can be observed that there is progressive increase in the hazard ratio with decreasing exceedance probabilities. After correcting for directivity using the modified Bradley (2010) GMPE, the hazard ratio is essentially unaffected for the 50% in 50-year PE. In contrast, it can be observed from Figure 7.16b and Figure 7.17b that there is a slight reduction in hazard ratio for the smaller exceedance probabilities at periods less than T = 0.4 s. This can be attributed to deamplification of spectral ordinates predicted by the SB11 model to account for the occurrence of non-pulse-like ground motions, as described previously in Section 7.5.2.1. Amplification due to directivity occurs in the period range 0.7 s $\leq T \leq$ 3 s, and is especially notable at the 2% in 50-year PE (the largest increase is approximately two times that of the 10% in 50-year PE). The low levels of amplification can be attributed to the low probabilities of pulse occurrence predicted by the S13 model for the background fault sources. This is consistent with the fact that the background seismicity for Christchurch is dominated by reverse faults and that the S13 model always predicts smaller pulse probabilities for non strike-slip faults due to reasons mentioned previously in Chapter 4. The consideration of background seismicity in the Canterbury as exclusively reverse faulting events is presumably a conservative assumption, since such events produce on average larger ground shaking than strike-slip events. However, the above point may mean that this is in fact unconservative at long periods, where strike-slip events give a notably larger probability of directivity.

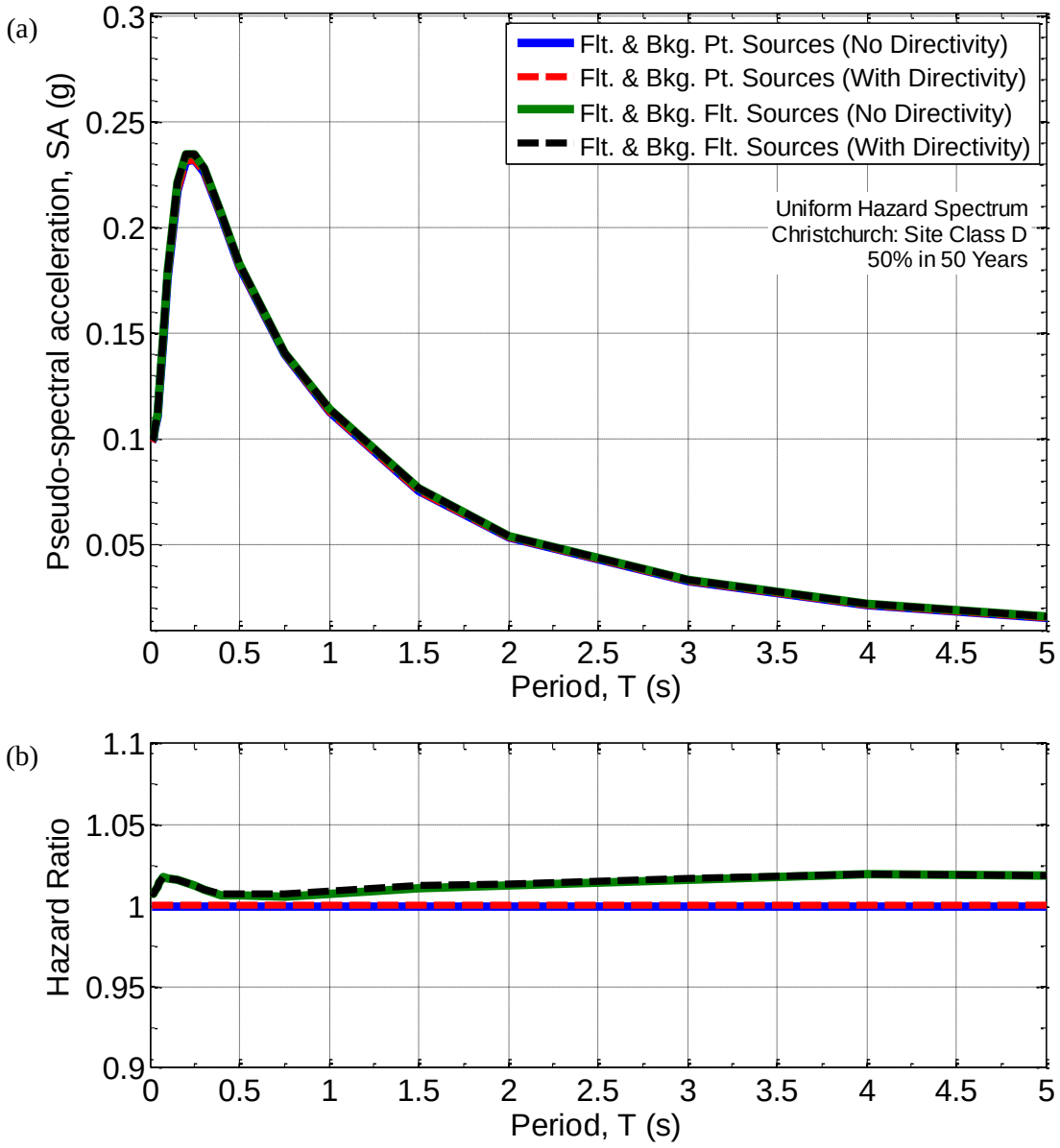

Figure 7.15: (a) UHS for a typical site in Christchurch both with and without considering the effects of near-fault directivity at an exceedance probability of 50% in 50 years; and (b) Hazard ratio illustrating the increase/decrease in hazard as a result of considering directivity effects.

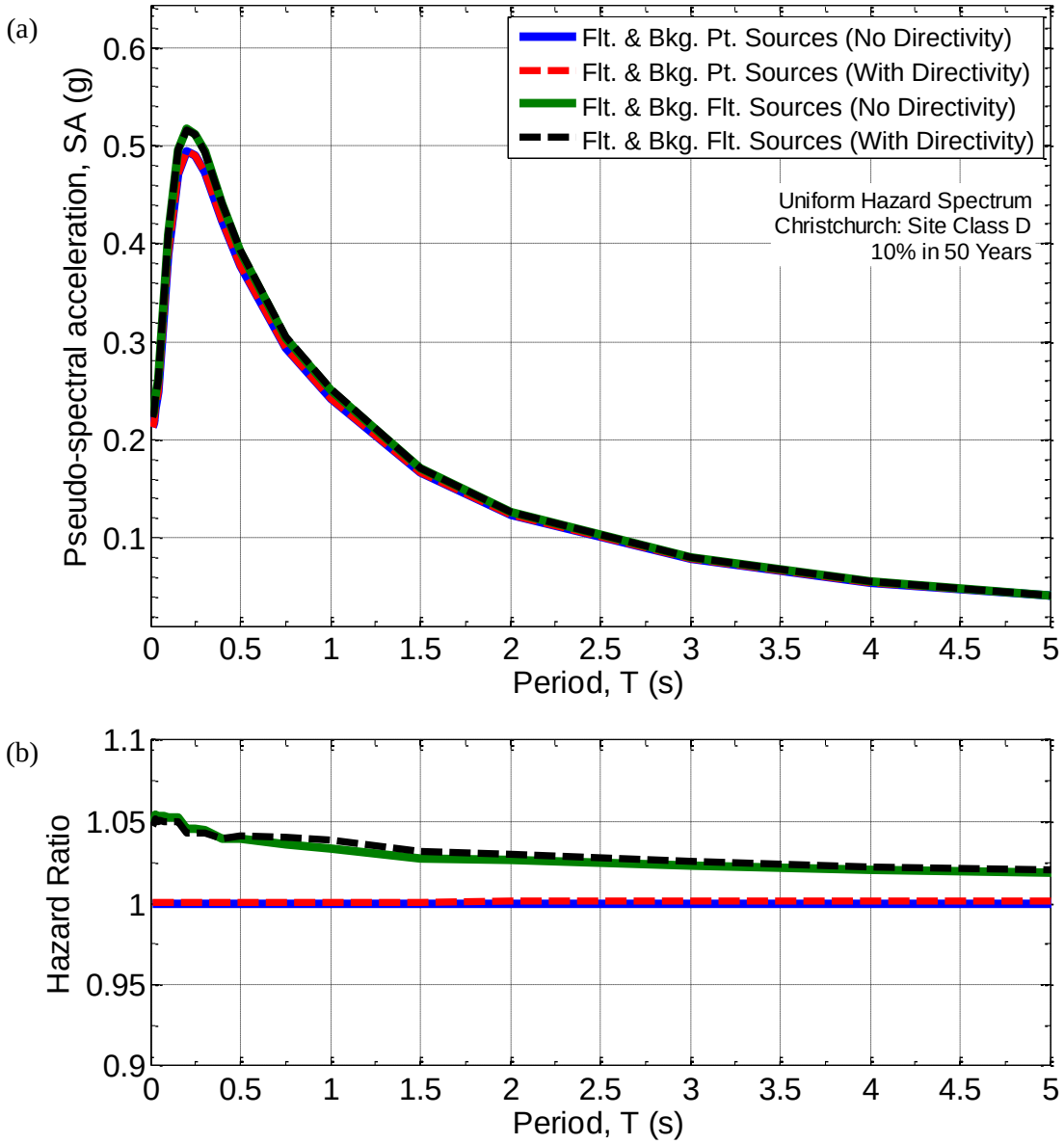

Figure 7.16: (a) UHS for a typical site in Christchurch both with and without considering the effects of near-fault directivity at an exceedance probability of 10% in 50 years; (b) Hazard ratio illustrating the increase/decrease in hazard as a result of considering directivity effects.

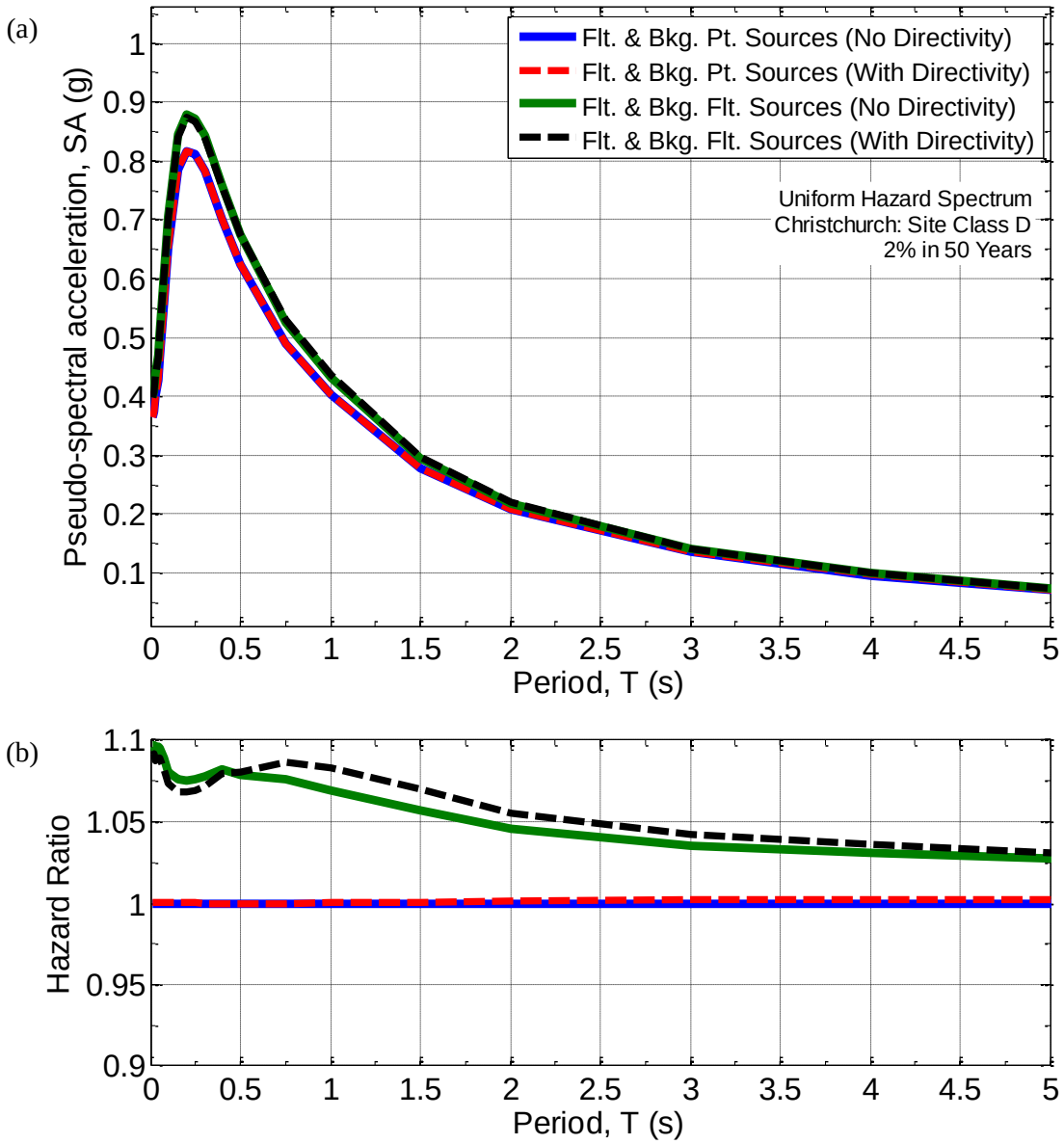

Figure 7.17: (a) UHS for a typical site in Christchurch both with and without considering the effects of near-fault directivity at an exceedance probability of 2% in 50 years; and (b) Hazard ratio illustrating the increase/decrease in hazard as a result of considering directivity effects.

Another useful exercise is to link the predominant sources obtained from deaggregation for SA corresponding to periods at which the largest directivity amplification was observed previously. For the location in Christchurch, it is appropriate to consider the deaggregation of hazard for $SA(1\text{ s})$ at the 2% in 50-year PE (refer to Figure 7.18) based on the period range (i.e. $0.7\text{ s} \leq T \leq 3\text{ s}$) over which the amplification was observed. It is evident that the hazard is controlled by: (i) small-to-moderate magnitude earthquakes ($M_w < 7.0$) on background fault sources at relatively short distances ($R_{rup} \leq 50$ km); and (ii) large magnitude earthquakes on the Alpine Fault (M_w8.1, R_{rup} = 133 km; 9.4% contribution), Porter's Pass Fault (M_w7.45, R_{rup} = 44 km 7.4% contribution), Pegasus Fault (M_w7.04, R_{rup}

= 22 km 3.9% contribution) and Ashley Fault (M_w7.18, R_{rup} = 31 km 3.8% contribution). It was identified previously that the fault sources produce marginal levels of directivity amplification based on the low pulse probabilities resulting from the large source-to-site distances. Hence, it was deduced that the observed amplification is caused mainly by the background fault sources. This is not reflected by the mean magnitude ($M_{w,mean}$ = 6.91) and distance ($R_{rup,mean}$ = 46.4 km) from the deaggregation of hazard for SA(1 s), which is likely due to a skewing effect caused by the fault sources. Although not shown here, the deaggregation of hazard considering only background fault sources provides a mean magnitude and distance of 6.45 and 27.6 km, respectively. Based on the empirical model of Shahi & Baker (2011) illustrated in Equation (7.9), this corresponds to a median pulse period of 1.9 s, which falls within the aforementioned period range corresponding to directivity amplification.

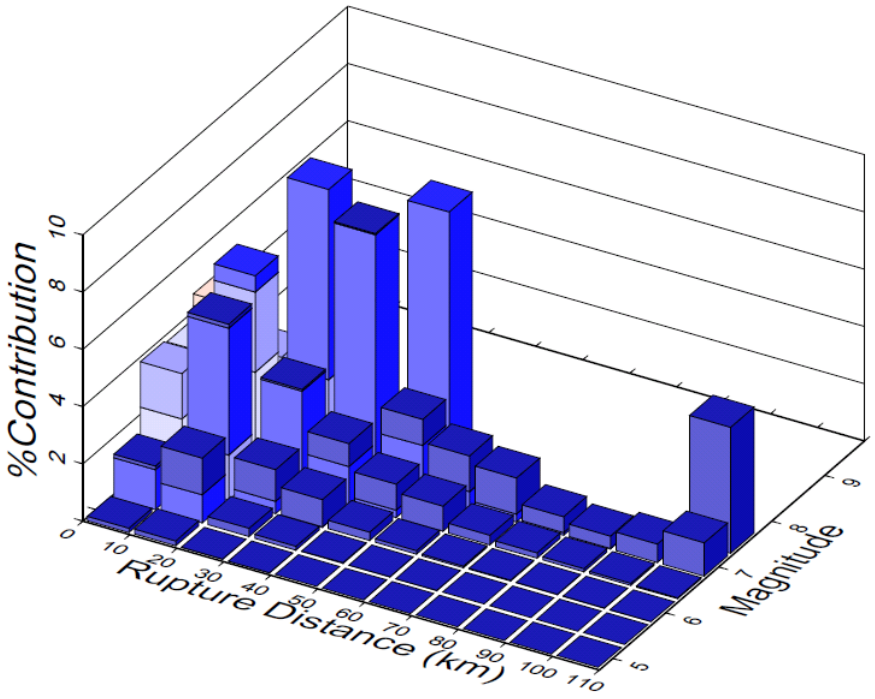

Figure 7.18: Seismic hazard deaggregation for SA(1 s) for a typical site in Christchurch at an exceedance probability of 2% in 50 years. Note that the hazard calculations are performed considering directivity effects and treating background sources as finite-faults.

7.6.2 Example 2: Otira

In this example, a generic location in Otira (latitude: -42.8302°; longitude: 171.5647°) corresponding to site class B (weak rock) conditions, as defined in NZS1170.5:2004 (Standards New Zealand, 2004) is considered. The importance of fault-based seismicity in the region is clearly illustrated by the deaggregation plots for PGA and SA(1 s) in Figure 7.19. It

is noted that both plots correspond to an exceedance probability of 2% in 50 years and are representative of short and long-period ground motion, respectively. The seismic hazard for Otira is dominated by the Kelly Fault, which is capable of producing M_w7.25 earthquakes and is located at a distance of R_{rup} = 1.5 km from the site. This is followed by significantly smaller contributions from the Browning (M_w6.89, R_{rup} = 4.6 km) and Alpine faults (M_w8.1, R_{rup} = 11.7 km) in both cases. The result above is in contrast to the Christchurch example considered previously, where the short-period ground motion was dominated by background sources and the contribution of fault sources became notable at longer vibration periods.

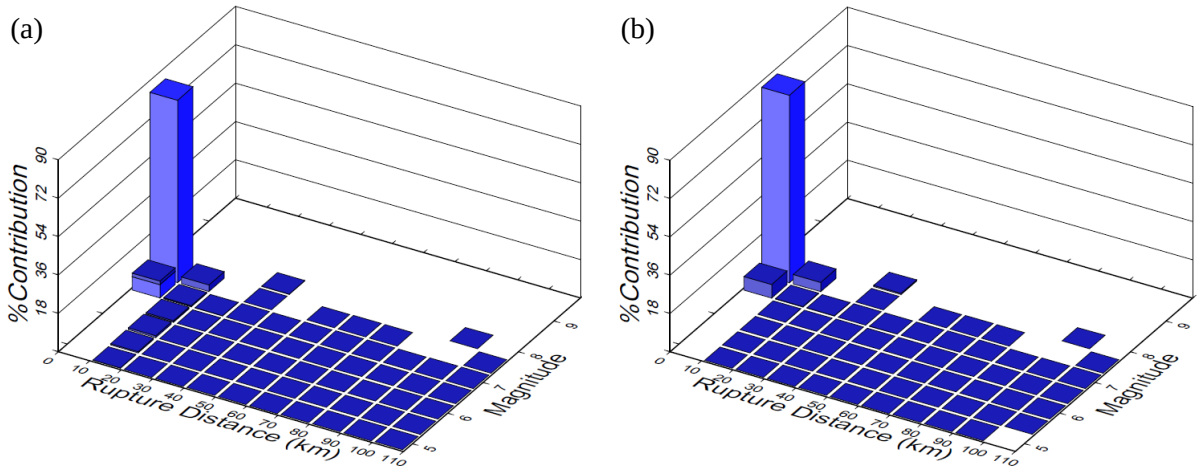

Figure 7.19: Seismic hazard deaggregation for a typical site in Otira for an exceedance probability of 2% in 50 years: (a) PGA; and (b) SA(1 s), considering both fault and background (point-source) seismicity sources.

A fewer number of IMs are considered in this example to illustrate salient features of the seismic hazard for the site of interest. Although the contribution of background sources to the seismic hazard at Otira is negligible, it is still useful to examine the effect of representing the point-sources as finite-faults. Figure 7.20 illustrates the seismic hazard curves for SA(0.2 s) and SA(1 s) in the same manner as Figure 7.12 considering only background sources. Also shown is the 'error ratio' which is calculated by normalising the hazard corresponding to each 50-year exceedance probability with that obtained using the 'exact' finite-fault representation of background sources. Firstly, it can be observed that the error resulting from the point-source assumption in the NZ ERF increases with decreasing probability of exceedance. While the error is negligible for the 50% in 50-year PE, an under-estimation of approximately 18% and 22% occur at the 2% in 50-year PE for SA(0.2 s) and SA(1 s), respectively. Due to the smaller source-to-site distances resulting from the use of fault geometry corresponding to the maximum M_w in the G-R, the resulting hazard at the 50%, 10% and 2% in 50-year PE is over-estimated by approximately 45%, 57% and 46%, respectively. Once again, this clearly

indicates the need to appropriately characterise the dimensions of potential background earthquakes.

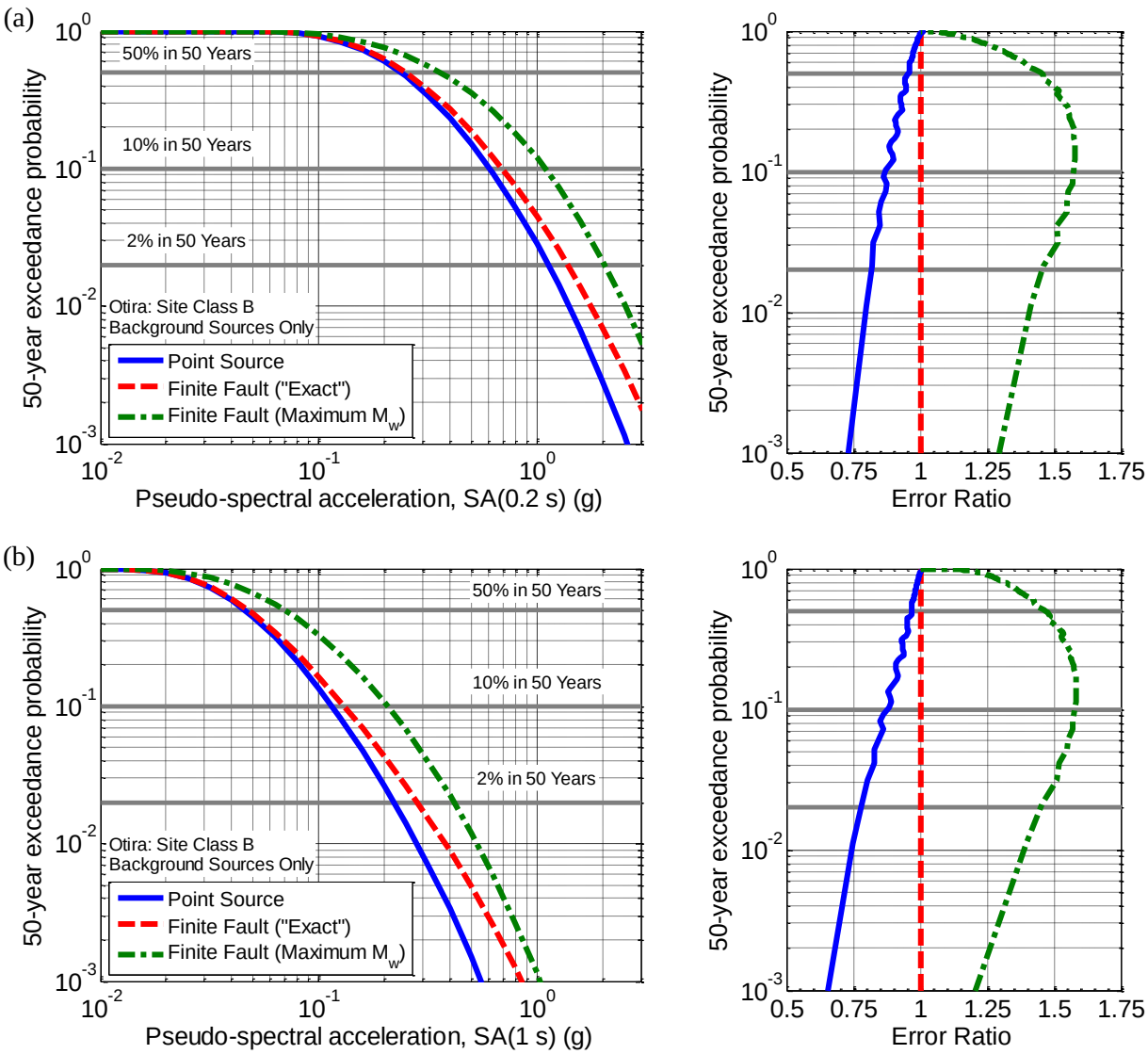

Figure 7.20: Importance of characterising background earthquake sources using the 'exact' finite-fault geometry illustrated using seismic hazard curves calculated for a site in Otira and for two IMs including: (a) SA(0.2 s); and (b) SA(1 s). The plots on the right-hand side of each panel illustrate an 'error ratio' to demonstrate (i) the under-estimation of hazard resulting from the point-source approximation; and (ii) over-estimation of the hazard resulting from the use of fault geometry corresponding to the maximum M_w in the magnitude-frequency distribution.

Despite the appreciable increase in hazard as a result of using a finite-fault representation for the point-sources, it can be observed from Figure 7.21 that in the context of the overall hazard, the increase does not bear any significance, particularly at lower exceedance probabilities. This can be attributed to the fault sources contributing a majority of the seismic hazard for both IMs considered, as highlighted by the overlapping hazard curves computed using fault sources only and a combination of both types of seismicity. Similar to

the previous example, an 'error ratio' (i.e. $UHS_{(Flt.\ \&\ Bkg.\ Pt.)}$ / $UHS_{(Flt.\ \&\ Bkg.\ Flt.)}$) is illustrated in Figure 7.22 to quantify the under-prediction resulting in the overall hazard (for SA at all vibration periods) from the point-source assumption for background sources. The error is approximately 5-6% for all vibration periods in the case of the 50% in 50-year PE. At lower exceedance probabilities, it can be seen that the error is negligible at all periods due to the significance of fault-based seismicity as described above.

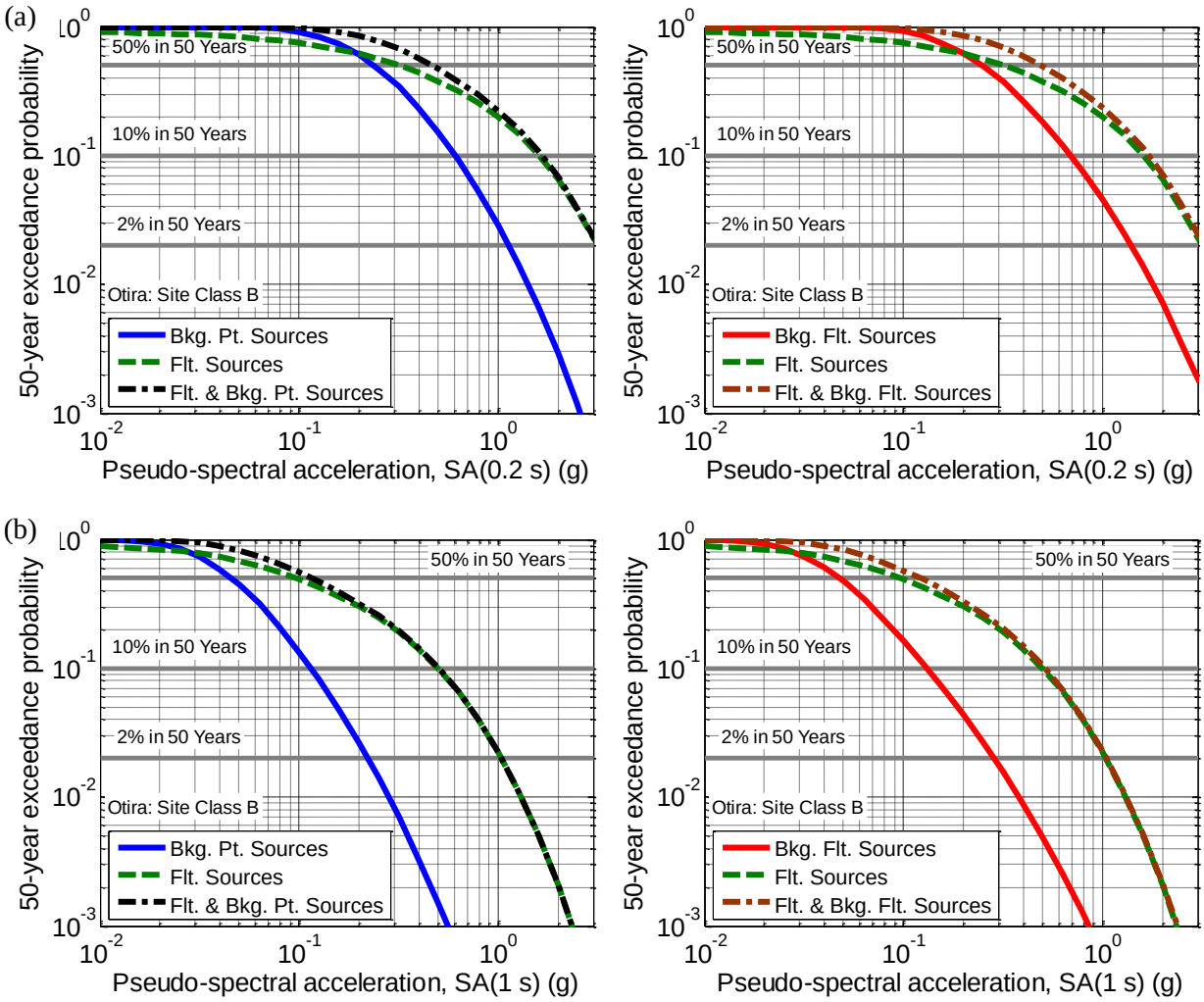

Figure 7.21: Comparison of the seismic hazard curves calculated for a typical site in Otira and for two IMs including: (a) SA(0.2 s); and (b) SA(1 s). The hazard curves are shown considering: (i) background sources only (left panel: point-source representation; right panel: finite-fault representation); (ii) fault sources only; and (iii) a combination of both background and fault-based seismicity.

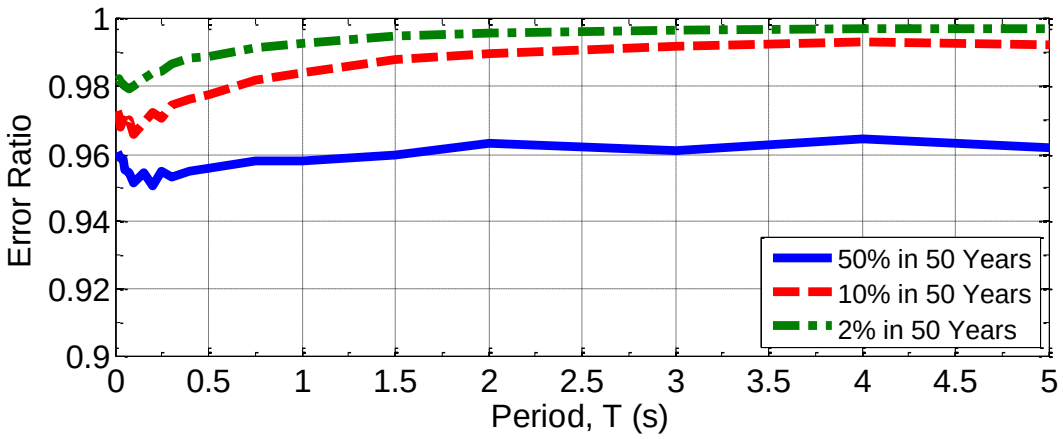

Figure 7.22: Comparison of the 'error ratio' calculated for a site in Otira for three exceedance probabilities (defined as the ratio of UHS considering background point and fault sources and UHS considering background fault and fault sources).

To quantify the effect of near-fault directivity for the site in Otira, seismic hazard analyses were conducted for vibration periods between 0.01s and 10 s with and without consideration of the approach adopted herein. As before, the analyses were repeated using both point-source and 'exact' finite-fault representations of the background sources. Figure 7.23 (10% in 50 years) and Figure 7.24 (2% in 50 years) illustrate: (i) uniform hazard spectra with and without accounting for directivity effects; and (ii) a 'hazard ratio' defined as the ratio of all UHS normalised by the base case i.e. UHS considering fault and background point-sources without directivity.

The results of both figures highlight the fact that near-fault directivity effects are significant for the Otira site at vibration periods greater than T = 2 s. It is important at this point to revisit the fact that the UHS represents an envelope of spectral ordinates resulting from a combination of ground motions with different magnitudes, distances and pulse periods. As a result, the narrowband nature of the amplification predicted by the SB11 model is somewhat masked in Figure 7.23(a-b) and Figure 7.24(a-b). This observation is consistent with the findings of previous researchers including Shahi & Baker (2011) and Chioccarelli & Iervolino (2012).

Because the hazard is dominated by fault sources at all vibration periods, it can be seen from the hazard ratios (for both PE) that the effect of considering directivity for the background fault sources is negligible. The significant directivity amplification for Otira can be attributed to higher pulse probabilities predicted by the S13 model due to the proximity and strike-slip faulting mechanism of the aforementioned fault sources which control the

seismic hazard. In the previous example, the amplification became notable for the 2% in 50-year PE. However, in this case, it is evident that the increase in hazard is similar for the two exceedance probabilities. For example, the largest increase in hazard is 34% for the 10% in 50-year PE and 32% for the 2% in 50-year PE, both of which occur at T = 5 s. The marginal increase in hazard for periods less than T = 2 s can be explained by the large magnitudes of the fault sources contributing to the hazard, thereby resulting in longer pulse periods. In fact, for the 2% in 50-year PE, it can be seen that a de-amplification of spectral ordinates is predicted by the SB11 model.

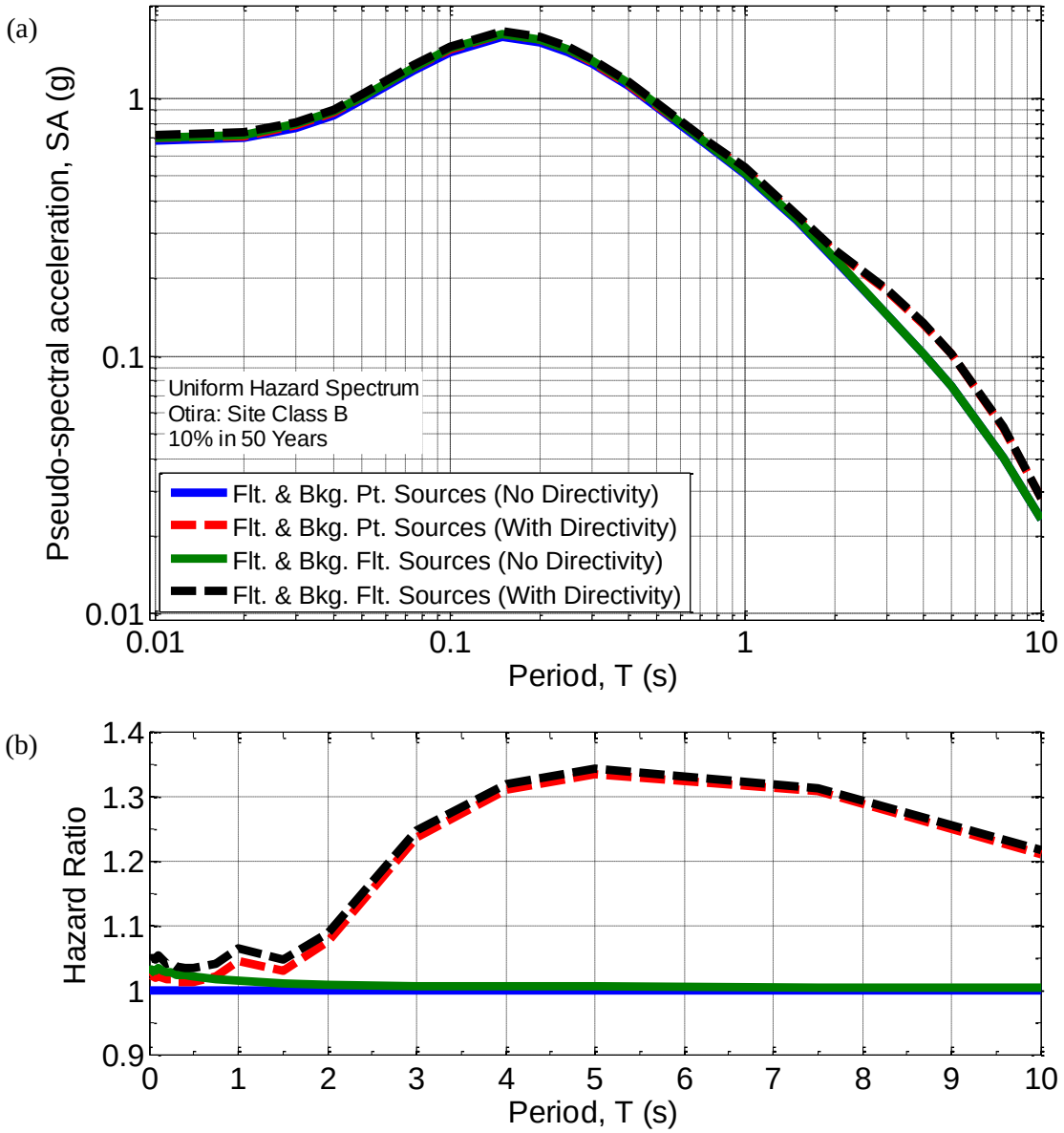

Figure 7.23: (a) UHS for a typical site in Otira both with and without considering the effects of near-fault directivity at an exceedance probability of 10% in 50 years; and (b) Hazard ratio illustrating the increase/decrease in hazard as a result of considering directivity effects.

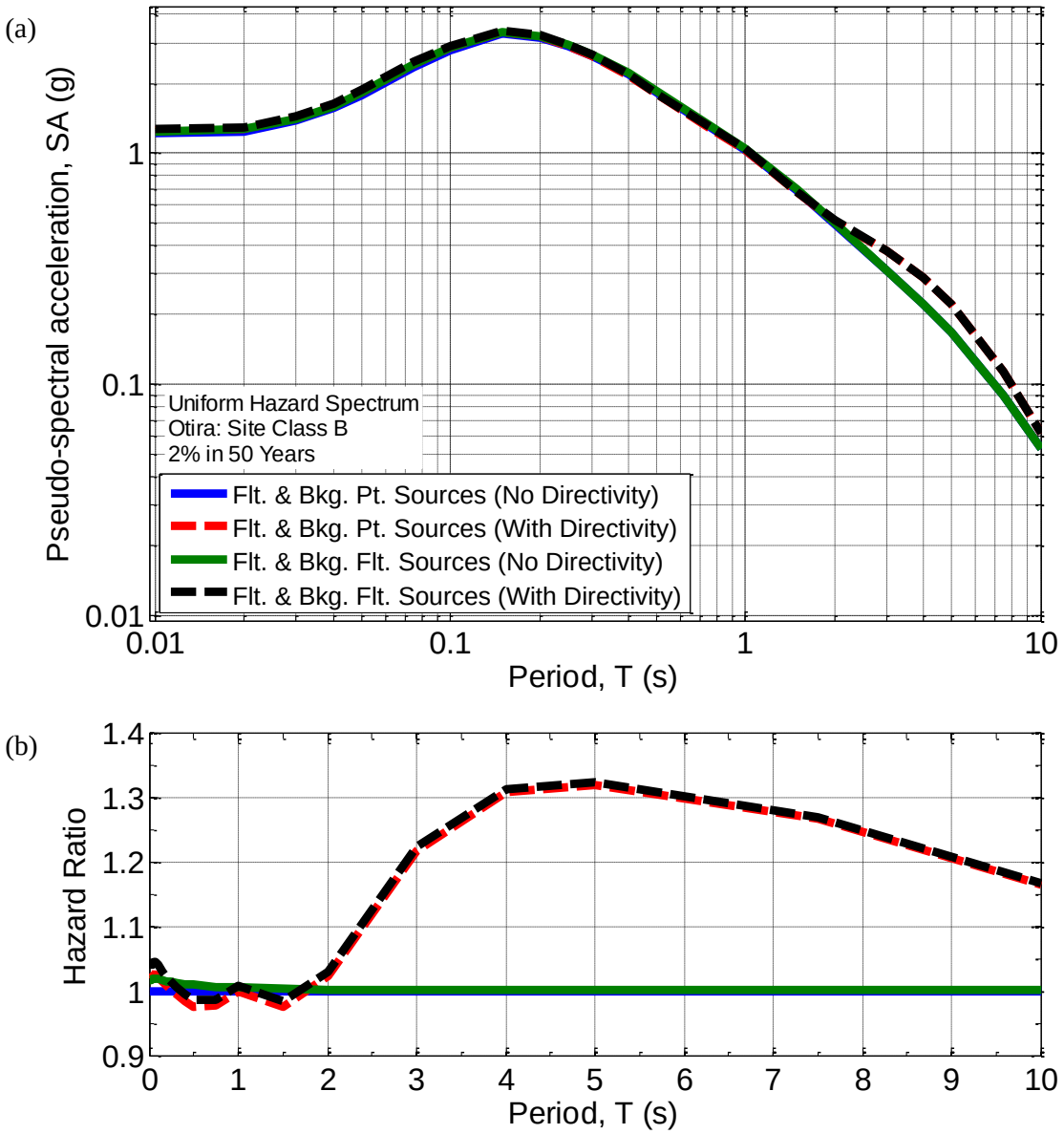

Figure 7.24: (a) UHS for a typical site in Otira both with and without considering the effects of near-fault directivity at an exceedance probability of 2% in 50 years; and (b) Hazard ratio illustrating the increase/decrease in hazard as a result of considering directivity effects.

Given that the maximum directivity amplification for Otira was observed at T = 5 s, it is logical to expect that the pulse period associated with the mean earthquake magnitude from the deaggregation for SA(5 s) would also be similar. Figure 7.25 illustrates the deaggregation plot for the latter IM and the trends identified previously for SA(1 s) (refer to Figure 7.19) are also applicable in this case. The median pulse period predicted by the SB11 model for the mean M_w of 7.32, is equal to 4.6 s, which is in the period range corresponding to the maximum observed directivity amplification.

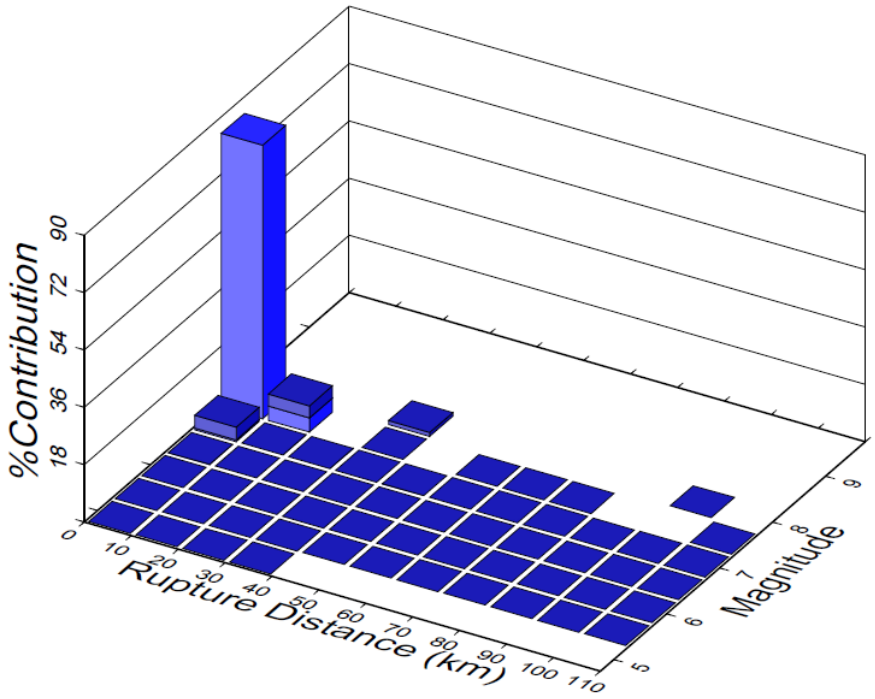

Figure 7.25: Seismic hazard deaggregation for SA(5 s) for a typical site in Otira at an exceedance probability of 2% in 50 years. Note that the hazard calculations are performed considering directivity effects and treating background sources as finite-faults.

7.7 Comparison with NZS1170.5:2004 guidelines for near-fault directivity effects

In this section, a comparison between the directivity amplification obtained from NZ-specific PSHA and the NZS1170.5:2004 prescription using the near-fault factor, N, is carried out. It should be recalled that the near-fault factor in NZS1170.5:2004 is based on the broadband directivity model of Somerville et al. (1997) and amplifies the design response spectra depending upon the vibration period and source-to-site distance (Standards New Zealand, 2004). More importantly, NZS1170.5:2004 is based on the results of seismic hazard analyses carried out using the McVerry et al. (2006) GMPE, which predicts the 'larger component' of SA i.e. the larger value of SA (for a given period, T) obtained from two as-recorded orthogonal components of ground motion, as defined in Equation (7.18):

$$SA_{Larger} = \max\left(SA_1, SA_2\right) \tag{7.18}$$

On the other hand, the seismic hazard analyses carried out in Section 7.6 used the Bradley (2010) GMPE, which predicts the geometric mean of SA (for a given period, T) obtained from two as-recorded orthogonal components of ground motion, as defined in Equation (7.19):

$$SA_{GeoMean} = \sqrt{SA_1 * SA_2} \tag{7.19}$$

Therefore, prior to carrying out the aforementioned comparison, it is important to convert the directivity amplification obtained from PSHA to the 'larger component' using ground motion directionality ratios.

Because the directivity pulse is typically polarised in the fault-normal direction (FN), SA_{FN} represents the 'larger component' in relation to the fault-parallel direction. In this study, it is assumed that SA_{FN} also represents the 'largest component' of ground motion i.e. the 100th percentile value of SA obtained after rotating the horizontal components of ground motion though all non-redundant orientations, also known as $SA_{RotD100}$ (Boore et al., 2006; Boore, 2010). Appropriate ratios developed by Bradley (2013) and Shahi & Baker (2013) are used herein to convert the geometric mean directivity amplification ($DA_{GeoMean}$) to the orientation-independent 'largest component' directivity amplification ($DA_{RotD100}$), as illustrated in Equation (7.20). It should be noted that $DA_{GeoMean}$ represents the UHS considering directivity normalised by the UHS without considering directivity.

$$\begin{aligned} DA_{RotD100} &= DA_{GeoMean} * \frac{SA_{RotD50}}{SA_{GeoMean}} * \frac{SA_{RotD100}}{SA_{RotD50}} \\ &= \frac{SA_{GeoMean_{with\ Directivity}}}{SA_{GeoMean_{without\ Directivity}}} * \frac{SA_{RotD50}}{SA_{GeoMean}} * \frac{SA_{RotD100}}{SA_{RotD50}} \end{aligned} \tag{7.20}$$

where SA_{RotD50} represents the 50th percentile value of SA obtained after rotating the horizontal components of ground motion through all non-redundant orientations; and $\frac{SA_{RotD50}}{SA_{GeoMean}}$ and $\frac{SA_{RotD100}}{SA_{RotD50}}$ are period-dependent directionality ratios obtained using models developed by Bradley (2013) and Shahi & Baker (2013), respectively. Figure 7.26 provides an illustration of the relationships for both ratios as well as their product.

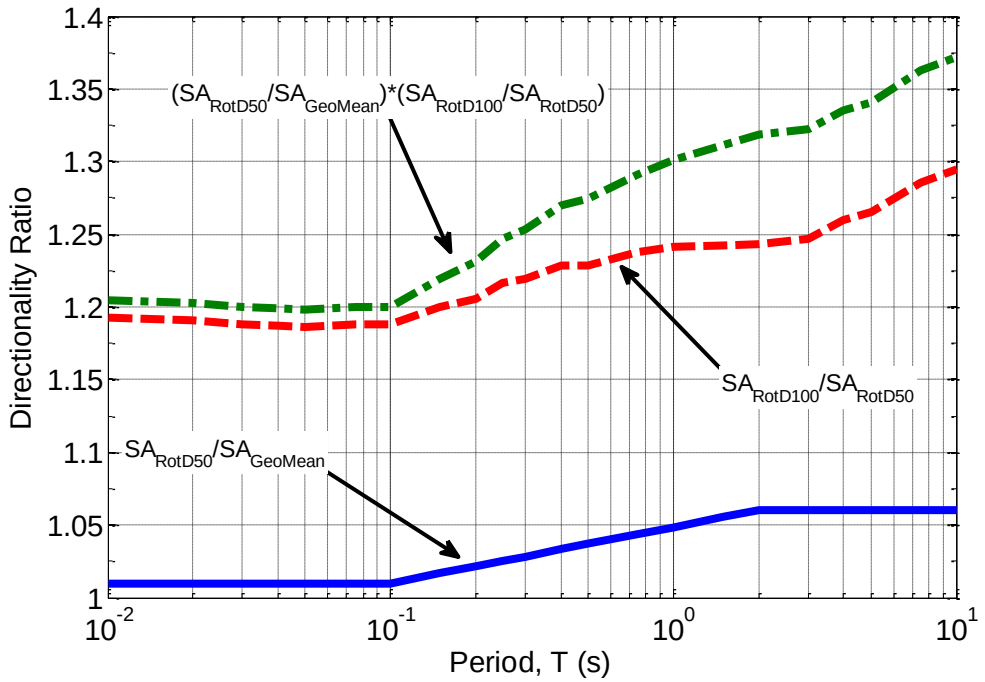

Figure 7.26: Period-dependent relationships for the ratio of SA_{RotD50} to $SA_{GeoMean}$ and $SA_{RotD100}$ to SA_{RotD50} developed by Bradley (2013) and Shahi & Baker (2013), respectively. Also shown is the product of both ratios which is used to convert $SA_{GeoMean}$ to $SA_{RotD100}$.

After having converted the directivity amplification estimated from PSHA for Christchurch and Otira using Equation (7.20), it is now appropriate to carry out a comparison with the near-fault factor. Figure 7.27 and Figure 7.28 illustrate this comparison for both locations, respectively. It is noted that the maximum permissible increase allowed by the design standard for the near-fault factor is used herein. For Christchurch, it can be observed that for T < 2.5 s, the observed amplification exceeds the code-based prescription by up to approximately 40% for the three exceedance probabilities considered. At longer periods, the trend is reversed, with the increase in hazard defined by the near-fault factor being up to 26% greater than the PSHA amplification in each case. In reality, it should be noted that the near-fault factor is not applied for the seismic design of structures in Christchurch because it is not located within 20 km of any major faults (Standards New Zealand, 2004). Hence, it is likely that the current design guidelines for the Christchurch region do not adequately account for the effects of near-fault directivity.

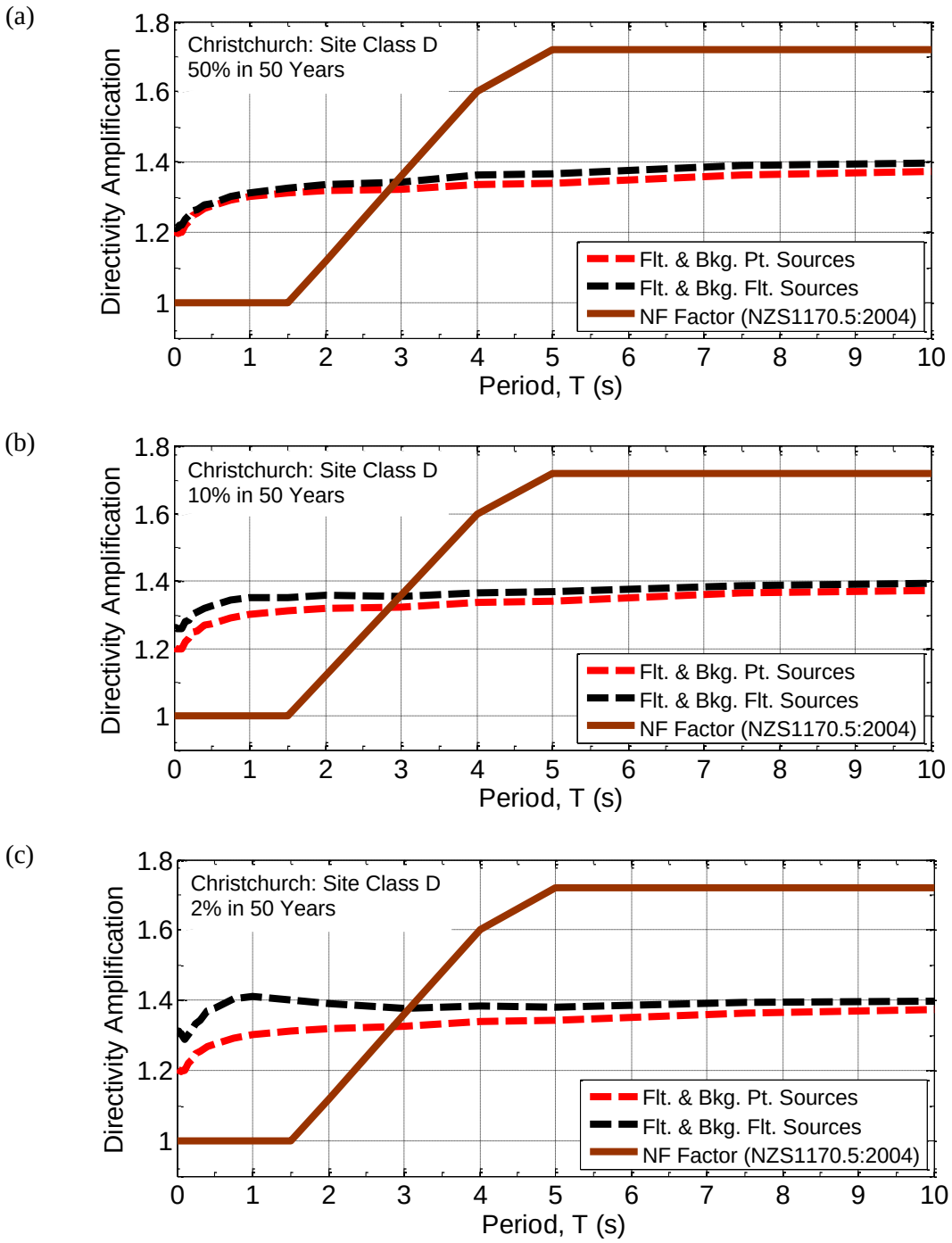

Figure 7.27: Comparison of the directivity amplification obtained from PSHA for a typical location in Christchurch with the near-fault factor from the NZS1170.5: 2004.

For the location in Otira, it is evident from Figure 7.28 that the NZS1170.5:2004 near-fault factor amplification is lower than the PSHA directivity amplification for $T < 3$ s for all three exceedance probabilities. Similar to the previous example, the largest under-prediction in this case is as high as 40%. These comparisons clearly indicate that the changes to the near-fault factor are warranted in the development of a future seismic design standard for NZ. Moreover, the narrowband nature of the directivity pulse is not captured by the Somerville et

al. (1997) model, which forms the basis of the code-based directivity prescription, as mentioned previously.

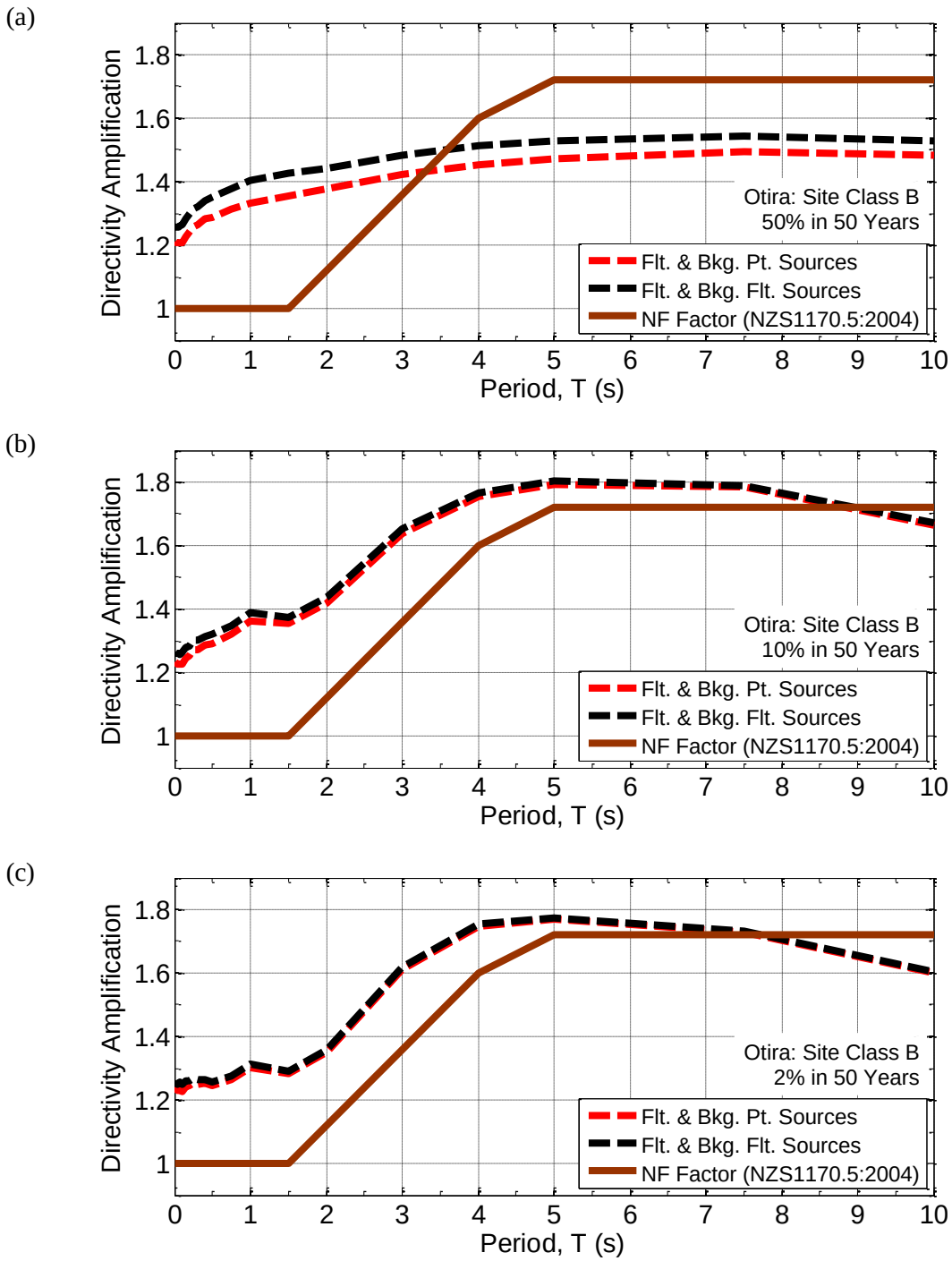

Figure 7.28: Comparison of the directivity amplification obtained from PSHA for a typical location in Otira with the near-fault factor from the NZS1170.5: 2004.

7.8 Conclusions

This chapter has focused on explicitly incorporating the effects of near-fault directivity in New Zealand-specific PSHA using a recently developed empirical model by Shahi & Baker (2011). The directivity model accounts for both the 'narrowband' nature of the directivity pulse and probability of pulse occurrence at the site of interest. Based on the findings of a recent study by Bradley (2012), it was deemed necessary to consider the distributed/background seismicity as finite-fault sources, as opposed to their conventional treatment as point-sources. More importantly, this allowed the directivity phenomenon to be considered appropriately for the background earthquakes.

The significance (or lack thereof) of explicit inclusion of directivity in PSHA was illustrated for the entire vibration period range (0.01 s $\leq T \leq$ 10 s) at typical sites located in Christchurch and Otira, two locations whose seismic hazard is comprised of notably different seismic sources. In both cases, using the 'exact' finite-fault representation of the background sources resulted in improved estimates of the hazard, with larger ground motion intensities being predicted at longer periods. For example, in Christchurch (where background sources provide a significant contribution to the total hazard), the increase in the 2475-year return period hazard for PGA and SA(3 s) was approximately 10% and 15%, respectively. Based on the results of PSHA, it was found that the maximum increase in hazard due to directivity effects is less than 10% for Christchurch at the 2% in 50-year PE, and occurred in the period range, 0.7 s $\leq T \leq$ 3 s. At higher exceedance probabilities, the observed increase was either marginal or non-existent. The low levels of amplification were attributed to (i) large source-to-site distances of fault sources; (ii) small-to-moderate magnitudes of the contributing background earthquakes; and (iii) relatively low pulse probabilities assigned to the background sources as a result of their reverse faulting-mechanism. In contrast, notable directivity amplification (15-35% increase in hazard for the periods greater than 2 s at exceedance probabilities of 10% and 2% in 50 years) was observed at Otira. This was consistent with the proximity of the site to major sources of seismicity including the strike-slip Kelly, Browning and Alpine faults. Comparisons of the observed amplification at both sites with the near-fault factor indicated that the NZS1170.5:2004 prescription for near-fault effects is generally inadequate for a large range of vibration periods. More importantly, based on the methodology outlined in this chapter, directivity effects could be directly incorporated

in seismic hazard analyses underpinning design codes – thus removing the need for a 'near-fault' factor.

7.9 References

Abrahamson, N. A. (2000). Effects of rupture directivity on probabilistic seismic hazard analysis. In *Proceedings of the 6th International Conference on Seismic Zonation*. Palm Springs, California.

Ang, A. H.-S., & Tang, W. H. (2007). *Probability Concepts In Engineering* (2nd ed.). New York: Wiley.

Baker, J. W. (2008). *An introduction to probabilistic seismic hazard analysis (PSHA)*. Stanford University. Retrieved from http://www.stanford.edu/~bakerjw/Publications/Baker_(2008)_Intro_to_PSHA_v1_3.pdf

Baker, J. W. (2011). Conditional Mean Spectrum: Tool for Ground-Motion Selection. *Journal of Structural Engineering*, **137**(3):322–331. doi:10.1061/(ASCE)ST.1943-541X.0000215

Bazzurro, P., & Cornell, C. A. (1999). Disaggregation of seismic hazard. *Bulletin of the Seismological Society of America*, **89**(2):501–520.

Berryman, K. R., Cochran, U. A., Clark, K. J., Biasi, G. P., Langridge, R. M., & Villamor, P. (2012). Major Earthquakes Occur Regularly on an Isolated Plate Boundary Fault. *Science*, **336**(6089): 1690–1693. doi:10.1126/science.1218959

Boore, D. M. (2010). Orientation-Independent, Nongeometric-Mean Measures of Seismic Intensity from Two Horizontal Components of Motion. *Bulletin of the Seismological Society of America*, **100**(4): 1830–1835. doi:10.1785/0120090400

Boore, D. M., Watson-Lamprey, J., & Abrahamson, N. A. (2006). Orientation-Independent Measures of Ground Motion. *Bulletin of the Seismological Society of America*, **96**(4A):1502–1511. doi:10.1785/0120050209

Bradley, B. A. (2012). *Ground Motion and Seismicity Aspects of the 4 September 2010 and 22 February 2011 Christchurch Earthquakes* (Technical report prepared for the Canterbury Royal Commission) (p. 62). Department of Civil and Natural Resources Engineering, University of Canterbury.

Bradley, B. A. (2013). *Examination of ground motion directionality in the Christchurch earthquakes: Ratio of geometric mean to larger component* (Technical Report Prepared for GNS Science and the). Chr: University of Canterbury.

Bradley, B. A., & Cubrinovski, M. (2011). Near-source Strong Ground Motions Observed in the 22 February 2011 Christchurch Earthquake. *Seismological Research Letters*, **82**(6): 853–865. doi:10.1785/gssrl.82.6.853

Bradley, B. A., Stirling, M. W., McVerry, G. H., & Gerstenberger, M. (2012). Consideration and Propagation of Epistemic Uncertainties in New Zealand Probabilistic Seismic-Hazard Analysis. *Bulletin of the Seismological Society of America*, **102**(4):1554–1568. doi:10.1785/0120110257

Bradley, B. A. (2010). *NZ-Specific Pseudo-Spectral Acceleration Ground Motion Prediction Equations Based on Foreign Models* (Research Report No. 2010-03) (p. 316). Department of Civil and Natural Resources, University of Canterbury.

Bradley, B. A. (2012). A ground motion selection algorithm based on the generalized conditional intensity measure approach. *Soil Dynamics and Earthquake Engineering*, **40**:48–61.

Chioccarelli, E., & Iervolino, I. (2012). Near-source seismic hazard and design scenarios. *Earthquake Engineering & Structural Dynamics*, n/a–n/a. doi:10.1002/eqe.2232

DeMets, C., Gordon, R. G., & Argus, D. F. (2010). Geologically current plate motions. *Geophysical Journal International*, **181**(1):1–80.

Field, E. H., Jordan, T. H., & Cornell, C. A. (2003). OpenSHA: A developing community-modelling environment for seismic hazard analysis. *Seismological Research Letters*, **74**(4):406–419.

GeoNet. (2011). *Historical Earthquakes*. Retrieved November 1, 2013, from http://info.geonet.org.nz/display/quake/Historical+Earthquakes

Gledhill, K., Ristau, J., Reyners, M., Fry, B., & Holden, C. (2011). The Darfield (Canterbury, New Zealand) Mw 7.1 Earthquake of September 2010: A Preliminary Seismological Report. *Seismological Research Letters*, **82**(3):378–386. doi:10.1785/gssrl.82.3.378

Gutenberg, B., & Richter, C. F. (1944). Frequency of earthquakes in California. *Bulletin of the Seismological Society of America*, **34**(4):185–188.

Hanks, T. C., & Bakun, W. H. (2002). A bilinear source-scaling model for M-log A observations of continental earthquakes. *Bulletin of the Seismological Society of America*, **92**(5):1841–1846.

Iervolino, I., & Cornell, C. A. (2008). Probability of occurrence of velocity pulses in near-source ground motions. *Bulletin of the Seismological Society of America*, **98**(5):2262–2277. doi:10.1785/0120080033

Kramer, S. L. (1996). *Geotechnical Earthquake Engineering*. Upper Sadle River, New Jersey: Prentice Hall.

Mai, P. M. (2005). Hypocenter Locations in Finite-Source Rupture Models. *Bulletin of the Seismological Society of America*, **95**(3):965–980. doi:10.1785/0120040111

MATLAB (Version 7.10.0). (2010). Natick, Massachusetts: The MathWorks Inc.

McGuire, R. K. (2004). *Seismic Hazard and Risk Analysis*. Berkeley, California: Earthquake Engineering Research Institute.

McVerry, G. H., Gerstenberger, M. C., Rhoades, D. A., & Stirling, M. W. (2012). Spectra and Pgas for the Assessment and Reconstruction of Christchurch. In *2012 NZSEE Conference Proceedings*. Christchurch, New Zealand.

McVerry, G. H., Zhao, J. X., Abrahamson, N. A., & Somerville, P. G. . (2006). New Zealand acceleration response spectrum attenuation relations for crustal and subduction zone earthquakes. *Bulletin of the New Zealand Society for Earthquake Engineering*, **39**(4):1–58.

Rowshandel, B. (2010). Directivity Correction for the Next Generation Attenuation (NGA) Relations. *Earthquake Spectra*, **26**(2):525–559. doi:10.1193/1.3381043

Schwartz, D. P., & Copper, K. J. (1984). Fault Behavior and Characteristic Earthquakes: Examples From the Wasatch and San Andreas Fault Zones. *Journal of Geophysical Research*, **89**(b7): 5681–5698. doi:10.1029/JB089iB07p05681

Shahi, S. K. (2013, January). *A probabilistic framework to include the effects of near-fault directivity in seismic hazard assessment*. Stanford University, Stanford.

Shahi, S. K., & Baker, J. W. (2011). An empirically calibrated framework for including the effects of near-fault directivity in probabilistic seismic hazard analysis. *Bulletin of the Seismological Society of America*, **101**(2):742–755. doi:10.1785/0120100090

Shahi, Shrey K., & Baker, J. W. (2013). *NGA-West2 Models for Ground-Motion Directionality*. Pacific Earthquake Engineering Research Center. Retrieved from http://128.32.145.86/publications/peer_reports/reports_2013/webPEER-2013-10-Shahi-Baker.pdf

Somerville, P. G. (2003). Magnitude-scaling of the near fault rupture directivity pulse. *Physics of the Earth and Planetary Interiors*, **137**(1-4):201–212. doi:10.1016/S0031-9201(03)00015-3

Somerville, P. G., Smith, N. F., Graves, R. W., & Abrahamson, N. A. (1997). Modification of empirical strong ground motion attenuation relations to include the amplitude and duration effects of rupture directivity. *Seismological Research Letters*, **68**(1):199–222.

Spudich, P., & Chiou, B. S. J. (2008). Directivity in NGA Earthquake Ground Motions: Analysis Using Isochrone Theory. *Earthquake Spectra*, **24**(1):279–298. doi:10.1193/1.2928225

Standards New Zealand. (2004). *NZS1170.5:2004, Structural Design Actions, Part 5: Earthquake actions- New Zealand*. Wellington, New Zealand.

Stirling, M., McVerry, G., Gerstenberger, M., Litchfield, N., Van Dissen, R., Berryman, K., … Jacobs, K. (2012). National Seismic Hazard Model for New Zealand: 2010 Update. *Bulletin of the Seismological Society of America*, **102**(4):1514–1542. doi:10.1785/0120110170

Stirling, M. W., Gerstenberger, M., Litchfield, N., McVerry, G. H., Smith, W. D., Pettinga, J. R., & Barnes, P. (2007). *Updated probabilistic seismic hazard assessment for the Canterbury Region*. Retrieved from http://ecan.govt.nz/publications/Reports/canterbury-probabilistic-seismic-hazard-assessment-report.pdf

Stirling, Mark W., Mc Verry, G. H., & Berryman, K. R. (2002). A new seismic hazard model for New Zealand. *Bulletin of the Seismological Society of America*, **92**(5):1878–1903.

Strasser, F. O., Arango, M. C., & Bommer, J. J. (2010). Scaling of the source dimensions of interface and intraslab subduction-zone earthquakes with moment magnitude. *Seismological Research Letters*, **81**(6):941–950.

Tothong, P., Cornell, C. A., & Baker, J. W. (2007). Explicit directivity-pulse inclusion in probabilistic seismic hazard analysis. *Earthquake Spectra*, **23**(4):867–891. doi:10.1193/1.2790487

USGS. (2012). *Earthquake Glossary*. Retrieved November 1, 2013, from http://earthquake.usgs.gov/learn/glossary/?term=active%20fault

Villamor, P., Van Dissen, R., Alloway, B. V., Palmer, A. S., & Litchfield, N. (2007). The Rangipo fault, Taupo rift, New Zealand: An example of temporal slip-rate and single-event displacement variability in a volcanic environment. *Geological Society of America Bulletin*, **119**(5-6):529–547.

Wells, D. L., & Coppersmith, K. J. (1994). New empirical relationships among magnitude, rupture length, rupture width, rupture area, and surface displacement. *Bulletin of the Seismological Society of America*, **84**(4):974–1002.

Youngs, R. R., & Coppersmith, K. J. (1985). Implications of fault slip rates and earthquake recurrence models to probabilistic seismic hazard estimates. *Bulletin of the Seismological society of America*, **75**(4):939–964.

8 Conclusions

In this thesis, near-fault ground motions resulting from several important events in the 2010-11 Canterbury earthquake sequence were rigorously examined to identify and document evidence of forward-directivity effects. The identification process involved the use of state-of-the-art pulse classification algorithms whose performance was subsequently scrutinised based on the results obtained. Using the observed forward-directivity ground motions, the efficacy of models (where applicable, including those developed in the present study) used to predict: (i) the probability of directivity pulse occurrence; (ii) the effects of directivity on acceleration response spectrum amplitudes; and (iii) the period and amplitude of the directivity pulse were determined. Such an elaborate exercise has not been previously possible in a New Zealand (NZ) context primarily due to a lack of well-recorded near-fault ground motions resulting from moderate-to-large magnitude earthquakes. The above efforts culminated in the explicit incorporation of directivity effects in probabilistic seismic hazard analysis for NZ. A summary of the main findings from previous chapters and their implications are provided in the sections to follow.

8.1 Characteristics of observed forward-directivity effects in the 2010-11 Canterbury earthquakes

The objective of Chapter 3 was to carry out an extensive analysis of near-fault ground motions resulting from the Canterbury earthquakes in an effort to identify observations of forward-directivity effects. In particular, the following events were considered:

- M_w7.1 Darfield Earthquake (4 September 2010)
- M_w6.2 Christchurch Earthquake (22 February 2011)
- M_w5.3 and M_w6.0 Earthquakes (13 June 2011)
- M_w5.8 and M_w5.9 Earthquakes (23 December 2011)

Although previous studies by Bradley (2012b) and Bradley & Cubrinovski (2011) have also examined directivity effects in the Darfield and Christchurch earthquakes, respectively, the level of rigour applied in the identification and characterisation (both in terms of period and amplitude) of directivity pulses in the present study was significantly greater. A wavelet-based pulse classification algorithm developed by Baker (2007) (B07) was initially employed to identify directivity pulses in an automated manner. The algorithm uses wavelet analysis to extract the main pulse-like feature from the velocity time-series and then calculates a pulse indicator (PI) score to classify the ground motion as pulse-like or non-pulse-like. Further criteria are applied to determine whether the extracted pulse arrives early and has significant amplitude. The automated approach failed to classify a number of ground motions which clearly demonstrated evidence of an early-arriving directivity pulse. This deficiency in model prediction was attributed to (i) incorrect pulse extraction resulting from the inability of the algorithm to distinguish between the directivity pulse and pulse-like motion caused by other physical phenomena (e.g. basin-induced surface waves and manifestation of acceleration 'spikes' due to liquefaction as low-frequency pulses in the velocity time-series); and (ii) insufficiency of the PI score as a sole classification metric. In an effort to ensure correct pulse extraction and characterisation, a 'manual' approach was adopted by truncating the time over which a pulse could be extracted. The classification process was further guided by careful examination of the horizontal velocity trajectory plots and source-to-site geometry.

The above analysis resulted in the classification of 59 pulse-like ground motions which, in the author's opinion, were caused by forward-directivity effects in the Canterbury earthquakes. It is noted that directivity effects in ground motions from the M_w5.3 June and M_w5.8 December earthquakes were generally insignificant in terms of amplitude, which prompted their removal from the list of pulse-like motions. In the Darfield event, the principal directivity pulse was observed in an orientation normal to the inferred rupture propagation along the central and eastern segments of the predominantly strike-slip Greendale fault towards Christchurch. On the other hand, several ground motions from the Christchurch and 13 June 2011 (M_w6.0) earthquakes contained velocity pulses in orientations which were not normal to the modelled finite faults, inferred as a result of the complex rupture process involving multiple fault planes. Using a simplified approach to define the pulse orientation, it was found that a majority of the pulses from the two events were aligned with fault-normal orientations corresponding to at least one fault plane of these complex ruptures. Although potential reasons were given for the observed trends, it was difficult to

confirm their validity based on kinematic finite fault models (FFM) alone. It is anticipated that ongoing efforts to carry out physics-based broadband ground motion simulation (Bradley, personal communication, 2012) will provide further insight into the complex interaction of source-, path- and site-effects which resulted in the ground motions examined in the present study.

Another wavelet-based pulse classification algorithm, developed by Shahi (2013), was also considered in this study on the basis of its improved classification criteria in relation to the B07 algorithm. However, upon applying the algorithm to near-fault ground motions from the Canterbury earthquakes, superior pulse classification results could not be obtained due to the aforementioned reasons which were not considered by Shahi (2013) when modifying the B07 algorithm. Hence, the use of other approaches (i.e. visual examination of the velocity time-series, horizontal velocity trajectory plots and source-to-site geometry) in conjunction with the automated algorithms appears warranted in identifying velocity pulses in ground motions as a result of forward-directivity, on an event-specific basis. In doing so, it must be accepted that some level of bias can potentially be introduced due to subjectivity in the classification process. When dealing with large strong motion datasets, the B07 and S13 algorithms provide an extremely efficient means of identifying pulse-like and non-pulse-like motions. The classified pulses can be subsequently scrutinised using manual approaches to determine whether they were caused by directivity effects or other aforementioned effects. Such an approach was used by Baker (2007) and Shahi (2013) in identifying directivity pulses from the NGA and NGA-West2 strong ground motion databases, respectively.

8.2 Empirical modelling of forward-directivity effects

8.2.1 Pulse probability

Empirical models to predict the probability of pulse occurrence at sites located in the near-fault region are typically required to incorporate near-fault directivity effects in seismic hazard analyses that make use of empirical ground motion prediction equations (GMPEs). They can also be used in hindsight as to whether pulse-like motions from specific events occurred at locations where relatively large pulse probabilities are predicted. Chapter 4 evaluated pulse probability models developed by Iervolino & Cornell (2008) (IC08), Shahi & Baker (2010) (SB10) and Shahi (2013) (S13) using observations from four significant events

(4 September 2010 M_w7.1 Darfield, 22 February 2011 M_w6.2 Christchurch, 13 June 2011 M_w 6.0 June and 23 December 2011 M_w 5.9 December earthquakes) in the Canterbury earthquake sequence. It is noted that each of these models is purely a function of the source-to-site geometry. In particular, logistic regression models were fitted to the observations of pulse/non-pulse observations from all events with predictions from the three models acting as the main predictor variable. This was justified by the fact that the pulse classification process is binary in nature. A comparison of the fitted models across all four events revealed that the predictions for strike-slip events (i.e. Darfield and June earthquakes) are better than those associated with non strike-slip events (i.e. Christchurch and December earthquakes). This was attributed to the fact that models for strike-slip events always predict larger pulse probabilities, which is perhaps also indicative of the 'cleaner' nature of the current understanding of the geometry and physics in these events, as suggested by Iervolino & Cornell (2008).

Based on the results of logistic regression analysis, it was found that the S13 model (developed using forward-directivity ground motions from the latest NGA-West2 database) provided the most improved predictions in relation to the IC08 and SB10 models. As a result, it was considered appropriate to adopt the S13 model for further use in Chapters 5 and 7. In addition, pulse probability contour maps for the Darfield, Christchurch, June and December earthquakes were developed using the S13 model. Observations of forward-directivity ground motions generally coincided with larger predicted pulse probability contours. However, the comparison of observed pulses and prediction probabilities was effective in highlighting the fact that the occurrence of directivity pulses does not depend on source-to-site geometry alone, but also other physical phenomena related to source-, path- and site-effects. For the purposes of empirical ground motion modelling, it must be appreciated that the complexity of the above phenomena has inhibited the incorporation of physical parameters in pulse probability models. Another source of discrepancy in the above comparison for the Christchurch and June earthquakes resulted from the fact that the source-to-site geometry required as inputs in the models is based on a single rupturing fault plane, in contrast to the known multiple-fault rupturing events in this earthquake sequence (Beavan et al. 2012).

8.2.2 Response spectrum amplification due to directivity effects

Forward-directivity effects are not explicitly modelled by conventional GMPEs for pseudo-spectral acceleration (SA) used in seismic hazard assessments. This could potentially

lead to an under-estimation of the hazard for a site located in the near-fault region. In fact, a recent study by Bradley (2012a) concluded that NZ-specific GMPEs are unable to capture the increase in long-period spectral ordinates due to forward-directivity effects based on comparisons with observed ground motions from the Darfield and Christchurch earthquakes. Several empirical models have been proposed by researchers in the past to essentially 'correct' the predictions of GMPEs for directivity effects. Models which monotonically increase or decrease the predicted spectral amplitudes over a wide range of periods are classified as 'broadband', whereas those which predict amplification in the vicinity of the directivity pulse period are referred to as 'narrowband'. Similar to Chapter 4, the predictive capabilities of empirical models for response spectrum amplification were examined using observations of forward-directivity ground motions from the Canterbury earthquakes in Chapter 5. Specifically, broadband models developed by Somerville et al. (1997) (S97), Abrahamson (2000) (AB00) and Rowshandel (2010) (R10) were considered, as well as a more recent narrowband model developed by Shahi & Baker (2011) (SB11).

Using a direct comparison of the observed and predicted directivity amplification, it was found that broadband models, which form the basis of the near-fault factor (N) in the New Zealand loadings standard, NZS1170.5:2004 (Standards New Zealand, 2004), notably under-predicted the observed amplification of moderate-to-long period spectral ordinates. While the SB11 model over-predicted the directivity amplification, the maximum amplification was predicted in the region surrounding the pulse period, consistent with the fact that the directivity pulse is inherently narrowband in nature. However, for the purposes of forward prediction, it must be accepted that the predicted amplification will always occur over a wider range of periods as a consequence of considering uncertainties in the directivity pulse occurrence probability and period, as well as the contribution of multiple earthquake sources to the total seismic hazard.

Residual analysis played an important role in identifying potential bias demonstrated by the directivity models on an event-specific basis. The trends identified from the direct comparison above were largely confirmed by the residuals. While the strike-slip version of the S97/AB00 model provided a notable reduction of the mean residuals in the Darfield event for periods greater than 0.6 s, the non strike-slip version predicted a deamplification of spectral ordinates for several sites in the Christchurch earthquake. Similar trends were also observed using the R10 model, with the effect of the predicted amplification for the Darfield

earthquake becoming significant for periods greater than 4 s. The SB11 narrowband model generally provided similar or improved predictions in relation to its broadband counterparts. More importantly, the greatest reduction in the mean residuals occurred in the region surrounding the pulse period for all four events considered. Based on its consistency with theoretical considerations and empirical observations, the SB11 model was adopted in Chapter 7 to explicitly model the effects of directivity in seismic hazard analysis for NZ.

In addition to forward-directivity effects, the positive bias exhibited by all directivity models at periods greater than 5 s was inferred as being a result of additional amplification of SA amplitudes caused by: (i) basin-generated surface waves; and (ii) non-linear surficial soil response in the Darfield and Christchurch earthquakes. This is unsurprising given the highly simplified manner in which both physical phenomena are modelled by empirical GMPEs. For example, the B10 GMPE accounts for basin effects using the $Z_{1.0}$ parameter, which represents the depth to an average shear-wave velocity of $V_{s,30}$ = 1000 m/s. Due to the unavailability of site-specific depths, the empirical model of Chiou & Youngs (2008) was initially used, which resulted in poor predictions of the observed long-period SA amplitudes. By increasing $Z_{1.0}$ for sites which demonstrated basin effects in the two events, a systematic reduction in the mean residuals was observed at all periods. While improved predictions were obtained for SA at long periods, a significant over-prediction was observed at short-to-moderate vibration periods. It is expected that ongoing efforts (e.g. Lee et al., 2013) to characterise the geometric and mechanical properties of the Canterbury basin will provide basin depths which can be used with confidence in empirical ground motion modelling for the Christchurch region.

8.2.3 Prediction of directivity pulse period and amplitude

The results of numerous studies have highlighted that the period and amplitude of the directivity pulse largely govern the response of structures subjected to forward-directivity ground motions. This has prompted researchers to develop empirical relationships for both parameters, which are typically a function of moment magnitude, source-to-site distance, site conditions and fault type. These models can be used to define simplified velocity pulse shapes for use in seismic response analyses. Models for the pulse period are also essential in the use of narrowband directivity models in seismic hazard calculations for the near-fault region.

In Chapter 6, pulse periods and amplitudes observed in the Canterbury earthquakes (characterised in Chapter 3) were used to determine the efficacy of several existing empirical models. While the observed pulse periods from the Darfield and Christchurch earthquakes were notably under-predicted, favourable predictions were obtained for the June (M_w6.0) and December (M_w5.9) 2011 events. The elongation in observed pulse periods from the two larger magnitude earthquakes was inferred as being a result of both the effect of nonlinear site response and influence of the Canterbury basin, which appear to be less significant for the June and December events due to smaller shaking amplitudes and shorter rupture durations. On the other hand, empirical relationships for the pulse amplitude (defined by the peak ground velocity, PGV) generally provided accurate estimates for source-to-site distances between 1 km and 10 km. At larger distances, the slower apparent attenuation of the observed PGVs in the Darfield earthquake was not well-captured by the models.

The availability of the most up-to-date, and larger, NGA-West2 (NGAW2) pulse-like ground motion dataset allowed the development of revised empirical models for both pulse parameters using a mixed-effects regression model. In particular, pulse period models were developed considering: (i) earthquake magnitude dependence only; (ii) magnitude and rake angle dependence and (iii) magnitude, rake angle and site class dependence (i.e. to examine the effects of site response). Model (ii), in particular, is a novel contribution in that it captures the effect of faulting mechanism on pulse period using a continuous predictor variable (i.e. rake angle), as compared to previous models which use a binary 'strike-slip' and 'non-strike-slip' classification. In doing so, predictions consistent with theory and empirical evidence were obtained. A simple model for predicting PGV as a function of magnitude and source-to-site distance was also developed using pulse-like ground motions recorded within 20 km of the causative rupture in the NGAW2 database.

The inclusion of a larger dataset in the model development above did not result in improved pulse period estimates (particularly for the Darfield and Christchurch earthquakes), which was effective in highlighting the importance of region-specific features on directivity characteristics. In contrast, the NGAW2 model for PGV provided significantly improved predictions in relation to its predecessors for distances greater than 10 km.

8.3 Inclusion of near-fault directivity in NZ-specific PSHA

The conventional PSHA framework used to conduct routine seismic hazard assessments in NZ does not account for the effects of near-fault directivity. In order to address this issue, Chapter 7 initially focused on explicitly including the recent narrowband directivity model of Shahi & Baker (2011) in the Bradley (2010) GMPE. Prior to the application of the modified GMPE in NZ-specific PSHA, it was necessary to appropriately model the background sources in the NZ seismicity model. Specifically, point sources were converted to an 'exact' finite-fault representation using dimensions obtained from magnitude-scaling relationships. This also allowed the effect of near-fault directivity to be considered for background earthquakes.

Typical sites in Christchurch and Otira were considered in this study, which are locations with notable differences in the sources contributing to the seismic hazard. Due to the smaller source-to-site distances resulting from the use of finite-fault sources to represent background seismicity, larger estimates of the seismic hazard were obtained for both locations in comparison with the conventional and unconservative assumption of point sources. The under-estimation of seismic hazard resulting from the point-source assumption increases at longer vibration periods, but because long-period spectral ordinates in PSHA are typically dominated by modelled faults, then eventually the point-source assumption generally leads to the largest errors at short-to-moderate vibration periods. Hence, the results re-affirm the findings of a recent study by Bradley (2012a), in which the consistency of the NZ seismicity model in this regard was scrutinised using observed ground motions from the Canterbury earthquakes.

The probabilistic seismic hazard analyses including directivity models were conducted for $SA(0.01 \text{ s} \leq T \leq 10 \text{ s})$ at exceedance probabilities (PE) of 50%, 10% and 2% in 50 years. For Christchurch, the maximum increase in hazard caused by directivity effects was found to be less than 10% at the 2% in 50-year PE, and occurred in the period range, $0.7 \text{ s} \leq T \leq 3$ s. The effects of explicit directivity inclusion were either marginal or non-existent at higher exceedance probabilities. Reasons for the small levels of predicted directivity amplification in Christchurch include: (i) large source-to-site distances of modelled fault sources (which represent the most likely large magnitude earthquakes, for which directivity effects will be most significant); (ii) predominantly small-to-moderate magnitudes of the

contributing background earthquakes; and (iii) relatively low pulse probabilities assigned to the background sources as a result of their reverse faulting-mechanism. The seismic hazard at Otira, in contrast, was dominated by major fault-sources including the Kelly, Browning and Alpine faults. Due to the proximity of these faults to the site (R_{rup} < 12 km), and their ability to produce large magnitude earthquakes ($6.89 \leq M_w \leq 8.1$), the amplification due to directivity effects was significant and reached its peak at T = 5 s. In particular, a 15-35% increase in hazard was observed for periods greater than 2 s at exceedance probabilities of 10% and 2% in 50 years.

Appropriate directionality ratios were used to convert the directivity amplification obtained from PSHA to allow a comparison with the near-fault factor (N) prescribed in NZS1170.5:2004, which is based on the larger component definition of horizontal ground motion. The comparisons clearly emphasised the fact that current seismic design guidelines to consider near-fault effects warrant revision to be consistent across NZ.

8.4 References

Abrahamson, N. A. (2000). Effects of rupture directivity on probabilistic seismic hazard analysis. In *Proceedings of the 6th International Conference on Seismic Zonation*. Palm Springs, California.

Baker, J. W. (2007). Quantitative classification of near-fault ground motions using wavelet analysis. *Bulletin of the Seismological Society of America*, **97**(5):1486–1501. doi:10.1785/0120060255

Bradley, B. A. (2012a). *Ground Motion and Seismicity Aspects of the 4 September 2010 and 22 February 2011 Christchurch Earthquakes* (Technical report prepared for the Canterbury Royal Commission) (p. 62). Department of Civil and Natural Resources Engineering, University of Canterbury.

Bradley, B. A. (2012b). Strong ground motion characteristics observed in the 4 September 2010 Darfield, New Zealand earthquake. *Soil Dynamics and Earthquake Engineering*, **42**, 32–46. doi:10.1016/j.soildyn.2012.06.004

Bradley, B. A., & Cubrinovski, M. (2011). Near-source Strong Ground Motions Observed in the 22 February 2011 Christchurch Earthquake. *Seismological Research Letters*, **82**(6):853–865. doi:10.1785/gssrl.82.6.853

Bradley, B. A. (2010). *NZ-Specific Pseudo-Spectral Acceleration Ground Motion Prediction Equations Based on Foreign Models* (Research Report No. 2010-03) (p. 316). Department of Civil and Natural Resources, University of Canterbury.

Chiou, B.-J., & Youngs, R. R. (2008). An NGA Model for the Average Horizontal Component of Peak Ground Motion and Response Spectra. *Earthquake Spectra*, **24**(1):173–215. doi:10.1193/1.2894832

Iervolino, I., & Cornell, C. A. (2008). Probability of occurrence of velocity pulses in near-source ground motions. *Bulletin of the Seismological Society of America*, **98**(5):2262–2277. doi:10.1785/0120080033

Lee, R. L., Bradley, B. A., Pettinga, J. R., Hughes, M., & Graves, R. W. (2013). A 3D seismic velocity model of Canterbury, New Zealand for broadband ground motion simulation. Presented at the 2013 Southern California Earthquake Centre (SCEC) Annual Meeting, Palm Springs, California, USA.

Rowshandel, B. (2010). Directivity Correction for the Next Generation Attenuation (NGA) Relations. *Earthquake Spectra*, **26**(2):525–559. doi:10.1193/1.3381043

Shahi, S., & Baker, J. W. (2010). Regression models for predicting the probability of near-fault earthquake ground motion pulses, and their period. In *Proceeding of 11th International conference on applications of statistics and probability in civil engineering*. Retrieved from http://shreyshahi.com/papers/Shahi%20Baker%20(2010)%20ICASP.pdf

Shahi, S. K. (2013, January). *A probabilistic framework to include the effects of near-fault directivity in seismic hazard assessment*. Stanford University, Stanford.

Shahi, S. K., & Baker, J. W. (2011). An empirically calibrated framework for including the effects of near-fault directivity in probabilistic seismic hazard analysis. *Bulletin of the Seismological Society of America*, **101**(2):742–755. doi:10.1785/0120100090

Somerville, P. G., Smith, N. F., Graves, R. W., & Abrahamson, N. A. (1997). Modification of empirical strong ground motion attenuation relations to include the amplitude and duration effects of rupture directivity. *Seismological Research Letters*, **68**(1):199–222.

Standards New Zealand. (2004). *NZS1170.5:2004, Structural Design Actions, Part 5: Earthquake actions- New Zealand*. Wellington, New Zealand.

9 Appendices

The appendices associated with this thesis are provided as self-contained documents.

9.1 Appendix A: Observed ground motions in the 13 June 2011 and 23 December 2011 earthquakes

9.2 Appendix B: Plots of strong ground motions from the 4 September 2010 M_w7.1 Darfield earthquake

9.3 Appendix C: Plots of strong ground motions from the 22 February 2011 M_w6.2 Christchurch earthquake